EFFECT OF H_2S AND CO_2 IN HPHT WELLS ON TUBULARS AND CEMENT

FINAL REPORT

Authors:

Ramadan Ahmed, Principal Investigator

Subhash Shah, Co-Principal Investigator

Samuel Osisanya, Co-Principal Investigator

Shokrollah Hassani, Postdoctoral Research Associate

Omotayo Omosebi, Research Assistant

Rida Elgaddafi, Research Assistant

Himanshu Maheshwari, Research Assistant

Aman Srivastava, Research Assistant

Jueun Hwang, Research Assistant

Mounraj Sharma, Research Assistant

Sagar Tale, Research Assistant

Jiwon Jeon, Research Assistant

Prepared under BSEE Project # E12PC00035

by

THE UNIVERSITY OF OKLAHOMA

June 09, 2015

Note: This report has been reviewed by the Bureau of Safety and Environmental Enforcement and approved for publication. Approval does not signify that the contents necessarily reflect the views and policies of the Service, nor does mention of the trade names or commercial products constitute endorsement or recommendation for use.

1. EXECUTIVE SUMMARY

This final report presents accomplishments of BSEE Project # E12PC00035 (Effect of H_2S and CO_2 in High-Pressure High-Temperature (HPHT) Wells on Tubulars and Cement) performed during the project period from September 22, 2011 to March 21, 2015. This research project is aimed at: i) Investigating the impacts of H_2S and CO_2 environment on oil and gas tubulars and cement; ii) Establishing how commonly used tubulars and cement are affected by exposure to H_2S and/or CO_2 in HPHT wells; iii) Determining the capability of these materials to function properly in harsh downhole environments; iv) Developing new cement formulations which are suitable for HPHT sour gas environment; v) Evaluating corrosion resistance of common steel used in the field; vi) selecting special steel materials that have better sour gas corrosion resistant under HPHT conditions; and vii) providing recommendations and guidelines to ensure long term integrity of the well. In order to achieve the project objectives, extensive literature survey has been conducted to perform theoretical and modeling studies, and better understand the mechanisms of oil well cement degradation and tubular corrosion under harsh downhole condition.

Cement degradation

Cement degradation mechanisms such as carbonation and leaching and associated theories have been investigated. The relationship between cement degradation and downhole operating parameters such as temperature, pressure, and acid gas concentration has been examined. The outcomes of the theoretical analysis provided useful information to develop experimental setup and test matrices. Moreover, the analysis has presented theories and necessary information to formulate cement degradation model that predicts the effects of temperature, CO_2 content and pressure on the physicochemical properties of degraded aged cement. In order to validate the model and better understand cement degradation in acidic environment, extensive experimental investigation was conducted. Test setups were developed to perform degradation (aging) experiments and measure important cement properties such as porosity, permeability, shear bond and compressive strengths, and mineralogical composition. Changes occurring in these properties are used to assess the level of degradation resulting from acid attack and other environmental factors. To carry out the degradation experiments, cement cores and shear bond samples were prepared and aged in 2% NaCl solution saturated with methane gas containing acidic gases (CO_2 and H_2S) for fourteen days. Tests were carried out varying temperature (100 to 430°F), pressure (3000 to 9000 psi), and CO_2 concentration (0 to 100%). Experiments were performed with or without the presence of H_2S. Two conventional (baseline) cement formulations (Class H and Class G cements with 35% silica flour) were considered in the investigation.

Conventional Cement

Results obtained from testing baseline cements showed that temperature, pressure and CO_2 content have strong impact on the degradation process. They determine the rate and mechanism of cement degradation. They affect most of physicochemical phenomena involved in the degradation process such as dissolution, diffusion, carbonation reaction, bicarbonation, and leaching. Low-temperature (less than 225°F) and/or low-pressure (less than 3000 psi) condition favors incomplete carbonation, which forms scawtite thereby decreasing the porosity and permeability. Nevertheless, above 225°F, carbonation becomes the dominant process. In the presence of excess carbonic acid, calcium carbonate is converted to calcium bicarbonate, which is water-soluble and susceptible to leaching. Intensified-leaching

increases porosity and permeability of cement, leading to more acid penetration and attack. At extreme high temperature (430°F), the interaction between pore fluid and cement matrix intensifies, leading to rapid dissolution of binding materials (portlandite and calcium silicate hydrates), which results in substantial reduction in cement mechanical strength and increase in porosity and permeability. After aging fluid system with H_2S, reduction in cement porosity and permeability due to carbonation was not observed. Instead, the porosity and permeability increased due to formation of secondary ettringite, which causes molecular expansion. Abundant amount of ettringite crystals were observed in scanning electron microscope (SEM) images of cores aged in fluid system with H_2S.

Studies on New Cement Formulations

In addition to baseline cement studies, extensive cement additive screening and formulation studies were performed to develop new acid resistant cement formulations. Different cement additives including hydroxyapatite, magnesium oxide, fly ash, zinc oxide, latex, and microsilica were considered in the screening study. Based on the outcomes of the screening study, two acid-resistant cement formulations have been developed for Class H and Class G cements using hydroxyapatite and magnesium oxide as additives. After aging under various conditions, porosity, permeability compressive and bond strengths of samples of the new formulations were measured to evaluate their acid resistance. In addition, the changes occurring in the mineralogical composition of the samples were investigated using Fourier Transform Infrared Spectroscopy (FTIR). The results indicated that Class H based hydroxyapatite and magnesium oxide containing cements are the most viable formulations that can withstand acid attack under HPHT conditions.

Corrosion of Tubulars

Although the industry is exploring and producing oil and gas from extreme environments and sour gas resources, very limited studies have been conducted to evaluate corrosion behavior of tubulars in CO_2 and H_2S containing brine system. In this project, extensive investigation has been performed to study corrosion of tubulars under high-pressure wellbore conditions. Corrosion is complex material-degradation phenomena. There are several types of corrosion including uniform corrosion, pitting corrosion, crevice corrosion, galvanic corrosion, sulfide stress cracking. This study is focused on the investigation of uniform corrosion and sulfide stress cracking under HPHT condition. Different carbon steel grades (API T95, C110, Q125 and AISI C1045) were considered in experimental investigation. Uniform corrosion experiments were carried out under low-pressure (120 psi varying temperature from 78 to 176°F) and high-pressure (3000 to 9000 psi, 100°F) conditions.

Uniform Corrosion under Low-Pressure

Low-pressure corrosion experiments were conducted using weight loss and electrical measurement (linear polarization resistance, LPR) techniques. The experiments were performed on carbon steel (Grade C1045) using brine saturated with N_2 gas containing CO_2. The effects of the carbon dioxide concentration, temperature, and salt content on corrosion of the carbon steel were investigated. CO_2 corrosion rates decreased with the increase in the salt content. The relationship between CO_2 content and corrosion rate is strongly influenced by temperature and salt content. Results indicate the occurrence of increased corrosion in the presence of CO_2. Although the corrosion rate increased with

increasing CO_2 concentration, the trend changed at high concentration and slight reduction in corrosion rate was predominantly observed at high concentrations. Both measuring techniques provided similar trend. Although corrosion rate reduction with CO_2 content is uncommon, similar corrosion rate trend has been reported in the literature. The reduction can be because of Fe^{2+} concentration increase resulting from increase in CO_2 content. As CO_2 content approaches 100%, Fe^{2+} concentration exceeds its solubility limit resulting in the formation of porous protective scale, which has adverse effect on corrosion process.

Uniform Corrosion under High-Pressure

Corrosion behavior of API grade steels (T95, C110 and Q125) was theoretically and experimentally investigated considering the effects of pressure and gas composition on corrosion rate. T95 and Q125 grades demonstrated similar corrosion rate trend with concentration. At low concentration (less than 25% CO_2), the corrosion rate increased with CO_2 content, resulting in increased CO_2-solubility and reduced pH. Reduction in pH facilitates the corrosion process. As the CO_2 content increases, carbonic acid concentration in the solution increases, accelerating the cathodic reactions and therefore increasing the corrosion rate. The corrosion rate increasing-trend with CO_2 concentration has been found consistent with previous studies. Above 25% CO_2, increasing CO_2 content reduced corrosion rate. This could be attributed to formation of protective layer. However, as the concentration is increased above 50%, this trend was changed and the rate was increased. These results are consistent with low-pressure corrosion rate measurements obtained from Grade 1045 carbon steel. Grade C110 showed slightly different corrosion rate trend. At low CO_2 concentration (less than 25%), the average corrosion rate greatly increased with the concentration. In the intermediate concentration range (25 to 75%), the corrosion rate was approximately constant. Slight reduction in the corrosion rate was observed when the concentration was increased above 75%. In general, Q125 showed better uniform corrosion resistance than the other API grade steels.

Sulfide Stress Cracking (SSC) Corrosion

Sulfide Stress Cracking is a natural phenomenon caused by permeation of hydrogen atom into crystalline structure of a metal. A new corrosion test setup has been developed to investigate SSC behavior of metals in corrosive environment containing H_2S. During the test, a mini-pipe, which was exposed to the corrosive environment, was stretched to 85% of its yield stress. Tested duration was seven days in a corrosion cell. Highly embrittled material is expected to fail before the completion of the experiments. However, most of the tested mini-pipe specimens did not fail during the test. Therefore, their mechanical properties were measured using the tensile strength testing (TST) apparatus. Among many mechanical properties measured by the TST apparatus, ultimate tensile strength (UTS) and plastic strain to failure (PSF) are found to be useful in assessing the level of embrittlement occurring during the exposure. PSF of corroded and uncorroded mini-pipes were measured and compared.

Studies show that the SSC is highly affected by the pH of corrosive fluid surrounding the metal. Hence, corrosion experiments were conducted varying CO_2 content. Tests were performed using three API grade steels (T95, C110 and Q125). Results showed consistent PSF and UTS trends with CO_2 concentration. At low concentration (0 to 10% CO_2), PSF and UTS of the steels reduced with concentration. The reduction indicates the embrittlement occurring in the material. However, as CO_2

content was increased above 10%, the trend was reversed and slight improvements in PSF and UTS were observed. The trend reversal could be due to corrosion related phenomena, which maximize the sulfide stress cracking corrosion around 10% CO_2 for these particular sets of experiments. In general, sulfide embrittlement tends to reduce PSF and UTS of the steels. This observation is in agreement with published research results in the area of sulfide stress cracking corrosion. Moreover, UTS measurements are consistent with the API grade number assignment (i.e. Q125 exhibited the highest UTS and T95 showed the lowest). However, PSF data did not follow API grade numbering. C110 displayed the lowest PSF values at all concentrations. Moreover, it was the only steel grade, which showed a complete failure when tested at 10% CO_2. As expected, T95 displayed the highest SSC resistance.

TABLE OF CONTENTS

1. EXECUTIVE SUMMARY **2**

TABLE OF CONTENTS **6**

LIST OF FIGURES **10**

LIST OF TABLES **20**

2. WELL CEMENT DEGRADATION **22**

2.1. INTRODUCTION 22

2.1.1. Overview *22*

2.1.2. Statement of the Problem *22*

2.1.3. Objectives *23*

2.1.4. Research Methodology *23*

2.1.5. Scope of Work *24*

2.2. LITERATURE REVIEW ON CEMENT DEGRADATION 25

2.2.1. Experimental Studies *27*

2.2.1.1. Cement Degradation in Carbonic Acid Environment 27

2.2.1.2. Cement Degradation after H_2S Attack 29

2.2.2. Theoretical and Modeling Studies *33*

2.2.2.1. Cement Degradation under CO_2 Exposure 33

2.2.2.2. Cement Degradation under H_2S Exposure 35

2.2.2.3. Cement Degradation in Mixed H_2S and CO_2 System 37

2.2.2.4. Cement Degradation involving Minor Cement Components 38

2.2.3. Effects of Environmental Parameters *41*

2.2.3.1. Temperature Effect 41

2.2.3.2. Effects of pH on Oil Well Cement 43

2.2.4. Acid Resistant (AR) Cement *44*

2.2.4.1. Additives Used to Formulate AR Cement 44

2.2.4.2. Carbonic Acid Resistant Cements 47

2.2.4.3. Hydrogen Sulfide Resistant Cements 49

2.3. EXPERIMENTAL INVESTIGATIONS 51

2.3.1. Test Matrix *51*

2.3.2. Test Materials *53*

2.3.3 Test Equipment *53*

2.3.3.1. Compressive and Bonding Strength Measurement Techniques 53

2.3.3.2. Porosity and permeability 56

2.3.3.3. FTIR Mineralogy 56

2.3.3.4. SEM Imaging 57

2.3.3.5. Cement Consistometer 57

2.3.3.6. Rotational viscometer 58

2.3.3.7. Filter Press 58

2.3.3.8. Cement Blender 58

2.3.3.9. Mud Balance 58

2.3.4. Cement Slurry Preparation Procedure *59*
2.3.4.1. Slurry Formulations 59
2.3.4.2. Mixing 59
2.3.4.3. Slurry Properties 59
2.3.5. Test Sample Preparation Procedures *61*
2.3.5.1. Curing Procedure 62
2.3.5.2. Bonding Sample Preparation Procedure 62
2.3.5.3. Cement Core Preparation Procedure 63
2.3.6. Cement Aging Experiment *64*
2.3.6.1. Experimental Setup 64
2.3.6.2. Test Procedure 65
2.4. RESULTS 65
2.4.1. Performance of Baseline Cement Formulations *65*
2.4.1.1. Porosity and Permeability 66
2.4.1.2. Compressive Strength 75
2.4.1.3. Shear Bond Strength 83
2.4.1.4. FTIR Analysis 87
2.4.2. Acid Resistance of New Cement Formulations *96*
2.4.2.1. Additive Screening Study 96
2.4.2.2. Detailed Analysis of Acid Resistance of New Cement Formulations 111
2.4.2.3. Experimental Results Showing Acid Resistance of New Cement Formulations 133
2.4.2.4. Performance of Other Additive Cement Formulations 147
2.5. MODELING CEMENT DEGRADATION 165
2.5.1. Overview *165*
2.5.2. Model Assumptions *166*
2.5.3. Model Formulation *166*
2.5.3.1. Hydration Model 167
2.5.3.2. Porosity Model 172
2.5.3.3. Degradation Model 172
2.5.3.4. Mechanical Strength Degradation Model 178
2.5.3.5. Model Predictions 183
2.6. CONCLUSIONS AND RECOMMENDATIONS 184
2.6.1. Conclusions *184*
2.6.2. Recommendations *185*

3. TUBULAR CORROSION 186

3.1. INTRODUCTION 186
3.1.1. Overview *186*
3.1.2. Statement of the Problem *187*
3.1.3. Objectives *187*
3.2. SULFIDE STRESS CRACKING (SSC) CORROSION 187
3.2.1. Literature Review *187*
3.2.1.1. Experimental Studies 187
3.2.1.2. Theoretical Background 192

3.2.1.3. Measurement Techniques 196
3.2.2. Experimental Investigations 203
3.2.2.1. Test Conditions 203
3.2.2.2. Measurement Technique 204
3.2.2.3. Experimental Set Up 204
3.2.2.4. Specimen Preparation and Placement Procedures 208
3.2.2.5. SCC Test Procedure 209
3.2.2.6. TST Setup and Procedure 210
3.2.2.7. Results 211
3.2.3. SSC Model 216
3.2.3.1. Hydrogen Permeation Model 216
3.2.3.2. Numerical Procedures 217
3.2.3.3. Validation of SSC model 217
3.2.3.4. Sensitivity Analysis 218
3.2.4. Conclusions 221
3.3. UNIFORM CORROSION 221
3.3.1. Literature Review 221
3.3.1.1. Effect of NaCl on CO_2 Corrosion 221
3.3.1.2. Effect of pH on CO_2 Corrosion 222
3.3.1.3. Effect of Temperature on CO_2 Corrosion 222
3.3.1.4. Effect of Flow Velocity and Flow Regime on CO_2 Corrosion 223
3.3.1.5. Effect of CO_2 Partial Pressure on CO_2 Corrosion 224
3.3.2. Theoretical Studies 224
3.3.2.1. H_2S-CO_2 corrosion 224
3.3.2.2 Electrochemistry of CO_2 Corrosion 229
3.3.2.3 Electrochemistry of H_2S Corrosion 230
3.3.2.4 Uniform Corrosion under Dynamic Flow Conditions 231
3.3.3. Uniform Corrosion Models 231
3.3.3.1. CO_2 Corrosion Model for Non-Scale Forming Condition 231
3.3.3.2. CO_2 Corrosion Models for Scale-Forming Conditions 237
3.3.3.3. H_2S Corrosion Model 242
3.3.3.4. H_2S-CO_2 Corrosion Models 246
3.3.4. Measurement Techniques 251
3.3.4.1. Linear Polarization Resistance 251
3.3.4.2. Electrochemical Impedance Spectroscopy 252
3.3.5. Experimental Study at Low Pressure 254
3.3.5.1. Test Conditions 255
3.3.5.2. Measurement Techniques 256
3.3.5.3. Specimen Preparation and Placement Procedures 258
3.3.5.4. Experimental Set Up 258
3.3.5.5. Test Procedure 261
3.3.5.6. Results 262
3.3.6. Experimental Study at High Pressure 267
3.3.6.1. Test Conditions 267

3.3.6.2. Measurement Techniques 268
3.3.6.3. Specimen Preparation and Placement Procedures 268
3.3.3.4. Experimental Setup 269
3.3.3.5. Test Procedure 270
3.3.3.6. TST Setup and Procedure 271
3.3.3.7. Results and Analysis 273
3.3.7. Modeling 280
3.3.7.1. Model Description 280
3.3.7.2. Assumptions and Limitations 280
3.3.7.3. Model Formulation 280
3.3.7.4. Model Validation and Testing 283
3.3.7.5. Summary 285
3.3.8. Conclusions 285

NOMENCLATURES 286

REFERENCES 289

APPENDIX A: EXPERIMENTAL DATABASE 304

APPENDIX B: GAS SOLUBILITY MODELS 304

APPENDIX C: NUMERICAL SCHEME FOR DEGRADATION DEPTH MODEL 304

APPENDIX D: MECHANICAL STRENGTH DEGRADATION MODEL 304

APPENDIX E: MACKINAWITE STABILITY LIMIT MODELS 304

APPENDIX F: CORROSION BEHAVIOR OF TUBULARS UNDER SOUR GAS ENVIRONMENT 304

APPENDIX G: MECHANISTIC CO2-H2S CORROSION MODEL 304

APPENDIX H: PARAMETERS USED TO PREDICT CORROSION RATE 304

APPENDIX I: IMPROVED MECHANISTIC CO2-H2S CORROSION MODEL 304

LIST OF FIGURES

Fig. 2.1: SEM-BSE image of cement cured for 28 days at 22°C and 0.1 MPa (Kutchko et al. 2007) 26
Fig. 2.2: CO_2 leakage through primary (A) or secondary cement (C) interfaces between casing and cement (B), formation and cement (D) and through casing (E) (Duguid et al. 2006).....27
Fig. 2.3a: Cement core samples after 15-day of aging in water saturated with CO_2 (Santra et al. 2009) 29
Fig. 2.3b: Measured penetration depth (Santra et al. 2009).....29
Fig. 2.4: Schematic view of a pore in a hardened cement paste matrix under sulfate attack, showing nucleation and growth of ettringite by through-solution (left) and topo-chemical (right) mechanisms (Naik 2003).....31
Fig. 2.5: ΔL vs days for different sulfate ions concentration in class G cement (Morales et al. 2003) 32
Fig. 2.6: ΔW vs Days for different sulfate ions concentration in class G cement (Morales et al. 2003) 32
Fig. 2.7: SEM image of Class G cement showing presence of acicular needle like ettringite (Morales et al. 2003)....33
Fig. 2.8a: Microscopic image of sectioned-cement core after CO_2 exposure (Kutchko et al. 2007) 34
Fig. 2.8b: Formation of distinct zones in the degraded cement specimen (Kutchko et al. 2007) 34
Fig. 2.9: Portland cement samples before and after CO_2 exposure at 180°C and 280 bars (Rimmelé et al. 2008).....35
Fig. 2.10: Mechanism of sulfate attack of cement (Morales et al. 2003) 37
Fig. 2.11: Cement samples aged in: a) pure CO_2; and b) H_2S-CO_2 system (Kutchko et al. 2011) 38
Fig. 2.12: SEM observation of powdered Class G cement aged in H_2S and CO_2 saturated brine: a) Polished section showing pyrites as white minerals; b) Euhedral pyrite observed in cement sample (Jacquemet et al. 2005) ..39
Fig. 2.13a: Compressive strength variation with temperature(Noik and Rivereau 1999) 42
Fig. 2.13b: Permeability variation with temperature (Noik and Rivereau 1999).....42
Fig. 2.14: Compressive strength vs. aging time at different temperatures (Dubois et al. 1999).....42
Fig. 2.15: Compressive strength vs. temperature after 28 days of aging (Johnson and Garvin 1972) 42
Fig. 2.16: Permeability of three different cement cores (Jennings 2005) 43
Fig. 2.17: Thermo-Gravimetric Analysis: a) before CO2 treatment; and b) after CO2 treatment (Santra and Sweatman 2011) 48
Fig. 2.18 Microscopic image of half-core sample after 88 hr aging in CO_2 in wet supercritical CO_2 fluid (Barlet-Gouédard et al. 2006) 49
Fig. 2.19 Cement specimens after one-week aging in H_2S-saturated saline water :a) 15% Mn_3O_4-Cement system; and ii) 30% Fe_2O_3-Cement (Lécolier et al. 2008) 50
Fig. 2.20: Test setup for measuring compressive and bonding strength of cement samples 54
Fig. 2.21: Compressive and bond strength measurement setup.....54
Fig. 2.22: Compressive strength test measurements: a) Load rate vs. time; and b) Stress vs. time 55
Fig. 2.23: Shear bonding test sample and pipe holder 56
Fig. 2.24: Automated Porosimeter-Permeameter (AP-608) 56
Fig. 2.25: FTIR Equipment (Thermo Scientific Model Nicolet 6700).....57
Fig. 2.26: SEM equipment.....57
Fig. 2.27: CTE Model 200 atmospheric consist-o-meter.....57
Fig. 2.28: OFITE Model 900 viscometer 58
Fig. 2.29: Low-pressure filter press.....58
Fig. 2.30: Rheological reading for base slurries of Class G and H 60
Fig. 2.31: Consist-o-meter reading for base slurries of class G and H 61
Fig. 2.32: Nomenclature of the samples.....61
Fig. 2.33: Sample size distribution for aging cell experiments 62
Fig. 2.34: a) Steel pipe; and b) Steel pipes with hardened cement for SBS measurement 63
Fig. 2.35: Cured cylindrical samples for porosity and permeability and compressive strength testing 63

Fig. 2.36: A schematic of the aging cell setup 64
Fig. 2.37: Effect of temperature on CO_2 solubility in 1M NaCl solution 66
Fig. 2.38: Effects of temperature on porosity and permeability of baseline cores aged at 6000 psi and 10% CO_2 67
Fig. 2.39: Effects of temperature on porosity and permeability of baseline cores aged at 6000 psi and 40% CO_2 67
Fig. 2.40: Effects of temperature on porosity and permeability of baseline cores aged at 6000 psi and 100% CO_2 67
Fig. 2.41: Effects of temperature on porosity and permeability of baseline cores aged at 3000 psi and 100% CO_2 68
Fig. 2.42: Effects of temperature on porosity and permeability of baseline cores aged at 9000 psi and 100% CO_2 68
Fig. 2.43: Porosity (a) and permeability (b) of samples aged for 14 days at 350°F and 10% CO_2 and different pressures 69
Fig. 2.44: Porosity (a) and permeability (b) of samples aged for 14 days at 350°F and 40% CO_2 and different pressures 69
Fig. 2.45: Porosity (a) and permeability (b) of samples aged for 14 days at 350°F and 100% CO_2 and different pressures 69
Fig. 2.46: Phase diagram of CO_2 (Vestergaard and Robinson 2003) 70
Fig. 2.47: Effects of CO_2 concentration on porosity and permeability of baseline cores aged at 225°F and 3000 psi 71
Fig. 2.48: Effects of CO_2 concentration on porosity and permeability of baseline cores aged at 350°F and 3000 psi 71
Fig. 2.49: Porosity of Class H samples aged at 6000 psi and different temperatures in: a) fluid system without H_2S; b) fluid system with H_2S 72
Fig. 2.50: Permeability of Class H samples aged at 6000 psi and different temperatures in: a) fluid system without H_2S; b) fluid system with H_2S 72
Fig. 2.51: FTIR data for Class H samples aged at 100°F and 6000 psi in fluid system: a) without H_2S; and) b with H_2S 73
Fig. 2.52: SEM images of Class H sample aged at 100°F and 6000 psi: a) ettringite formed in a pore in the middle zone; b) ettringite formed in a pore in the inner zone; c) empty pore close to the specimen external surface; d) presence of CH, CSH and unhydrated cement particles 73
Fig. 2.53: Porosity of Class G cement samples aged at 6000 psi and different temperatures in: a) fluid system without H_2S; b) fluid system with H_2S 74
Fig. 2.54: Permeability of Class G cement samples aged at 6000 psi and different temperatures in: a) fluid system without H_2S; b) fluid system with H_2S 75
Fig. 2.55: Effects of temperature on compressive strength of baseline cores aged at 6000 psi and 10% CO_2 76
Fig. 2.56: Effects of temperature on compressive strength of baseline cores aged at 6000 psi and 40% CO_2 76
Fig. 2.57: Effects of temperature on compressive strength of baseline cores aged at 6000 psi and 100% CO_2 77
Fig. 2.58: Effect of temperature on compressive strength at 100% CO_2 and 3000 psi 77
Fig. 2.59: Effect of temperature on compressive strength at 100% CO_2 and 9000 psi 78
Fig. 2.60: Effects of pressure on compressive strength of cement cores at 225°F and 10% CO_2 concentration 79
Fig. 2.61: Compressive strengths of cements after aging in brine saturated with 100% CO_2 at: a) 225°F, and b) 350°F 79
Fig. 2.62: Compressive strength vs. CO_2 concentration for cements aged at 225°F and 3000 psi 80
Fig. 2.63: Porosity and permeability vs. CO_2 concentration for cements aged at 225°F and 3000 psi 80
Fig. 2.64: FTIR of Class H cement aged at 225°F and 3000 psi: a) virgin zone; b) middle zone; and c) outermost zone 81
Fig. 2.65: Compressive strength vs. CO_2 concentration for cements aged at 350°F and 3000 psi 81
Fig. 2.66: Porosity and permeability vs. CO_2 concentration for cements aged at 350°F and 3000 psi 81
Fig. 2.67: FTIR results of Class H cement sample aged at 350°F and 3000 psi: a) virgin zone; b) middle zone; and c) outermost zone 82
Fig. 2.68: Compressive strength of Class H samples aged at 6000 psi and different temperatures in: a) fluid system

without H_2S; b) fluid system with H_2S 82
Fig. 2.69: The effect of temperature at 6000 psi with different CO_2 concentrations: a) 10%; b) 40%; and c) 100% ..83
Fig. 2.70: Effect of aging pressure on SBS of samples aged at 350°F for 14 days in brine saturated with different CO_2 concentrations: a) 10%; b) 40%; and c) 100% 84
Fig. 2.71: Influence of aging pressure on shear bond strength at 40% CO_2 concentration and different temperature: a) 225°F; and b) 350°F 84
Fig. 2.72 Penetration depth observed after applying Phenolphthalein solution to identify degraded zone (T = 225°F) 85
Fig. 2.73: Influence of CO_2 concentration on shear bond strength at 225°F 85
Fig. 2.74: Influence of CO_2 concentration on shear bond strength at 350°F 86
Fig. 2.75: SBS of Class H sample aged for 14 days in brine saturated with methane containing 10% CO_2 at 6000 psi and different temperatures in fluid system: a) with H_2S; b) without H_2S 86
Fig. 2.76: Mineralogy comparison for samples aged at 100% CO_2, 225°F, 6000 psi and 2% brine solution for 14 days: a) FTIR; and b) XRD 87
Fig. 2.77: Aged cement core in Batch 006: a) Mineralogical profile; and b) Photograph 88
Fig. 2.78: Summarized FTIR data of baseline Class H cement samples aged at 3000 psi, and 10% CO_2 for 14 days: a) Virgin zone; b) Middle zone; and c) Outermost zone 89
Fig. 2.79: Summarized FTIR data of baseline Class H cement samples aged at 3000 psi, and 40% CO_2 for 14 days: a) Virgin zone; b) Middle zone; and c) Outermost zone 89
Fig. 2.80: Summarized FTIR data of baseline Class H cement samples aged at 3000 psi, and 100% CO_2 for 14 days: a) Virgin zone; b) Middle zone; and c) Outermost zone 89
Fig. 2.81: Summarized FTIR data of baseline Class H cement samples aged at 6000 psi, and 10% CO_2 for 14 days: a) Virgin zone; b) Middle zone; and c) Outermost zone 89
Fig. 2.82: Summarized FTIR data of baseline Class H cement samples aged at 6000 psi, and 40% CO_2 for 14 days: a) Virgin zone; b) Middle zone; and c) Outermost zone 90
Fig. 2.83: Summarized FTIR data of baseline Class H cement samples aged at 6000 psi, and 100% CO_2 for 14 days: a) Virgin zone; b) Middle zone; and c) Outermost zone 90
Fig. 2.84: Summarized FTIR data of baseline Class H cement samples aged at 9000 psi, and 10% CO_2 for 14 days: a) Virgin zone; b) Middle zone; and c) Outermost zone 90
Fig. 2.85: Summarized FTIR data of baseline Class H cement samples aged at 9000 psi, and 40% CO_2 for 14 days: a) Virgin zone; b) Middle zone; and c) Outermost zone 90
Fig. 2.86: Summarized FTIR data of baseline Class H cement samples aged at 9000 psi, and 100% CO_2 for 14 days: a) Virgin zone; b) Middle zone; and c) Outermost zone 91
Fig. 2.87: Summarized FTIR data of baseline Class H cement samples aged at 225°F, 10% CO_2 for 14 days: a) Virgin zone; b) Middle zone; and c) Outermost zone 91
Fig. 2.88: Summarized FTIR data of baseline Class H cement samples aged at 225°F, 40% CO_2 for 14 days: a) Virgin zone; b) Middle zone; and c) Outermost zone 92
Fig. 2.89: Summarized FTIR data of baseline Class H cement samples aged at 225°F, 100% CO_2 for 14 days: a) Virgin zone; b) Middle zone; and c) Outermost zone 92
Fig. 2.90: Summarized FTIR data of baseline Class H cement samples aged at 350°F, 10% CO_2 for 14 days: a) Virgin zone; b) Middle zone; and c) Outermost zone 92
Fig. 2.91: Summarized FTIR data of baseline Class H cement samples aged at 350°F, 40% CO_2 for 14 days: a) Virgin zone; b) Middle zone; and c) Outermost zone 92
Fig. 2.92: Summarized FTIR data of baseline Class H cement samples aged at 350°F, 100% CO_2 for 14 days: a) Virgin zone; b) Middle zone; and c) Outermost zone 93
Fig. 2.93: Summarized FTIR data of baseline Class H cement samples aged at 225°F, 3000 psi for 14 days: a) Virgin

zone; b) Middle zone; and c) Outermost zone 94
Fig. 2.94: Summarized FTIR data of baseline Class H cement samples aged at 350°F, 3000 psi for 14 days: a) Virgin zone; b) Middle zone; and c) Outermost zone 94
Fig. 2.95: Summarized FTIR data of baseline Class H cement samples aged at 225°F, 6000 psi for 14 days: a) Virgin zone; b) Middle zone; and c) Outermost zone 94
Fig. 2.96: Summarized FTIR data of baseline Class H cement samples aged at 350°F, 6000 psi for 14 days: a) Virgin zone; b) Middle zone; and c) Outermost zone 94
Fig. 2.97: Summarized FTIR data of baseline Class H cement samples aged at 225°F, 9000 psi for 14 days: a) Virgin zone; b) Middle zone; and c) Outermost zone 95
Fig. 2.98: Summarized FTIR data of baseline Class H cement samples aged at 350°F, 9000 psi for 14 days: a) Virgin zone; b) Middle zone; and c) Outermost zone 95
Fig. 2.99: FTIR data for Class H samples aged at 225°F and 6000 psi in fluid system: a) without H_2S; b) with H_2S 95
Fig. 2.100: FTIR data for Class H samples aged at 350°F and 6000 psi: a) in fluid system without H_2S; b) in fluid system with H_2S 96
Fig. 2.101: Rheological data of MS-10 and baseline slurries 99
Fig. 2.102: Porosity (a) and Permeability (b) of unaged MS-10 and baseline samples 100
Fig. 2.103: Compressive strength (a) and Shear bond strength (b) of unaged MS-10 and baseline samples 100
Fig. 2.104: Porosity (a) and Permeability (b) of unaged latex and baseline samples 101
Fig. 2.105: Compressive strength (a) and Shear bond strength (b) measurements of unaged latex and baseline samples 101
Fig. 2.106: Rheological data of LTMS and baseline slurries 103
Fig. 2.107: Porosity (a) and Permeability (b) of unaged LTMS and baseline cements 104
Fig. 2.108: Compressive strength (a) and Shear bond strength (b) of unaged LTMS and baseline cements 104
Fig. 2.109: Viscometeric readings of MGO-5 and baseline slurries 105
Fig. 2.110: Porosity (a) and Permeability (b) of unaged MGO-5 and baseline samples 106
Fig. 2.111: Compressive (a) and Shear bond strength (b) of unaged MGO-5 and baseline samples 106
Fig. 2.112: Dial readings of HOAP and baseline slurries 107
Fig. 2.113: Porosity (a) and Permeability (b) of unaged HOAP and baseline samples 108
Fig. 2.114: Compressive and shear bond strengths of unaged HOAP and baseline samples 108
Fig. 2.115: Consistency of cement slurry containing ZnO 109
Fig. 2.116: Thickening time of fly ash and baseline cements 110
Fig. 2.117: Porosity (a) and permeability of unaged fly ash and baseline samples 111
Fig. 2.118: Porosity of aged (orange) and unaged (blue) samples: a) HHO; and b) HS 113
Fig. 2.119: Porosity of unaged and aged (in the presence of H_2S) samples: a) HHO; and b) HS 114
Fig. 2.120: Permeability of aged (orange) and unaged (blue) samples: a) HHO; and b) HS 114
Fig. 2.121: Permeability of unaged and aged (in the presence of H_2S) samples: a) HHO; and b) HS 115
Fig. 2.122: Porosity of aged (orange) and unaged (blue) samples: a) GHO; and b) GS 115
Fig. 2.123: Porosity of unaged and aged (in the presence of H_2S) samples: a) GHO; and b) GS 116
Fig. 2.124: Permeability of aged (orange) and unaged (blue) samples: a) GHO; and b) GS 116
Fig. 2.125: Permeability of unaged and aged (in the presence of H_2S) samples: a) GHO; and b) GS 117
Fig. 2.126: Compressive strength of aged and unaged samples: a) HHO; and b) HS 118
Fig. 2.127: Compressive strength of aged (orange) and unaged (blue) samples: a) GHO; and b) GS 118
Fig. 2.128: Compressive strength of unaged and aged (in the presence of H_2S) samples: a) HHO; and b) HS 118
Fig. 2.129: Compressive strength of unaged and aged (in the presence of H_2S) samples: a) GHO; and b) GS 119
Fig. 2.130: Shear bond strength of aged (orange) and unaged (blue) samples: a) HHO; and b) HS 120
Fig. 2.131: Shear bond strength of unaged and aged (in the presence of H_2S) samples: a) HHO; and b) HS 120

Fig. 2.132: FTIR results in inner zone of HOAP and baseline HS samples aged at different conditions: a) Exp. 9; b) Exp. 12; c) Exp. 13; d) Exp. 15; e) Exp. 19; f) Exp. 23; and g) Exp. 29 121
Fig. 2.133: FTIR results (middle zone) of HOAP and baseline HS samples aged at different conditions: a) Exp. 9; b) Exp. 12; c) Exp. 13; d) Exp. 15; e) Exp. 19; f) Exp. 23; and g) Exp. 29 122
Fig. 2.134: FTIR results (outer zone) of HOAP and baseline HS samples aged at different conditions: a) Exp. 9; b) Exp. 12; c) Exp. 13; d) Exp. 15; e) Exp. 19; f) Exp. 23; and g) Exp. 29 123
Fig. 2.135: Porosity of aged (orange) and unaged (blue) samples: a) HSMG; and b) HS 125
Fig. 2.136: Porosity of unaged and aged (in the presence of H_2S) samples: a) HSMG; and b) HS 125
Fig. 2.137: Permeability of aged (orange) and unaged (blue) samples: a) HSMG; and b) HS.....126
Fig. 2.138: Permeability of unaged and aged (in the presence of H_2S) samples: a) HSMG; and b) HS.....126
Fig. 2.139: Porosity of aged (orange) and unaged (blue) samples: a) GSMG; and b) GS.....127
Fig. 2.140: Permeability of aged (orange) and unaged (blue) samples: a) GSMG; and b) GS.....127
Fig. 2.141: Porosity of unaged and aged (in the presence of H_2S) samples: a) GSMG; and b) GS 127
Fig. 2.142: Permeability of unaged and aged (in the presence of H_2S) samples: a) GSMG; and b) GS.....128
Fig. 2.143: Compressive strength of aged (orange) and unaged (blue) samples: a) HSMG; and b) HS 128
Fig. 2.144: Compressive strength of unaged and aged (in the presence of H_2S) samples: a) HSMG; and b) HS 129
Fig. 2.145: Compressive strength of aged (orange) and unaged (blue) samples: a) GSMG; and b) GS 129
Fig. 2.146: Compressive strength of unaged and aged (in the presence of H_2S) samples: a) GSMG; and b) GS 130
Fig. 2.147: Shear bond strength of aged and unaged samples: a) HSMG; and b) HS 130
Fig. 2.148: Shear bond strength of unaged and aged (in the presence of H_2S) samples: a) HSMG; and b) HS 131
Fig. 2.149: FTIR results of inner zone of MGO-5 and baseline HS samples aged at different conditions: a) Exp. 8; b) Exp. 10; c) Exp. 7A; d) Exp. 14; e) Exp. 20; and f) Exp. 22.....131
Fig. 2.150: FTIR results of middle zone of MgO and baseline HS samples aged at different conditions: a) Exp. 8; b) Exp. 10; c) Exp. 7A; d) Exp. 14; e) Exp. 20; and f) Exp. 22.....132
Fig. 2.151: FTIR results of outer zone of MgO and baseline HS samples aged at different conditions: a) Exp. 8; b) Exp. 10; c) Exp. 7A; d) Exp. 14; e) Exp. 20; and f) Exp. 22.....133
Fig. 2.152: Porosity and permeability of HOAP and baseline samples (aging at 100°F, 6000 psi and 40 % CO_2) 135
Fig. 2.153: Shear bond strength of baseline and HOAP samples (aging condition: 100°F, 6000 psi and 40 % CO_2) .135
Fig. 2.154: Compressive strengths of baseline and HOAP cements (aging at 100°F, 6000 psi and 40 % CO_2) 136
Fig. 2.155: Middle cross-section of cores after aging at 350°F with 100% CO_2 gas: a) GHO; b) HHO; c) GS; and d) HS 136
Fig. 2.156: Compressive strengths of baseline and HOAP cements (aging at 350°F, 6000 psi and 100 % CO_2) 137
Fig. 2.157: Shear bond strength of baseline and HOAP samples (aged at 350°F, 6000 psi and 100 % CO_2) 138
Fig. 2.158: Summarized FTIR data for HOAP and baseline samples (innermost Zone) 138
Fig. 2.159: Summarized FTIR data for HOAP and baseline samples (middle zone) 139
Fig. 2.160: Summarized FTIR data for HOAP and baseline samples (outermost zone) 139
Fig. 2.161: Porosities of MGO-5 and baseline cements: a) unaged; and b) aged.....141
Fig. 2.162: Permeabilities of MGO-5 and baseline cements: a) unaged; and b) aged.....141
Fig. 2.163: Compressive strength of MGO-5 and baseline cements: a) unaged; and b) aged.....142
Fig. 2.164: Shear bond strength of MGO-5 and baseline cements: a) unaged; and b) aged.....142
Fig. 2.165: Summarized FTIR data of HSMG and baseline HS samples aged at 225°F, 9000 psi, 40% CO_2 for 14 days: a) Outermost zone; b) Middle zone; and c) Innermost zone 143
Fig. 2.166: Porosities of MGO-5 and baseline samples: a) Unaged; and b) aged at 350°F, 9000 psi and 40% CO_2...144
Fig. 2.167: Permeabilities of MGO-5 and baseline samples: a) Unaged; and b) aged at 350°F, 9000 psi and 40% CO_2 144
Fig. 2.168: FTIR peaks of MGO and baseline samples aged at 350°F and 9000 psi for 14 days in 2% brine saturated

with 40% CO_2: a) inner most zone; b) middle zone; and c) outer most zone 145
Fig. 2.169: Compressive strength of MGO-5 and baseline samples: a) Unaged; and b) aged at 350°F, 9000 psi, 40% CO_2 for 14 days.....146
Fig. 2.170: SBS of MGO-5 and baseline samples: a) Unaged; and b) aged at 350°F, 9000 psi, 40% CO_2 for 14 days 146
Fig. 2.171: Porosity of aged (orange) and unaged (blue) Class H based cores: a) HSMS; and b) HS 147
Fig. 2.172: Permeability of aged (orange) and unaged (blue) Class H based cores: a) HSMS; and b) HS 148
Fig. 2.173: Porosity of aged (orange) and unaged (blue) Class G based cores: a) GSMS; and b) GS 148
Fig. 2.174: Permeability of aged (orange) and unaged (blue) Class G based cores: a) GSMS; and b) GS 149
Fig. 2.175: Compressive strength of aged (orange) and unaged (blue) Class H based cores: a) HSMS; and b) HS ...149
Fig. 2.176: Compressive strength of aged (orange) and unaged (blue) Class G based cores: a) GSMS; and b) GS ...150
Fig. 2.177: SBS of aged (orange) and unaged (blue) Class H based cores: a) HSMS; and b) HS.....150
Fig. 2.178: Schematic of a cylindrical samples and zones selected in the cross section 151
Fig. 2.179: FTIR results of inner zones of HSMS and HS samples aged at different conditions: a) Exp. 21; b) Exp. 25; and c) Exp. 26 151
Fig. 2.180: FTIR results of middle zones of HSMS and HS samples aged at different conditions: a) Exp. 21; b) Exp. 25; and c) Exp. 26 152
Fig. 2.181: FTIR results of middle zones of HSMS and HS samples aged at different conditions: a) Exp. 21; b) Exp. 25; and c) Exp. 26 152
Fig. 2.182: Porosity and permeability of latex and baseline cores (aged at 350°F with 40% CO_2) 154
Fig. 2.183: Middle cross sections of cores aged at 350°F with 40% CO_2 gas: a) GSLT; b) HSLT; c) GS; and d) HS.....154
Fig. 2.184: Compressive strength of baseline and latex-based cements aged at 350°F with 40% CO_2 155
Fig. 2.185: Shear bond strength of latex and baseline cements aged at 350°F with 40% CO_2 155
Fig. 2.186: Summarized FTIR of latex and baseline cements: a) innermost; b) middle; and c) outermost zones 156
Fig. 2.187: Porosity of aged (orange) and unaged (blue) samples: a) HSLM; and b) HS.....157
Fig. 2.188: Permeability of aged (orange) and unaged (blue) samples: a) HSLM; and b) HS.....158
Fig. 2.189: Porosity of aged (orange) and unaged (blue) samples: a) GSLM; and b) GS.....158
Fig. 2.190: Permeability of aged (orange) and unaged (blue) samples: a) GSLM; and b) GS 158
Fig. 2,191: Compressive strength of aged (orange) and unaged (blue) samples: a) HSLM; and b) HS 159
Fig. 2.192: Compressive strength of aged (orange) and unaged (blue) samples: a) GSLM; and b) GS.....159
Fig. 2.193: Average shear bond strength of aged (orange) and unaged (blue) samples: a) HSLM; and b) HS 160
Fig. 2.194: FTIR results of inner zones of LTMS and baseline HS samples aged at different conditions: a) Exp. 24; b) Exp. 27; and c) Exp. 28 160
Fig. 2.195: FTIR results (middle zone) of LTMS and baseline HS samples aged at different conditions: a) Exp. 24; b) Exp. 27; and c) Exp. 28 161
Fig. 2.196: FTIR results (outer zone) of LTMS and baseline HS samples aged at different conditions: a) Exp. 24; b) Exp. 27; and c) Exp. 28 161
Fig. 2.197: Porosity and permeability of cement cores aged at 350°F (Experiment 4, Batch 005) 162
Fig. 2.198: Compressive strength of unaged and aged baseline and fly ash cement cores aged at 350ºF (Experiment 4, Batch 5) 163
Fig. 2.199: Shear bond strengths of samples before and after 6 days of aging (Experiment #3).....164
Fig. 2.200: Class H cement after 6 days aging (Experiments # 3): a) with fly ash; and b) without fly ash 164
Fig. 2.201: Shear bond strength of unaged and aged samples (Experiment # 2) 165
Fig. 2.202: Simplified block diagram of cement degradation model 166
Fig. 2.203: Model prediction of degree of hydration for Class H and Class G cements.....170
Fig. 2.204: Model validation for degree of hydration while curing oil well cement.....171
Fig. 2.205: Temperature effect on degree of hydration of Class G cement 171

Fig. 2.206: Pressure effect on degree of hydration of Class H cement....171
Fig. 2.207: Comparison of predicted initial porosity with experimental data....172
Fig. 2.208: Predicted degradation depth for Class G and Class H at T=350°F, P_{CO2} = 600 psi, NaCl = 2%wt....177
Fig. 2.209: Predicted degradation depth for Class H cement at T=350°F, NaCl = 2%wt, P = 6000 psi....177
Fig. 2.210: Effect of salt concentration on solid-phase calcium profile of Class H cement at P=6000 psi, T=350°F, CO_2 = 10%, t = 14 days....178
Fig. 2.211: Comparison of solid-phase calcium profile different cement classes at P = 6000 psi, T = 350°F, CO_2 =10%, t = 14 days....178
Fig. 2.212: CO_2 concentration effect on solid-phase calcium profile of Class G cement P = 6000 psi, T=350°F, NaCl = 2 wt%, t = 14 days....178
Fig. 2.213: Temperature effect on solid-phase calcium profile of Class G cement P = 6000 psi,T = 350°F, NaCl = 2 wt%, t = 14 days....178
Fig. 2.214: Comparison of strength predictions during curing with experimental data (Akkaya et al. 2003)....179
Fig. 2.215: Comparison of strength predictions with experimental data after curing....179
Fig. 2.216: Strength predictions during curing Class G and Class H cement....180
Fig. 2.217: Comparison of chemical shrinkage in class G and class H during curing....180
Fig. 2.218 : Stress distribution in a degraded cement sample....181
Fig. 2.219: Comparison of compressive strength of Class G cement predictions with measurements: a) varying pressure at 10% CO_2 and 350°F; and b) varying CO_2 concentration at 6000 psi and 350°F....182
Fig. 2.220: Model predictions: a) porosity; and b) liquid phase calcium concentration for Class H and Class G cements....183
Fig. 2.221: Model predictions: a) solid phase calcium concentration; and b) calcium carbonate concentration for Class H and Class G cements....183
Fig. 2.222: Validation of model predictions: a) Effect of pressure; and b) Effect of CO_2 concentration for Class H and Class G cements....184
Fig. 3.1: Corrosion rate vs. pH (Hashizume et al. 2000)....190
Fig. 3.2: Temperature effect on time to failure....190
Fig. 3.3: Effect of temperature on critical stress intensity factor for different materials (Szklarz 1998)....192
Fig. 3.4: Effect of inhibitor concentration on Kissc for different materials at 250°C (Szklarz 1998)....192
Fig. 3.5: Stress Corrosion Cracking Mechanism (Heidary et al. 2008)....194
Fig. 3.6: Stress distribution in minipipe wall (Cernocky et al. 2005)....196
Fig. 3.7: Tensile test specimen in an environmental chamber (Kim et al. 2010)....196
Fig. 3.8: Real-pipe specimen (Maldonado and Bruno 2005)....197
Fig. 3.9: Mini-pipe specimen (Cernocky et al. 2007)....197
Fig. 3.10: Mini-pipe without sleeve in frame (Cernocky et al. 2005)....198
Fig. 3.11: Experimental set up for testing mini-pipe specimens (Been and Crozier 2014)....199
Fig. 3.12: Hydrogen permeation vs time (Been and Crozier 2014)....199
Fig. 3.13: C-ring test specimen (NACE TM0177)....200
Fig. 3.14: FPB test experimental set up (Skogsberg et al. 2001)....200
Fig. 3.15: Stress vs. strain for API grade steels (Koh et.al. 2003)....202
Fig. 3.16: Stress vs. strain curves for L-80 in NACE solutions and air (re-drawn from Kermani and MacCuish 1990)....202
Fig. 3.17: Schematics of cement degradation and tubular corrosion facilities....205
Fig. 3.18: Corrosion test setup....206
Fig. 3.19: Schematic of tubular corrosion test facility....206
Fig. 3.20: Design of SCC cell....207

Fig. 3.21: Assembly of SCC cell with heating jacket and hydraulic cylinder....207
Fig. 3.22: Control volume for mini-pipe, adapter and pulling rod assembly 208
Fig. 3.23: Mini-pipe specimen....208
Fig. 3.24: Mini-pipe holders 208
Fig. 3.25: Assembly of mini-pipe, adapters, pulling rod and vessel lid 209
Fig. 3.26: TST apparatus....210
Fig. 3.27: TST apparatus....210
Fig. 3.28: Stress vs. strain for corroded sample (Mini-pipe 1) 212
Fig. 3.29: Stress vs. strain for un-corroded sample (Mini-pipe 2)....212
Fig. 3.30: Stress vs. strain for un-corroded sample (Mini-pipe 3)....212
Fig. 3.31: Crack characteristics of broken mini-pipe specimens....212
Fig. 3.32: Operating window of Q-125 (Redrawn from Morana and Nice 2009) 213
Fig. 3.33: Stress vs. strain of mini-pipes: a) Mini-pipe 7 (corroded); and b) Mini-pipe 2 (baseline/uncorroded) 214
Fig. 3.34: Plastic strain to failure versus CO_2 concentration: a) T95; b) C110; and b) Q125....214
Fig. 3.35: Ultimate tensile strength versus CO_2 concentration: a) T95; b) C110; and b) Q125....215
Fig. 3.36: Comparison of model susceptibility prediction with experimental data: a) P-110; b) Q-125; c) C110; and d) L-80....218
Fig. 3.37: Sensitivity analysis for SSC model at pressure ratio of 1/6 219
Fig. 3.38: Solubility of H_2S and CO_2 vs. temperature 220
Fig. 3.39: Change in H_2S solubility vs. change in H_2S partial pressure 220
Fig. 3.40: Variation in pH vs. variation in CO_2 partial pressure....220
Fig. 3.41: Change in solubility of H_2S and CO_2 with variation in salt concentration 220
Fig. 3.42: Corrosion rates vs. temperature, pH 4, P_{CO2}=1 bar, C_{Fe2+} < 5ppm, 100 ppm acetic species ($HAc + Ac^-$), v = 0.5 m/s (Nešić 2007) 223
Fig. 3.43: Predicted and measured corrosion rates showing the effect of fluid velocity in the absence of iron carbonate scales at 20°C, P_{CO2}=1 bar, CFe2+ < 2 ppm....223
Fig. 3.44: Influence of temperature and CO_2 partial pressure on the rate of corrosion (Ropital 2010)....224
Fig. 3.45: Predicted and measured corrosion rates vs. CO_2 partial pressure at 60°C, pH 5, 1 m/s 224
Fig. 3.46: Schematic of the H_2S-CO_2 corrosion process (Sun and Nesic 2009)....225
Fig. 3.47: Corrosion rate vs. H_2S concentrations in CO_2 saturated brine (5% NaCl) (Ramirez and Ruiz 1998) 226
Fig. 3.48: Corrosion product diagram for H_2S-CO_2 environment (Smith 1993) 227
Fig. 3.49: Corrosion product diagram for H_2S-CO_2 environment (a) pH=4 and (b) pH=7 (Smith et al. 2011)....229
Fig.3.50: Summary of overall CO_2 corrosion process....232
Fig.3.51: Predicted CO_2 corrosion rate vs. experimental data (Dayalan et al. 1995)....234
Fig. 3.52: Free energy vs. extent of reaction (Glasstone et al. 1941) 234
Fig. 3.53: Change in free energy as a function of extent of reaction (Glasstone et al. 1941)....236
Fig. 3.54: Steps of overall CO_2-corrosion process under scale forming conditions 238
Fig. 3.55: Predicted CO_2 corrosion rate vs. experimental data (Dayalan et al. 1998)....238
Fig. 3.56: Model predictions and experimental data at 347K and 0.5 molar NaCl concentration 242
Fig. 3.57: Model predictions and experimental data at 299K and 0.5 molar NaCl concentration 242
Fig. 3.58: Measured and prediction corrosion rate vs. time for different H_2S gas concentrations under stagnant conditions (P = 1 bar, T = 80ºC, and pH 5.0-5.5) reaction times of 1 and 24 hours (Sun and Nešić 2007) 244
Fig. 3.59: Measured and predicted scale retention vs. time for different H_2S gas concentrations under stagnant conditions (P = 1 bar, T = 80ºC, and pH 5.0-5.5) reaction time of 1 and 24 hours (Sun and Nešić 2007).....245
Fig. 3.60: Predicted vs. measured corrosion rate (P = 1 bar, H_2S concentration ranging from 0.0075% to 10%, temperature 25°C, 60°C, and 80°C, reaction time of 1 hour and 24 hours, pH from 5.0 to 5.5, and velocity

from 0 to 8000 rpm) (Sun et al. 2007).....245
Fig. 3.61: Schematic of H_2S-CO_2 model computational procedure.....249
Fig. 3.62: Comparison between experimental data (Singer et al. 2007), Sun and Nešić model (2009), and prediction using modified model 250
Fig. 3.63: Comparison between predictions and measurements: a) data (Kvarekval et al. 2003); and b) data (Kvarekval et al. 2003; Sun and Nešić model 2009) 250
Fig. 3.64: Linear polarization plot (Roberge 1999) 251
Fig. 3.65: Polarization diagram for an active system with anodic and cathodic branches (Roberge 1999) 252
Fig. 3.66: Hypothetical polarization diagram for a passivating system with anodic and cathodic branches (Roberge 1999) 252
Fig. 3.67: Equivalent circuit models proposed for the interpretation of EIS results measured in corroding systems: (a) simplest representation of an electrochemical interface; (b) one relaxation time constant with extended diffusion; (c) two relaxation time constants; and (d) the impedance of pitting processes of Al-based materials (Epelboin et al. 1972) 253
Fig. 3.68: Complex-plane presentation of simulated data corresponding to the model circuit in Fig. 3.67a when Rs=10 Ω, Rp= 100 KΩ, and Q decomposes into Cdl=40μF and n=0.8 (Epelboin et al. 1972) 254
Fig. 3.69: Bode representation of the same data illustrated in Fig. 3.68 in complex plane format (Epelboin et al. 1972) 254
Fig. 3.70: Instantaneous corrosion rate vs. time (LPR data) 257
Fig. 3.71: Cylindrical PTFE block with electrodes.....258
Fig. 3.72: Schematic of moderate pressure experimental setup.....259
Fig. 3.73: Modified test setup for low pressure corrosion study.....259
Fig. 3.74: Corrosion rate vs. time obtained before installing a heating jacket 259
Fig. 3.75: Autoclave cover with PTFE block 260
Fig. 3.76: GAMRY G300 Potentiostat for LPR measurement (Courtesy GAMRY Instrument).....260
Fig. 3.77: GAMRY DC-105 startup interface.....262
Fig. 3.78: Corrosion rate versus CO_2 concentration and temperature for 2% NaCl solution (WL method) 264
Fig. 3.79: Corrosion rate versus CO_2 concentration and temperature for 2% NaCl solution (LPR Method).....264
Fig. 3.80: Corrosion rate versus CO_2 concentration and temperature for 1% NaCl solution (WL method) 265
Fig. 3.81: WL vs. LPR corrosion rate measurements: a) 1% NaCl; and b) 2% NaCl 266
Fig. 3.82: Corrosion coupon covered with protective coating.....269
Fig. 3.83: Specimen holder 269
Fig. 3.84: Dynamic corrosion cell.....270
Fig. 3.85: Coupon used for static and dynamic corrosion test 270
Fig. 3.86: Base of the specimen holder.....271
Fig. 3.87: Rotating cylinder 271
Fig. 3.88: Grips for flat coupons.....272
Fig. 3.89: Applied instantaneous load versus elongation for C110 coupon 272
Fig. 3.90: Corrosion rates of API grade steels as function CO_2 concentration measured at 6000 psi and 100°F: a) T95; b) C110; and c) Q125.....275
Fig. 3.91: Comparison of corrosion rate measurements at different CO_2 concentrations (Carbon steel 1045).....276
Fig. 3.92: Corrosion rate of C110 versus CO_2 concentration at 100°F and different pressures.....276
Fig. 3.93: Corrosion rate of C110 as a function CO_2 concentration (3000 psi and 100°F) 276
Fig. 3.94: Corrosion rates of API grade steels at different pressures (50% CO_2 and 100°F) 277
Fig. 3.95: Corrosion rate of C110 at different pressures (100% CO_2 and 100°F) 277
Fig. 3.96: Corrosion rate versus pressure at 100°F and 0% CO_2 277

Fig. 3.97: Corrosion rate of T95 as a function of H_2S concentration (100°F, 50% CO_2 and 6000 psi) 278
Fig. 3.98: Corrosion rate of C110 as a function of H_2S concentration (100°F, 50% CO_2 and 6000 psi) 278
Fig. 3.99: Corrosion rate of Q125 as a function of H_2S concentration (100°F, 50% CO_2 and 6000 psi) 278
Fig. 3.100: Effect of rotational speed on corrosion rate of Q125 at 6000 psi, 100°F and 50% CO_2 279
Fig. 3.102: Model prediction and measurements for C110 at 3000 psi, 100°F and different CO_2 concentrations ...284
Fig. 3.103: Model prediction and measurements for T95 at 6000 psi, 100°F and different CO_2 concentrations 284
Fig. 3.104: Model prediction and measurements for C110 at 6000 psi, 100°F and different CO_2 concentrations ...284
Fig. 3.105: Model prediction and measurements for Q125 at 6000 psi, 100°F and different CO_2 concentrations...284
Fig. 3.106: Model prediction and measurements at 9000 psi, 100°F, 50% CO_2 and different materials 285

LIST OF TABLES

Table 2.1: Typical composition and properties of API classes of cement 25
Table 2.2: Applicability of various classes of cement (Bourgoyne et al. 1986) 26
Table 2.3: Comparing the effects of using two different filter materials in cement (Santra et al. 2009) 28
Table 2.4: Slurry compositions (Santra et al. 2009) 28
Table 2.5 Permeability change before and after aging the sample (Jennings 2005) 43
Table 2.6: Potential cement additives to formulate AR cement 44
Table 2.7: Comparison of conventional and CO_2 resistant cement (Barlet-Gouédard et al. 2006) 48
Table 2.8a: Test Matrix 1- Studying the effect of CO_2 concentration at 100°F 51
Table 2.8b: Test Matrix 2 - Studying the effects of pressure and CO_2 concentration at 225°F 51
Table 2.8c: Test Matrix 3 - Studying the effects of pressure and CO_2 concentration at 350°F 51
Table 2.8d: Test Matrix 4 - Studying the effects of pressure and CO_2 concentration at 430°F 51
Table 2.9: Test Matrix 5 - Studying the effects of pressure, H_2S and CO_2 concentration at 100°F 51
Table 2.10: Test Matrix 6- Studying the effect of H_2S concentration at 6000 psi 51
Table 2.11: Test Matrix 7 - Studying the effects of pressure and temperature at 100% CH4 51
Table 2.12: Test parameters for aging experiments conducted to date 52
Table 2.13: Compositions of the baseline slurries 59
Table 2.14: Properties of baseline slurries 60
Table 2.15: Sample arrangement in aging cell 65
Table 2.16: Interpretations of FTIR results presented in Figs. 2.78 to 2.86 88
Table 2.17: Interpretations of FTIR results presented in Figs. 2.87 to 2.92 91
Table 2.18: Interpretations of FTIR results presented in Figs. 2.93 to 2.98 93
Table 2.19: Compositions of microsilica based slurries (MS-10) 98
Table 2.20: Properties of MS-10 and baseline slurries 99
Table 2.21: Summary of latex cement slurry testing results (Reports 17 to 24) 102
Table 2.22: Composition of latex slurry 102
Table 2.23: Compositions of LTMS slurries 103
Table 2.24: Properties of LTMS slurries 103
Table 2.25: Formulations of MgO based cement (MGO-5) slurries 105
Table 2.26: Properties of MGO-5 and baseline cement slurries 105
Table 2.27: Formulations of HOAP based cement slurries 107
Table 2.28: Properties of HOAP and baseline slurries 107
Table 2.29: Formulation of Class H cement with fly ash (HSF) 110
Table 2.30: Formulation of Class G cement with fly ash (GSF) 110
Table 2.31: Porosity and permeability of fly ash and baseline samples 111
Table 2.32: Aging conditions for HOAP samples 112
Table 2.33: Aging conditions for MGO samples 124
Table 2.34: Composition of the HOAP slurries 134
Table 2.35: Properties of hydroxyapatite containing cement slurries 134
Table 2.36: Degradation depth of HOAP and baseline samples aged at 350°F 137
Table 2.37: Formulations of MgO based cement (MGO-5) slurries 140
Table 2.38: Properties of MGO-5 and baseline cement slurries 140
Table 2.39: Aging conditions for the MGO-5 samples 140
Table 2.40: Aging conditions for the MGO-5 samples 143
Table 2.41: Aging conditions for MS-10 samples 147

Table 2.42: Degradation depth of baseline and latex-based cements 154
Table 2.43: Aging conditions for LTMS samples 157
Table 2.44: Test parameters for aging experiments.....162
Table 2.45: Cement clinker composition, water requirement and curing conditions.....171
Table 2.46: Amount of calcium in hydrated oil well cements 176
Table 3.1: Comparison of P-110and Q-125 performance.....191
Table 3.2: Compositions of steel alloys (Dezhi et al. 2012; Tucroni et al. 2001; Szklarz 1988) 191
Table 3.3: Properties of tested materials (Horstemeier et al. 2010).....201
Table 3.4: Specimen corrosion testing conditions.....203
Table 3.5: Mechanical properties of samples before and after corrosion test 211
Table 3.6: Parameters of Flux equations 248
Table 3.7: Test parameters of low-pressure corrosion experiments.....255
Table 3.8: Chemical composition of Grade 1045 carbon steel 258
Table 3.9: Test parameters and results of low-pressure corrosion experiments conducted to date 263
Table 3.10: Test conditions for HPHT uniform corrosion tests.....267
Table 3.11: Corrosion rate and mechanical properties of specimens before and after corrosion test.....273
Table 3.12: Values of rate constant of the electrochemical reactions 282

2. WELL CEMENT DEGRADATION

2.1. Introduction

Cement is a widely used material in a number of industrial applications involving acids and HPHT conditions. In the processing industry, storage tanks and high-pressure autoclaves handling strong acids have brick linings. Specially designed thermal resistant cements are used as mortar for securing the bricks at elevated temperatures and pressures. In the petroleum industry, well cementing is a routine procedure that is applied during drilling of oil and gas wells. This procedure requires cementing a series of steel casings into the well as the drilled depth increases. The main function of the casing is to support the wellbore and seal off overpressure formations. The cement provides a hydraulic seal to isolate different fluid-bearing zones of the rock formation from one another and from the surface. Moreover, the cement prevents the casing from corrosion. Properly placed cement can effectively isolate different formation zones (i.e. zonal isolation). Adequate zonal isolation allows the production of oil and gas from the producing formations and prevents leaks into the surface and to other subsurface formations (Ahmed et al. 2009).

2.1.1. Overview

The origin of cement degradation can be due to mechanical or chemical process or both. Mechanical degradation occurs when the cement is exposed to extreme loading conditions resulting from casing ballooning, thermal expansion and volume change during hydration. Well cement is very susceptible to chemical attack. Cement exposed to water saturated with acidic gases undergoes a combination of oxidation–reduction, sulfidation and carbonation reactions, which are strongly affected by the pH of the liquid phase.

The performance of well cement is regularly measured in terms of zonal isolation and compressive strength. The desired zonal isolation is achieved through proper formulation of the cement slurry and effective displacement of the mud by the cement. Correctly conducted cement jobs often result in cement with very low permeability and strong bondage between the cement-casing and cement-rock interfaces. Even though cement exhibits low initial permeability, its sealing properties vary with time as it interacts with the surrounding fluid under downhole conditions. Depending on the nature of the fluid in contact with the cement, severe degradation can occur with significant change in permeability and mechanical integrity. Limited laboratory studies (Krilov et al. 2000; Lécolier et al. 2008; Lécolier et al. 2010; Fakhreldin et al. 2010) have been conducted to assess the degradation behavior of oil well cement under acidic wellbore environment.

2.1.2. Statement of the Problem

Currently, the industry is exploring and producing oil and gas from extreme environments such as deepwater HPHT wells and sour gas resources. For the coming years, the production of gas from these resources is expected to increase. A recent study (Lécolier et al. 2010) indicated that substantial amount of the world's remaining gas reserves contain more than 2% Carbon dioxide and/or substantial amounts of hydrogen sulfide. In gas injection wells, the CO_2 and H_2S concentrations can be considerable (Fakhreldin et al. 2010). The presence of these corrosive gases under HPHT conditions further

complicates the well construction design. Appropriate design procedures require careful selection of casing and cementing materials that don't degrade when exposed to sour gases.

Oil field cements are vulnerable to acid attack and harsh downhole environments. Different physicochemical mechanisms are involved in the deterioration of cement properties. Very limited studies have been conducted to develop acid resistant oil field cement that can be used in sour gas resources. Published data on degradation mechanisms of cement-based materials exposed to H_2S and CO_2 environments are very scarce (Fakhreldin et al. 2010). More studies are needed to better understand the degradation mechanisms and develop new solutions that are required to ensure long-term integrity of oil field cement.

2.1.3. Objectives

A good primary cement job results in consistent cement matrix in the annulus and at the casing shoe. The cement provides zonal isolation by preventing fluid movement through annular space outside the casing, supports the casing, and protects casing string from corrosive formation fluids. For cement to perform its functions effectively over a long period, it needs to withstand the deleterious effects of severe temperature, pressure, corrosive fluids, and acidic gases (H_2S and CO_2). This study aims to develop a better understanding of the role of acidic gases in the chemical degradation of cement under downhole conditions. The study is focused on Class G and Class H based cements as they are most widely used in the oil industry. The investigation concentrates on examining the effects of acidic gases on the physical properties (mechanical strength, porosity, permeability, and shear bond strength) of cement.

Considering the severity of the possible cement failure in the well, it becomes imperative to understand cement degradation mechanism, and develop methods to reduce the degradation using special additives. Hence, the objectives of this study are:

- To understand the mechanisms of acid attack on conventional and special cements under HPHT harsh borehole conditions.
- To develop methods to quantify the degradation of oil well cement due to acid attack.
- To investigate effects of different downhole parameters (temperature, pressure, and CO_2 concentration) on the degradation of cement.
- To better understand carbonation and leaching, which take place during degradation of cement in acidic environment.
- To develop new cement formulations for lowering the degradation rate due to acid attack.
- To study the effects of different additives on cement degradation.

2.1.4. Research Methodology

In order to achieve the aforementioned objectives, experimental and theoretical approaches have been considered in this investigation. An extensive literature review has been conducted to assess vast information available in the public domain. More focus has been given to mechanisms of acid attack on oil well cement under HPHT conditions. The review has provided background information for the theoretical and modeling studies.

Degradation of well cement strongly depends on its formulation as well as compositions of liquid and gas phases, which are in contact with the cement. In this study, degradation mechanisms

such as carbonation and leaching and associated theories have been investigated. We have examined the relationship between degradation and downhole operating parameters such as temperature, pressure, and acid gas concentration. The outcomes of the theoretical analysis provided useful information in understanding the mechanisms that are involved in the cement degradation process. Moreover, the analysis has presented suitable theories and necessary information to formulate a degradation model that accounts for effects of temperature and pressure on the physicochemical properties of aged (i.e. exposed) cement.

In addition to the theoretical analysis and modeling, experimental investigations were performed to validate the model and study degradation behavior of oil well cements in acidic environment. The degree of degradation was measured as change in critical properties of cement such as porosity, permeability, compressive and shear bond strengths, and mineralogy. Furthermore, experiments were conducted to develop special cement formulations that are resistant to acid attack. Several cement additives were considered in the first phase of formulation study. Acid resistant formulations that showed superior performance were selected for further investigation. Two types of acid resistant formulations (magnesium oxide and hydroxyapatite-based formulations) were developed. The formulations were rigorously tested to evaluate their performance.

2.1.5. Scope of Work

Cement degradation is very sensitive to downhole conditions (temperature, pressure and acid gas concentration). In order to perform tests under simulated borehole conditions, cement degradation (aging) experiments were carried out varying temperature from 100 to 430°F, pressure from 3000 to 9000 psi, and CO_2 concentration from 0 to 100%. Normally, aging duration was 14 days in each test. Some aging experiments were conducted for extended period (28 days) to study effect of aging duration on degradation. Two different oil well cement classes (Class G and Class H) were considered in the investigation.

In order to quantify the level of degradation, properties (mechanical strength, porosity, permeability, and shear bond strength) of aged and unaged samples were measured and compared. In addition, FTIR, XRD, SEM and SEM-EDS analysis were conducted to determine the change in mineralogical composition, phase composition, morphology, and elemental composition, respectively. XRD was used to validate the use of FTIR for mineralogical studies. SEM imaging helped in finding the degree of hydration of cement and identifying different degraded zones including carbonation front.

Two types of cement samples (cores and bond samples) were prepared to carry out the experiments. Cylindrical cement cores were prepared from cured cement slabs. Shear bond samples were made from steel pipe and cement. After mixing, cement slurry was poured into steel pipes and cured in 2% brine (NaCl) solution. FTIR and XRD samples were collected from different location on aged and unaged cement cores.

To develop acid resistant formulations, different cement additives were considered in the investigation including magnesium oxide, hydroxyapatite, microsilica, latex, fly ash, and latex-microsilica. Cement slurries with various formulations of these additives were prepared and tested for their flowability, acceptable filtration loss, and consistency. Slurries with acceptable properties (i.e. similar to that of baseline cement) were cured and used to prepare cores for further testing. Mechanical and physical properties (porosity, permeability, compressive and shear bond strengths) of the cores were

measured and compared with corresponding baseline samples. Additive cement formulations, which showed comparable mechanical and physical properties to baseline cement, were further tested in the aging cell. Formulations, which demonstrated unacceptable mechanical and physical properties were modified and retested again to assess if acceptable mechanical and physical properties can be attained with minor modifications.

2.2. Literature Review on Cement Degradation

Deterioration of cement in aggressive environment leads to increased porosity and permeability that drastically affects the sealing and isolation performance of the cement. The increase in porosity and permeability further intensifies the degradation process by allowing more aggressive fluid to penetrate into the cement and reaches the undamaged zone. The depth of penetration depends upon several factors, namely, permeability, porosity, the calcium content of the cement system, and composition of the surrounding fluid.

In order to prevent cement degradation by acid attack, it is important to understand the composition of cement, properties of cement slurry, types of additives and its use. The major components of dry Portland cement are lime, silica, alumina and iron oxide. These components are present in the following crystalline phases and constitute the major part of the cement:

- C_3S – Tri-Calcium Silicate (Alite) – $3CaO.SiO_2$
- C_2S – Di-Calcium Silicate (Belite)– $2CaO.SiO_2$
- C_3A – Tri-Calcium Aluminate – $3CaO.Al_2O_3$
- C_4AF – Tetra-Calcium Aluminoferrite – $4CaO.Al_2O_3.Fe_2O_3$

Apart from the above components, minerals like potassium sulfate, sodium, magnesium oxide, free lime are also present in the cement. The chemical composition of oil well cement is slightly different from that of regular Portland cement. Oil well cements have lower C_3A contents, and they are coarsely ground. Moreover, they may contain friction-reducing additives and special retarders such as starch and sugars.

The API has defined three standard types and eight standard classes of cement for use in oil wells (Bourgoyne et al. 1986). The cement types are classified on the basis of resistance towards sulfate attack as: Ordinary (O), Medium Sulfate Resistant (MSR) and High Sulfate Resistant (HSR). The cement classes (Classes A through H) are established on the basis of temperature, pressure and depth applicability. **Tables 2.1 and 2.2** present composition and applicability of various classes of cement, respectively.

Table 2.1: Typical composition and properties of API classes of cement

API Classes	Components				Fineness (cm^2 / gm)	Water / Cement Ratio
	C_3S	C_2S	C_3A	C_4AF		
A	53	24	8	8	1500 - 1900	0.46
B	47	32	3	12	1500 - 1900	0.46
C	70	10	3	13	2000 - 2400	0.56
D	26	54	2	12	1100 - 1500	0.38
G	52	32	8	12	1400 - 1600	0.44
H	52	32	8	12	1200 - 1400	0.38

Table 2.2: Applicability of various classes of cement (Bourgoyne et al. 1986)

API	Usage	Grade
Class A	Shallow Depth – up to 6000 ft	O
Class B	Shallow Depth – up to 6000 ft	MSR and HSR
Class C	High early strength at shallow depth – up to 6000 ft	O, MSR and HSR
Class D	Moderately High temperature and Pressures – between 6000 - 10000 ft	MSR and HSR
Class E	HPHT Wells – between 10000 - 14000 ft	MSR and HSR
Class F	Extreme HPHT – between 10000 - 16000 ft	MSR and HSR
Class G	Basic cement for various depths and temperature and can be incorporated with accelerators and retarders – Up to 8000 ft	MSR and HSR
Class H	Basic cement for various depths and temperature and can be incorporated with accelerators and retarders – Up to 8000 ft	MSR

There are a number of special blends of Portland cement with additives, or cements based on other chemistry that do not fall specifically into any general classification. These include pozzmix cements that incorporate organic resin technology, expanding cements that increase in volume as the cement sets, silica and lime cements for high temperature wells, and low heat generating cements for permafrost applications. These cements are seldom used in general completions because they are more expensive than Portland cements or have other traits that are less desirable than those of Portland cements.

Due to varied depth applicability, compatibility with several additives and easy availability, Class G and Class H cements are most commonly used for oil wells (Bourgoyne et al. 1986). Both classes have almost similar composition except for particle size and water cement ratio. Class H is usually coarser than Class G cement and the water requirement is also lower (38%) than Class G (44%). This difference in the particle size along with different water requirement leads to varied performance of the cements.

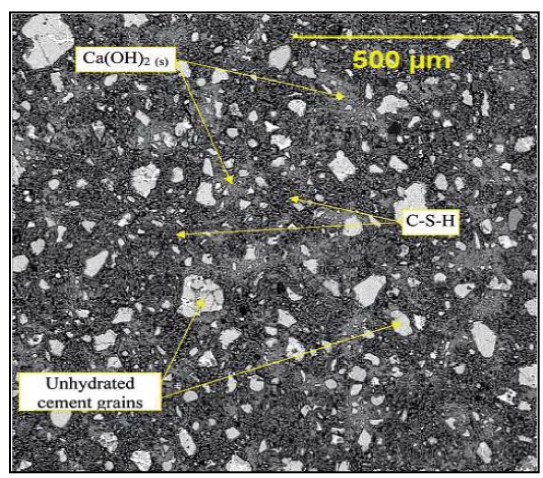

Fig. 2.1: SEM-BSE image of cement cured for 28 days at 22°C and 0.1 MPa (Kutchko et al. 2007)

During cement hydration, the main reaction products (**Fig. 2.1**) formed are tobermorite gel ($3CaO.2SiO_2.3H_2O$), which is known as CSH phase and portlandite ($Ca(OH)_2$). The tobermorite gel is the main binding material. Reaction equations for hydration of C_3S and C_2S are written as:

$$2(3CaO.SiO_2) + 6H_2O \rightarrow 3CaO.2SiO_2.3H_2O + 3Ca(OH)_2 \quad (2.1)$$

$$2(2CaO.SiO_2) + 4H_2O \rightarrow 3CaO.2SiO_2.3H_2O + Ca(OH)_2 \text{ (slow reaction)} \quad (2.2)$$

The C_3A also hydrates very rapidly and produces most of the heat of hydration observed during the first few days. To control this rapid hydration, gypsum is added to the clinker. The C_3A is attacked very fast with the water containing sulfates.

$$3CaO.Al_2O_3 + 12H_2O + Ca(OH)_2 \rightarrow 3CaO.Al_2O_3.Ca(OH)_2.12H_2O \text{ (fast reaction)} \quad (2.3)$$

$$3CaO.Al_2O_3 + 10H_2O + CaSO_4.2H_2O \rightarrow 3CaO.Al_2O_3.CaSO_4.12H_2O \quad (2.4)$$

C_4AF is hydrated in the presence of portlandite and it has only minor effects on the physical properties of the cement.

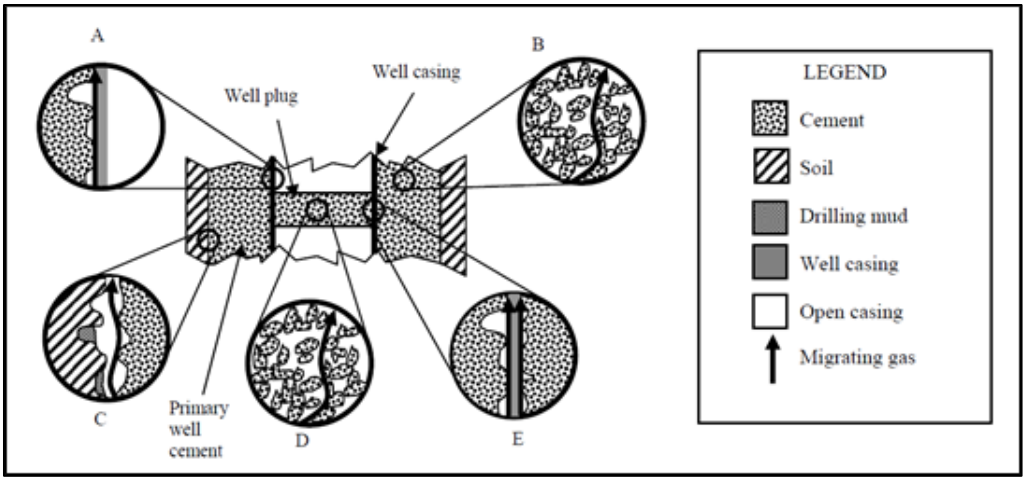

Fig. 2.2: CO_2 leakage through primary (A) or secondary cement (C) interfaces between casing and cement (B), formation and cement (D) and through casing (E) (Duguid et al. 2006)

According to Duguid et al. (2006), CO_2 leakage from a wellbore can take place in 5 different ways (**Fig. 2.2**). Leakage that occurs through primary or secondary cement can be at the interfaces between: (i) casing and cement (A), (ii) formation and cement (C); and (iii) through the cement (D and B). Degradation opens a pathway for the stored CO_2 to escape again into the atmosphere.

2.2.1. Experimental Studies

2.2.1.1. Cement Degradation in Carbonic Acid Environment

The degradation rate of the cementitious material in the presence of acidic fluid depends upon the acid concentration, pH of the solution and also the type and amount of hydrated phases present in the reaction. For instance, the dissolution of Fe^{3+} and Al^{3+} is slower and occurs at a lower pH value. So when the pH lowers, portlandite ($Ca(OH)_2$) and Tobermorite gel (CSH) initially dissolve and then calcium aluminate and ferrite hydrates dissolve. When pH is between 4 and 6, calcium hydrates dissolve leaving behind aluminate and ferrite hydrate. However, at low pH values (pH ≈ 2), only silica gel is left after the alteration process of the cementitious material (Lecolier et al. 2008).

Incorporating filler materials such as silica fumes and fly ash can reduce the content of $Ca(OH)_2$ and CSH in cement (**Table 2.3**) thereby reducing the formation of calcium carbonate which forms water soluble calcium bicarbonate (Santra et al. 2009).

Table 2.3: Comparing the effects of using two different filter materials in cement (Santra et al. 2009)

Filler	Silica Fumes	Fly Ash
Filler material content	35%	98%
Particle size	Finer	Coarser
Porosity & permeability	Less	More
Water-solid Ratio	High	Low
$Ca(OH)_2$	Low	High
Depth of penetration tends to:	1) Reduce due to low $Ca(OH)_2$ content 2) Reduce due to reduction of ϕ and k 3) Increase due to increased W/S Ratio	1) Increase due to high $Ca(OH)_2$ content 2) Increase due to increased ϕ and k 3) Reduce due to low W/S Ratio

Table 2.4: Slurry compositions (Santra et al. 2009)

Sample, No.	Cement, %	Silica Fume, %	Fly Ash, %
1	100	0	0
2	83.3	16.7	0
3	71.4	28.6	0
4	62.5	37.5	0
5	55.6	44.4	0
6	50	50	0
7	83.3	0	16.7
8	71.4	0	28.6
9	62.5	0	37.5
10	55.6	0	44.4
11	50	0	50

Depth of CO_2 penetration depends upon the following two factors: i) permeability of the original rock (before carbonation) that controls rate of acid penetration in the rock; and ii) amount of $Ca(OH)_2$ in the pore fluid that facilitates formation of $CaCO_3$, which plugs the pores and results in decreased porosity and acid penetration. Therefore, to lower the depth of penetration, the amount of $Ca(OH)_2$ needs to be lowered by increasing the amount of filler materials such as silica fume and fly ash. To study the effects of filler materials on the carbonation process, Santra et al. (2009) conducted experiments using 11 samples (**Table 2.4**). After aging for 15 days at 2000 psi and 200°F in the presence of fresh water saturated with CO_2, the samples were cut in half to examine the degree of penetration. Penetration depth was determined by examining different colors formed on carbonated and uncarbonated portions of the sample. The images of the samples presented in **Fig. 2.3a** shows that Samples 5 and 6 were fully penetrated due to extensive CO_2 invasion, which was confirmed by TGA (Thermo-Gravimetric Analysis) and XRD (Santra et al. 2009). **Figure 2.3b** compares the measured depth of penetrations using different filler materials and shows the effect of concentration of the fillers.

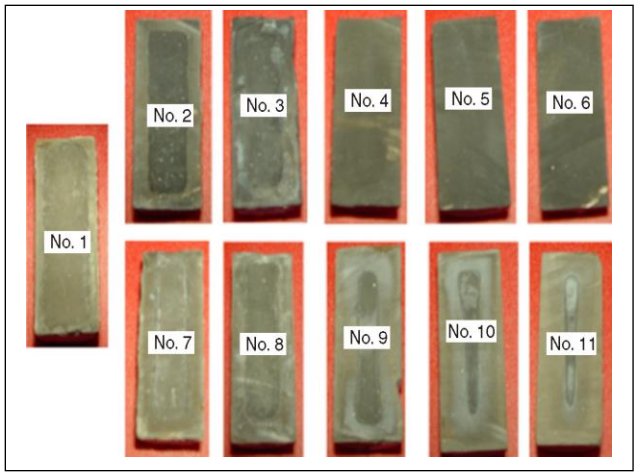

Fig. 2.3a: Cement core samples after 15-day of aging in water saturated with CO_2 (Santra et al. 2009)

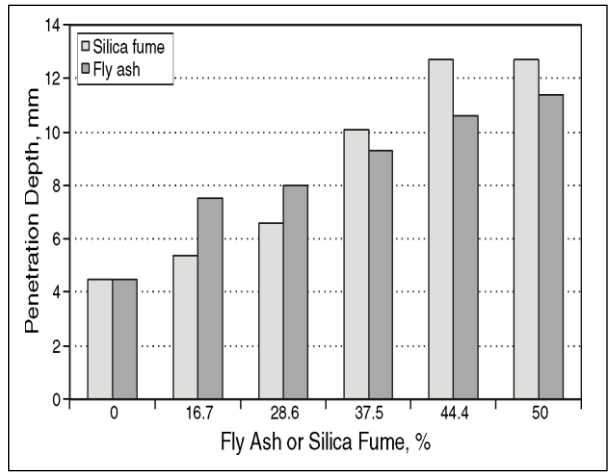

Fig. 2.3b: Measured penetration depth (Santra et al. 2009)

2.2.1.2. Cement Degradation after H_2S Attack

Calcium tri-sulfo-aluminate hydrate (Ettringite) [$Ca_6[Al(OH)_6]_2\cdot(SO_4)_3\cdot 26H_2O$] and mono-sulfo-aluminate hydrate (monosulfate) [$3(CaO)(Al_2O_3)(CaSO_4)\cdot 12H_2O$], are minor hydration products of mature Portland cement (Glasser et al. 2008; Taylor 1997). They are formed by the hydration of C_3A and C_4AF. The amount of these minor phases in the cement depends on the quantities of ferrite and tricalcium aluminate present in the cement, level of hydration and curing conditions (Neville 2004). The primary ettringite formed before hardening of the cement slurry is not associated with expansion and internal stress. However, the ettringite formed after the hardening of the slurry (secondary ettringite) may lead to expansion, internal stress and cement degradation (Zhang et al. 2013; Kutchko et al. 2011; Collepardi 2003; Mehta 1983).

Formation of Ettringite

A number of studies (Glasser et al. 2008; Collepardi 2003; Zhou and Glasser 2001) documented the formation of ettringite in cements and concrete from different sulfate sources. Secondary ettringite is formed when calcium (in form of lime or CSH), aluminum (in form of hydrated ferrite and C_3A), sulfate (formed from H_2S), and H_2O present in the hardened cement. Depending on the source of sulfate ions, there are two primary methods of secondary ettringite formation, which are also referred to as sulfate attack in this section:

- Internal sulfate attack occurs when the sulfate ions are present or formed in the porous space of cement.
- External sulfate attack takes place when sulfate ions from the environment penetrate the cement matrix.

Internal sulfate attack is considered as the main mechanism of ettringite formation in cement. During the attack, the sulfur is provided by an external source as aqueous H_2S (Kutchko et al. 2011). In experimental analysis of cement samples, abundant ettringite was observed in aqueous H_2S–CO_2 exposed cement as compared to only CO_2 exposed cement suggesting that the primary source of sulfate

for ettringite formation is the H_2S (Kutchko et al. 2011). The hydrosulfuric acid penetrates into the cement and reacts with ionic species present in the pore fluid of the cement. The acid forms sulfate as described by Eq. (2.5a). This internal source of sulfate is then available for ettringite formation.

$$8Fe(OH)_3 + \mathrm{HS}^- \leftrightarrow 8Fe^{2+} + SO_4{}^{2-} + 5H_2\mathrm{O} + 15\mathrm{OH}^- \quad \text{(2.5a)}$$

Different formation mechanisms and chemical formulae for secondary ettringite are proposed (Zhang et al. 2013; Kutchko et al. 2011; Collepardi 2003; Morales et al. 2003; Mehta 1983). Formation of ettringite can occur either by a through-solution mechanism or by topo-chemical growth (Naik 2003). Depending on the formation pathway, the mechanism of cement degradation by ettringite varies. These mechanisms are discussed in the Section 2.2.2.4. Although formulae for ettringite vary depending on the pathway and species, an approximation is given by Eq. (2.5b). Here the calcium is supplied by the C_3A, which reacts with sulfate ions in the solution to form secondary ettringite (Kutchko et al. 2011).

$$6\mathrm{Ca}^{2+} + 2\mathrm{Al(OH)}^{4-} + 4\mathrm{OH}^- + 3\mathrm{SO_4}^{2-} + 26\mathrm{H_2O} \leftrightarrow \mathrm{Ca_6[Al(OH)_6]_2(SO_4)_2.26H_2O} \quad \text{(2.5b)}$$

Other approaches (Zhang et al. 2013; Tixier 2000) consider that calcium ions released from dissolution of portlandite and CSH are involved in the formation of ettringite. The sulfate ions react with Ca^{2+} ions and unhydrated C_3A or tetra calcium aluminate hydrate or monosulfate to form secondary ettringite as described from Eqs. (2.6) to (2.8). Studies observed that the calcium flux during sulfate attack test (1.1 mol/m^2/days$^{0.5}$) was smaller than that obtained for leaching in pure water (1.3 mol/m^2/days$^{0.5}$). However, the fluxes of hydroxyl ions were similar in both the sulfate solution as well as pure water (Planel et al. 2006). Thus, it was concluded that Ca^{2+} ions used in the formation of ettringite were supplied by the dissolution of portlandite (CH).

$$(3\mathrm{CaO.Al_2O_3}) + 3\mathrm{Ca}^{2+} + 3\mathrm{SO_4}^{2-} + 32\mathrm{H_2O} \rightarrow \mathrm{Ca_6Al_2(SO_4)_3(OH)_{12}.26H_2O} \quad \text{(2.6)}$$

$$\mathrm{Ca_4Al_2(OH)_{14}6H_2O} + 3\mathrm{Ca}^{2+} + 3\mathrm{SO_4}^{2-} + 20\mathrm{H_2O} \rightarrow \mathrm{Ca_6Al_2(SO_4)_3(OH)_{12}.26H_2O} + \mathrm{Ca(OH)_2} \quad \text{(2.7)}$$

$$\mathrm{Ca_4Al_2(OH)_{12}SO_46H_2O} + 2\mathrm{Ca}^{2+} + 2\mathrm{SO_4}^{2-} + 20\mathrm{H_2O} \rightarrow \mathrm{Ca_6Al_2(SO_4)_3(OH)_{12}.26H_2O} \quad \text{(2.8)}$$

Expansion of Ettringite

Ettringite is an expansive material (Zhang et al. 2013; Kutchko et al. 2011; Collepardi 2003; Tixier 2000; Mehta 1983). Hence, the formation and expansion of secondary ettringite may disintegrate the cement. Presently, it is unclear to what extent does cement degradation occur due to hydrosulfuric acid attack and secondary ettringite formation within the well bore (Zhang et al. 2013). The validity of ettringite related mechanism has been analyzed but no satisfactory evidence for ettringite expansion is available (Tixier 2000).

Ettringite crystalline structure contains 26 to 32 water molecules. Therefore, the formation of ettringite involves considerable expansion and weight growth (Morales et al. 2003). Based on studies (Naik 2003; Ping and Beaudoin 1992) on cement and concrete, the degradation of cement by ettringite can be either during the formation of ettringite itself or by expansion of colloidal ettringite. Ping and

Beaudoin (1992) summarized the two widely accepted theories of cement expansion by ettringite formed by through-solution and topo-chemical mechanisms in a concise manner as the Swelling Theory and the Crystal Growth Theory, respectively.

Through-solution growth (Swelling Theory): Some studies suggest that the formation of ettringite itself is not expansive, but it has a colloidal structure that can adsorb significant quantities of water causing expansion (Mehta 1983; Tixier 2000). The colloidal ettringite is formed by through-solution mechanism. It has a high specific surface and a peculiar crystal structure with a negative net charge that possibly results in expansions by large adsorption of water molecules and inter-particle repulsion (Naik 2003). In a through solution growth of ettringite (**Fig. 2.4**, left), all the reacting components such as calcium hydroxide, sulfate ions and the aluminate phase are present in the pore solution as ions. The components nucleate as colloidal ettringite crystals at different points in the pore solution and start growing when the solution cannot hold them any further. As the growth of ettringite crystals is within the solution, the growth mechanism is called the through-solution mechanism. The volume of ettringite exceeds the volume of the pores causing internal pressure to build up inside the pores until it reaches the material tensile strength resulting in cement cracking. The Swelling Theory assumes that expansion occurs because of hydration and swelling of colloidal ettringite.

Topo-chemical growth (Crystal Growth Theory): In a topo-chemical growth mechanism (Fig. 2.4, right), the calcium hydroxide and sulfate ions in the pore solution react with the aluminate phase in the solid pore walls. The resulting ettringite crystals nucleate and grow as thin needles from the solid pore walls. These needle-like structures strike the pore walls to exert expansive stresses. Expansion and cracking occur if these stresses become greater than the tensile strength of the surrounding matrix (Naik 2003; Basheeduzaffar 1992). However, Mehta (1983) suggested that due to the large differences in the structure of monosulfate hydrate and tetra calcium aluminate hydrate, transformation of these components to ettringite by solid-state reaction is most unlikely.

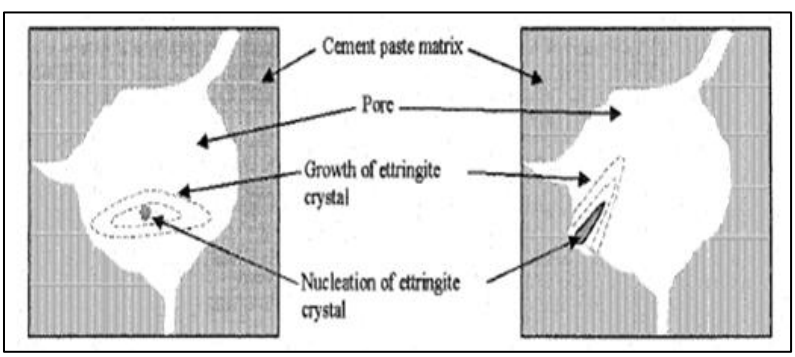

Fig. 2.4: Schematic view of a pore in a hardened cement paste matrix under sulfate attack, showing nucleation and growth of ettringite by through-solution (left) and topo-chemical (right) mechanisms (Naik 2003)

To study the effects of sulfate concentration on expansion and formation of secondary ettringite, Morales et al. (2003) conducted experiments on Class G cement at 90 and 185°F. No clear co-relation was established between length change (ΔL) and sulfate concentration (**Fig. 2.5**). However, it was observed that the change in weight (ΔW) increases with increase in sulfate ions concentration at 90°F (**Fig. 2.6**). It was suggested that ettringite forms within cement pores and continues to grow till it

fills the free space. During this incubation period, no trend was observed between ΔL and days; however, ΔW increased. During propagation period, the internal pressure may start building up inside pores until it reaches the material tensile strength causing the cement to crack and an increase in ΔL is observed. No trend was observed on specimens tested at 185°F. This could be due to the fact that ettringite is unstable and dissolves at temperatures around 190°F.

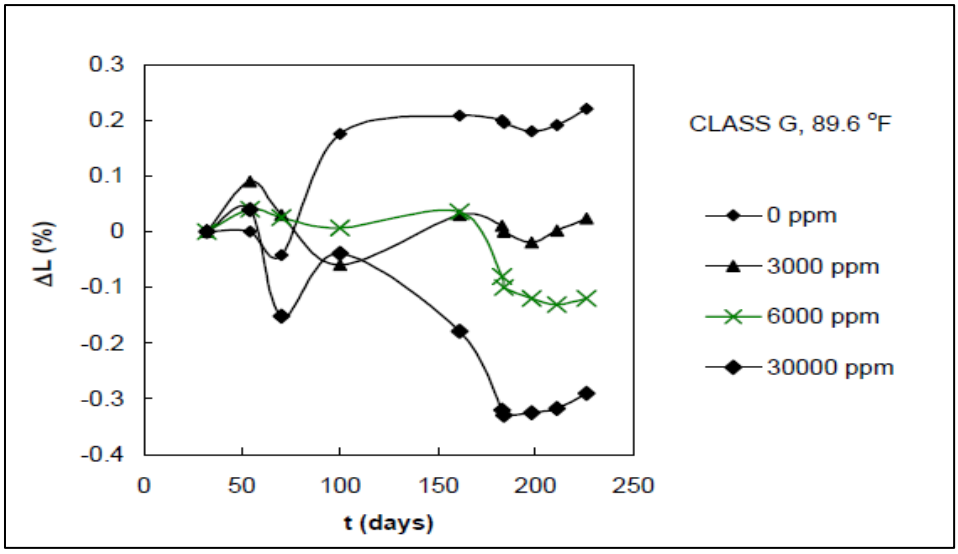

Fig. 2.5: ΔL vs days for different sulfate ions concentration in class G cement (Morales et al. 2003)

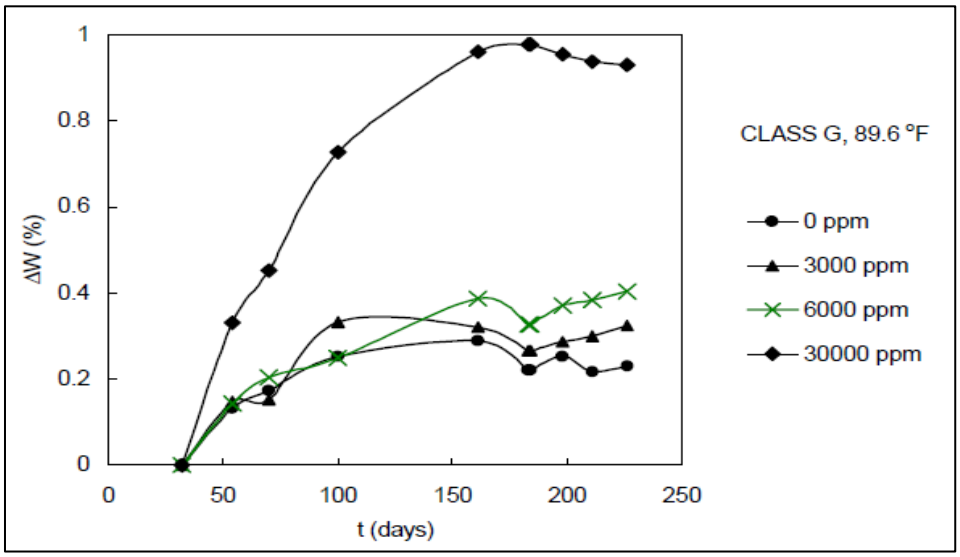

Fig. 2.6: ΔW vs Days for different sulfate ions concentration in class G cement (Morales et al. 2003)

The secondary ettringite formation can be a destructive process and lead to cement degradation by cracking and spalling. However, some studies (Kutchko et al. 2011) suggested that the effect of secondary ettringite formation can be minimal depending on the rate of CO_2 ingress into cement. CO_2 may actually dissolve the ettringite and re-precipitate calcium compounds to help improve the overall cement integrity.

Detection of ettringite formation is very challenging. While the structural and surface OH in portlandite exhibits a distinct FTIR peak at a wave number of 3645 cm^{-1}, ettringite exhibits broad stretching peaks at 3550 and 3300 cm^{-1} (Myneni et al. 1998). When compared to structurally simple metal-hydroxides and sulfates, ettringite has several types of OH groups such as: OH exposed at the surfaces (Al-OH, Ca_2-OH, Ca-$(OH)_2$), structural OH ($AlCa_2$-OH; Ca-$(OH)_2$), and free H_2O in the channels. These varieties of OH bonding environments produce broad IR absorption bands around 3550, 3300, and 1640 cm^{-1}, which are not conclusively resolved into individual vibrations. Thus, ettringite is difficult to identify via FTIR. Ettringite crystals have acicular needle like structures observed by SEM. **Figure 2.7** shows an SEM image indicating presence of ettringite crystals in cement. In addition, the formation of ettringite can be detected by XRD analysis.

Fig. 2.7: SEM image of Class G cement showing presence of acicular needle like ettringite (Morales et al. 2003)

2.2.2. Theoretical and Modeling Studies

2.2.2.1. Cement Degradation under CO_2 Exposure

Once the cement is placed in the annular space, it comes in contact with the formation fluid containing brine and CO_2. After its placement, hydration, carbonation and leaching processes occur. When cement hydrates in water, it forms CH and CSH, which is the major binding material responsible for the strength development. CH has limited binding property. It forms weak cement matrix (Brandl et al. 2010). CSH and CH can be easily attacked by carbonic acid to form $CaCO_3$, which plugs the pores of the cement thereby decreasing its porosity and permeability. However, in presence of excess carbonic acid, calcium carbonate is converted to bicarbonate (Krilov 2000). Calcium bicarbonate is water-soluble and dissolves quickly in brine (formation fluid). Consequently, leaching of cementitious materials (CH and CSH) takes place leading to increase in porosity and permeability and reduction in strength.

The degradation of cement occurring under downhole conditions involves a number of chemical and physical processes including: i) ionic transport in porous material; ii) chemical reaction between cement hydration products and dissolved acid gases (carbonation, and sulfidation); and iii) dissolution and leaching of carbonation/bicarbonation products from the matrix.

Carbon dioxide is water-soluble gas. It dissolves in water or aqueous solutions quickly forming acidic solution. The reaction reduces the pH of the solution. Temperature, partial pressure of CO_2 and other ions present in water, such as salts, influence the pH. The produced carbonic acid penetrates into the cement matrix and attacks the main hydration products or binding materials (portlandite and CSH). The reaction (i.e. carbonation reactions) produces calcium carbonate ($CaCO_3$), amorphous silica (silica gel, $SiO_2.H_2O$) and water as:

$$H_2CO_3 + Ca(OH)_2 \rightarrow CaCO_3 + 2H_2O \quad (2.9)$$

$$CSH + H_2CO_3 \rightarrow CaCO_3 + \text{amorphous silica} + H_2O \quad (2.10)$$

The first reaction (Eq. 2.9) is considered faster than the second one (Eq. 2.10). These reactions cause densification, which increases the cement hardness and decreases its permeability, resulting in reduced CO_2 diffusion and expansion up to 6% in volume that can create micro to macro cracks in the cement matrix (Santra et al. 2009). The produced $CaCO_3$ is converted to calcium bicarbonate and leached out by the carbonic acid as:

$$CaCO_3 + H_2CO_3 \rightarrow Ca(HCO_3)_2 \quad (2.11)$$

The leaching or dissolution of $CaCO_3$ occurs when the cement is surrounded by carbonated aqueous solution. The dissolution tends to increase porosity and permeability, and degrade mechanical properties of the cement. However, if the above reaction stops after the carbonation of the calcium hydroxide, the $CaCO_3$ formed would cause an increase in compressive strength and a decrease in permeability (Fakhreldin et al. 2010).

Cement specimens aged in the aqueous phase under high-pressure conditions showed an altered region containing distinct zones (**Figs. 2.8a** and **2.8b**) situated in a radial pattern in cylindrical samples (Kutchko et al. 2007).

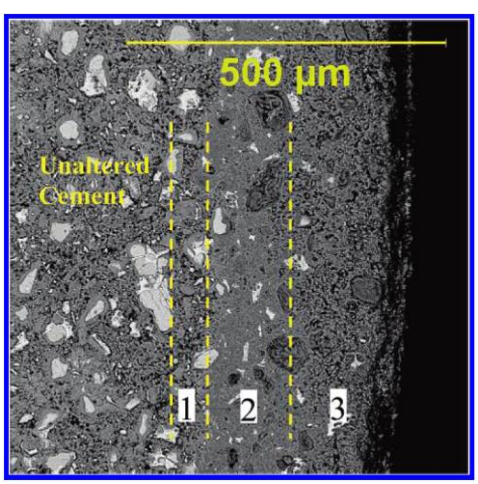

Fig. 2.8a: Microscopic image of sectioned-cement core after CO_2 exposure (Kutchko et al. 2007)

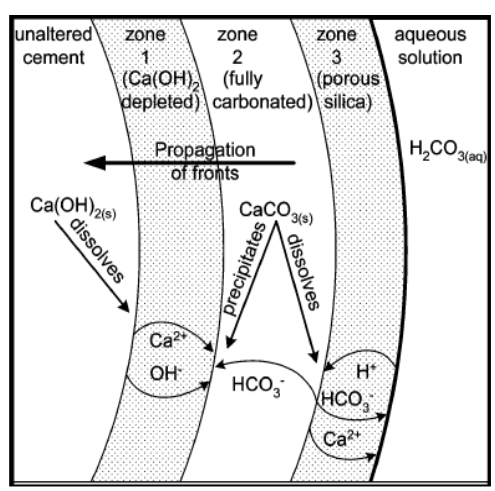

Fig. 2.8b: Formation of distinct zones in the degraded cement specimen (Kutchko et al. 2007)

Microscopic examination showed the presence of:

- Unaltered central zone.
- Zone 1 with slightly increased porosity and decreased $Ca(OH)_2$.
- Zone 2 with decreased porosity and increased calcium content.
- Zone 3 with low calcium content and increased porosity as a result of dissolution.

These changes taking place in the cement matrix are due to the interaction between the components of the cement and CO_2-saturated brine resulting in the carbonation and bicarbonation of the CSH and $Ca(OH)_2$. These distinct zones are formed as a result of the balance between dissolution reaction and species transport in the porous cement. More recently, a similar study (Rimmelé et al. 2008) was conducted to investigate the effects of wet supercritical CO_2 and CO_2-saturated water on cement degradation. Results (**Fig. 2.9**) demonstrated surface carbonation of the cement sample after two days of exposure to wet supercritical CO_2 and CO_2-saturated water at 180°C and 280 bars. After 3 months of exposure, the carbonation became clear as the samples showed a thick white layer on their surface, which indicate the formation of calcium carbonate. The carbonation is commonly accompanied by the development of cracks. After 6 months of aging, the carbonated rim on the surface of the samples was flaked out as the carbonation layer became very thick. The pH of water used for aging the cement cores reduced from 13 to 6.5 after the exposure.

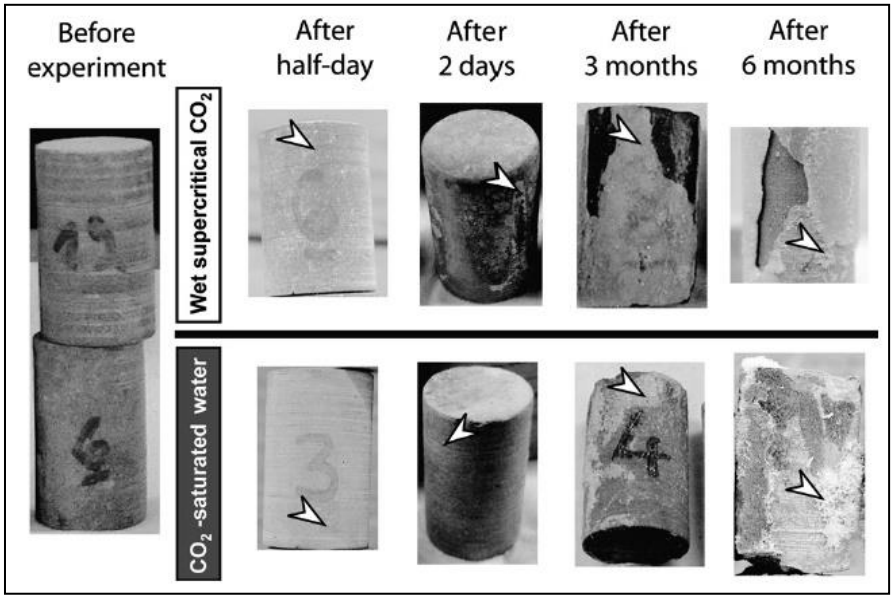

Fig. 2.9: Portland cement samples before and after CO_2 exposure at 180°C and 280 bars (Rimmelé et al. 2008)

2.2.2.2. Cement Degradation under H_2S Exposure

Like carbon dioxide, H_2S dissolves in aqueous liquids and form weak acid solution. The acid attacks some of the components of set cement resulting in the formation of CaS, FeS, and $Ca(HS)_2$, CaS and Al_2S_3 when H_2S concentration is high (Renpu 2011). The H_2S attack depends strongly on the pH of the acid solution and composition of the cement. Intuitively, the impact of H_2S degradation on cement is

expected to be limited as it predominately attacks minor components of cement (ferrites) by sulfidation (Fakhreldin et al. 2010). Moreover, portlandite and hydrated calcium aluminate (C_3A) in set cement may react with the acid causing cement failure due to the formation of expansive reaction products. The C_3A content of the cement needs to be reduced by adding tetra calcium alumino-ferrite (C_4AF) to minimize the expansion ratio. The portlandite content can be controlled by introducing activated SiO_2-rich materials such as silica flour or volcanic ash. These materials can react with the portlandite and generate CSH phase, which is less reactive than portlandite.

Furthermore, as the H_2S reduces the pH of the solution, it facilitates the dissolution and leaching of hydration products that diminishes the mechanical strength of the cement (Kutchko et al. 2011). The presence of methane gas in the system may also promote the degradation of cement in H_2S containing environment (Renpu 2011).

Due to the complexity of cement chemistry, the mechanisms of chemical attack on cement are complicated. During H_2S exposure, the chemical changes occurring within the hydrated cement matrix lead to the degradation of the cement, resulting from sulfate attack, which is identified as expansive attack because the acid penetrates into the cement pores and forms voluminous water-insoluble products (crystals). As the size of the crystals grows, the pressure inside the cement pores will increase resulting in cracks, fractures, and fragments. The American Society of Testing and Material (ASTM) defines the sulfate attack as the chemical or physical reaction, or both, occurring between the sulfate and calcium aluminate hydrates, which leads to deterioration of the cement. Morales et al. (2003) presented the chemical reaction between the C_3A and gypsum, which is commonly added to the clinker to regulate the rate of the hydration that occurs during the first 24 hours of hydration forming a primary ettringite ($Ca_6Al_2(SO_4)_3(OH)_{12}\cdot 26(H_2O)$). They proposed the following three steps as mechanism for sulfate attack.

Step 1. Formation of Primary Ettringite: The primary ettringite is formed during the first 24 hours of hydration:

$$3(CaO.Al_2O_3) + 3(CaSO_4.2H_2O) \rightarrow Ca_6[Al(OH)_6]_2(SO_4)_3.26H_2O \quad (2.12)$$

Step 2. Formation of calcium mono-sulfo-aluminate hydrate: As cement hydration takes place, gypsum concentration reduces and therefore ettringite is transformed into calcium mono-sulfo-aluminate hydrate.

$$Ca_6[Al(OH)_6]_2(SO_4)_3.26H_2O+2(CaO.Al_2O_3)+4H_2O \rightarrow 3(CaO.Al_2O_3.CaSO_4.12H_2O) \quad (2.13)$$

Step 3. Formation of secondary ettringite: When hydrated cement is placed in an environment containing high sulfate concentrations, as could be the case of many formations, the calcium mono-sulfo-aluminate hydrate and the calcium hydroxide present in the cement paste will react with the sulfate ions coming from the environment to form secondary ettringite.

$$3(CaO.Al_2O_3.CaSO_4.12H_2O) + 2(CaSO_4.2H_2O) +16\ H_2O \rightarrow 3(CaO.Al_2O_3.3CaSO_4.32H_2O) \quad (2.14)$$

The product of the final reaction, represented by Eq. (2.14), is ettringite, which is a crystal compound that contains 32 water molecules. Therefore, the formation of ettringite results in considerable expansion and volume growth. As the reaction takes place, the expansive products (mainly ettringite) begin filling the cement pores and under confined conditions generate internal pressure that causes cement cracking and strength loss (**Fig. 2.10**). Kutchko et al. (2011) also proposed a two-step mechanism for sulfate attack shown below:

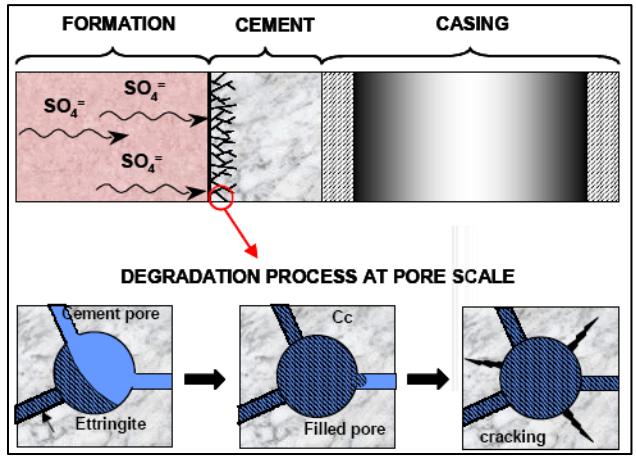

Fig. 2.10: Mechanism of sulfate attack of cement (Morales et al. 2003)

Step 1. Formation of Sulfate: Sulfur migrates into the cement and reacts with species of the cement pore solution to form sulfate via:

$$8Fe(OH)_{3(am)} + HS^- \leftrightarrow 8Fe^{2+} + SO_4^{2-} + 5H_2O + 15OH^- \quad (2.15)$$

Step 2. Formation of Ettringite: The stability of ettringite is strongly affected by the temperature, pH, and the activity of calcium. Even though reaction equation for ettringite formation varies with the reaction path and reactants present in the system, it can be approximated as follows:

$$6Ca^{2+} + 2Al(OH)_4^- + 4OH^- + 3SO_4^{2-} + 26H_2O \leftrightarrow Ca_6[Al(OH)_6]_2.(SO_4)_2.26H_2O \quad (2.16)$$

Morales et al (2003) used Eq. (2.17) to predict the degradation depth of sulfate attack. The sulfate effective diffusion coefficient (D_{eff}) can be determined by curve fitting the experimental results to the analytical solution of Fick's second law of diffusion. A semi-infinite diffusion process with a constant surface concentration (C_s) can be assumed. C_o is the bulk sulfate concentration.

$$C(X,t) = C_s - (C_s - C_o).\,\mathrm{erf}\left(\frac{X}{2\sqrt{D_{eff}t}}\right) \quad (2.17)$$

2.2.2.3. Cement Degradation in Mixed H_2S and CO_2 System

The mechanism of cement degradation in a system containing a mixture of H_2S and CO_2 is different from those occurring in pure gas systems. In pure H_2S system, the primary source of sulfate attack resulting from ettringite formation is the H_2S. However, in a mixed H_2S and CO_2 system, as the CO_2 follows H_2S penetration into the cement, the pH is lowered as carbonation progresses (pH < 12). Once the pH decreases approximately below 10.5, ettringite dissolve in the solution. As a result, ettringite crystals are not observed in the carbonated zone as they dissolve due to the lower pH (less than 10.5) of the pore fluid. In addition, ettringite crystals are highly soluble at temperature greater than 90°C and therefore are not observed in high-temperature experiments.

A laboratory study (Kutchko et al. 2011), conducted on cement exposed to pure CO_2 and mixed gas systems, showed the formation of the typical carbonation rim when cement was exposed to pure CO_2 system (**Fig. 2.11a**). In mixed gas system, a similar carbonation rim was formed (**Fig. 2.11b**). However, the samples displayed additional sequence of oxidation–reduction and sulfidation reactions. Ettringite and pyrite were formed in the interior region and carbonated rim of the samples, respectively. The pore water pH buffering is believed to have great impact on the mineralogical change occurring in the samples.

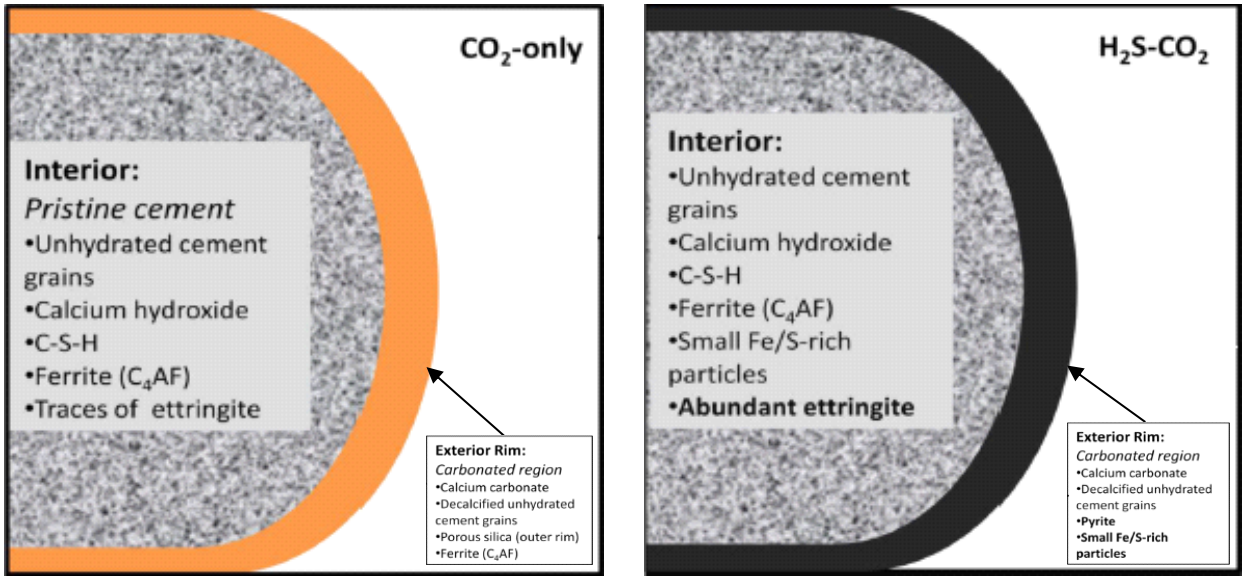

(a) (b)

Fig. 2.11: Cement samples aged in: a) pure CO_2; and b) H_2S-CO_2 system (Kutchko et al. 2011)

Temperature plays an important role on the cement sulfate attack. A decrease in the degree of sulfate attack was reported (Morales et al. 2003) with an increase in temperature, which has been supported by many authors. The reason of this observation is that the solubility of the ettringite increases with the increase in the temperature until it becomes completely soluble above 150°F. However, below this temperature, the cement paste should be improved to reduce the effect of the sulfate attack. According to Morales et al. (2003), the effect of sulfate attack can be reduced by decreasing the permeability using pore blocking additives such as latex, sodium silicate, or microsilica.

2.2.2.4. Cement Degradation involving Minor Cement Components

In presence of CO_2, hydrosulfuric acid reacts with minor components of cement to form pyrite, ettringite and gypsum. In this case, the degradation of cement by H_2S is minimal. However, the formation of these minerals may lead to expansion and development of microscopic cracks within the cement (Jacquemet et al. 2011; Kutchko et al. 2007; Krilov et al. 2000). The reaction pathway for formation of these minerals, their properties and the degradation mechanism of cement due to formation of these minerals is discussed here.

Pyrite Formation

Pyrite is one of the most common sulfide mineral with the chemical formula FeS_2. It is formed in cement when an iron atom, which is present within the cement matrix, reacts with two sulfur atoms provided by H_2S. Formation of pyrite was observed (Jacquemet et al. 2005 and 2011; Kutchko et al. 2011) in H_2S exposed cement samples. A study conducted on powdered Class G cement (Jacquemet et al. 2005) confirmed the formation of pyrite in the pore spaces created by dissolution of quartz and/or C_2S within matrix (**Fig. 2.12**). As shown by image analysis on SEM micrographs (Fig. 2.12), the mean proportion of pyrite was around 2% by volume.

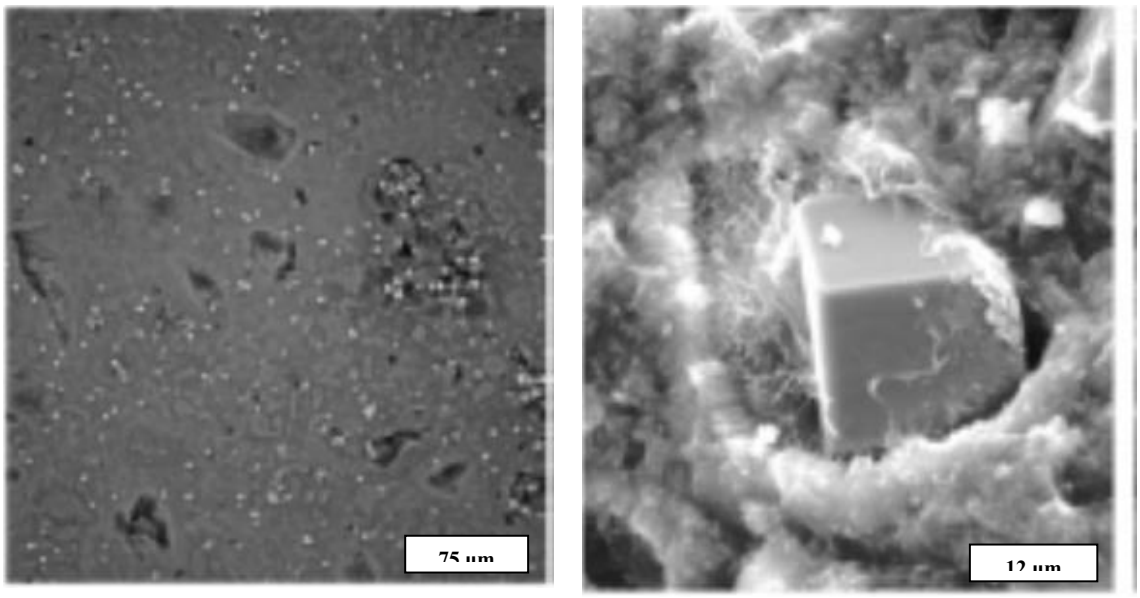

(a) **(b)**

Fig. 2.12: SEM observation of powdered Class G cement aged in H_2S and CO_2 saturated brine: a) Polished section showing pyrites as white minerals; b) Euhedral pyrite observed in cement sample (Jacquemet et al. 2005)

Laboratory experiments (Jacquemet et al. 2005) suggest the occurrence of a combined reaction involving cement carbonation and sulfidation. It is anticipated that calcium rich Tobermorite phase (Tobermorite 1) reacts with carbonic and hydrosulfuric acids to form calcium depleted Tobermorite phase (Tobermorite 2) along with formation of calcite and pyrite as describe in Eq. (2.18).

$$\mathrm{Tob1} + 0.1\,C_4AF + 0.6\,SiO_2 + 0.6\,H_2S + 1.6\,CO_2 + 0.2\,Fe \leftrightarrow \mathrm{Tob2} + 1.6\,CaCO_3 + 0.1\,FeS_2 + 0.2\,H_2 \quad \text{..... (2.18)}$$

where,

$\mathrm{Tob1} = Ca_{5.4}Si_{5.5}Al_{0.4}O_{16}(OH)_2.4H_2O$ ---------- (CSH gel)

$\mathrm{Tob2} = Ca_4Si_{6.1}Al_{0.5}O_{16}(OH)_2.4H_2O$ ---------- (Calcium depleted CSH gel)

The molar consumptions of H_2S and CO_2 during the experiments were 6% and 16%, respectively. The Fe in the above equation was provided by the steel. Thus, the H_2S consumption was essentially attributed to the sulfidation of steel. A different mechanism has been suggested by Kutchko et al. (2011) for the formation of pyrite. It is believed that hydrosulfuric acid reacts with hydration products, mainly C_4AF, to form pyrite and sulfate ions. When the pH of the pore solution is high, HS^- reduces Fe^{3+} to Fe^{2+} producing sulfate ions.

$$8Fe(OH)_3 + HS^- \leftrightarrow 8Fe^{2+} + SO_4{}^{2-} + 5H_2O + 15OH^- \quad (2.19)$$

The Fe^{2+} released by the reduction of $Fe(OH)_3$ reacts with HS^- to form pyrite via meta stable intermediate compound FeS (Rickard and Luther 1997). This pathway is also called the H_2S pathway. The reactions are as follows:

$$Fe^{2+} + HS^- \leftrightarrow FeS_{am} + H^+ \quad (2.20)$$

$$FeS + H_2S \leftrightarrow FeS_2 + H_2 \quad (2.21)$$

It is seen from the above equations that hydrogen is produced during the formation of pyrite via the H_2S pathway. In the experiments conducted to determine the reaction of carbonic and hydrosulfuric acids on Class G cement, hydrogen was identified as a byproduct in synthetic fluid inclusions and in residual gas (Jacquemet et al. 2011). Thus, it can be concluded that pyrite formation in cement is by the H_2S pathway. In addition to this mechanism, pyrite can be formed (Kutchko et al. 2011) through the polysulfide pathway as:

$$FeS + S_x^{2-} \leftrightarrow FeS_2 + S_{(x-1)}^{2-} \quad (2.22)$$

Reducing conditions favor the H_2S pathway whereas oxidizing conditions promote the polysulfide pathway (Rickard and Luther 1997). Studies (Jacquemet et al. 2011; Zhang et al. 2013) suggest that formation of pyrite in cement is not accompanied by any expansion or micro cracking and does not result in cement degradation. However, in the presence of oxygen and moisture, pyrite has the potential to oxidize and form ferrous sulfate and sulfuric acid. The free sulfuric acid may react with the calcite present to produce gypsum that tends to expand and crack the cement (Kutchko et al. 2011). Although this is one of the possible mechanisms for the deterioration of cement in H_2S environment, the mechanism and extent of degradation of cement due to pyrite formation is not fully understood.

Gypsum

It is widely believed that sulfate attack is mainly attributed to the formation of ettringite and the expansions related to the process. However, sulfate attack can also lead to mechanical damage due to the formation of gypsum (Planel et al. 2006; Wang 1994). When adequate supply of aluminate is no longer maintained in the solution, the formation of ettringite may cease and gypsum may precipitate (Mehta 1983). As stated earlier, continued removal of Ca^{2+} ions from the solution through gypsum

precipitation by SO_4^{2-} may result in further dissolution of CH. This eventually would lead to depletion of all the solid CH from the area. In such a scenario, decalcification of CSH may commence resulting in further cement degradation.

2.2.3. Effects of Environmental Parameters

When in contact with acidic fluid containing H_2S and CO_2, Portland cement degrades over a period of time, which results in loss of well integrity and zonal isolation. It is required to ensure long term integrity of cementing materials and safe continuation of operations.

2.2.3.1. Temperature Effect

Temperature can strongly affect the properties of oil well cement. The effect of temperature on the cement properties depends on the composition of the cement including calcium to silica ratio. At high temperature (greater than 230°F) and high calcium to silica ratio, the tobermorite phase (CSH) transforms into less stable α-C_2SH phase (dicalcium silicate hydrate), resulting in increased permeability and low compressive strength. This can be minimized by adding more silica to the cement and allowing more stable tobermorite to form. At higher temperatures (greater than 302°F), the tobermorite converts into xonotlite and/or gyrolite. This conversion improves the cement properties and its performance. The following equations summarize possible CSH high temperature transformations. At high calcium-to-silica ratios and temperature greater than 230°F:

$$CSH \rightarrow \alpha\text{-}C_2SH \quad (2.23)$$

At low calcium-to-silica ratios (i.e. cement containing more than 35% silica) and temperature between 230°Fand 302°F:

$$CSH \rightarrow \text{Tobermorite } (C_5\text{-}S_6\text{-}H_5) \quad (2.24)$$

At low calcium-to-silica ratios and temperature above 302°F:

$$\text{Tobermorite } (C_5\text{-}S_6\text{-}H_5) \rightarrow \text{Xonotlite } (C_6\text{-}S_6\text{-}H) \quad (2.25)$$

Noik and Rivereau (1999) presented compressive strength (**Fig. 2.13a**) and permeability (Fig. **2.13b**) measurements obtained from experiments conducted using silica-containing Class G cement. Tests were carried out at different temperatures (120, 140, and 180°C) and for periods of up to 2 years. Fig. 2.13a presents variations in compressive strength of the cement specimens as a function of time at three different temperatures. Data points are highly scattered. However, they apparently indicate the trend of the compressive strength. The results show mixed trends. For lower temperature tests (120 and 140°C), the compressive strength decreased with aging time as some of the CSH phase converted to more stable phase (α-C_2SH). For specimens aged at 180°C, the compressive strengths slightly increased indicating the transformation of tobermorite into xonotlite phase, which was confirmed by X-Ray Diffraction (XRD) and Nuclear Magnetic Resonance (NMR) methods.

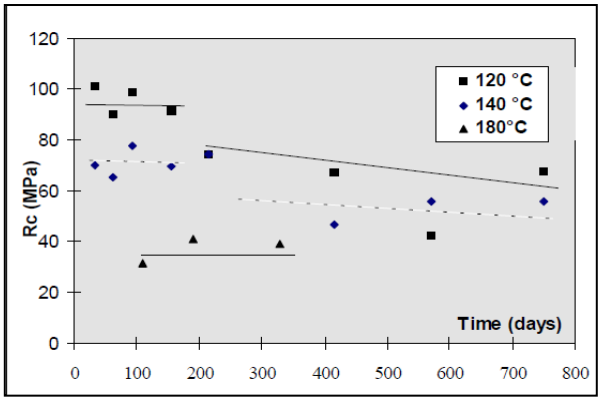

Fig. 2.13a: Compressive strength variation with temperature(Noik and Rivereau 1999)

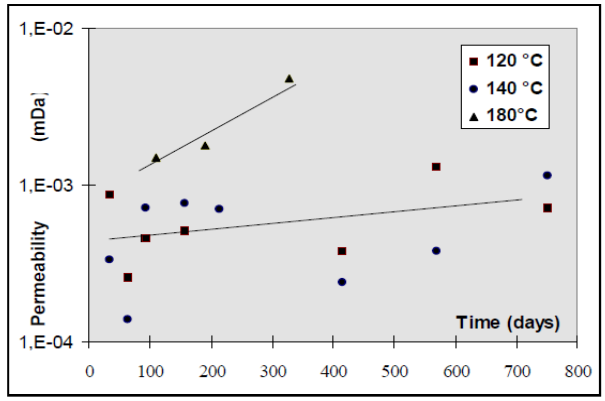

Fig. 2.13b: Permeability variation with temperature (Noik and Rivereau 1999)

Fig. 2.13b shows that the permeability change occurred during high temperature aging. Like the compressive strength measurements, permeability data points display high scattering. Lower temperature aging tests (120 and 140°C) showed slight increase in permeability. At 180°C, a substantial increase in permeability was observed, even though high temperature favors the formation of xonotlite phase. This contradicts the presumptions of other investigators (Brandl et al. 2010) that the formation of xonotlite phase enhances the sealing property of cement by reducing the cement permeability.

Compressive strength of cement can be affected by temperature and aging time. Short-term compressive strength of cement was studied by Dubois et al. (1999). Cement slurry formulations were prepared by adding 20 to 40% crushed sand and 10 to 30% silica fume to the neat cement. The results showed (**Fig. 2.14**) that the compressive strength slightly decreased as temperature was increased from 90 to 120°C, which is believed to be due to CSH phase transformation into a more stable α-C_2SH phase. However, at higher temperature (140°C), the compressive strength slightly increased with the aging time indicating the conversion of the tobermorite into xonotlite and/or gyrolite. Similar results (**Fig. 2.15**) have also been reported by Johnson and Garvin (1972). Cement aged at increased temperature showed a reduction in compressive strength. Additives such as bentonite have substantial influence on the temperature sensitivity of the cement. At temperature above 160°C, the compressive strength trend changes. This could be due to the conversion of tobermorite to xonotlite at higher temperatures.

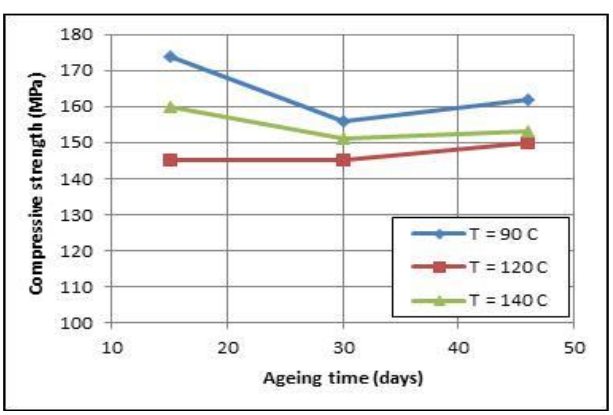

Fig. 2.14: Compressive strength vs. aging time at different temperatures (Dubois et al. 1999)

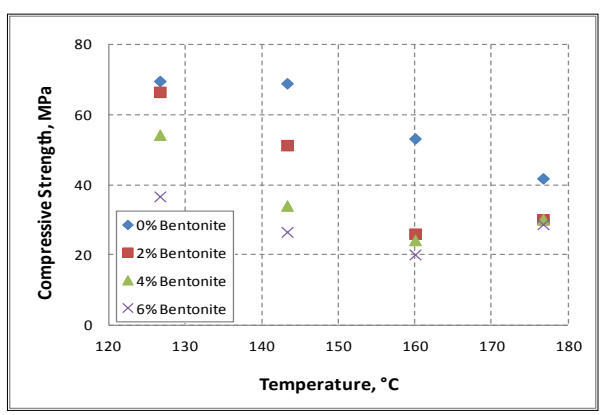

Fig. 2.15: Compressive strength vs. temperature after 28 days of aging (Johnson and Garvin 1972)

Thermal retrogression of cement greatly depends on its composition. Jennings (2005) experimentally investigated long-term permeability, shrinkage and compressive strength of different cement core samples exposed to high temperature and high-pressure environment. Three types of cement samples that are shown below were considered in the investigation.

- 72 PCF: 71-lbm/ft^3–hollow ceramic spheres (HCS) blend + fluid loss additives (0.15% by weight of blend: BWOB) + dispersant (0.06 gallon/sack) + retarder (0.025 gallon/sack) + anti-settling (0.15% BWOB) + defoamer (2 pt/10 bbls) and total mixing fluid at 8.80 gallon/sack.
- 101 PCF: 101 lbm/ft^3 – Class G (HSR) + pre-hydrated Bentonite (1.9% BWOC) + silica flour (35% BWOC) + fluid loss additives (0.60% BWOC) + dispersant (0.05 gallon/sack) + retarder (0.025 gal/sack) + defoamer (2 pt/10 bbls) at total mixing fluid of 11.47 gal/sack.
- 118 PCF: 118 lbm/ft^3 – Class G (HSR) + silica flour(35% BWOC) + fluid loss additives(0.60% BWOC) + dispersant(0.10 gal/sack) + retarder(0.03 gal/sack) + defoamer (1 pt/10 bbls) and total mixing fluid at 6.26 gal/sack.

Results show substantial increase in the permeability of samples (72 PCF and 101 PCF) that were made without adding silica flour (**Table 2.5**). The thermal retrogression appears to take place gradually with time (**Fig. 2.16**). The 118 PCF cement exhibited minimum permeability that decreased with aging. This observation is consistent with other similar studies (Brandl et al. 2010) conducted to examine high temperature degradation and/or retrogression of cement.

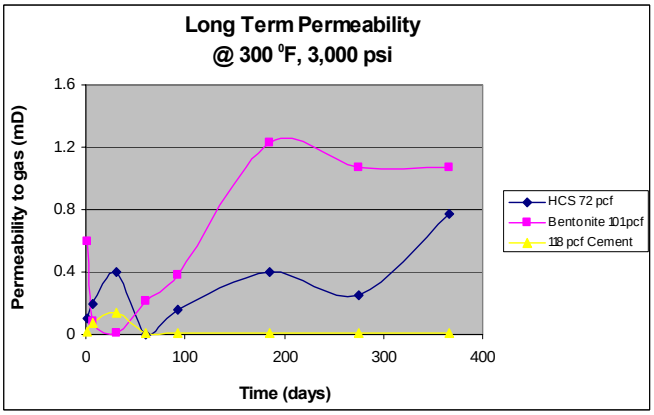

Fig. 2.16: Permeability of three different cement cores (Jennings 2005)

Table 2.5 Permeability change before and after aging the sample (Jennings 2005)

Cement Sample	Temp.	Pressure	Permeability (mD)	
			Before	After
72 PCF	300°F	3000 psi	0.10	0.77
101 PCF	300°F	3000 psi	0.60	1.07
118 PCF	300°F	3000 psi	0.02	0.01

2.2.3.2. Effects of pH on Oil Well Cement

When in contact with acidic aqueous solutions, H_3O^+ ions penetrate within cement matrix and dissolve solid hydration products. Experimental works have shown that the rate of acid attack depends on chemical composition of cement as well as pH of the acid solution. Dissolution of ferrite and aluminate phases and induced leaching of Fe^{3+} and Al^{3+} is slower and occurs at lower pH values than the carbonation and leaching of Ca^{2+} from the cement matrix. As pH decreases, portlandite with stability pH of 12.6, CSH with stability pH of 10 to 11, calcium aluminate and ferrite hydrates are successively dissolved (Lecoiler et al. 2006).

2.2.4. Acid Resistant (AR) Cement

2.2.4.1. Additives Used to Formulate AR Cement

Cement additives may not have direct effect on the nature of the cementitious material; however, they can delay or prevent acidic related degradation. A number of studies have been conducted to assess the benefits of different additives in improving acid resistance of well cement. A summary of the cement additive considered in these studies is presented in **Table 2.6**.

Table 2.6: Potential cement additives to formulate AR cement

Additive	Property	Studies	Its Effects on cement
Microsilica	Ultrafine pozzolanic substance which can fill up the pore space	Group 1	The micro-silica has been widely studied due to its pozzolanic reaction with CH group, it has the potential to protect the cement against carbonation.
Latex	Reduces the porosity and permeability of the set cement.	Group 2	It improves expansion tendency of the cement.
MgO and/ or Cao	Act as expanding additives	Group 3	Improve sealing performance. They are effective up to 392°F. The optimum concentration is 3-5%.
Calcium Hydroxyapatite or $Ca_5(OH)(PO_4)_3$	Incorporates CO_2 without altering the structure	Group 4	The addition of calcium hydroxyapatite can improve strength of the cement and CO_2 absorbing property.
Dolomite or $MgCO_3$	Thermally decomposes into $CaCO_3$ and MgO in the presence of CO_2.	Group 5	It helps in improving cement strength and reducing its porosity and permeability. However, with time it can cause cracking problems.
Amine Based Sorbent	$2RNH_2 + CO_2 + H_2O \leftrightarrow (RHN_3)_2CO_3$	Group 6	It is used as a sorbent for H_2S and CO_2 in oil refineries.
Zinc Oxide, ZnO	Cement retarder	Group 7	Reacts with H_2S
Fly ash	Cement filler	Group 8	Reduces portlandite and C-S-H contents of the cement

Group 1: Daou and Piot (2009); Grabowski and Gillott (1989); Sasaki et al. (1985); Shadizadeh et al. (2010); Shahriar (2011); Eilers and Root (1976); Eilers et al. (1983); Santra et al. (2009); Mueller and Dillinbeck (1991); Dillinbeck et al. (1990);
Group 2: Abdul Rahman et al. (1997); Jones and Carpenter (1991); Fuquan et al. (2006); Ray and Gupta (1994); Hou et al. (2010);
Group 3: Rubiandini et al. (2005); Zhang et al. (2011 and 2012); Nokken (2010); Ali and Mullick (1998); Ghofrani and Plack (1993); Agzamov et al. (2012), Buntoro and Rubiandini (2001); Cheung (1999); Mehta and Monteiro (2006);
Group 4: Sugama et al. (2006); Teraoka et al. (1998); Sugama and Carciello (1992 and 1993); Martin and Brown (1995);
Group 5: Hashimoto et al. (1980);
Group 6: Strazisar et al. (2009);
Group 7: Lecolier et al. (2008); and
Group 8: Santra et al. (2009).

Microsilica

Microsilica is a pozzolanic and amorphous material that has extremely fine particle size (less than 1 micron). Its chemical composition is similar to silica flour (SiO_2); however, it has smaller particle size than silica flour. Being a pozzolanic material, it has limited cementitious property unless mixed with

water in presence of calcium hydroxide. Because of its fine particle size and large surface area, extra water for hydration is required. The potential use of microsilica in Portland cement formulation has been previously studied (Eilers and Root 1976; Dillinbeck III et al. 1990; Eilers et al. 1983; Grabowski and Gillott 1989; Mueller and Dillinbeck 1991). Although it is able to fulfill the silica content requirement, the integrity and strength of the cement is a major issue in acidic environment. The studies revealed that microsilica can prevent degradation of cement by affecting rate as well as reducing the initial porosity and permeability. Hence, microsilica has been included in this study.

Latex

Latexes used as cement additives are colloidal solutions usually consisting of 50% by weight of small - spherical particles of polymer (0.01 to 1 µm) and 50% water. In order to obtain a stable colloidal mix, surface acting agents are added, which may lead to entrapment of air. Anti-foaming agents are usually added to the commercial latex to avoid this problem. The use of latex in well cements has been studied (Abdul-Rahman and Chong 1997; Fuquan et al. 2006; Hou et al. 2010; Zeng et al. 2012; Reddy et al. 2010; Jones and Carpenter 1991; Pavlock et al. 2012; Jennings et al. 2003) since early 90's. The prime advantage identified with the additive is that it controls fluid loss from the cement and prevents gas seepage. The studies suggested the use of latex in closely spaced reservoirs to prevent gas seepage between various zones (Jones and Carpenter 1991).

Among various kinds of latex available in the market, styrene butadiene is the most common latex used for construction and well cementing applications. It can be either anionic or neutral depending on the type of surfactant used. The latex is known to be highly sensitive towards temperature and mechanical effects (Abdul-Rahman and Chong 1997). With temperatures above 212°F, it is possible for the latex to flocculate and settle down (Fuquan et al. 2006). This limits the addition of latex in the oil well cement as an additive. By introducing a strong hydrophilic carboxyl ion (such as acetic acid, citric acid) the flocculation can be reduced inducing chemical stability (Hou et al. 2010). The mechanical stability needs to be taken care with respect to the mixing procedure. Large shear rates may lead to damage of the polymer and may cause entrapment of air bubbles. Due to its ability to prevent gas seepage and minimize fluid invasion, the latex cement has been selected in this study.

Latex-Microsilica

Another technique to utilize latex is to use it with microsilica. Although it has not been proposed for use in well cement, extensive studies (Rossignolo et al. 2003; Rossignolo and Agnesini 2002 and 2004; Rossignolo 2009), which were conducted on latex-microsilica, recommended it for construction purpose. Wan (2011) noted the use of latex and microsilica together in order to obtain a stronger matrix. Because of its ability to reduce gas migration and provide better cement bond, latex-microsilica cement formulation has been considered in this study.

Magnesium Oxide

Magnesium oxide is an expanding cement additive. Its expanding property has been studied (Zhang et al. 2012 and 2011; Nokken 2010; Ali and Mullick 1998; Ghofrani and Plack 1993; Agzamov et al. 2013; Rubiandini et al. 2005; Buntoro and Rubiandini 2001; Cheung 1999) extensively. As reported by Rubiandini et al. (2005), the use of magnesium oxide as an expanding additive in cement was proposed by Danjuschewskij (1983).

Magnesium oxide is industrially produced by calcining dolomite ($CaMg(CO_3)_2$). The temperature at which the calcination is performed defines the reactivity of magnesium oxide formed. Calcination above 1652°F tends to lower the reactivity and causes MgO to hydrate very slowly. MgO calcined at temperatures below 1652°F hydrate faster, causing expansion of cement in early stages. The calcination temperature for the magnesium oxide used in this investigation is approximately 2282°F.

The hydration of MgO basically involves formation of $Mg(OH)_2$ crystals, which occupy the pore space and provide swelling of the cement matrix (Rubiandini et al. 2005). Swelling or expansion is required to take place at the precise point of time during setting of the cement in the well and reduce its porosity and permeability. Expansion that occurs in the liquid slurry phase does affect the cement properties. Expansion after the complete setting causes cracking of the cement, which is highly undesirable. Hence, expansion needs to occur during the gelling or setting phase of the cement so that the porous space of the cement is effectively reduced (Ghofrani and Plack 1993).

Experimental results (Rubiandini et al. 2005) showed the expansion property of MgO and compressive and shear bond strength improvements obtained after its addition. The additives showed more expansion with increased calcination temperature. It was also observed that 3 – 5% BWOC MgO content was optimal to provide high compressive and shear bond strengths at temperatures above 482°F (Buntoro and Rubiandini 2001). Ghofrani and Plack (1993) also observed similar results with MgO when subjected to hydration.

Extensively documented properties of MgO are: i) the formation of $Mg(OH)_2$ crystals; ii) swelling of cement that helps in reducing porosity and permeability; and iii) improvement in compressive and shear bond strengths. Although $Mg(OH)_2$ undergoes carbonation to form $MgCO_3$, these crystals are insoluble in water. Hence, they do not easily leach out like calcium bicarbonate (Cheremisinoff 1995). These properties made MgO a suitable cement additive for HPHT applications. Despite a number of studies have been conducted on magnesium oxide, the full extent of its benefit is not well realized. This is because the level of expansion is highly dependent on number of factors including temperature, pressure, composition and properties of surrounding fluid, and composition of the cement sample. Hence, magnesium oxide, with calcination temperature of 2282°F, has been considered in this study.

Calcium Hydroxyapatite

Calcium hydroxyapatite (also known as hydroxyapatite) is a natural occurring mineral form of calcium apatite. The human bone structure is 50% composed of hydroxyapatite and it is often used for dental and orthopedic prostheses because of its biocompatibility (Teraoka et al. 1998). The use of hydroxyapatite-based cements in oil well was brought forward by the work performed at Brookhaven National Laboratory (Sugama 2006) through their CAP (calcium aluminate phosphate) cement project.

Limited studies were conducted to evaluate the performance of hydroxyapatite as a cement additive. It has been observed that after acid attack, the strength of hydroxyapatite-based (HOAP) cement reduces (Sugama and Carciello 1992, 1993; Martin and Brown 1995). Further, investigation is needed to study the performance of this additive. Hence, hydroxyapatite has been selected as potential additives in this study.

Dolomite

Dolomite thermally decomposes into $CaCO_3$ and MgO crystals when it is in contact with carbonic acid. Such reaction towards carbonic acid can help in protecting the cement against the acid attack. However, MgO and $CaCO_3$ crystals continue to grow with the reaction (Hashimoto et al. 1980). The growth of crystals results in cement expansion and cracks leading to a serious acid attack. Therefore, dolomite has not been considered in this study.

Amine Based Sorbents

Amine-based sorbents such as monoethanolamine (MEA), diethanolamine (DEA), methyldiethanolamine (MDEA), diisopropanolamine (DIPA) are used in refineries as sorbents to sweeten sour gases, (i.e. absorb CO_2 and H_2S). However, the procedure requires the sorbent in liquid form, and it is performed under highly controlled conditions in the refinery towers. Such level of precision is difficult to achieve under downhole conditions. Consequently, even though amine-based sorbents have capability to react with H_2S and CO_2, they might be difficult to incorporate in the well cements as additive; hence, they have not been considered in this study.

Zinc Oxide

Sasaoka et al. (1994) conducted an experimental study on the reaction between ZnO and H_2S under various conditions. The paper focused on use of ZnO as a sorbent for H_2S in solid-state fuel cells. One of the objectives was to examine the reaction in presence of water or carbon dioxide. In absence of water or carbon dioxide, formation of elemental sulfur was observed, which confirmed the catalytic decomposition of H_2S in presence of the sorbent ZnO. With inclusion of water in the system, the formation of elemental-sulfur was reduced. This was explained using two possible reasons. First, the active elemental-sulfur is reacting with water to form H_2S. Second, as water is a similar molecule to H_2S, a competitive adsorption of water could inhibit the reaction with H_2S. Hence, zinc oxide has been selected in this study.

Fly Ash

Incorporating pozzolanic fillers such as fly ash effectively decreases portlandite and C-S-H contents of cement thereby reducing the potential for the formation of calcium carbonate, which further reacts with the acid to form water-soluble calcium bicarbonate that can be easily leached out. To study the effects of filler materials on the carbonation process, Santra et al. (2009) conducted experiments with samples-containing different quantities of silica and fly ash. After aging for 15 days at 2000 psi and 200°F in the presence of fresh water saturated with CO_2, the samples were cut in half to examine visually the degree of penetration. The penetration depth was determined by examining different colors formed on carbonated and uncarbonated portions of the sample when phenolphthalein indicator was applied. The results showed that the addition of fly ash did improve the resistance of the cement against acid attack as reported by earlier studies (Garev et al. 2007 and Black et al. 2007). Fly ash has been considered in this study.

2.2.4.2. Carbonic Acid Resistant Cements

Recently, Santra and Sweatman (2011) reported the analysis of two different cement samples before and after the CO_2 treatment (i.e. water + supercritical CO_2). The two samples were: i) Cement sample A

– CO_2 resistant formulation; and ii) Neat Portland cement – Class G cement at 15.8 ppg density. They used the TGA method as a characterization tool. The TGA method is a type of testing performed on samples to determine the change in sample weight in relation to the temperature. **Figure 2.17a** shows the TGA results of the neat cement and System A before the CO_2 treatment. The peaks represent the initial amounts of portlandite. The portlandite amount is significantly less in system A than in the neat cement. **Figure 2.17b** shows the TGA results after the CO_2 treatment. The peak represents the amount of $CaCO_3$ formed. This shows that cement system A is a better option because it has less amount of the substance (portlandite i.e. $Ca(OH)_2$), which can react with CO_2 to form $CaCO_3$.

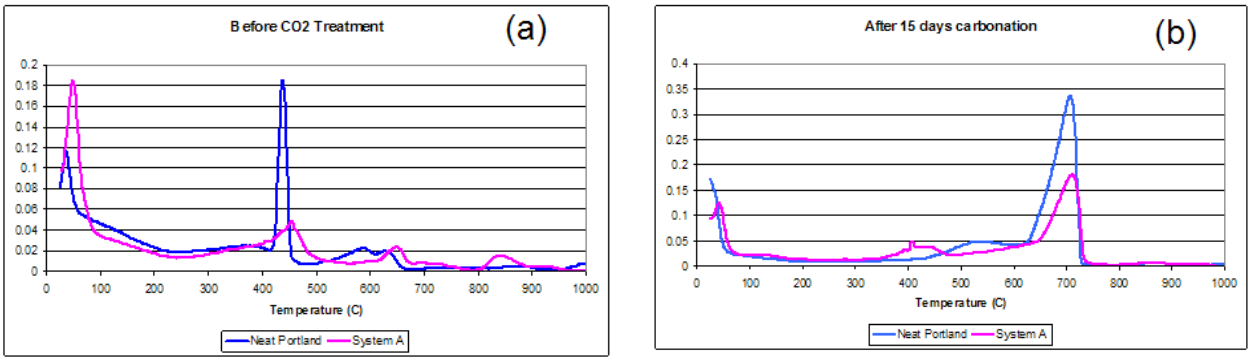

Fig. 2.17: Thermo-Gravimetric Analysis: a) before CO2 treatment; and b) after CO2 treatment (Santra and Sweatman 2011)

Table 2.7: Comparison of conventional and CO_2 resistant cement (Barlet-Gouédard et al. 2006)

Cement Sample	Temperature	Pressure	Porosity	Sample Size
Conventional Portland cement (class G, 1.89 g/cm^3, water/cement ratio equal to 0.44)	90°C [194°F]	28 MPa [4061 psi]	In wet supercritical CO_2, the porosity decreased continuously, from initially 33 to 15% after 6 weeks. In the first two days, it decreased rapidly from 33 to 27%, and then the decrease slowed down. In water-saturated with CO_2, the porosity decreased rapidly from 33 to 9% during the first three weeks. The carbonation front reached the center of the cores. After three weeks, the porosity increased from 9 to 21% in three more weeks.	0.5-inch-diameter x 1-inch (1.27-cm OD x 2.54-cm) and 1- inch-diameter x 2-inch (2.54-cm OD x 5.08-cm).
A new CO_2-resistant material	90°C [194°F]	28 MPa [4061 psi]	CO_2-resistant material remains stable from the first two days to a longer duration.	

After aging, the core samples were cut in half and examined using a microscope (**Fig. 2.18**). The aged cement cores displayed a particular geometry with concentric zones at different test durations on back-scattered electron images. From the core towards the rim of samples, the cement sample consisted of: i) uncarbonated zone; ii) dissolution front; iii) carbonation front; and iv) dissolution back-front. The uncarbonated zone is the inner part of the core, surrounded by the dissolution front. The dissolution front is a highly porous zone where CSH progressively dissolves. The carbonation front is a 50 to 100 µm-large zone of very low porosity. The dissolution back-front is located at the rear of the carbonation front. In this zone, neo-formed carbonates are dissolved, increasing the porosity and

resulting in severe degradation of the cement. In contrast, a homogeneous pattern with a limited carbonation threshold is observed with the CO_2-resistant material, which has good mechanical behavior over a wide density range. This material remains comparably inert in both wet supercritical CO_2 and water-saturated with CO_2. Weight, density, compressive strength, microstructural characterizations and high porosity measurements confirm good CO_2-resistance of the new cement.

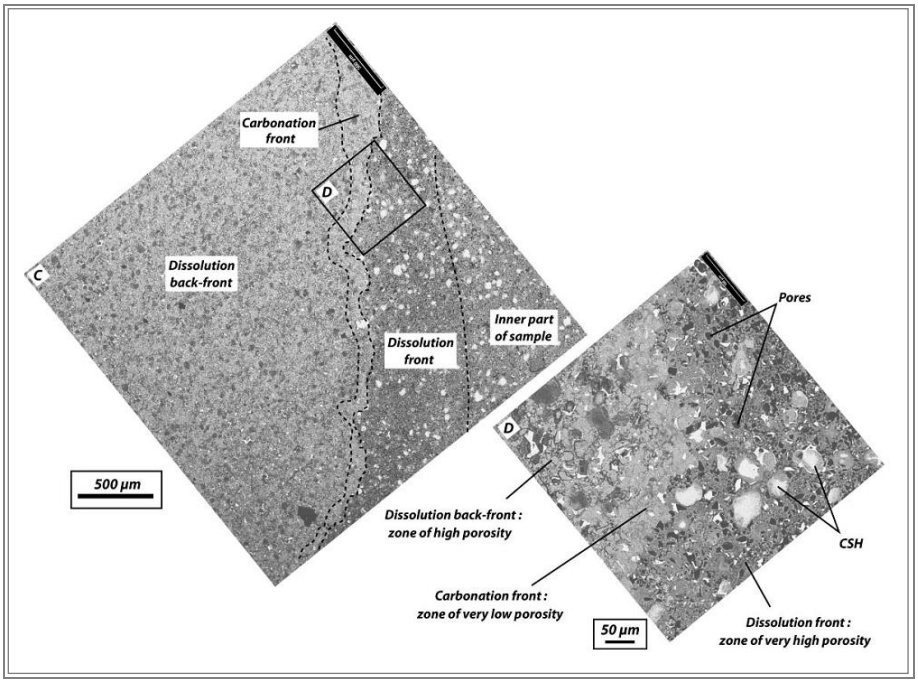

Fig. 2.18 Microscopic image of half-core sample after 88 hr aging in CO_2 in wet supercritical CO_2 fluid (Barlet-Gouédard et al. 2006)

Another similar study (Lécolier et al. 2006) considered different cement samples (silica containing cements, conventional cement, and mortar) and two types of aging fluids, namely: reservoir fluid and H_2S saturated brine. The permeability of cement samples containing silica decreased while the conventional cement showed a substantial increase in permeability. The reason for the increase in permeability is due to excessive calcium leaching (dissolution of portlandite and decalcification of CSH).

2.2.4.3. Hydrogen Sulfide Resistant Cements

When H_2S reacts with water, it forms a weak acid and lowers the pH. Portland cement reactive to acidic solutions and as a result it degrades when exposed to acidic fluids. It is important to understand the interactions of the acid and components of set cement that react with H_2S and the mechanisms of species transport in the porous cement thereby preventing the deterioration of cement.

In brine saturated with H_2S, the acid attack occurs when the H_3O^+ ions penetrate into the cement matrix and react with hydration products. Lécolier et al. (2006) studied durability of different cementing materials (silica containing cements, conventional cement, and mortar) in reservoir fluid and H_2S saturated brine containing 12.6% NaCl and 0.42% Na_2SO_4. All samples were cured at 80°C and 7 MPa. Aging was performed at 120°C and 15 MPa in non-agitated cell. Cement specimens (D = 1" and L = 2") were fully immersed in the brine solution. The ratio between the aging fluid and sample volume

was approximately 2. System pressure quickly reduced during the first hours when the H_2S gas dissolved in the liquid. The permeability of silica-containing samples decreased while the conventional cement showed a substantial increase in permeability. The reason for the permeability increase is attributed to excessive calcium leaching (dissolution of portlandite and decalcification of CSH).

Cement additives may not have direct effect on the nature of the cementitious material, but at the same time, they can prevent it from acidic degradation. The two metallic oxides proposed by Lecolier et al. (2008) that have a high affinity for H_2S are: i) Fe_2O_3 (Hematite); and ii) Mn_3O_4 (Hausmanite). Cement specimens containing these additives were tested by aging in H_2S-saturated saline water. Incorporating hematite leads to strong damaging of cement matrix due to acid reaction, resulting in total destruction (**Fig. 2.19a**); however, adding Mn_3O_4 showed encouraging results (**Fig. 2.19b**).

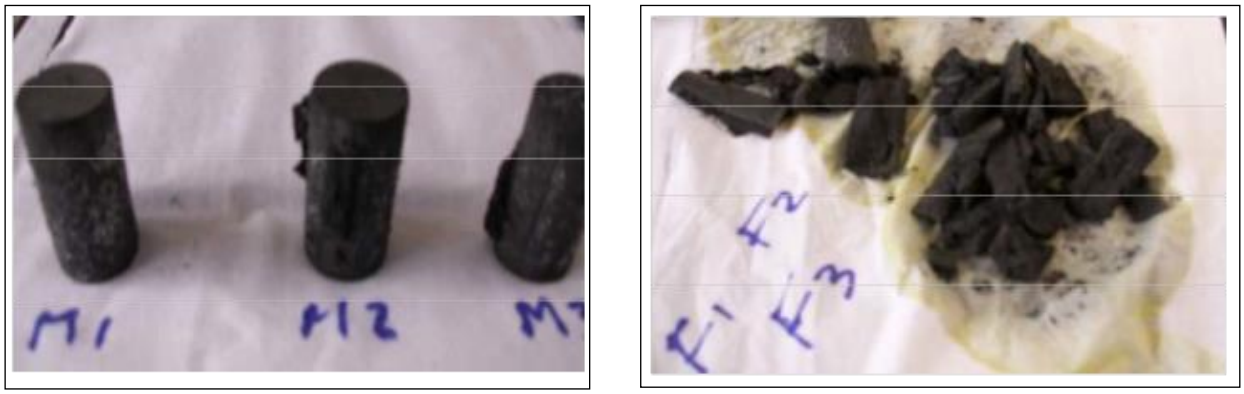

(a) (b)

Fig. 2.19 Cement specimens after one-week aging in H_2S-saturated saline water :a) 15% Mn_3O_4-Cement system; and ii) 30% Fe_2O_3-Cement (Lécolier et al. 2008)

The reaction of cement with H_2S in some cases results in production of expanding products that can generate micro-cracks in the system. These micro-cracks increase the porosity and permeability of the affected cement. However, in case of Mn_3O_4 based cement, there was no significant expansion noticed. Introducing Mn_3O_4 substantially reduced the adverse effect of H_2S but it could not 'completely' eliminate the degradation. In spite of these observations, another study (Jacquemet et al. 2005) conducted on crushed cement using mixture of H_2S and CO_2 showed the dominating effect of CO_2 on cement degradation. The mineralogy of aged and un-aged cement samples were analyzed using XRD method. The analysis showed reduction in tobermorite and ferrite contents. The residual gas analysis showed traces of H_2S and CO_2. The initial gas mixture composition was 66% H_2S and 34 mol% CO_2. The gases were consumed during the aging process and the initial concentration changed. The amount of consumed H_2S and CO_2 ranged from 1 to 15 mol% and 65 to 75 mol%, respectively. The H_2S attack was limited since the H_2S reactivity is only responsible for the sulfidation of ferrites (Ca_2AlFeO_5 or C_4AF) into pyrite (FeS).

2.3. Experimental Investigations

2.3.1. Test Matrix

Five test matrices (**Tables 2.8** to **2.11**) have been developed to examine the effects of pressure, temperature, CO_2 concentration and the presence of H_2S on the degradation behavior of well cements. Test parameters of the experiment are summarized in **Table 2.12**. Mechanical and physical properties (porosity, permeability, and compressive and bond strengths) of unaged and aged samples were measured to assess the level of degradation and performance of the new formulation.

Table 2.8a: Test Matrix 1- Studying the effect of CO_2 concentration at 100°F

Pressure/CO_2 Conc.	10% CO_2	40% CO_2	100% CO_2
6000 psi	Batch 008	Batch 011	Batch 012

Table 2.8b: Test Matrix 2 - Studying the effects of pressure and CO_2 concentration at 225°F

Pressure/CO_2 Conc.	10% CO_2	40% CO_2	100% CO_2
3000 psi	Batch 026	Batch 022	Batch 024
6000 psi	Batch 007	Batch 015	Batch 010
9000 psi	Batch 027	Batch 023	Batch 025

Table 2.8c: Test Matrix 3 - Studying the effects of pressure and CO_2 concentration at 350°F

Pressure/CO_2 Conc.	10% CO_2	40% CO_2	100% CO_2
3000 psi	Batch 020	Batch 016	Batch 018
6000 psi	Batch 006	Batch 013	Batch 014
9000 psi	Batch 021	Batch 017	Batch 019

Table 2.8d: Test Matrix 4 - Studying the effects of pressure and CO_2 concentration at 430°F

Pressure/CO_2 Conc.	10% CO_2	40% CO_2	100% CO_2
3000 psi	-	-	Batch 031
6000 psi	Batch 028	Batch 029	Batch 030
9000 psi	-	-	Batch 032

Table 2.9: Test Matrix 5 - Studying the effects of pressure, H_2S and CO_2 concentration at 100°F

Pressure/CO_2 Conc.	0% CO_2	10% CO_2	40% CO_2
3000 psi	Batch 041	-	
6000 psi	Batch 036	Batch 033	Batch 037
9000 psi	Batch 038	Batch 039	Batch 040

Table 2.10: Test Matrix 6- Studying the effect of H_2S concentration at 6000 psi

CO_2 Conc./Temp	100°F	225°F	350°F
10% CO_2	Batch 008	Batch 011	Batch 012

Table 2.11: Test Matrix 7 - Studying the effects of pressure and temperature at 100% CH4

Pressure/Temp.	225°F	350°F	430°F
3000 psi			Batch 031
6000 psi		Batch 002/003	Batch 030
9000 psi		Batch 001	Batch 032

Table 2.12: Test parameters for aging experiments conducted to date

Batch #	Temp. (ºF)	Pressure (psi)	Concentration %			Brine (%)	Aging Period (days)	Exp. #	Additive Batch #
			CH_4 (%)	CO_2 (%)	H_2S (ppm)				
001	350	9000	100	0	0	9	6	1	001-FLAS
002	350	6000	100	0	0	2	14 & 28	2	002-FLAS
003	350	6000	100	0	0	2	14		003-FLAS
004	350	6000	90	10	0	2	6	3	004-FLAS
005	350	6000	90	10	0	2	14 & 28	4	005-FLAS
006	350	6000	90	10	0	2	14		006-FLAS
007	225	6000	90	10	0	2	14	5	
008	100	6000	90	10	0	2	14	6	
009	225	6000	60	40	0	2	14	7	
010	225	6000	0	100	0	2	14	8	002-MGO
011	100	6000	60	40	0	2	14	9	002-HOAP
012	100	6000	0	100	0	2	14	10	003-MGO
013	350	6000	60	40	0	2	14	11	004-LT
014	350	6000	0	100	0	2	14	12	003-HOAP
015	225	6000	60	40	0	2	14	7A	004-MGO
016	350	3000	60	40	0	2	14	13	004-HOAP
017	350	9000	60	40	0	2	14	14	005-MGO
018	350	3000	0	100	0	2	14	15	005-HOAP
019	350	9000	0	100	0	2	14	16	
020	350	3000	90	10	0	2	14	17	005-MS-10
021	350	9000	90	10	0	2	14	18	006-MS-10
022	225	3000	60	40	0	2	14	19	006-HOAP
023	225	9000	60	40	0	2	14	20	006-MGO
024	225	3000	0	100	0	2	14	21	008-MS-10
025	225	9000	0	100	0	2	14	22	007-MGO
026	225	3000	90	10	0	2	14	23	007-HOAP
027	225	9000	90	10	0	2	14	24	002-LTMS
028	430	6000	90	10	0	2	14	25	009 – MS-10
029	430	6000	60	40	0	2	14	26	010 – MS-10
030	430	6000	100	0	0	2	14	27	003 - LTMS
031	430	3000	100	0	0	2	14	28	004 - LTMS
032	430	9000	100	0	0	2	14	29	008 - HOAP
033	100	6000	90	10	300	2	14	30	009 - HOAP
034	225	6000	90	10	300	2	14	31	008 - MGO
035	350	6000	90	10	300	2	14	32	010 - HOAP
036	100	6000	100	0	300	2	14	33	011 - HOAP
037	100	6000	60	40	180	2	14	34	010 - MGO
038	100	9000	100	0	300	2	14	35	012 - HOAP
039	100	9000	90	10	300	2	14	36	011 - MGO
040	100	9000	60	40	180	2	14	37	013 - HOAP
041	100	3000	100	0	300	2	14	38	012 - MGO

2.3.2. Test Materials

In order to prepare baseline cement slurries, standard API cement formulation for high-temperature application was used. Accordingly, cement slurries containing cement, water, silica flour, antifoam Agent and Hydroxy-Ethyl-Cellulose (HEC) went prepared. A brief discussion of materials used in slurry preparation and their specific role is presented here.

Water: Reaction of dry cement with water results in the hydration of cement. The amount of water to be added is dependent on the cement class. According to API 10A specification, the water requirement for Class H cement is 38% by weight of cement (BWOC) and for Class G cement, it is 44% BWOC. Addition of other components, such as silica flour to the slurry will increase the total water requirement. In this research, tap water was used for hydration of cement.

Silica Flour: CSH gel is the major component of hydrated cement. It was observed in several studies that during hydration of cement approximately above 230°F, C/S (CaO/SiO_2) ratio of greater than 1 result in the formation of di-calcium silicate hydrate (α-C_2SH), which has low compressive strength. On the other hand, a low C/S ratio warrants the formation of high-compressive-strength CSH (tobermorite gel) that has low porosity and permeability (Grabowski and Gillott 1989; Eilers et al. 1976 and 1983; Lea 1971). Thus, in order to maintain the C/S ratio below 1, 35% BWOC of silica flour was added. The increased quantity of silica resulted in increased water requirement of cement (38.5% by weight of silica flour).

HEC: 0.1% Hydroxy-Ethyl-Cellulose, a natural polymer, was added during preparation of slurry to reduce the fluid loss from the cement.

Antifoam Agent: Cement antifoamer is used to prevent the formation of foam during blending of cement slurry; thus, preventing the formation and entrapment of air within the cement. The antifoamer helps to maintain slurry density within the desired range.

2.3.3 Test Equipment

Degradation of cement significantly changes its property and performance. In order to assess the degradation of cement occurring after exposure to acidic environment, different tests were conducted to measure the change in physical, chemical and mineralogical properties of samples. The measurements include compressive and bonding strength, porosity, permeability, mineralogy, and microscopic properties.

2.3.3.1. Compressive and Bonding Strength Measurement Techniques

Mechanical properties such as compressive and bonding strengths are very important characteristics of oil well cement. **Figure 2.20** shows schematic of experimental setup developed to measure bonding and confining compressive strengths of cement. The setup (**Fig. 2.21**) consists of : i) confining cell; ii) power cylinders to apply compression force on the specimens; iii) air-operating pump to develop the confining pressure; iv) syringe pump to supply hydraulic power to the cylinders; v) supporting frame to hold the bonding test samples in place; and vi) instrumentation and data acquisition (DAQ) system.

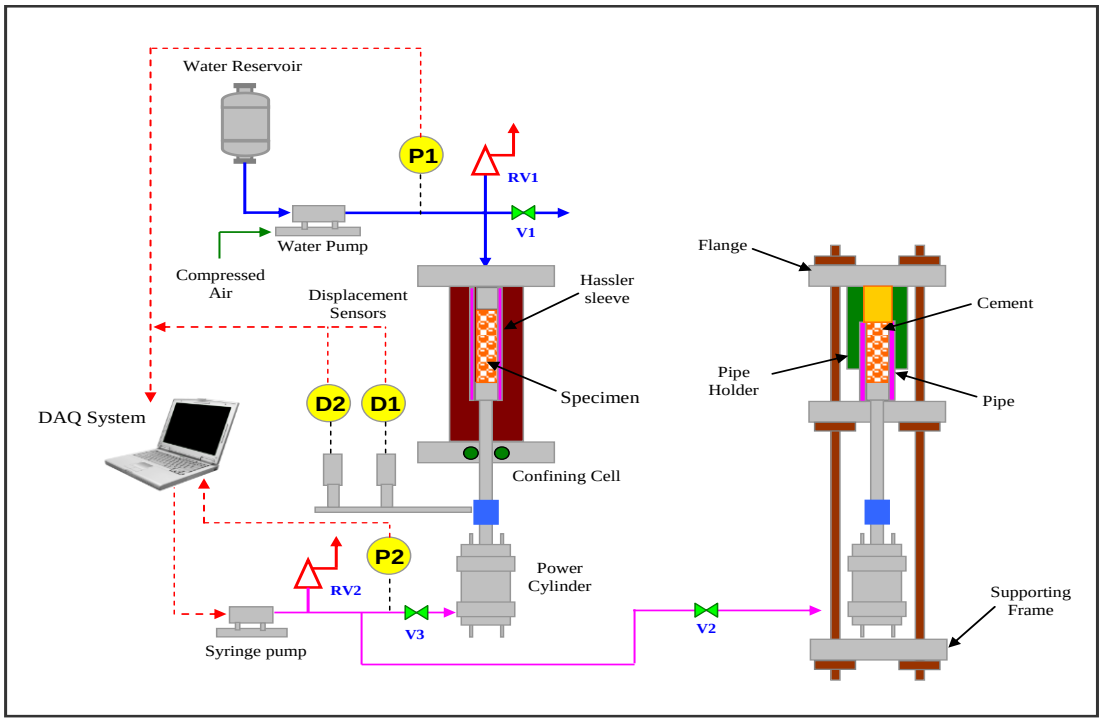

Fig. 2.20: Test setup for measuring compressive and bonding strength of cement samples

Fig. 2.21: Compressive and bond strength measurement setup

The confining cylinder has a shaft with a specimen holder that is connected to the power cylinder. High accuracy displacement sensors that are attached to the shaft measures the level of strain developed in the specimen. During the test, the cement sample is placed in the Hassler sleeve and

mounted on the plunger attached to the cylinder shaft. Then, the plunger on cylinder lid is inserted into the Hassler sleeve and the lid is pressed to seal completely the cylinder. After screwing and tightening the lid holder on the cylinder, the confining pressure is increased using the water injection pump. Subsequently, the syringe pump is started to apply compression force on the sample. As the sample compresses, the displacement sensors measure the movement of the plunger or piston rod at the shaft coupling. At a constant pump rate, the compressive force developed in the sample (i.e. stress load) increases with time. The DAQ system controls the speed of the syringe pump to maintain a constant stress-loading rate. The sample is compressed and deformed until a complete mechanical failure occurs. During the test, the DAQ system display and records all the measurements.

For compressive strength tests, the confining pressure was maintained at 1000 psi. Stress loading rate in the final stage of the test was kept in the range of 28 to 42 psi/second as required by ASTM standard C39-C39M-12. Speed of motor was adjusted based on the measured stress-loading rate using the DAQ system. **Figures 2.22a** and **2.22b** show examples of loading rates and compressive and bonding stresses monitored during the test for class G and class H cement samples containing 35% silica.

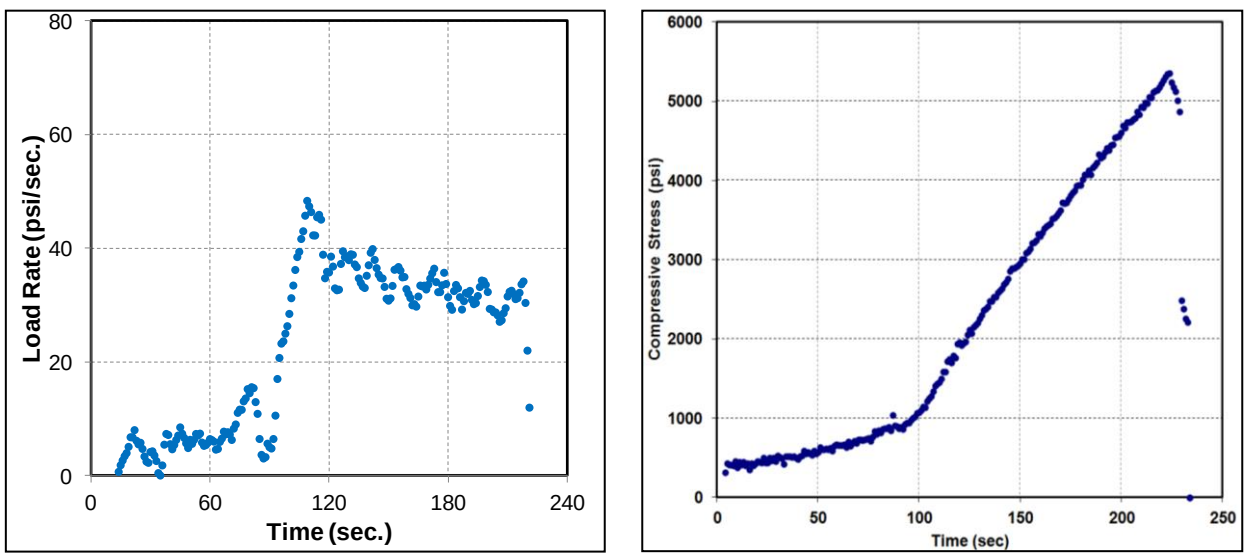

(a) (b)

Fig. 2.22: Compressive strength test measurements: a) Load rate vs. time; and b) Stress vs. time

The bonding strengths of cement samples were measured using the setup developed for measuring compressive strength (Fig. 2.21). The setup has supporting frame with a power cylinder and sliding flanges to hold the sample. The power cylinder is attached to the supporting frame that keeps a bonding sample and its holder in place. To perform the test, the sample (short pipe together with hardened cement) is placed on a plunger coupled with the piston rod. Then, the sample holder (pipe holder) and the supporting flange are placed on the top of the sample and secured using four bolts. The test begins when the syringe pump is turned on to apply the force on the sample using the plunger. At a constant pump rate (i.e. plunger velocity), the applied force increases with time. The DAQ system is set to control the speed of the syringe pump to maintain roughly a constant bonding shear stress loading rate of 20 psi/second. The test is stopped when abrupt reduction in the shear stress is observed.

The shear bond strength of cement indicates the force required to break the bond between cement and casing. Test specimens were prepared by casting cement slurry into a 1-inch diameter carbon steel pipe (**Fig. 2.23**) that has a length of 1.5". One piece of a long 1-inch diameter seamless steel pipe was cut to small pieces (1.5" length) to have an identical pipe surface roughness in all the bonding samples. Once the slurry was set in the pipe, the specimen were cured and then placed in the aging cell. The maximum pressure developed by the syringe pump during the test was used to determine the shear bond strength.

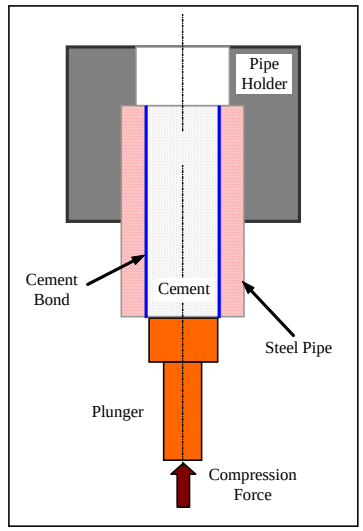

Fig. 2.23: Shear bonding test sample and pipe holder

2.3.3.2. Porosity and permeability

In order to measure the permeability and porosity, cement slurries were cured for 5 days; and then cored and sanded from both sides (bottom and top). To measure porosity and permeability, the specimens were first placed in an oven for 24 hours to dry at 110°F. Porosity and permeability of the dried specimens were measured using a fully automated Porosimeter-Permeameter (CSI Model AP-608). The equipment (**Fig. 2.24**) was calibrated and leak-tested to obtain reliable and accurate measurements.

The apparatus uses unsteady state method to determine the permeability. It provides both gas and klinkenberg corrected liquid permeabilities. Two different gases (helium and nitrogen) were used for these measurements. Nitrogen was used for measuring permeability. Porosity measurements were conducted using helium. In these experiments, the confining pressure was maintained at 500 psi. Tests were performed maintaining differential pressure of 200 psi.

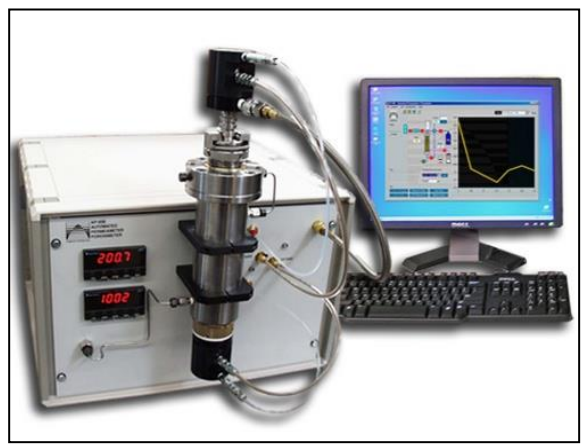

Fig. 2.24: Automated Porosimeter-Permeameter (AP-608)

2.3.3.3. FTIR Mineralogy

Fourier transform infrared spectroscopy (FTIR) analysis was conducted to examine mineralogical changes occurring during degradation. The analysis was performed using an optical spectrometer (Thermo Scientific Model Nicolet 6700) shown in **Fig. 2.25**.

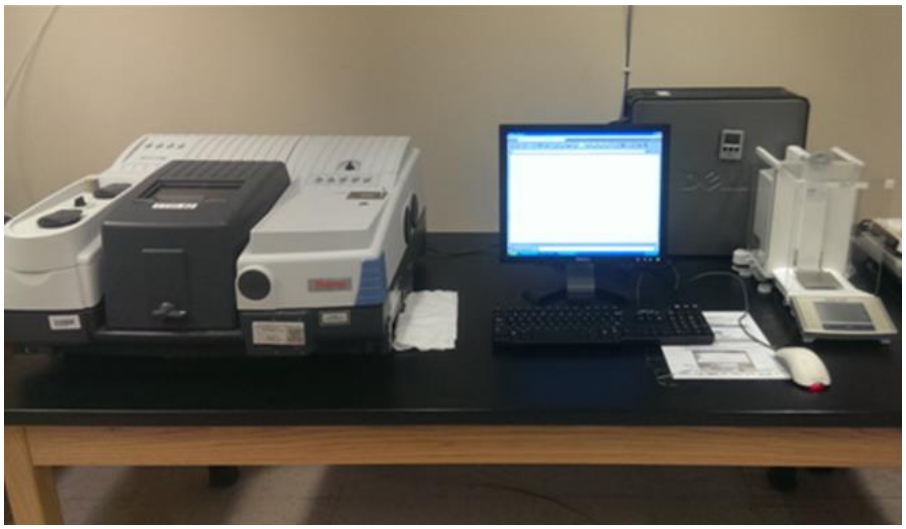

Fig. 2.25: FTIR Equipment (Thermo Scientific Model Nicolet 6700)

2.3.3.4. SEM Imaging

Scanning electron microscope (SEM) imaging was performed using FEI equipment shown in **Fig. 2.26**. The imaging was conducted to observe degree of hydration, distribution of CH, CSH and $CaCO_3$ particles and different degradation zones such as the virgin zone, carbonate zone and the leaching front.

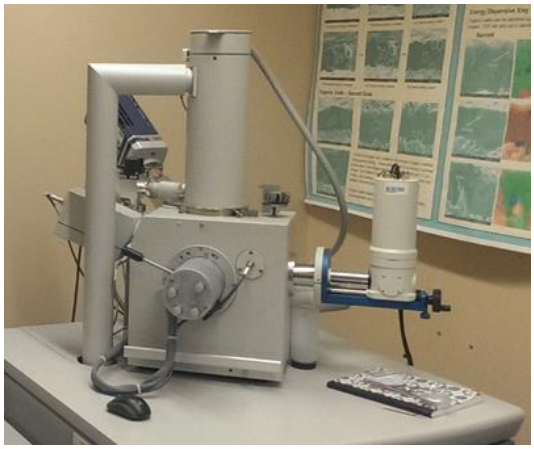

Fig. 2.26: SEM equipment

2.3.3.5. Cement Consistometer

CTE Model 200 atmospheric consist-o-meter (**Fig. 2.27**) was used to measure the consistency and subsequently the thickening time of the slurries at 135°F. Although this temperature is less than the down-hole conditions, to which the cement is going to perform, it serves to compare the additive slurry with the baseline. The additive slurry should have thickening time similar to baseline slurry with maximum difference of 50 minutes. The consistency curve usually has exponential trend as shown in **Fig. 2.31**.

Fig. 2.27: CTE Model 200 atmospheric consist-o-meter

2.3.3.6. Rotational viscometer

Cement slurry rheology is extremely important characteristics of the fluid, which needs to be optimized. As the focus of the current work was not rheology; hence, it was essential for the slurry to have flow-ability rather than optimal rheological parameters. The rheological properties of the slurries were measured using the OFITE Model 900 viscometer (**Fig. 2.28**). The measurements were obtained as per the API standards (R1B1 bob and spindle geometry with spring factor = 1). Tests were performed under ambient room temperature, varying the rotor speed from 3 to 300 RPM.

Fig. 2.28: OFITE Model 900 viscometer

2.3.3.7. Filter Press

Industry standard low-pressure filter press (OFITE Model 142-53) was used to perform filter loss tests. The press (**Fig. 2.29**) has a cell body to hold slurry sample, a pressure inlet for pressurization, a base cap with screen and filter paper to simulate permeable formation, CO_2 charger to pressurize the sample and pressure regulator to accurately control the cell pressure.

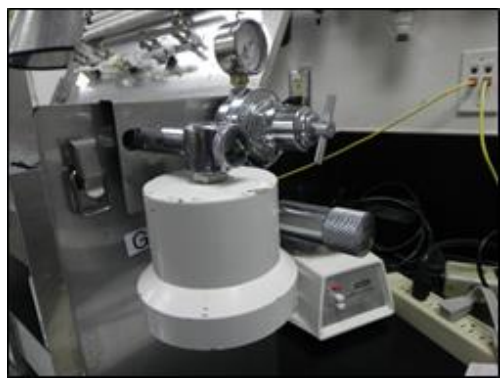

Fig. 2.29: Low-pressure filter press

2.3.3.8. Cement Blender

Cement slurry was prepared as per API RP 10B procedure. The API procedure requires using a special high-speed mixer with 4,000 and 12,000 rpm preset speeds. API standard blender (Grace Model M3080 Variable Speed Mixer) was used to prepare cement slurries. The blender allows automatic mixing sequences, which are exactly configured to meet the API speed requirements for cement slurries.

2.3.3.9. Mud Balance

The actual slurry density was measured using the standard atmospheric mud balance, which is commonly used in the field. It was imperative to have the density of additive slurry and baseline slurry close to each other so that the set cement properties can be compared. Higher density slurry has the ability to form a less porous matrix and vice-versa. If the density of additive slurry is considerably higher than the baseline slurry, the matrix structure substantially changes and the effect of additive cannot be properly assessed. Hence, theoretical densities of additive and baseline slurries (using ideal calculations) were approximately matched so that actual densities remain in the same order.

2.3.4. Cement Slurry Preparation Procedure

2.3.4.1. Slurry Formulations

Compositions of the baseline slurries are presented in **Table 2.13**. Class H and Class G cements were tested as they are the most widely used cements in the industry due to their applicability for wide range of temperatures and depth with use of additives. In order to prevent thermal retrogression at high temperatures (> 230°F), silica flour was added to the cement slurry. Hydroxyethyl cellulose (HEC) was used to control fluid loss and prevent lumping of cement particles. Anti-foamer was used to minimize the entrapment of air in the cement slurry during slurry preparation.

Table 2.13: Compositions of the baseline slurries

Materials	Amount	
	Class H (HSR)	Class G (HSR)
Cement	100% BWOC	100% BWOC
Silica Flour	35% BWOC	35% BWOC
HEC	0.1% of water for Silica	0.1% of water for Silica
Anti-Foaming Agent	0.1 gal/sk of cement	0.1 gal/sk of cement
Water for Cement	38% BWOC	44% BWOC
Water for Silica Flour	38.5% BWOC	38.5% BWOC

* BWOC = by weight of cement

2.3.4.2. Mixing

The quantity of cement, water and other components required to prepare the desired volume of slurry were calculated considering the ideal mixing case. API standard specification was followed during the preparation of the slurries. Cement mixer (M/S Grace, Model M3080) with 1-liter capacity and an API standard blade was used. Slurries were mixed using two speeds. First, the agitator speed was maintained at 4,000 rpm while water, cement powder and additives were mixed for at least 15 seconds. Subsequently, the lid was placed on the top of the mixer and the speed was increased to 12,000 rpm and run for additional 35 seconds.

2.3.4.3. Slurry Properties

After the preparation of cement slurries, there properties such as density, rheology, filtration loss and thickening time were to measure. The properties of baseline slurries are presented in (**Table 2.14**). One of the objectives of the study was to determine the effect of use of specialized additives to prevent or delay acid attack. In order to assess correctly the effect of additives, properties of additive slurries were approximately matched to those of the baseline slurries.

Table 2.14: Properties of baseline slurries

Property	Class H Value	Class G Value
Measured Density	16.20 ppg	15.45 ppg
Filtration Loss at 7.5 min.	50 ml	60 ml
Rheological Properties	Power Law Fluid n = 0.44 K = 14.4 lbf.s^n/100ft2	Power Law Fluid n = 0.35 K = 10.5 lbf.s^n/100ft2
Thickening Time	170 min.	135 min.

Density: The slurry density was measured using the standard atmospheric OFITE mud-balance used in the oilfield. As density also affects rate and extent of cement degradation, the density of additive slurry was adjusted to that of baseline slurry.

Rheology: The rheological properties of the slurries were measured as per the API standards using the OFITE Model 900 Viscometer to verify its flowability. **Figure 2.30** presents the rheological measurements for baseline slurries of Class H and Class G cements. Both the slurries follow approximately Power Law model with n and K values presented in Table 2.14.

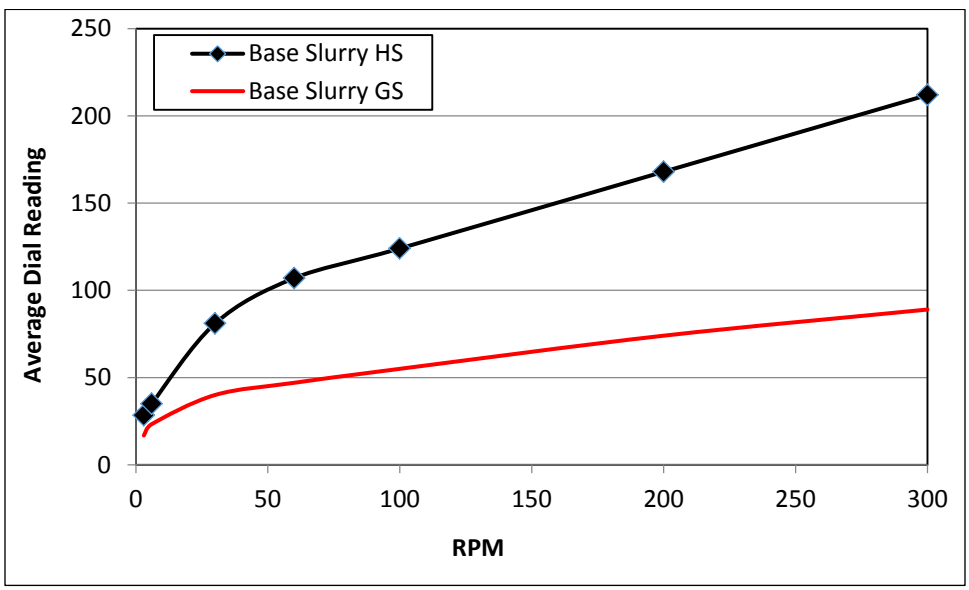

Fig. 2.30: Rheological reading for base slurries of Class G and H

Filtration Loss: The filtration loss of the slurry was measured using OFITE Portable Fluid Loss Apparatus at 100 psi and ambient temperature. The fluid loss of additive slurry was adjusted to a value comparable to that of the baseline slurry using fluid-loss control agents.

Thickening Time: The measurement of the unit for thickening time defined by API is Bearden units of consistency, Bc. Thickening time cement slurry is defined as the time taken for the slurry to reach Bc value of 100. Above 100, the slurry is expected to be very thick and may not be pumped. The thickening

time of the slurries was measured using an atmospheric consist-o-meter (CTE Model 200) at 135°F. Fig. 2.31 presents the consist-o-meter readings for both class H and G slurries.

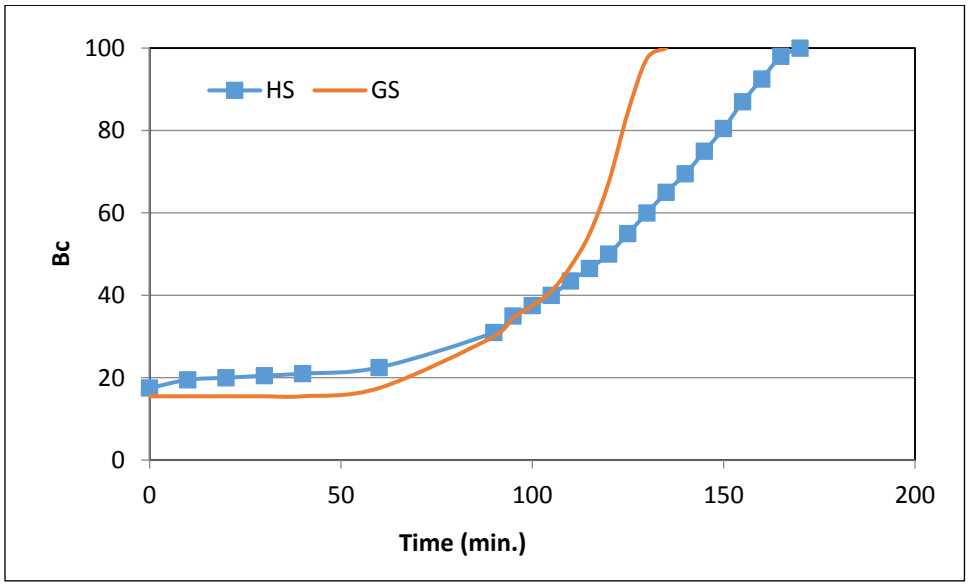

Fig. 2.31: Consist-o-meter reading for base slurries of class G and H

2.3.5. Test Sample Preparation Procedures

The slurry was then poured into a mold and kept in a 2% brine-filled autoclave to cure. In order to cure the samples at elevated temperature, the cooker was kept in an oven at 200°F for 5 days (120 hrs.). After 5 days, the cement was taken out of the mold and cylindrical cores (1" OD X 1.5" long) were cut. These cores were kept in an aging cell filled with 2% brine, for 14 days at various experimental conditions of temperatures, pressures and CO_2 concentrations.

Figure 2.32 describes the nomenclature (sample identification code) used for describing the samples. The first term of the sample nomenclature corresponds to the batch number while the second term describes the class of cement used (Class G and Class H). The presence of S in the second term indicates the use of silica flour. For samples with additive, two letters representing the additive used are also added to the second term. Aging locations of the aged samples are represented by the shelf number on which they were placed in the aging cell. If the samples are unaged the code is '00'. As each shelf can house 5 samples, the next term indicates the count of samples from '01' to '05'.

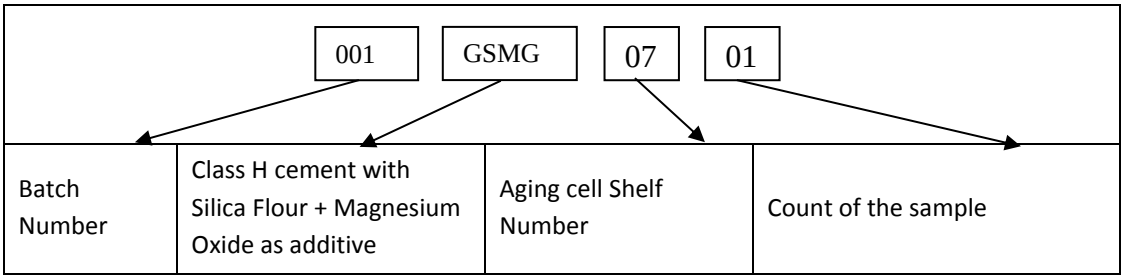

Fig. 2.32: Nomenclature of the samples

Totally seventy samples were prepared for each batch of cement degradation experiment. A flow chart representing sample size distribution is presented in **Fig. 2.33**. The samples were used to assess degradation occurring after exposure to acidic environment in the aging cell. The degradation was evaluated based on change in porosity, permeability, compressive strengths and shear bond strengths. For each batch of experiment, 4 aged and 4 unaged samples were used to measure porosity and permeability of the cores. Similarly, 12 unaged and 24 aged samples were used to determine compressive strength of the cores.

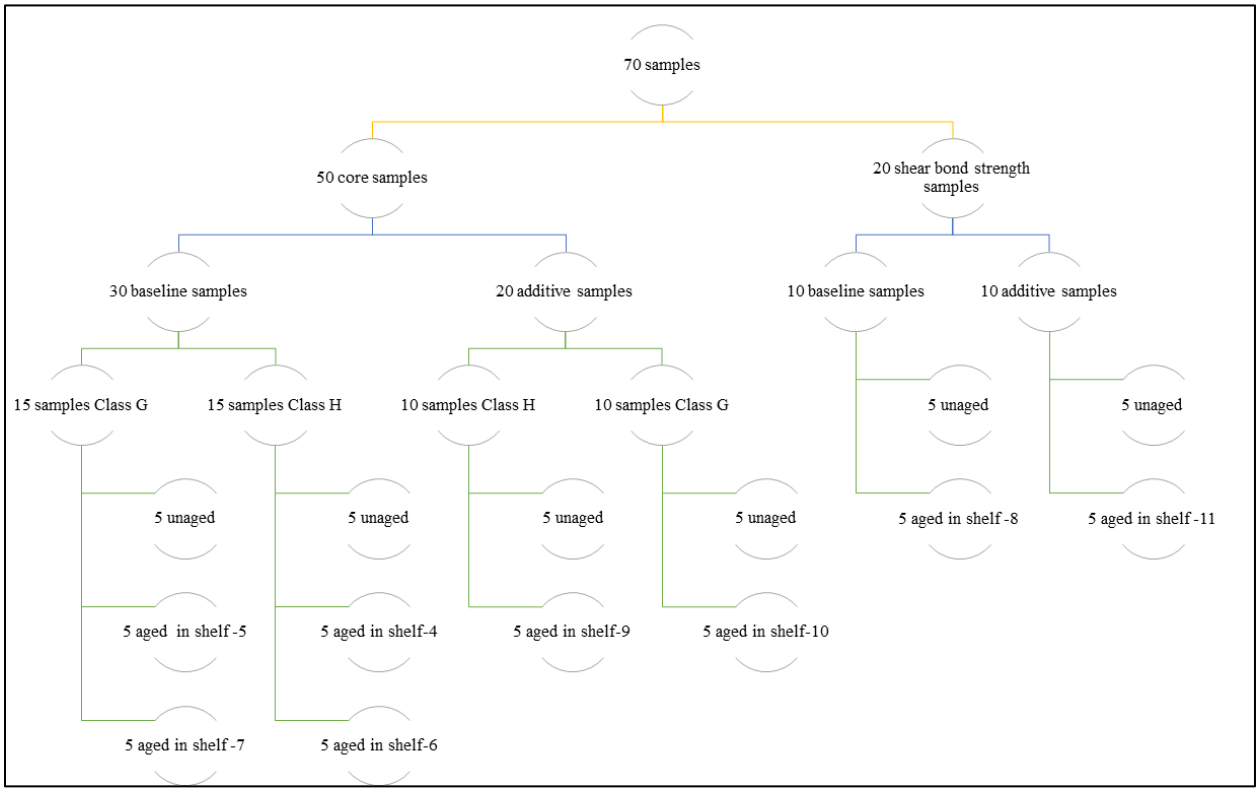

Fig. 2.33: Sample size distribution for aging cell experiments

2.3.5.1. Curing Procedure

Once the slurry was prepared as per the API RP 10B procedure it was poured in rectangular rubber molds (to prepare compressive strength and porosity samples), and into carbon steel pipes of size 1.75" length and 1" OD (for shear bond strength samples). Subsequent to pouring the slurry, the molds and carbon steel pipes were immersed in 2% by weight NaCl brine inside a pressure vessel. The sealed pressure vessel was kept for 5 days in convective ovens maintained at 200°F. The aforementioned curing and hardening procedure was followed throughout the research for each batch of cement. The baseline and additive slurries were cured and hardened under similar conditions for the same time to maintain the same degree of hydration.

2.3.5.2. Bonding Sample Preparation Procedure

For the preparation of shear bond strength (SBS) samples, the slurries were directly poured into the carbon steel pipes (**Fig. 2.34**). Prior to pouring the cement slurry, the outside surface of the pipes was

cleaned using an electric scrubber and coated with high temperature resistant primer and paint to minimize corrosion. 0.39” long rubber cork was used to seal one end of the carbon steel pipe. The slurry was poured inside the pipes and kept for curing and hardening, which results in the formation of a bond between cement and inside surface of the steel pipes. The bonded cement and the steel pipe are together referred to as SBS sample. One set of the samples, referred to as ‘aged samples’ was then subjected to aging conditions, while the other set, referred to as ‘unaged samples’ was kept at ambient conditions. After completion of the test, the pipes were immersed in concentrated citric acid for 8-10 hours to clean their surfaces. The pipes were then scrubbed from outside and painted with high temperature resistant primer and paint. The insides of the pipes were scrubbed with citric acid using lab towels to obtain smoothness. The pipes were re-used for the next samples. New pipes were used when the surface of the used pipes appeared rough or scratch patterns is developed.

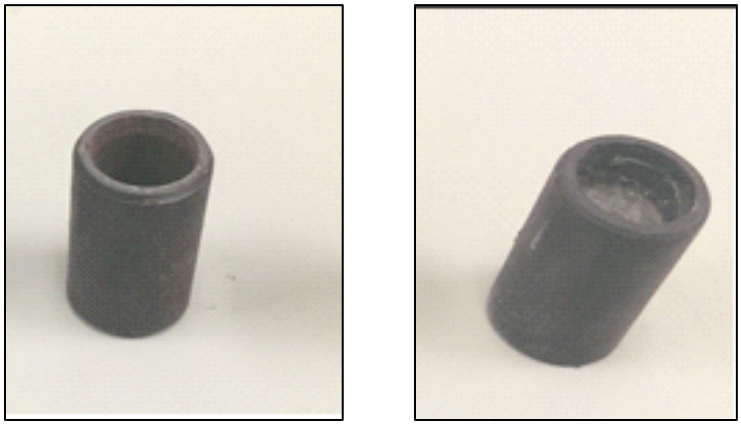

(a) **(b)**

Fig. 2.34: a) Steel pipe; and b) Steel pipes with hardened cement for SBS measurement

2.3.5.3. Cement Core Preparation Procedure

Cured and hardened blocks of cement samples were used to prepare cylindrical cores of size 1.5” length and 1” diameter. The samples (**Fig. 2.35**) were used to measure compressive strength, porosity and permeability of cements. The samples were ground and polished to the exact dimensions. One set of the samples, referred to as ‘aged samples’ was then subjected to aging conditions while the other set, referred to as ‘unaged samples’ was kept at ambient conditions in 2% brine solution.

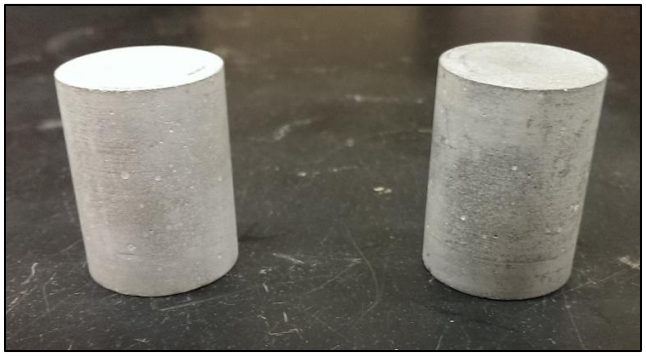

Fig. 2.35: Cured cylindrical samples for porosity and permeability and compressive strength testing

2.3.6. Cement Aging Experiment

2.3.6.1. Experimental Setup

A test setup has been developed to age samples under simulate HPHT downhole conditions. **Figure 2.36** presents a schematic of the setup. As seen from the figure, the setup consists of: i) aging cell that has 3 liter volume capacity; ii) three gas cylinders filled with test gases (CO_2, methane, and methane mixed with H_2S); iii) gas injection cylinder (capacity 250 ml) to accurately control the composition of the gas phase in the aging cell; iv) measuring instruments and data acquisition (DAQ) system. The injection cylinder equipped with a floating piston to separate the cylinder into two chambers. The lower chamber is used to meter and inject the gases needed for the aging process. The upper chamber is connected to an oil pump and reservoir. The oil pump fills the upper chamber and moves the piston downward to pressurize and inject the gas phase into the aging cell. The hydraulic oil flows back to the oil reservoir, when the lower chamber is refilled with gas coming from one of the test gas cylinders. The location of the piston is determined from the liquid-level measured in the oil tank. During the aging test, first cement cores and shear bond samples were placed in the cells using specially design shelf (round multilayer rack). The cell is filled with brine until all the samples and cores were completely immersed in the brine. Then, the lid is placed on cell and the gas inlet line is connected. Gas injection begins by opening the valve between the injection cylinder and aging cell. Gas is injected into the cell repeatedly until the cell pressure (P2) reaches the desired value.

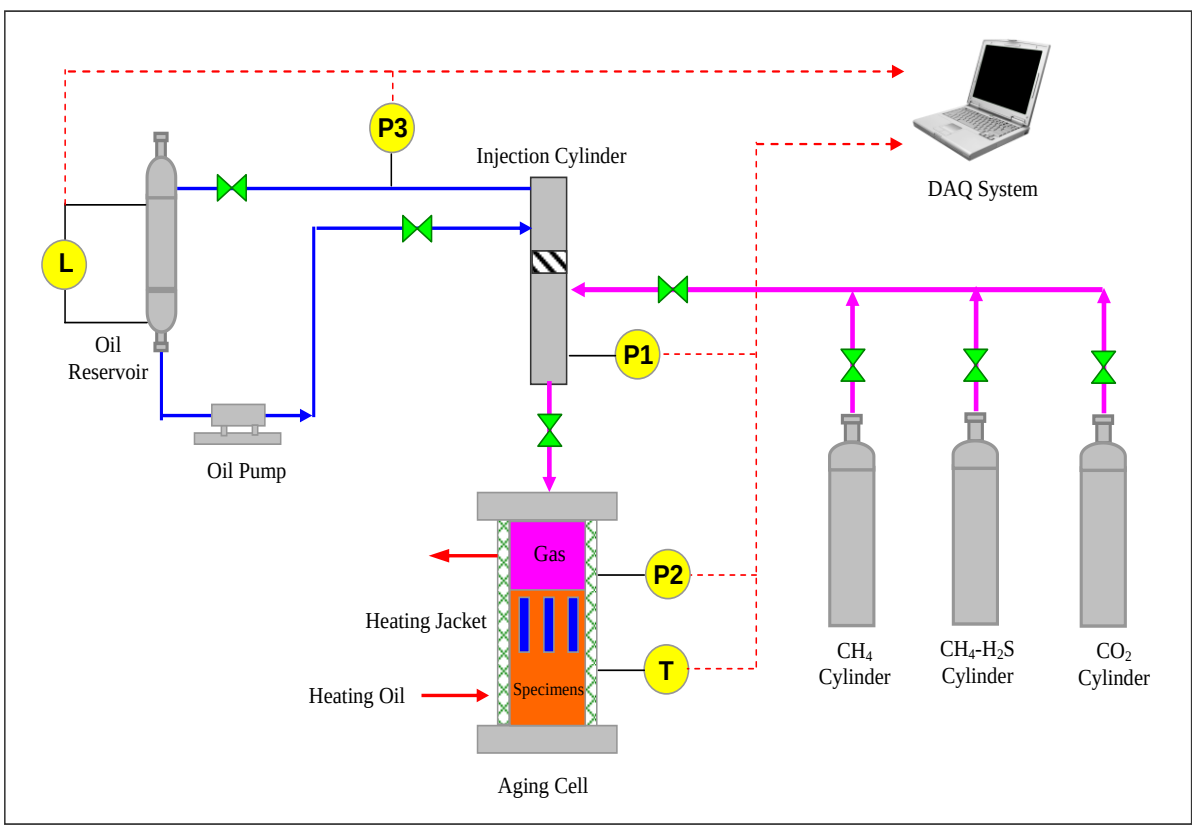

Fig. 2.36: A schematic of the aging cell setup

2.3.6.2. Test Procedure

Table 2.15 shows sample arrangement in the aging cell. The aging cell is equipped with a sample racking system that has 11 shelves out of which the bottom three shelves were kept empty during this research. The full length (inside) of the aging cell is 30 inches. The samples were arranged on the racking system (5 samples per shelf) and then carefully placed in the cell. Subsequently, the cell was filled with 2% NaCl (by weight) solution up to a level of 24". The samples were completely immersed in the brine. The remaining 6-inch space of the autoclave was used for gas injection. The autoclave was sealed and heated to the desired temperature by circulating heating oil through the heating jacket. When the autoclave temperature reached critical temperature of CO_2 (87°F), gas injection was initiated. This was performed in order to keep the CO_2 in the gaseous form during the injection. CO_2 and CH_4 were injected into the autoclave consecutively using the injection cylinder. The injection was stopped when the desired cell pressure was achieved.

Table 2.15: Sample arrangement in aging cell

Shelf	Sample
11	Additive Bonding Samples – Class H
10	Additive Cement Core Samples – Class G
9	Additive Cement Core Samples – Class H
8	Bonding Samples – Class H
7	GS Cement Core Sample
6	HS Cement Core Sample
5	GS Cement Core Sample
4	HS Cement Core Sample
3	Empty
2	Empty
1	Empty

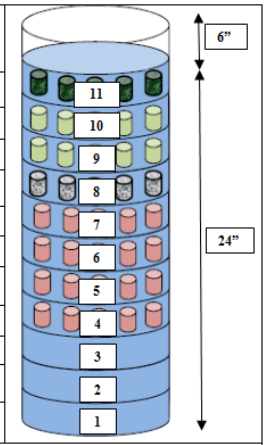

Legend	
Additive Bonding Sample (Class H)	
Additive Cement Core Sample (Class G/ Class H)	
Bonding Sample (Class H)	
Cement Core Sample (Class G/ Class H)	

2.4. Results

Appendix A presents the experimental database developed during the project. The database summarizes all useful data collected during cement degradation and corrosion studies. It shows performance of conventional and new additive-based cement formulations in terms of change in performance indicators such as porosity, permeability, shear bond and compressive strengths) under HPHT acidic environments.

2.4.1. Performance of Baseline Cement Formulations

The performance of oil well cement is determined through its sealing and structural integrity. Cement seals the annular space between casing and formation by hindering fluid flow. The ability of cement to perform this function is determined by its porosity (Ø) and permeability (k). As Ø and k values decreases, the sealing integrity of well cement is improved and vice versa. Structural integrity assesses the ability of well cement to provide mechanical support for the casing without being subjected to failure under in-situ stress conditions of tectonic activities and production or injection operations. Usually, compressive and shear bond strengths are indicators of this mechanical integrity. Compressive strength is the maximum stress cement can withstand before it is subjected to failure while shear bond strength is the maximum stress at which the bond between casing and cement is lost. These mechanical

integrity parameters are strongly correlated to sealing integrity parameters (i.e. porosity and permeability). Generally, compressive strength increases as porosity and permeability decreases due to increase in grain-to-grain contact. Exposure of cement to CO_2-brine fluid system results in the precipitation and dissolution of minerals (e.g. calcium carbonate, calcium bicarbonate, calcium silicate carbonates). Depending on the strength of these minerals, mechanical strength may either improve or degrade. Predominantly, porosity and permeability decrease as minerals precipitate and this increases compressive strength. The growth of minerals would also lead to expansion of the cement matrix against a rigid metallic pipe thereby improving shear bond strength. However, dissolution of minerals results in highly porous and permeable cement (i.e. low compressive strength) whose matrix is likely to shrink thereby weakening the bond between cement and casing.

2.4.1.1. Porosity and Permeability

Degradation associated with acid attack often changes sealing performance of cement by increasing its porosity and permeability. The rate of cement degradation in borehole environment is strongly affected by concentration of acidic gases, temperature, and pressure.

Effects of Temperature

Temperature play very important role in determining degradation of cement under acidic environment. This is because it affects most of physicochemical phenomena such as dissolution, diffusion, carbonation reaction, bicarbonation, and leaching, which are highly involved in the degradation process. Degradation process is facilitated with increased solubility of CO_2 and binding components of cement (CH and CSH) in water. Carbon dioxide and calcium hydroxide exhibit abnormal solubility in water. At high pressure and high temperature (approximately more than 350°F), carbon dioxide shows abnormal solubility (**Fig. 2.37**). Hence, under HPHT condition, the effect of temperature on cement degradation is difficult to predict. A solubility model used to generate Fig. 2.37 is presented in Appendix B.

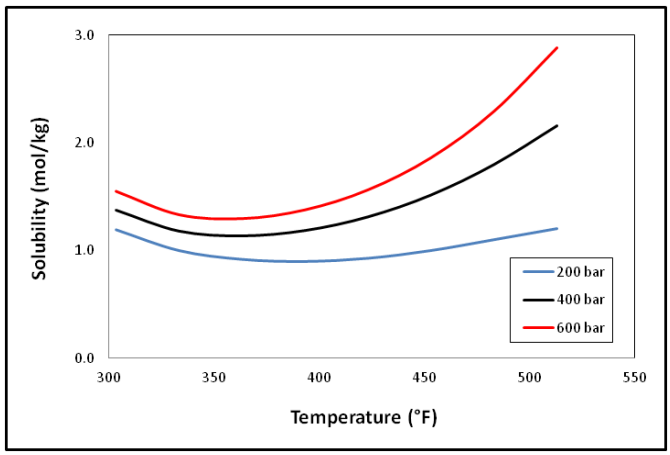

Fig. 2.37: Effect of temperature on CO_2 solubility in 1M NaCl solution

Furthermore, temperature has influence on the product of carbonation reaction. Low temperature condition favors incomplete carbonation. **Figures 2.38** to **2.40** demonstrate the effects of temperature on degradation of baseline cements at 6000 psi. The general trend that is observed here is that at low temperatures (less than 225°F) incomplete carbonation, which forms scawtite thereby decreasing the porosity and permeability. Nevertheless, as the temperature increases above 225°F, both porosity and permeability increase due to carbonation and subsequent leaching of bicarbonate from the cement.

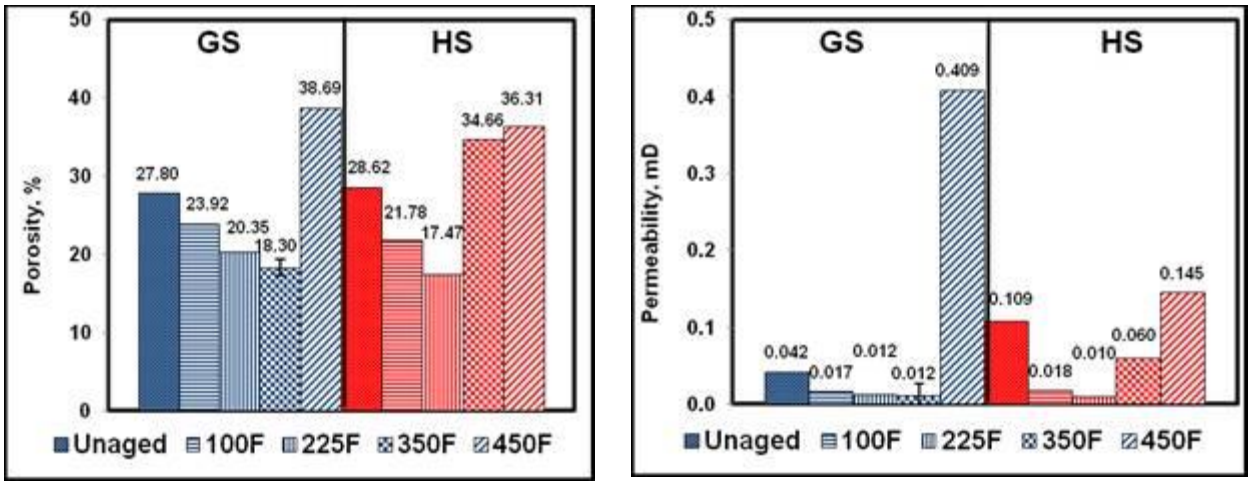

(a) (b)

Fig. 2.38: Effects of temperature on porosity and permeability of baseline cores aged at 6000 psi and 10% CO_2

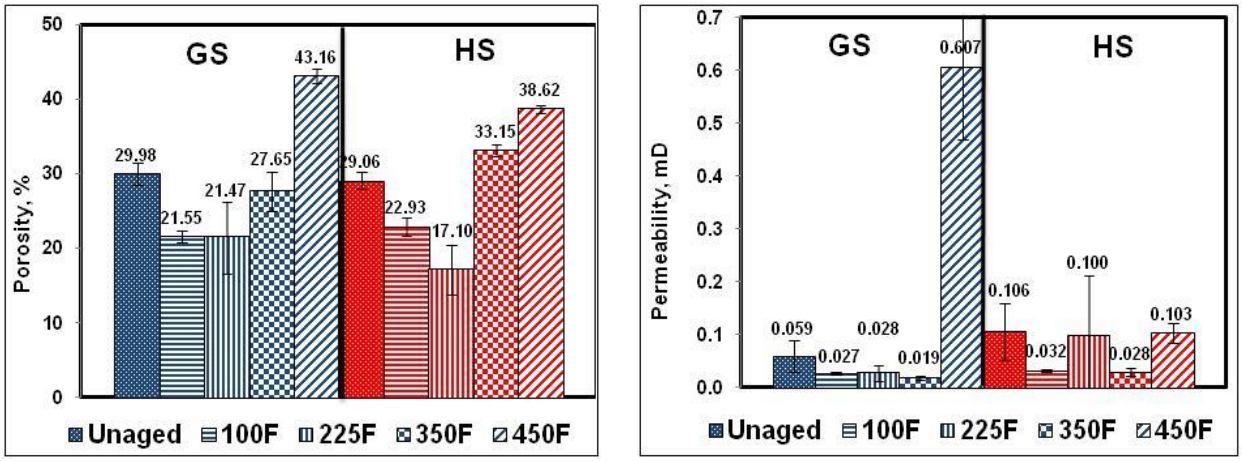

(a) (b)

Fig. 2.39: Effects of temperature on porosity and permeability of baseline cores aged at 6000 psi and 40% CO_2

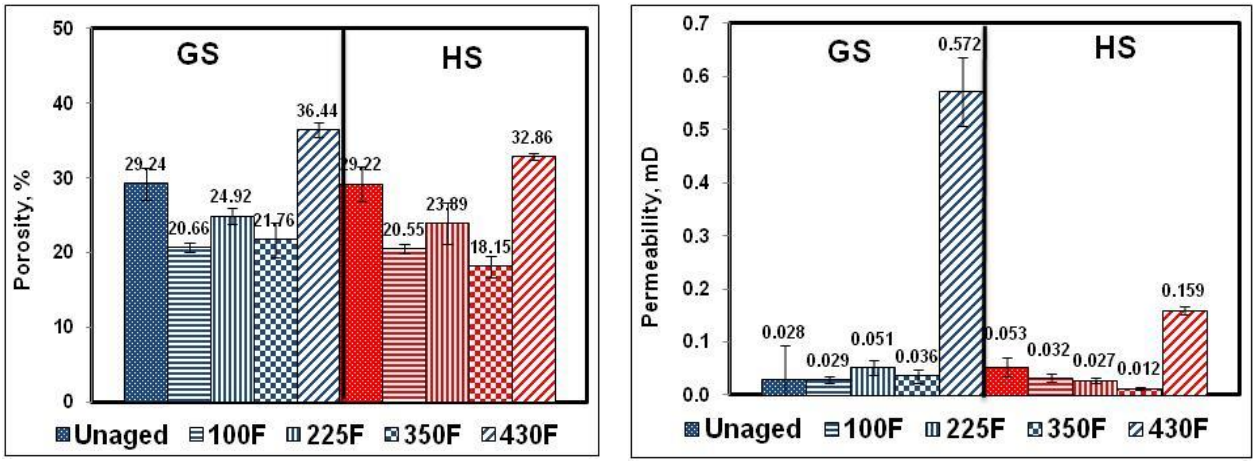

(a) (b)

Fig. 2.40: Effects of temperature on porosity and permeability of baseline cores aged at 6000 psi and 100% CO_2

Figures 2.41 and **2.42** compare the effects of temperature on porosity and permeability of baseline cements at different pressures (3000 and 9000 psi). As observed at 6000 psi, incomplete carbonation resulted in scawtite formation at low temperatures causing reduction in porosity and permeability. However, as the temperature increased, porosity and permeability of the cores increase due to carbonation and successive leaching of bicarbonate from the cement matrix. In addition, the trends of porosity and permeability with temperature for samples aged at lower CO_2 concentrations (10 and 40% CO_2) are similar to the ones observed at high CO_2 concentration (100% CO_2).

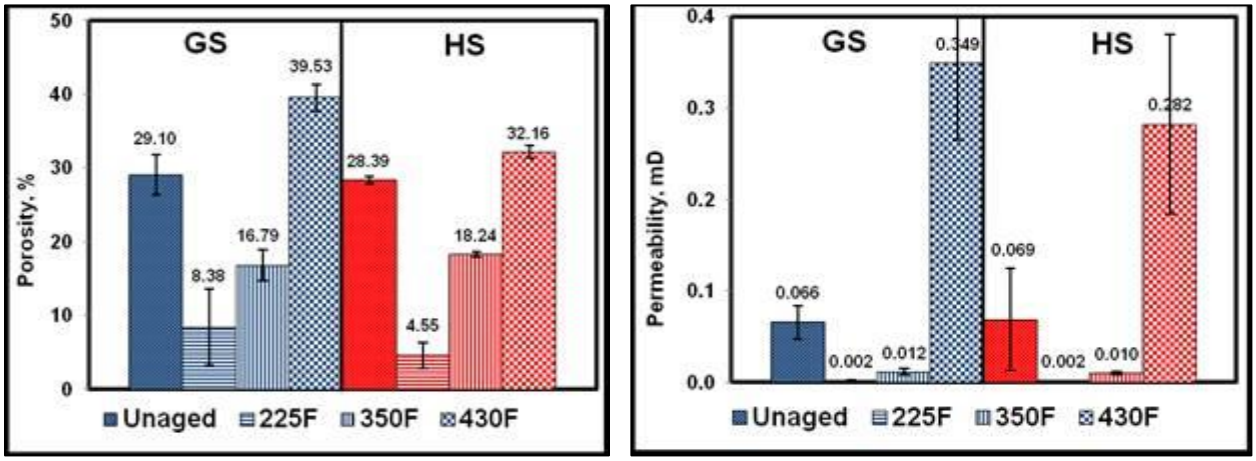

(a) (b)

Fig. 2.41: Effects of temperature on porosity and permeability of baseline cores aged at 3000 psi and 100% CO_2

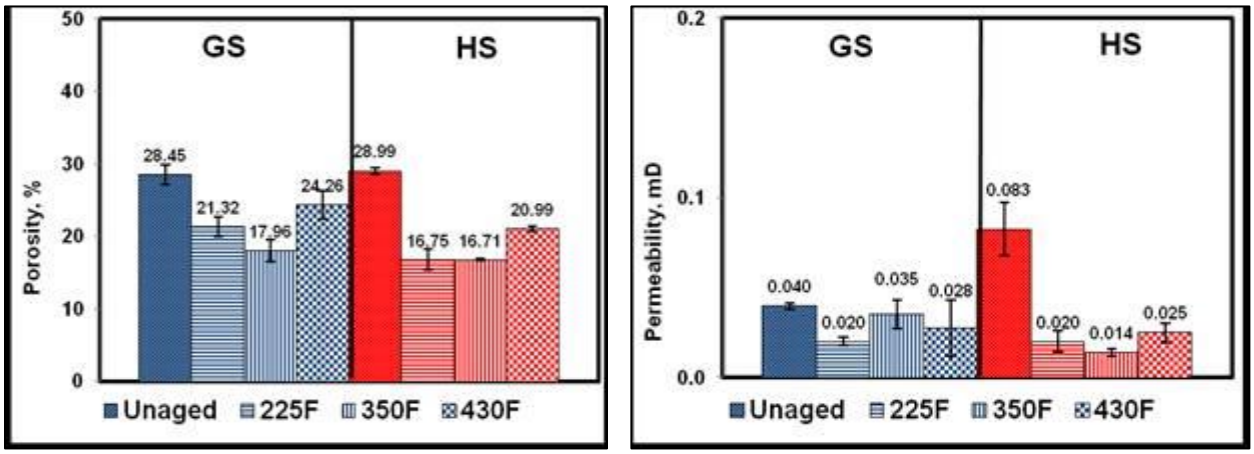

(a) (b)

Fig. 2.42: Effects of temperature on porosity and permeability of baseline cores aged at 9000 psi and 100% CO_2

Effects of Pressure

Figures 2.43 to **2.45** demonstrate porosity and permeability of samples aged at 350°F and different pressures (3000, 6000 and 9000 psi) and CO_2 concentrations (10, 40 and 100%). Porosity and permeability of the samples significantly vary with pressure. For both cement classes, the trends of porosity and permeability are very similar at 40% CO_2 gas concentration. There is a decrease in both porosity and permeability from unaged to 3000 psi, then an increase from 3000 to 6000 psi and then

again a decrease from 6000 to 9000 psi pressure. For Class H cement, the decrease observed at 3000 psi is much more prominent as compared to the one at 9000 psi.

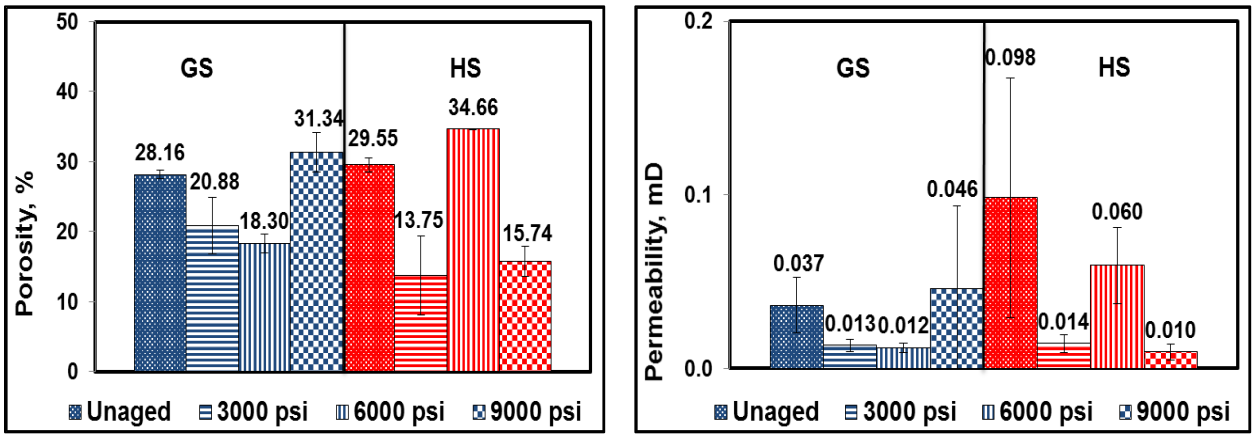

(a) (b)

Fig. 2.43: Porosity (a) and permeability (b) of samples aged for 14 days at 350°F and 10% CO_2 and different pressures

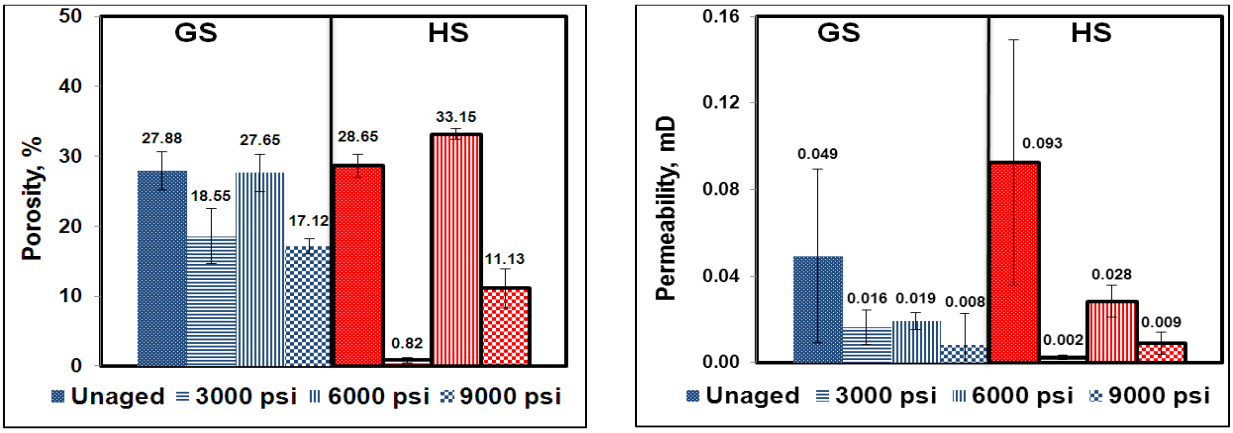

(a) (b)

Fig. 2.44: Porosity (a) and permeability (b) of samples aged for 14 days at 350°F and 40% CO_2 and different pressures

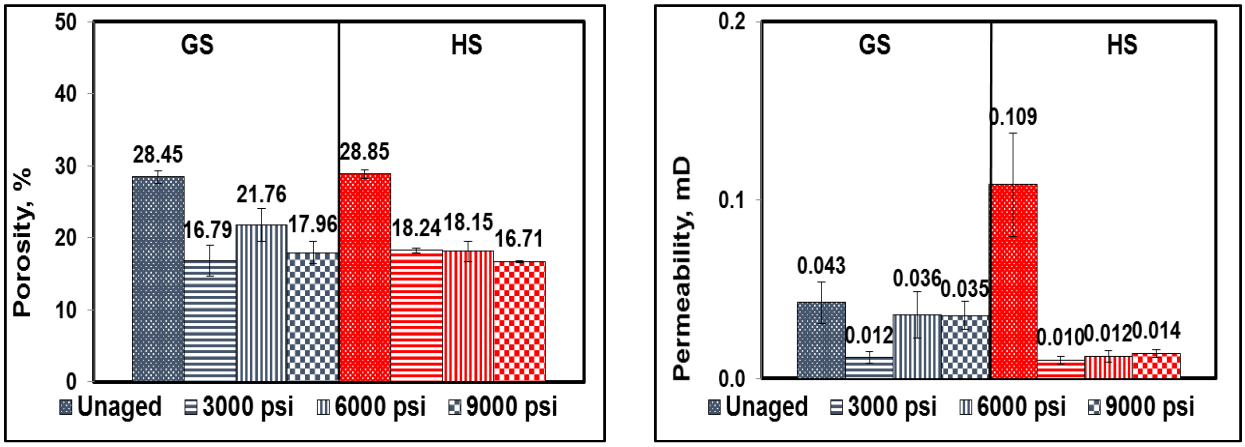

(a) (b)

Fig. 2.45: Porosity (a) and permeability (b) of samples aged for 14 days at 350°F and 100% CO_2 and different pressures

When the pressure is as low as 3000 psi, the condition favors incomplete carbonation, which leads to the formation of scawtite phase (Harker 1965; Lea 1971). When more CO_2 reacts with scawtite it forms $CaCO_3$ thereby completing the carbonation process. At low pressures, solubility of CO_2 in brine is low; hence, less carbonic acid is present in the brine to degrade the cement. At 3000 psi, the reduction in porosity and permeability could be due to the incomplete carbonation of CSH (i.e. formation of scawtite). This incomplete carbonation prevents formation of $CaCO_3$, and as a result, limits the formation of soluble bicarbonate. Hence, leaching process that tends to increase porosity and permeability of the cores does not occur. Therefore, the reduction in porosity and permeability observed at lower pressures is attributed to the precipitation of scawtite, which became the predominant process. However, at 6000 psi, increased gas solubility resulted in complete carbonation and subsequent bicarbonate formation, which was proceeded by leaching, thereby increasing the porosity and permeability of the cement.

At 9000 psi, reduction in porosity and permeability was observed. According to Roger (1996), when portlandite (CH) reacts with super critical CO_2 (**Fig. 2.46**) under high pressure condition, it forms dense, rounded and closely packed crystals thereby plugging the pores and capillaries, which decreases the porosity and permeability while increasing the strength of the cement.

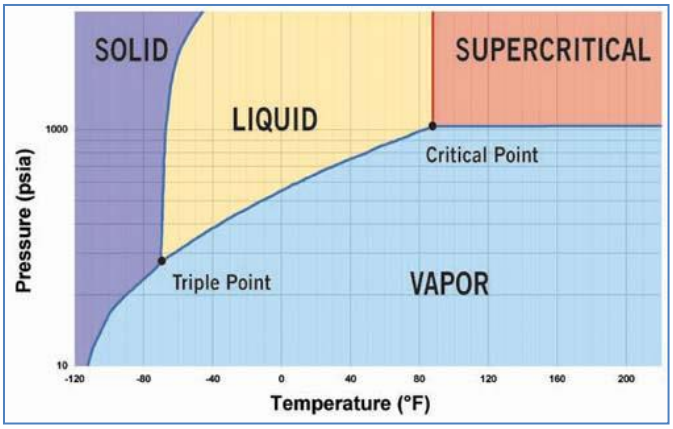

Fig. 2.46: Phase diagram of CO_2 (Vestergaard and Robinson 2003)

At 100% CO_2 concentration, the trends of porosity and permeability of Class G cement are very similar to that observed at 40% CO_2. For Class H cement however, the trends of porosity and permeability observed at 100% CO_2 is different from the one shown at 40%.

Effects of CO_2 Concentration

Figures 2.47 and **2.48** demonstrate the effects of CO_2 concentration on porosity and permeability of aged samples at 3000 psi and different temperatures (225°F and 350°F). For both classes of cement, the general trends of porosity and permeability are consistent. At low temperature (225°F), increase in CO_2 concentration reduced porosity and permeability of the samples. At high temperature (350°F), Class G cement showed a similar trend. However, Class H cement exhibited reduction in porosity and permeability at 40% CO_2 and increase at 100% CO_2. This could be attributed to the leaching of the carbonated binding components such as CSH and portlandite.

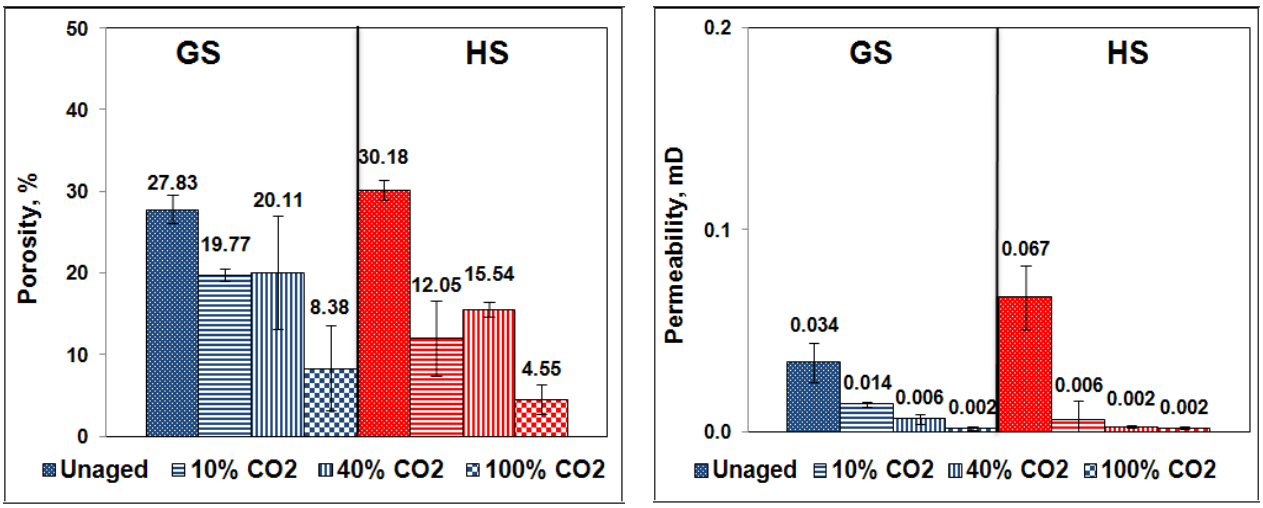

(a) (b)

Fig. 2.47: Effects of CO_2 concentration on porosity and permeability of baseline cores aged at 225°F and 3000 psi

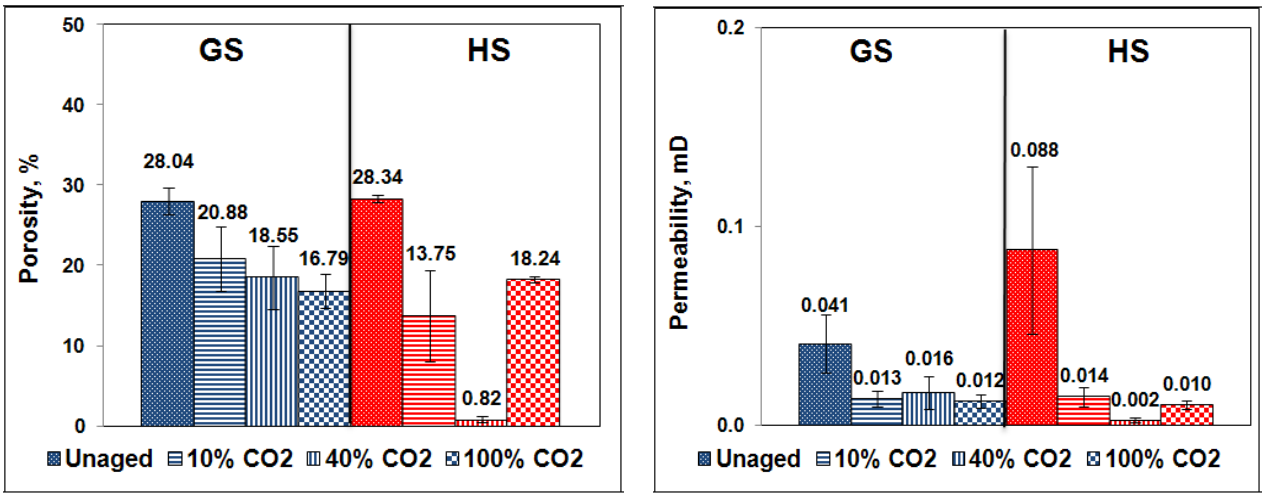

(a) (b)

Fig. 2.48: Effects of CO_2 concentration on porosity and permeability of baseline cores aged at 350°F and 3000 psi

Effects of H_2S

Figures 2.49 and **2.50** compare porosity and permeability of Class H cement samples aged in fluid systems with and without H_2S at three different temperatures. For core aged at 100°F in fluid system without H_2S, the porosity decreased (Fig. 2.49). For the same temperature, the permeability of the core decreased from 0.115 to 0.018 mD (Fig. 2.50). The decrease in porosity and permeability is attributed to the formation of carbonates by the reaction of CO_2 with CH and CSH. However, for samples aged in fluid system with H_2S, this decrease in porosity and permeability is not observed. In fact, the porosity and permeability increased for these samples. It has been observed in literature that reaction of aqueous H_2S with ferrites and aluminates at temperatures below 190°F results in formation of ettringite (Kutchko et al. 2011 and Jacquemet et al. 2005). The formation of secondary ettringite may result in molecular expansion. Abundant ettringite was observed in SEM images of cores aged in fluid system with H_2S (**Fig.**

2.52). The FTIR data (**Fig. 2.51**) demonstrates that the increase in porosity and permeability of samples aged in fluid system with H_2S may also be due to less degree of carbonation in the samples. Thus, molecular expansion due to the formation of ettringite, or less carbonation can be attributed to the increase in porosity and permeability at 100°F.

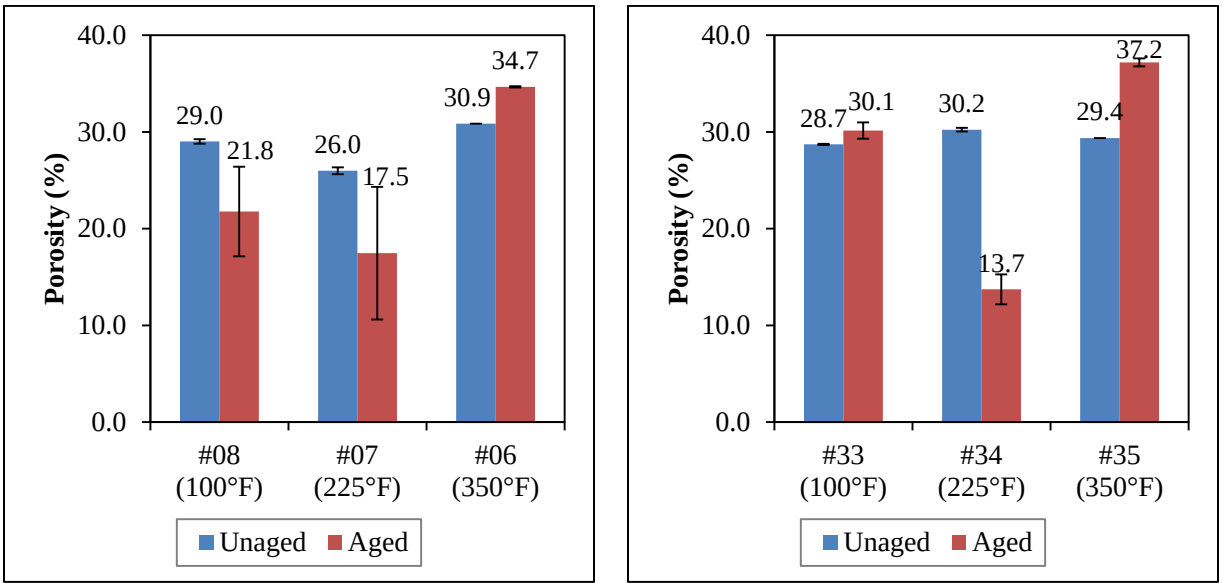

(a) (b)

Fig. 2.49: Porosity of Class H samples aged at 6000 psi and different temperatures in: a) fluid system without H_2S; b) fluid system with H_2S

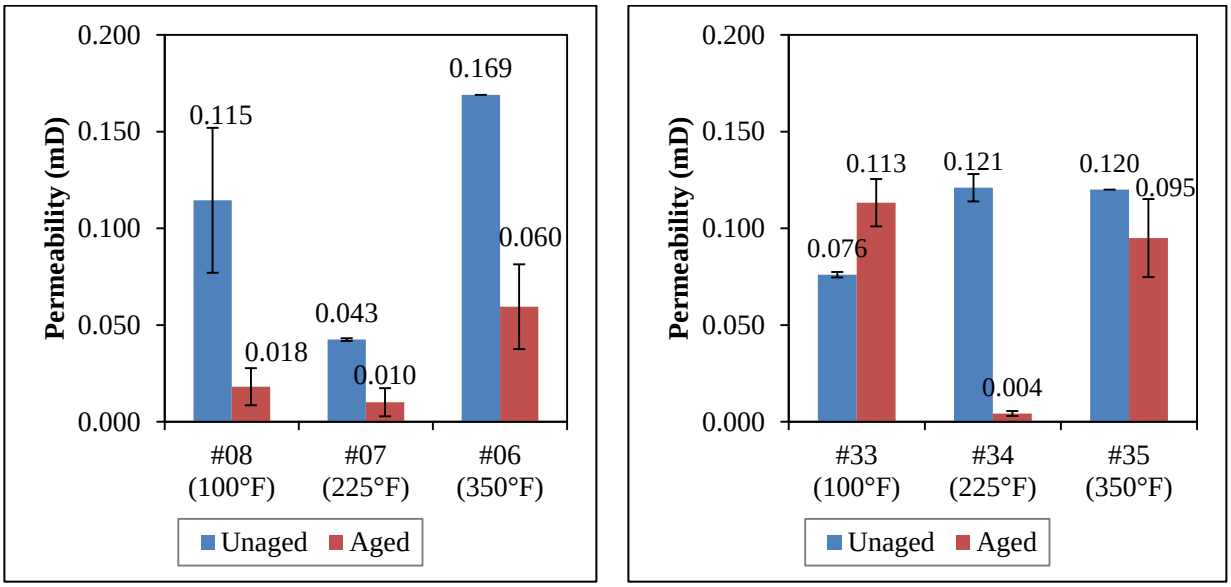

(a) (b)

Fig. 2.50: Permeability of Class H samples aged at 6000 psi and different temperatures in: a) fluid system without H_2S; b) fluid system with H_2S

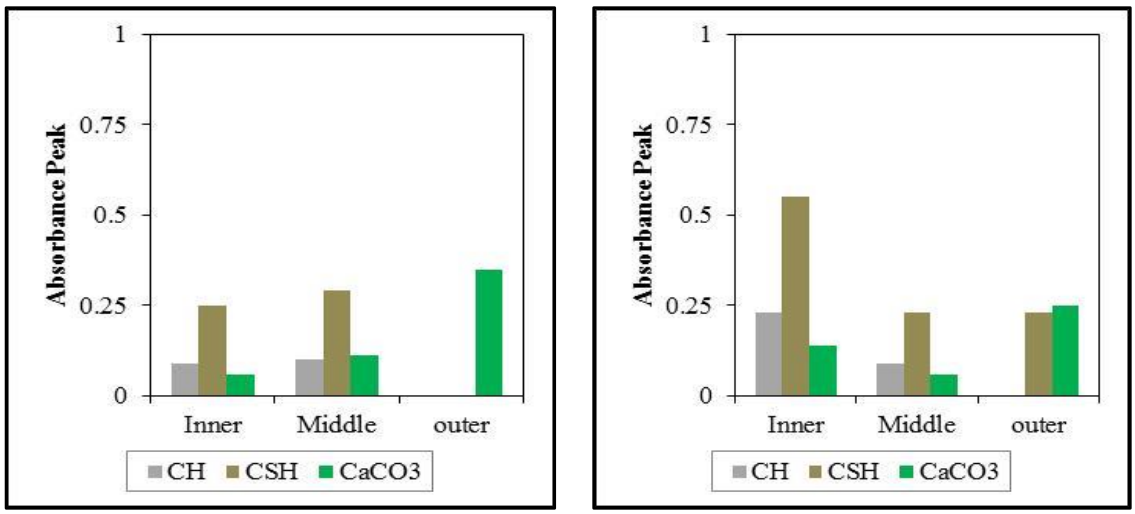

(a) **(b)**

Fig. 2.51: FTIR data for Class H samples aged at 100°F and 6000 psi in fluid system: a) without H_2S; and) b with H_2S

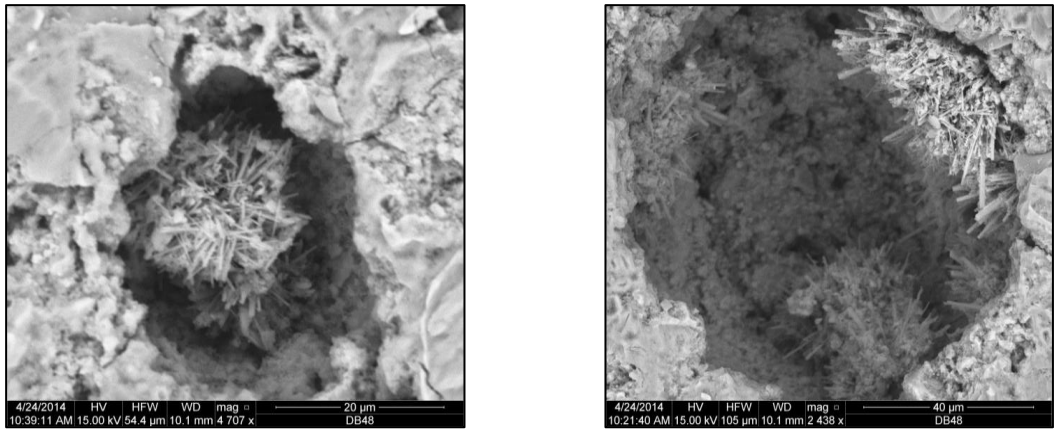

(a) **(b)**

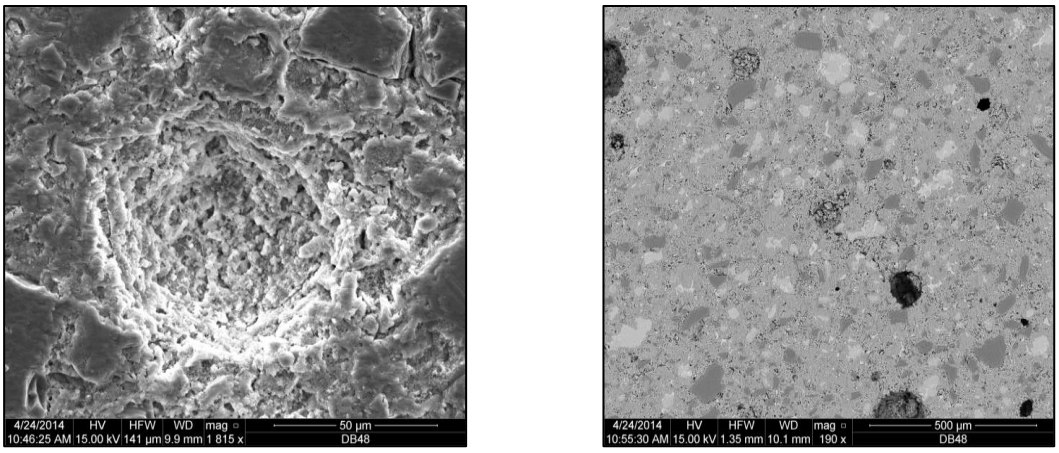

(c) **(d)**

Fig. 2.52: SEM images of Class H sample aged at 100°F and 6000 psi: a) ettringite formed in a pore in the middle zone; b) ettringite formed in a pore in the inner zone; c) empty pore close to the specimen external surface; d) presence of CH, CSH and unhydrated cement particles

At 225°F, the porosity of aged samples is lower than the unaged samples irrespective of the presence of H_2S in the aging fluid (Fig. 2.49). Considering the standard deviation, one can conclude that the decrease in porosity after aging is almost similar for samples aged in fluid systems with and without H_2S. However, there is a significant difference in the permeability values of samples aged with and without the presence of H_2S (Fig. 2.50). This difference may be attributed to the low permeability value of unaged samples in Batch #07. The effect of ettringite formation is not observed at 225°F as ettringite dissolves above 190°F.

At 350°F, the porosities of samples aged in both fluid systems are higher than the porosity of the corresponding unaged samples (Fig. 2.50). The increase in porosity may be a result of formation of water soluble calcium bicarbonate due to higher level of CO_2 diffusing into the pores at higher temperature. The increase in porosity may also be due to high level of calcium ion leaching resulting from increased rate of diffusion. However, no such increase in the permeability of aged samples is observed (Fig. 2.50). In fact the permeability of aged samples was less than that of the unaged samples. This may be due to plugging of some of the connecting pores by calcium carbonate.

The porosity and permeability of Class G cement samples aged in fluid systems with and without H_2S is presented in **Figs. 2.53 and 2.54**, respectively. It is observed that at 100°F the porosity and permeability of samples aged in fluid systems without H_2S is lower than the porosity of unaged samples. The decrease in porosity and permeability is attributed to carbonation. For samples aged in fluid systems with H_2S, the porosity and permeability of aged and unaged samples is almost similar. In these samples, the decrease in porosity and permeability due to carbonation may be offset by the increase in porosity and permeability due to ettringite formation or due to less degree of carbonation.

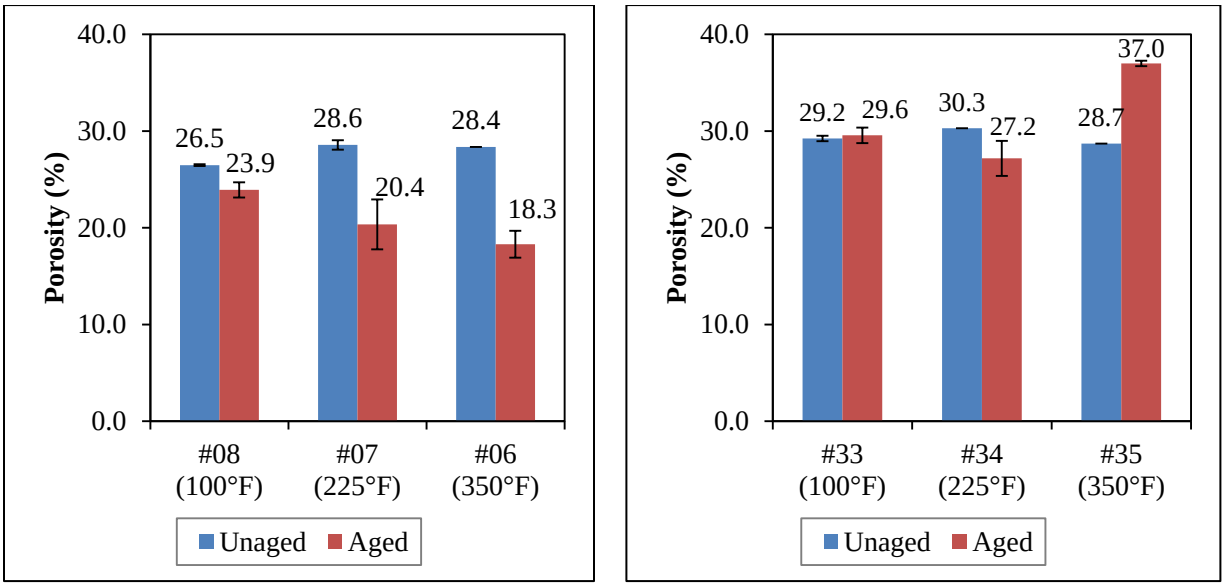

(a) (b)

Fig. 2.53: Porosity of Class G cement samples aged at 6000 psi and different temperatures in: a) fluid system without H_2S; b) fluid system with H_2S

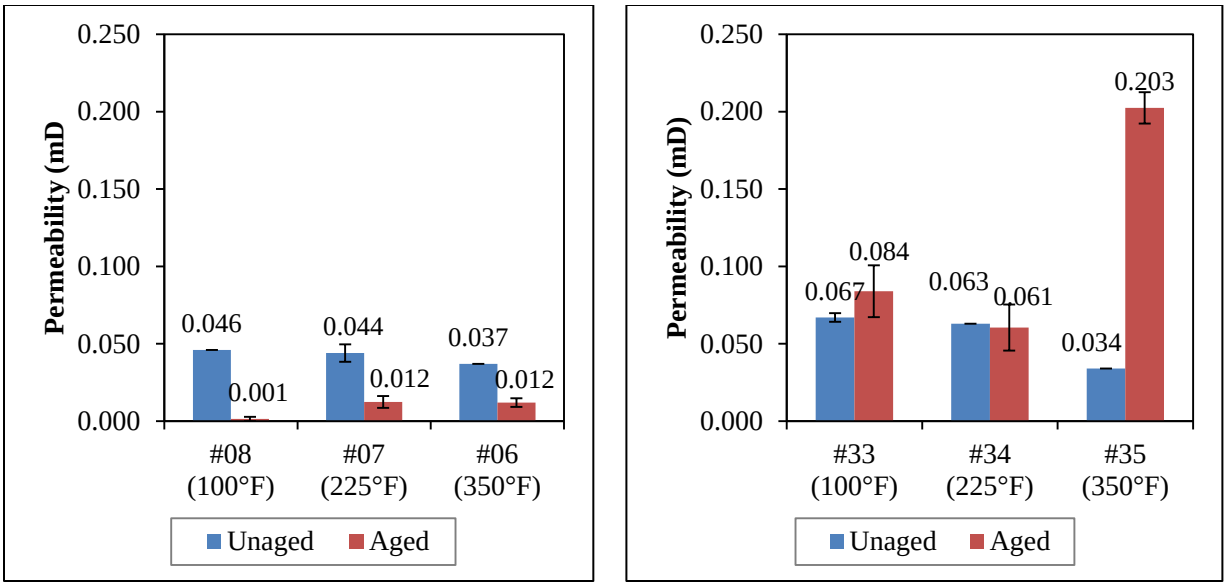

(a) (b)

Fig. 2.54: Permeability of Class G cement samples aged at 6000 psi and different temperatures in: a) fluid system without H_2S; b) fluid system with H_2S

2.4.1.2. Compressive Strength

When a cement sample is in contact with brine, the difference in concentration between the interstitial pore fluid and cement matrix causes the dissolution of ions into the pore fluid. This leads to diffusion of ions from the pore fluid to the bulk fluid causing reduction in calcium ion concentration in the cement, resulting in weaker cement matrix primarily because of dissolution of calcium-bearing binding components of cement (portlandite and tobermorite gel). In the presence of CO_2, dissolved binding components react with CO_2 and form $CaCO_3$, which precipitates and fills pore spaces in the cement causing an overall increase in compressive strength. With further acid attack, $CaCO_3$ reacts with the acid and forms easily soluble $Ca(HCO_3)_2$ resulting in leaching of the binding components from the matrix causing strength retrogression. The process of carbonation, dissolution, and leaching are strongly dependent on acidic gas concentration, pressure and temperature.

Effects of Temperature

Figures 2.55 to **2.57** demonstrate the effects of temperature on compressive strength of baseline (Class G and Class H) cement at different CO_2 concentrations and intermediate pressure (6000 psi). Temperature has impact on a number of physicochemical processes involved during cement degradation including carbonation, dissolution, ionic transport, and leaching. For Class G cement, most of these processes offset each other leading to mixed trend in compressive strength at low CO_2 concentrations (10 and 40% CO_2). At high CO_2 concentration (100%), Class G cement strength showed consistent trend with temperature change; first increase in strength at low temperature, which is followed by progressive strength reduction. Class H cement showed a similar trend at different concentrations. As the temperature increases, significant strength gain was observed due to carbonation, then progressive strength reduction due to cement leaching.

At extreme high temperature (430°F), the interaction between pore fluid and cement matrix intensifies, leading to dissolution of hydrated binding materials (portlandite and calcium silicate hydrates), which results in substantial reduction in cement mechanical strength. Furthermore, the results presented in the figures, show the effect of CO_2 concentration on the strength. Increase in CO_2 concentration from 10 to 40% had minimal effect on compressive strength of Class G cement; only slight increase or decrease in strength was observed as concentration changes. Class H cement strength predominately improved with increase in CO_2 content of the gas. This is mainly due to carbonation occurring at higher CO_2 concentration. However, as the temperature increases, CO_2 gas solubility reduces resulting in diminished carbonation that can be dominated by leaching, which is intensified by increased temperature.

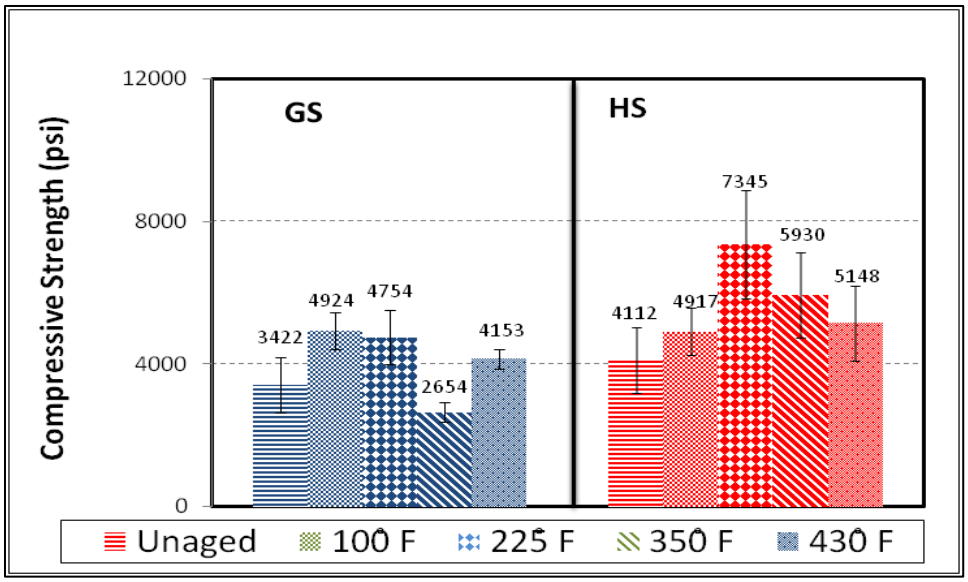

Fig. 2.55: Effects of temperature on compressive strength of baseline cores aged at 6000 psi and 10% CO_2

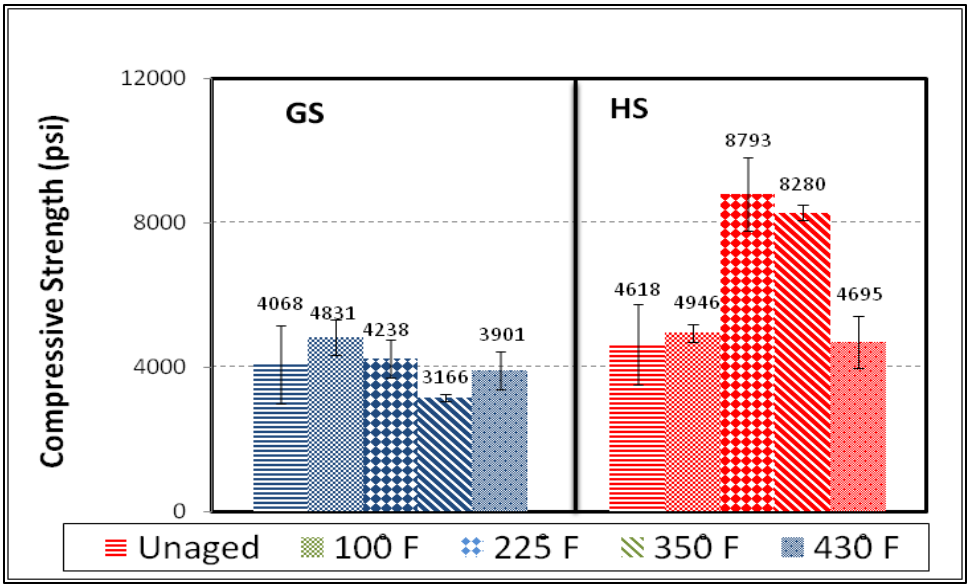

Fig. 2.56: Effects of temperature on compressive strength of baseline cores aged at 6000 psi and 40% CO_2

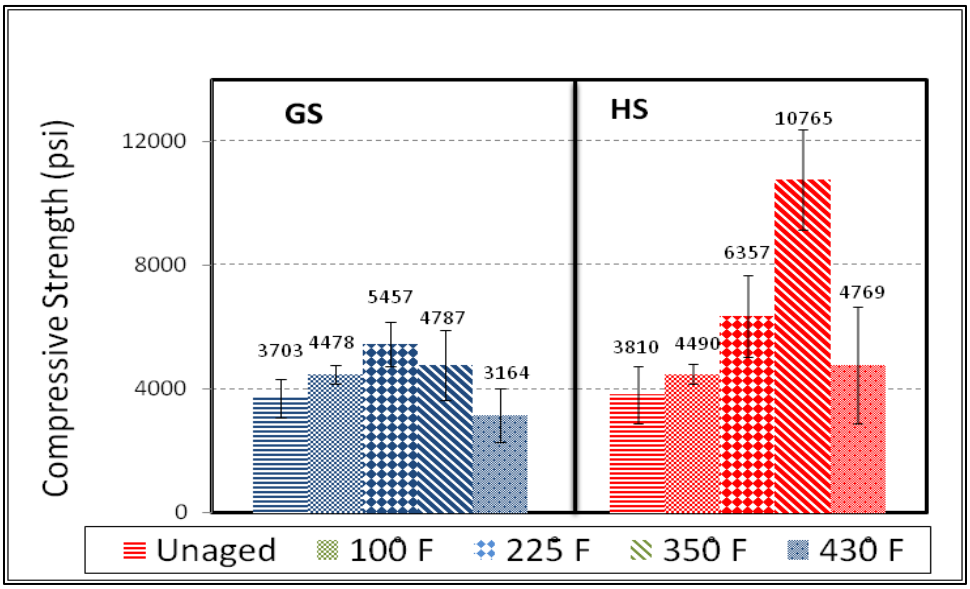

Fig. 2.57: Effects of temperature on compressive strength of baseline cores aged at 6000 psi and 100% CO_2

Compressive strengths of baseline cements aged in 2% brine saturated with 100% CO_2 are shown in **Fig. 2.58**. At 3000 psi, although CO_2 solubility decreases with temperature (Fig. 2.37, 200 Bar), temperature favors carbonation reaction of the carbonic acid with hydrated cement products (CSH and CH). Carbonation results in precipitation of calcite that fills the pores of the cement, thereby increasing compressive strength. However, at higher temperatures, the precipitated calcium carbonate is further attacked by carbonic acid forming calcium bi-carbonate, which can be easily leached out of the cement causing strength retrogression.

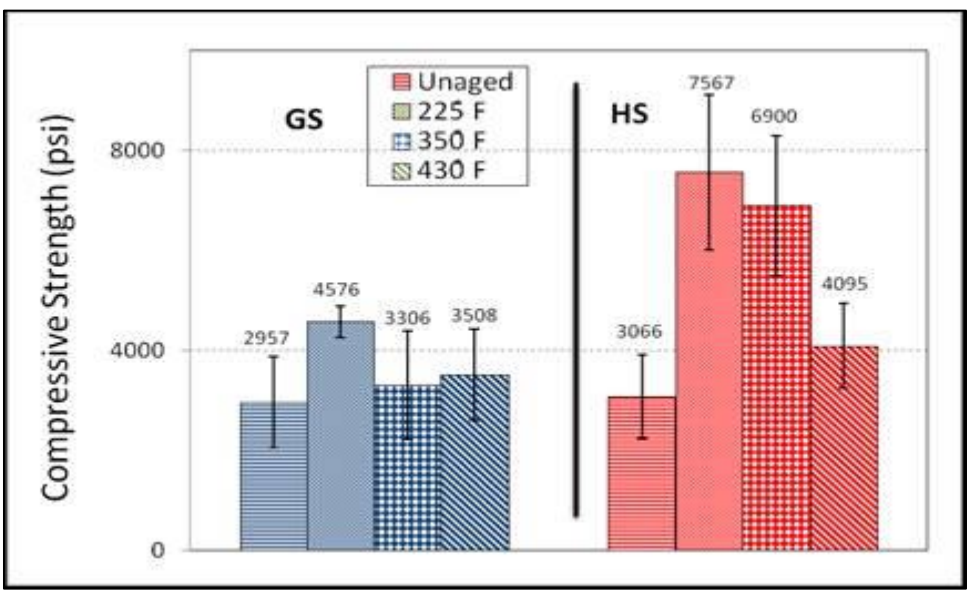

Fig. 2.58: Effect of temperature on compressive strength at 100% CO_2 and 3000 psi

After aging at 430°F, 3000 psi, compressive strength improved in both classes of cements due to carbonation. For aged samples, increasing temperature reduced strength. The maximum strength gain occurred at 225°F due to carbonation, and then strength reduced as the temperature was increased. Class H cement showed substantial strength retrogression at extremely high temperature (430°F). The reduction is possibly due to leaching of calcite and/or formation of scawtite. Low pressure (3000 psi) favors incomplete carbonation that yields scawtite. According to Eilers et al. (1983), small amount of scawtite formation improves strength while excessive amount leads to loss of integrity. In addition, strength retrogression can happen due to phase transformation occurring in CSH.

Consistent with low-pressure (3000 psi) measurements, cement samples gained strength after aging under high pressure (9000 psi) condition (**Fig. 2.59**). Class G cement gained strength after aging at 225°F primarily because of calcite precipitation. However, between 225 and 350°F, the strength reduced indicting a switch from carbonation dominated to leaching dominated process. A different trend is demonstrated by Class H cement. With increasing temperature, strength increased below 350°F due to carbonation and reduced above 350°F because of leaching and/or thermal retrogression.

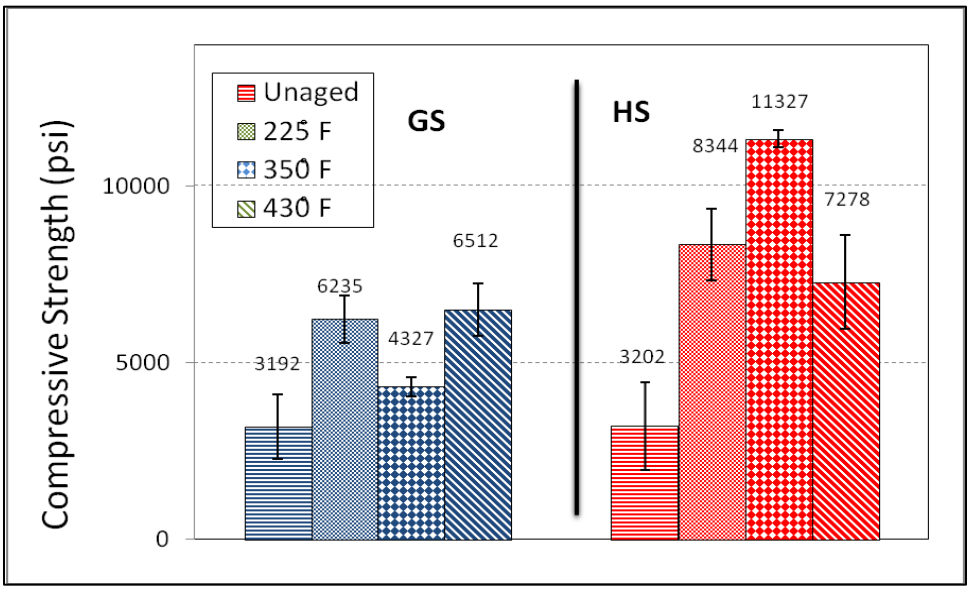

Fig. 2.59: Effect of temperature on compressive strength at 100% CO_2 and 9000 psi

Effects of Pressure

The formation of scawtite is favorable at low CO_2 partial pressure (i.e. low system pressure and/or low CO_2 concentration). The effect of pressure on cement compressive strength at 225°F and 10% CO_2 concentration presented in **Fig. 2.60**. At low aging pressure (3000 psi), strength increased in both cements due to the formation of scawtite. As the temperature was increased to 6000 psi, most of the scawtite was fully carbonated, resulting in the formation of calcite, which caused the strength to increase. Calcite formation peaked at 6000 psi. However, more CO_2 was dissolved with further increase in pressure, resulting in leaching of the fully carbonated phases and reduction of strength. In general, Class H cement exhibited higher strength than Class G cement after aging under HPHT conditions.

Figure 2.61 shows compressive strength of baseline cements after aging in 2% brine saturated with 100% CO_2. At 225°F, CO_2 solubility increases with aging pressure and precipitation of scawtite is likely at low aging pressure while full carbonation and leaching are possible occurrences at high aging pressures. Mixed trend in Class H cement at 225°F may have occurred because of complex nature of cement degradation, which involves two offsetting processes (carbonation and leaching). Similar mixed trend is observed with Class G cement at 350°F. Despite these anomalies, results show enhancement of carbonation as pressure is increased due to improvement in CO_2 solubility.

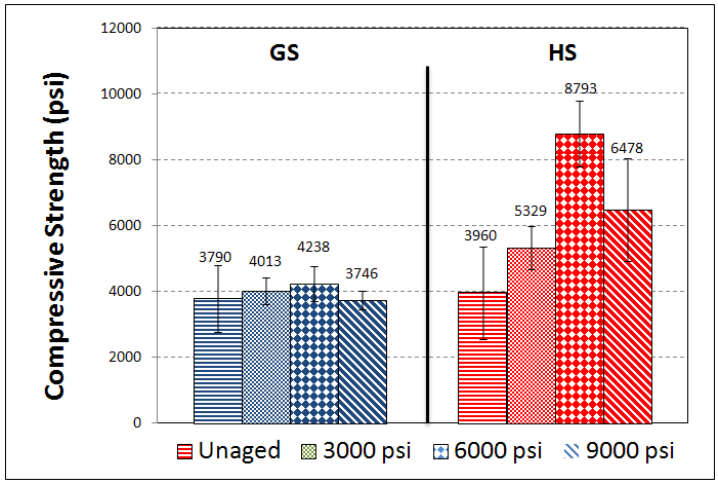

Fig. 2.60: Effects of pressure on compressive strength of cement cores at 225°F and 10% CO_2 concentration

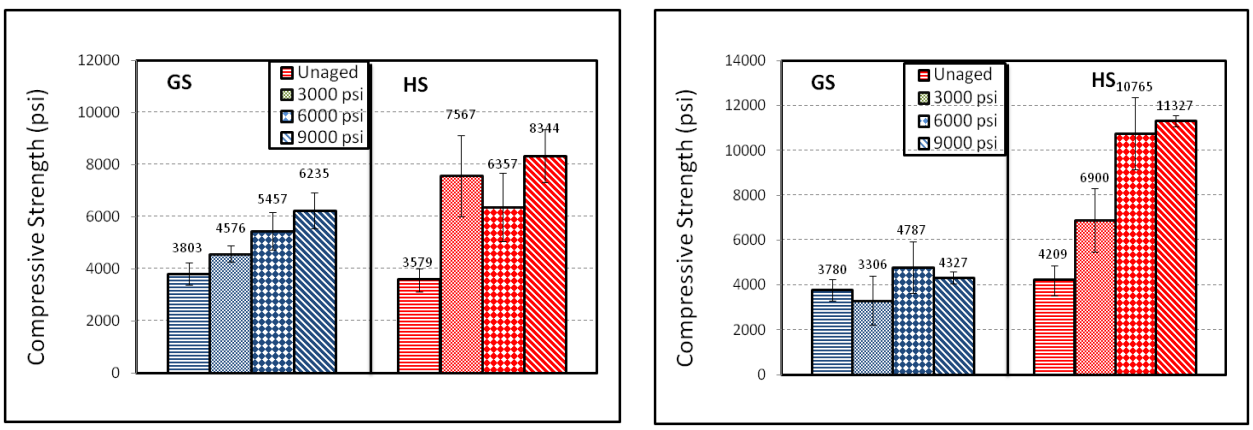

(a) **(b)**

Fig. 2.61: Compressive strengths of cements after aging in brine saturated with 100% CO_2 at: a) 225°F, and b) 350°F

Effects of CO_2 Concentration

At Intermediate Temperature (225°F): The principal mechanisms that lead to cement degradation in carbonic acid environment are carbonation and leaching. Of these mechanisms, the rate controlling process is carbonation and subsequent leaching, both processes being affected by the concentration of carbon dioxide. **Figures 2.62** and **2.63** show mechanical (compressive strength) and physical properties (porosity and permeability) of Class H and Glass G cements as a function of CO_2 concentration at 225°F and 3000 psi. Lines in Fig. 2.63 represent permeability data. As CO_2 concentration increases, compressive strength of both well cements increased while porosity and permeability decreased. When carbonic acid attacks cement, cement binding components (CSH and CH) dissolve into the pore fluid and react with the acid to form calcium carbonate (calcite). Due to its low solubility, calcium carbonate precipitates, and fills the pores of the cement, thereby resulting in reduction in ϕ-k. However, carbonate precipitation improves mechanical strength. With continuous supply of CO_2, the precipitated calcite is

converted to water-soluble calcium bicarbonate, which is subsequently leached out further, leading to increased porosity and permeability, and reduced strength. Both carbonation and leaching processes take place simultaneously during acid exposure. Thus, the physical and mechanical properties are dictated by the dominant process and parameters such as CO_2 concentration that affect it considerably.

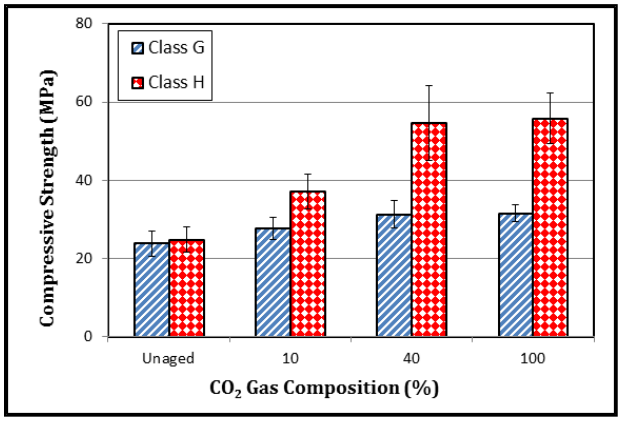

Fig. 2.62: Compressive strength vs. CO_2 concentration for cements aged at 225°F and 3000 psi

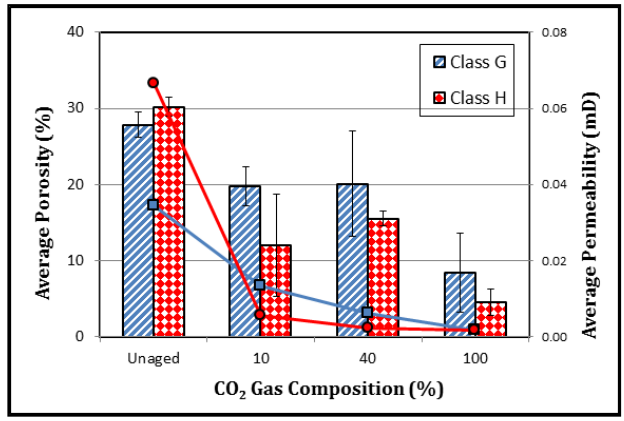

Fig. 2.63: Porosity and permeability vs. CO_2 concentration for cements aged at 225°F and 3000 psi

As CO_2 concentration increases, additional CO_2 dissolves in brine. This increases carbonic acid concentration and reduces the pH of the solution. Subsequently, solubility of calcite increases since low pH facilitates dissolution. At low temperature and pressure, the binding components are carbonated faster than subsequent conversion to bicarbonate. However, in some cases, the rate of carbonation may be low and bicarbonation becomes the rate controlling mechanism. While these results hold for 14 days of exposure adopted in this study, effect of leaching may become more pronounced with prolonged exposure.

Furthermore, phase transformation of partially carbonated (calcium silicate carbonate) and un-carbonated CSH may have contributed to the trend observed in experimental data. Although the effect of pressure on CSH and calcium silicate carbonate (CSC) phase transformation is not well understood, the effect of temperature is well-documented (Taylor 1964; Eilers et al. 1983; Nelson et al. 1981; Richardson 2008). Transformation of CSH to tobermorite ($5CaO.6SiO_2.5H_2O$) or clinotobermorite is likely to occur at approximately 225°F and C/S ≈ 1. Of the CSH phases, tobermorite is the strongest and the least permeable (Meller et al. 2007; Sanders and Smothers 1957).

To explain the compressive strength and ϕ-k measurements further, FTIR results are presented in **Fig. 2.64**. The FTIR spectrum peaks of calcium hydroxide, CSH and calcium carbonate were extracted from FTIR spectra of different zones for the cores. In virgin (inner) and middle zones, only CSH was preserved while all the portlandite was consumed regardless of the CO_2 concentration. This is due to high reactivity and quick dissolution of portlandite in carbonic acid environment, which resulted in the formation of $CaCO_3$ in all zones.

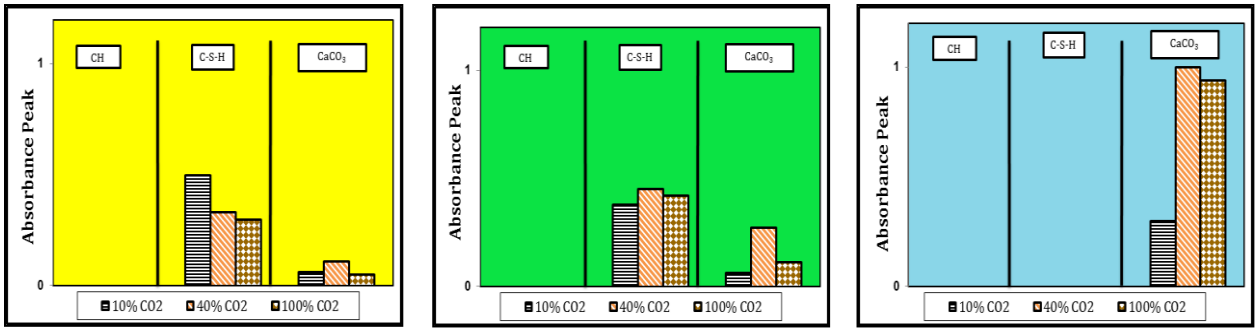

(a) (b) (c)

Fig. 2.64: FTIR of Class H cement aged at 225°F and 3000 psi: a) virgin zone; b) middle zone; and c) outermost zone

Overall, Class H cement demonstrated better integrity for zonal isolation than Class G cement because it is stronger, less porous, and less permeable after exposure. This observation is in agreement with experimental studies conducted by Bruckdorfer (1986) in which Class H cement was found to be more CO_2-resistant. This justifies its suitability as the standard cement used for oil and gas well cementing in the US Gulf coast, the Midcontinent, and the Permian basin while Class G is used primarily in the western US, Canada, and most other parts of the world (Smith 1991).

At High Temperature (350°F): In this section, the effects of CO_2 concentration on compressive strength (**Fig. 2.65**) as well as ϕ-k of Class G and Class H cements (**Fig. 2.66**) are investigated. For Class H cement, the trend is similar to the results obtained from tests conducted at 225°F: strength increased while ϕ-k decreased as CO_2 concentration was increased. However, close examination of the experimental data reveals that elevated temperature accelerated the rate of leaching at high CO_2 concentrations (40% and above). However, carbonation was still dominating. As a result, strength improved and ϕ-k decreased compared to the unaged sample.

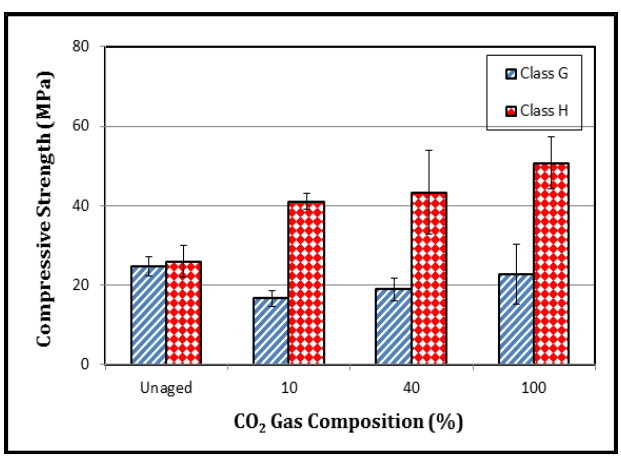

Fig. 2.65: Compressive strength vs. CO_2 concentration for cements aged at 350°F and 3000 psi

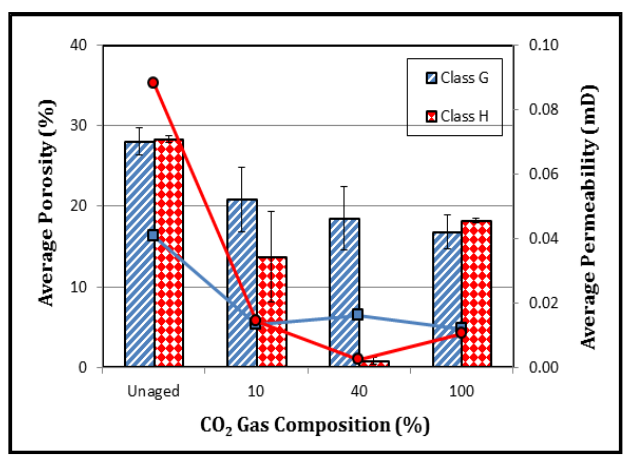

Fig. 2.66: Porosity and permeability vs. CO_2 concentration for cements aged at 350°F and 3000 psi

FTIR data (**Fig. 2.67**) reveals the preservation of CSH in virgin and middle zones of the samples at any CO_2 concentration. However, CH was almost completely consumed indicating its high solubility and reactivity toward carbonic acid. Due to limited ionic diffusion in the cement matrix, the acid concentrations in the outer and inner zones vary greatly. CSH was not significantly consumed in virgin and middle zones, even though the acid was able to reach all the zones. The preservation of CSH maintained the mechanical strength. In the outer zone, acid concentration is high, pH is low, and ionic transport is very high. This condition intensifies dissolution and carbonation of CH and CSH, resulting in complete consumption of CH and CSH.

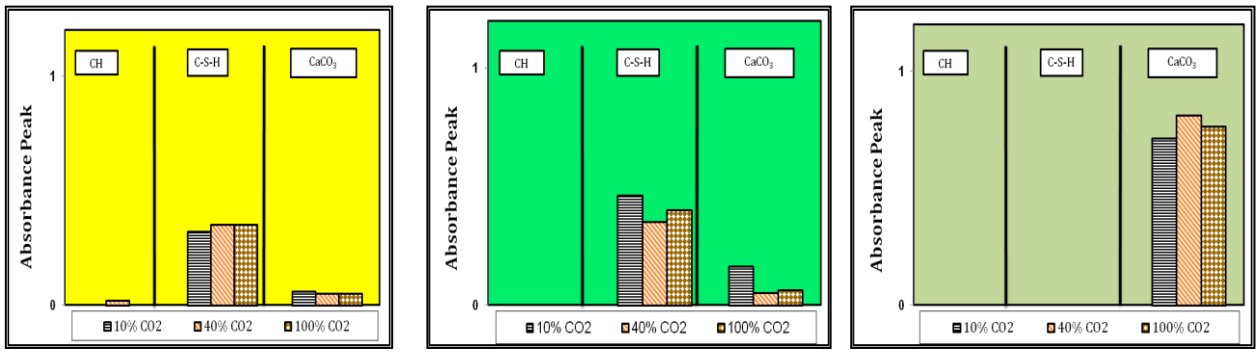

(a) (b) (c)

Fig. 2.67: FTIR results of Class H cement sample aged at 350°F and 3000 psi: a) virgin zone; b) middle zone; and c) outermost zone

Effects of H_2S

Figure 2.68 presents the compressive strength data for Class H cement samples aged in fluid systems with and without H_2S at different temperatures. The compressive strengths of samples aged at 100°F in fluid system without H_2S are almost similar to those of the unaged samples.

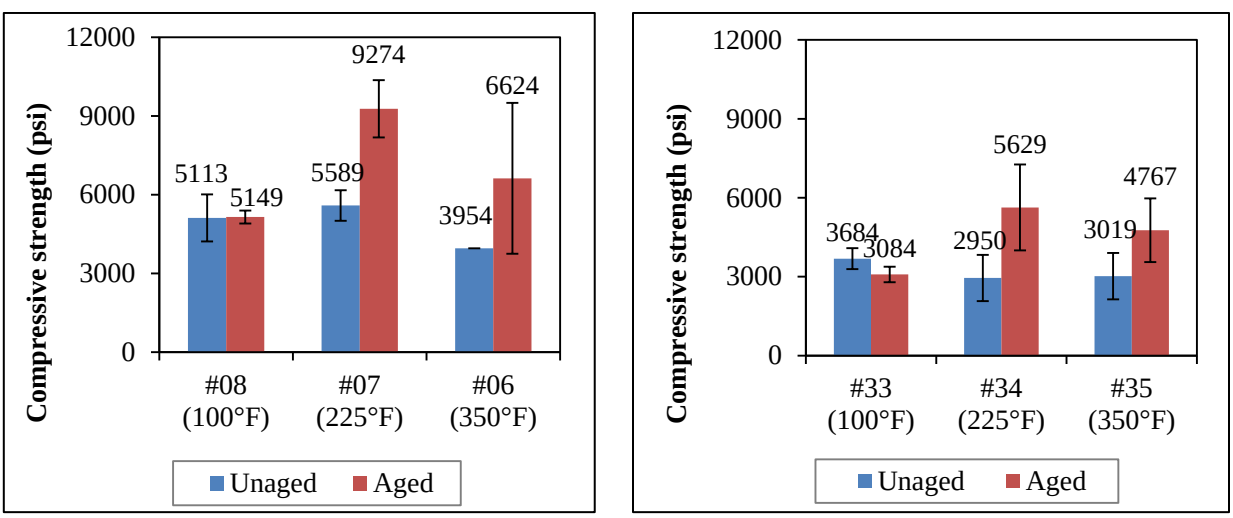

(a) (b)

Fig. 2.68: Compressive strength of Class H samples aged at 6000 psi and different temperatures in: a) fluid system without H_2S; b) fluid system with H_2S

At this low temperature (Fig. 2.68), the increase in compressive strength is due to carbonation which offsets the decrease in compressive strength caused by higher dissolution of CH. Thus, no significant net change in compressive strength is observed at 100°F. However, there is some decrease in compressive strength of samples aged in fluid systems with H_2S which may be due to formation of ettringite. As can be seen from FTIR data the decrease in compressive strength may be because of reduction of carbonates formed in the samples. Increase in compressive strength is observed at 225°F for samples aged in fluid systems with and without H_2S. The increase in compressive strength is due to the formation of calcium carbonate. In addition, solubility of CH decreases with increase in temperature resulting in less increase of porosity. The presence of H_2S does not seem to have any significant effect on the compressive strength of the samples. At 350°F, the increase in compressive strength of samples aged in fluid systems with and without H_2S is almost the same (Fig. 2.68). Thus, H_2S does not seem to affect the compressive strength of samples significantly.

2.4.1.3. Shear Bond Strength

Resembling compressive strengths, shear bond strength (SBS) of cement strongly affected by degradation phenomena such as dissolution, carbonation, bicarbonation, and leaching. The formation of $CaCO_3$ during carbonation tends to increase the volume of the cement within the limited pipe space, creating very tight condition, which improves the shear bond. Nevertheless, bicarbonation and leaching have adverse effect on SBS. They tend to shrink the cement, reducing tightness at the interface between the pipe and the cement, which is necessary for maintaining strong bond. Temperature, pressure, CO_2 concentration and the presence of H_2S strongly affect the degradation process.

Effects of Temperature

Figure 2.69 shows influence of temperature on shear bond strength (SBS) of Class H cement at different CO_2 concentrations and 6000 psi. Tests conducted at different CO_2 concentrations showed similar SBS trend. The SBS increased with temperature until 350°F, and then it showed reduction. Increasing the temperature up to 350°F promoted carbonation and caused the cement to expand resulting in increased SBS. However, at high temperature (430°F), leaching and thermal retrogression offset the effect of carbonation and as a result, the SBS decreased when the temperature was increased above 350°F.

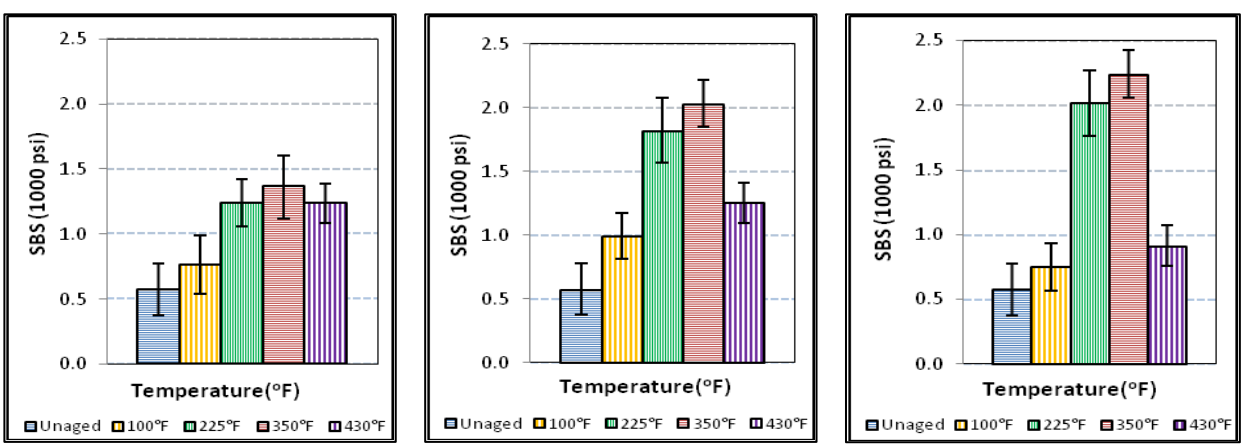

(a) (b) (c)

Fig. 2.69: The effect of temperature at 6000 psi with different CO_2 concentrations: a) 10%; b) 40%; and c) 100%

Effects of Pressure

Increased pressure improves solubility of CO_2 in water at a given temperature. In other words, pressurization increases acidity of the surrounding solution. **Figure 2.70** demonstrates the effect of pressure on the SBS of Class H cement at different CO_2 concentrations (10, 40 and 100%). Unaged samples were not exposed to CO_2 environment; hence, they exhibited considerably lower SBS than aged samples. Tests conducted at 10 and 40% CO_2 concentrations (Fig. 2.70a and 2.70b) showed unexpected SBS trend. Measurements obtained at 6000 psi displayed reduction in SBS. However, when the carbon dioxide concentration was increased to 100%, the maximum SBS was obtained by aging the samples at 6000 psi.

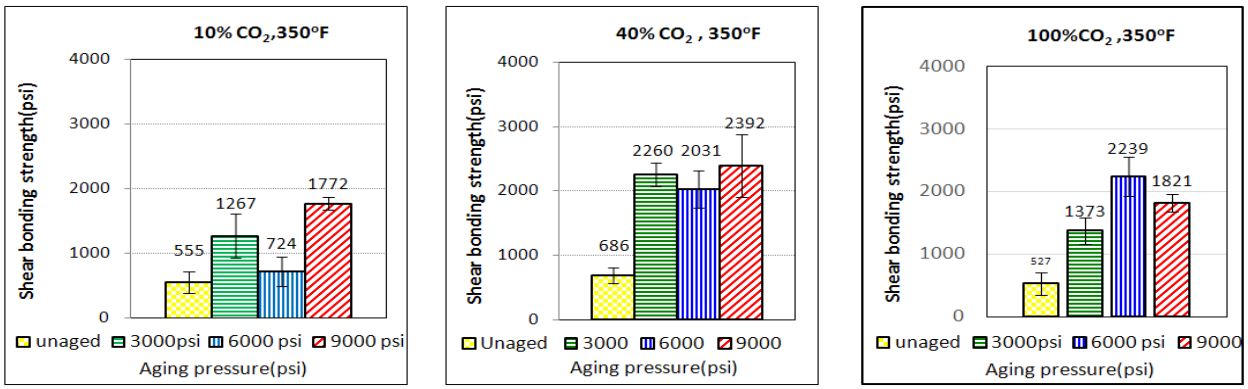

(a) (b) (c)

Fig. 2.70: Effect of aging pressure on SBS of samples aged at 350°F for 14 days in brine saturated with different CO_2 concentrations: a) 10%; b) 40%; and c) 100%

At higher aging pressures, acid penetration increases (Sauki et al. 2010). **Figure 2.71** shows the influence of aging pressure on SBS at different temperatures (225°F and 350°F). Bond strength increased with pressure due to improvement in carbonation resulting from increased pressure that causes more gas to dissolve in the brine. The formation of $CaCO_3$ tends to increase the volume of the cement within the limited pipe space, creating very tight condition, which improves the bond. Penetrated depth measurements obtained from bisected SBS sample (only the cement portion) are in agreement with the SBS measurements (**Fig. 2.72**).

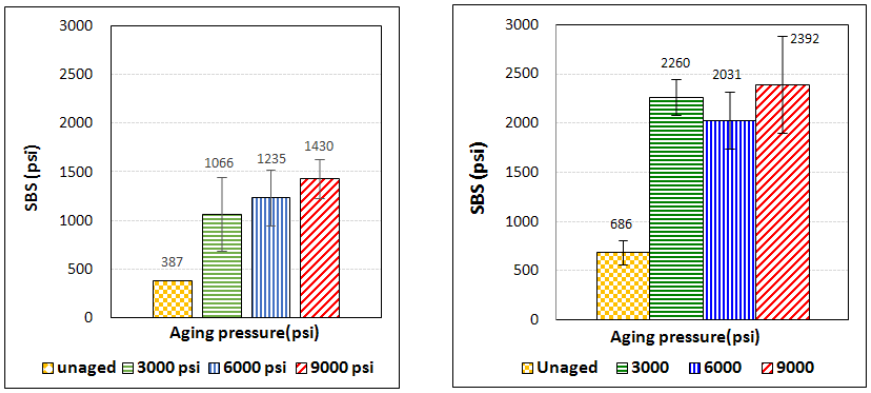

(a) (b)

Fig. 2.71: Influence of aging pressure on shear bond strength at 40% CO_2 concentration and different temperature: a) 225°F; and b) 350°F

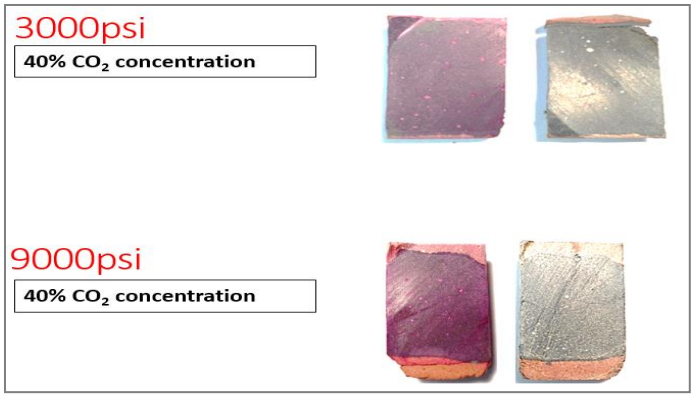

Fig. 2.72 Penetration depth observed after applying Phenolphthalein solution to identify degraded zone (T = 225°F)

Effects of CO_2 Concentration

The effects of CO_2 concentration on shear bond strength (SBS) at 225°F and 350°F are presented in **Figs. 2.73** and **2.74**. Although the trend of SBS remained unchanged with the pressure, it varied with temperature. At 225°F, the SBS consistently increased with CO_2 concentration because of carbonation, which makes the cement to expand. As expected, increased pressure results in additional carbonation and hence higher bond strength. Tests conducted at 350°F showed a different trend (Fig. 2.74). The SBS increased as the concentration of CO_2 was increased from zero to 40 percent. However, when the concentration increased above 40%, reduction in bond strength was observed. At low concentrations (less than 40%), carbonation of the cement dominated the leaching process leading to improved strength. As the CO_2 concentration was increased, additional CO_2 dissolved in brine, resulting in high carbonic acid concentration in the solution. This condition facilitated bicarbonation process and subsequent leaching (partial) of carbonation products causing shrinkage of the matrix and reduction in SBS. Tests conducted at high pressure (9000 psi), exhibited similar SBS trend that indicates maximum SBS at 40% CO_2 concentration. As anticipated, increasing pressure mostly increased the SBS.

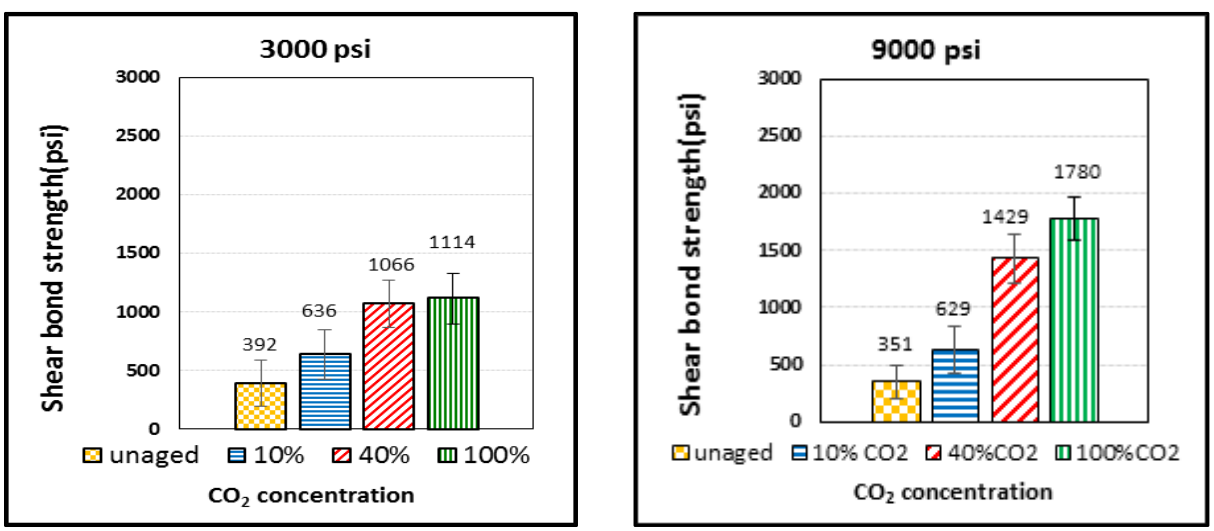

Fig. 2.73: Influence of CO_2 concentration on shear bond strength at 225°F

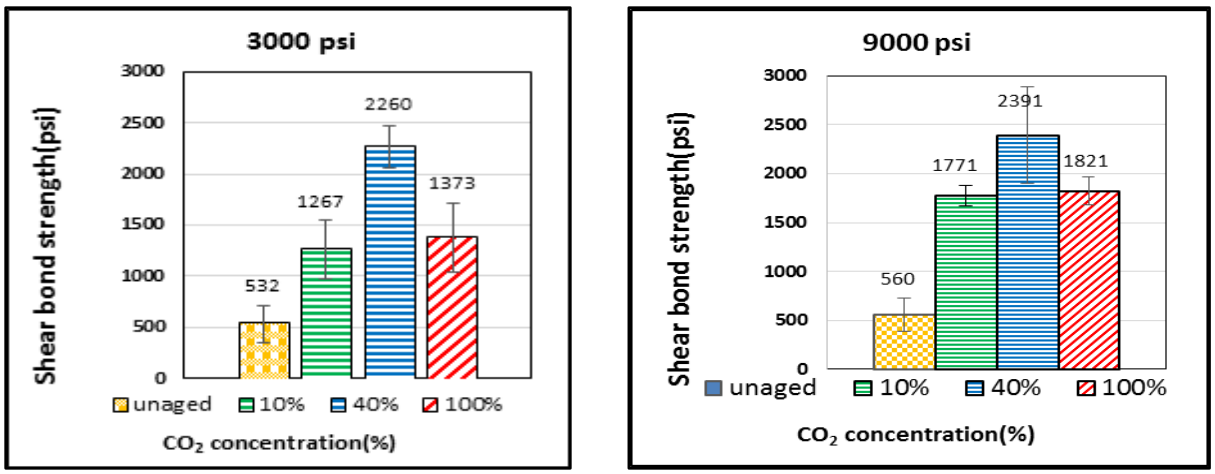

Fig. 2.74: Influence of CO_2 concentration on shear bond strength at 350°F

Effects of H_2S

The presence of H_2S gas in the system can affect the degradation of cement. Shear bond samples were aged in fluid system with and without the presence of H_2S gas to examine the impact of sour gas on SBS of Class H cement. **Figure 2.75** shows the effect of H_2S gas on SBS at 6000 psi and different temperatures with and without the presence of H_2S.

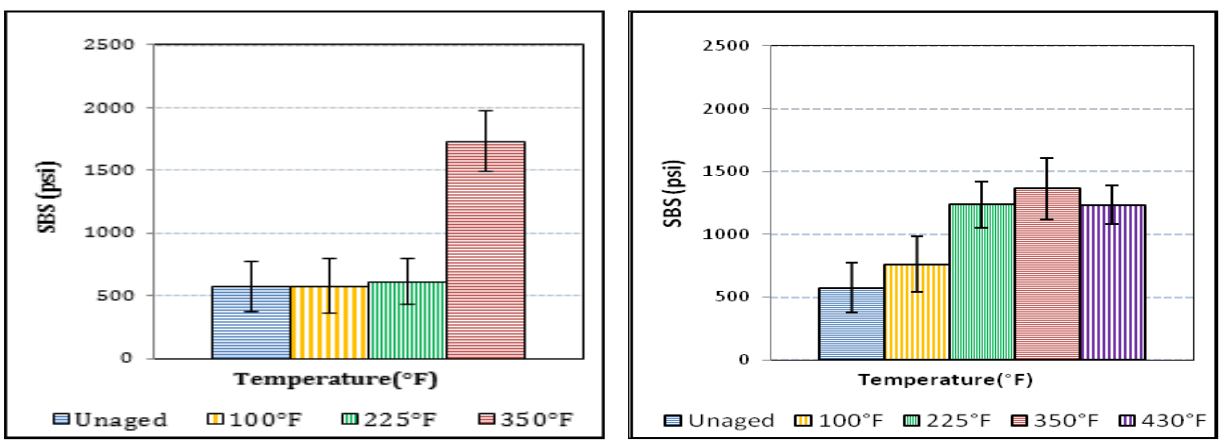

(a) (b)

Fig. 2.75: SBS of Class H sample aged for 14 days in brine saturated with methane containing 10% CO_2 at 6000 psi and different temperatures in fluid system: a) with H_2S; b) without H_2S

When samples were aged in fluid system without H_2S at temperature less than 350°F, SBS increased with temperature due to carbonation (Fig. 2.75b). Carbonation dominates by precipitating $CaCO_3$ thereby reducing porosity and permeability, and increasing compressive and bond strengths of the cement. When the samples were aged in fluid system containing H_2S, SBS was not improved with temperature up to 225°F. At low temperature, H_2S solubility in brine is higher than that of CO_2. As a result, the presence of dissolved H_2S substantially reduces the solubility of CO_2 and formation of carbonic acid. With limited carbonic acid attack, minimal cement carbonation occurs. At 350°F, enormous increase in SBS was observed after aging in fluid system with H_2S. This is due to the combined

effect of cement carbonation and formation of gypsum at high temperatures. At high temperature (350°F), solubility of CO_2 increases while that of H_2S reduces. The condition favors the carbonation of cement to some extent and SBS development. At the same time, limited H_2S can dissolve to form ferrites, which has the potential to produce gypsum that increases molecular volume and leads to expansion and SBS improvement. The SBS enhancement is in agreement with other cement property measurements such porosity, permeability and compressive strength.

2.4.1.4. FTIR Analysis

Comparison between FTIR and XRD Results

Fourier Transform Infrared Spectroscopy (FTIR) and X-Ray Diffraction (XRD) techniques are commonly used in cement degradation studies. XRD provides more detailed and accurate mineralogical composition of cement than FTIR. In other word, FTIR provides a qualitative analysis whereas XRD provides both qualitative and quantitative analysis of the sample mineralogy. Moreover, it is able to differentiate between different phases.

In order to validated our FTIR results, limited number of XRD tests were conducted on both aged and unaged samples. **Figure 2.76** presents FTIR and XRD results of the same samples, which were aged at 225°F and 6000 psi for 14 days in 2% brine saturated with 100% CO_2. The amounts of carbonated ($CaCO_3$) and uncarbonated (CH and CSH) binding components of the cement present in the samples are displayed. Similar composition trends are observed in both measurement techniques. However, some anomalies can be explained by describing the working principles of FTIR and XRD techniques.

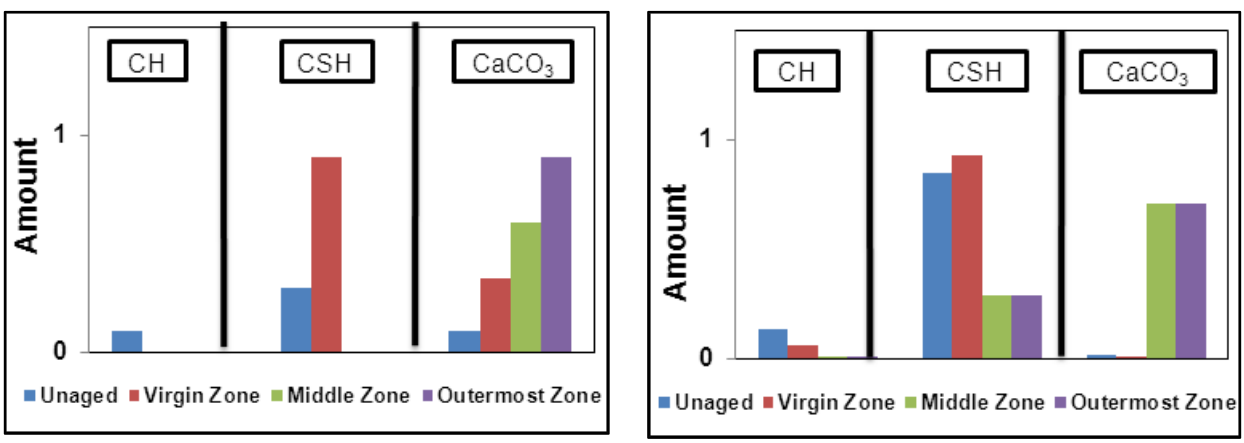

(a) (b)

Fig. 2.76: Mineralogy comparison for samples aged at 100% CO_2, 225°F, 6000 psi and 2% brine solution for 14 days: a) FTIR; and b) XRD

In FTIR method, the entire -CO_3 bonds are shown at wavenumber 1480 cm^{-1}. Hence, it does not specifically indicate the amount of $CaCO_3$ present in the sample. The CO_3 bonds can be from scawtite, which is partially carbonated CSH that exhibits CO_3 bonds. XRD results demonstrate the presence of more CSH phase. This is because XRD is able to distinguish between CSH and scawtite phases. However, FTIR results show the scawtite as the CO_3 bond. Consequently, FTIR measurements displayed strong $CaCO_3$ peak. CSH peaks shown in XRD of middle and outermost zones are mostly from scawtite, as a

result, CSH peaks are absent in the FTIR graphs of middle and outermost zones. In addition, the $CaCO_3$ peaks of unaged and virgin zone are very high in FTIR as compared to XRD. This is also due to scawtite, which is seen as $–CO_3$ bond by FTIR but XRD identifies it as CSH (Carbonated CSH).

Figure 2.77 presents mineralogical profile and a photo of aged cement core in Batch #006. FTIR peaks of CH, CSH and $CaCO_3$ are displayed (Fig. 2.77a) as a function of distance from center of the core. A photo of the core taken after laterally slicing at the middle is presented in Fig. 2.77b. FTIR samples were taken from three different zones (innermost/virgin, middle, and outermost) of the core. The results indicate reduction in CH and CSH contents and increase in $CaCO_3$ concentration with radial distance from the center.

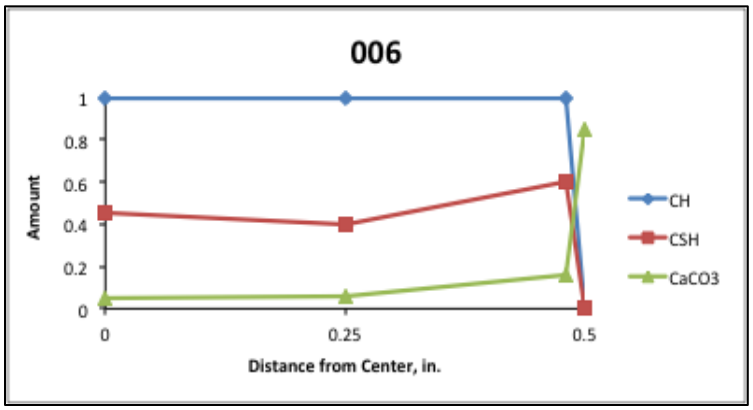

Fig. 2.77: Aged cement core in Batch 006: a) Mineralogical profile; and b) Photograph

Effect of Temperature

Figures 2.78 to **2.86** show how the pressure affects the degradation of baseline cement at different temperatures (100, 225 and 350°F). Result interpretations are summarized in **Table 2.16**.

Table 2.16: Interpretations of FTIR results presented in Figs. 2.78 to 2.86

Figure	Zone	Discussion
Figs. 2.78, 2.79 & 2.80	Virgin	CH was completely carbonated. Some amount of CSH was preserved
	Middle	Ditto
	Outermost	Both CH and CSH were completely carbonated.
Figs. 2.81, 2.82 & 2.83	Virgin	Some amount of CH was preserved at 100 and 350 °F. Some amount of CSH was preserved.
	Middle	Ditto
	Outermost	Both CH and CSH were completely carbonated.
Figs. 2.84, 2.85 & 2.86	Virgin	CH was completely carbonated. Some amount of CSH was preserved
	Middle	CSH was completely carbonated at 100% CO_2.
	Outermost	Both CH and CSH were completely carbonated.

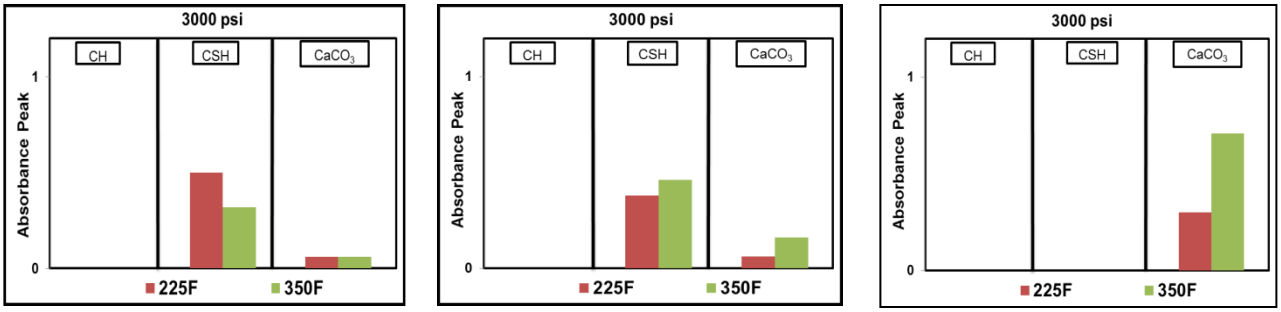

(a) (b) (c)

Fig. 2.78: Summarized FTIR data of baseline Class H cement samples aged at 3000 psi, and 10% CO_2 for 14 days: a) Virgin zone; b) Middle zone; and c) Outermost zone

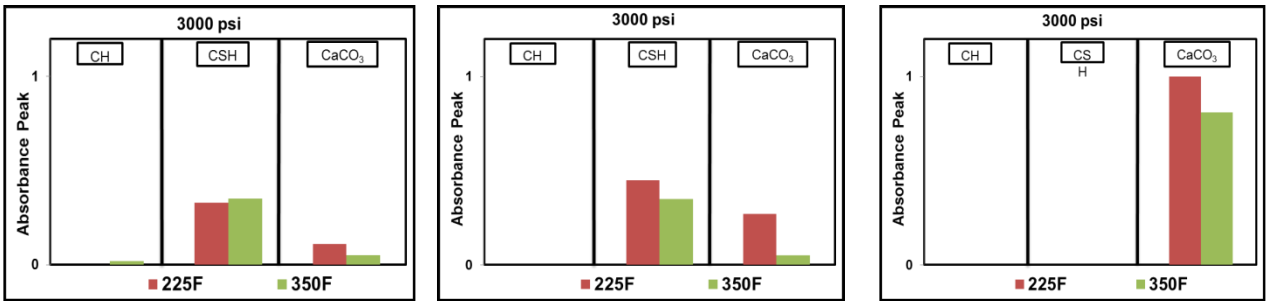

(a) (b) (c)

Fig. 2.79: Summarized FTIR data of baseline Class H cement samples aged at 3000 psi, and 40% CO_2 for 14 days: a) Virgin zone; b) Middle zone; and c) Outermost zone

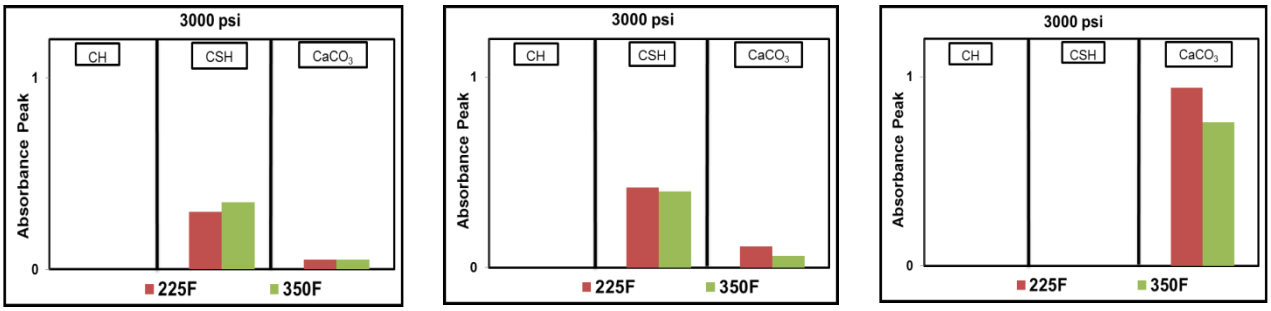

(a) (b) (c)

Fig. 2.80: Summarized FTIR data of baseline Class H cement samples aged at 3000 psi, and 100% CO_2 for 14 days: a) Virgin zone; b) Middle zone; and c) Outermost zone

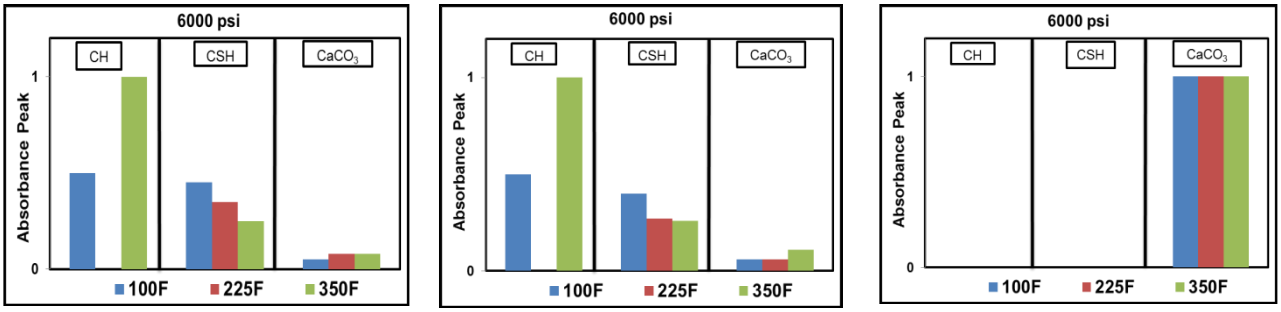

(a) (b) (c)

Fig. 2.81: Summarized FTIR data of baseline Class H cement samples aged at 6000 psi, and 10% CO_2 for 14 days: a) Virgin zone; b) Middle zone; and c) Outermost zone

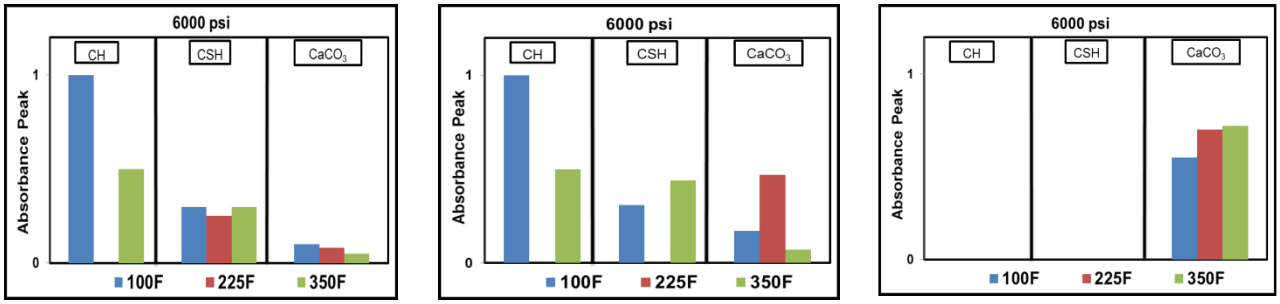

(a) (b) (c)

Fig. 2.82: Summarized FTIR data of baseline Class H cement samples aged at 6000 psi, and 40% CO_2 for 14 days: a) Virgin zone; b) Middle zone; and c) Outermost zone

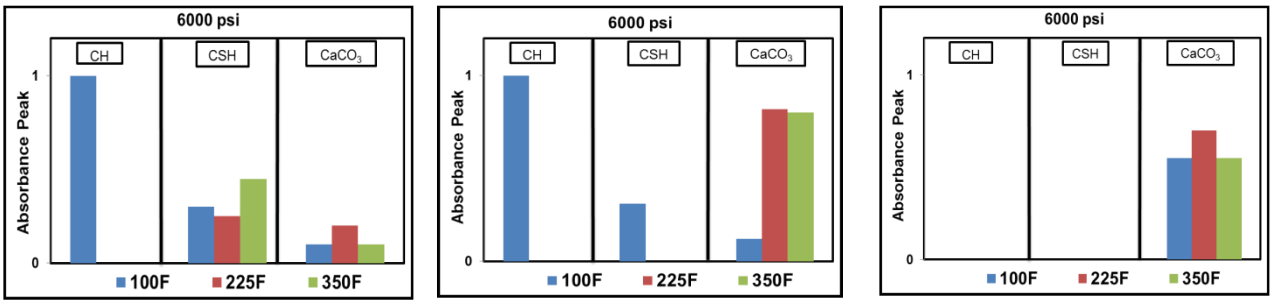

(a) (b) (c)

Fig. 2.83: Summarized FTIR data of baseline Class H cement samples aged at 6000 psi, and 100% CO_2 for 14 days: a) Virgin zone; b) Middle zone; and c) Outermost zone

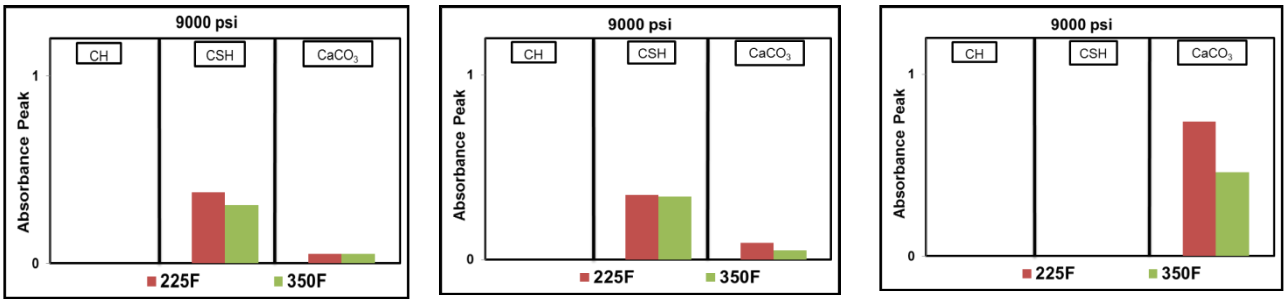

(a) (b) (c)

Fig. 2.84: Summarized FTIR data of baseline Class H cement samples aged at 9000 psi, and 10% CO_2 for 14 days: a) Virgin zone; b) Middle zone; and c) Outermost zone

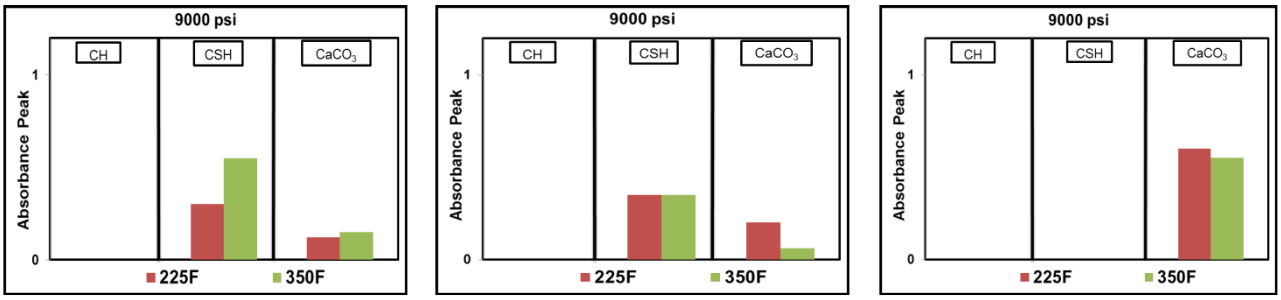

(a) (b) (c)

Fig. 2.85: Summarized FTIR data of baseline Class H cement samples aged at 9000 psi, and 40% CO_2 for 14 days: a) Virgin zone; b) Middle zone; and c) Outermost zone

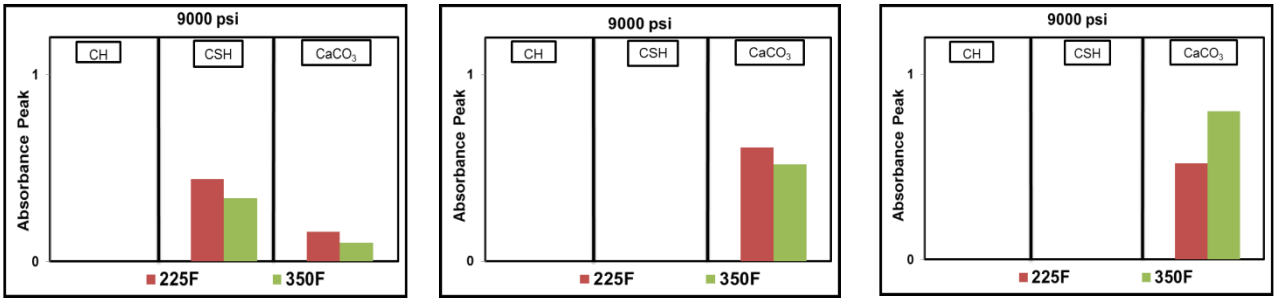

(a) (b) (c)

Fig. 2.86: Summarized FTIR data of baseline Class H cement samples aged at 9000 psi, and 100% CO_2 for 14 days: a) Virgin zone; b) Middle zone; and c) Outermost zone

Effects of Pressure

Figures 2.87 to **2.92** show how pressure affects the degradation of cement at different temperatures (225°F and 350°F). Result interpretations are summarized in **Table 2.17**. As expected, the outer zone is fully carbonated. At 225°F, CSH was less preserved at 6000 psi than other test pressures (3000 and 9000 psi). However, CH component of the cement was only preserved at high temperature (350°F). This could be due to reduction in solubility of CO_2 as the temperature increases.

Table 2.17: Interpretations of FTIR results presented in Figs. 2.87 to 2.92

Figures	Zone	Discussion
Figs. 2.87, 2.88 & 2.89	Virgin	CH was not preserved throughout and carbonation increased with increasing CO_2 concentration
	Middle	The highest carbonation of CSH was occurred at 6000 psi.
	Outermost	Leaching tends to dominate with increasing pressure.
Figs. 2.90, 2.91 & 2.92	Virgin	CH was maximum preserved at 40% CO_2.
	Middle	Maximum degradation occurred at 100% CO_2 where it gradually increased with increasing pressure.
	Outermost	At 10% CO_2, increasing pressure promoted carbonation up to 6000 psi, then leaching became dominant. At 40% CO_2, increasing pressure promoted leaching. At 100% CO_2, the trend is unexpected.

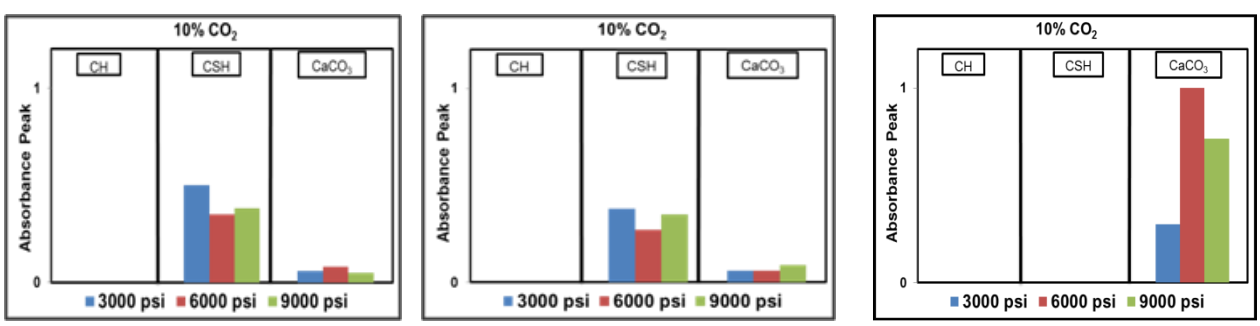

(a) (b) (c)

Fig. 2.87: Summarized FTIR data of baseline Class H cement samples aged at 225°F, 10% CO_2 for 14 days: a) Virgin zone; b) Middle zone; and c) Outermost zone

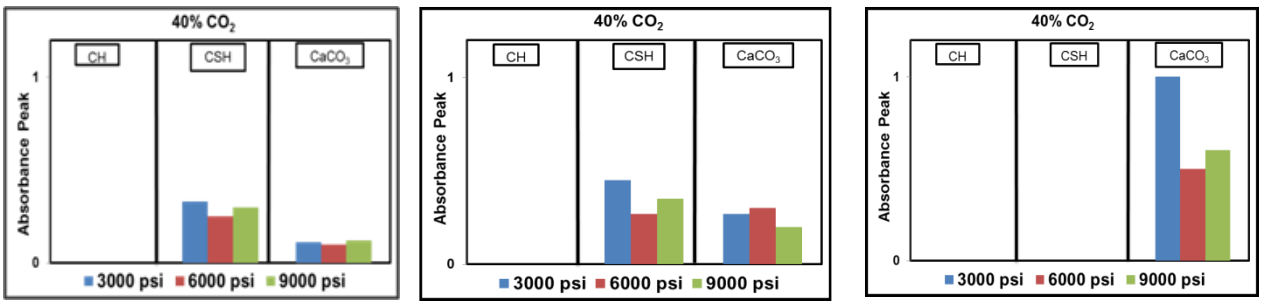

(a) (b) (c)

Fig. 2.88: Summarized FTIR data of baseline Class H cement samples aged at 225°F, 40% CO_2 for 14 days: a) Virgin zone; b) Middle zone; and c) Outermost zone

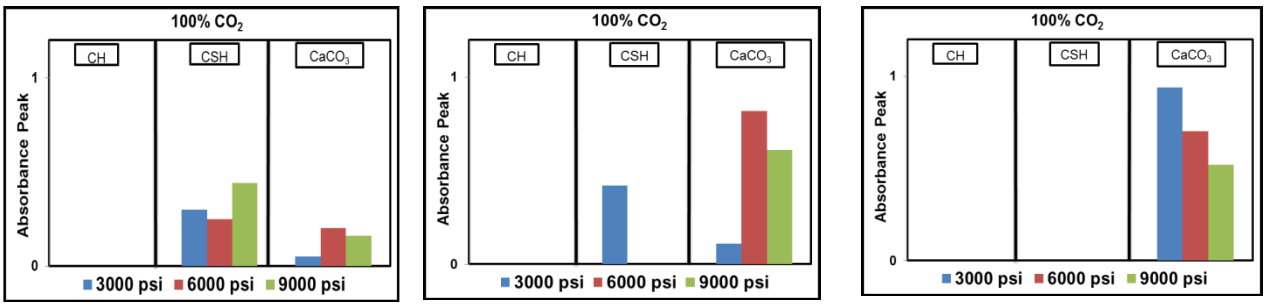

(a) (b) (c)

Fig. 2.89: Summarized FTIR data of baseline Class H cement samples aged at 225°F, 100% CO_2 for 14 days: a) Virgin zone; b) Middle zone; and c) Outermost zone

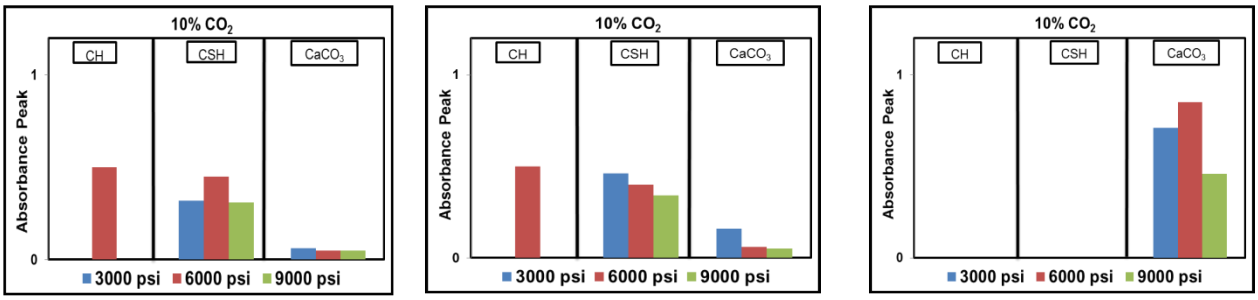

(a) (b) (c)

Fig. 2.90: Summarized FTIR data of baseline Class H cement samples aged at 350°F, 10% CO_2 for 14 days: a) Virgin zone; b) Middle zone; and c) Outermost zone

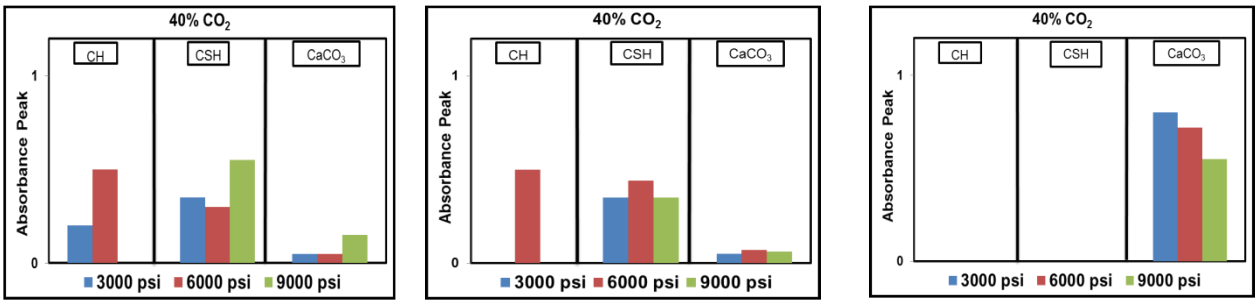

(a) (b) (c)

Fig. 2.91: Summarized FTIR data of baseline Class H cement samples aged at 350°F, 40% CO_2 for 14 days: a) Virgin zone; b) Middle zone; and c) Outermost zone

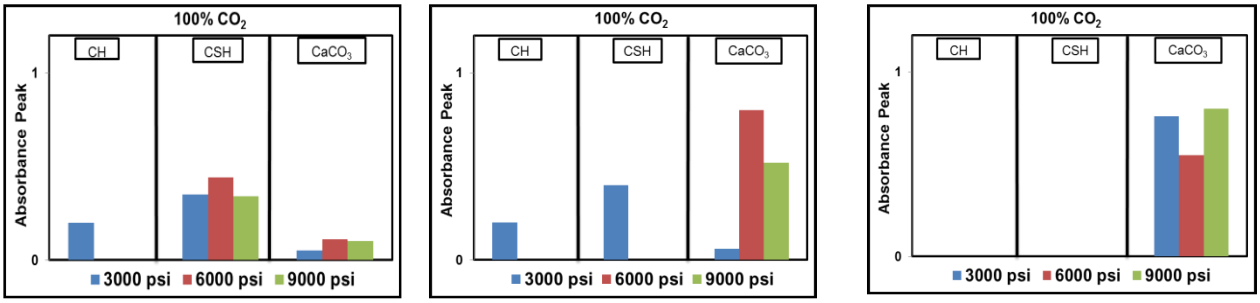

(a) (b) (c)

Fig. 2.92: Summarized FTIR data of baseline Class H cement samples aged at 350°F, 100% CO_2 for 14 days: a) Virgin zone; b) Middle zone; and c) Outermost zone

Effects of CO_2 Concentration

Figures 2.93 to **2.98** illustrate the effect of CO_2 concentration in the gas phase on the composition of aged cement at different temperatures (225°F and 350°F). Interpretation of the results is summarized in **Table 2.18**. In all cases, the outer zone is fully carbonated. This is expected, as the outer zone is the most exposed zone for the acid attack. In some cases, results from the outer zone show reduction in $CaCO_3$ content with increasing CO_2 content of the gas. This could be attributed to the conversion of $CaCO_3$ to $Ca(HCO_3)_2$ and eventually leaching out of the cement matrix. CH is more reactive than CSH. It is only preserved in the virgin zone of a core aged at 6000 psi and 350°F. However, at high CO_2 concentration (100%), CH was completely carbonated. Increased pressure tends to facilitate the carbonation of CSH. At high pressures (6000 and 9000 psi) and high concentration of CO_2, CSH was completely consumed by the acid. FTIR results that show the effects of pressure and temperature on baseline cement degradation are presented in monthly Report #27.

Table 2.18: Interpretations of FTIR results presented in Figs. 2.93 to 2.98

Figures	Zone	Discussion
Figs. 4 & 5	Virgin	CH was absent while CSH was present. Limited carbonation occurred.
	Middle	CH was absent. However, CSH was present. Slightly higher carbonation than the virgin zone.
	Outermost	CH and CSH were absent. Carbonation was considerable. Test with 100% CO_2 showed slight leaching.
Figs. 6 & 7	Virgin	CH was absent at 225°F in all zones.
	Middle	More CSH was present at 350°F than 225°F.
	Outermost	More carbonation occurred when CO_2 content of the gas was increased.
Figs. 8 & 9	Virgin	No major difference between 225°F and 350°F results.
	Middle	No major difference between 225°F and 350°F results.
	Outermost	CH and CSH were fully carbonated. As CO_2 concentration increased, leaching became dominate at 225°F.

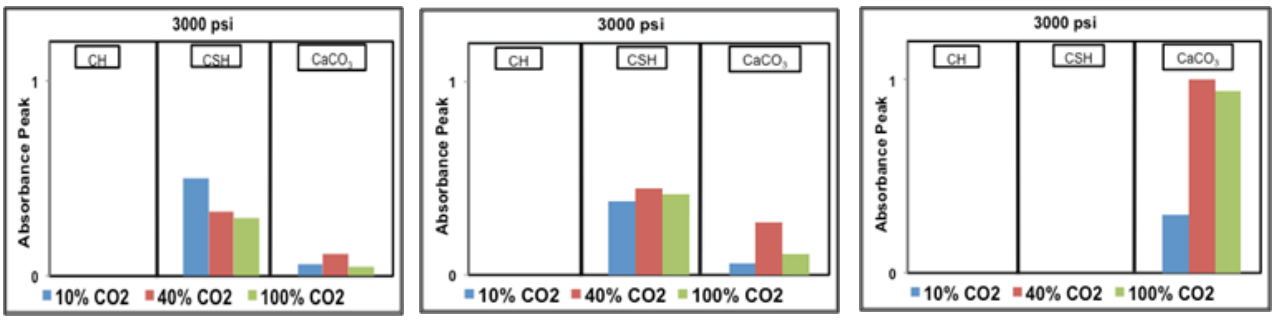

(a) (b) (c)

Fig. 2.93: Summarized FTIR data of baseline Class H cement samples aged at 225°F, 3000 psi for 14 days: a) Virgin zone; b) Middle zone; and c) Outermost zone

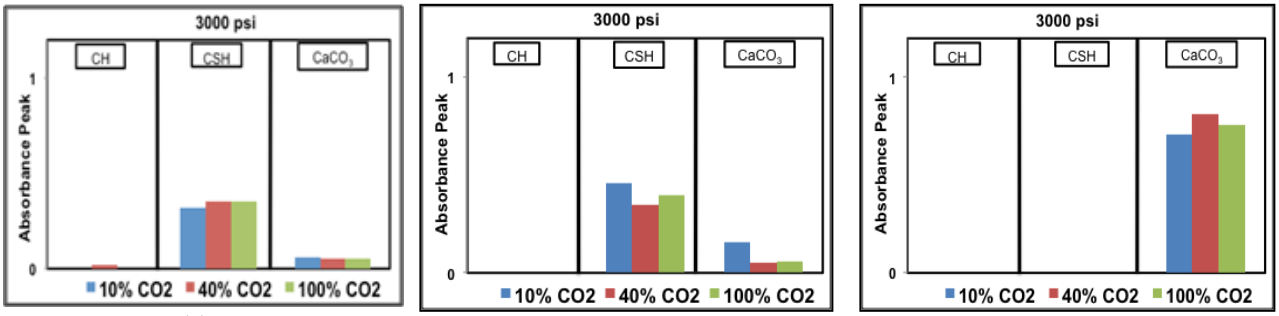

(a) (b) (c)

Fig. 2.94: Summarized FTIR data of baseline Class H cement samples aged at 350°F, 3000 psi for 14 days: a) Virgin zone; b) Middle zone; and c) Outermost zone

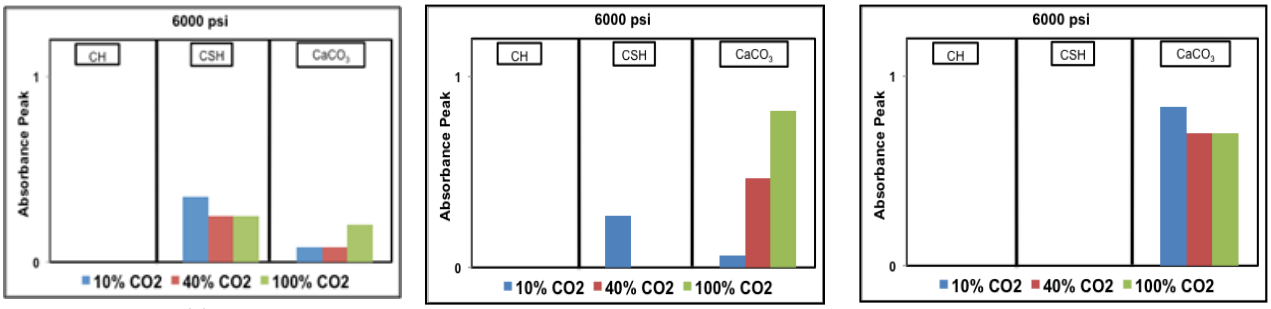

(a) (b) (c)

Fig. 2.95: Summarized FTIR data of baseline Class H cement samples aged at 225°F, 6000 psi for 14 days: a) Virgin zone; b) Middle zone; and c) Outermost zone

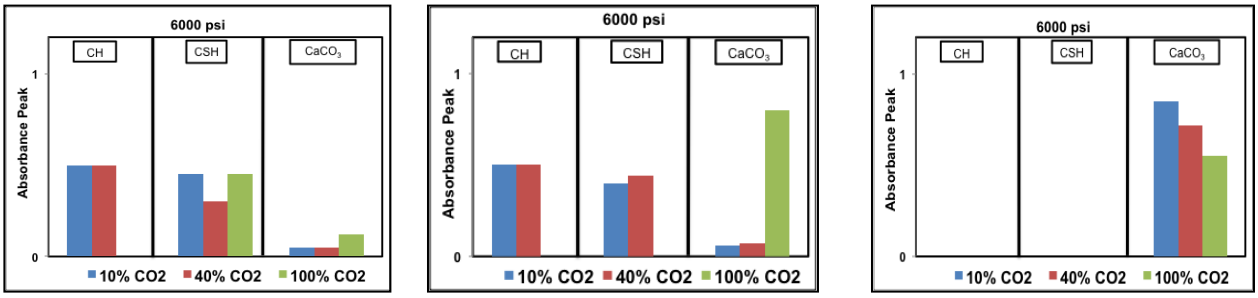

(a) (b) (c)

Fig. 2.96: Summarized FTIR data of baseline Class H cement samples aged at 350°F, 6000 psi for 14 days: a) Virgin zone; b) Middle zone; and c) Outermost zone

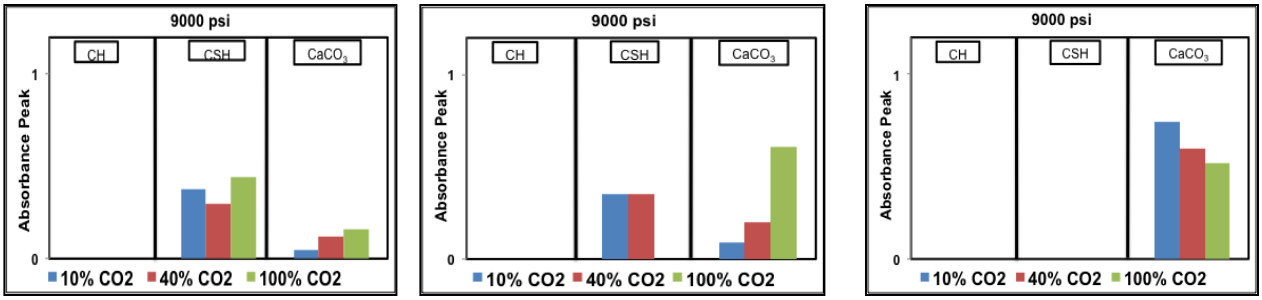

(a) (b) (c)

Fig. 2.97: Summarized FTIR data of baseline Class H cement samples aged at 225°F, 9000 psi for 14 days: a) Virgin zone; b) Middle zone; and c) Outermost zone

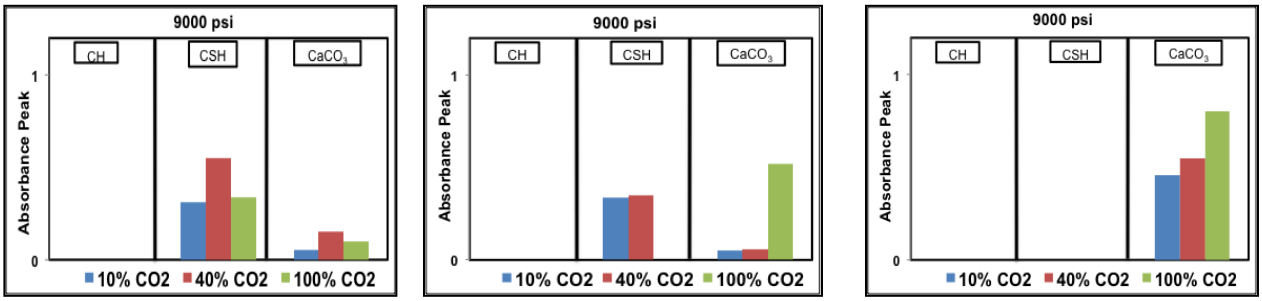

(a) (b) (c)

Fig. 2.98: Summarized FTIR data of baseline Class H cement samples aged at 350°F, 9000 psi for 14 days: a) Virgin zone; b) Middle zone; and c) Outermost zone

Effects of H_2S

FTIR mineralogy of Class H baseline samples aged in fluid systems with and without H_2S at different temperatures is discussed in this section. As discussed earlier, ettringite and pyrite cannot be identified using FTIR. **Figure 2.99** shows the FTIR data for Class H cement samples aged in fluid systems with and without H_2S at 225°F.

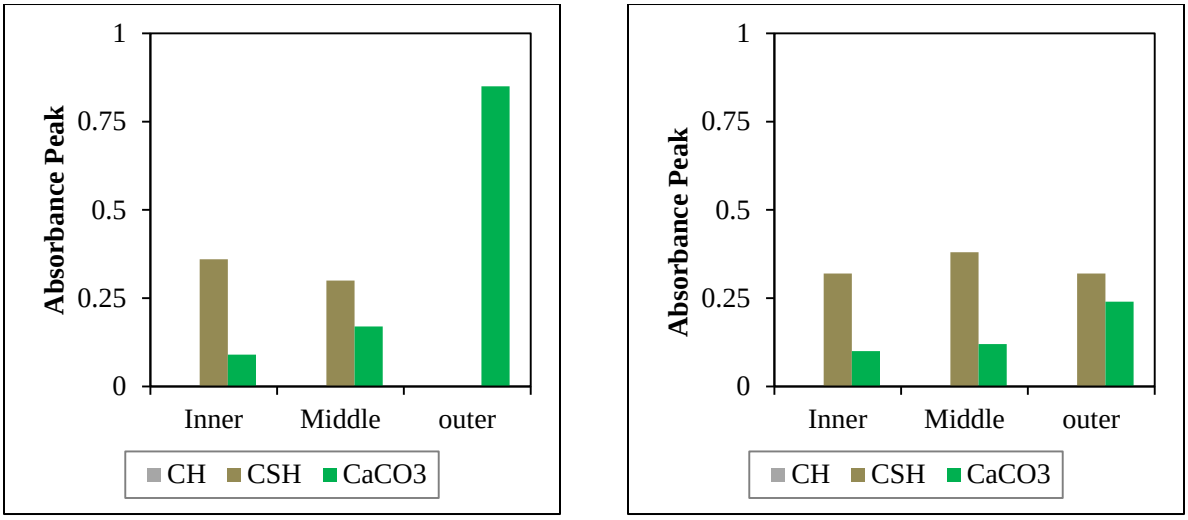

(a) (b)

Fig. 2.99: FTIR data for Class H samples aged at 225°F and 6000 psi in fluid system: a) without H_2S; b) with H_2S

CH and CSH peaks in Fig. 2.99 were not observed in the outer layer of samples aged in fluid system without H_2S. A very high carbonate peak was also observed for these samples. However, for samples aged in fluid system with H_2S, the CSH peak was present. Moreover, the carbonate peak was lower than that of sample aged in fluid system without H_2S. Thus, the level of carbonation was higher for samples aged in fluid system without H_2S.

FTIR data of Class H cement samples, aged in systems with and without H_2S at 350°F is presented in **Fig. 2.100**. It is seen that the FTIR data is not conclusive for samples aged in system with H_2S, as there were no CH peaks in the middle and inner layers; however, some CH was observed in the outermost layer. Consistent with the results of the aging test conducted at 225°F, the degree of carbonation is higher for samples aged in fluid system without H_2S.

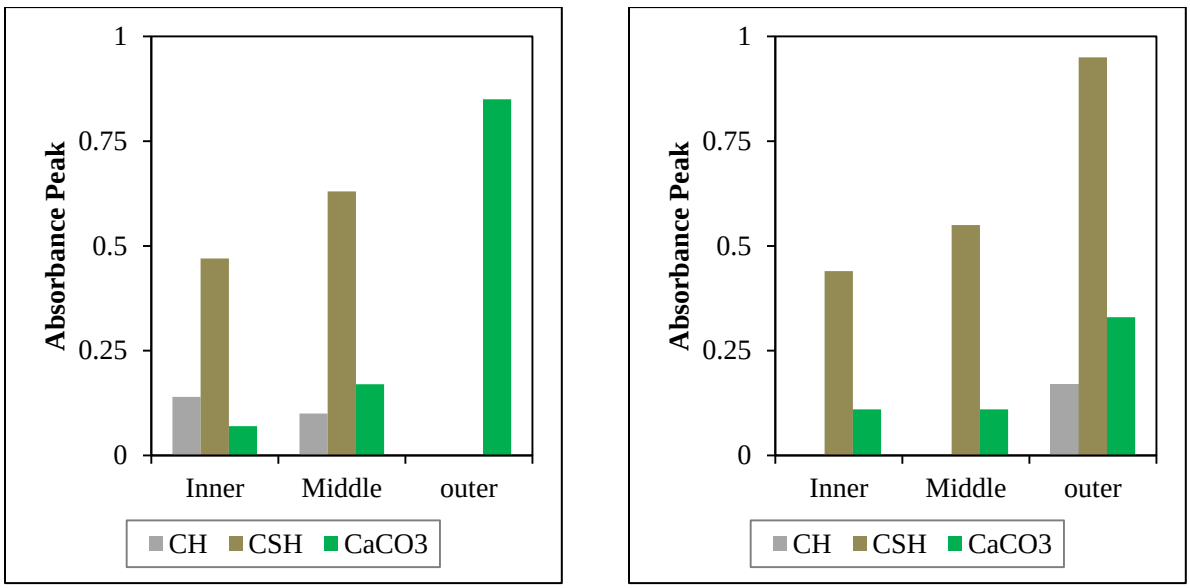

Fig. 2.100: FTIR data for Class H samples aged at 350°F and 6000 psi: a) in fluid system without H_2S; b) in fluid system with H_2S

2.4.2. Acid Resistance of New Cement Formulations

2.4.2.1. Additive Screening Study

Additive containing cement (additive cement) samples were rigorously tested before they were kept in the aging cell. Performance evaluation method was established for selecting additive cement formulations that meet basic characteristics of conventional oil well cement (baseline cement) in unaged condition.

Methodology

In order to conduct the additive screening study, initial cement formulations were developed for each selected additives. The formulations were based on the findings of literature review, inputs from TAB members, and studying the behavior of the additives. Subsequently, physical properties of the formulated slurries were measured and compared with those of the baseline cement slurries. The following pre-aging tests were performed to select suitable additives:

I. Slurry Properties

Slurry Density: Applying ideal mixing rules, the theoretical density of the additive cement slurry was determined based on its formulation. The density of the slurry was adjusted to be in the range of that of the baseline slurry by slightly modifying its formulation. The actual density of the slurry was measured immediately after its preparation. Conventional oil field mud balance was used to measured slurry density.

Slurry Viscosity: Rheological properties of the slurries were measured and compared with that of baseline cement slurry. Standard oil field viscometer (OFITE Model 900 Viscometer) was used to measure slurry viscosity. The viscosity measurements were taken immediately after the slurry was prepared.

Filtration Loss: The filtration loss of cement slurry was tested using a standard filter press. The test was performed using freshly prepared slurry. Measurements of the additive cement slurry were compared with that of the baseline.

Slurry Consistency: The thickening time of the slurry was measured with the consist-o-meter and compared with that of the baseline cement slurry. A very long or short thickening time was compensated with use of accelerators or retarders. The consist-o-meter test was conducted immediately after the slurry was prepared.

II. Hardened Cement Properties

Additive slurries that provided acceptable density, viscosity, fluid loss and consistency were further investigated for their suitability. Additive slurries were prepared and cured with baseline cement slurries. After preparation, the slurries were poured into rubber molds, immersed into 2% brine (NaCl) solution and placed in an oven for 5 days. Oven temperature was maintained at 200°F. In addition, parts of the slurries were poured into one-end plugged steel pipes to prepare shear bond strength (SBS) samples. SBS samples were also immersed in brine and cured in the oven together with other samples. After curing, hardened slurry samples were taken out of the rubber molds and 1-inch diameter cores were cut from the hardened cement. Subsequently, the following tests were performed to check if the additive cement meets the required physical properties.

Visual Test: After curing and coring, the cement cores and SBS samples were examined for any irregularity such as micro cracks or other types of physical damages.

Compressive Strength: Confined compressive strength of the cores were measured and compared with that of the baseline cement. Cores with compressive strength similar or better than the unaged conventional cement were selected for further testing. The confined compressive strengths of the cement samples were measured using a special setup developed in this project (Figs. 2.20 and 2.21). The confining pressure was 1000 psi for all the tests. The tests were conducted as per the ASTM-

C39/C39M-12 standard.

Shear Bonding: Selected samples were able to show shear bond strength (SBS), which was comparable with that of the unaged conventional cements. SBS of the samples were measured using a setup developed during the investigation (Figs. 2.20 and 2.21). The contact length of the cement column with the pipe wall was measured to compute the bond area between cement and the pipe. During the test, a hydraulic piston was used to push the cement from the bottom side to break the bond. The shear bond strength of the cement was determined using the contact surface area and the pressure required to break the bond.

Porosity and Permeability: Porosity and permeability of the samples were measured using an automated porosity and permeability testing device (Coretest Model AP-608). Confining pressure of 500 psi and differential pressure of 200 psi were used during the tests (Figs. 2.24). The samples were dried for 24 hours in an oven at 100°F to avoid presence of any moisture in the pore spaces prior to the measurement. Helium gas was used as test fluid.

Microsilica

Light microsilica with bulk density of 288 – 352 kg/m^3 and particle size of less than a micron was used as a cement additive. Several preliminary tests were performed using different cement formulations (Reports # 15 to 24) before the hardened slurry was tested. These tests were required to formulate the slurry that has similar or comparable properties as the corresponding baseline cement slurries and hardened cores. The changes in the compositions were required to optimize the concentration of microsilica and secondary additives such as anhydrous citric acid, Sodium Poly-naphthalene Formaldehyde Sulfonate (NSF) and silica flour. The final microsilica based slurry formulations are presented in **Table 2.19**.

Table 2.19: Compositions of microsilica based slurries (MS-10)

Component	Class G	Class H
Water for cement	44% bwoc	38 % bwoc
Water for Silica Flour	38.5% bwoc	38.5% bwoc
Anti-Foaming Agent	0.1 gal/sk of cement	0.1 gal/sk of cement
Citric Acid	0.02% bwoc	0% bwoc
NSF	1.25% bwoc	1.25% bwoc
HEC	0.1% of water for Silica	0.1% of water for Silica
Cement	100% bwoc	100% bwoc
Silica Flour	25% bwoc	25% bwoc
Microsilica	10% bwoc	10% bwoc

Slurry properties obtained as per the procedure presented in Section 2.3.4.3 are shown in **Table 2.20**. Properties of MS-10 and baseline slurries were comparable. It is important to note that microsilica based slurry formulations were mixed for 2 minutes at 12,000 RPM, whereas the baseline cement formulations were prepared according to the API standard (mixing the slurry at 4,000 RPM for 15 seconds, followed by a 35-second mixing at 12,000 RPM). The special mixing procedure for

microsilica-based slurry was suggested by Grabowski and Gillott (1989) to ensure homogenous mixing and consistent slurry properties.

Table 2.20: Properties of MS-10 and baseline slurries

Property	HSMS	HS	GSMS	GS
Theoretical Density	16.01 ppg	15.96 ppg	15.55 ppg	15.51 ppg
Measured Density	16.20 ppg	16.20 ppg	15.50 ppg	15.45 ppg
Filtration Loss at 7.5 min.	44 ml	50 ml	54 ml	60 ml
Rheological Properties	Bingham PV = 33.52 cP YP = 8.7 lbf/100ft^2	Power Law n = 0.44 K = 14.4 lbf.s$^{0.44}$/100ft^2	Bingham PV = 23.94 cP YP = 9.57 lbf/100ft^2	Power Law n = 0.35 K = 10.5 lbf.s$^{0.35}$/100ft^2
Thickening Time	220 min.	170 min.	145 min.	135 min.

Figure 2.101 shows viscometer measurements of MS-10 and baseline slurries. The dial readings of microsilica slurries were less than that of the baseline slurries, which means that microsilica slurries were less viscous. As a result, they are expected to have better flowability, which is the basic requirement for cement slurry.

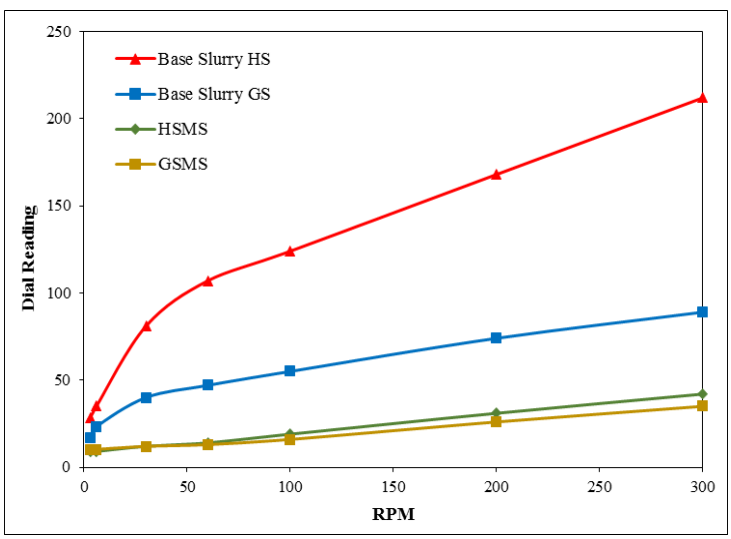

Fig. 2.101: Rheological data of MS-10 and baseline slurries

After hardening, the slurry samples were cored and cement properties such as porosity, permeability, and compressive and shear bond strengths were measured. The unaged porosity and permeability of MS-10 samples were significantly less than that of the baseline samples (**Fig. 2.102**). The values presented in the figure are average values obtained from four samples. The smaller particle size of microsilica was able to fill up the pore space in the matrix and reduce the pore volume as anticipated. The low porosity and permeability is beneficial in reducing the penetration of the acid in the matrix.

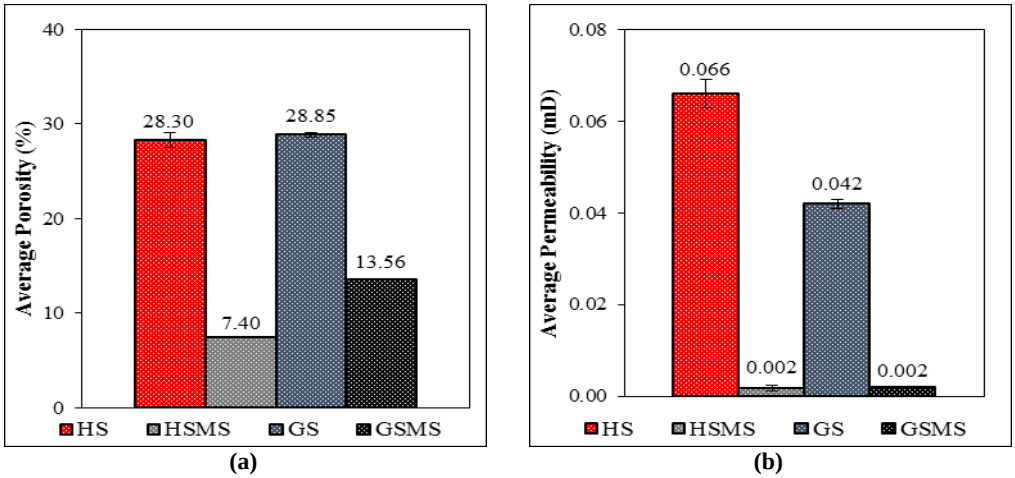

Fig. 2.102: Porosity (a) and Permeability (b) of unaged MS-10 and baseline samples

The average compressive and shear bond strengths of MS-10 samples (**Fig. 2.103**) were slightly higher than that of the baseline samples. This suggests that the matrix properties of the cement system containing microsilica are better than those of the baseline samples. After obtaining encouraging results, microsilica samples were selected for further testing under HPHT acidic environment.

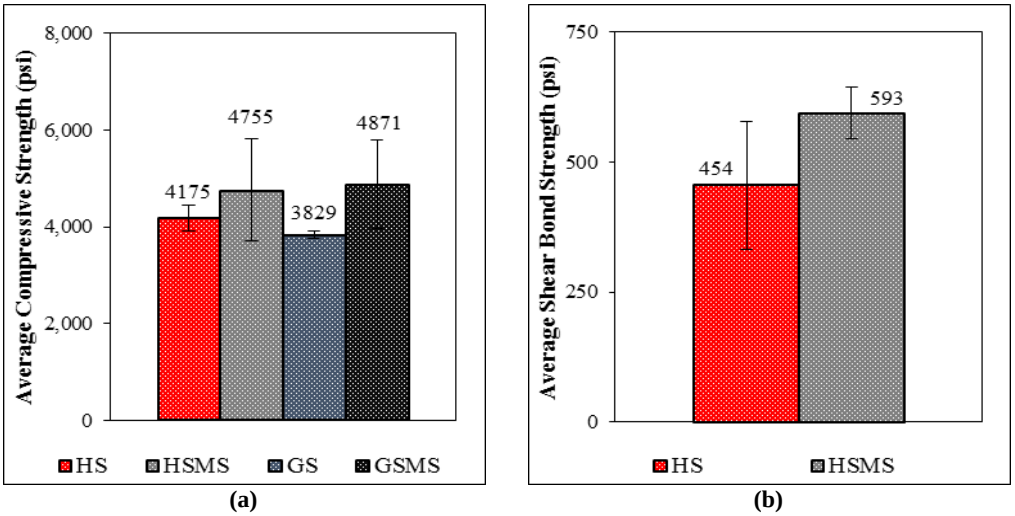

Fig. 2.103: Compressive strength (a) and Shear bond strength (b) of unaged MS-10 and baseline samples

Latex

Latex was selected as a cement additive for preliminary screening study as per the literature review. For the testing, styrene butadiene latex (Styrofan 1186) was used as recommended by the Technical Advisory Board (TAB) members. The latex was in liquid form, containing approximately 50% active polymer components. In order to cure the slurry at 200°F, cationic agent was required to prevent thermal degradation and flocculation (Hou et al. 2010). For this purpose, concentrated acetic acid (0.43% bwoc) was added as recommended by Fuquan et al. (2006).

The latex based cement was prepared with latex concentration of 10% bwoc. This concentration has been recommended by previous studies (Hou et al. 2010). However, during slurry preparation, large amount of air bubbles were formed. The rheology and filtrate loss of latex slurry were found to be better than baseline slurry, even though the density of the slurry was substantially less than that of the baseline cement (Reports #17 to 24).

Consistent with the density reduction, porosity and permeability of unaged latex samples were more than those of baseline samples (**Fig. 2.104**). In addition, latex samples exhibited higher compressive and shear bond strengths than the baseline samples (**Fig. 2.105**). The entrapment of air in latex slurry can be the reasons behind the increase in porosity and reduction in compressive strength. Class G cement was more susceptible towards increase in the porosity. Several different formulations of latex based cement were prepared and tested yielding similar problem of high porosity and permeability. The outcomes of the tests are summarized in **Table 2.21**. In reference to the list of solution methods presented in Table 2.21, the last option was to use a filler material such as microsilica along with latex.

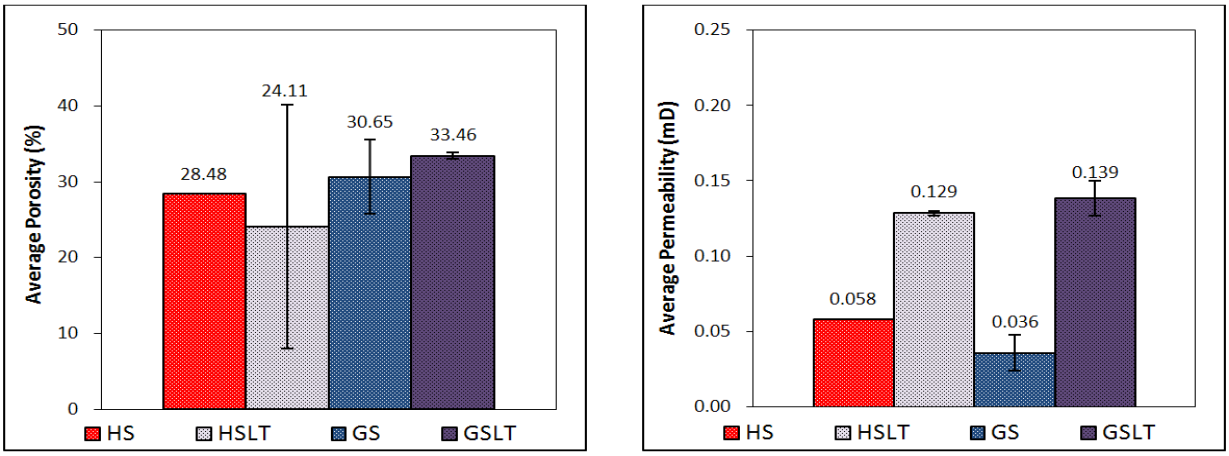

(a) (b)

Fig. 2.104: Porosity (a) and Permeability (b) of unaged latex and baseline samples

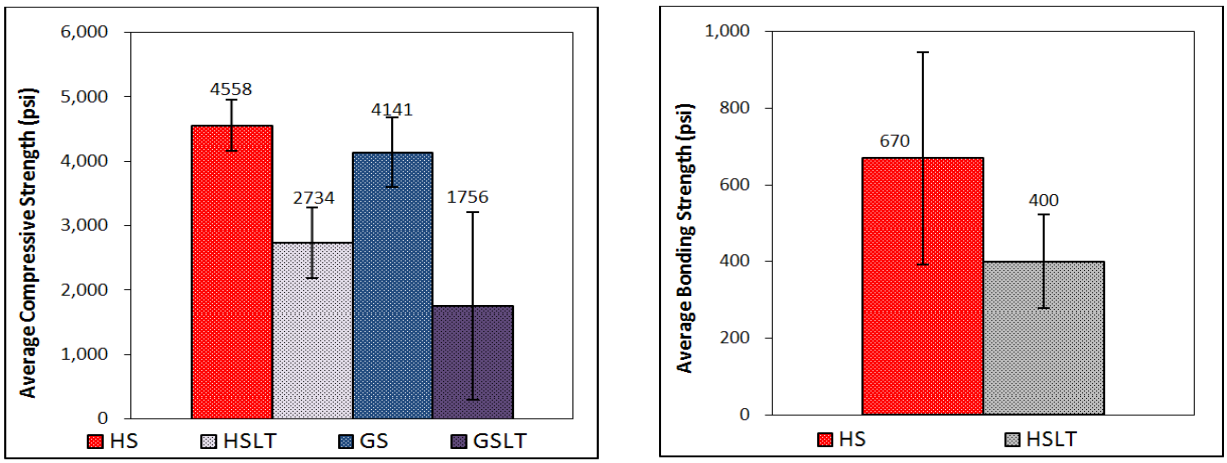

(a) (b)

Fig. 2.105: Compressive strength (a) and Shear bond strength (b) measurements of unaged latex and baseline samples

Table 2.21: Summary of latex cement slurry testing results (Reports 17 to 24)

Possible Reasons for Porosity Increased	Measures Taken	Remarks/Outcomes
Property of latex to entrap air	Reduce mixing speed	Not recommended by API
	Use larger amount of surfactant	Not highly effective as tests revealed
	Use pressurized curing	Not applicable for the current research as baseline slurries were cured at atmospheric pressure
Small particle size of latex, which is not able to bond with cement and hence creates gaps which may act as micro-cracks.	Improve bonding between latex and cement using a carboxylate – SBR latex	Tested for several compositions, carboxylate group results in thick slurry.
	Use filler material such as microsilica to fill in the pore space and cracks	LTMS slurry was tested. Its porosity was extremely low.

As it was observed in a number of unaged sample tests, the permeabilities of latex samples (HSLT and GSLT) were higher than those of baseline samples. The reason for increased permeability could be entrapment of air bubbles in the latex. The composition of the latex slurry is presented in **Table 2.22**. Even though latex showed higher unaged core permeability than the baseline, other properties were comparable. As a result, it has been selected for further testing under HPHT acidic environment.

Table 2.22: Composition of latex slurry

Component	Percentage Amount
Cement	100%
Silica Flour	35% bwoc
SBR Latex	10% bwoc
Acetic Acid (Emulsifier)	0.43% bwoc
HEC	0.1% of water for fillers
Antifoam Agent	0.1 gal/sack of cement
Water for Cement	38% bwoc – Class H 44% bwoc – Class G
Water for Silica Flour	38.5% of silica flour
bwoc = by weight of cement	

Latex with Microsilica

To prepare latex-microsilica based slurry, 10% latex and 10% microsilica were added to the baseline cement. This formulation was adopted from a similar study (Hou et al. 2010) conducted on latex cement. Several tests were performed with different LTMS slurry formulations to obtain optimized dispersant concentration to be used (Reports #23 and 24). The final compositions of the slurries are presented in **Table 2.23**.

Table 2.23: Compositions of LTMS slurries

Component	Class G	Class H
Water for cement	44% bwoc	38% bwoc
Water for Silica Flour	38.5% bwoc	38.5% bwoc
Anti-Foaming Agent	0.1 gal/sk of cement	0.1 gal/sk of cement
Citric Acid	0.02% bwoc	0.002% bwoc
NSF	0.75% bwoc	0.75% bwoc
HEC	0.1% of water for Silica	0.1% of water for Silica
Cement	100% bwoc	100% bwoc
Silica Flour	25% bwoc	25% bwoc
Micro-silica	10% bwoc	10% bwoc
SB Latex	10% bwoc	10% bwoc

As suggested by Allan (1997), latex was added in the cement system after the addition of all solids to minimize the entrapment of air. The LTMS slurry properties (**Table 2.24**) were close to that of the baseline slurry. The density of Class H based LTMS slurry was slightly (about 1 ppg) less than that of baseline Class H. Filtration loss and thickening time were in acceptable range.

Table 2.24: Properties of LTMS slurries

Property	HSLM	HS	GSLM	GS
Theoretical Density	15.38 ppg	15.96 ppg	14.99 ppg	15.51 ppg
Measured Density	15.30 ppg	16.20 ppg	14.80 ppg	15.45 ppg
Filtration Loss at 7.5 min.	27 ml	50 ml	30 ml	60 ml
Rheological Propertie vision s	Bingham PV = 28.73 cP YP = 5.39 lbf/100ft^2	Power Law n = 0.44 K = 14.4 lbf.s$^{0.44}$/100ft^2	Bingham PV = 23.94 cP YP = 7.07 lbf/100ft^2	Power Law n = 0.35 K = 10.5 lbf.s$^{0.35}$/100ft^2
Thickening Time	230 min.	170 min.	160 min.	135 min.

Fig. 2.106 presents viscometeric readings of LTMS and baseline slurries. The additive slurries were less viscous than the baseline slurries. This means they are more flowable than the baseline. Porosities of unaged LTMS and baseline samples were similar (**Fig. 2.107a**). However, the permeabilities of LTMS samples were significantly less than those of the baseline samples (**Fig. 2.107b**).

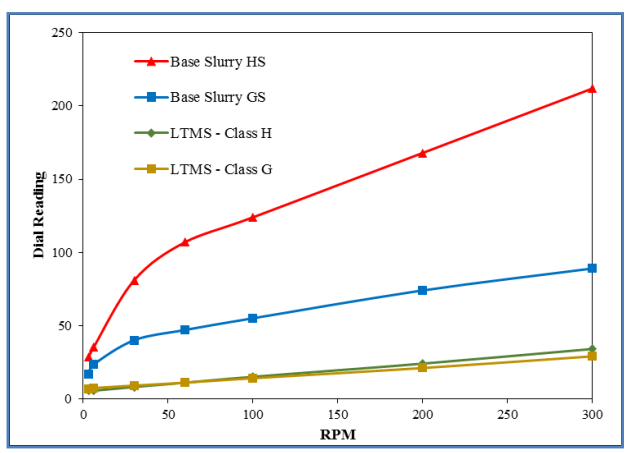

Fig. 2.106: Rheological data of LTMS and baseline slurries

Compressive strengths of HSLM samples were considerably less than that of the baseline samples. This observation was a major setback because the strength reduction could be due to entrapment of air in the system as observed in latex

cement previously. Despite this, GSLM samples exhibited almost comparable compressive strength. Moreover, the shear bond strengths of latex-microsilica samples were higher than that of the baseline samples (**Fig. 2.108**).

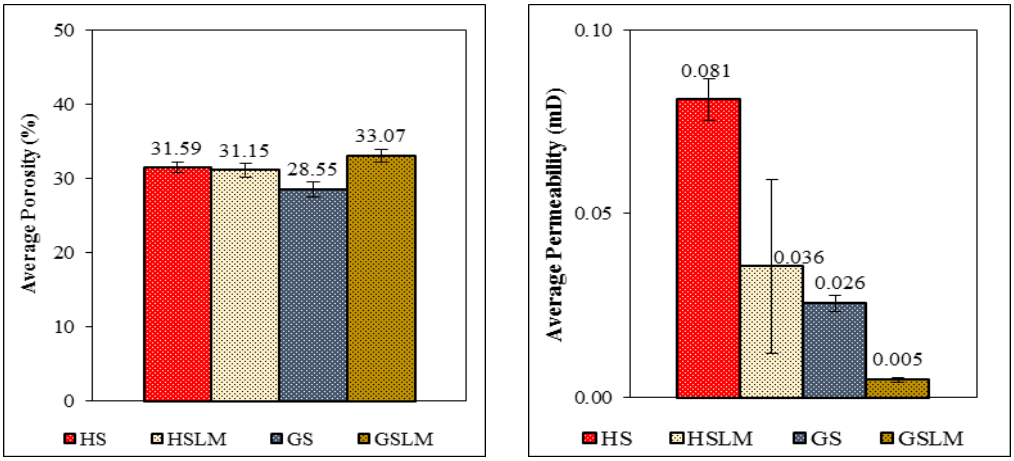

(a) (b)

Fig. 2.107: Porosity (a) and Permeability (b) of unaged LTMS and baseline cements

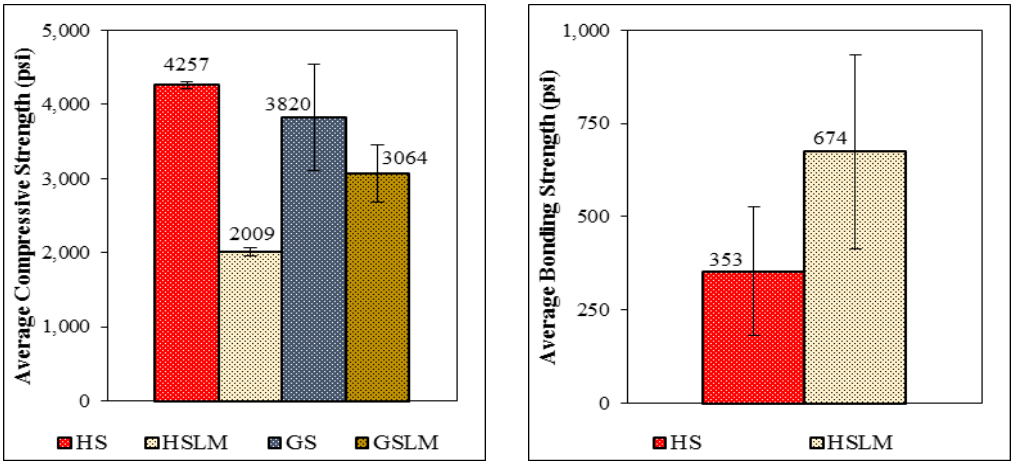

(a) (b)

Fig. 2.108: Compressive strength (a) and Shear bond strength (b) of unaged LTMS and baseline cements

Although the results obtained from unaged samples were mixed (some show property improvements while other indicate poor performance), the LTMS slurry has been selected for final screening test. Hence, slurries and core samples were prepared and aged at three different conditions to evaluate their degradation behavior.

Magnesium Oxide

Cement slurries containing magnesium oxide were also considered in the additive screening study. Slurry properties of Class H and Class G cements containing magnesium oxide (HSMG and GSMG) were investigated. Magnesium oxide was able to provide acceptable slurry with 5% BWOC as per the

recommendation of Rubiandini et al. (2005). **Table 2.25** presents the compositions of magnesium oxide based cement slurries. Properties of the slurries were measured and found to be very similar to those of the baseline slurries (**Table 2.26**).

Table 2.25: Formulations of MgO based cement (MGO-5) slurries

Component	Class G	Class H
Water for cement	44% bwoc	38% bwoc
Water for Silica Flour	38.5% bwoc	38.5% bwoc
Anti-Foaming Agent	0.1 gal/sk of cement	0.1 gal/sk of cement
HEC	0.1% of water for Silica	0.1% of water for Silica
Cement	100% bwoc	100% bwoc
Silica Flour	35% bwoc	35% bwoc
MgO	5% bwoc	5% bwoc

Table 2.26: Properties of MGO-5 and baseline cement slurries

Property	HSMG	HS	GSMG	GS
Theoretical Density	16.15 ppg	15.96 ppg	14.99 ppg	15.51 ppg
Measured Density	16.30 ppg	16.20 ppg	14.80 ppg	15.45 ppg
Filtration Loss at 7.5 min.	58 ml	50 ml	62 ml	60 ml
Rheological Properties	Power Law n = 0.52 K = 7.9 $lbf.s^{0.52}/100ft^2$	Power Law n = 0.44 K = 14.4 $lbf.s^{0.44}/100ft^2$	Power Law n = 0.40 K = 9.9 $lbf.s^{0.40}/100ft^2$	Power Law n = 0.35 K = 10.5 $lbf.s^{0.35}/100ft^2$
Thickening Time	160 min.	170 min.	130 min.	135 min.

Figure 2.109 shows the viscometer readings of MGO and baseline slurries. For practical range of shear rate, the MgO slurries were less viscous than the baseline slurries. After testing the slurry properties, seven cement cores of GSMG and HSMG, and three bonding samples of HSMG were prepared and tested. The samples were cured for 5 days at 200ºF in 2% brine. The porosity and permeability measurements showed expected results (**Fig. 2.110**). The permeability of MGO-5 (HSMG and GSMG) samples were significantly less than that of the baseline (HS and GS) cores due to MgO addition, which makes the cement matrix to expand and shrink the pores.

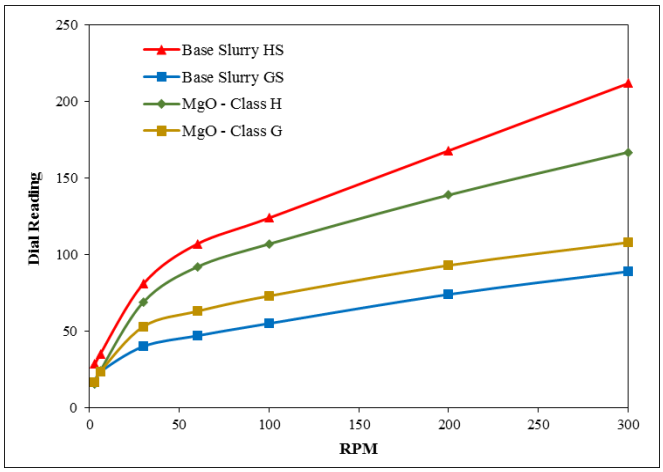

Fig. 2.109: Viscometeric readings of MGO-5 and baseline slurries

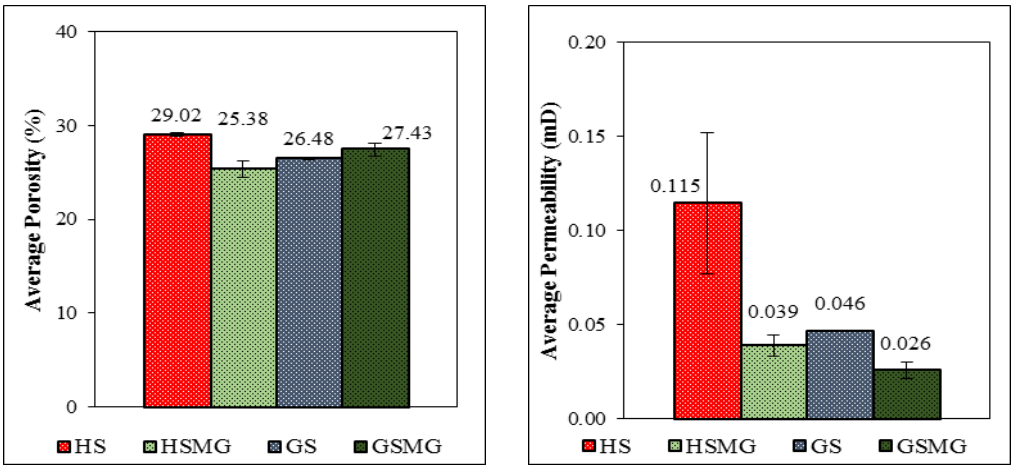

(a) (b)

Fig. 2.110: Porosity (a) and Permeability (b) of unaged MGO-5 and baseline samples

In addition to their porosity and permeability, MGO-5 cores were tested for their compressive and bonding strengths. MGO-5 and baseline samples displayed very similar compressive and shear bond strengths. Increase in compressive and shear bond strengths of MGO-5 samples were anticipated; however, incomplete hydration of MgO to $Mg(OH)_2$ crystals, due to curing at 200°F, resulted in properties that were similar to those of the baseline samples (**Fig. 2.111a**). Shear bond strength (**Fig. 2.111b**) obtained for the HSMG samples were slightly lower than that of the baseline HS samples.

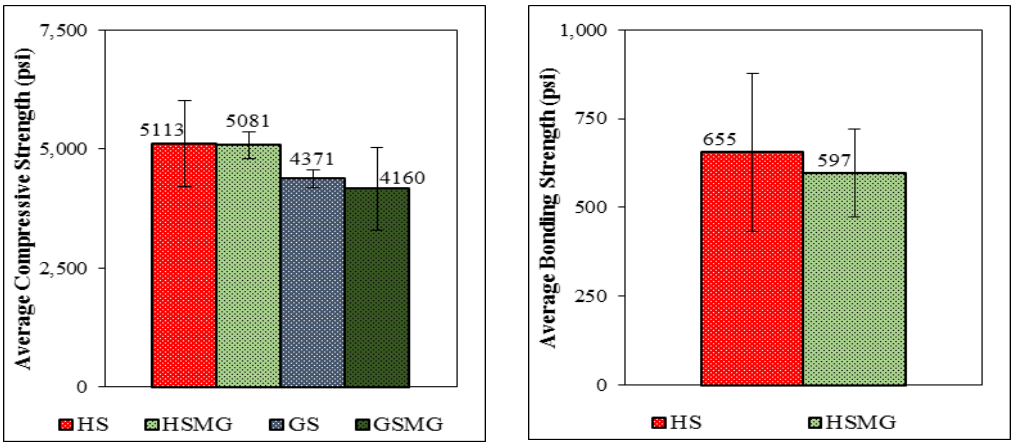

(a) (b)

Fig. 2.111: Compressive (a) and Shear bond strength (b) of unaged MGO-5 and baseline samples

Extensive testing of slurry and core properties of the MGO-5 showed suitability of the slurry for the intended applications. MgO based cements were found to be acceptable (i.e. slurry properties within the range of baseline cement slurries); therefore, they have been selected for final screening study.

Calcium Hydroxyapatite (HOAP)

Different concentrations (5%, 15% and 30%) of hydroxyapatite containing cement slurries were

prepared and tested. It was observed that with addition of hydroxyethylcellulose (HEC) and silica flour, the slurries were very thick. HEC is added to reduce fluid loss. Based on the literature survey, HOAP is expected to reduce the filter loss by forming a structured matrix. Considering this hypothesis, addition of HEC was abandoned, even though present in very small quantities. Silica flour is added to the cement to prevent conversion of tobermorite (CSH) to α-CSH at higher temperature to avoid strength retrogression. Calcium hydroxyapatite based cements are resistant to high temperature and they do not require silica flour to prevent strength retrogression (Sugama 2006). This property of calcium hydroxyapatite was considered and the silica flour was excluded in the formulation of HOAP cement.

To test the hypothesis of not using HEC and silica flour on the matrix properties, it was essential to prepare the HOAP slurries. The water requirement for HOAP is 23% by weight of HOAP (Reddy et al. 2010). Even without HEC and silica flour, the slurries were still very thick. Hence, citric acid (0.125% bwoc) was added in order to disperse and retard the slurries (**Table 2.27**). Then, the slurry properties were measured and found to be very similar to those of the baseline cement (**Table 2.28**).

Table 2.27: Formulations of HOAP based cement slurries

Component	Class G	Class H
Water for cement	44% bwoc	38% bwoc
Water for HOAP	23% by weight of HOAP	23% by weight of HOAP
Anti-Foaming Agent	0.1 gal/sk of cement	0.1 gal/sk of cement
Citric Acid	0.125% bwoc	0.125% bwoc
Cement	100% bwoc	100% bwoc
HOAP	5% bwoc	5% bwoc

Table 2.28: Properties of HOAP and baseline slurries

Property	HHO	HS	GHO	GS
Theoretical Density	16.39 ppg	15.96 ppg	15.77 ppg	15.51 ppg
Measured Density	16.40 ppg	16.20 ppg	15.70 ppg	15.45 ppg
Filtration Loss at 7.5 min.	67 ml	50 ml	65 ml	60 ml
Rheological Properties	Power Law n = 0.31 K = 21.6 $lbf\ s^{0.31}/100ft^2$	Power Law n = 0.44 K = 14.4 $lbf\ s^{0.44}/100ft^2$	Power Law n = 0.34 K = 20.3 $lbf\ s^{0.34}/100ft^2$	Power Law n = 0.35 K = 10.5 $lbf\ s^{0.35}/100ft^2$
Thickening Time	165 min.	170 min.	130 min.	135 min.

Figure 2.112 shows viscometeric readings of HOAP and baseline slurries. The readings of HOAP slurries were between those of baselines (Class H and Class G) slurries, which indicate acceptable fluidity.

Based on these encouraging results, HOAP core were prepared and their properties were measured. Porosities of unaged HOAP cores were almost similar to those of the baseline samples; however, their permeabilities were lower than

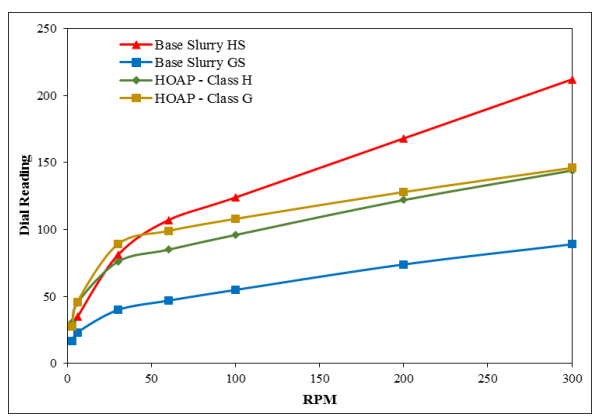

Fig. 2.112: Dial readings of HOAP and baseline slurries

those of the corresponding baseline samples (**Fig. 2.113**). Reduction in permeability due to the addition of calcium hydroxyapatite may help in limiting the extent of acid penetration under downhole conditions.

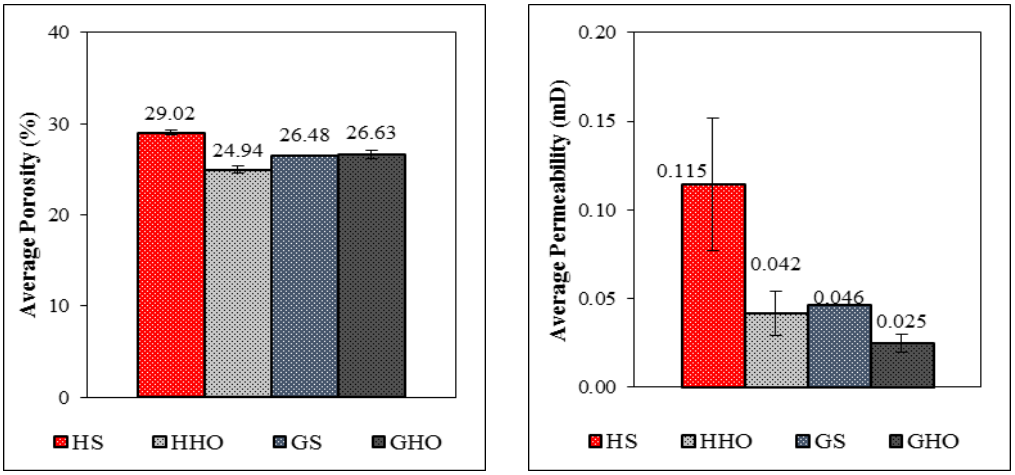

(a) **(b)**

Fig. 2.113: Porosity (a) and Permeability (b) of unaged HOAP and baseline samples

HOAP and baseline cement samples exhibited comparable compressive and shear bond strengths (**Fig. 2.114**). Similar properties for unaged samples indicate analogous matrix structures for the baseline and additive cement cores. The most useful characteristic of hydroxyapatite is to prevent the carbonation through chemical interaction; hence, the actual performance of HOAP against carbonic acid attack can only be observed after aging samples under simulated harsh downhole conditions. Therefore, HOAP cement slurries have been selected for final screening study.

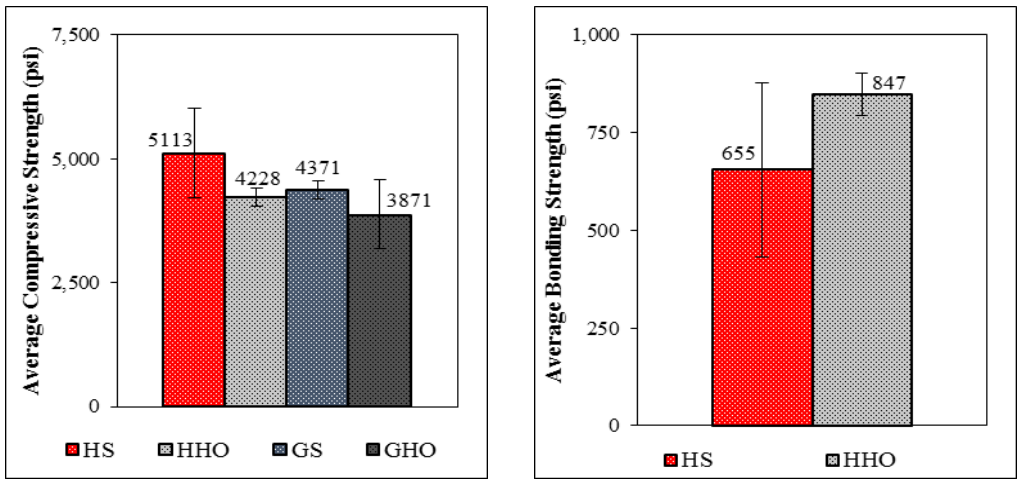

(a) **(b)**

Fig. 2.114: Compressive and shear bond strengths of unaged HOAP and baseline samples

Zinc Oxide

An experimental study (Sasaoka et al. 1994) conducted on the reaction between Zinc oxide (ZnO) and H_2S under various conditions showed encouraging results that indicate the potential of ZnO in hindering cement degradation. Based on this, ZnO has been selected as one of the potential cement additives for improving acid resistance. However, ZnO is known to be a very heavy cement retarder even after the addition of common accelerators such as NaCl.

Before aging ZnO cement samples in H_2S containing environment, the slurry properties had to be tested for their suitability by comparing them with that of baseline cements. A number of studies (Olmo et al. 2001; Arliguie and Grandet 1985) investigated the retardation property of ZnO. The retardation effect of ZnO arises from its ability to create an amorphous layer of $Zn(OH)_2$, which in combination with $Ca(OH)_2$ creates calcium-zinc-hydrate. The calcium-zinc-hydrate seems to form a protective layer that inhibits the normal hydration of cement grains by hindering the transport of hydration water to C_3S (Tri-Calcium Silicate) phase (Hamilton and Sammes 1999), thereby retarding the overall hydration reaction.

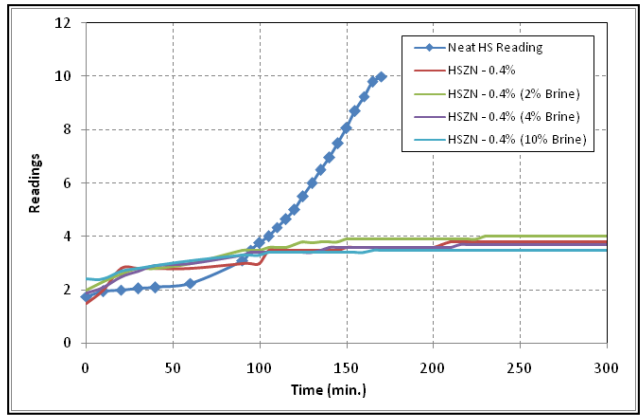

Fig. 2.115: Consistency of cement slurry containing ZnO

In order to examine the retardation effect of ZnO, the consistency of cement slurry samples containing ZnO and NaCl were studied (**Fig. 2.115**). Consist-o-meter readings are compared to those of the baseline slurry (Class H cement containing silica). The value of 10 indicates 100 B_c, which corresponds to the API thickening time for the baseline. Cement slurry samples with different concentrations of salt were prepared to offset the retardation effect of ZnO. Regardless of the salt concentration, ZnO containing slurries were unable to thicken during the test period. For all ZnO containing samples, the consist-o-meter readings showed a significant retardation. With the addition of small quantity of ZnO (0.4% BWOC), the slurry hydration (thickening) was effectively delayed for more than 5 hours. Chloride ions of NaCl were unable to accelerator the thickening. When tested with other accelerator, similar results were obtained. Therefore, ZnO might not be an effective additive in the cement due to its heavy retardation property. As a result, it has not been selected for further study.

Fly Ash

There is a general belief that incorporating pozzolanic fillers such as silica fumes and fly ash effectively decreases portlandite and C-S-H contents of the cement thereby reducing the formation of calcium carbonate, which further reacts with the acid to form water soluble calcium bicarbonate that can be easily leached out (Santra et al. 2009). Before aging the fly ash cements under acidic environment, their slurry and core properties were tested and compared with that of baseline cements. Fly ash Class F was used in this research because it has lower sulfate content. The amount of fly ash added to the cement was 100% by weight (**Tables 2.29** and **2.30**).

Table 2.29: Formulation of Class H cement with fly ash (HSF)

Material	Percent	Mass (g)	Specific Gravity	Volume (cc)
HEC	0.1% of water of filler	0.45	-	-
Cement	100%	860	3.14	273.9
Silica Fume	35% of cement	301	2.63	114.4
Fly Ash	100% of cement	860	2.63	327.0
Water for cement	38% cement	327	1.00	326.8
Water for Silica	38.5% silica	116	1.00	115.8
Water for Fly ash	38.5% fly ash	331	1.00	330.9
Total		**2795**		**1488.9**
Density (g/cc)	**1.88**			
Density (lbm/gal)	**15.66**			

Table 2.30: Formulation of Class G cement with fly ash (GSF)

Material	Percent	Mass (g)	Specific Gravity	Volume (cc)
HEC	0.1% of water of filler	0.45	-	-
Cement	100%	860	3.14	273.9
Silica Fume	35% of cement	301	2.63	114.4
Fly Ash	100% of cement	860	2.63	327.0
Water for cement	44% cement	378	1.00	378.4
Water for Silica	38.5% silica	116	1.00	115.8
Water for Fly ash	38.5% fly ash	331	1.00	330.9
Total		**2846**		**1540.5**
Density (g/cc)	**1.85**			
Density (lbm/gal)	**15.42**			

Figure 2.116 shows comparison of thickening time for fly ash and baseline cement samples. In this graph, B_c is the consistometer reading that ranges between 0 and 10. At t = 0, when B_c = 0, the slurry has just being prepared and is least resistant to pumping. At t = t_1, when B_c = 10, the slurry becomes very thick and unpumpable. Experimental results showed that Class G cement without fly ash has lowest thickening time. Adding fly ash to the cement increased the thickening time for both Class H and Class G cements.

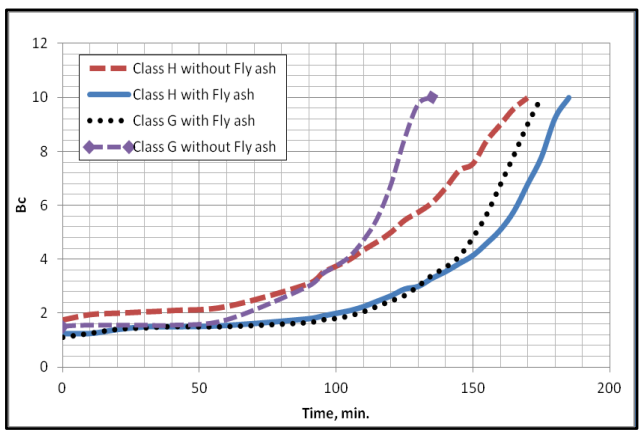

Fig. 2.116: Thickening time of fly ash and baseline cements

Porosity and permeability of fly ash and baseline cements were measured after curing for five days at temperature of 200°F (**Table 2.31**). Class G cement with fly ash showed the minimum porosity while other samples showed almost the same porosity of approximately 25%. Class H cement without fly ash had the maximum permeability (**Fig. 2.117**). Class G cement with and without fly ash and class H cement with fly ash exhibited comparable permeability, which is roughly 0.02 mD.

Table 2.31: Porosity and permeability of fly ash and baseline samples

CGS Units											
Core #	Core dimensions			Porosity					Permeability		Remarks
	Diameter	Length	Weight	V_b	V_g	V_p	Porosity	Gr. Density	K_{air}	K_{klink}	
	mm	mm	g	cc	cc	cc	%	g/cc	mD	mD	
1Go1	25.36	37.98	32.55	19.18	14.09	5.09	26.54%	2.31	0.035	0.018	Class G without Fly ash
1Go2	25.32	36.72	31.52	18.49	13.55	4.94	26.72%	2.33	0.043	0.022	
1Go3	25.34	30.27	26.24	15.27	11.29	3.98	26.06%	2.32	0.036	0.019	
1Ho1	25.26	38.30	33.53	19.19	13.83	5.36	27.93%	2.42	0.102	0.060	Class H without Fly ash
1Ho2	25.28	37.32	32.74	18.73	13.39	5.34	28.51%	2.44	0.116	0.070	
1Ho3	25.33	38.22	33.90	19.26	13.73	5.53	28.71%	2.47	0.113	0.068	
1Hf1	25.24	37.56	31.13	18.79	13.94	4.85	25.81%	2.23	0.050	0.027	Class H with Fly ash
1Hf2	25.17	37.62	31.45	18.72	14.10	4.62	24.68%	2.23	0.042	0.022	
1Hf3	25.18	36.97	30.31	18.41	13.55	4.86	26.40%	2.24	0.056	0.031	
1Gf1	25.30	33.58	29.46	16.88	13.46	3.42	20.26%	2.19	0.038	0.020	Class G with Fly ash
1Gf2	25.25	38.40	33.76	19.23	15.31	3.92	20.38%	2.20	0.036	0.018	
1Gf3	25.20	39.13	33.94	19.52	15.43	4.09	20.95%	2.20	0.040	0.021	

Slurry and core properties of fly ash cements (GSF and HSF) were tested and compared with properties of baseline cements. Fly ash based cements showed acceptable (i.e. slurry properties within the range of baseline cement slurries) property suitable for cementing applications; therefore, they have been selected for testing in the aging cell under HPHT conditions.

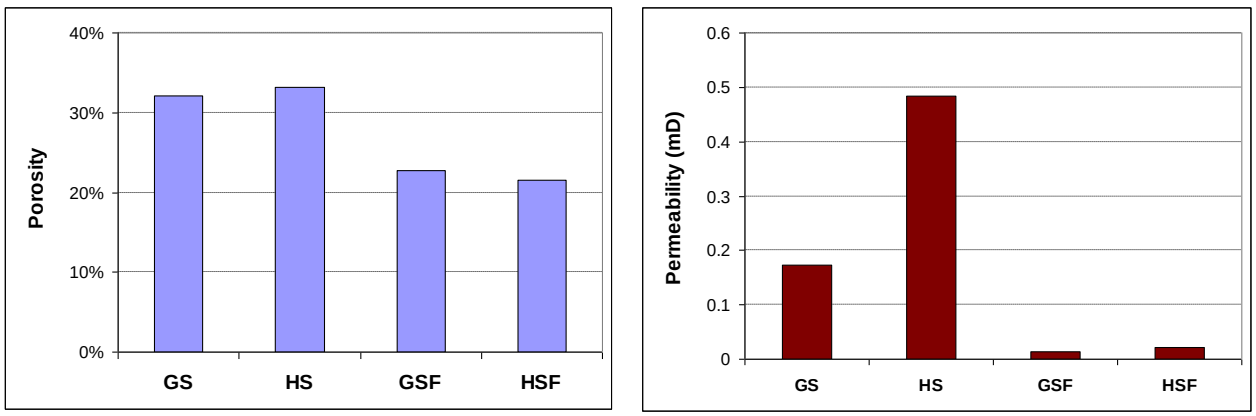

(a) (b)

Fig. 2.117: Porosity (a) and permeability of unaged fly ash and baseline samples

2.4.2.2. Detailed Analysis of Acid Resistance of New Cement Formulations

After exposure to harsh simulated downhole conditions for 14 days, the cement matrix of baseline samples mostly depicted carbonation. This was observed as increase in compressive and shear bond strengths and reduction in porosity and permeability of the baseline samples. In addition, FTIR examinations confirm the conversion of CH and CSH into $CaCO_3$ in carbonated cement. Four of the additive cements (microsilica cement, latex cement, microsilica-latex cement and fly ash based cement) did not show better performance than the baseline cement. These cement formulations were not able to prevent acid penetration into their pores or carbonation of CH and CSH better than the baseline.

Class H based MGO-5 cement was able to resist acid attack under different test conditions. Leaching and carbonation of MGO-5 cement was prevented under HPHT carbonic acid environment by the addition of 5% MgO. However, Class G based MGO-5 cement displayed mixed performance; and hence, its reliability is quite questionable.

Addition of hydroxyapatite has been very effective in controlling acid attack under HPHT carbonic acid environment. In the range of 100 to 350°F, the matrix was able to protect the CH and CSH components of the matrix, along with maintaining the porosity and permeability and shear bond strength to similar levels. At high temperature (430°F), major strength retrogression was observed. Hence, hydroxyapatite cement formulation is suitable and performs better than the baseline cement in the temperature range of 100 to 350°F.

Calcium Hydroxyapatite

The hydroxyapatite containing cement (HOAP) is one of the new formulations that showed promising results in the initial screening study. To investigate the performance of this formulation, HOAP and baseline samples were prepared and aged under different conditions (**Table 2.32**). During aging, samples were immersed for 14 days in 2% brine saturated with CO_2 and H_2S containing methane gas.

Table 2.32: Aging conditions for HOAP samples

HOAP Batch #	Exp. #	Baseline Batch #	Temp. (ºF)	Pressure (psi)	Concentration		
					CH_4 (%)	CO_2 (%)	H_2S (ppm)
002	9	11	100	6000	60	40	0
003	12	14	350	6000	0	100	0
004	13	16	350	3000	60	40	0
005	15	18	350	3000	0	100	0
006	19	22	225	3000	60	40	0
007	23	26	225	3000	90	10	0
008	29	32	430	9000	100	0	0
009	30	33	100	6000	90	10	300
010	32	35	350	6000	90	10	300
011	33	36	100	6000	100	0	300
012	35	38	100	9000	100	0	300
013	37	40	100	9000	60	40	180

The matrix properties (porosity, permeability, compressive strength and shear bond strength, FTIR analysis) of aged and unaged samples were measured to quantify the level of degradation occurring during aging and compare the performance of HOAP with the baseline cement.

Porosity and Permeability

Figure 2.118 illustrates the porosity for Class H based HOAP and baseline samples. In all the experiments, porosity of baseline decreased after aging due to carbonation. On the other hand, only three of HHO samples (Experiments #12, 23 and 29) showed porosity reduction after aging. The reduction that occurred in these samples could be due to partial carbonation of the matrix; and hence, the results from compressive strength, shear bond strength and FTIR measurements need to be

analyzed to better understand the impacts of different test parameters. For Experiment #23, the reduction for HHO samples was 29%, which is considerably less than that of the baseline samples (60%). Measurements from Experiments #12 and 29 showed substantial decrease in porosity of the samples when aged at 350 and 430°F, respectively. The high temperature enhances ionic diffusion through the cement, resulting in rapid acid penetration and carbonation. Moreover, above 350°F, increasing temperature tends to increase CO_2 solubility, which facilitates the carbonation process.

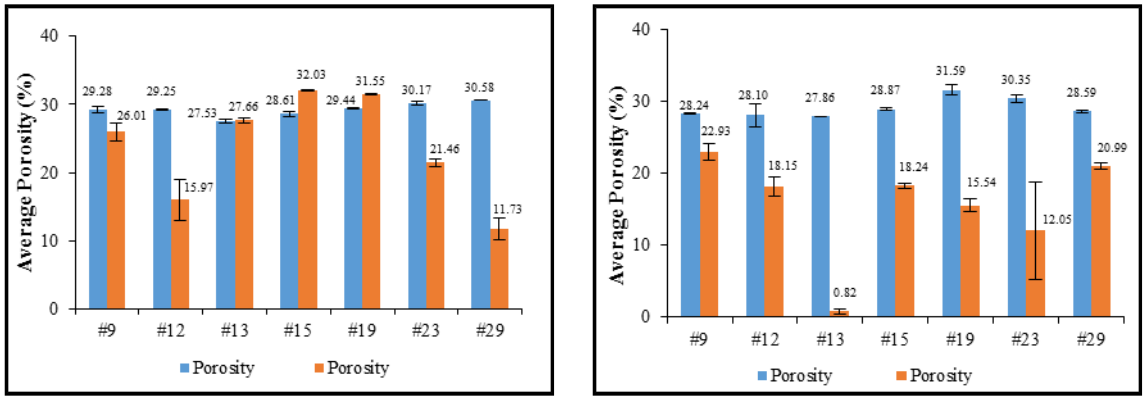

(a) **(b)**

Fig. 2.118: Porosity of aged (orange) and unaged (blue) samples: a) HHO; and b) HS

One of the baseline samples (Experiment #13), displayed very low porosity after aging (0.82%). This reduction is not realistic with respect to carbonation process. The possible reason for this reduction could be deposition of salt on the outer surface of the slurry resulting in blocking of pores on the outer zone.

Recent aging tests (Experiments #30, 32, and 37) were conducted in the presence of H_2S. Results presented in **Fig. 2.119** shows the performance of HHO cement. After aging, the change in HHO cement porosity was negligible, while the baseline cement showed increase in porosity in two experiments (Experiments #30 and 32). These experiments were conducted under low CO_2 concentration conditions. Hence, leaching is expected to dominate the degradation process. As a result, baseline samples showed increase in porosity while the additive samples exhibited a slight reduction. These results are consistent with our previous observations when tests were conducted without the presence of H_2S, HHO cement preserved its original property after exposure to acidic environment.

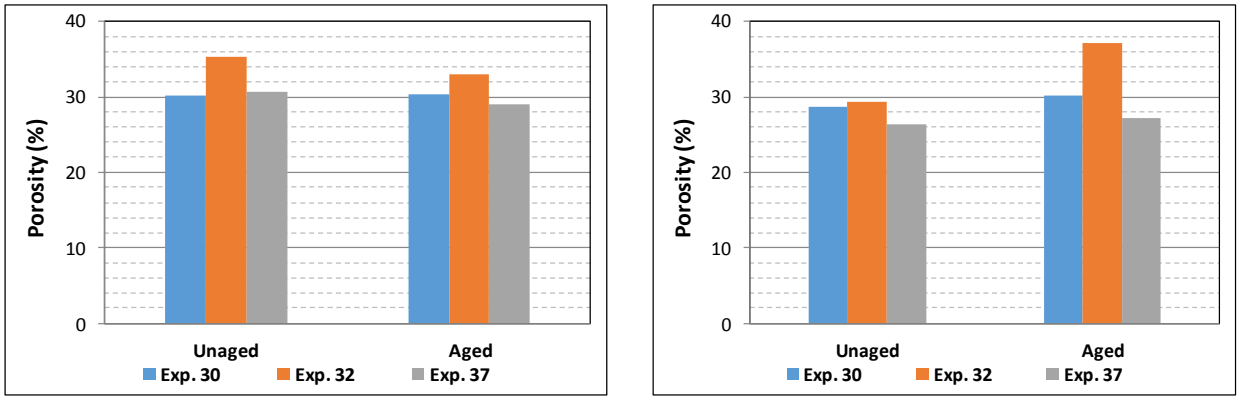

Fig. 2.119: Porosity of unaged and aged (in the presence of H_2S) samples: a) HHO; and b) HS

Most of the HOAP samples showed slight change in porosity after aging, which suggests minimal carbonation and preservation of CH and CSH components of the cement. In addition, permeability of HOAP and baseline samples indicates different trends (**Fig. 2.120**). The scale of the permeability chart has been modified to logarithmic for better visualization. The drastic reduction in permeability of baseline samples demonstrated severe carbonation resulting in blocking of the pore throats. On the other hand, HOAP samples remain predominately immune against carbonation. Permeability reductions observed in Experiments # 12 and 19 were less significant than that of the baseline samples.

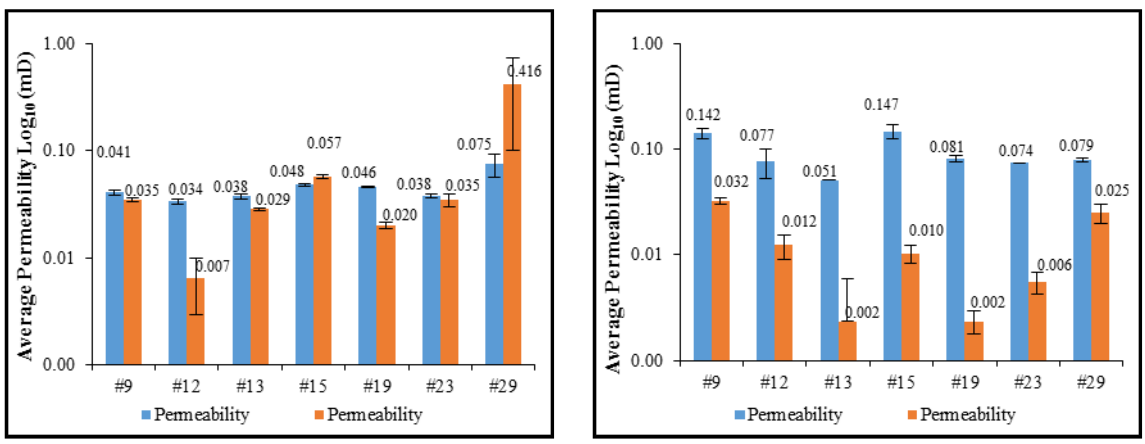

Fig. 2.120: Permeability of aged (orange) and unaged (blue) samples: a) HHO; and b) HS

Substantial permeability increase was observed in Experiment # 29 that can be attributed to high temperature (430°F), which causes rapid ionic diffusion in the cement leading to harsh leaching condition.

In addition to CO_2, the presence of H_2S also affects the degradation behavior of oil well cement. Tests conducted in the presence of H_2S demonstrated the effectiveness of hydroxyapatite in minimizing carbonation and leaching processes. Permeability of HHO samples decreased (**Fig. 2.121**) when aged under different conditions due to the formation of ettringite, which reduces the pore space and

subsequently porosity and permeability. However, in the presence of leaching, the reduction in permeability resulting from the formation of ettringite can be offset by the leaching process and this causes increase in permeability as indicated in baseline (HS) samples. For both types of samples (additives and baseline), the maximum reduction in permeability was observed in Experiment #37, in which the samples were aged in fluid containing high concentration of CO_2 (40%). This means that, in addition to the formation of ettringite, considerable amount of calcium carbonate was formed as the cement reacts with carbonic acid. The precipitation of calcium carbonate in the pore resulted in the reduction in porosity and permeability of the cement samples.

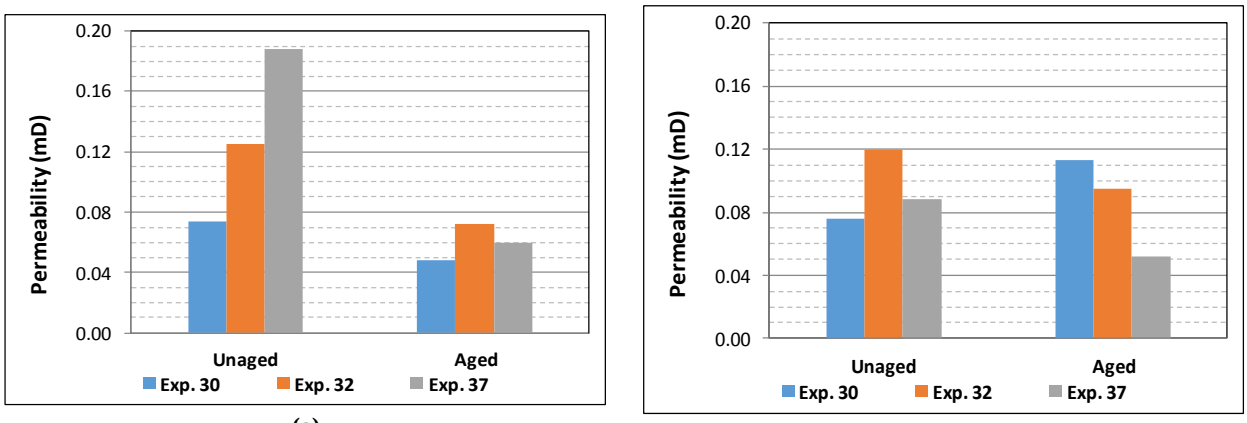

(a) (b)

Fig. 2.121: Permeability of unaged and aged (in the presence of H_2S) samples: a) HHO; and b) HS

Class G based HOAP (GHO) and baseline samples demonstrated (**Fig. 2.122**) reduction in porosity after aging, except for two tests (Experiments #15 and 19). Increases in porosity in Experiments #15 and 19 could be due to combine effects of high temperature (350°F) and high CO_2 concentration (100% CO_2) leading to heavy leaching rather than carbonation. The baseline samples on the other hand demonstrated a consistent porosity decline due to carbonation.

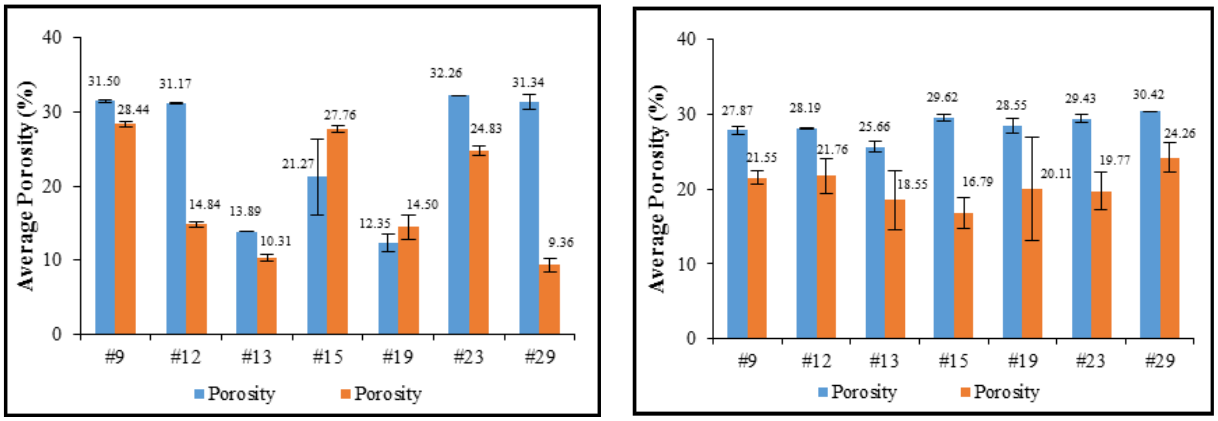

(a) (b)

Fig. 2.122: Porosity of aged (orange) and unaged (blue) samples: a) GHO; and b) GS

Results of aging tests conducted in the presence of H_2S (**Fig. 2.123**) demonstrated acid

resistance of the GHO cement. After aging, the porosity of GHO cement slightly reduced. This is attributed to the formation of ettringite as hydrosulfuric acid reacts with the binding components of cement (CH and CSH). On the other hand, baseline cement exhibited mixed trend indicating the presence of leaching, which offsets the impact of ettringite formation on porosity. These measurements are consistent with results obtained from Class H based additive cement (HHO).

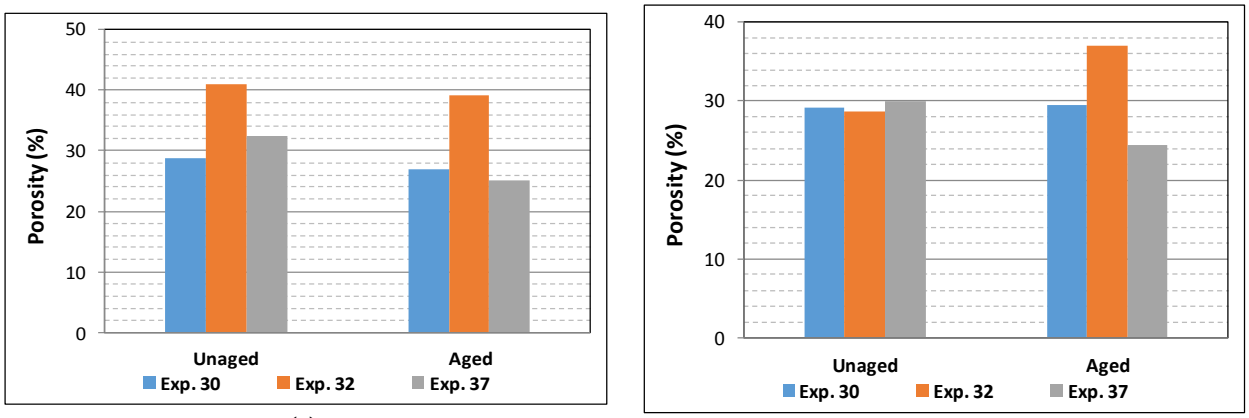

Fig. 2.123: Porosity of unaged and aged (in the presence of H_2S) samples: a) GHO; and b) GS

Permeability of Class G baseline samples predominantly decreased after aging (**Fig. 2.124**). Some samples showed minor increase in permeability, which is in the order of the margin of error. However, the corresponding HOAP sample (GHO) displayed mixed results. In general, the performance of GHO cement is as good as the baseline cement. In Experiments #29, porosity of GHO samples diminished significantly while permeability increased dramatically. Similar inconsistency between permeability and porosity measurements were observed in HHO samples. Possible reason for the inconsistency could be carbonation of the matrix at high temperature (430°F), when hydroxyapatite fails to act as an additive against acid attack.

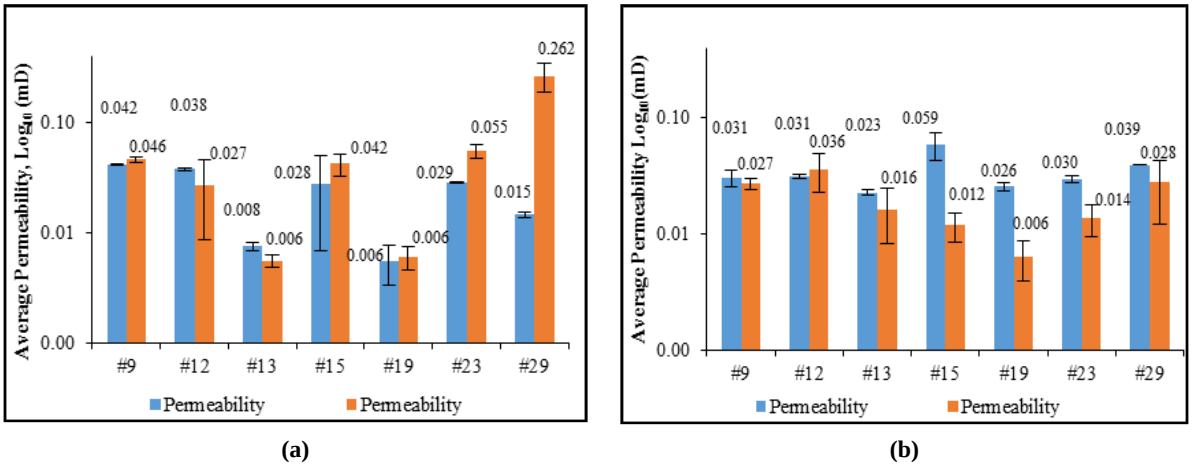

Fig. 2.124: Permeability of aged (orange) and unaged (blue) samples: a) GHO; and b) GS

Permeability measurements obtained from samples aged in an environment containing H_2S showed (**Fig. 2.125**) the effectiveness of hydroxyapatite in limiting leaching of the cement. Except for high-temperature experiment (Experiment #32), permeability of GHO samples slightly decreased when aged under different conditions due to the formation of ettringite in the pore space, which reduces porosity and permeability of cement. When aged at high temperature (350°F), permeability of GHO samples slightly increased. Since GHO cement formulation does not include silica, it is prone to structural transformation occurring at high temperatures (greater than 230°F). This transformation can facilitate the leaching process leading to increase in permeability. Moreover, ettringite solubility increases with temperature, resulting in increased porosity and permeability. Consistent with the porosity measurements, baseline cement exhibited increase in permeability in two experiments (Experiments #30 and 32) demonstrating the presence of leaching, which offsets the carbonation process. However, at high CO_2 concentration (Experiment #37), carbonation dominated the leaching process leading to reduction in permeability, which is consistent with the porosity measurement.

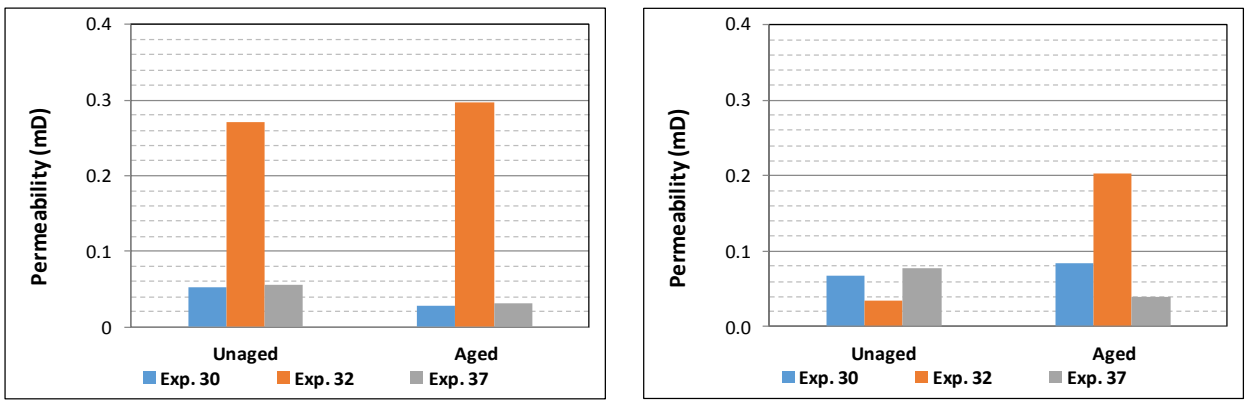

(a) (b)

Fig. 2.125: Permeability of unaged and aged (in the presence of H_2S) samples: a) GHO; and b) GS

Compressive Strength

HOAP samples displayed consistent decrease in compressive strength after aging (**Figs. 2.126** and **2.127**). In spite of this, the baseline samples showed a prominent increase except in some cases (Experiments #9, 13 and 15). The increase is attributed to carbonation of the cement binding components to form $CaCO_3$. Interestingly, the moderate reduction in the strength of HOAP could be due to carbonation of calcium hydroxyapatite. Carbonated hydroxyapatite has lower compressive strength than uncarbonated hydroxyapatite (Sugama and Carciello 1992 and 1993; Martin and Brown 1995). This also indicates that HOAP is able to act as a reactive additive against carbonic acid attack. At high temperature (430°F, Experiment #29), there was a substantial decrease in the strength, which demonstrated the presence of thermal retrogression. Although the decrease in the strength is a major concern in using the HOAP for high temperature applications (above 430°F), the obtained strength after the aging was still above the accepted industry standards (500 psi).

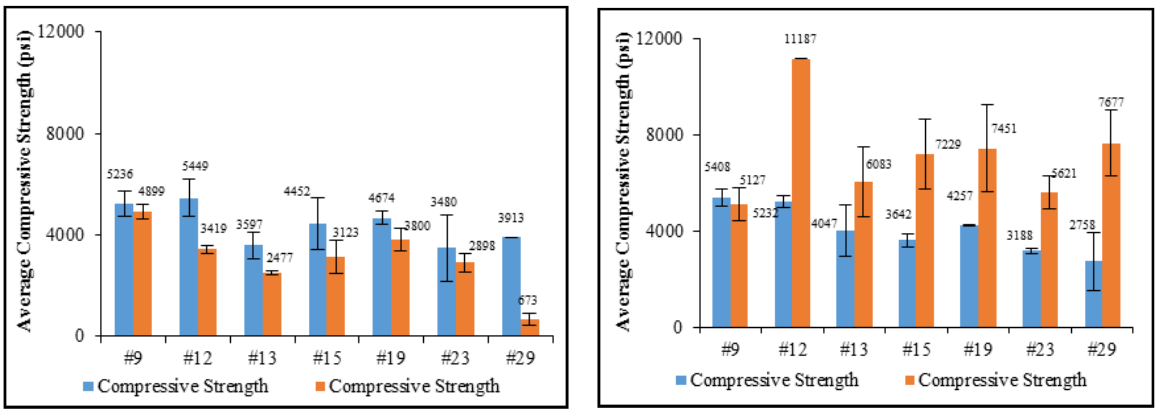

(a) **(b)**

Fig. 2.126: Compressive strength of aged and unaged samples: a) HHO; and b) HS

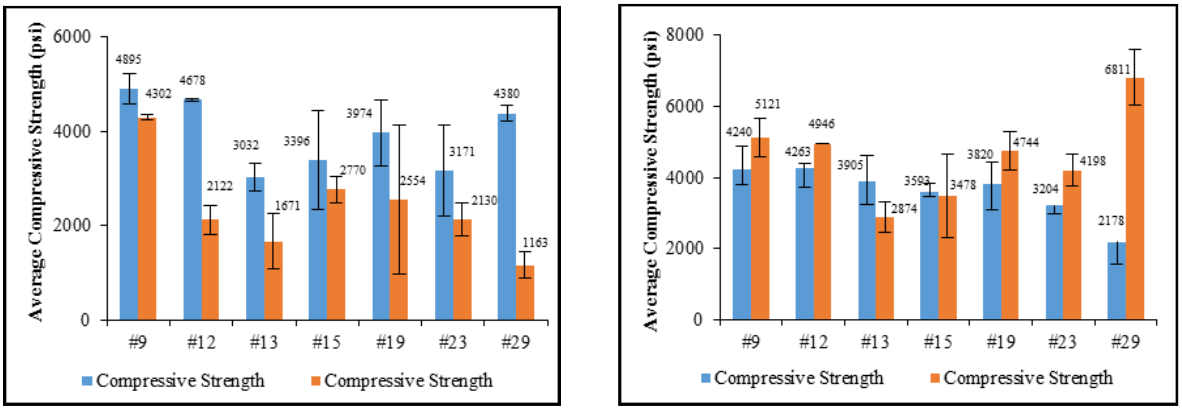

(a) **(b)**

Fig. 2.127: Compressive strength of aged (orange) and unaged (blue) samples: a) GHO; and b) GS

Before aging, compressive strength of additive and baseline cements were in the same range. After aging, compressive strength of HHO samples aged in environment containing H_2S showed mostly improvement in strength after the exposure (**Fig. 2.128**).

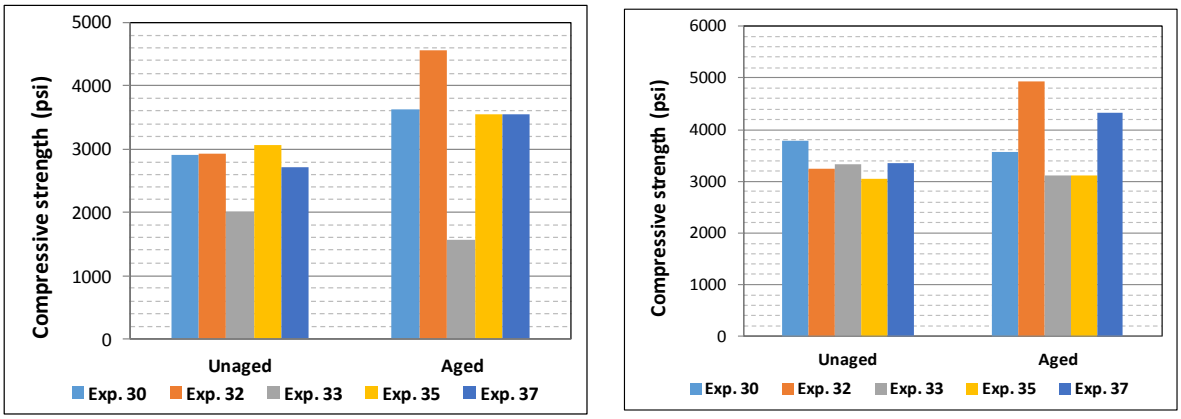

(a) **(b)**

Fig. 2.128: Compressive strength of unaged and aged (in the presence of H_2S) samples: a) HHO; and b) HS

The improvement in strength can be attributed to the formation of ettringite. Both reduction and improvement in strength was observed when samples were tested without the presence of CO_2 (Experiments #33 and 35). These variations are in the order of measurement error. Baseline samples did not display consistent improvement in strength. Carbonation was mostly prominent in the presence of CO_2 in the aging fluid system.

Unaged compressive strength of GHO samples vary significantly. This could be the result of small variation in the mixing procedure of the cement. Although efforts were made to replicate the mixing procedure, similar strength measurements were not obtained for GHO samples. Aging experiments conducted in environment containing H_2S showed mostly reduction in strength of GHO samples after the exposure (**Fig. 2.129)**. The improvement in strength can be attributed to the formation of ettringite. Unaged baseline samples from different batches display similar compressive strength. After aging, baseline samples showed slight and inconsistent changes in compressive strengths. In the presence of carbon dioxide (Experiments #30 and 37), slight improvement in strength was observed.

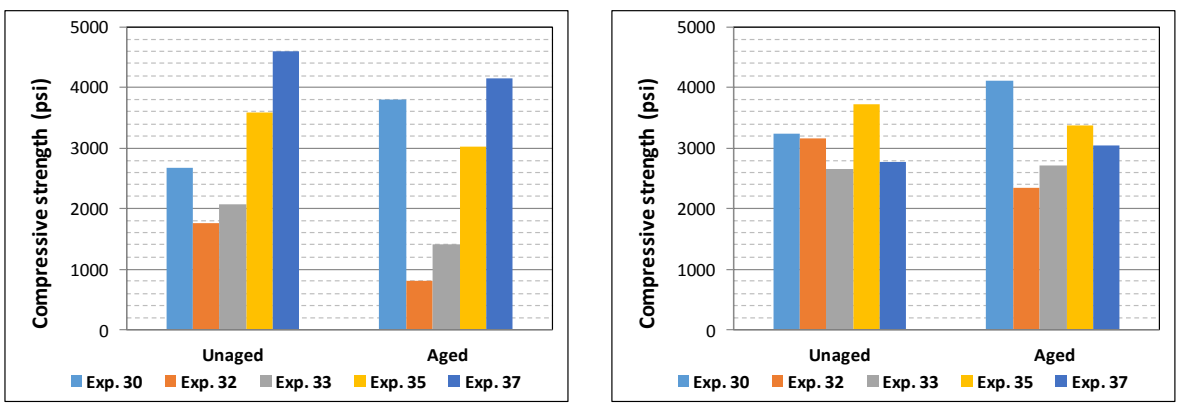

(a) **(b)**

Fig. 2.129: Compressive strength of unaged and aged (in the presence of H_2S) samples: a) GHO; and b) GS

Shear Bond Strength

The shear bond strength (SBS) of HOAP samples mostly remained the same after aging (**Fig. 2.130**). This implies that HOAP cement is not susceptible towards carbonation and expansion. Samples in Experiment #9 conducted at 100°F, showed the largest increase in the SBS. This can be due to increased solubility of CO_2 at low temperature causing carbonation of hydroxyapatite, which may lead to expansion and increase of the SBS. Consistent with compressive strength data, results of Experiment #29 conducted at 430°F indicated extreme reduction in the shear bond strength. This is attributed to thermal retrogression that makes the hydroxyapatite cement very weak.

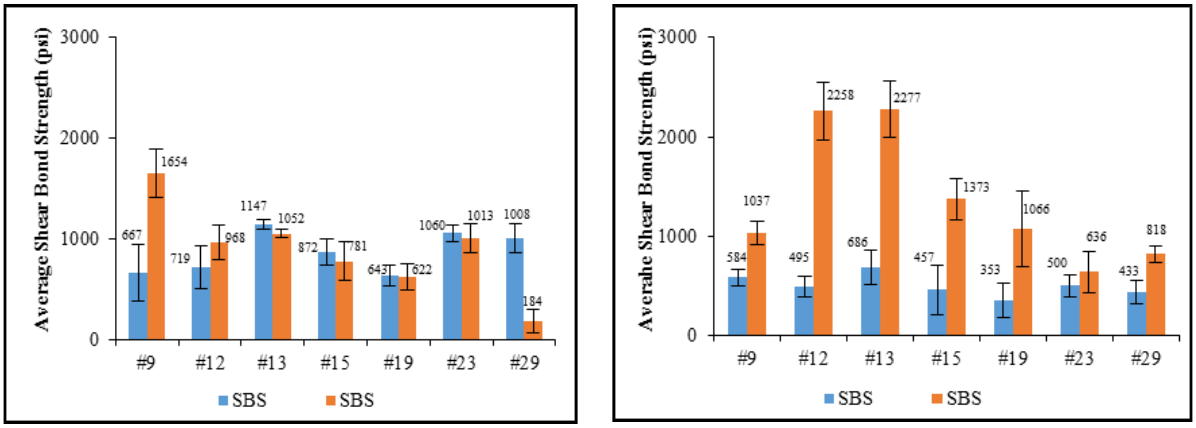

(a) (b)

Fig. 2.130: Shear bond strength of aged (orange) and unaged (blue) samples: a) HHO; and b) HS

In the presence of H_2S, HHO samples mostly exhibited slight change in SBS (**Fig. 2.131**). Experiment # 37 is an exceptional case in which the unaged sample SBS was considerably low. In general, the additive samples displayed higher SBS than baseline samples. After aging, SBS of baseline samples consistently increase. Three of these experiments (Experiments #30, 32, and 37) were conducted in the presence of CO_2 and therefore it is expected that carbonation caused the SBS improvement. However, the rest of the experiments (Experiments #33 and 35) were performed in the absence of CO_2. Hence, only the formation of ettringite is expected to improve the SBS.

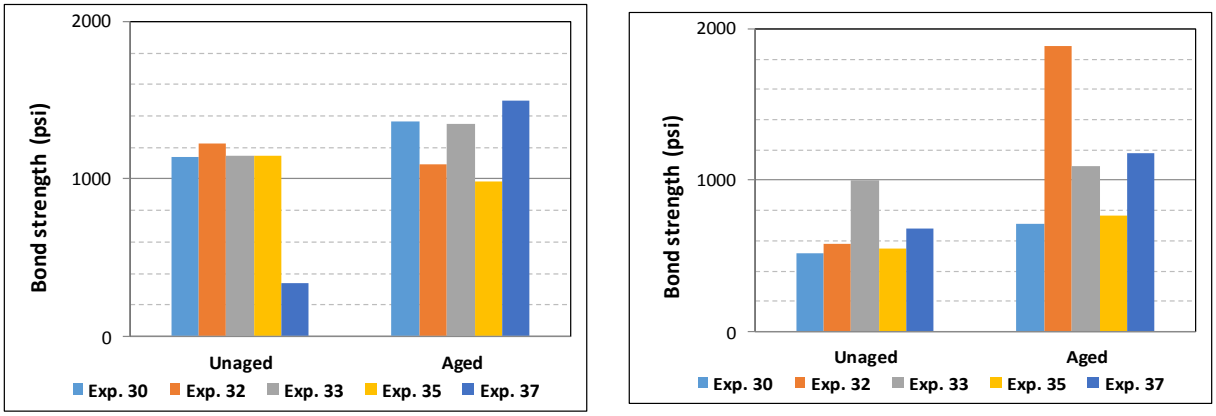

(a) (b)

Fig. 2.131: Shear bond strength of unaged and aged (in the presence of H_2S) samples: a) HHO; and b) HS

FTIR Analysis

The minerals under focus for the FTIR analysis are CH, CSH and $CaCO_3$. The carbonated form of HOAP also shares similar wavelength as $CaCO_3$ and hence is not distinguishable in the spectrum. The CO_3^{2-} bond peak shows the presence of $CaCO_3$ carbonated calcium hydroxyapatite in the samples. To perform the FTIR tests, additive and baseline cores (with radius R) were first dried and then cut transversely. Three zones in the cylindrical cement cores were identified as outermost ($r \approx R$), middle ($r \approx R/2$) and innermost ($r \approx 0$) zones. Small amount of representative cement sample was cut from each zone and

finely grinded. The amounts of CH, CSH and $CaCO_3$ found in these zones indicate the level of carbonation occurring in each zone.

Inner Zone: FTIR mineralogy results of inner zones of HOAP and baseline cores are displayed in **Fig. 2.132**. Except for Experiment # 9, which was conducted at 100°F, CH was not preserved in all the baseline samples. However, CH and CSH were preserved in HOAP samples noticeably indicating the performance of hydroxyapatite. CSH component of the matrix varied for each experiment. In some experiments, the baseline samples preserved higher level of CSH in the inner zone. The HOAP samples showed varying amount of CSH. HOAP may have been able to intercalate CSH in the matrix distorting the structure. Interestingly the CH and CSH components in Experiment #29 (430°F) are more in HOAP samples, indicating a preserved state even after thermal retrogression, which resulted in high-permeability and low compressive and bond strengths.

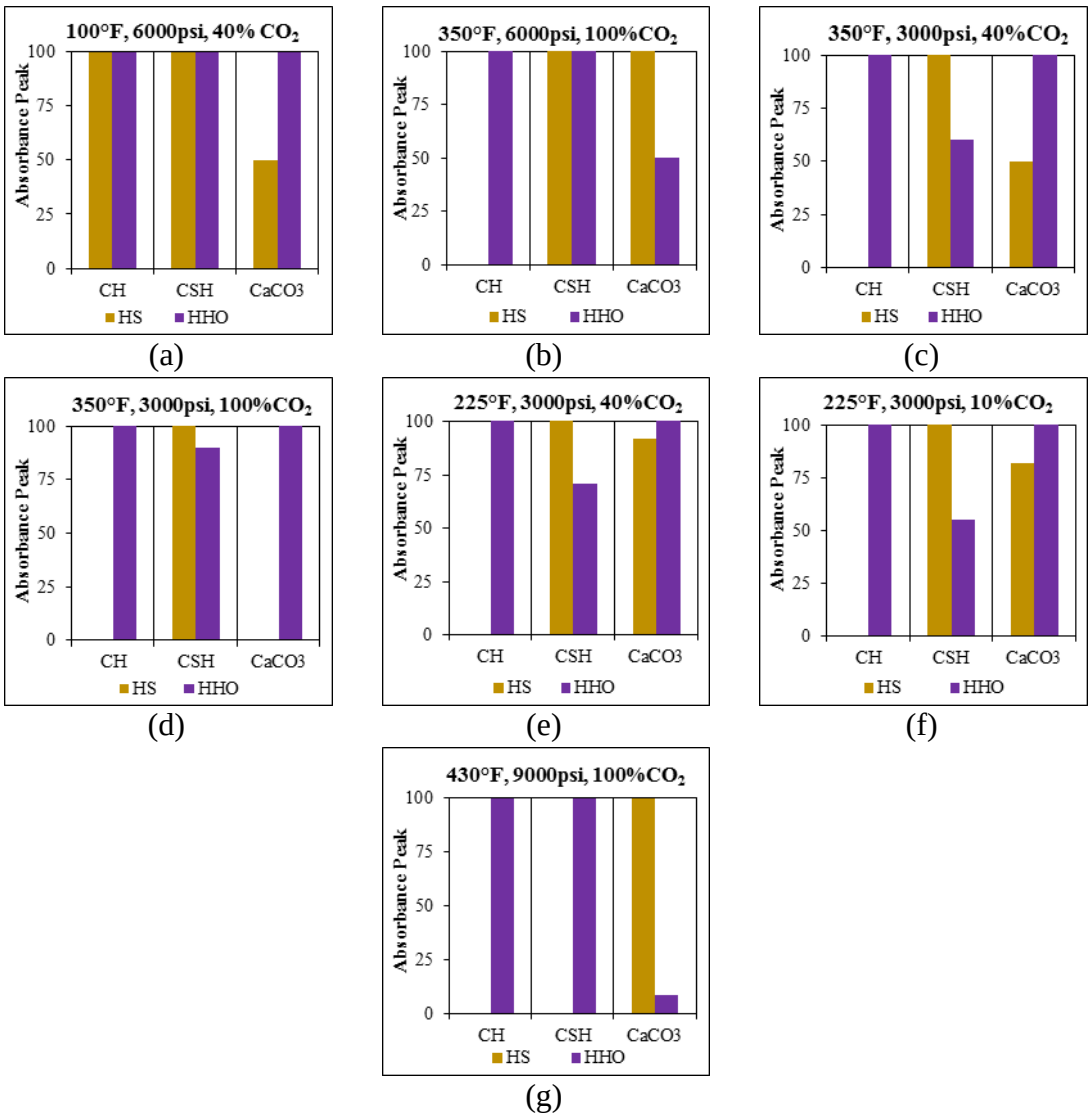

Fig. 2.132: FTIR results in inner zone of HOAP and baseline HS samples aged at different conditions: a) Exp. 9; b) Exp. 12; c) Exp. 13; d) Exp. 15; e) Exp. 19; f) Exp. 23; and g) Exp. 29

Middle Zone: The FTIR results obtained from the middle zones of HOAP and baseline samples are presented in **Fig. 2.133**. Being exposed to the harsh condition more than the inner zone, the middle zone is expected to show a reduced presence of CH and CSH. The HOAP samples were able to prevent degradation of CH while it was completely carbonated from baseline samples. In addition, HOAP samples mostly preserved CSH, although the amount varies from experiment to experiment. Experiment #13 is the only test that CSH was completely carbonated from HOAP samples. The CSH was completely carbonated in the baseline samples during Experiments #12, 13 and 15.

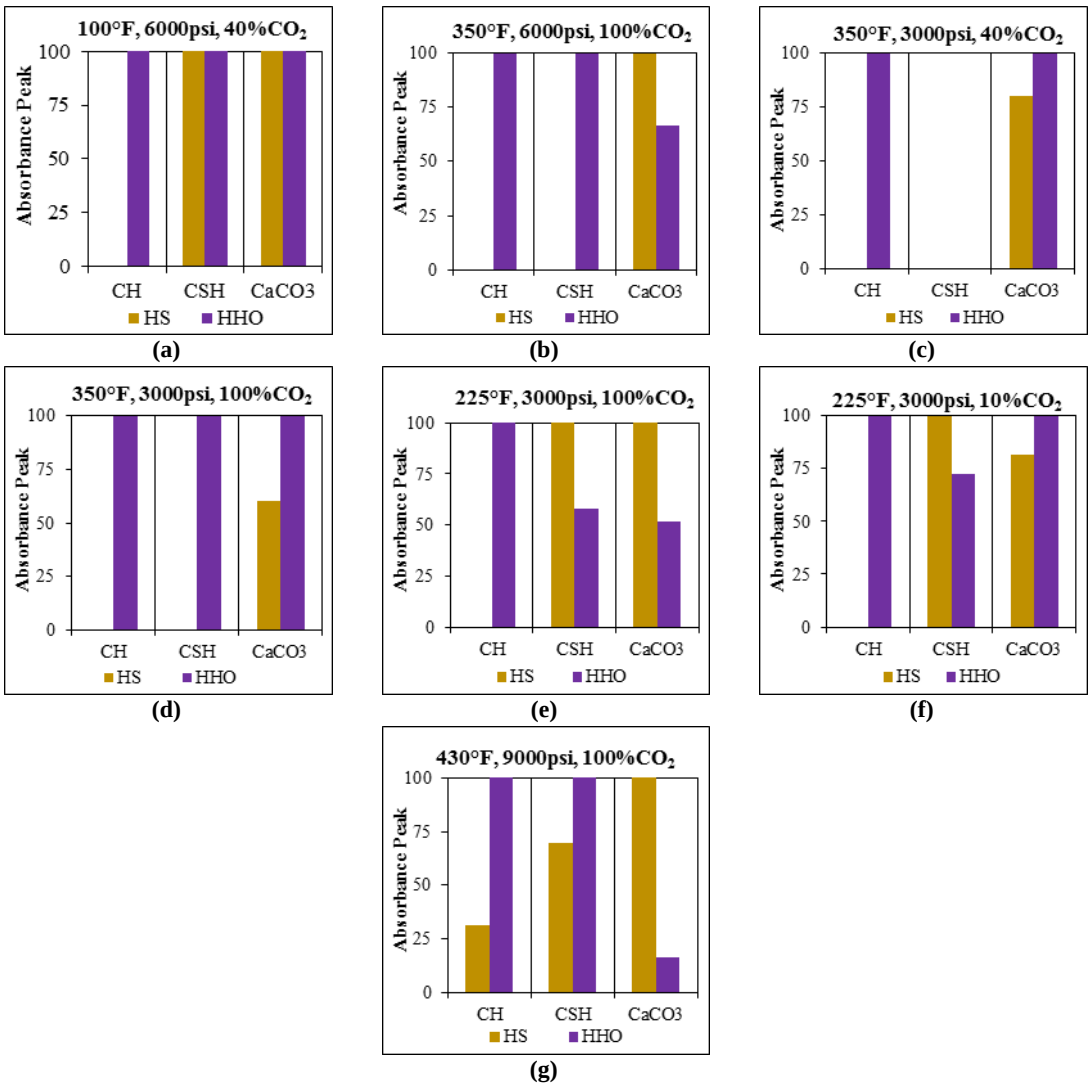

Fig. 2.133: FTIR results (middle zone) of HOAP and baseline HS samples aged at different conditions: a) Exp. 9; b) Exp. 12; c) Exp. 13; d) Exp. 15; e) Exp. 19; f) Exp. 23; and g) Exp. 29

Outer Zone: The outer layer is highly exposed to the acid attack. Therefore, it is expected to have maximum amount of $CaCO_3$ and minimum levels of CH and CSH content. The FTIR results obtained from the outer zones of HOAP and baseline samples are presented in **Fig. 2.134**. In most cases, the CH and CSH components were completely consumed. The baseline samples mostly display strong $CaCO_3$ peaks

and limited peaks of CH (one case) and CSH (two cases) implying strong acid attack and carbonation. The HOAP samples showed slightly better performance than baseline samples. They showed one peak of CH and three peaks of CSH. The HOAP samples also preserved the essential component (CSH) in their outer most zone even under extreme condition (430°F, 9000 psi and 100% CO_2), which resulted in dramatic permeability increase (Experiment #29).

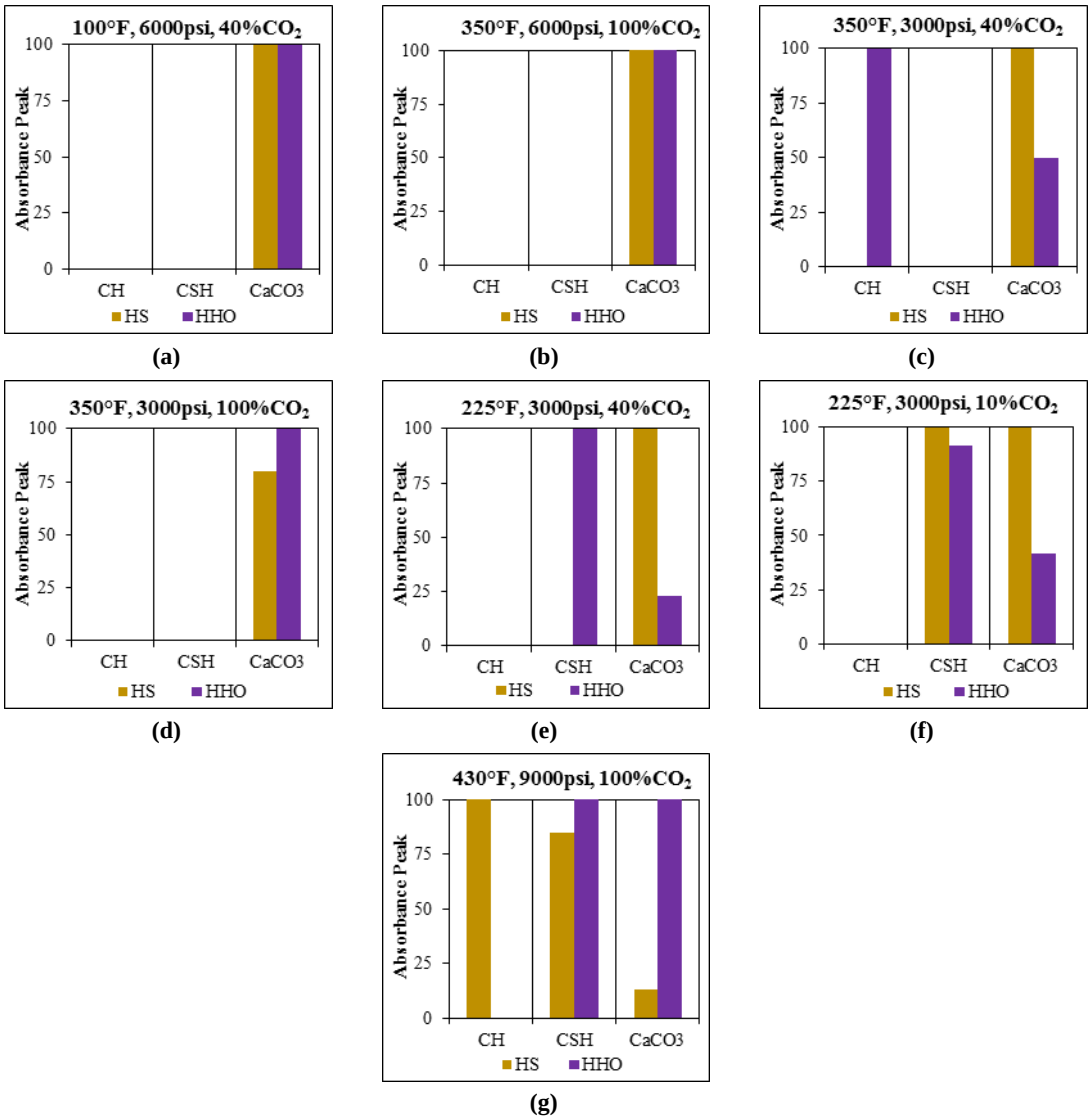

Fig. 2.134: FTIR results (outer zone) of HOAP and baseline HS samples aged at different conditions: a) Exp. 9; b) Exp. 12; c) Exp. 13; d) Exp. 15; e) Exp. 19; f) Exp. 23; and g) Exp. 29

<u>Summary</u>

Consistent porosity, permeability and shear bond strength of HOAP samples after aging, along with a slight reduction in the compressive strength due to limited carbonation indicate the protection of the main binding components of the cement (CH and CSH) from carbonic acid attack. In addition, the FTIR mineralogy results evidently demonstrated the presence of CSH and CH in the matrix of HOAP samples while they were completely carbonated in baseline samples. This proves that HOAP is able to react with

CO_2 and protect the matrix from carbonation. However, at higher temperature (430°F), the samples exhibited severe thermal retrogression in the strength.

Magnesium Oxide

The hydration of MgO involves formation of $Mg(OH)_2$ crystals, which occupy the pore space and result in expansion of the cement matrix. The expansion is required to take place at the precise point of time during setting of the cement in the well, and to reduce cement porosity and permeability. Expansion that occurs in the liquid slurry phase does affect the cement properties. Expansion after the complete setting causes cracking of the cement, which is highly undesirable. Hence, expansion has to occur during the setting phase of the cement so that the porous space of the cement is effectively reduced.

In this project, magnesium oxide is one of the additives selected for developing acid resistant cement formulations. To test the performance the new formulations, 5% magnesium oxide cements (MGO-5) and baseline samples were aged under different conditions presented in **Table 2.33**. Aged and unaged sample properties (porosity, permeability, compressive and shear bond strengths and FTIR mineralogy) were measured and analyzed.

Table 2.33: Aging conditions for MGO samples

MGO Batch #	Exp. #	Baseline Batch #	Temp. (ºF)	Pressure (psi)	Concentration		
					CH_4 (%)	CO_2 (%)	H_2S (ppm)
2	8	10	225	6000	0	100	0
3	10	12	100	6000	0	100	0
4	7A	15	225	6000	60	40	0
5	14	17	350	9000	60	40	0
6	20	23	225	9000	60	40	0
7	22	25	225	9000	0	100	0
8	31	34	225	6000	90	10	300
10	34	37	100	6000	60	40	180
11	36	39	100	9000	90	10	300
12	38	41	100	3000	100	0	300

Porosity and Permeability

Figure 2.135 depicts porosities of aged and unaged Class H based MGO-5 (HSMG) and baseline (HS) samples. Aging was conducted predominantly in brine (2% NaCl) saturated with methane gas containing CO_2. All baseline samples showed substantial reduction in the porosity, which is attributed to carbonation. However, MGO-5 samples showed limited reduction in porosity resulting from expansion of the matrix (through formation of $Mg(OH)_2$) and partial carbonation that occurred simultaneously. The formation of $Mg(OH)_2$ crystals is beneficial because it can reduce the pore space and prevent penetration of the acid into the matrix thereby limiting the carbonation process.

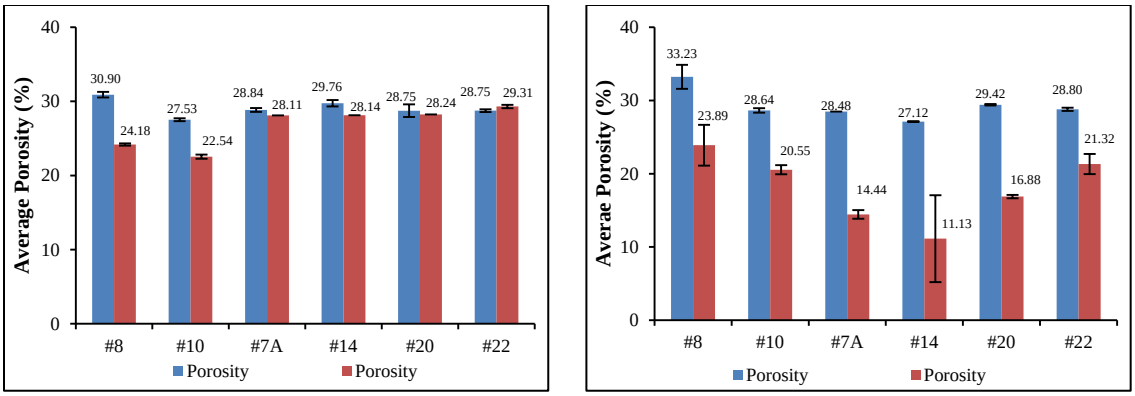

(a) (b)

Fig. 2.135: Porosity of aged (orange) and unaged (blue) samples: a) HSMG; and b) HS

Furthermore, the performances of the new formulations were tested in the presence of H_2S. **Figure 2.136** present porosities of aged and unaged HSMG and baseline samples. Baseline samples aged in CO_2-H_2S containing environment (Experiments #31 and 36) showed substantial reduction in the porosity, which is attributed to carbonation. However, HSMG samples showed mixed results (i.e. slight porosity increase in Experiment #31 and moderate porosity reduction in Experiment #36). The reduction in porosity is attributed to expansion of the matrix. The formation of $Mg(OH)_2$ crystals is expected to reduce the pore space and prevent acid penetration and subsequently the carbonation process.

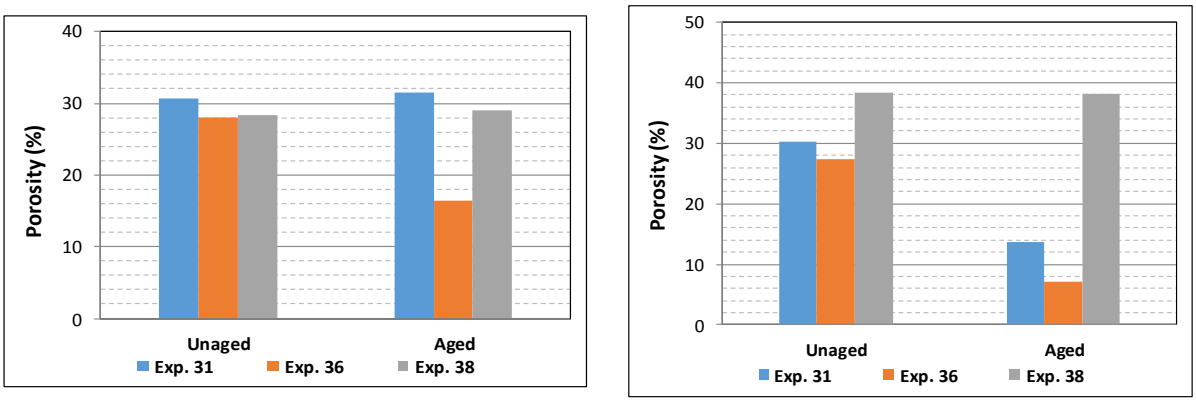

(a) (b)

Fig. 2.136: Porosity of unaged and aged (in the presence of H_2S) samples: a) HSMG; and b) HS

Consistent with the porosity data, permeability of HSMG and baseline samples showed substantial reduction after aging (**Fig. 2.137**). However, permeability alone cannot be used to compare the performance of the MGO-5 samples, as it tends to be highly sensitive to experimental errors and development of micro-cracks resulting from abrupt change in test parameters such as pressure and temperature. It is important to note that porosity and permeability reductions of HSMG samples were less than those of the baseline samples. The $Mg(OH)_2$ crystallization blocks the pore space and limits further decrease in porosity due to carbonation.

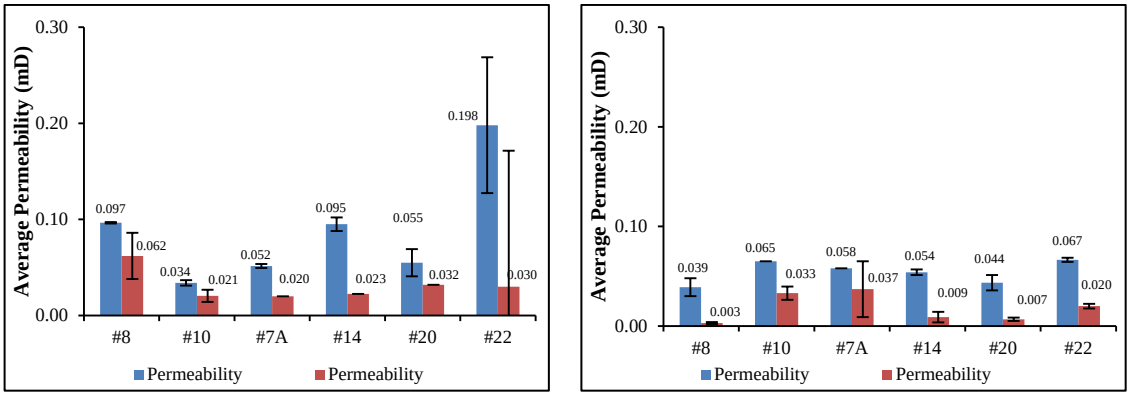

(a) (b)

Fig. 2.137: Permeability of aged (orange) and unaged (blue) samples: a) HSMG; and b) HS

In the presence of H_2S, permeability of baseline samples showed (**Fig. 2.138**) substantial reduction after aging, while HSMG samples displayed reduction in only one of the experiments (Experiment #31). The reduction in permeability was more pronounced when aging was carried out in CO_2 containing environment (Experiments #31 and 36). Hence, examining the changes observed in porosity and permeability of HSMG samples, it could be concluded that the addition of magnesium oxide reduces the penetration of carbonic acid and consequently limits the reduction in porosity and permeability resulting from carbonation.

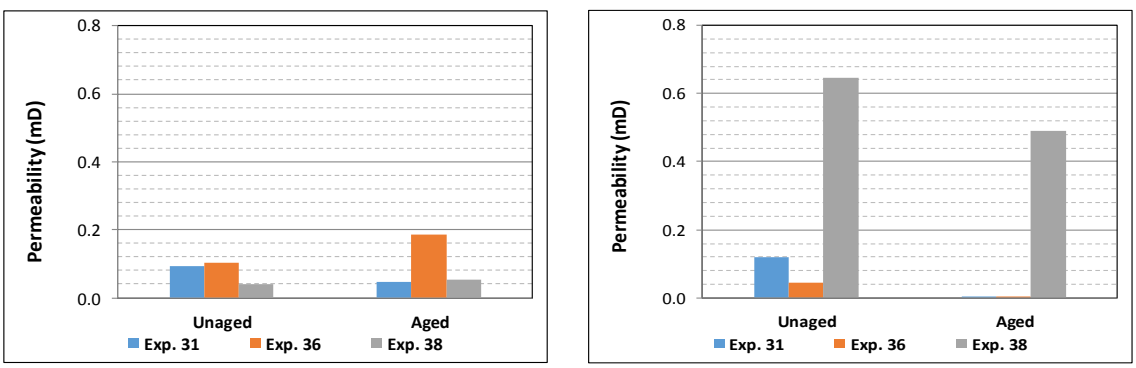

(a) (b)

Fig. 2.138: Permeability of unaged and aged (in the presence of H_2S) samples: a) HSMG; and b) HS

Class G based MGO-5 (GSMG) samples did not show a consistent decrease in the porosity or permeability (**Figs. 2.139** and **2.140**). Even though baseline samples displayed consistent decrease in porosity resulting from carbonation, measurements from GSMG samples were mixed. In addition, permeability measurements of some of GSMG samples (Experiments #8 and 14) demonstrated excessive increase, which indicates poor performance. Such an increase in permeability is attributed to severe leaching or development of micro cracks. There is inconsistency in the performance of GSMG.

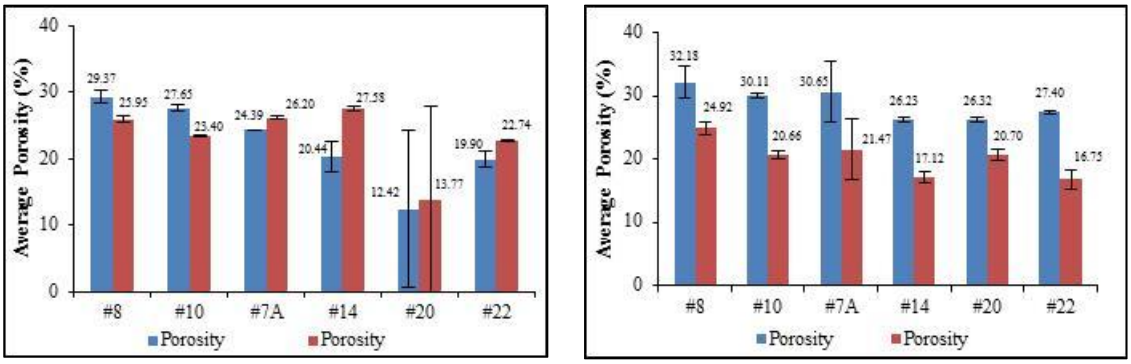

(a) (b)

Fig. 2.139: Porosity of aged (orange) and unaged (blue) samples: a) GSMG; and b) GS

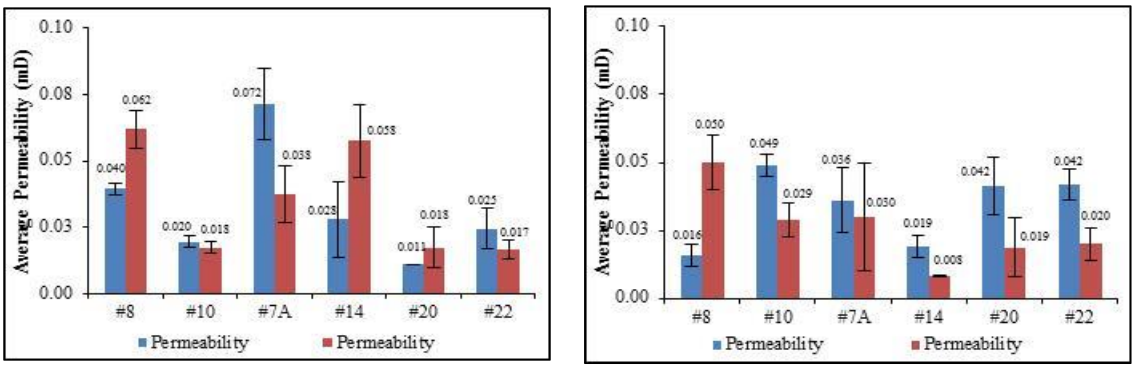

(a) (b)

Fig. 2.140: Permeability of aged (orange) and unaged (blue) samples: a) GSMG; and b) GS

Aging tests conducted in the presence of H_2S showed very similar results. GSMG samples porosity or permeability predominately increased after aging while baseline samples displayed mostly decrease in porosity and permeability due to carbonation (**Figs. 2.141** and **2.142**). Measurements from GSMG samples indicate poor performance resulting from severe leaching and formation of micro cracks.

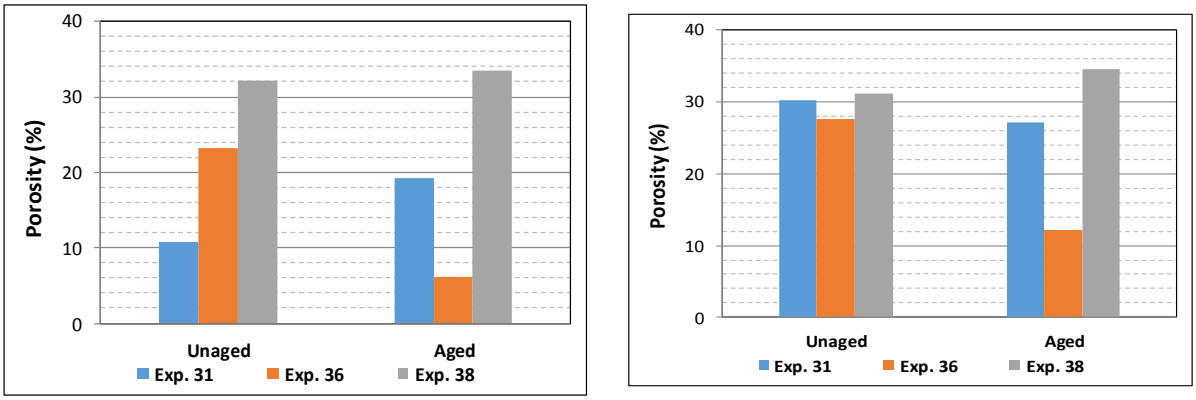

(a) (b)

Fig. 2.141: Porosity of unaged and aged (in the presence of H_2S) samples: a) GSMG; and b) GS

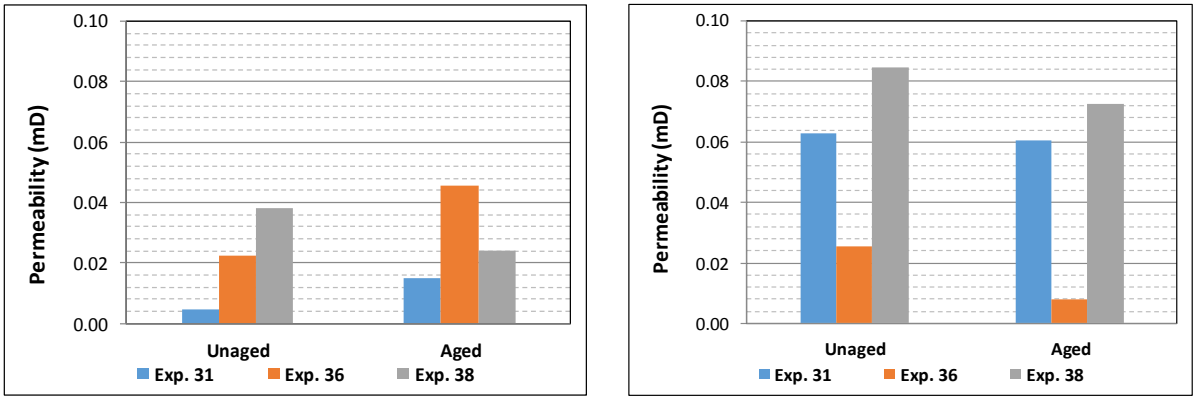

Fig. 2.142: Permeability of unaged and aged (in the presence of H_2S) samples: a) GSMG; and b) GS

Compressive Strength

The compressive strength for all baseline samples increased after aging due to carbonation of the matrix (**Fig. 2.143**). The improvement in strength is due to deposition of carbonate crystals in the pore space reinforcing the structure. The HSMG samples demonstrated a similar increase in the strength, which may be attributed to matrix expansion and carbonation. Results of Experiment #10 show minimal change in compressive strength of the baseline and HSMG samples. This could be due to aging at low temperature (100°F) and high CO_2 concentration (100% CO_2), which accelerates the dissolution and leaching of CH and CSH from the matrix (Nakarai et al. 2006). The strength gained by the carbonation can be offset by the leaching of the CH and CSH in the presence of excess carbonic acid. Similar results were obtained when the samples were aged in H_2S containing environment (**Fig. 2.144**).

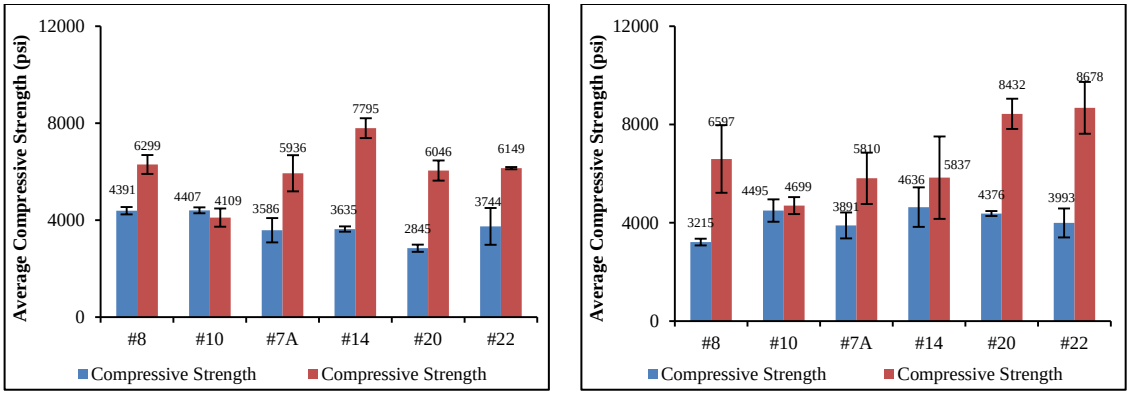

Fig. 2.143: Compressive strength of aged (orange) and unaged (blue) samples: a) HSMG; and b) HS

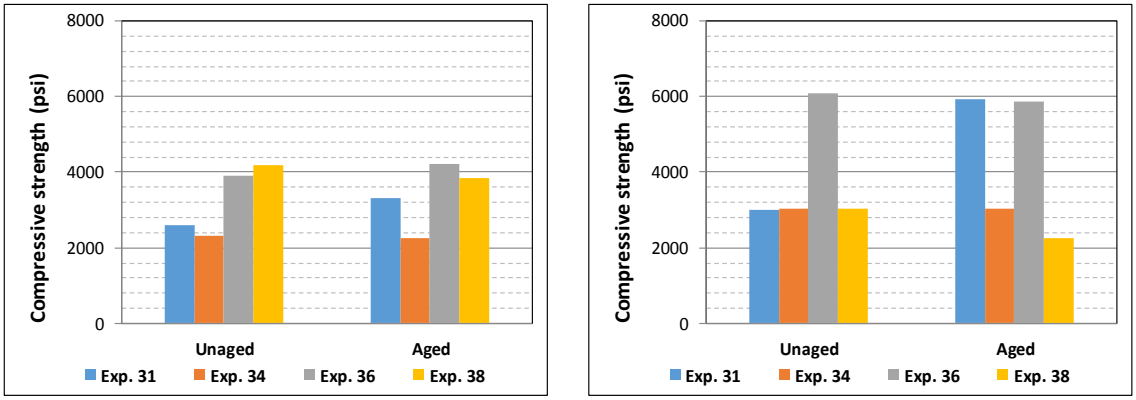

(a) (b)

Fig. 2.144: Compressive strength of unaged and aged (in the presence of H_2S) samples: a) HSMG; and b) HS

Compressive strengths of GSMG and baseline cements were predominately increased after aging (**Fig. 2.145**). However, the average strength improvement for GSMG samples was slightly lower than that of the baseline samples.

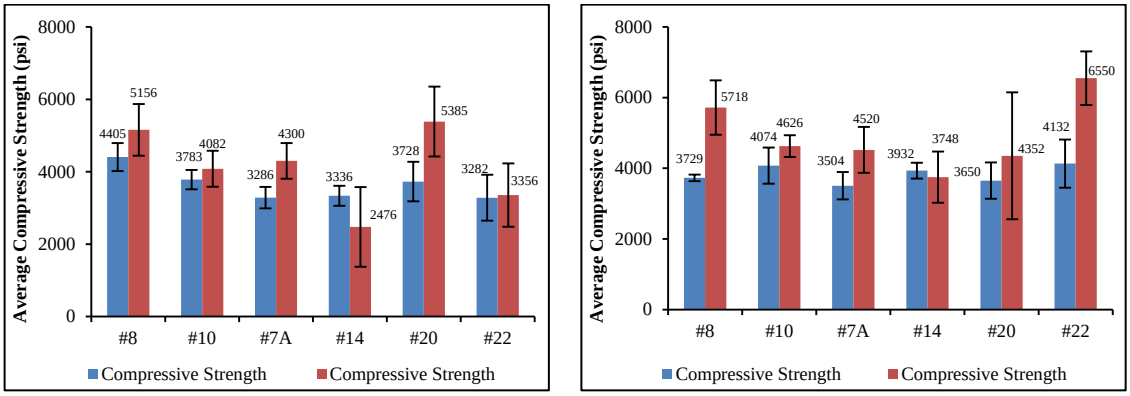

(a) (b)

Fig. 2.145: Compressive strength of aged (orange) and unaged (blue) samples: a) GSMG; and b) GS

Furthermore, like the porosity results, GSMG samples displayed inconsistent increase and decrease in their compressive strength. Baseline samples showed better consistence than the additive samples. Very similar results were obtained when the samples were tested in H_2S containing environment (**Fig. 2.146**).

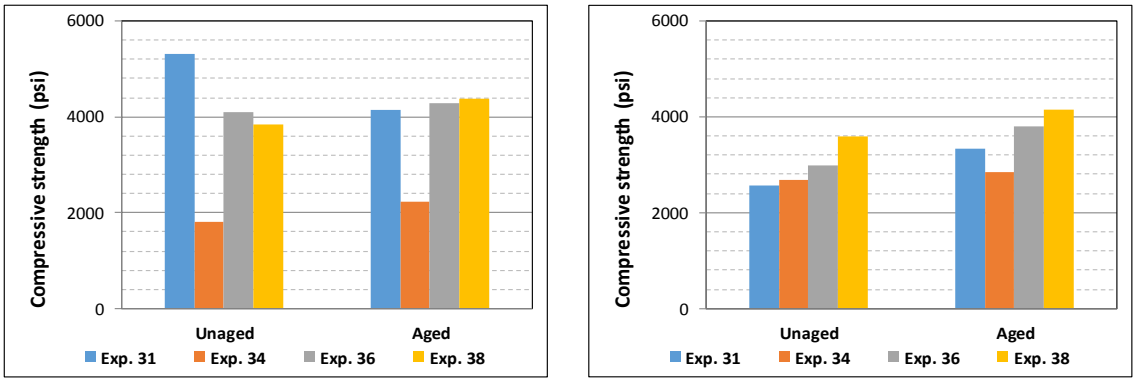

(a) (b)

Fig. 2.146: Compressive strength of unaged and aged (in the presence of H_2S) samples: a) GSMG; and b) GS

Shear Bond Strength

As the cement matrix expands, the shear bond strength is expected to increase. The MGO-5 and baseline samples showed steady increase in the shear bond strength (**Fig. 2.147**). In the presence of CO_2, baseline samples are expected to expand due to carbonation. The expansion of MgO takes place due to hydration occurring inside the matrix, while carbonation caused by acid attack is happening as the same time. However, measuring the extent of hydration of MgO and carbonation of CH and CSH in the matrix to quantify the expansion level is challenging. Results of Experiment #10 indicate the lowest increment in the shear bond strength in both samples due to leaching of CH component because of low temperature (100°F) and high CO_2 concentration (100% CO_2). When experiments conducted in the presence of H_2S, similar results were obtained (**Fig. 2.148**).

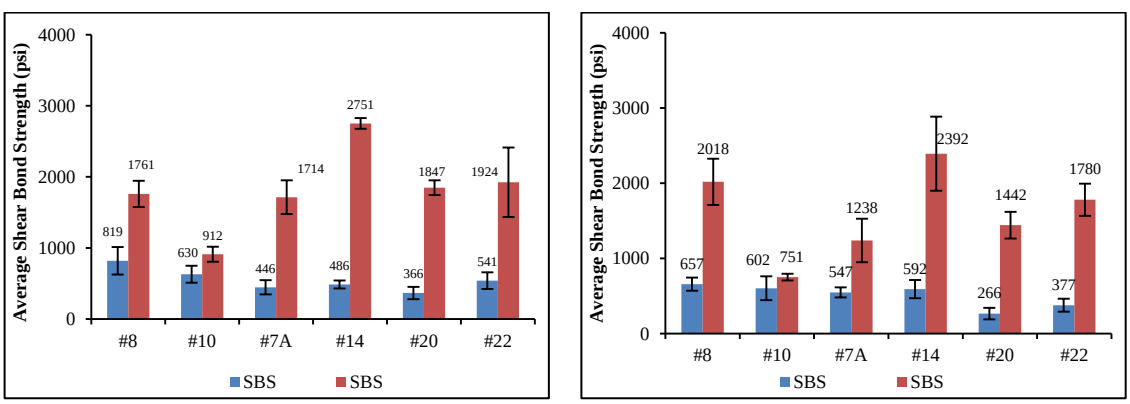

(a) (b)

Fig. 2.147: Shear bond strength of aged and unaged samples: a) HSMG; and b) HS

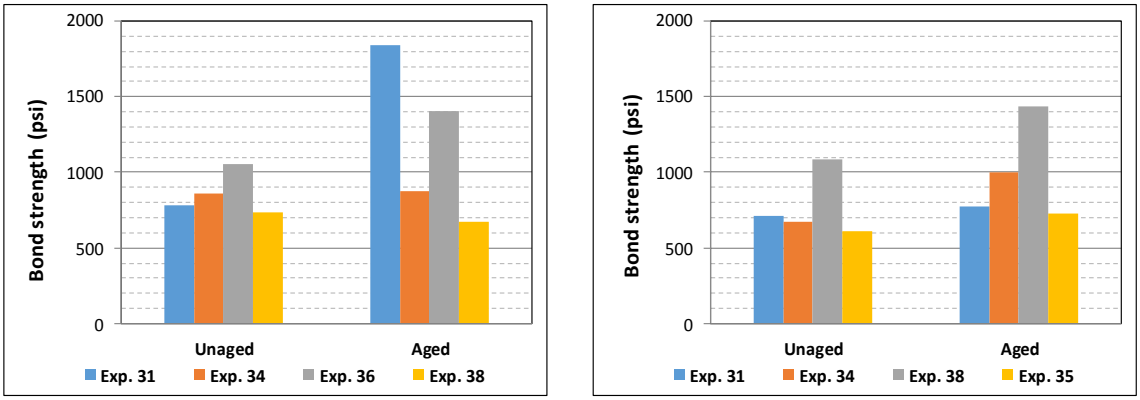

(a) (b)

Fig. 2.148: Shear bond strength of unaged and aged (in the presence of H_2S) samples: a) HSMG; and b) HS

FTIR Analysis

FTIR results of Class H based MGO-5 and baseline samples are presented in this section. The minerals under focus for the FTIR analysis are CH, CSH, $CaCO_3$ (denoted by CCO3) and $Mg(OH)_2$ (denoted by MH). MgO and $MgCO_3$ can also be identified at wavelengths of 500 cm^{-1} and 880/1480 cm^{-1}, respectively. However, the noise in the FTIR spectrum is in the order of hundreds (0 – 500 1/cm); hence, very low measurements like that of MgO may not provide reliable information. FTIR results of the inner zone are presented in **Fig. 2.149.**

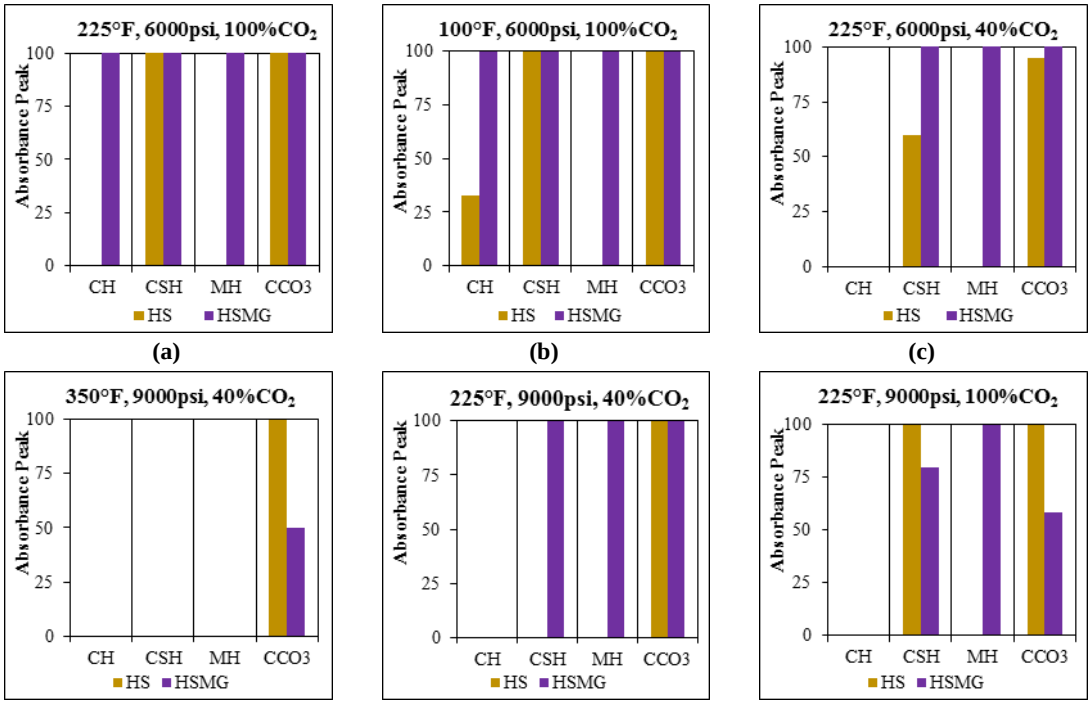

(a) (b) (c)

(d) (e) (f)

Fig. 2.149: FTIR results of inner zone of MGO-5 and baseline HS samples aged at different conditions: a) Exp. 8; b) Exp. 10; c) Exp. 7A; d) Exp. 14; e) Exp. 20; and f) Exp. 22

Inner Zone: Results indicate the presence of CH and CSH components along with $Mg(OH)_2$ in the matrix. All experiments except the one conducted at 350°F (Experiment #14), demonstrated the presence of CH and/or CSH. The presence of $Mg(OH)_2$ in the cement demonstrate the reduction of carbonic acid penetration. $Mg(OH)_2$ crystals also undergo carbonation forming $MgCO_3$, which is insoluble compound that precipitates in the matrix. Unlike $CaCO_3$, $MgCO_3$ does not react readily with carbonic acid to form a soluble product (Cheremisinoff 1995) that can be leached out by the surrounding fluid. Hence, carbonation of $Mg(OH)_2$ to $MgCO_3$ is beneficial in limiting acid attack.

The $CaCO_3$ bars in the FTIR spectrum shown in the charts include both $MgCO_3$ and $CaCO_3$. Hence, it can be misleading to assess the performance of MGO-5 by comparing $CaCO_3$ peaks alone; other peaks can be used to evaluate its performance. According to the results, the performance of MGO-5 in Class H cement seems to be effective to a certain extent. MGO-5 cement expected to resist acid attack by generating $Mg(OH)_2$ crystals during carbonation. The formation of crystals in the pore space reduces porosity and permeability of the cement and limits the penetration of acid.

Middle Zone: The middle zone is expected to show more carbonation than the inner zone (**Fig. 2.150**). The CH and CSH were only preserved when aged at 100°F and 100% CO_2 (Experiment #10). Results are consistent with the inner zone measurements. $Mg(OH)_2$ was preserved in the three experiments. The CSH, which was preserved in the inner zone during Experiments #8 and 22 was completely carbonated in the middle zone.

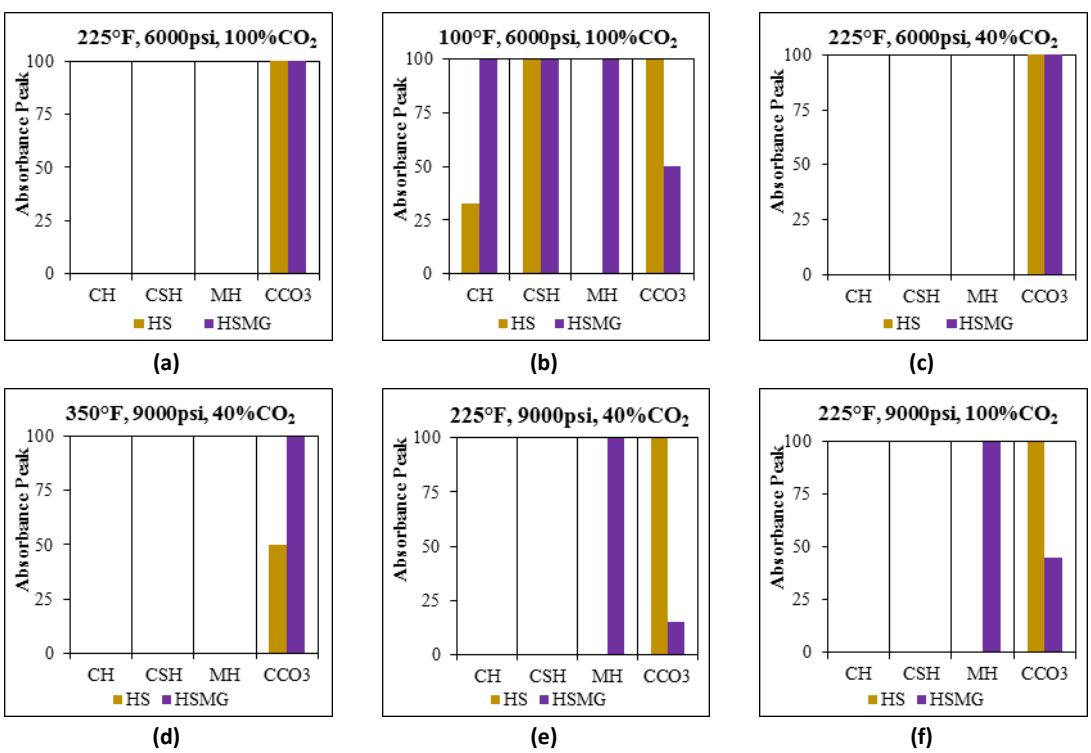

Fig. 2.150: FTIR results of middle zone of MgO and baseline HS samples aged at different conditions: a) Exp. 8; b) Exp. 10; c) Exp. 7A; d) Exp. 14; e) Exp. 20; and f) Exp. 22

Outermost Zone: The outermost zone is the most degraded zone due to direct exposure. Only $CaCO_3$ was found to be present in all the samples. It should be noted that the $CaCO_3$ peaks also comprise $MgCO_3$ content (**Fig. 2.151**).

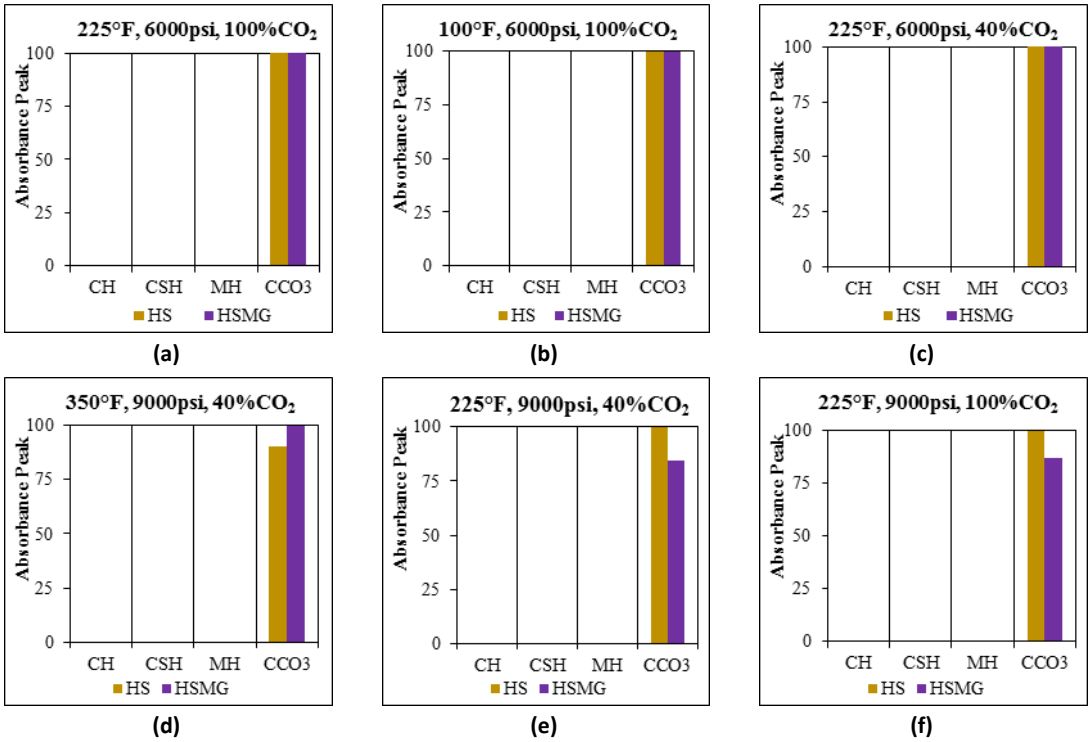

Fig. 2.151: FTIR results of outer zone of MgO and baseline HS samples aged at different conditions: a) Exp. 8; b) Exp. 10; c) Exp. 7A; d) Exp. 14; e) Exp. 20; and f) Exp. 22

Summary

According to the experiment results, MgO was able to act as an expanding agent in the cement. The formation of $Mg(OH)_2$ leads to expansion of matrix, which is highly dependent on temperature. Although the magnesium hydroxide crystals were able to reduce porosity, they were susceptible to carbonation, which forms $MgCO_3$. The advantage of the formation of $MgCO_3$ over $CaCO_3$ is that, it does not form soluble product that can be easily leached out when it reacts with the acid. According to FTIR study, the presence of CH and CSH component in the inner zone confirms a protected MGO-5 matrix, even though the middle and outer zone indicate a leached zone.

2.4.2.3. Experimental Results Showing Acid Resistance of New Cement Formulations

Extensive additive screening and cement formulation study indicated that hydroxyapatite and magnesium oxide containing cement (HOAP and MGO-5) are the most viable formulations that can withstand acid attack under HPHT conditions. Addition of magnesium oxide or hydroxyapatite is expected to preserve cement properties such as porosity, permeability, and compressive and bonding strength after exposure to acidic environment.

Acid Resistance of Hydroxyapatite Cement

Twelve aging experiments were performed to evaluate performance of hydroxyapatite-based cement (HOAP). Samples were subjected to different aging conditions (Table 2.32). For all batches of aging experiments, slurry compositions (**Table 2.34**) and properties were maintained the same. Properties of the slurries are presented in **Table 2.35**.

Table 2.34: Composition of the HOAP slurries

Component	Unit	GHO	HHO
Cement	%	100	100
Hydroxyapatite	% BWOC	5	5
Antifoam Agent	gal/sack of cement	0.1	0.1
Water for Cement	% BWOC	44	38
Water for HOAP	% BWOC	23	23

BWOC = by weight of cement

Table 2.35: Properties of hydroxyapatite containing cement slurries

Slurry	GHO	HHO
Amount	5% bwoc	5% bwoc
Remarks	No Silica Flour and HEC	No Silica Flour and HEC
Density (ppg)	15.80 ppg	16.65 ppg
API Fluid Loss	82 ml	88 ml
Thickening Time	60 minutes	90 minutes

Hydroxyapatite cement samples are expected to react with the acid to form carbonated-hydroxyapatite ($Ca_5(PO_4)_3CO_3$), according to the following reaction:

$$2Ca_5(PO_4)_3(OH) + CO_3^{2-} \rightarrow 2Ca_5(PO_4)_3(CO_3) + OH^- \quad \text{.....} \quad (2.26)$$

The formation of carbonated-hydroxyapatite layer around the core prevents the cement from further acid attack. The hexagonal structure of the hydroxyapatite remains intact without disruption due to the formation of carbonated-hydroxyapatite (Sugama 2006). However, after aging, a slight expansion is still observed in the samples, which can be as a result of carbonation of $Ca(OH)_2$ and CSH present in the cement matrix.

<u>Performance under Low Temperature Conditions</u>

Batch #002 samples were aged at 100°F using 40% CO_2 gas. After aging, the samples were cut in the middle to examine the depth of degradation. The samples did not exhibit feasible discoloration that indicates changes in property. However, reduction in porosity and permeability (**Fig. 2.152**) were observed while their shear bond strengths were improved substantially (**Fig. 2.153**) due to expansion of the cement resulting from carbonation. More carbonation is expected in HS samples than HOAP cores resulting in high tendency of expansion and increased bonding strength. However, at 100°F, leaching may be higher for HS samples. Leaching counterbalances the effects of carbonation and adversely affects SBS improvement.

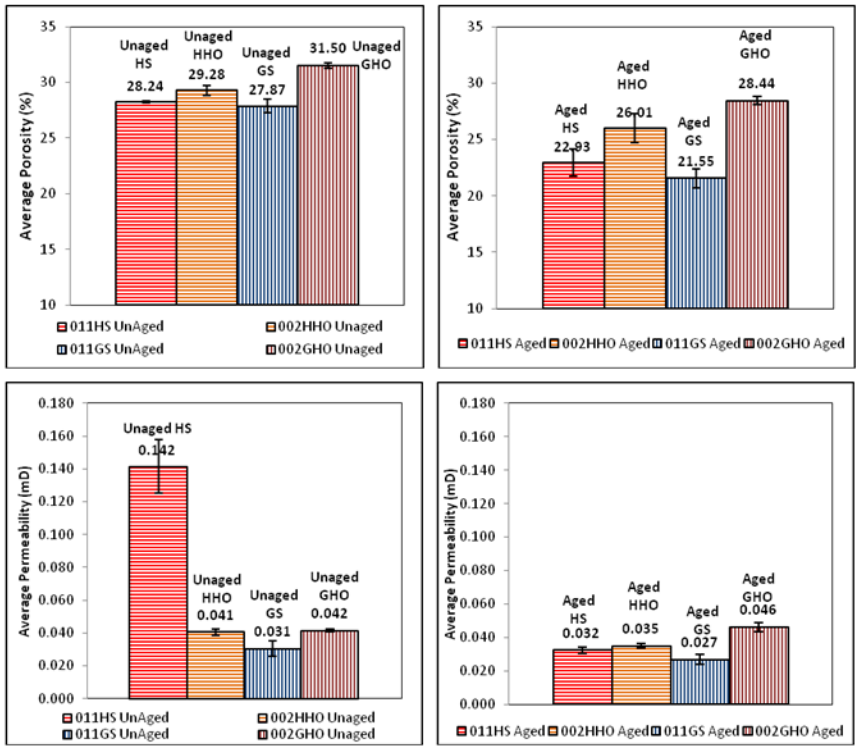

Fig. 2.152: Porosity and permeability of HOAP and baseline samples (aging at 100°F, 6000 psi and 40 % CO_2)

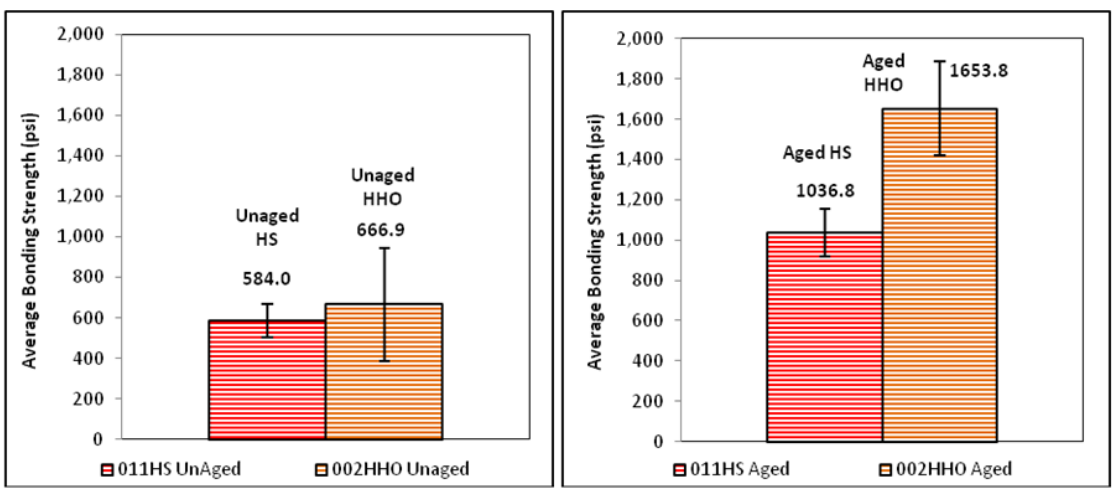

Fig. 2.153: Shear bond strength of baseline and HOAP samples (aging condition: 100°F, 6000 psi and 40 % CO_2)

Compressive strength of aged and unaged samples were approximately the same (**Fig. 2.154**). This suggests the presence of mild carbonation without discoloration of the cores. Only small variations within the range of measurement discrepancy were observed. The trend of compressive strength measurements are similar to those obtained for permeability tests. The reason can be attributed to the formation of thin carbonated layer on the outer rim of HOAP samples that prevents further penetration of CO_2 or occurrence of comparable levels of carbonation and leaching that maintains the strength of the cores more or less the same.

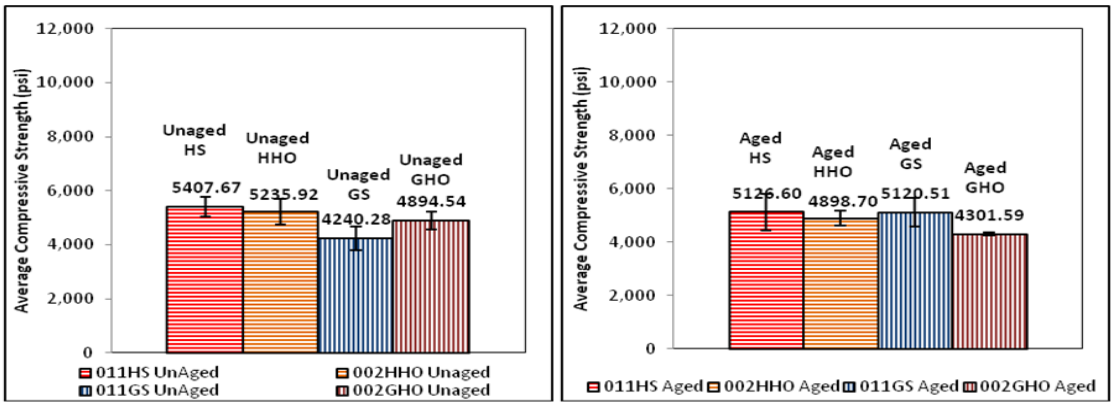

Fig. 2.154: Compressive strengths of baseline and HOAP cements (aging at 100°F, 6000 psi and 40 % CO_2)

Performance under High Temperature Conditions

When aged at high temperature (350°F) and high CO_2 concentration (100% CO_2 gas), both the HOAP and baseline cement samples showed (**Fig. 2.155**) a clear discoloration indicating the degradation depth.

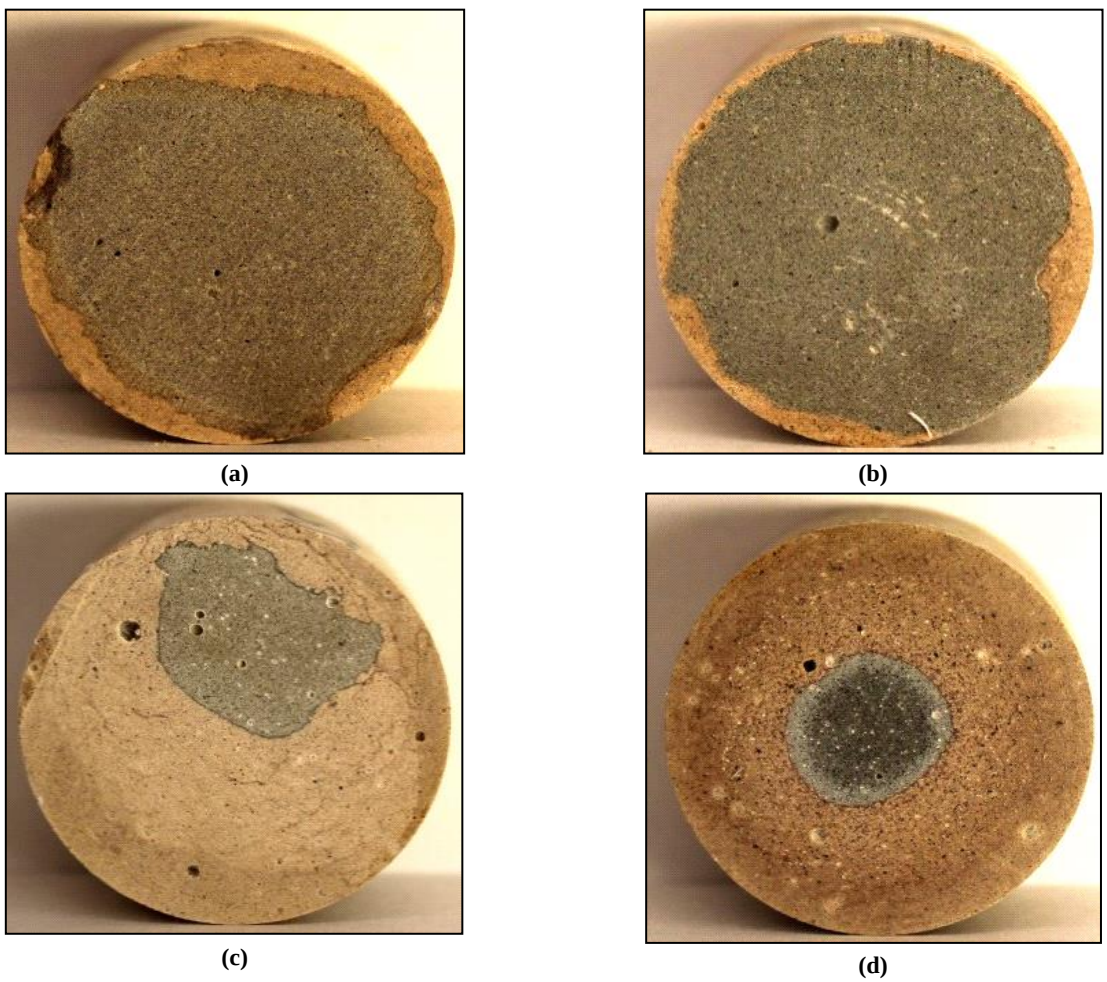

Fig. 2.155: Middle cross-section of cores after aging at 350°F with 100% CO_2 gas: a) GHO; b) HHO; c) GS; and d) HS

It can be clearly observed (Fig. 2.155) that HOAP samples experienced very less degradation as compared to the baseline cement samples. The discoloration front, which can be related to the depth of penetration of CO_2, is observed only as a very small outer rim in the HOAP samples. Due to the non-uniformity of the degradation depth, an average degradation depth is calculated and used to compare the samples. Results (**Table 2.36)** indicate substantial difference in degradation depth between the baseline cement and HOAP samples. The introduction of hydroxyapatite into the cement system considerably improved the resistance of the cement against carbonic acid attack.

Table 2.36: Degradation depth of HOAP and baseline samples aged at 350°F

Core #	Average carbonated depth (in.)	Std. Dev.
HHO	0.046	0.022
HS	0.353	0.018
GHO	0.063	0.051
GS	0.351	0.203

At high temperature (350°F), HOAP samples showed reduction in compressive strength while the baseline samples displayed improvement (**Fig. 2.156**). The increase in strength of baseline cement is due to carbonation which results in precipitation of $CaCO_3$ in the pore space. The strength improvement is consistent with the degradation measurements obtained from baseline samples. The precipitated $CaCO_3$ in the pore provides reinforcement to the cement matrix, resulting in improvement of the compressive strength. Studies on HOAP containing cement are very limited. It is not clear why the strength of HOAP samples reduced after aging. Possible explanations could be leaching and/or thermal retrogression. HOAP samples did not exhibit substantial carbonation as presented in the degradation depth measurements. In addition, when it is carbonated, it does not precipitate in the pore space. However, it becomes a part of the matrix without increasing the compressive strength. As a result, leaching can dominate the aging process causing reduction in strength. Another reason is that silica flour, which is needed to prevent thermal retrogression, was not added in the HOAP slurries to maintain slurry properties within acceptable range. The lack of excess silica in the cement system can result in thermal retrogression, when the cement is exposed to high temperatures (i.e. greater than 230°F).

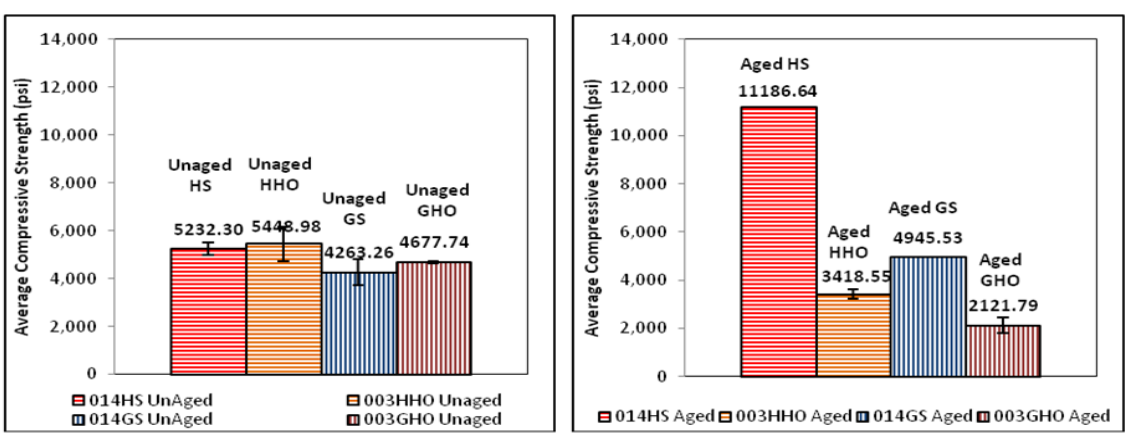

Fig. 2.156: Compressive strengths of baseline and HOAP cements (aging at 350°F, 6000 psi and 100 % CO_2)

For samples aged at 350°F and 100% CO_2, the HOAP samples showed a lower increase in SBS than the HS samples (**Fig. 2.157**). This could be attributed to temperature retrogression resulting from lack of excess silica to prevent the formation of weak CSH phase (α-CSH). This observation is consistent with compressive strength measurements.

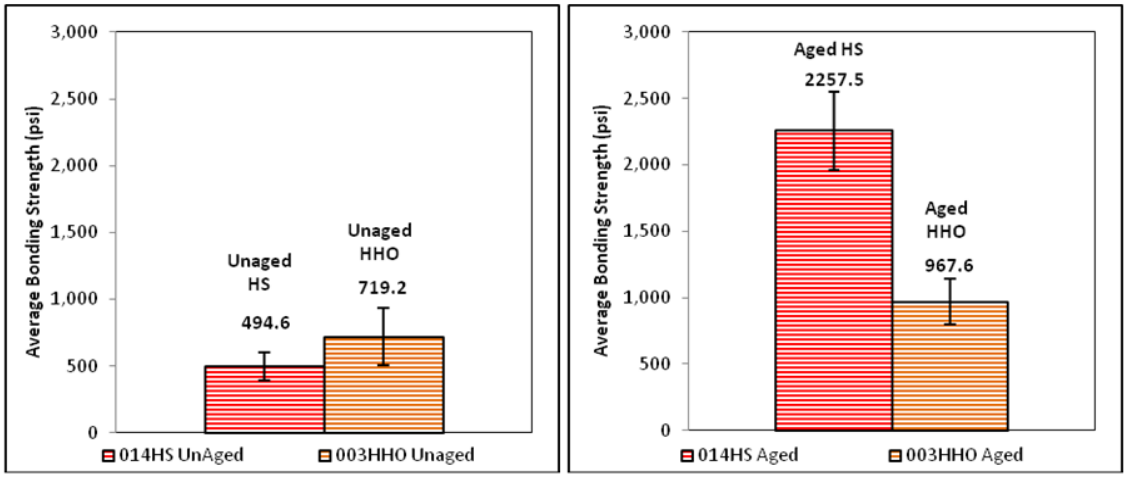

Fig. 2.157: Shear bond strength of baseline and HOAP samples (aged at 350°F, 6000 psi and 100 % CO_2)

<u>Performance Comparison using FTIR Measurements</u>

The porosity, permeability, degradation depth, compressive strength and shear bond strength measurements indicate a lesser amount of calcium carbonate formation in the HOAP samples. The Fourier Transform Infrared Spectroscopy (FTIR) tests were carried by taking samples from the outermost, middle and innermost zones of a transversely cut cement cores. Spectrum peaks of relevant molecular bonds that indicate the level of CH, CSH and $CaCO_3$ in each zone are summarized and presented from **Figs. 2.158** to **2.160**.

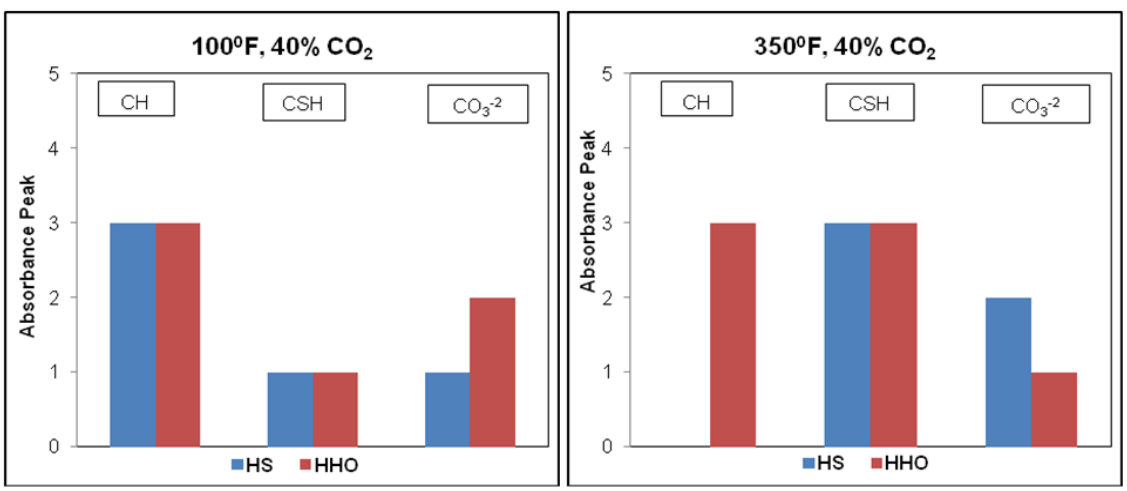

Fig. 2.158: Summarized FTIR data for HOAP and baseline samples (innermost Zone)

In the inner zone of the sample (Fig. 2.158), the amounts of CH and CSH were almost the same in both HS and HOAP samples after aging at 100°F and 40% CO_2. However, the amount of carbonate was higher in HOAP than HS samples. The source of this carbonate bond can be calcium carbonate and/or carbonated-hydroxyapatite ($Ca_5(PO_4)_3.CO_3$) formed from the HOAP. The type of carbonate is not distinguishable from FTIR result. On the other hand, after aging at 350°F and 100% CO_2, the CH present in the HS samples was fully carbonated while abundant amount of CH was found in the HOAP sample. In all zones, the level of carbonation is higher in the HS sample than in HOAP samples when aged at 350°F. This means that the amount of carbonate, including $CaCO_3$ and $Ca_5(PO_4)_3.CO_3$, formed in HOAP samples is lesser than calcium carbonate formed in HS samples.

FTIR results from the middle zone also displayed (Fig. 2.159) acceptable carbonation resistance of HOAP samples. After aging, CH was completely absent in the HS sample; however, it was still present in abundant amount in HOAP samples. After aging at 100°F, the amount of CSH and $CaCO_3$ was almost same in both HS and HOAP samples. However, after aging at high temperature (350°F) the CSH was not found in the HS samples indicating complete carbonation of the matrix, while abundant amount of CSH was present in HOAP samples. In addition, the amount of carbonate formed in HOAP samples was less than that formed in HS cores. The outer zone showed a complete carbonation of the matrix in both cases (Fig. 2.160). This result was expected as the outer rim is most vulnerably exposed to the harsh environment.

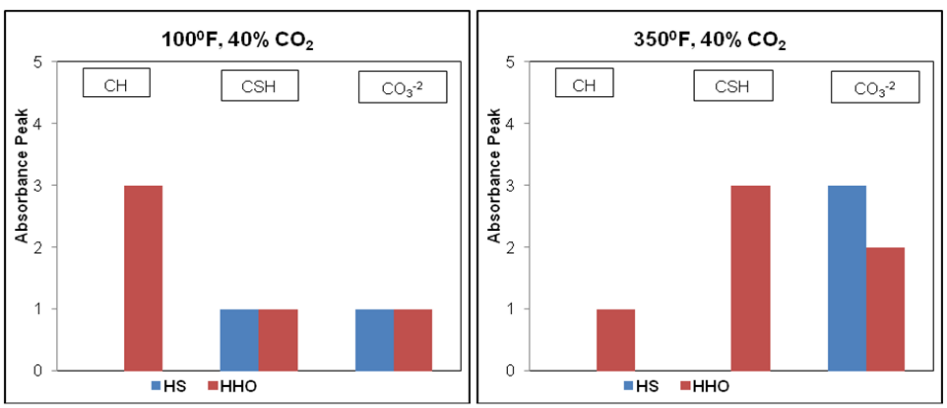

Fig. 2.159: Summarized FTIR data for HOAP and baseline samples (middle zone)

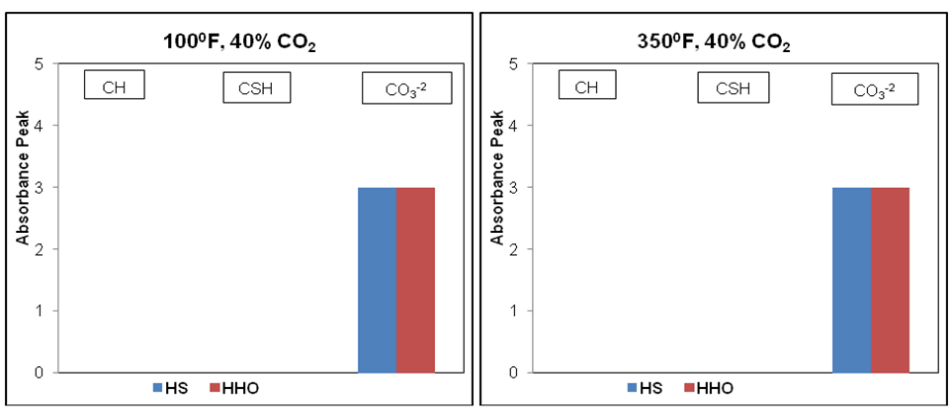

Fig. 2.160: Summarized FTIR data for HOAP and baseline samples (outermost zone)

Acid Resistance Magnesium Oxide Cement

Additive screening and cement formulation study indicated that magnesium oxide containing cement (MGO-5) is viable formulations that can withstand acid attack under HPHT conditions. During the investigation, ten aging experiments were performed to evaluate performance of magnesium oxide-based cements. Samples were exposed to different aging conditions (Table 2.33). During the investigation, slurry compositions (**Table 2.37**) and properties (**Table 2.38**) were maintained approximately the same.

Table 2.37: Formulations of MgO based cement (MGO-5) slurries

Component	Class G	Class H
Water for Cement	44% BWOC	38% BWOC
Water for Silica Flour	38.5% BWOC c	38.5% BWOC c
Anti-Foaming Agent	0.1 gal/sk of Cement	0.1 gal/sk of Cement
HEC	0.1% of Water for Silica	0.1% of Water for Silica
Cement	100% BWOC	100% BWOC
Silica Flour	35% BWOC	35% BWOC c
MgO	5% BWOC	5% BWOC

Table 2.38: Properties of MGO-5 and baseline cement slurries

Property	HSMG	HS	GSMG	GS
Theoretical Density	16.15 ppg	15.96 ppg	14.99 ppg	15.51 ppg
Measured Density	16.30 ppg	16.20 ppg	14.80 ppg	15.45 ppg
Filtration Loss at 7.5 min.	58 ml	50 ml	62 ml	60 ml
Rheological Properties	Power Law n = 0.52 K = 7.9 $lbf.s^{0.52}/100ft^2$	Power Law n = 0.44 K = 14.4 $lbf.s^{0.44}/100ft^2$	Power Law n = 0.40 K = 9.9 $lbf.s^{0.40}/100ft^2$	Power Law n = 0.35 K = 10.5 $lbf.s^{0.35}/100ft^2$
Thickening Time	160 min.	170 min.	130 min.	135 min.

Performance under Intermediate Temperature Conditions

In Batch #006, tests with MGO-5 samples were conducted under HPHT conditions presented in **Table 2.39**. After aging, the properties (porosity, permeability, compressive strength and shear bond strength) of aged and unaged cores were measured.

Table 2.39: Aging conditions for the MGO-5 samples

MGO-5	Temp. (°F)	Pressure (psi)	CO_2 (%)	CH_4 (%)	NaCl (%)	Days	Baseline	Exp. No.
Batch 006	225	9000	40	60	2	14	Batch 023	20

After aging, porosity of baseline cements showed considerable reduction due to carbonation in the matrix, which occurred because of acid penetration (Fig. 2.161). Most of MGO-5 samples exhibited slight reduction in porosity and permeability (**Figs. 2.161** and **2.162**), which is attributed to the simultaneous effects of carbonation and matrix expansion (i.e. pore shrinkage) due to $Mg(OH)_2$

formation. Class G based MGO-5 samples showed increase in permeability. The reversal of permeability trend is mainly due to high sensitivity of permeability towards the physicochemical phenomena occurring during aging. For aged samples, porosity and permeability trends are consistent. However, it was inconsistent for unaged samples. Limited porosity and permeability changes occurred in MGO samples after aging indicate the effectiveness of magnesium oxide in preventing the penetration of carbonic acid and carbonation of cement matrix.

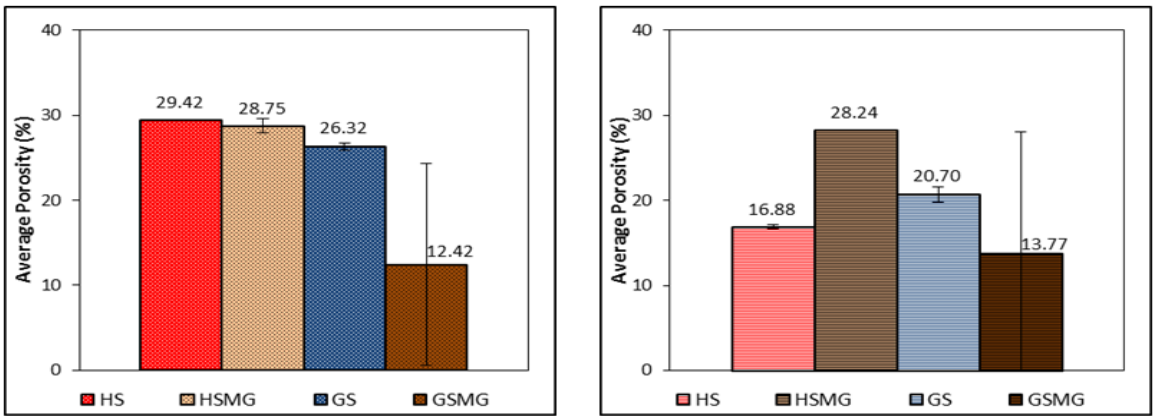

Fig. 2.161: Porosities of MGO-5 and baseline cements: a) unaged; and b) aged

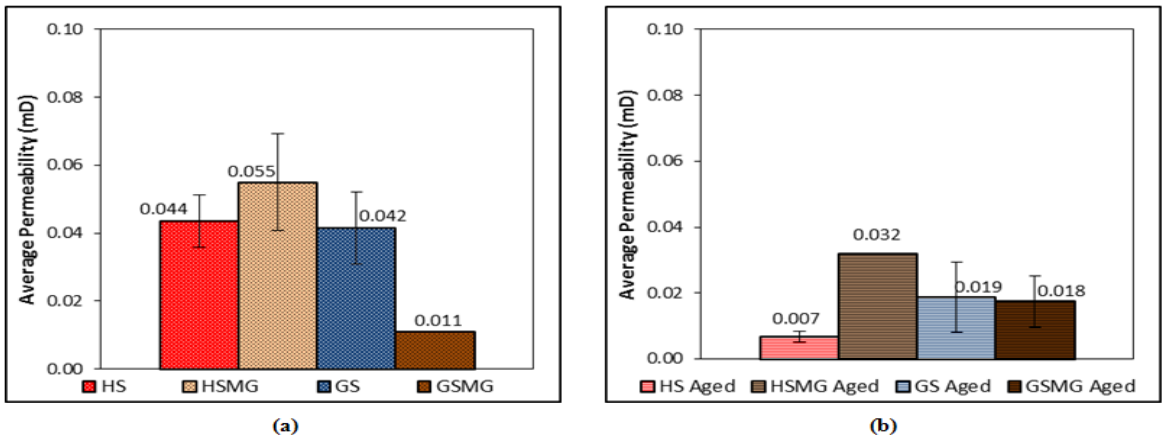

Fig. 2.162: Permeabilities of MGO-5 and baseline cements: a) unaged; and b) aged

Compressive strengths of MGO-5 and baseline cements are presented in **Fig. 2.163**. Compressive strength of unaged HSMG samples was significantly lower than that of baseline cores. However, GSMG samples exhibited more or less the same compressive strengths as the baseline samples. Hence, the formation of $Mg(OH)_2$ did not increase the initial compressive strength after hydration. After aging, all samples showed improvement in strength. Compressive strengths of MGO-5 samples were substantially increased due to further hydration of MgO, and carbonation of $Mg(OH)_2$ and $Ca(OH)_2$. The baseline samples displayed a lesser amount of compressive strength improvement (i.e. percentage increase) than the MGO-5 samples. This can be due to the carbonation process, which is limited to $Ca(OH)_2$. However it was observed that the porosity of MGO-5 samples did not change

significantly after aging, which indicate lesser penetration of carbonic acid due to formation of $Mg(OH)_2$ crystals. Hence, it can be concluded that MGO-5 samples showed lesser acid penetration and consequently, lower carbonation, though they exhibited increased compressive strength due to the formation of $Mg(OH)_2$ crystals in the pore space.

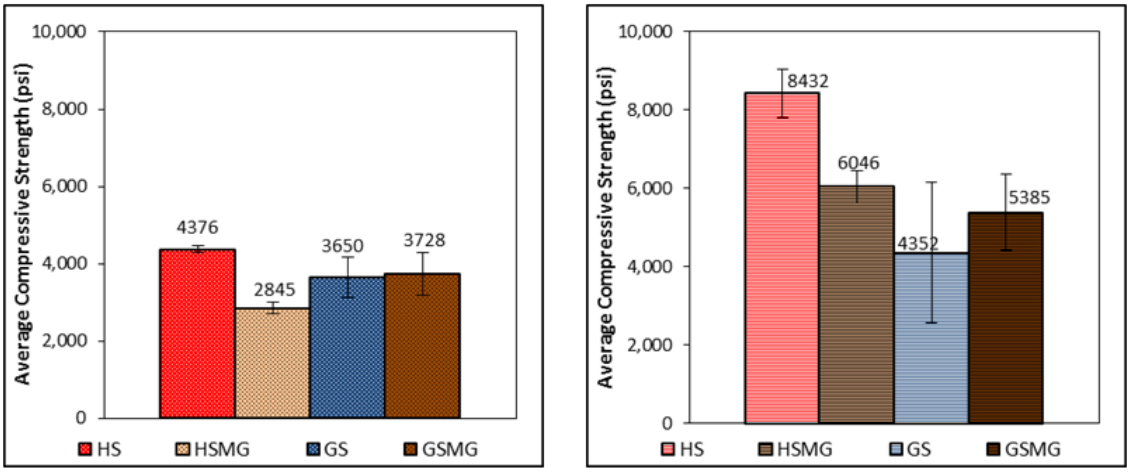

Fig. 2.163: Compressive strength of MGO-5 and baseline cements: a) unaged; and b) aged

The shear bond strength (SBS) measurements are presented in **Fig. 2.164**. Baseline HS samples showed increased SBS after aging due to carbonation and expansion of the matrix. At the same time, HSMG samples exhibited increased SBS due to carbonation and formation of $Mg(OH)_2$ crystals. It is challenging to compare the level of carbonation upcoming in the HSMG samples using the SBS data alone. Hence, FTIR tests were performed to examine the mineralogical changes occurred after aging.

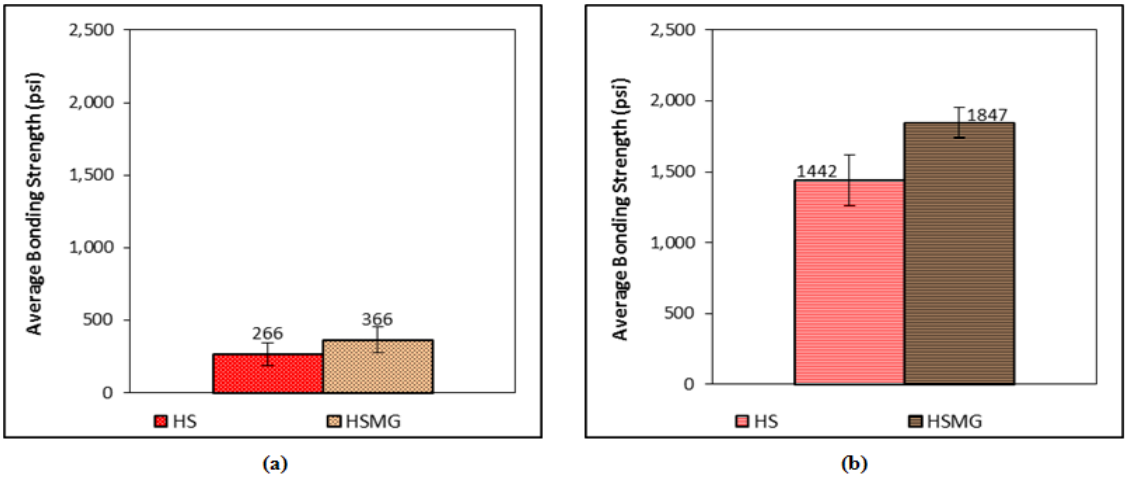

Fig. 2.164: Shear bond strength of MGO-5 and baseline cements: a) unaged; and b) aged

FTIR spectrum is simplified in the form of bar charts for easy interpretation (**Fig. 2.165**). The outer and middle zones show presence of $CaCO_3$ and $MgCO_3$ only. The inner zone, however, shows

presence of CSH and $Mg(OH)_2$ in the HSMG samples, indicating that the matrix has not been carbonated completely. This promising indication of performance MGO cement justifies its application in HPHT acidic environment.

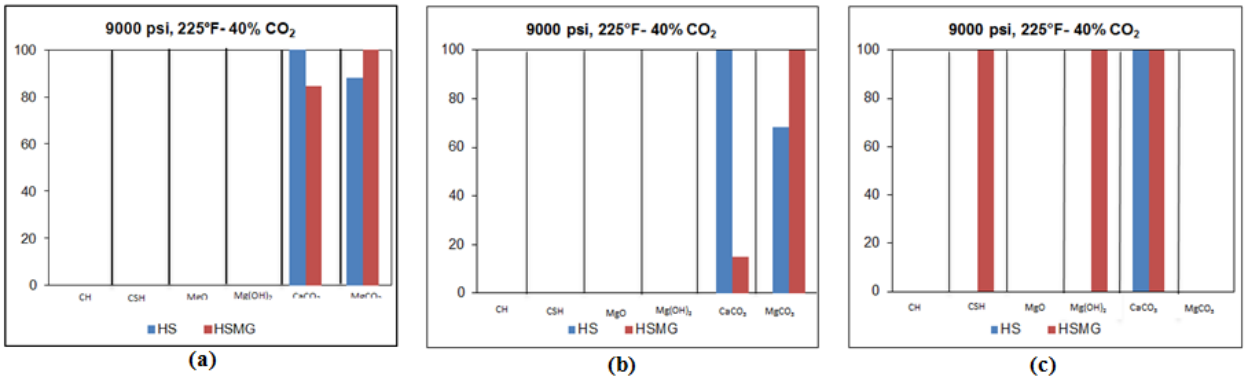

Fig. 2.165: Summarized FTIR data of HSMG and baseline HS samples aged at 225°F, 9000 psi, 40% CO_2 for 14 days: a) Outermost zone; b) Middle zone; and c) Innermost zone

Performance under High Temperature Conditions

An aging experiment (Batch #005) conducted with MGO-5 and baseline samples under high temperature condition (**Table 2.40**) demonstrated the performance of the new cement formulations. After aging, the properties (porosity, permeability, compressive strength and shear bond strength) of aged and unaged cores were measured.

Table 2.40: Aging conditions for the MGO-5 samples

MGO-5	Temp. (°F)	Pressure (psi)	CO_2 (%)	CH_4 (%)	NaCl (%)	Days	Baseline	Exp. No.
Batch 005	350	9000	40	60	2	14	Batch 017	15

Porosity and permeability of MGO-5 and baseline samples are presented in **Figs. 2.166** and **2.167**, respectively. The unaged porosities of all the samples are in the same range except for GSMG, which showed lower porosity than the baseline samples. On the other hand, the permeability of the unaged samples varies significantly. The permeability of MGO-5 samples is higher than their respective baseline cement samples. As these measurements were taken just after curing of the samples; the difference is mainly due to variation in composition and hydration process of the cements. After aging, decrease in the porosity was predominately observed, except in the case of GSMG samples, which displayed a considerable increase in porosity. This increase can be attributed to leaching of the calcium bicarbonate formed after complete carbonation of $Ca(OH)_2$ and CSH. Class H based MgO samples (HSMG) exhibited substantial reduction in permeability after aging. This reduction can be attributed to the expansion of $Mg(OH)_2$ crystals in the matrix, which prevents the carbonation. This has been verified using FTIR analysis, which is presented next.

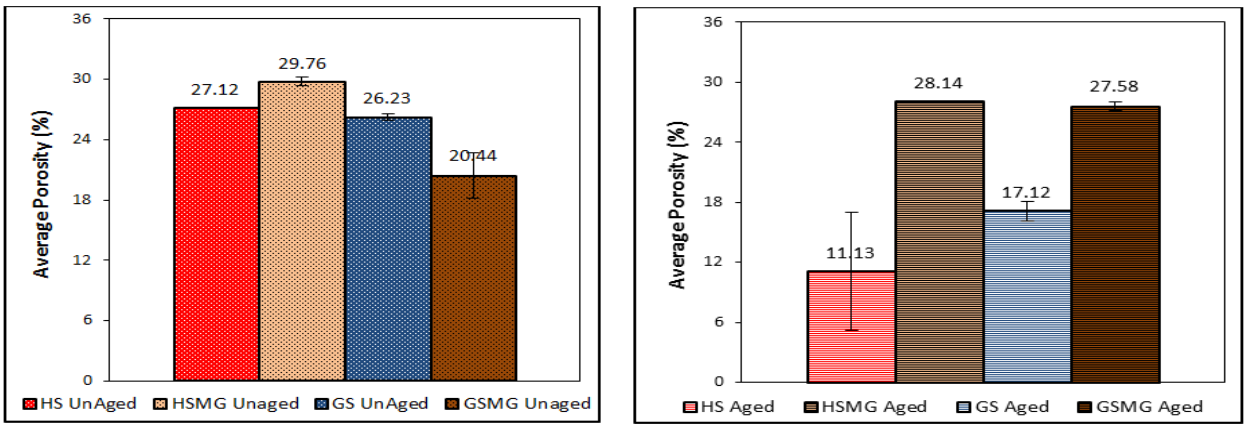

(a) (b)

Fig. 2.166: Porosities of MGO-5 and baseline samples: a) Unaged; and b) aged at 350°F, 9000 psi and 40% CO_2

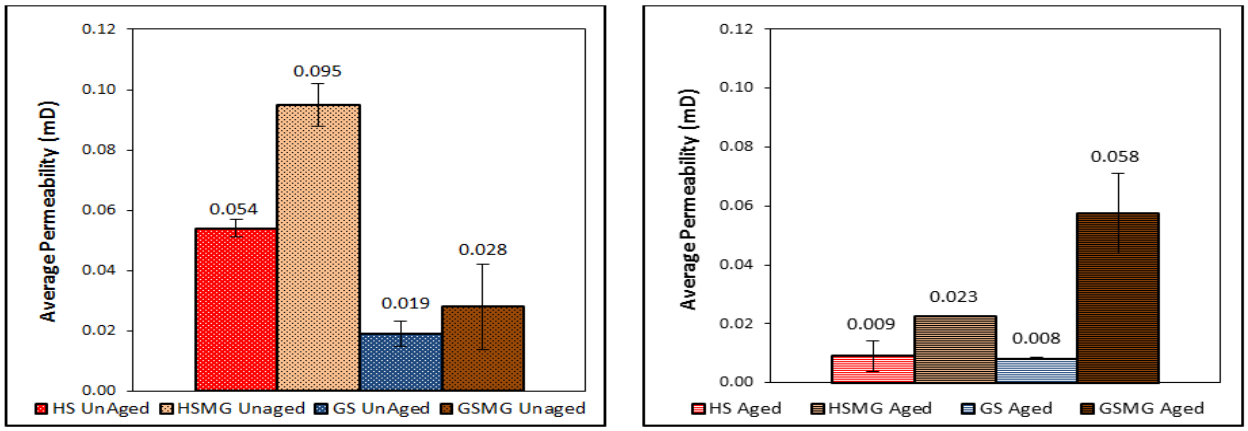

(a) (b)

Fig. 2.167: Permeabilities of MGO-5 and baseline samples: a) Unaged; and b) aged at 350°F, 9000 psi and 40% CO_2

In order to verify the penetration of CO_2 in the MGO-5 samples, FTIR experiments were carried out by taking samples from inner, middle and outer zones of aged HS and HSMG samples. Summarized FTIR spectrum charts are presented in **Fig. 2.168**. The charts present spectrum peaks of $Ca(OH)_2$, CSH, $CaCO_3$, MgO, $Mg(OH)_2$ and $MgCO_3$ at different locations (inner, middle and outer most zones) in the samples. FTIR results obtained from the inner zone indicate complete carbonation of CH and CSH in both the samples. The result from outer and middle zones showed complete conversion of MgO to $MgCO_3$ and $Mg(OH)_2$. No $MgCO_3$ was found in the inner zones of the samples. In HSMG samples, $Mg(OH)_2$, which precipitates in the pore space was present in inner and middle zones. The $Mg(OH)_2$ crystals help in decreasing porosity and permeability, and improve compressive and shear bond strength of the cement. The amount of $CaCO_3$ in HSMG samples is less than the baseline samples in the inner zone, indicating lesser carbonation of the matrix. It should be noted that, although peak for $MgCO_3$ can be identified at 880 cm^{-1}, all carbonates provided major peak around 1480 cm^{-1}. Hence, $CaCO_3$ and $MgCO_3$ cannot be clearly distinguished using the peaks at 1480 cm^{-1}. The middle and outer zones of MGO-5 showed higher content of $CaCO_3$ along with presence of $MgCO_3$.

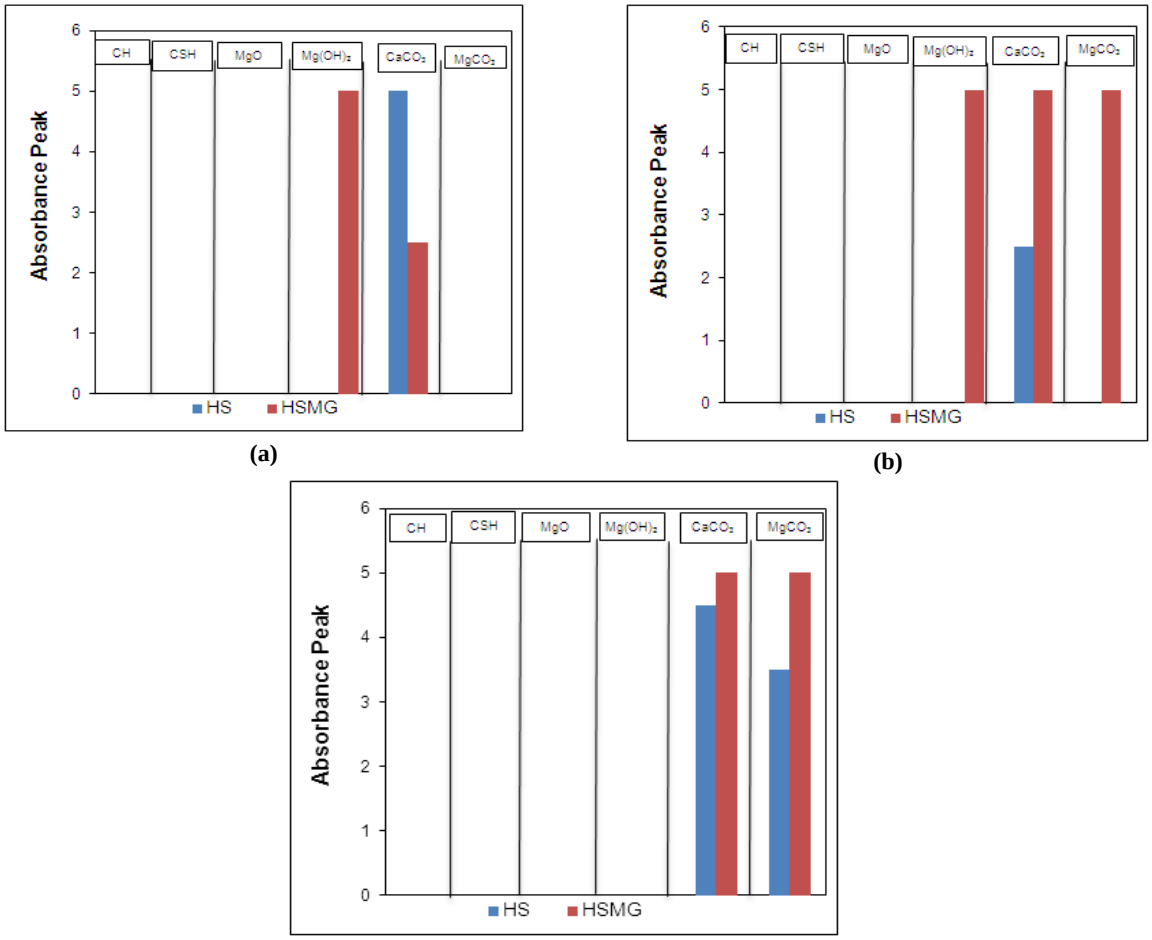

Fig. 2.168: FTIR peaks of MGO and baseline samples aged at 350°F and 9000 psi for 14 days in 2% brine saturated with 40% CO_2: a) inner most zone; b) middle zone; and c) outer most zone

Compressive strengths of MGO-5 and baseline cement samples are presented in **Fig. 2.169**. The strengths of all unaged samples were in the same range. After aging, increase in the compressive strength was observed for Class H based cores (HS and HSMG). The strength improvement is attributed to carbonation of the matrix and deposition of $CaCO_3$ crystals in the pore space. For MGO samples, this improvement is also due to matrix expansion by the formation of $Mg(OH)_2$ crystals from hydration of MgO. The matrix expansion results in pore shrinkage and strength improvement. In spite of this, the aging made Class G based cores (GS and GSMG) slightly weaker. The reduction in the strength of GS and GSMG samples is mainly attributable to leaching of the soluble products such as $Ca(HCO_3)_2$ and $Mg(HCO_3)_2$, which are formed after carbonation process. The GSMG cores exhibited more strength reduction than the baseline GS samples. This could be because of more leaching tendency of the GSMG samples as they contain higher MgO content than the baseline cement. As observed in the porosity and permeability results of GSMG, the increase in the respective values may lead to this decrease in the compressive strength. Hence, adding MgO did not improve performance of Class G cement under HPHT conditions.

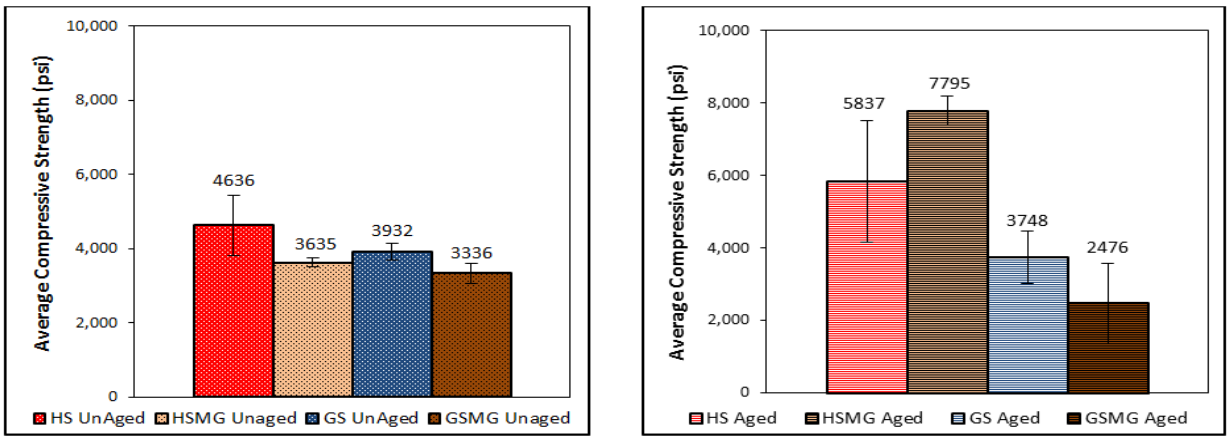

(a) (b)

Fig. 2.169: Compressive strength of MGO-5 and baseline samples: a) Unaged; and b) aged at 350°F, 9000 psi, 40% CO_2 for 14 days

Shear bond strengths of HSMG and baseline HS samples are presented in **Fig. 2.170**. For both aged and unaged cases, the SBS values do not vary significantly with the types (i.e. HS or HSMG) of cement samples. However, substantial (four to five folds) increase in SBS is observed due to carbonation after aging the samples under CO_2 containing environment. More importantly, the aged HSMG samples showed slightly higher SBS than the baseline samples, even though their unaged SBS values were lower than those of the baseline samples. The result demonstrated the benefits of adding MgO in improving performance of Class H cement.

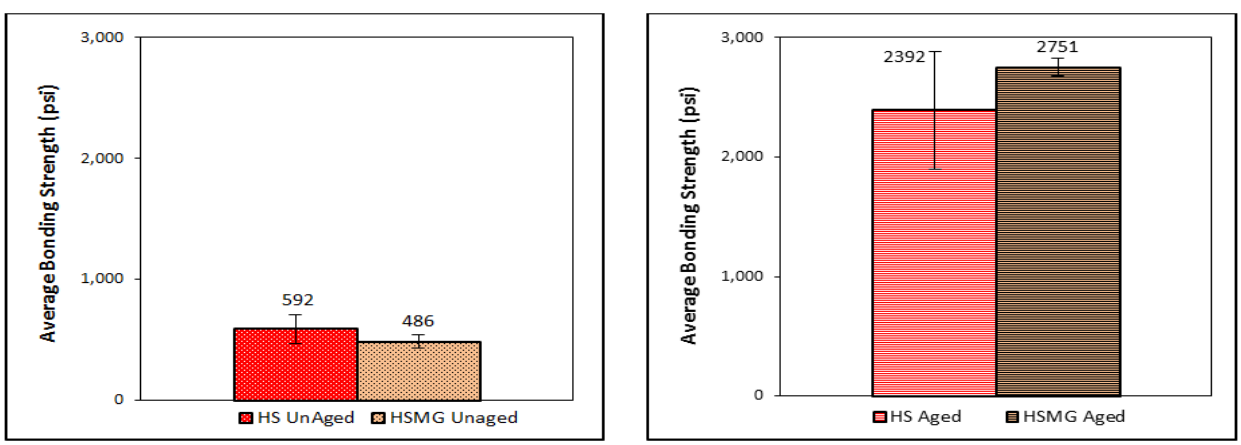

(a) (b)

Fig. 2.170: SBS of MGO-5 and baseline samples: a) Unaged; and b) aged at 350°F, 9000 psi, 40% CO_2 for 14 days

Addition of 5% BWOC of MgO to the cement has been effective in preventing acid attack according to the experimental results. Although HSMG showed good performance at 9000 psi and 350°F, performance of Class G based MGO cement (GSMG) was comparable with the baseline cement. Such result with Class G cement was only observed at 9000 psi. High-pressure may have caused breaking of the $Mg(OH)_2$ crystals or the matrix.

2.4.2.4. Performance of Other Additive Cement Formulations

Additive cement formulations that were selected from the initial screening were tested again for their performance in HPHT acidic environment. The cores were prepared and aged in a high-pressure autoclave. During experiment, all the aged cores were completely immersed in 2% NaCl solution (brine) saturated with methane gas containing CO_2 and H_2S. After aging, physical properties (porosity, permeability, compressive and bond strengths) of the cores were measured and compared with properties of unaged cores to quantify the degree of degradation. In addition, FTIR mineralogy, SEM, EDX and XRD analyses were performed to assess the degradation of additive cements.

Microsilica Cement

Three HPHT experiments were conducted with microsilica based cements (MS-10). The aging conditions of these experiments are presented in **Table 2.41**. Baseline samples were also aged simultaneously under similar conditions; hence, the parallel HS and GS batches mentioned for each condition in the table refers to the baseline samples, which were in the aging cell along with corresponding additive samples.

Table 2.41: Aging conditions for MS-10 samples

Experiment No.	Microsilica Batches	Temp. (°F)	Pressure (psi)	CO2 Conc. (%)	Baseline Batch
21	Batch 008	225	3000	100	Batch 024
25	Batch 009	430	6000	10	Batch 028
26	Batch 010	430	6000	40	Batch 029

After aging, porosity, permeability, compressive and shear bond strengths tests were performed. In addition, FTIR analysis was conducted to assess the level of degradation occurring in the samples.

<u>Porosity and Permeability</u>

Figures 2.171 and **2.172** depict unaged and aged porosity and permeability (ϕ-k) of Class H based microsilica and baseline cements. The decrease in ϕ-k indicates carbonation in the matrix and the increase demonstrates leaching.

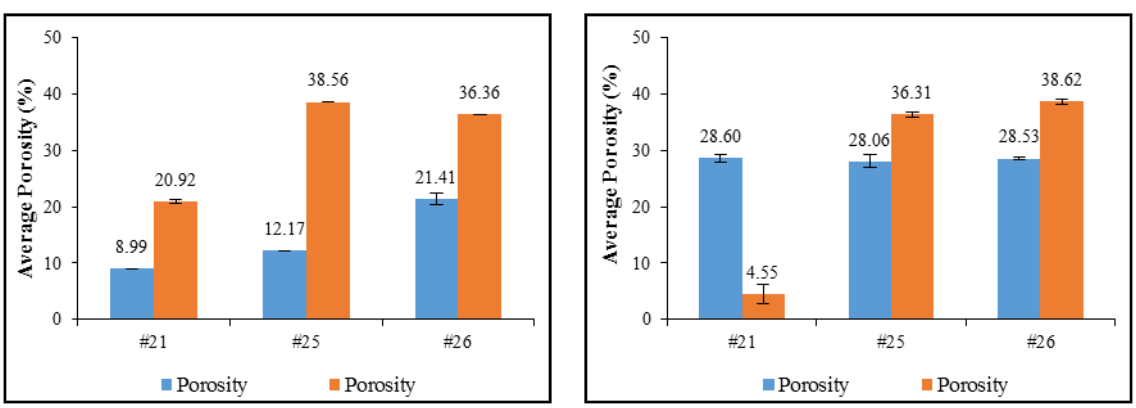

(a) (b)

Fig. 2.171: Porosity of aged (orange) and unaged (blue) Class H based cores: a) HSMS; and b) HS

At temperature 225°F and 100% CO_2 concentration, ϕ-k of baseline samples increased due to carbonation (Experiment #21). At higher temperature (430°F), significant leaching occurred and ϕ-k of the samples increased. It can be deduced that excessive temperature (430°F) leads to rapid diffusion of ions form the matrix, causing major leaching.

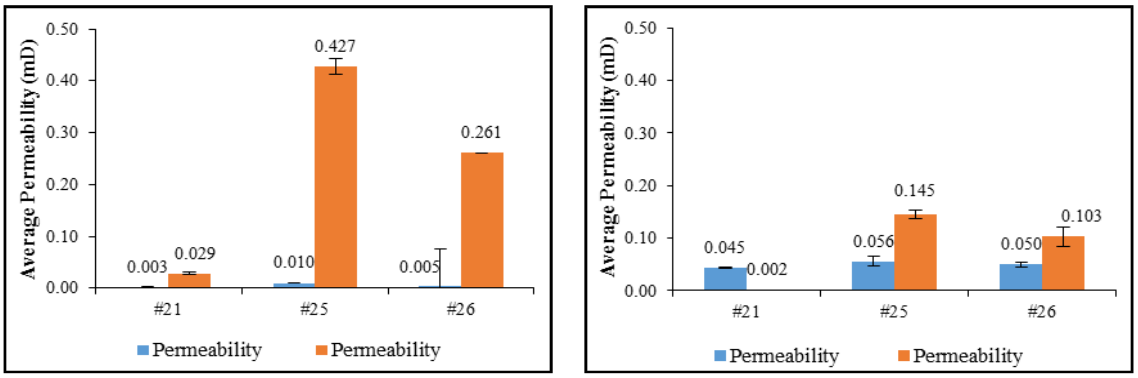

(a) (b)

Fig. 2.172: Permeability of aged (orange) and unaged (blue) Class H based cores: a) HSMS; and b) HS

The microsilica samples indicated a consistent increase in ϕ-k irrespective of the temperature. The level of increase was significantly higher for microsilica samples than the baseline. Such high ϕ-k increase is detrimental to the integrity of the cement matrix. One possible reason for the huge increment in the ϕ-k of microsilica could be incomplete pozzolanic reaction occurring at higher temperature. Pozzolanic reactions are exothermic; and hence, they tend to slow down at higher temperatures (Siddique and Khan 2011). The incomplete pozzolanic reaction results in poor unconsolidated CSH, which is formed resulting from the interaction of microsilica and CH. Due to continuous carbonation and leaching, the matrix resulted in the partially carbonated and weaker matrix.

Results of Class G based microsilica and baseline samples indicate almost similar trends as the Class H. Increases in the ϕ-k values of microsilica samples were observed in all the three experiments (**Figs. 2.173** and **2.174**). Large permeability increment, which makes the cement susceptible to acid penetration, was considerably higher for microsilica samples as compared to baseline cement.

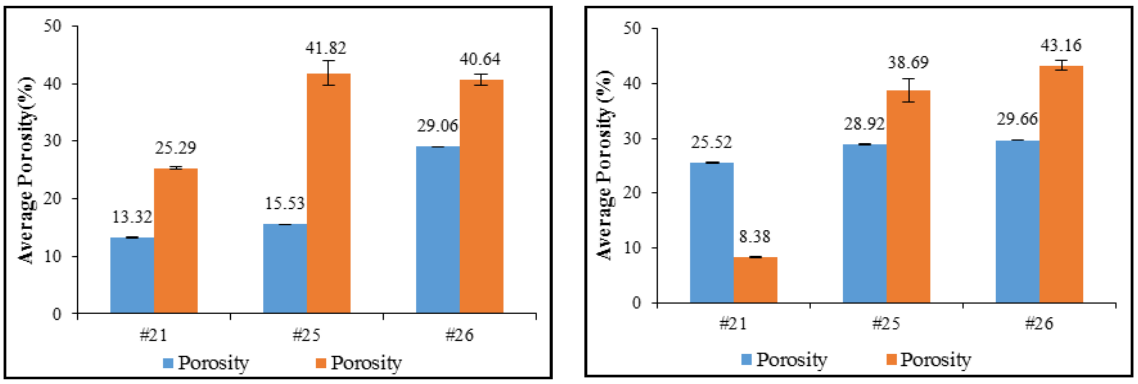

(a) (b)

Fig. 2.173: Porosity of aged (orange) and unaged (blue) Class G based cores: a) GSMS; and b) GS

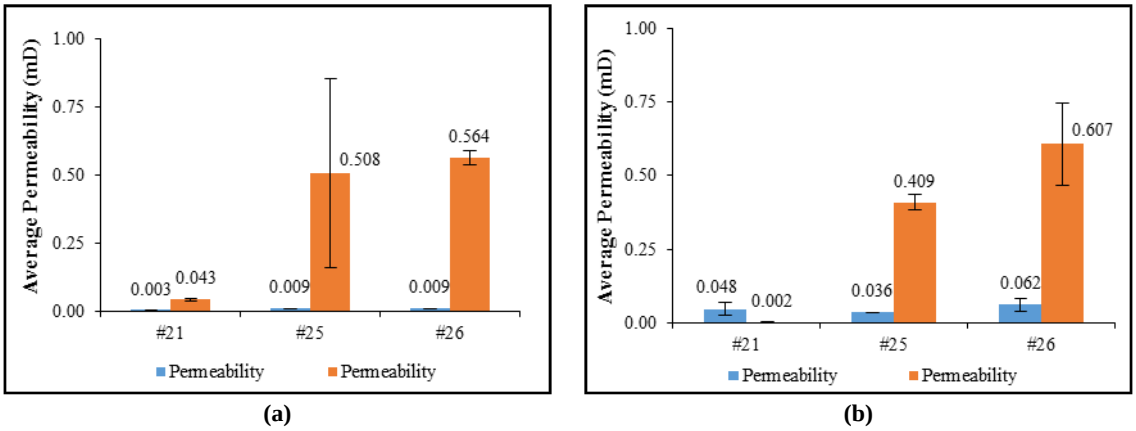

(a) (b)

Fig. 2.174: Permeability of aged (orange) and unaged (blue) Class G based cores: a) GSMS; and b) GS

Compressive Strength

Figures 2.175 and **2.176** present compressive strength of microsilica and baseline samples (aged and unaged) for Class H and Class G, respectively. Baseline samples consistently showed increased strength after aging, which suggest carbonation of the matrix. At 225°F and 100% CO_2 (Experiment #21), microsilica samples indicated slight carbonation. At 430°F with 10% CO_2 (Experiment #25), HSMS samples exhibited a slight increase in the strength, while the GSMS cores showed a small decrease. Unaged microsilica samples displayed significant variation in strength. This indicates that compressive strength of microsilica samples are very sensitive to other factors that have minor influence on mechanical properties of conventional cements (baseline).

At 430°F, increasing the CO_2 concentration from 10 to 40% (Experiment #26), the matrix of HSMS became extremely weak. Compressive strength measurements of aged GSMS samples demonstrated considerable scattering, which can indicate inconsistency in the integrity of the matrix due to severe degradation. Few microsilica samples also showed cracks after aging and were eliminated from the test. This suggests formation of highly permeable and weak matrix of microsilica cement when aged at high temperature (430°F) and increased CO_2 concentration (40%).

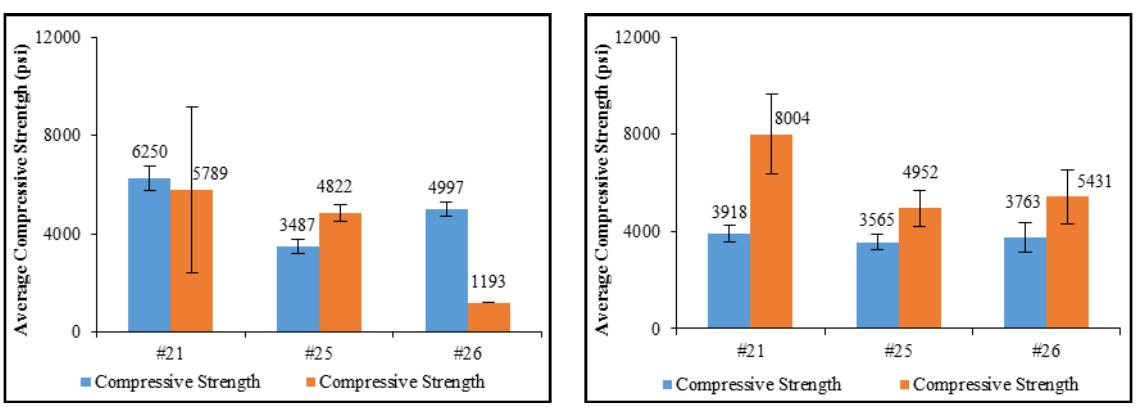

(a) (b)

Fig. 2.175: Compressive strength of aged (orange) and unaged (blue) Class H based cores: a) HSMS; and b) HS

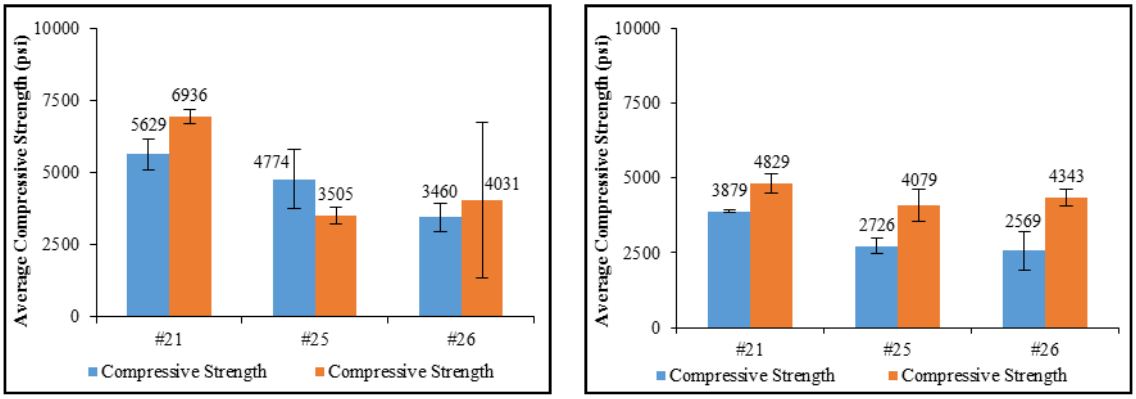

(a) (b)

Fig. 2.176: Compressive strength of aged (orange) and unaged (blue) Class G based cores: a) GSMS; and b) GS

Shear Bond Strength

The shear bond strength (SBS) of microsilica and baseline samples (**Fig. 2.177**) increased after aging. For microsilica samples, the increase was minimal at 430°F and 10% CO_2 (Experiment #25). However, this particular test showed the highest measurement scattering for unaged microsilica samples. In addition, the SBS of aged microsilica samples was the lowest one, which may indicate leaching of carbonated zone of the samples. In other words, the samples might have carbonated and leached out at the same time, maintaining SBS value approximately constant. This can be attributed to incomplete pozzolanic reactions as mentioned previously. In general, the microsilica samples displayed similar performance as the baseline samples.

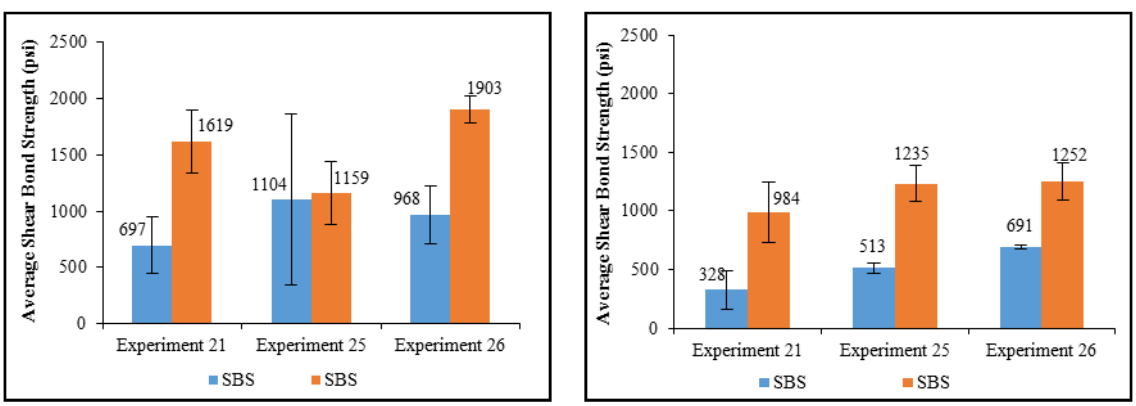

(a) (b)

Fig. 2.177: SBS of aged (orange) and unaged (blue) Class H based cores: a) HSMS; and b) HS

FTIR Analysis

In order to investigate the level of degradation, FTIR analysis was conducted on samples used to measure ϕ-k. The level of degradation was evaluated by monitoring major binding components of the cement (CH and CSH) and the main product of the carbonation process ($CaCO_3$). To perform the FTIR

tests, microsilica and baseline cores were first dried and then cut transversely. Three zones in the cylindrical cement cores were identified as outermost, middle and innermost zones (**Fig. 2.178**). Small amount of representative cement sample was cut from each zone and finely grinded. The amounts of calcium carbonate and calcium hydroxide (CH) found in these zones indicate the level of carbonation occurring in each zone.

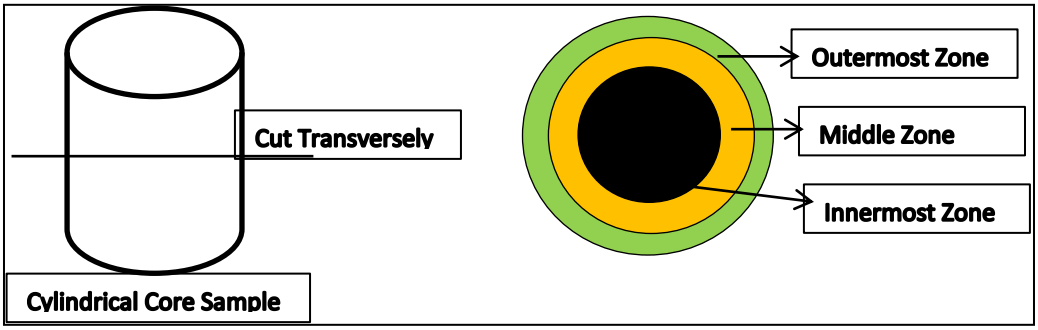

Fig. 2.178: Schematic of a cylindrical samples and zones selected in the cross section

Inner Zone: The inner zone is expected to be the least degraded zone, as it is at the center of the core and farthest away from the bulk fluid. Microsilica (HSMS) and baseline (HS) samples exhibited (**Fig. 2.179**) similar mineralogy after aging in Experiment #21 and 25. Results of the FTIR analysis show the presence of substantial amount of CSH, which may indicate preserved matrix. However, in Experiment #26, which was conducted at 430°F and 40% CO_2, the HSMS samples were highly degraded according to permeability and compressive strength measurements. The presence of CH and CSH in the matrix could be attributed to incomplete pozzolanic reaction. Moreover, higher $CaCO_3$ content as compared to HS signifies a highly carbonated matrix. Even though, the contents of CH and CSH in microsilica cement were higher than those of the baseline HS samples, microsilica cement samples were more carbonated than the baseline samples.

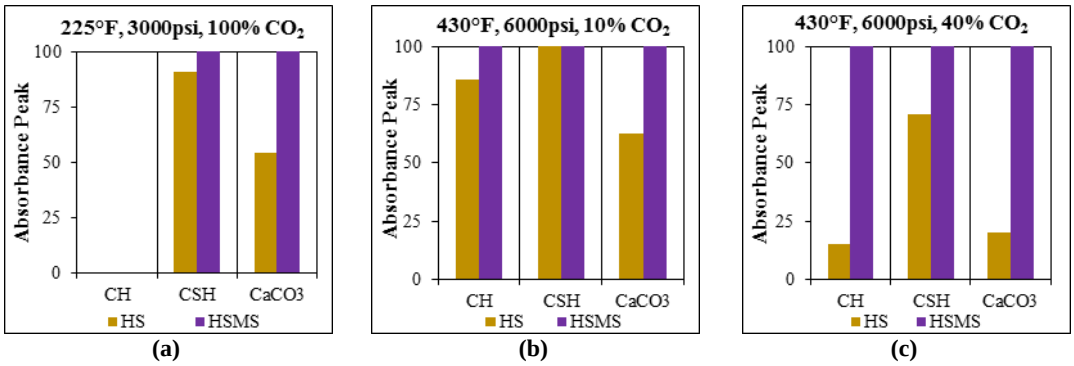

Fig. 2.179: FTIR results of inner zones of HSMS and HS samples aged at different conditions: a) Exp. 21; b) Exp. 25; and c) Exp. 26

Middle Zone: The middle zone showed greater amount of carbonation being closer to the bulk fluid. Microsilica samples displayed higher or similar content of $CaCO_3$ as compared to the baseline samples in

all the experiments (**Fig. 2.180**). On the other hand, their CH and CSH contents were almost similar or less than those of the baseline samples. The microsilica did show better resistance against acid attack than the baseline samples.

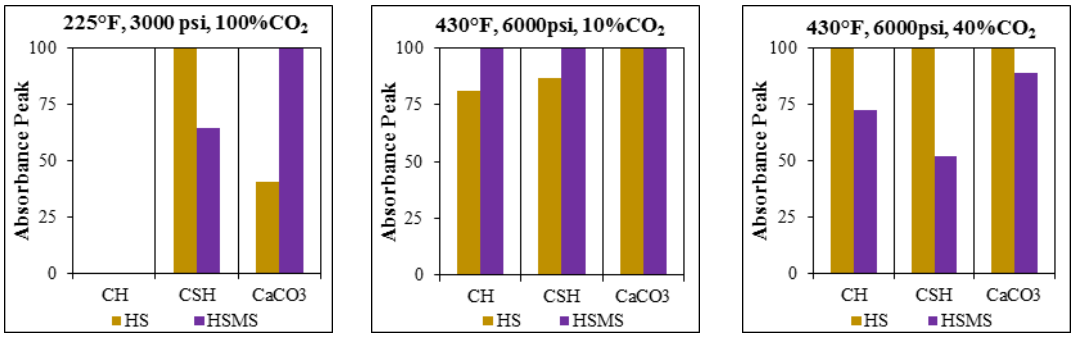

Fig. 2.180: FTIR results of middle zones of HSMS and HS samples aged at different conditions: a) Exp. 21; b) Exp. 25; and c) Exp. 26

The outer zone is the most exposed part of the sample. The zone is selected for evaluation since usually it shows substantial degradation. The outer zones of both microsilica and baseline samples demonstrated significant carbonation of the binding materials (**Fig. 2.181)**. However, when subjected to 430°F and 40% CO_2 (Experiment #26) the baseline samples showed unanticipated result by preserving CH and CSH in the matrix. Although $CaCO_3$ was present in the samples, the presence of CH and CSH in the baseline HS samples indicates more degradation of microsilica samples than the baseline samples.

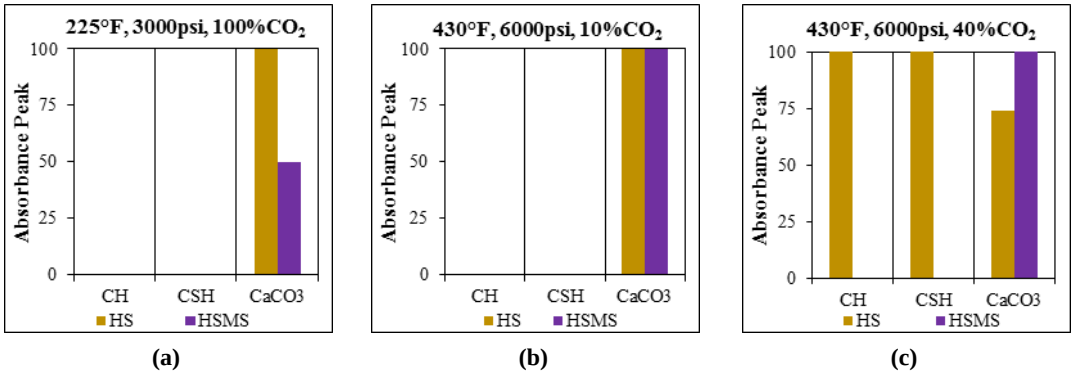

Fig. 2.181: FTIR results of middle zones of HSMS and HS samples aged at different conditions: a) Exp. 21; b) Exp. 25; and c) Exp. 26

<u>Summary</u>

The results of these three experiments show that the addition of microsilica does not improve the performance of the baseline cement. As result, porosity and permeability of microsilica samples were predominately increased after aging. This is an indication of severe leaching of the matrix that reduces the compressive strength. In agreement with this, compressive strength for Class H based microsilica (HSMS) samples cement showed significant reduction with increase in temperature. Class G based microsilica cement was stronger than the HSMS. Cracking of core samples inside the aging cell in

Experiment #26 (430°F and 40% CO_2), indicated weakening of the microsilica samples. The shear bond strength measurements of the additive cement exhibited almost similar performance as the baseline samples. Possible explanation of these results is attributed to partial pozzolanic reactions at 430°F.

The FTIR results showed slightly lower amount of CH and CSH components in the matrix of microsilica than the baseline samples. Evidently, the performance of microsilica cement against acid attack and carbonation is not better than the baseline samples. Moreover, the matrix damage through increased porosity and permeability renders the additive unsuitable for HPHT sour gas environment.

Latex Cement

Latex is often added to improve sealing properties of cement. The latex forms an emulsion with the cement. A similar experimental observation has been reported by Fuquan et al. (2006). The authors suggest the use of strong hydrophilic carboxyl group, such as formic acid or acetic acid, in order to stabilize the latex containing cement system at 200ºF or above.

Unaged latex cores exhibited higher permeability than the baseline samples (Section 2.4.2.4). In order to improve the performance of the cement styrene butadiene latex was substituted by SBR latex. However, the permeabilities of the SBR latex samples (HSLT and GSLT) were higher than those of baseline samples. In order to test if high permeability latex cement withstands acid attack, core samples with SBR latex were prepared and aged in 2% brine at 350°F and 6000 psi using 40% CO_2 gas. The composition of the slurry is presented in Table 2.22.

Porosity and Permeability

The porosity and permeability measurements obtained from latex and baseline cement samples are presented in **Fig. 2.182**. Porosity and permeability of unaged samples of latex cement were almost comparable with those of baseline samples. Except HS samples, all other samples showed slight reduction in porosity after aging. This result is expected, since carbonation reduces the pore space causing reduction in porosity and permeability. Consistent with this observation, the permeability of all the samples reduced after aging due to carbonation. The reduction observed in the GSLT sample was the least but still significant.

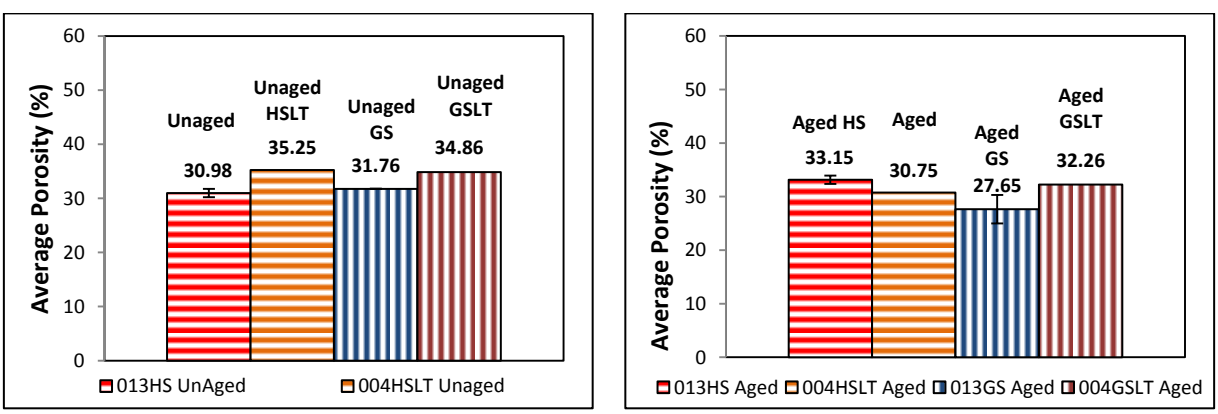

(a) (b)

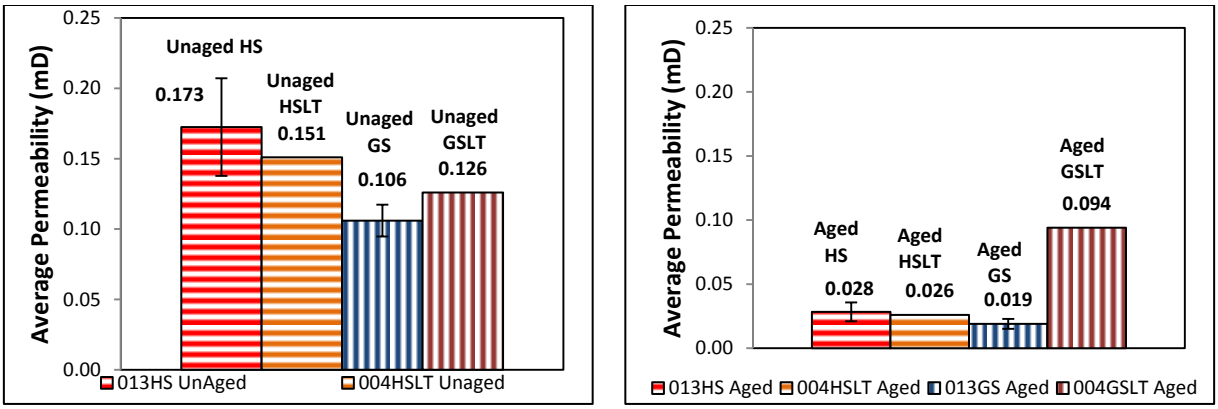

(c) (d)

Fig. 2.182: Porosity and permeability of latex and baseline cores (aged at 350°F with 40% CO_2)

Degradation Depth

Aged latex cement samples displayed a clear degraded zone (**Fig. 2.183**) when they were transversely cut. It was evidently observed that the degraded depths of latex cements were higher than those of the baseline samples. This confirms that even though the measured permeability was almost same for the latex and HS samples, the latex samples exhibited deeper penetration and degradation. The average degraded depth measurements are presented in **Table 2.42**. The increased depth values of latex samples indicate vulnerability towards carbonation.

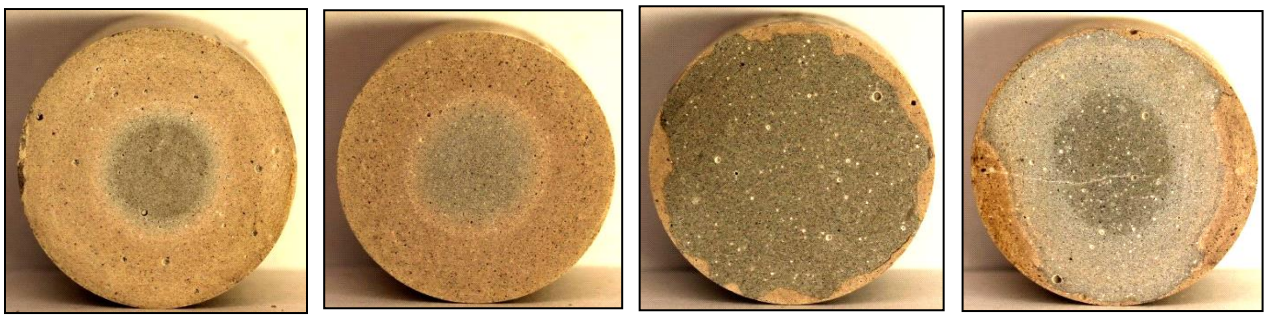

(a) (b) (c) (d)

Fig. 2.183: Middle cross sections of cores aged at 350°F with 40% CO_2 gas: a) GSLT; b) HSLT; c) GS; and d) HS

Table 2.42: Degradation depth of baseline and latex-based cements

Core #	Carbonated Depth Average (in.)	Std. Dev.
004HSLT	0.310	0.006
004GSLT	0.342	0.017
013HS	0.280	0.031
013GS	0.053	0.019

Compressive Strength

Compressive strengths of aged and unaged latex and baseline cement samples are presented in **Fig.**

2.184. Compressive strength of the latex samples increased more than the baseline samples. This is due to higher level of carbonation in the latex samples as compared to the baseline. High level of carbonation confirms poor performance of latex as a cement additive for acid attack reduction.

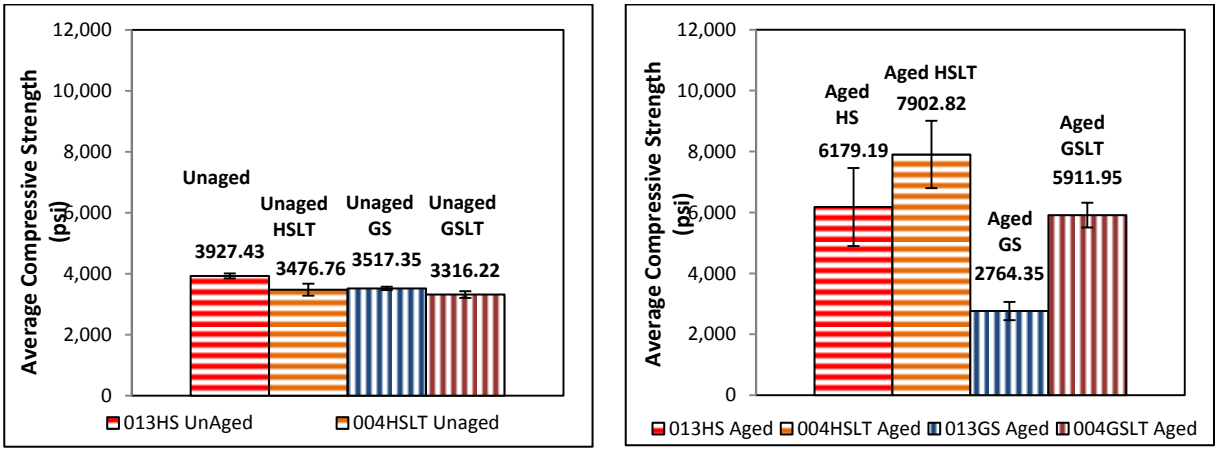

(a) (b)

Fig. 2.184: Compressive strength of baseline and latex-based cements aged at 350°F with 40% CO_2

<u>Shear Bond Strength</u>

Shear bond strengths of latex and baseline cements are presented in **Fig. 2.185**. Both samples show similar shear bond strength before and after aging. Although the addition of latex is expected to improve shear-bonding strength of the cement, results indicate minimal effect of latex on the bond strength. Moreover, the latex samples demonstrated the same level of bond strength improvement that suggests similar level of carbonation.

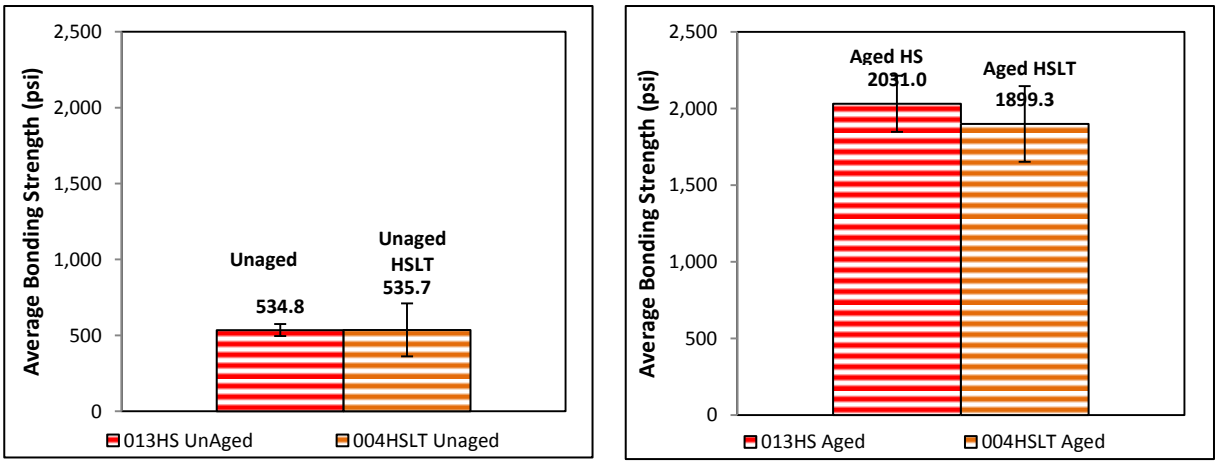

(a) (b)

Fig. 2.185: Shear bond strength of latex and baseline cements aged at 350°F with 40% CO_2

FTIR Analysis

In order to evaluate the carbonation level in the latex samples, the FTIR tests were conducted on samples taken from the inner, middle and outer zones of the latex and baseline cement cores. The results (**Fig. 2.186**) indicate poor performance of the latex cement in resisting the acid attack. In the latex cement core, carbonation occurred in outermost and middle zones while in the baseline cement, it occurred only in the outermost zone. Middle zone of aged latex samples had no traces of CH or CSH. Nevertheless, they displayed high content of CO_3^{2-} bond as compared to baseline samples. This confirms that latex did not prevent acid penetration. Instead, it reduced the capability of the cement to withstand acidic environment. Results of the outermost zone showed the same level of degradation in both cases. In addition, the FTIR obtained from the inner most zone of the matrix indicates that the amount of uncarbonated CH and CSH is same in both latex and HS samples. Hence, CO_2 was not able to penetrate completely inside both the samples within two weeks of aging.

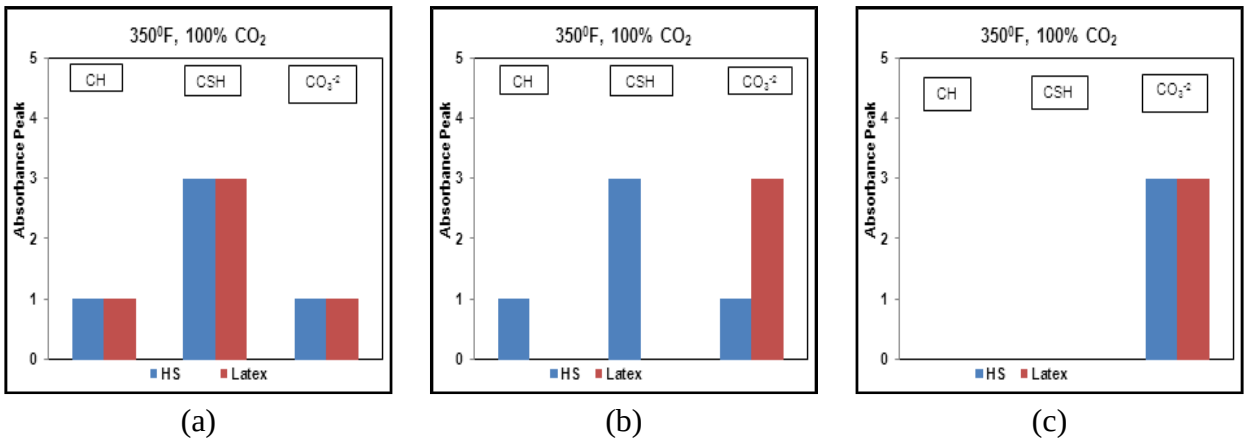

Fig. 2.186: Summarized FTIR of latex and baseline cements: a) innermost; b) middle; and c) outermost zones

Summary

Latex and baseline cores did not show significant porosity change after aging; however, their permeability deceased considerably except for GSLT, which exhibited minimal reduction. Moreover, latex had higher degradation depth compared to the baseline cement. Particularly, GSLT was severely penetrated as compared to GS. Furthermore, latex cores showed higher compressive strength than the baseline cement, which suggests incidence of intense carbonation. SBS of both samples were very similar. FTIR analysis results suggest the preservation of CH and CSH in the middle zone of the baseline core while the additive sample completely lost its CH and CSH content. In general, the performance of baseline cement is better than the latex cement under HPHT acidic environment. Latex is not suitable cement additive for controlling acid attack.

Latex-Microsilica Cement

The slurry compositions and properties of latex-microsilica cement (LTMS) are presented in Section 2.4.2.4. The aging conditions for LTMS samples are presented in **Table 2.43**. The first batch of latex-

microsilica cement cores were aged in 2% brine for 14 days under HPHT conditions and then tested. The samples exhibited the presence of CSH component after aging, indicating their resistance against acid attack.

Table 2.43: Aging conditions for LTMS samples

Exp. No.	LTMS Batch	Temp. (°F)	Pressure (psi)	CO_2 Conc. (%)	Baseline Batch
24	Batch 002	225	9000	10	Batch 027
27	Batch 003	430	6000	100	Batch 030
28	Batch 004	430	3000	100	Batch 031

The core property measurements (porosity, permeability, compressive strength, shear bond strength, and FTIR analysis) were conducted and the results are presented here.

Porosity and Permeability

Figure 2.187 depicts porosity of Class H cement based LTMS and baseline samples. The porosity of the baseline samples reduced 43% due to carbonation at 225°F. The LTMS samples on the other hand retained their original porosity, which indicates better performance. The permeability for baseline samples at similar conditions also showed almost 90% reduction while that of HSLM samples increased 77% (**Fig. 2.188**). This increment in permeability contradicts the consistent porosity measurements. When subjected to 430°F and 100% CO_2 (Experiment #27 and 28) at varying pressures, a significant increases in the porosity and permeability were observed with LTMS and baseline samples again. Such a porous and permeable matrix may be detrimental for the integrity of the cement. It is important to note that even with addition of latex and microsilica, the additive samples were not performing better than baseline samples.

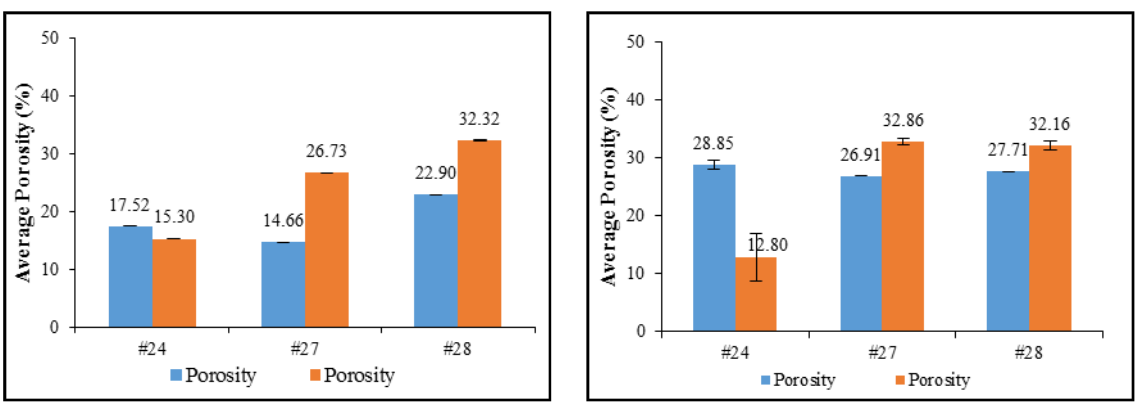

(a) (b)

Fig. 2.187: Porosity of aged (orange) and unaged (blue) samples: a) HSLM; and b) HS

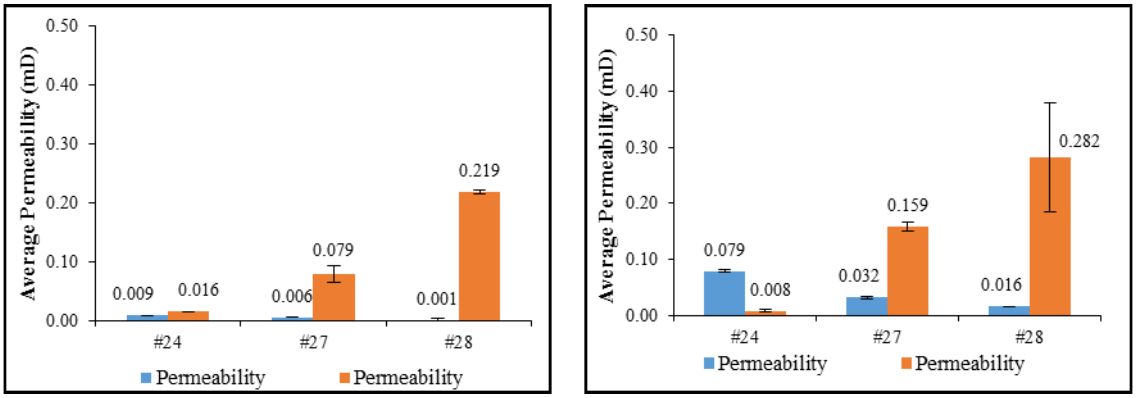

(a) (b)

Fig. 2.188: Permeability of aged (orange) and unaged (blue) samples: a) HSLM; and b) HS

Class G cement also showed similar trends of porosity and permeability changes as Class H samples (**Figs. 2.189** and **2.190**). The increment in permeability of GSLM samples, although significantly high, was not as excessive as that of HSLM samples.

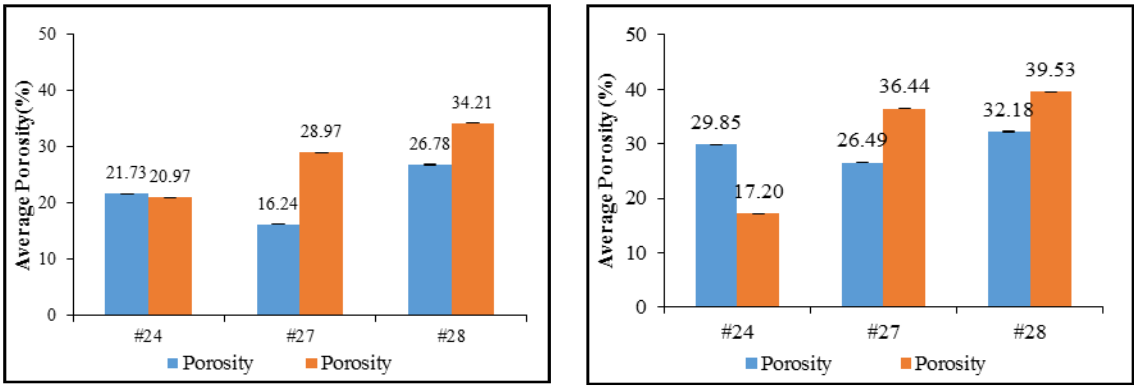

(a) (b)

Fig. 2.189: Porosity of aged (orange) and unaged (blue) samples: a) GSLM; and b) GS

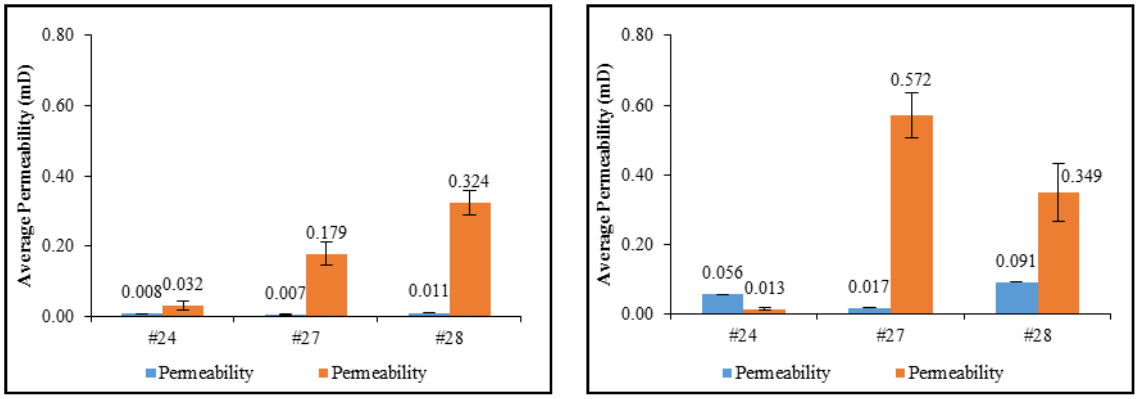

(a) (b)

Fig. 2.190: Permeability of aged (orange) and unaged (blue) samples: a) GSLM; and b) GS

Compressive Strength

At high temperature (Experiment #27 and 28), compressive strength of all the samples (additive and baseline) were consistent with porosity and permeability (ϕ-k) results (**Figs. 2.191** and **2.192**). Compressive strength increased after aging. However, at 225°F, all the samples show a different trend between compressive strength and ϕ-k. Results do not demonstrate the benefits of the additive in reducing degradation. The latex-microsilica samples behave in similar way as the baseline samples.

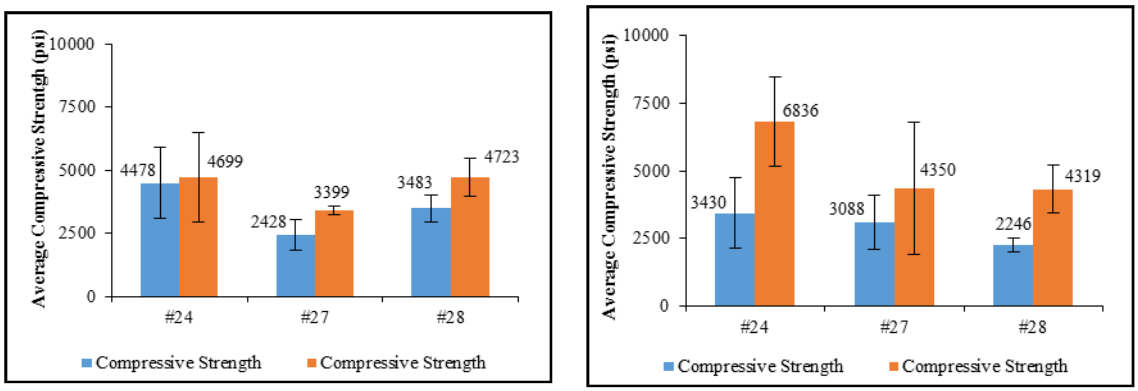

(a) (b)

Fig. 2,191: Compressive strength of aged (orange) and unaged (blue) samples: a) HSLM; and b) HS

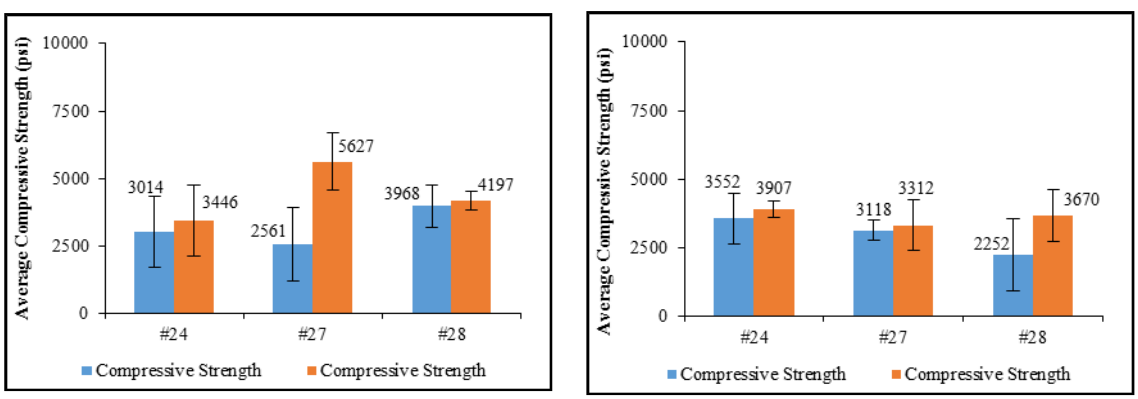

(a) (b)

Fig. 2.192: Compressive strength of aged (orange) and unaged (blue) samples: a) GSLM; and b) GS

Shear Bond Strength

Shear bond strength trends of LTMS and baseline samples are similar (**Fig. 2.193**), except for Experiment #24, which was conducted at 225°F. Shear bond strength of LTMS samples predominately reduced after aging. Increase in SBS was observed in Experiment #27. This conveys that the additive slurry did not have better bonding or sealing performance than the baseline cement.

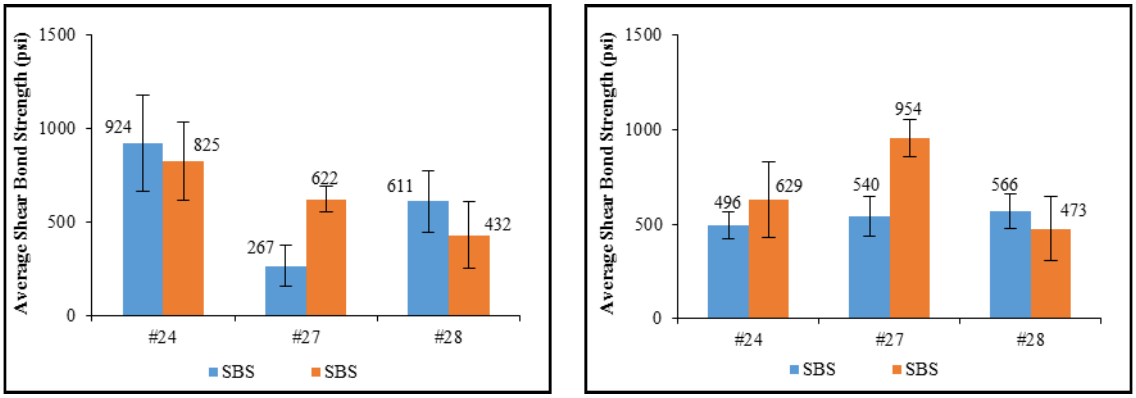

(a) (b)

Fig. 2.193: Average shear bond strength of aged (orange) and unaged (blue) samples: a) HSLM; and b) HS

FTIR Analysis

FTIR results of latex-microsilica and baseline samples are presented here. The minerals under focus are CH, CSH and $CaCO_3$. Similar to FTIR analysis of microsilica (Section 2.4.1.4), three zones (inner, middle, and outmost zones) on the LTMS and baseline cores were considered for the analysis.

Inner Zone: FTIR results of the samples from the inner zones of LTMS and baseline cores are depicted in **Fig. 2.194**. Aging at lower temperature (225°F) led to heavy leaching of baseline samples (Experiment #24). Although CH was completely carbonated in both LTMS and baseline samples, the former have retained certain amount of CSH in the matrix. The level of $CaCO_3$ was also higher for the LTMS samples indicating substantial carbonation. When aged at high temperature (430°F), the baseline samples were able to preserve the CH and CSH components. At higher pressure (6000 psi), the LTMS matrix showed complete loss of CH and CSH components (Experiment #27) while at low pressure (3000 psi), the least damage to the matrix was observed (Experiment #28). This observation is not consistent with permeability of LTMS samples that show huge increase after aging. The inconsistence could be as a result of partial pozzolanic reactions occurring at higher temperature (430°F). Other zones of the samples also need to be analyzed in order to better understand the degradation process.

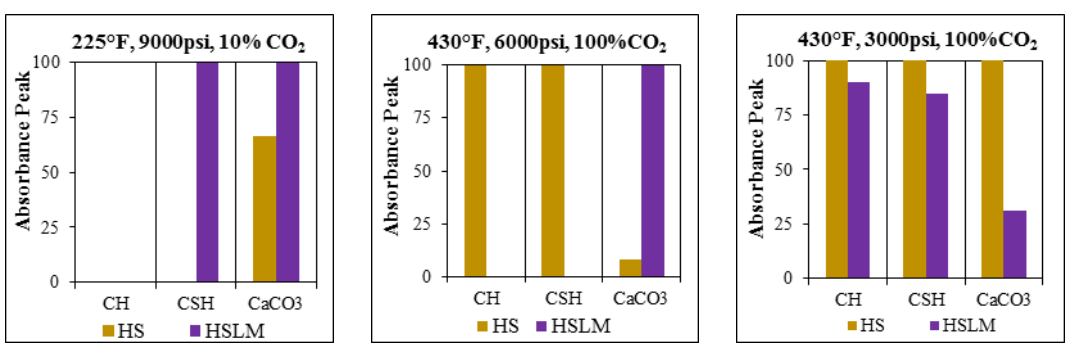

(a) (b) (c)

Fig. 2.194: FTIR results of inner zones of LTMS and baseline HS samples aged at different conditions: a) Exp. 24; b) Exp. 27; and c) Exp. 28

Middle Zone: FTIR results of the middle zones of LTMS and baseline cores are displayed in **Fig. 2.195**. The baseline cores preserved CH and CSH components after aging at 430°F while LTMS was unable to protect these components. However, at 225°F, LTMS cores were able to preserve the CSH component in the inner zone. This suggests that although LTMS samples performed better at lower temperature (225°F), they did not resist acid attack at high temperature (430°F) because increased temperature enhances CO_2 dissolution and carbonation of CH and CSH.

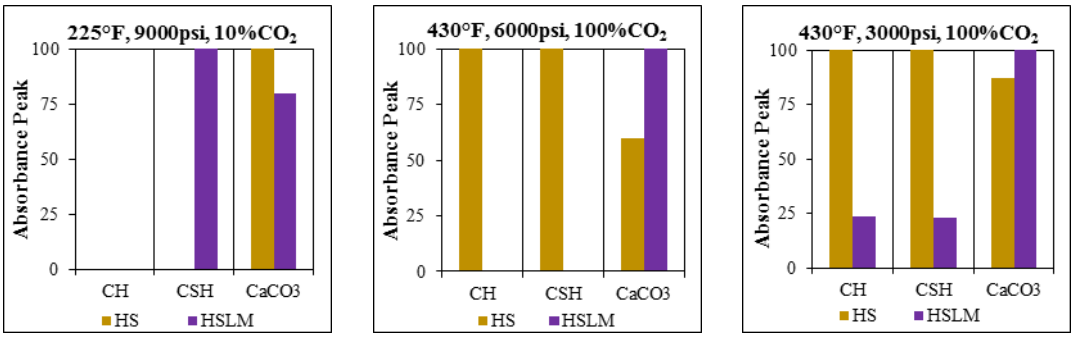

(a) (b) (c)

Fig. 2.195: FTIR results (middle zone) of LTMS and baseline HS samples aged at different conditions: a) Exp. 24; b) Exp. 27; and c) Exp. 28

Outer Zone: FTIR results of the outer zones of LTMS and baseline cores are shown in **Fig. 2.196**. Since this zone is the most exposed part of the cores, severe degradation is expected. In two aging experiments (Experiment #24 and #28), the binding components (CH and CSH) were completely consumed by the carbonation process. However, in Experiment #27, the baseline samples preserved their CH and CSH components at 6000 psi, 430°F and 100% CO_2 while LTMS completely lost these components. This indicates poor performance of the additive as compared to the baseline samples.

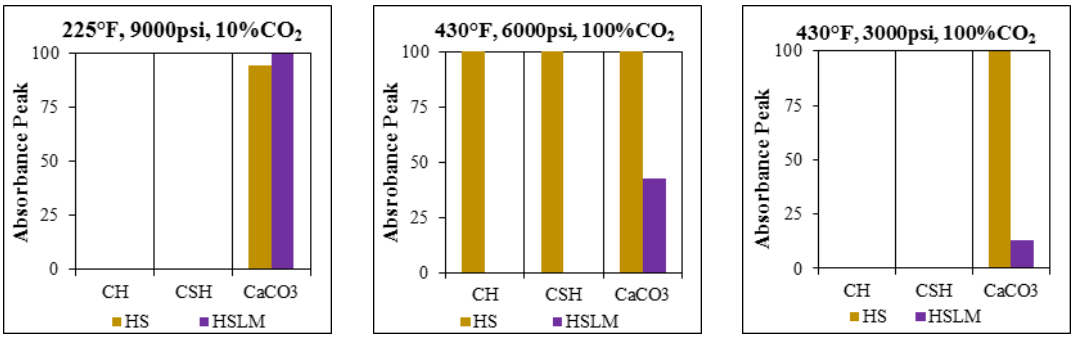

(a) (b) (c)

Fig. 2.196: FTIR results (outer zone) of LTMS and baseline HS samples aged at different conditions: a) Exp. 24; b) Exp. 27; and c) Exp. 28

<u>Summary</u>

Similar to the baseline cement, the LTMS cores showed substantial increase in the permeability and porosity after aging. For all the tests, the increase in permeability of LTMS cores was more than 72%, which shows major degradation in the matrix properties. The compressive strength of the additive cores

indicated similar performance as the baseline cores or indicated greater degree of carbonation. Although the FTIR results reveal presence of CH and CSH components in the inner most zone for HSLM cores, results from other zone show contradictory findings. In general, there is no noticeable difference between the performance of LTMS and baseline cement under HPHT acidic environment. The LTMS cores did not show better acid resistant than the baseline cores.

Cement with Fly Ash

Fly ash is commonly used additive in cementing application. It provides both economic and technical benefits. Class H fly ash was used in this investigation. The slurry properties and formulations are presented in Section 2.4.2.1. This was the first additive tested during the investigation. Experiments were performed varying aging duration, brine concentration and pressure. Test parameters for aging experiments of fly ash cement are summarized in **Table 2.44**. Six batch of fly ash samples were prepared and tested in brine (NaCl) saturated with 10% CO_2 containing method gas. Experiments were also conducted using 100% methane.

Table 2.44: Test parameters for aging experiments

Batch #	Temp. (°F)	Pressure (psi)	Partial Pressure %			Brine Conc. (%)	Aging Period (days)	Experiment #
			CH_4	CO_2	H_2S			
001	350	9000	100	0	0	9	6	1
002	350	6000	100	0	0	2	14 & 28	2
003	350	6000	100	0	0	2	14	
004	350	6000	90	10	0	2	6	3
005	350	6000	90	10	0	2	14 & 28	4
006	350	6000	90	10	0	2	14	

Porosity and Permeability

Figure 2.197 shows porosity and permeability of the samples before and after aging (2 and 4 weeks). The trends for baseline (HS and GS) samples are similar. Both porosity and permeability for these samples showed consistent trend. At the beginning, they displayed reduction, and then the trend reversed.

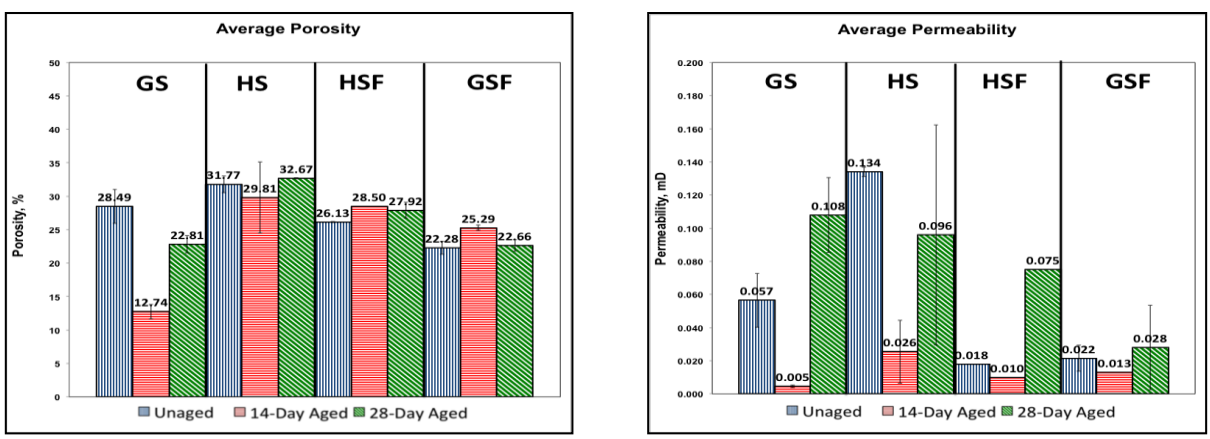

Fig. 2.197: Porosity and permeability of cement cores aged at 350°F (Experiment 4, Batch 005)

Fly ash cement sample (HSF and GSF) displayed a different trend. Porosity and permeability trends did not have consistent trend. However, the variation in porosity was minimal. After aging for two weeks their permeability decreased, and then it increased when the samples were aged for additional 2 weeks. In both GSF and HSF samples, porosity slightly reduced when the samples were aged for additional 2 weeks. The reason for this inconsistency between porosity and permeability trend could be the formation of micro cracks that do not increase the pore volume but increase the permeability by creating additional path for the fluid to flow and increase the connectivity of the pores. During the test, some of the fly ash cement cores exhibited brittleness and they were prone to cracking at low compressive loads. This resulted in unexpected failure of aged cores during the test and even during core handling. The cracking tendency can be related to internal weakening of cores due to high thermal stresses generated at high temperature (350°F).

Compressive Strength

Figure 2.198 summarizes compressive strength of samples aged in brine saturated with 10% CO_2 and 90% methane gas. Only limited numbers of cement cores containing fly ash were tested after aging since many of the samples were cracked and broken in the aging cell. Fly ash cement samples displayed considerable strength gain after aging for 2 weeks, and then reduction in strength was observed. The addition of fly ash did not limit the carbonation of the cement. The baseline samples demonstrated both improvement (Class H) and reduction (Class G) in strength with aging time. The strength reduction observed with Class G samples is mainly attributed to the leaching of cement by the carbonic acid. The compressive strength data indicated that the performance of baseline HS is better than the fly ash based cement samples. Compressive strength of HS samples was less affected by the acid attack.

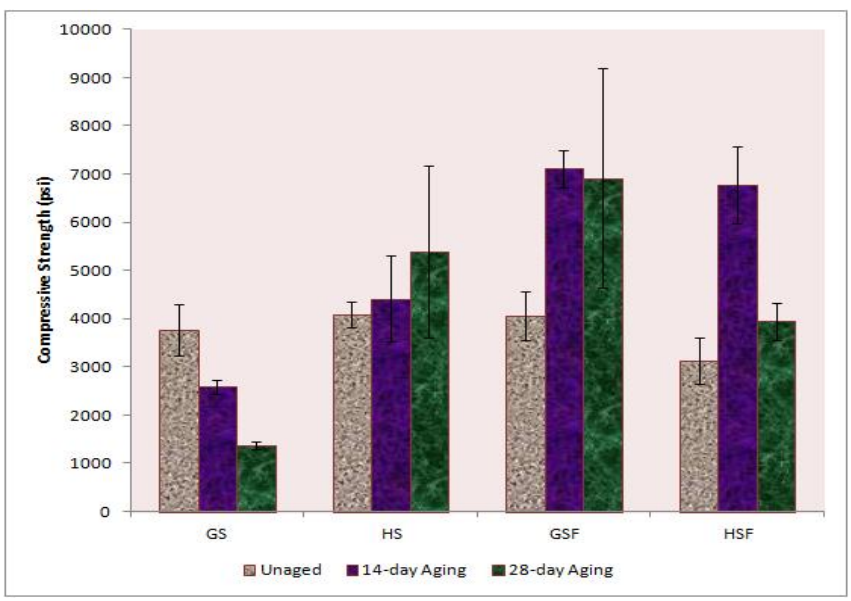

Fig. 2.198: Compressive strength of unaged and aged baseline and fly ash cement cores aged at 350ºF (Experiment 4, Batch 5)

Shear Bond Strength

Shear bonding strength of unaged and aged Class H cement samples with and without fly ash were measured. Before aging, samples with fly ash showed higher shear bonding strength (**Fig. 2.199**). However, after aging, the SBS of the samples with fly ash were considerably reduced due to acid attack. This behavior can be explained by low acid resistance of fly ash containing cement.

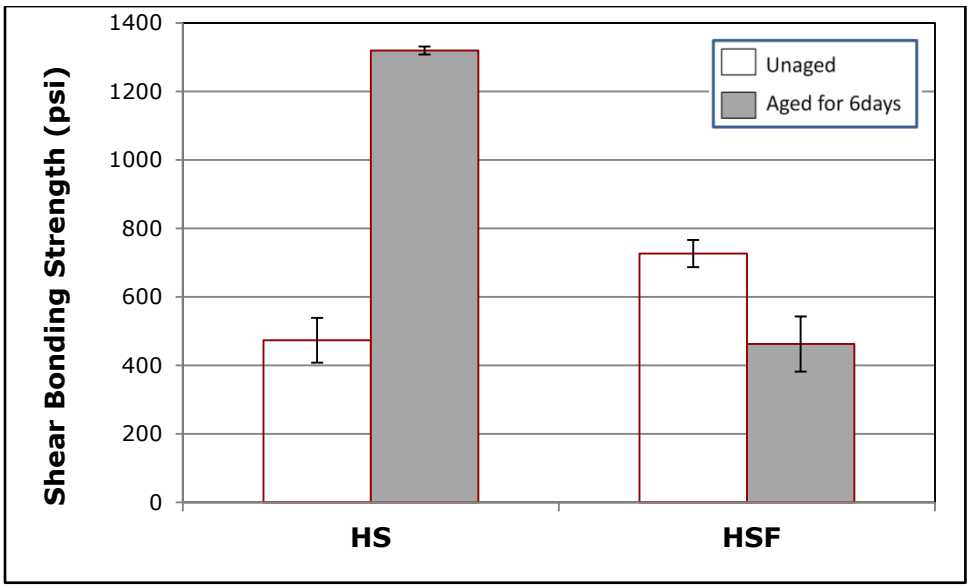

Fig. 2.199: Shear bond strengths of samples before and after 6 days of aging (Experiment #3)

Visual observation of the cement cores revealed that cores with fly ash were considerably attacked by carbonic acid. **Figure 2.200** shows the digital pictures of Class H cement with and without fly ash after 6 days of aging. Degradation depths for Class H and G samples with fly ash were approximately 2 mm. Phenolphthalein indicator was also applied to the samples to determine the degradation depth. Since $Ca(OH)_2$ content in the degraded zone is lower than the original content, the pH in degraded zone is expected to be lower than that of un-degraded part (sound zone) of the core. With Phenolphthalein indicator, pink color indicates higher pH values (more than 8.3). Figure 2.200a shows the Class H cement with fly ash after aging in brine saturated with methane gas containing 10% CO_2. Pink color at the center shows the sound zone of cement, which indicates higher pH (high alkalinity) due high concentration of calcium hydroxide. Degraded zone doesn't show a pink color because of low pH resulting from carbonation of calcium hydroxide.

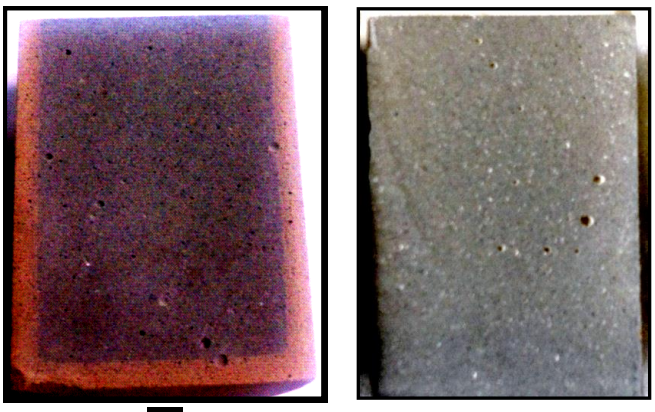

(a) (b)

Fig. 2.200: Class H cement after 6 days aging (Experiments # 3): a) with fly ash; and b) without fly ash

When fly ash samples were aged without the presence of CO_2 in the fluid system, their SBS increased. **Figure 2.201** presents shear bond strength of Class H cement with and without fly ash before and after 14 and 28 days of aging at 6000 psi of 100% CH_4 and 350°F. In this case, the aging increased the SBS of samples with fly ash. Therefore, acid attack is the key factor in reducing the shear bonding strength of fly ash containing samples.

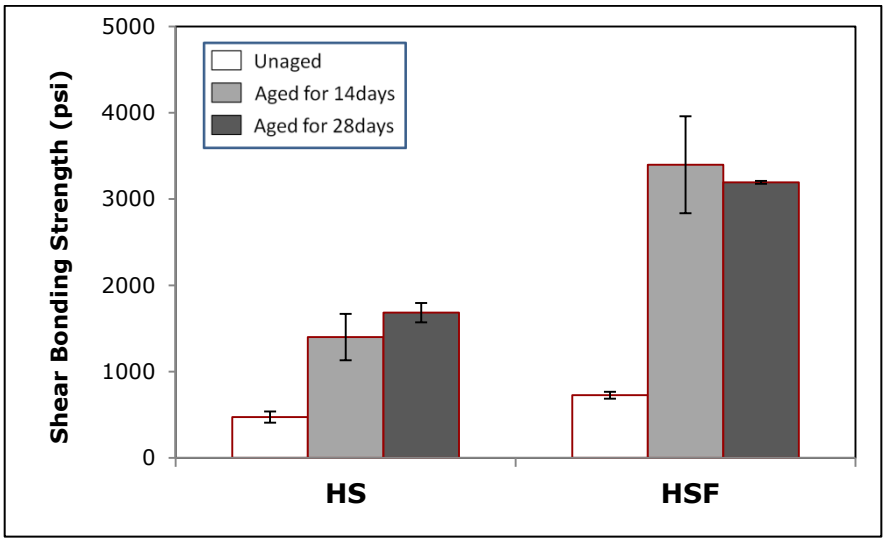

Fig. 2.201: Shear bond strength of unaged and aged samples (Experiment # 2)

Summary

All the measurements (porosity, permeability, compressive strength and SBS) of fly ash cement indicate its susceptibility to carbonic acid attack. Without carbonic acid, the SBS of fly ash cement increased after aging. However, when aged in acid environment, SBS substantially decreased.

Fly ash cement because of its low CH and CSH content, it is expected to have limited carbonation. Despite this, the compressive strength of fly ash cement increased more than the baseline cement, indicating greater carbonation of the matrix. Porosity and permeability measurements exhibited inconsistency that can be explained by crack formation in the cement during aging as the temperature increases. Even some samples were cracked and disintegrated during coring and after aging. In addition, degraded depth of fly ash samples was significantly higher than the baseline cement. Therefore, fly ash cement is not suitable for cementing HPHT wells producing carbon dioxide.

2.5. Modeling Cement Degradation

2.5.1. Overview

The major challenge in modeling cement degradation occurring in acidic environment is the involvement of different natural phenomena such as hydration, carbonation and leaching, which lead to change in important cement properties (porosity, permeability and strength). As the alteration in physical and mechanical properties takes place, the degradation process intensifies through further penetration of the aggressive fluid into the undamaged zone of the cement.

2.5.2. Model Assumptions

Modeling cement deterioration process is highly complex due to several controlling parameters and driving mechanisms. As a result, modeling assumptions are required to simplify the model to have adequate representation of cement degradation process. In this study, the following assumptions are made for the development of cement degradation model:

i. Hydration, carbonation and leaching are considered as major cement degradation mechanisms
ii. Bulk fluid is under static condition, hence no convective transport
iii. Degradation process is governed by reaction and diffusion
iv. Calcium leaching is solely responsible for the loss of cement integrity

2.5.3. Model Formulation

Figure 2.202 shows a simplified block diagram of cement degradation model. The key parameters to be predicted are degree of cement hydration, initial porosity of cured cement, saturated calcium concentration, penetration depth, new porosity and compressive strength.

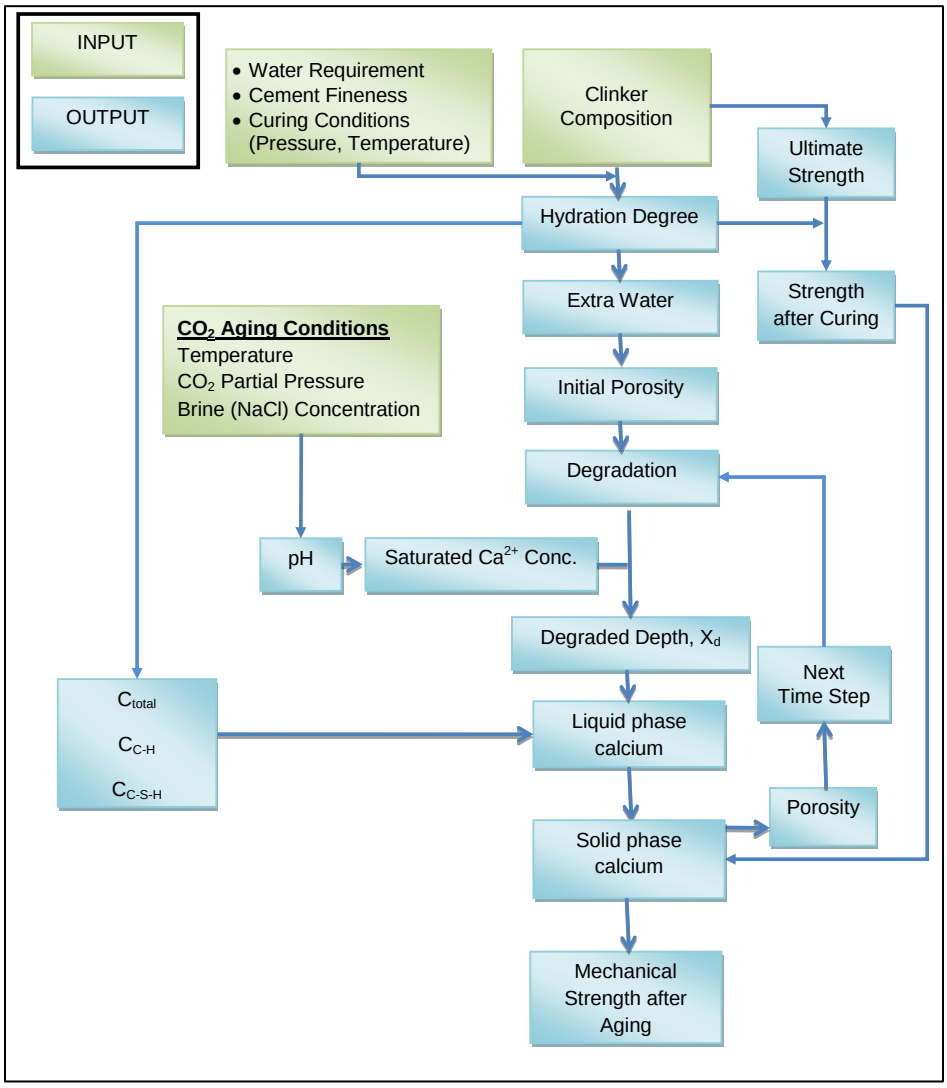

Fig. 2.202: Simplified block diagram of cement degradation model

Cement hydration degree is a function of cement composition, water/cement ratio, temperature and pressure. Once the degree of hydration is determined, initial porosity can be predicted from the extra water in hydrated cement. Most commonly, the degradation process is governed by diffusion process; therefore, loss in mechanical integrity due to dissolution of CH and C-S-H are predicted using Fick's law. Temperature, CO_2 pressure and NaCl concentration are used as initial conditions to predict the pH of the fluid system and consequently the saturated calcium concentration in pore solution of cement. Applying Mainguy and Coussy (2000) analytical model, predicted initial porosity and saturated calcium concentration are used in the diffusion model to calculate the depth of penetration. Next, solid-phase calcium profile in the penetrated zone is predicted by first calculating total calcium, CH and CSH concentrations from cement hydration equations and hydration model. New porosity of the penetrated zone is computed from the degraded depth and calcium concentration in solid phase. The molecular diffusion coefficient in the degraded zone is then recalculated using the newly computed cement properties. This iterative procedure is repeated at each time step for the entire period of exposure. By using the penetrated depth and sample dimensions, new compressive strength model is developed by adopting the methodology proposed by Carde et al. (1996).

2.5.3.1. Hydration Model

The first step in cement degradation modeling is to predict the degree of hydration. This is crucial for initial porosity and strength estimation after curing before the sample is exposed to carbonic acid environment. In addition, the initial amount of portlandite and calcium silicate hydrate can be predicted from the degree of hydration. In this study, the model proposed by Lin and Meyer (2009) is applied to predict the degree of hydration at the time when curing process is completed. Calculation procedure of this model is explained below:

Step 1: Compositions of C_3S, C_2S, C_3A and C_4AF are predicted using the following API – recommended oxide analysis.

$$C_3S = 4.07CaO - 7.6SiO_2 - 6.72Al_2O_3 - 1.43Fe_2O_3 - 2.85SO_3 \quad (2.27)$$

$$C_2S = 2.87SiO_2 - 0.754C_3S \quad (2.28)$$

$$C_3A = 2.65Al_2O_3 - 1.69Fe_2O_3 \quad (2.28)$$

$$C_4AF = 3.04Fe_2O_3 \quad (2.30)$$

These equations are valid only when $Al_2O_3 / Fe_2O_3 > 0.64$.

Step 2: Using above compositions, cement fineness and water-to-cement ratio, the following parameters can be determined:

$$A_o^{'} = -0.0767C_4AF + 0.0184 \quad (2.31)$$

$$A_o = A_o^{'}\left(\frac{\text{Blaine}}{350}\right) \quad \text{.....} \quad (2.32)$$

$$k = 0.56(C_3S)^{-0.206}(C_2S)^{-0.128}(C_3A)^{0.161} \quad \text{.....} \quad (2.33)$$

$$n_o = 10.945C_3S + 11.25C_2S - 4.10C_3A - 0.892 \quad \text{.....} \quad (2.34)$$

$$E_a = 22100(C_3A)^{0.30}(C_4AF)^{0.25}(\text{Blaine})^{0.35} \quad \text{.....} \quad (2.35)$$

$$\beta_1 = \frac{1}{9.33\left(\frac{\text{Blaine}}{100}\right)^{2.82} + 0.38} \quad \text{.....} \quad (2.36)$$

$$\beta_2 = \frac{\text{Blaine} - 220}{147.78 + 1.656(\text{Blaine} - 220)} \quad \text{.....} \quad (2.37)$$

where, 'Blaine' represents cement fineness, which varies from 270 to 420 m^2/kg. Large value means finer cement particles (Lin and Meyer 2009).

Step 3: The ultimate degree of hydration, at a particular temperature, is computed using the following equations:

$$\alpha_{u,293} = \frac{\beta_1 * \frac{w}{c}}{\beta_2 + \frac{w}{c}} \quad \text{.....} \quad (2.38)$$

$$\alpha_{u,T} = \alpha_{u,293} * \text{Exp}[-0.00003(T - 293)^2 * \text{SGN}(T - 293)] \quad \text{.....} \quad (2.39)$$

where

$$\text{SGN}(T - 293) = \begin{cases} 1, & \text{when } T \geq 293K \\ -1, & \text{when } T < 293K \end{cases} \quad \text{.....} \quad (2.40)$$

Theoretically, ultimate degree of hydration is computed using:

$$\alpha_{u,T} = \frac{\frac{w}{c}}{0.4} \quad \text{.....} \quad (2.41)$$

If the estimated ultimate degree of hydration exceeds the theoretical value, the theoretical value is selected.

Step 4: Rate of hydration, at a particular curing temperature and pressure, is computed from:

$$\dot{\alpha} = \frac{d\alpha}{dt} = A_\alpha n_\alpha * e^{-\frac{E_a}{RT}} * e^{\frac{E_a}{293R}} \quad \text{.....} \quad (2.42)$$

where,

$$A_\alpha = k\left(\frac{A_o}{k\alpha_u} + \alpha\right)(\alpha_u - \alpha) * e^{\left[0.02*\left(\frac{p}{p_{atm}} - 1\right)^{0.07}\left\{\frac{\alpha}{\alpha_u} - 1.5*\left(\frac{\alpha}{\alpha_u}\right)^2 + 0.4\right\}\right]} \quad \text{.....} \quad (2.43)$$

$$n_\alpha = e^{\left[-n_o\left\{1+(1-\alpha)^2 \ln\left(\frac{350}{Blaine}\right)\right\}\left\{e^{28*10^{-6}(T-293)^2}\right\}^{10\alpha^4}\alpha\right]} \quad \text{..... (2.44)}$$

Equation (2.42) is a non-linear ordinary differential equation and requires numerical procedure to obtain the solution.

Numerical Procedure

Applying forward finite difference approximation to find the solution of ordinary differential equation (2.42), the following expression can be obtained:

$$\frac{\alpha^{s+1} - \alpha^{s}}{\Delta t} = A_\alpha n_\alpha e^{-\frac{E_a}{RT}} e^{\frac{E_a}{293R}} \quad \text{..... (2.45)}$$

Rearranging the above equation yields:

$$\alpha^{s+1} = \alpha^{s} + \Delta t A_\alpha n_\alpha e^{-\frac{E_a}{RT}} e^{\frac{E_a}{293R}} \quad \text{..... (2.46)}$$

A function that compares the left side and right side of equation (2.46) can be defined as:

$$f(\alpha) = \alpha^{s+1} - \alpha^{s} - \Delta t A_\alpha n_\alpha e^{-\frac{E_a}{RT}} e^{\frac{E_a}{293R}} \quad \text{..... (2.47)}$$

The Newton-Raphson numerical iterative scheme is used to solve the equation above:

$$\alpha^{n+1} = \alpha^{n} - \frac{f(\alpha)}{f'(\alpha)} \quad \text{..... (2.48)}$$

The following representations are made in Eqs. (2.43) and (2.44) for ease of derivations:

$$Y_\alpha = \alpha\left\{1 + (1-\alpha)^2 \ln\left(\frac{350}{Blaine}\right)\right\} \quad \text{..... (2.49)}$$

$$Z_\alpha = \left\{e^{28*10^{-6}(T-293)^2}\right\}^{10\alpha^4} \quad \text{..... (2.50)}$$

$$X = -n_o YZ \quad \text{..... (2.51)}$$

$$s_\alpha = e^{\left[0.02\left(\frac{p}{P_{atm}}-1\right)^{0.07}\left\{\frac{\alpha}{\alpha_u}-1.5\left(\frac{\alpha}{\alpha_u}\right)^2+0.4\right\}\right]} \quad \text{..... (2.52)}$$

$$T_\alpha = k\left(\frac{A_o}{k\alpha_u} + \alpha\right)(\alpha_u - \alpha) \quad \text{..... (2.53)}$$

$$B_\alpha = A_\alpha n_\alpha * e^{-\frac{E_a}{RT}} * e^{\frac{E_a}{293R}} \quad \text{..... (2.54)}$$

Therefore:

$$n_\alpha = e^{X} \quad \text{..... (2.55)}$$

$$A_\alpha = T_\alpha s_\alpha \quad \text{..... (2.56)}$$

$$f(\alpha) = \alpha^{s+1} - \alpha^{s} - \Delta t B_{\alpha} \quad \text{.....} \quad (2.57)$$

Differentiating the above equations (Eqs. 2.49 to 2.57), the following expressions can be obtained:

$$f'(\alpha) = 1 - \Delta t B'_{\alpha} \quad \text{.....} \quad (2.58)$$

$$A'_{\alpha} = T_{\alpha} s'_{\alpha} + T'_{\alpha} s_{\alpha} \quad \text{.....} \quad (2.59)$$

$$n'_{\alpha} = X' e^{X} \quad \text{.....} \quad (2.60)$$

$$B'_{\alpha} = e^{-\frac{E_a}{RT}} * e^{\frac{E_a}{293R}} * (A_{\alpha} n'_{\alpha} + A'_{\alpha} n_{\alpha}) \quad \text{.....} \quad (2.61)$$

$$T'_{\alpha} = k\left[-\left(\frac{A_o}{k\alpha_u} + \alpha\right) + (\alpha_u - \alpha)\right] \quad \text{.....} \quad (2.62)$$

$$s'_{\alpha} = 0.02\left(\frac{p}{p_{atm}} - 1\right)^{0.07}\left[\frac{1}{\alpha_u} - \frac{3\alpha}{\alpha_u^2}\right] * e^{\left[0.02\left(\frac{p}{p_{atm}}-1\right)^{0.07}\left\{\frac{\alpha}{\alpha_u} - 1.5\left(\frac{\alpha}{\alpha_u}\right)^2 + 0.4\right\}\right]} \quad \text{.....} \quad (2.63)$$

$$X' = -n_o(Y'Z + Z'Y) \quad \text{.....} \quad (2.64)$$

$$Z'_{\alpha} = 10\alpha^4\left\{e^{28*10^{-6}(T-293)^2}\right\}^{10\alpha^4 - 1} \quad \text{.....} \quad (2.65)$$

$$Y'_{\alpha} = -2\alpha(1-\alpha)\ln\left(\frac{350}{Blaine}\right) + \left[1 + (1-\alpha)^2 \ln\left(\frac{350}{Blaine}\right)\right] \quad \text{.....} \quad (2.66)$$

Equations (2.58) – (2.66) are substituted into equation (2.48) and a MATLAB program was developed to compute the degree of hydration subject to convergence error of 10^{-5}.

Results

Figure 2.203 shows model prediction from the hydration model using the input data summarized in **Table 2.45**. Three stages of hydration can be observed from these plots; slow induction period, acceleration period and final slow reaction period. The induction period is characterized with low heat evolution and gradual nucleation of hydration products (i.e. CH and CSH).

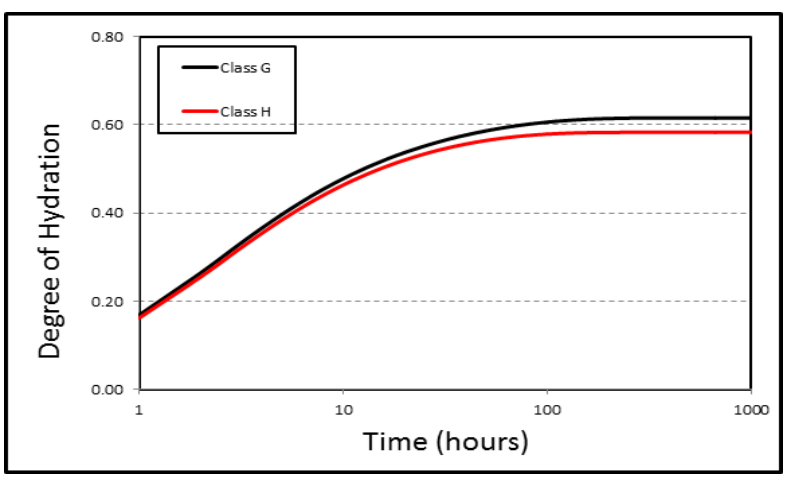

Fig. 2.203: Model prediction of degree of hydration for Class H and Class G cements

The cement begins to set during the acceleration period and early compressive strength development begins with accelerating growth of principal product of hydration (i.e. CSH). In the late stage, gradual densification of microstructure around residual unhydrated C_3S and CH re-crystallization occur (Bensted and Barnes 2002). Since less water is available to facilitate hydration of chemical compounds in Class H cement, only 58% of these compounds were hydrated compared to 60% in Class G. Both API oil well cements attained ultimate degree of hydration at approximately 100 hours; hence cement samples were cured for 5 days during the experimental investigation.

Table 2.45: Cement clinker composition, water requirement and curing conditions

Cement Class	W/C Ratio	C_3S	C_2S	C_3A	C_4AF	Blaine (m^2/kg)	Curing Temperature (^oF)	Curing Pressure (psi)
G	0.44	0.502	0.244	0.03	0.18	280	200	14.7
H	0.38	0.502	0.244	0.03	0.18	260	200	14.7

Remark: API recommends the following standard chemical composition: Maximum/Minimum C_3S composition = 0.58/0.48; Maximum C_3A composition = 0.03; Maximum $C_4AF + 2*C_3A$ composition = 0.24.

Model validation was conducted using experimental data originally published by Lerch and Ford (1948) and reported by Lin and Meyer (2009). The model appears to match reasonably with the experimental data (**Fig. 2.204**). While increase in curing temperature minimizes the curing time at which ultimate degree of hydration is attained, less degree of hydration is achieved since cement hydration is exothermic and pore water is rapidly consumed (**Fig. 2.205**). The model also shows that variation of curing pressure does not show significant effect on degree of hydration (**Fig. 2.206**).

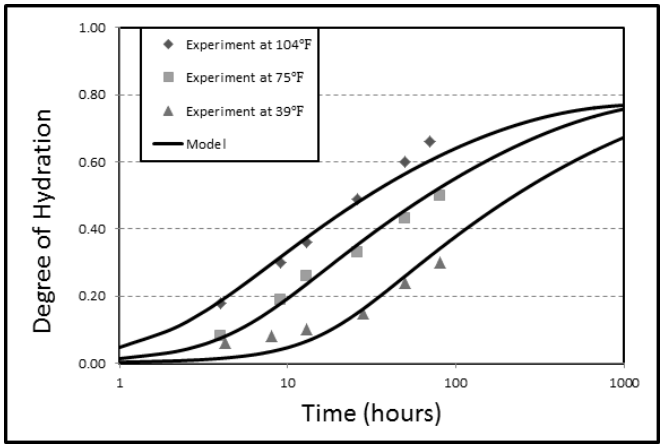

Fig. 2.204: Model validation for degree of hydration while curing oil well cement

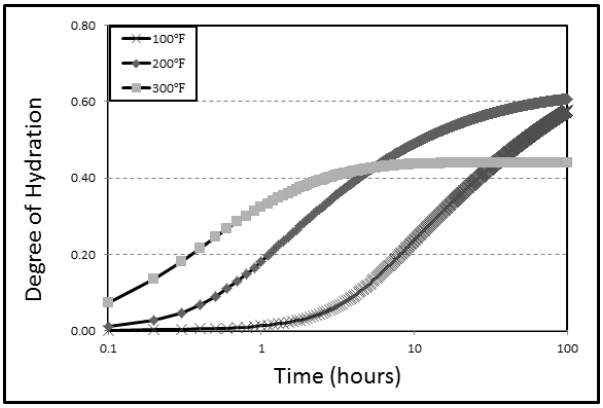

Fig. 2.205: Temperature effect on degree of hydration of Class G cement

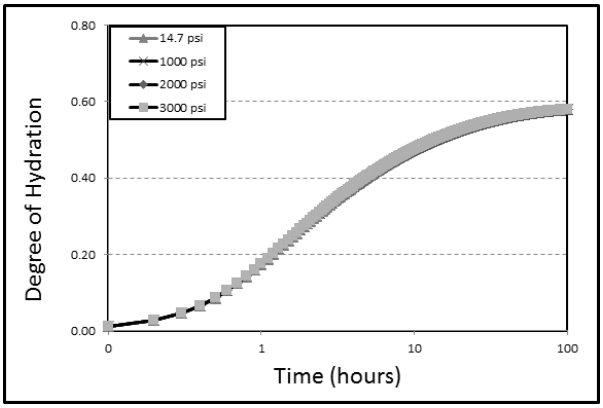

Fig. 2.206: Pressure effect on degree of hydration of Class H cement

2.5.3.2. Porosity Model

One major use of the degree of hydration is predicting initial porosity of the hydrated cement before exposure to CO_2-brine system, which alters this initial state after calcite precipitation and subsequent dissolution. Assuming no volumetric change during mixing and no air entrapment, extra (free) water after hydration is computed from hydration reaction kinetics and material balance. Then, the following relation can be used to compute porosity of the set slurry.

$$\text{Porosity} = \phi = \frac{\text{Pore Volume}}{\text{Bulk Volume}} = \frac{\text{Extra water}}{\text{Total Slurry volume}} \quad \text{.....} \quad (2.67)$$

Estimated initial porosities of Class G and Class H are approximately 30 and 24%, respectively. **Figure 2.207** shows comparison of the model prediction and experimentally measured porosity data with acceptable match.

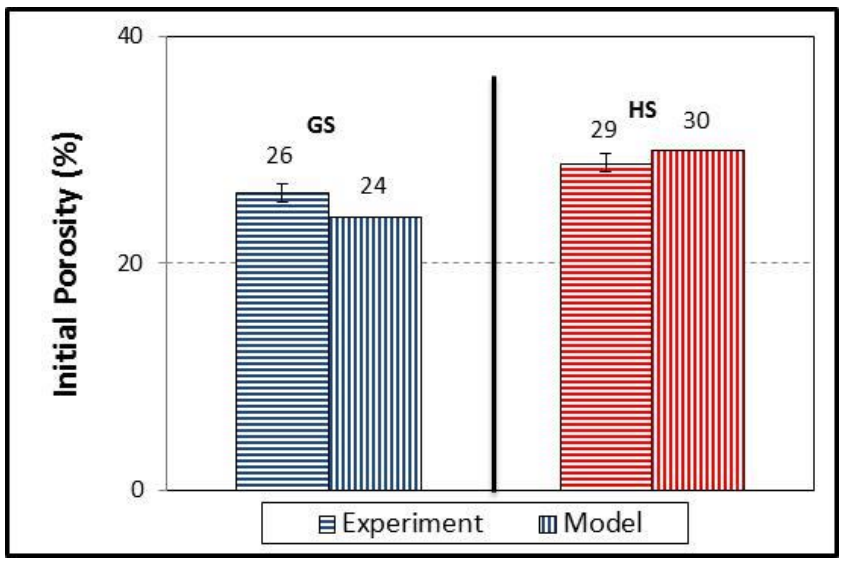

Fig. 2.207: Comparison of predicted initial porosity with experimental data

2.5.3.3. Degradation Model

Cement degradation models generally represent the dissolution process of calcium hydroxide and progressive gradual decalcification of calcium silicate hydrate. Ionic transfer (a diffusion process) between bulk fluid and pore solution are integrated with interaction between pore fluid and cement matrix, chemical species transport in the cement pores and mechanical strength models. This integrated model predicts degraded depth and relative compressive strength, considering temperature, CO_2 partial pressure, brine concentration and water-to-cement ratio as input parameters. Figure 2.202 shows the formulation and simplified numerical algorithm of the model.

In this section, procedure is outlined for application of Mainguy and Coussy (2000) analytical model to predict degraded depth. Further, the model is improved to predict degradation process in CO_2-brine environment.

Step 1: Determination of Saturation Concentration of Calcium Ions: C_{satu} is saturation concentration of calcium ions, which depends on temperature, brine concentration and concentration of CO_2. In pure

brine solution, the following model has been proposed by Nakarai et al. (2006):

$$C_{satu} = \frac{1}{2}\sqrt[3]{2K_{sp}} \quad \text{.....} \quad (2.68)$$

K_{sp} is the solubility product of calcium hydroxide, which depends on temperature and brine concentration. Effects of these variables are modeled in the following equation:

$$K_{sp} = 0.0125 * 10^{9}e^{-0.019T} + A\left(5 * 10^{4}\sqrt[3]{C_{NaCl}}\right) \quad \text{.....} \quad (2.69)$$

where,

$$A = \begin{cases} -2C_{NaCl}^{3} + 3C_{NaCl}^{2}, & \text{when } 0.0 \leq C_{NaCl} \leq 1.0 \\ 1, & \text{when } C_{NaCl} > 1.0 \end{cases} \quad \text{.....} \quad (2.70)$$

In CO_2-saturated brine solution where $pH < 7$ (i.e. acidic environment), C_{satu} corresponds to the maximum amount of calcite that is soluble in the pore solution. This requires analyzing ionic speciation of each component in pore solution. The chemical equilibrium reactions and associated dissociation constants involved in CO_2-corrosion of oil well cement can be summarized as:

Dissolution and dissociation of calcium carbonate in pore fluid occurs due to calcium concentration difference between the matrix and pore fluid:

$$CaCO_{3\,(s)} \rightleftharpoons Ca^{2+}{}_{(aq.)} + CO_3{}^{2-}{}_{(aq.)} \quad \text{.....} \quad (2.71)$$

The dissociation constant for this process is defined as:

$$K_{sp} = \left[Ca_{(aq)}^{2+}\right]\left[CO_{3(aq)}^{2-}\right] \quad \text{.....} \quad (2.72)$$

Dissolved CO_2 exists in equilibrium with CO_2 gas above the brine solution:

$$CO_{2\,(g)} \rightleftharpoons CO_{2\,(aq.)} \quad \text{.....} \quad (2.73)$$

Dissolved CO_2 exists in equilibrium with aqueous carbonic acid, Hence:

$$CO_{2\,(aq.)} + H_2O_{\,(l)} \rightleftharpoons H_2CO_{3\,(aq.)} \quad \text{.....} \quad (2.74)$$

Applying Henry's law, the relationship between CO_2 gas pressure and concentration of dissolved CO_2 in the brine solution can be expressed as:

$$K_h = \frac{\left[H_2CO_{3(aq)}\right]}{P_{CO_2}} \quad \text{.....} \quad (2.75)$$

The first dissociation equilibrium between $H_2CO_{3(aq.)}$ and $HCO_3^-{}_{(aq.)}$ is:

$$H_2CO_{3\,(aq.)} \rightleftharpoons H^+{}_{(aq.)} + HCO_3^-{}_{(aq.)} \quad (2.76)$$

The first dissociation constant of carbonic acid is expressed as:

$$K_{a1} = \frac{[H^+_{(aq)}][HCO^-_{3(aq)}]}{[H_2CO_{3(aq)}]} \quad (2.77)$$

The second dissociation equilibrium between $HCO_3^-{}_{(aq.)}$ and $CO_3^{2-}{}_{(aq.)}$ is:

$$HCO_3^-{}_{(aq.)} \rightleftharpoons H^+{}_{(aq.)} + CO_3^{2-}{}_{(aq.)} \quad (2.78)$$

The second dissociation constant of carbonic acid is defined as:

$$K_{a2} = \frac{[H^+_{(aq)}][CO^{2-}_{3(aq)}]}{[HCO^-_{3(aq)}]} \quad (2.79)$$

Dissociation of water:

$$H_2O_{(l)} \rightleftharpoons H^+{}_{(aq.)} + OH^-{}_{(aq.)} \quad (2.80)$$

Dissociation constant for water is:

$$K_w = [H^+_{(aq)}][OH^-_{(aq)}] \quad (2.81)$$

Electrical neutrality (charge balance) equation for the process is described as:

$$2[Ca^{2+}] + [H^+_{(aq)}] = [HCO^-_{3(aq)}] + 2[CO^{2-}_{3(aq)}] + [OH^-_{(aq)}] \quad (2.82)$$

Equilibrium concentrations of $[Ca^{2+}]$, $[H^+_{(aq)}]$, $[HCO^-_{3(aq)}]$, $[CO^{2-}_{3(aq)}]$, $[OH^-_{(aq)}]$, $[H_2CO_{3(aq)}]$ and $[CO_{2(aq)}]$ can now be obtained by solving the seven equations above (Eqs. 2.72, 2.74, 2.76, 2.78, 2.80, 2.82, and 2.83). Combining these equations yields the equilibrium calcium ion concentration (i.e. $[Ca^{2+}]$), which represents the maximum amount of calcium carbonate that can dissolve in pore fluid.

$$C_{Satu} = [Ca^{2+}]_{max} = \frac{K_{sp}}{K_h K_{a1} K_{a2}} \frac{[H^+]^2}{P_{CO_2}} \quad (2.83)$$

To account for the effect of temperature and brine concentration, the first and second dissociation constants of carbonic acid in brine solution are estimated using Millero et al. (2007) model in which the following expression has been obtained:

$$K_h K_{a1} = K_1 = \frac{[H^+_{(aq)}][HCO^-_{3(aq)}]}{[CO_{2(aq)}]} \quad \text{.....} \quad (2.84)$$

Step 2: Determination of Dimensionless Degraded Depth: Degradation depth of cement can be determined using the analytical solution (model) of the governing equation presented by Mainguy and Coussy (2000). Using this model, the degradation depth for 1D diffusion-dissolution problem can be obtained by solving the mass balance equation, diffusion equation (i.e. transport law of the solute through the porous medium), equilibrium equation (law governing the kinetics of dissolution), and initial condition at the time of exposure. To determine the degradation depth, first, Dimensionless depth, ξ_d, is determined by solving the following analytical solution:

$$\varepsilon \exp(-\xi_d^2) = \sqrt{\pi}\xi_d \mathrm{erf}(\xi_d) \quad \text{.....} \quad (2.85)$$

where dimensionless quantities in the previous equations are defined as:

$$\varepsilon = \frac{\emptyset C_{satu}}{C_{total}} \quad \text{.....} \quad (2.86)$$

$$\xi = \frac{x}{2\sqrt{Dt}} \quad \text{.....} \quad (2.87)$$

$$\mathrm{er}\,f(\xi_d) = \frac{2}{\sqrt{\pi}} \int_0^{\xi_d} e^{-t^2} \, dt \quad \text{.....} \quad (2.88)$$

where $\emptyset$ is porosity at any time and location and C_{total} is the solid-phase total calcium concentration. Numerical scheme presented in Appendix C is used to solve Eq. (2.85).

Step 3: Determination of Degradation Depth: Degraded depth, x_d, is estimated using:

$$x_d = 2\xi_d\sqrt{Dt} \quad \text{.....} \quad (2.89)$$

where diffusivity, $D\,(m^2/s) = 2.35 \times 10^{-13} \exp(9.95\,\emptyset)$. During degradation, porosity of the cement balance was time and location. Thus:

$$\emptyset = \emptyset_o + (1 - \emptyset_o)\big(C_{s,o} - C_s(x,t)\big)\frac{M_w}{\rho_s} \quad \text{.....} \quad (2.90)$$

where $\emptyset_o$ and $C_{s,o}$ are initial porosity and solid-phase calcium concentration (mol/L), respectively. M_w is the molecular weight of calcium (40.0 g/mol), and ρ_s is cement density. $C_s(x,t)$ is calcium concentration at any time and location (mol/L). $\emptyset_o$ is the initial porosity obtained from hydration model. $C_{s,o}$ is equal to the total calcium concentration associated with the amount of C-H and C-S-H present in the cement.

Step 4: Determination of Liquid-Phase Calcium Ion Concentration: In the degraded zone, liquid-phase

calcium ion concentrations are predicted using the following model:

$$\bar{C}_l = \begin{cases} \frac{C_l}{C_{satu}} = \frac{\mathrm{erf}(\xi)}{\mathrm{erf}(\xi_d)} & \text{when } 0.0 \le \xi \le \xi_d \\ 1 & \text{when } 0.0 \le \xi \le \xi_d \end{cases} \quad \text{.....} \quad (2.91)$$

Step 5: Determination of Solid-Phase Calcium Ion Concentration: Solid-phase calcium ion concentrations are then predicted using Nakarai et al. (2006) model.

$$C_s = f(C_l) = A\left[C_{CSH}\left(\frac{C_l}{C_{satu}}\right)^{\frac{1}{3}}\right] + B \quad \text{.....} \quad (2.92)$$

where,

$$A = \begin{cases} -\left(\frac{2}{x_1^3}\right)(C_l)^3 + \left(\frac{3}{x_1^2}\right)(C_l)^2 & (0.0 \le C_l \le x_1) \\ 1 & (x_1 < C_l) \end{cases} \quad \text{.....} \quad (2.93)$$

$$B = \begin{cases} 0 & (0.0 \le C_l \le x_2) \\ \frac{C_{CH}}{(C_{satu}-x_2)^3}(C_l - x_2)^3 & (x_2 < C_l) \end{cases} \quad \text{.....} \quad (2.94)$$

where x_1 is the liquid-phase calcium ion concentration when rapid transition of C-S-H gel into silica gel begins (mmol/L). x_2 is the liquid-phase calcium ion concentration when the calcium hydroxide has completely dissolved and dissolution of C-S-H gel begins (mmol/L). C_{CSH} is amount of calcium in the solid-phase of the C-S-H gel (mmol/m^3). C_{CH} is amount of calcium in the solid-phase of the calcium hydroxide (mmol/m^3) and C_{satu} is saturated liquid-phase calcium ion concentration (mmol/L). In this study, 2 mmol/L liquid-phase calcium ion concentration is assumed as the commencement of rapid transition of C-S-H gel into silica gel as recommended by a similar study (Nakarai 2006). Furthermore, as suggested by the same author, x_2 is assumed as C_{satu} - 2.99. C_{CSH} and C_{CH} for each cement classes are obtained from hydration chemistry and degree of hydration. **Table 2.46** shows the values of C_{CSH} and C_{CH} for this study. Once the solid-phase calcium concentration after exposure has been determined, mechanical strength model can then be applied.

Table 2.46: Amount of calcium in hydrated oil well cements

Cement Type	Portlandite	Calcium Silicate Hydrate	Total Solid-Phase Calcium before Exposure
Class G (mmol/m^3)	8149	13422	21571
Class H (mmol/m^3)	9435	15541	24976

Degradation depth obtained from the model is plotted in **Fig. 2.208** as a function of square root of time. The result shows that Class G cement is more penetrated than Class H cement after for 14 days of exposure to 2% brine solution saturated with methane containing CO_2 at 350°F. A study of CO_2 composition effect on degradation behavior of Class H cement is presented in **Fig. 2.209**. As more CO_2 is

injected, deeper penetration is achieved due to increased production of carbonic acid, which alters the state of equilibrium and leads to dissolution of calcite. Furthermore, the rate of degradation (i.e. slope of the plot) mainly is a function of cement composition and CO_2 partial pressure. This observation was observed in previous studies (Matteo et al. 2011; Matteo and Scherer 2012) in which temperature and solution pH (a function of CO_2 partial pressure) were reported as effective variables on degradation rate. Since solution pH is a function of CO_2 partial pressure, therefore, decreasing pH of the liquid phase (i.e. acidic environment) leads to high saturation concentration of calcium ion, which consequently results in depth of degradation increasing.

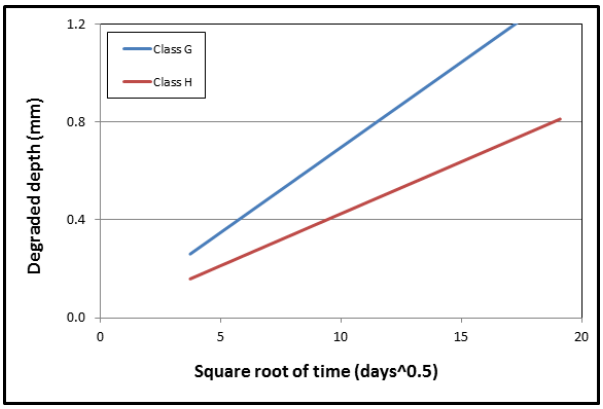

Fig. 2.208: Predicted degradation depth for Class G and Class H at T=350°F, P_{CO2} = 600 psi, NaCl = 2%wt

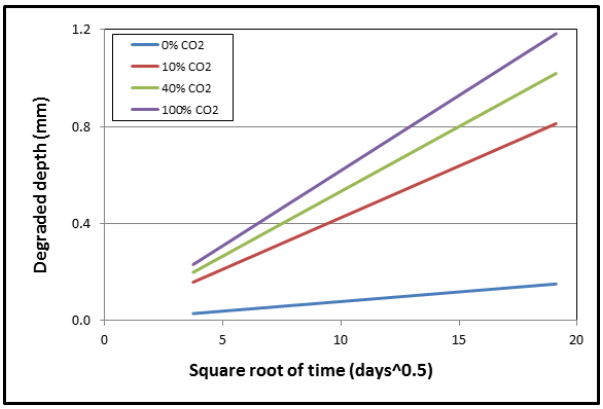

Fig. 2.209: Predicted degradation depth for Class H cement at T=350°F, NaCl = 2%wt, P = 6000 psi

Predicted solid-phase calcium concentration profile as a function of salt concentration in the bulk fluid is shown in **Fig. 2.210**. Increasing salinity of brine up to 5 wt% leads to slight decrease in degradation depth. Mechanical behavior of cement is affected by NaCl in different ways depending on temperature and concentration. Some experimental studies conducted at lower temperature and pressure (Barlèt-Gouédard et al. 2006; Duguid et al. 2005, 2008, 2009) have shown that sodium chloride (NaCl) increases dissolution rate during leaching. Furthermore, effect of water-to-cement ratio on solid-phase calcium is presented in **Fig. 2.211**. With less water requirement, Class H is more CO_2 resistant than Class G. This agrees with our experimental observations and results of other studies (Bruckdorfer 1986).

Results of simulation study conducted on CO_2 concentration show that loss of integrity is faster with increase in CO_2 partial pressure (**Fig. 2.212**). This is because of the shift in equilibrium position in response to increased production of carbonic acid and this result in dissolution of precipitated calcite. In addition, temperature effect was also studied (**Fig. 2.213**). Although more calcite precipitation is likely at temperature below approximately 250°F, calcium hydroxide (a key component of cement integrity) has been reported to be highly leached at low temperature (Nakarai 2006). Similarly, reduction in dissolution of portlandite protects the matrix against further penetration of carbonic acid at higher temperature. Although dissolution of calcite is more likely to occur at high temperature due to shift in equilibrium, our experimental measurements show mixed trend.

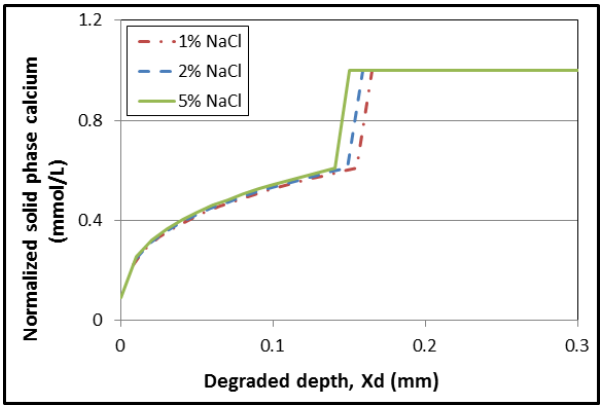

Fig. 2.210: Effect of salt concentration on solid-phase calcium profile of Class H cement at P=6000 psi, T=350°F, CO_2 = 10%, t = 14 days

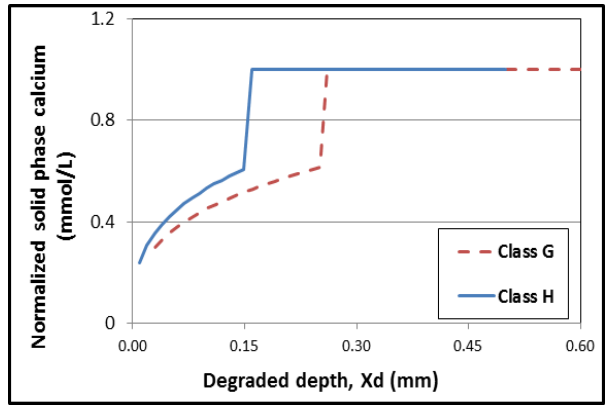

Fig. 2.211: Comparison of solid-phase calcium profile different cement classes at P = 6000 psi, T = 350°F, CO_2 =10%, t = 14 days

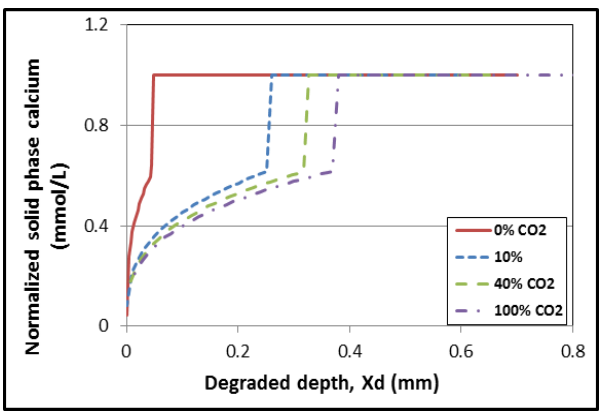

Fig. 2.212: CO_2 concentration effect on solid-phase calcium profile of Class G cement P = 6000 psi, T=350°F, NaCl = 2 wt%, t = 14 days

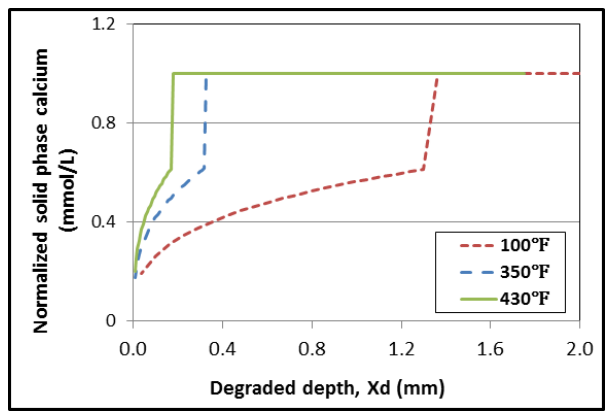

Fig. 2.213: Temperature effect on solid-phase calcium profile of Class G cement P = 6000 psi,T = 350°F, NaCl = 2 wt%, t = 14 days

2.5.3.4. Mechanical Strength Degradation Model

Compressive strength predictions are evaluated at three stages of the degradation process, which include ultimate strength before curing, strength after curing, and mechanical strength after CO_2 exposure.

Ultimate Strength before Curing

Major components of cement (C_3S and C_2S) are considered as main contributors to strength development. In the hydration reaction, the volume fraction of CSH to CH in hydrated cements is higher in C_2S than in C_3S; hence, for the same reacted amounts, C_2S contributes more to strength development than C_3S, since CSH contributes more to strength development than CH. To prevent strength retrogression at elevated temperature, 35% BWOC silica flour is usually mixed with the base slurry and its contribution is also included in ultimate strength computation. For cement with known volume fraction of C_3S and C_2S, Maekawa et al. (2009) presented the following equation for ultimate strength estimation.

$$\sigma_{\infty} = \frac{Ax_{C_3S}+Bx_{C_2S}}{x_{C_3S}+x_{C_2S}} x_c + Cx_{SF} \quad \text{.....(2.95)}$$

where A, B and C are material constants with values: 215, 250 and 300 MPa, respectively. x_c and x_{SF} are weight fractions of Portland cement and silica flour, respectively. Thus: $x_c + x_{SF} = 1$. x_{C_2S} and x_{C_3S} are volume fractions of C_2S and C_3S, respectively.

Mechanical Strength after Curing

Compressive strength development during cement curing is mostly affected by the degree of hydration. In this study, strength model proposed by Powers (1958) is used with slight modification in the value of empirical parameter K.

$$\sigma_c = \sigma_{\infty} \left[\frac{0.71\alpha}{0.32\alpha+\frac{w}{c}}\right]^k \quad \text{.....(2.96)}$$

where σ_{∞} is strength, α is degree of hydration, $\frac{w}{c}$ is water to cement ratio. k is empirical parameter, which is defined as:

$$k = f\left(\frac{w}{c}\right) \approx 13 - 16 * \left(\frac{w}{c}\right) \quad \text{..... (2.97)}$$

The above strength models were used to predict mechanical strength development while curing proceeds. **Figure 2.214** illustrates comparison of model prediction with literature data (Voigt and Shah 2003, Akkaya et al. 2003). Moreover, compressive strength predicted from the present model predominantly matched our compressive strength measurements for Class G and Class H cement samples cured at 200°F, 14.7 psi for 5 days (**Fig. 2.215**). Applying this model, comparison is made between strength estimated for Class G and Class H (**Fig. 2.216**).

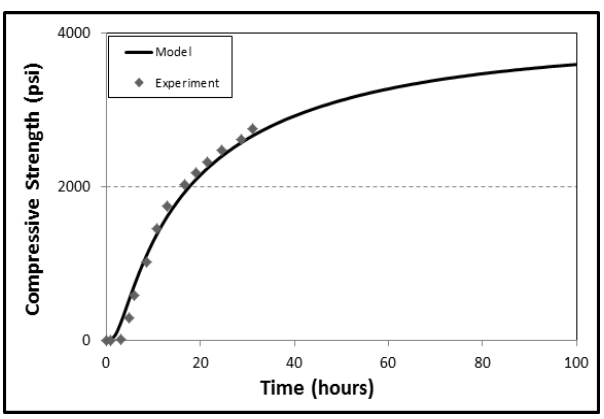

Fig. 2.214: Comparison of strength predictions during curing with experimental data (Akkaya et al. 2003)

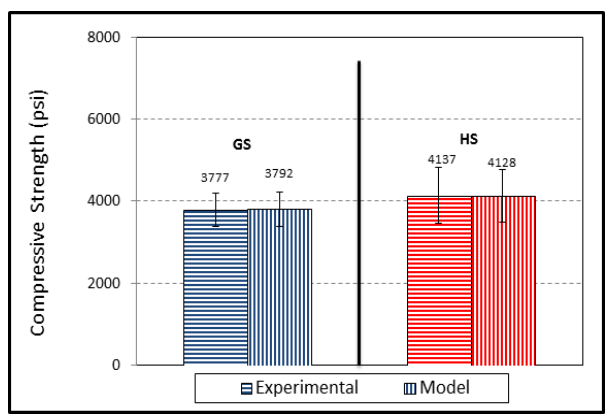

Fig. 2.215: Comparison of strength predictions with experimental data after curing

The result clearly shows that Class H cement exhibits better strength performance than Class G cement, although less degree of hydration was achieved. Several authors have noted that hydrated compounds are susceptible to chemical shrinkage, which leads to pore volume reduction. Lin and Meyer (2009) also presented the following model for estimate chemical shrinkage of cement during hydration and application of this model shows that more shrinkage is possible in Class H cement than Class G cement (**Fig. 2.217**).

$$v_{chsh} = \frac{0.0625\alpha}{0.32+\frac{w}{c}} \quad \text{.....} \quad (2.98)$$

where v_{chsh} is chemical shrinkage volume.

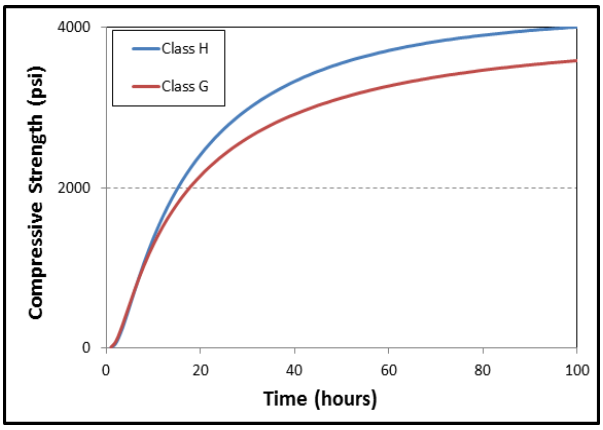

Fig. 2.216: Strength predictions during curing Class G and Class H cement

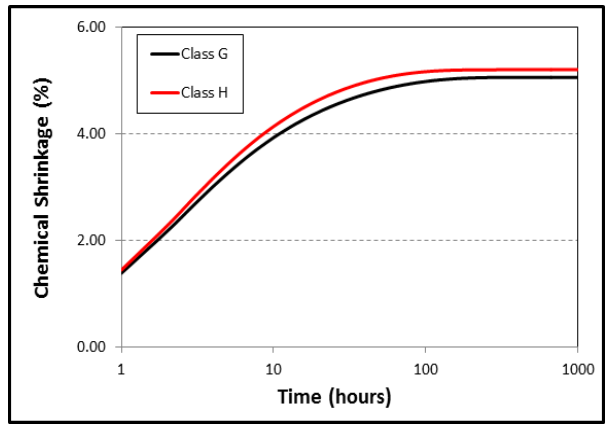

Fig. 2.217: Comparison of chemical shrinkage in class G and class H during curing

Mechanical Strength after CO_2 Aging

The next step is to predict alterations in mechanical strength after curing due to acidic attack. After exposure to CO_2 containing fluid, oil well cement is subjected to several interacting mechanisms which include diffusion, carbonation and leaching. The deterioration in mechanical strength arises from loss of calcium in portlandite and calcium silicate hydrates. Therefore, the distribution of calcium in the invaded zone is an indication of loss of strength. Two preliminary models are presented in this study. The first model assumes complete leaching of the calcium carbonate precipitated during carbonation while the second model accounts for leaching of only a proportion of the calcium carbonate. This means it accounts for porosity and permeability reduction occurring in carbonated zone of cement.

Model I: Applying elasto-plasticity theory, Carde et al. (1996) presented a methodology for formulating compressive strength models from solid-phase calcium profile in leached zone of cement materials. This methodology is adopted in developing a new mechanical strength model for cement that has been exposed to acidic environment under HPHT conditions.

Predicted solid-phase calcium profiles (Figs. 2.210 to 2.213) in cement after 14 days of acid attack show the effect of salt concentration, cement Class, CO_2 concentration, and temperature on cement degradation. Application of Carde's hypothesis implies that these profiles (as illustrated by **Fig. 2.218**) can be assumed for stress distribution in degraded cement. The underlying assumption here is that the reactions involving calcium (carbonation, leaching) are solely response for compressive strength alteration.

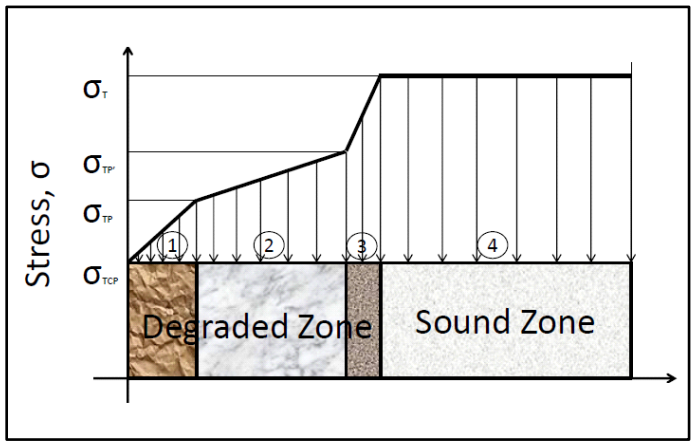

Fig. 2.218 : Stress distribution in a degraded cement sample

Based on the approach developed by Carde et al. (1996), reduction in compressive strength occurring after CO_2 exposure can be determined using the following analytical equations:

$$\frac{\Delta F}{F} = 1 - \frac{1}{\pi r^2}\left[\frac{F_1}{\sigma_T} + \frac{F_2}{\sigma_T} + \frac{F_3}{\sigma_T} + \frac{F_4}{\sigma_T}\right] \quad \text{..... (2.99)}$$

where the terms in the parenthesis are expressed as:

$$\frac{F_1}{\sigma_T} = 2\pi\left[\frac{R_P - R_{CP}}{R_1}\left\{\frac{r}{2}[r^2 - (r-R_1)^2] - \frac{1}{3}[r^3 - (r-R_1)^3]\right\} + R_P\left\{rR_1 - \frac{1}{2}[r^2 - (r-R_1)^2]\right\}\right] \quad \text{..... (2.100)}$$

$$\frac{F_2}{\sigma_T} = \frac{2\pi}{R_2 - R_1}\left[\begin{array}{c}\left(R_P' - R_P\right)\left\{\frac{r}{2}[(r-R_1)^2 - (r-R_2)^2] - \frac{1}{3}[(r-R_1)^3 - (r-R_2)^3]\right\} \\ +\left(R_P R_2 - R_P' R_1\right)\left\{r(R_2 - R_1) - \frac{1}{2}[(r-R_1)^2 - (r-R_2)^2]\right\}\end{array}\right] \quad \text{..... (2.101)}$$

$$\frac{F_3}{\sigma_T} = \frac{2\pi}{x_d - R_2}\left[\begin{array}{c}\left(1 - R_P'\right)\left\{\frac{r}{2}[(r-R_2)^2 - (r-x_d)^2] - \frac{1}{3}[(r-R_2)^3 - (r-x_d)^3]\right\} \\ +\left(R_P' x_d - R_2\right)\left\{r(x_d - R_2) - \frac{1}{2}[(r-R_2)^2 - (r-x_d)^2]\right\}\end{array}\right] \quad \text{..... (2.102)}$$

$$\frac{F_4}{\sigma_T} = \pi x_d(2r - x_d) \quad \text{..... (2.103)}$$

Detailed derivations of the above equations are presented in Appendix D.

The terms in the above model are defined in the nomenclature. Mechanical strength after CO_2 attack has been predicted using the model. To validate the model, lab measurements are compared with predictions considering the effects of pressure and CO_2 concentration on cement degradation. For the pressure effect, trend predicted by the current model for Class G cement shows acceptable agreement with the general trend of experimental measurements (**Fig. 2.219a**). As the pressure increases, consistent reduction of compressive strengths is predicted using the model while experimental data shows slight improvement in strength when the pressure is increased from 3,000 to 6,000 psi. These discrepancies could be attributed to data scattering, which is inherent in compressive strength measurements of degraded cement. The trend of model predictions shows the effect of

leaching process on cement strengths and its dominance over carbonation. As a result, the overall effect of pressure increase causes considerable reduction in strengths, resulting from increased acid concentration. In the CO_2 effect case study, similarly, model predictions present acceptable match with experimental data up to 40% CO_2 concentration (**Fig. 2.219b**). However, carbonation trend was not well captured at 100% CO_2 concentration, rather progressive decalcification ensued. This modeling approach does not provide satisfactory strength predictions for Class H cement.

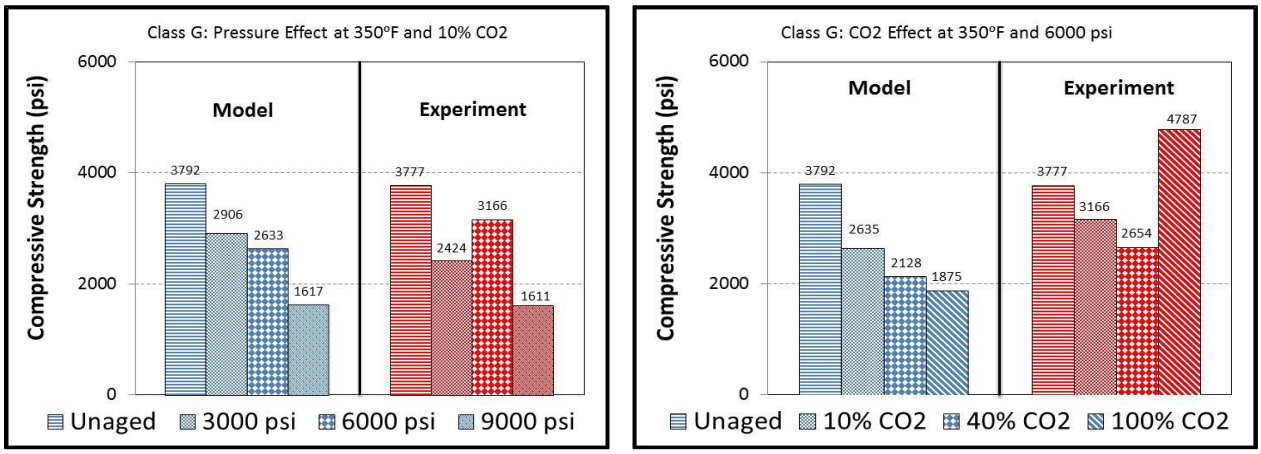

(a) (b)

Fig. 2.219: Comparison of compressive strength of Class G cement predictions with measurements: a) varying pressure at 10% CO_2 and 350°F; and b) varying CO_2 concentration at 6000 psi and 350°F

Model II: In this model, dissolution of calcium carbonate is assumed to be gradual so that its contribution to strength development can be investigated. The model accounts for porosity and permeability reduction in carbonated zone. Due to complexity of solid-phase calcium distribution in degraded cement, an empirical compressive strength model has been developed applying dimensional analysis. The model relates compressive strength to porosity (φ), sample volume (V), stress loading rate (R), average density (ρ_{cm}) of binding components in cement (calcium hydroxide and calcium carbonate). Thus:

$$\sigma_{cm} = \frac{k\rho_{cm}^{a}}{\varphi V^{b} R^{c}} \quad \text{..... (2.104)}$$

where k is determined from experiment,

$$\rho_{cm} = \frac{\sum \rho_i v_i}{\sum v_i} \quad \text{..... (2.105)}$$

$$\rho_{cm} = 1000 \frac{\sum C_i M_i v_i}{\sum v_i} \quad \text{.....(2.106)}$$

where, $i = solid\ minerals\ after\ degradation\ i.e. CH, CSH, CaCO_3$

$$M_i = Molar\ weight\ of\ solid\ minerals\ e.g. M_{CaCO_3} = 100\ g/mol, M_{Ca(OH)_2} = 74\ g/mol$$

$$C_i, v_i = Concentration, volume\ of\ solid\ minerals\ determined\ from\ numerical\ simulation$$

The dimensions of the independent variables are:

$\sigma_{cm} = ML^{-1}T^{-2}, \rho_{cm} = ML^{-3}, V = L^3, R = ML^{-1}T^{-3}$, ϕ=dimensionless. Therefore, $ML^{-1}T^{-2} = M^{a-c}L^{-3a-3b+c}T^{3c}$. Comparing the exponents and solving: a = 1/3, b = -2/9, and c = -2/3. Therefore, compressive strength can be expressed as a function of porosity, sample volume (V), stress loading rate, average density of binding components:

$$\sigma_{cm} = \frac{k\rho_{cm}^{1/3}V^{2/9}R^{2/3}}{\varphi} \quad \text{..... (2.107)}$$

2.5.3.5. Model Predictions

Model predictions of porosity, liquid and solid phase calcium profiles after degradation are presented from **Figs 2.220** to **2.221**.

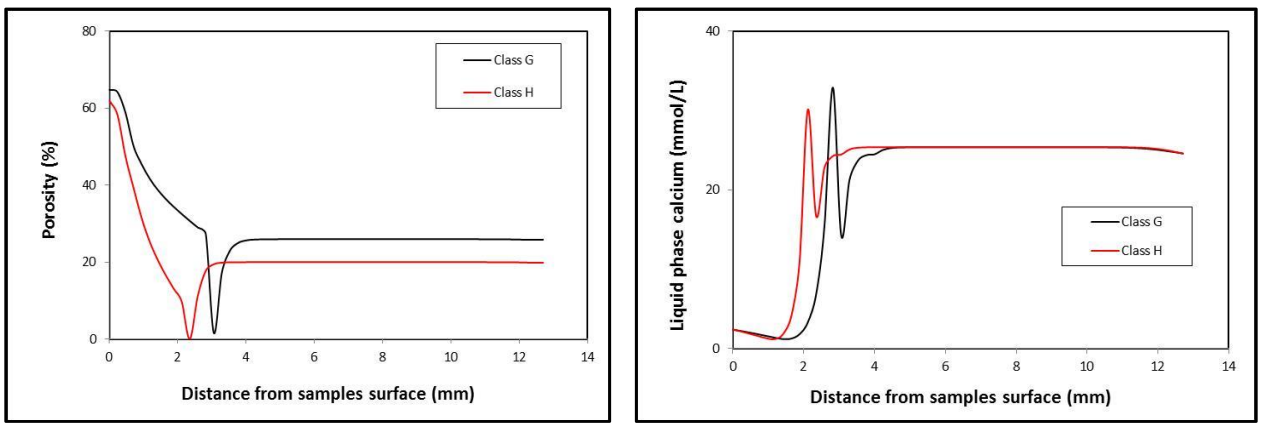

(a) (b)

Fig. 2.220: Model predictions: a) porosity; and b) liquid phase calcium concentration for Class H and Class G cements

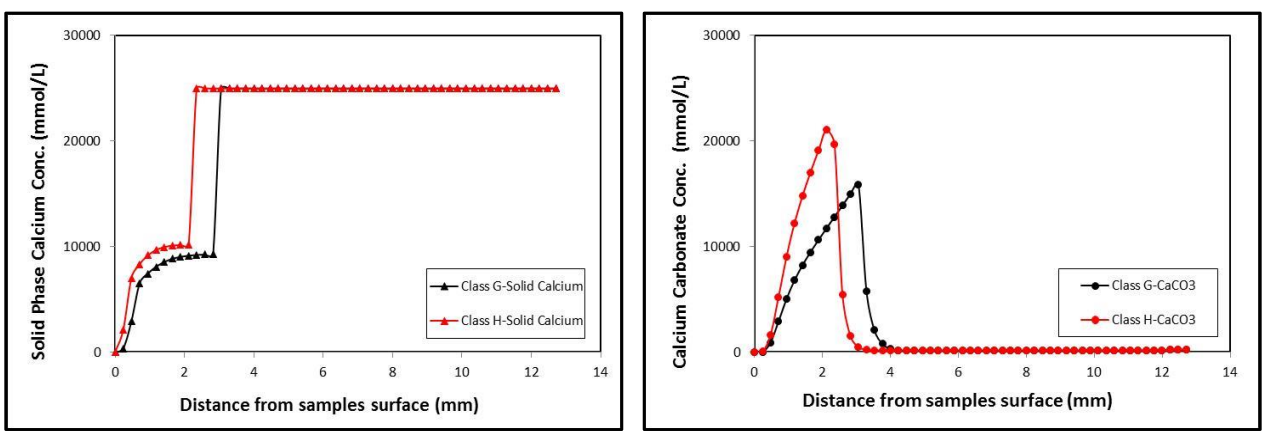

(a) (b)

Fig. 2.221: Model predictions: a) solid phase calcium concentration; and b) calcium carbonate concentration for Class H and Class G cements

Two experimental case studies with evidence of carbonation are used to validate the model (**Fig. 2.222**). The first case (Fig. 2.222a) presents pressure effect on compressive strength after aging at 430°F, 100% CO_2, 2wt% NaCl for 14 days. The second case (Fig. 2.222b) presents model comparison of CO_2 gas composition effect on strength of cores that were aged at 6000 psi, 430°F, 2wt% NaCl for 14 days. Model predictions show satisfactory agreement with experimental measurements.

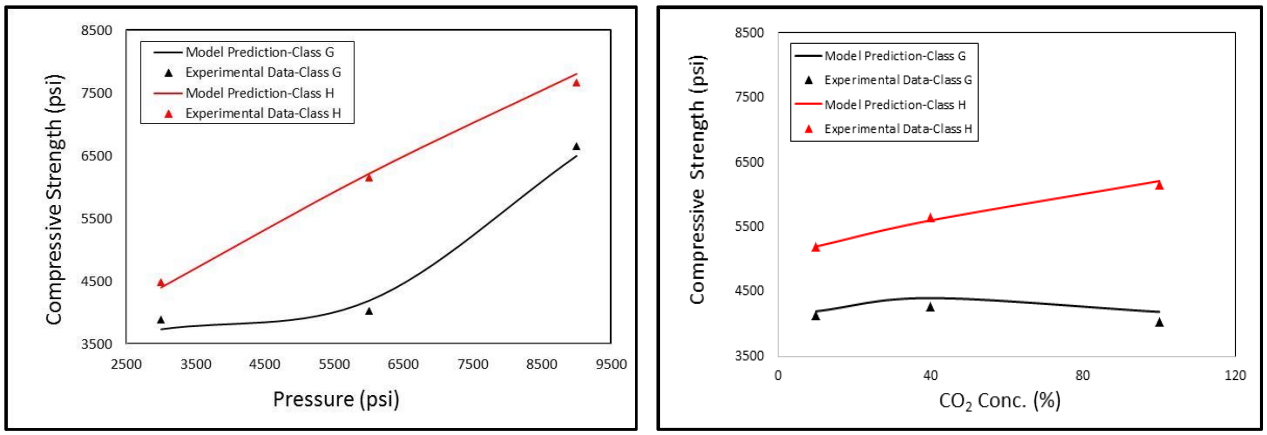

(a) (b)

Fig. 2.222: Validation of model predictions: a) Effect of pressure; and b) Effect of CO_2 concentration for Class H and Class G cements

2.6. Conclusions and Recommendations

2.6.1. Conclusions

- When exposed to pure carbonic acid environment, well cement undergoes carbonation and leaching. Carbonation reduces porosity, heals existing fractures (i.e. reduces permeability) and improves structural integrity (i.e. compressive and shear bond strength) while leaching leads to increase in porosity, permeability and loss of strength. The rate of degradation is controlled by temperature, CO_2 concentration and pressure.
- Below 225°F, solubility of CO_2 decreases with temperature. This leads to precipitation of calcite thereby improving the sealing and structural integrity of well cement. At high temperature (up to 350°F), CO_2 solubility increases with temperature. This facilitates the rate of leaching and leads to loss of zonal isolation and mechanical support for the casing. Minerology characterization also confirms structural transformation of calcium silicate hydrate at high temperature.
- As pressure increases, CO_2 solubility increases. Subsequently, calcite precipitation and dissolution ensue. Overall strength evolution is determined by aging temperature. At moderately low temperature (up to 225°F), performance of cement is improved through carbonation. At high temperature (up to 350°F), rate of degradation increases. At extremely high temperature (up to 430°F), reduction in solubility of portlandite preserves cement integrity.
- In CO_2-H_2S fluid system, cement degrades through combination of carbonation (and leaching), structural transformation and formation of secondary ettringite. At low temperature (greater

than 100°F), ettringite formation is severe; hence, it controls cement deterioration. At high temperature (greater than 225°F), ettringite dissolves and other mechanisms such as structural transformation, carbonation and leaching control the degradation process.

- In pure H_2S fluid system, expansion of ettringite is the principal mechanism through which cement degrades, especially at low temperature (greater than 100°F). At high temperature (greater than 225°F), dissolution of ettringite occurs hence structural phase transformation controls cement degradation.
- Overall, Class H cement demonstrates better integrity for zonal isolation and casing support than Class G cement because it is stronger (i.e. more carbonated than it is leached), less porous and less permeable (i.e. more CO_2-resistant) after 14 days of exposure. Model predictions agree with this observation.
- The performances of new cement formulations were tested which include hydroxyapatite (HOAP) cement, baseline cement containing 5% magnesium oxide (MGO-5), baseline cement containing microsilica, latex cement, latex-microsilica cement (LTMS) and fly ash cement. Among these cement formulations, HOAP and MGO-5 cements demonstrated the most promising potential as suitable CO_2-resistant cement formulations under HPHT condition. HOAP cement is limited in reactivity with CO_2 hence it is able to preserve and protect cement hydrates (i.e. CH and CSH) from excessive carbonic acid attack. In MGO-5 cement, magnesium oxide acted as expanding agent in the cement. Unlike calcium carbonate formed by baseline cement, it forms a less soluble magnesium carbonate ($MgCO_3$) after CO_2 attack, which minimizes its susceptibility to leaching.

2.6.2. Recommendations

- In CO_2 storage formations under HPHT condition, future wells should be designed and completed with Class H (low w/c ratio) Portland cement. However, formation integrity test should be conducted prior to cementing to determine if application of this high density API cement would not breakdown the formation. Furthermore, hydroxyapatite and MGO-5 (i.e. baseline cement containing 5% magnesium oxide) cements are also recommended for completing wells used for geological carbon storage. In addition, installation of CO_2-resistant downhole mechanical assembly in the section of the well adjacent to the storage zone is highly recommended.
- For producing wells, which were completed with Portland-based cement, cement samples should be retrieved and evaluated for structural compliance before such wells are used for CO_2 injection. In the event of non-compliance, workover remedial operations are highly recommended to ensure non-communicating seal between the storage zone and water-bearing rocks.
- Reaction of Portland-based cement with carbonated brine puts a question on its long-term durability. Therefore, the use of special cement additives such as magnesium oxide and hydroxyapatite should be considered. Although, these special cements are susceptible to thermal expansion (at high temperature) which might result in development of cracks, they can be blended with conventional cement formulations to minimize the degree of expansion.

3. TUBULAR CORROSION

3.1. Introduction

Corrosion is known as degradation of materials because of chemical and electrochemical reactions. Based on the mechanism of degradation, corrosion can be subdivided into several types including general corrosion, pitting corrosion, crevice corrosion, erosion-corrosion, galvanic corrosion, microbial corrosion, sulfide stress cracking, intergranular corrosion and other uncommon types of corrosion. Corrosion environment can be also be used to classify types such as CO_2 corrosion, H_2S corrosion, atmospheric corrosion, acid corrosion and high temperature corrosion. In the oil and gas industry, CO_2 and H_2S corrosions are two common types of corrosion, which cause a number of problems during oil and gas production. CO_2 and H_2S are the two well-known corrosive gases that are produced with formation fluid. Because of the diversity of corrosion related problems, CO_2 corrosion (sweet corrosion) is probably the material degradation mechanism most extensively assessed in this industry over the last 30 years. CO_2 is also injected into oil and gas wells for production enhancement or sequestration purposes. Corrosion control is considered as a major cost item in the industry. The total cost of corrosion in the US oil and gas industry is estimated (Heidersbach 2011) at $1.4 billion/year.

3.1.1. Overview

The corrosion of tubulars is considered as one of the major issues for exploitation of oil and gas resources containing acidic gases. The process of corrosion in brine saturated with acidic gases is complex and not fully understood, particularly under HPHT environment. A number of physicochemical phenomena such as ionic diffusion, electrochemical reaction, and dissolution of gases and corrosion products in brine are expected to affect the process of corrosion. The environment, and corrosion reactants and products play a great role in determining corrosion rate and mechanisms. Corrosion mechanisms of carbon dioxide and hydrogen sulfide are very different. High fluid velocity exacerbates CO_2 corrosion while corrosion in H_2S containing environment is considered independent of fluid velocity. Under ambient condition, H_2S corrosion is less severe than that of CO_2. Several forms of corrosion can occur in H_2S-containing environments, depending upon the tubular material, temperature, pressure, stress condition and H_2S concentration. At high temperature conditions, tubular corrosion can occur by direct reaction with H_2S gas, without the need for the presence of a liquid electrolyte. The presence of liquid electrolyte greatly facilitates the corrosion process. H_2S dissolves in water and forms a weak acid that can be highly corrosive under HPHT conditions. As a result, H_2S causes severe corrosion on oil field tubulars.

Like hydrogen sulfide, carbon dioxide forms a weak corrosive acid when dissolved in water. Corrosion products from carbonic acid do not often form a protective layer on the surface of the material. The quick removal of the corrosion products by the fluid aggravates the corrosion process. As a result, fluid velocity effects are considerable in CO_2 corrosion. However, depending on the environmental condition, a protective iron carbonate ($FeCO_3$) or Mackinawite (FeS) layer can form. In this case, the corrosion rate strongly depends on the factors that control the formation and retention of the protective layer. Without the formation of the protective layer, CO_2 corrosion rate can be very high. The corrosion rate of bare (unprotected) steel is a function of temperature, local fluid velocity (wall shear stress) and partial pressure of CO_2.

3.1.2. Statement of the Problem

Design and placement of well casings/tubulars is an important part of the drilling and completion process. Casing supports the wellbore and seals off overpressure formations. As a result, after its installation, the casing is exposed to different hydrostatic and mechanical forces, and harsh downhole environments that are conducive for acid attack and corrosion. Severe acid attack results in casing crack and failure, which may lead to uncontrolled flow of formation fluid to the surface and/or another formation. Successful placement of a casing in such wells requires better understanding of sulfide stress-cracking (i.e. a process called hydrogen embitterment) and uniform corrosion. The selection of a casing material must be based on criteria such as resistance to sulfide stress-cracking, uniform corrosion and mechanical degradation in harsh environments containing H_2S and CO_2 with water saturation.

Advanced corrosion studies are needed to evaluate the performances of oil field tubulars under downhole environments. Moreover, new materials that have the potential to resist acid attack under harsh conditions need to be investigated to provide the industry with the necessary information to select the most appropriate casing materials for a specific application.

3.1.3. Objectives

The objectives of this investigation are: i) to study stress-cracking in tubulars when simultaneously exposed to harsh downhole environment and loading conditions; ii) to investigate uniform corrosion characteristics of tubulars under borehole conditions; and iii) to study deterioration of mechanical properties of tubulars resulting from exposure to sour gases under HPHT conditions.

3.2. Sulfide Stress Cracking (SSC) Corrosion

The major corrosion problem in the oil and gas industry is associated with gases containing H_2S. To better understand the corrosion mechanisms, the solubility of hydrogen sulfide in brine and dissociation of hydrosulfuric acid have been investigated for the past two decades. The thermodynamic and kinetics of these processes are also very critical to develop models for sour gas corrosion. A number of correlations have been presented in the literature to predict solubility and dissociation constants at different pressure and temperature conditions.

3.2.1. Literature Review

Tubulars are extensively used in oil and gas resource-development and production. In some cases, reservoir fluids (oil and gas) contain H_2S, which leads to hydrogen embrittlement. This phenomenon is commonly known as Sulfide Stress Cracking (SSC). Studies on sulfide stress cracking on tubulars are limited. SSC is hydrogen embrittlement phenomenon caused by combined effect of stress and atomic hydrogen diffusion through the metal following corrosion by wet H_2S. SSC causes failure at much lower stress than ultimate tensile strength. A number of studies indicated that microstructure, hardness, applied stress and H_2S concentration are main factors, which affect susceptibility of an alloy to SSC.

3.2.1.1. Experimental Studies

SSC is the phenomenon caused by hydrogen embrittlement. Thus, hydrogen permeation into crystalline structure of a metal is important factor for SSC resistance. Tsay et al. (2005) and Kimura et al. (1996) evaluated hydrogen permeation rate of metals. The more hydrogen permeation rate, the lesser is the SSC resistance of the material. Chromium steel was found to be resistant to sour environment (Kimura

et al. 1996), even though Cr content did not increase threshold tensile stress of steel, which is required to initiate SSC. However, hydrogen permeation rate was significantly lower for Cr steel than Cr free steel. SSC resistance of steel strongly depends on its hardness, grain structure, molybdenum content, the level of cold work, environmental factors such as pH, pressure, temperature, and H_2S concentration.

Hardness

A number of studies (Kimura et al. 1996; Masouri and Zafar 2004, 2005) were conducted to relate hardness of steel and SSC resistance. Hardness has adverse effect on the SSC resistance of metals. This means that the higher the strength, the lower is the SSC resistance. NACE MR0175 specified the upper limit of steel hardness for sour gas application as 23 HRC (i.e. Hardness on Rockwell scale C). Inappropriate material selection led to premature failure of metals in sour environment. Masouri and Zafar (2005) conducted a case study on failure of V150 and L80 materials. They measured the hardness values of V150, which was found to be unsuitable for sour gas applications as per NACE MR0175 standards.

Various experiments performed by Ciaraldi (1986) showed the effects of hardness on SSC resistance of common steels. Historical development of steel grades (Bruce and Urband 1999; Waid and Stiglitz 1979) presented below demonstrates the direction of the industry toward the use of high strength steels. Grade L80 was approved by API in 1975, along with L-80 grade. Grades J-55 and K-55 were standard API grades. Grade C-90 was developed in 1979. This grade was approved by API in 1985 for sour environment. Grade T-95 was standardized by API in 1989 for sour services. C-100, C105 and C-110 are recently developed grades for sour services.

L-80, J-55 and K-55 do not have any minimum temperature limitation for operation in sour environment. These grades have good SSC resistance; however, they have lower yield strength, which limits their application in HPHT wells. C-90 and T-95 have better yield strength than L-80. According to API, tubulars must be produced as seamless pipe for sour application. In addition, C-95 has been approved by API for sour applications. It has high yield strength; nevertheless, it is difficult to produce the tubulars with controlled hardness. Furthermore, it cannot be used at lower temperature environment. C110 is recently developed steel grade. Tubular Corporation of America (TCA) performed several tests on C110 steel. Grain size testing proved that C110 have very fine grain size (ASTM 5 or finer) which is good for SSC resistance. TCA specified hardness of 25-26 for final tempered C110 tubulars (Bruce and Urband 1999). Moreover, C-90 grade has been developed using special internal and external quenching process. Previously, it was difficult to form a heavy walled material and still maintain uniform mechanical properties. However, the new internal external quenching system proved successful in maintaining uniform properties for casing and coupling stocks with wall thickness up to 1.5 inches (Waid and Stiglitz 1979).

Grain Structure and Non-Metallic Inclusions

Grain structure is one of the factors that determine SSC resistance of a metal. Austenite steels have good resistance to SSC. Studies (Tsay et al. 2005; Hashizume et al. 2000) showed improvement with SSC resistance with increase in austenite content. Austenite structure is known for hindering hydrogen embrittlement. Tsay et al. (2005) studied martensitic stainless steel (PH 13-8 Mo) to evaluate SSC resistance of the material. Four different samples were prepared by varying the aging conditions.

Samples were aged at 800, 900, 1000, 1100°F. Tensile and hydrogen-permeation rate tests were performed on each sample. For material aged at 1100°F, elongation was the highest and hydrogen permeation rate was the least. This indicates that the material has the highest SSC resistance. Further analysis showed that material aged at 1100°F had significant amount of austenite present in it. Austenite forms irreversible hydrogen traps, which impede hydrogen permeation inside the metal. In addition, the study showed the least hardness value for material aged at 1100°F.

Crack initiation and crack propagation are two most important steps in SSC. Grain structure controls crack propagation while non-metallic inclusions affect crack initiations. Various researchers (Chauveau et al. 2012; Craig 2005; Ciaraldi 1986; Tucroni et al. 2001; Cane and Cayard 1998) have studied the effect of microstructures on SSC resistance and concluded that following processes are beneficial for improving SSC resistance: i) Forming fine sized grain of prior austenite; ii) Obtaining fully martensitic structure during quenching process; iii) Tempering after quenching or cold work at suitable temperature; and iv) Reduce hardness of the material.

Cold Work

Cold work changes mechanical properties of the metals. An early experimental study (Baldy et al.1981) showed effects of cold work on mechanical properties of N-80 grade steel and C-Mn-Mo-V alloy. Mack et al. (2000) studied the effects of expansion on SSC resistance of various alloys used in manufacturing of expandable tubulars. Muraki et al. (2006) showed the effect of expansion on SSC resistance of API L-80 material. Both studies showed SSC resistance reduction after expansion. Mack et al. (2000) performed similar experiments on P-110 and L-80 specimens. The experiments were performed in two different environments: 2.5% H_2S and 100% H_2S. Results showed reduction in SSC resistance of L-80 in 100% H_2S environment after expansion but not in 2.5% H_2S. However, for P-110, SSC resistance reduction occurred both in 100% and 2.5% H_2S environments. Thus, reduction in SSC resistance after expansion depends on material type and concentration of H_2S.

Expandable casing technique has been recently developed in the oil industry. In this technique, diameter of the casing is increased after reaching bottom hole. However, the change in diameter occurring under wellbore conditions leads to change in mechanical properties of the casing and hence alteration of SSC resistance. Expanded tubulars showed change in SSC resistance after the expansion. Muraki et al. (2006) studied the effect of expansion on SSC resistance of API L80 material. C-ring and tensile tests were performed on as-received and post-expanded tubular materials. Results demonstrated the reduction of SSC resistance and strength improvement with the expansion. This reduction in SSC measurements was observed when the specimens were exposed to a sour environment with partial pressure of H_2S reaching 0.1 MPa. At low H_2S concentrations (partial pressure of H_2S less than 0.01 MPa), SSC resistance was not affected by the expansion.

Molybdenum Content

Sulfide stress cracking is a problem in oil and gas industry since high-strength steels are susceptible to SSC in sour environment. In general, high-strength steels have lower SSC resistance. Some studies have underlined importance of Molybdenum (Mo) content for environmental corrosion resistance.

Studies (Hashizume et al. 2000; Chauveau et al. 2012) showed that the SSC resistant of metals in sour environment is strongly related to depassivation pH, Mo content, austenite content and level of cold work. Depassivation pH (i.e. a critical pH value for the onset of intensive corrosion) is also a measure of performance of material in sour environment. Hashizume et al. (2000) and Chauveau et al. (2012) performed experiment to determine depassivation pH of steels. If surrounding pH is below depassivation pH, material undergoes severe corrosion. **Figure 3.1** shows result of experiment performed by Hashizume et al. (2000) using carbon steel (Steel A). For pH value of less than 3.8, corrosion rate sharply increases; however, for pH value greater than 4.0, the material showed a constant corrosion rate while the pH was varied. Thus, the depassivation pH is in between 3.8 and 4.0.

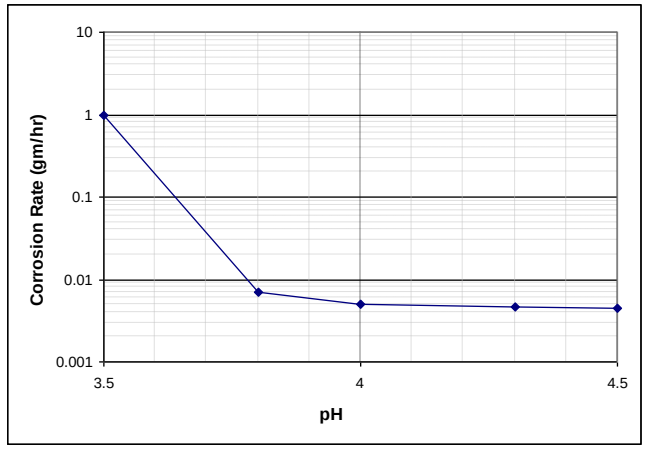

Fig. 3.1: Corrosion rate vs. pH (Hashizume et al. 2000)

A study (Hashizume et al. 2000) performed on steels with different Mo content showed that depassivation pH reduces with increase in Mo content. This suggests steel with higher Mo content to be used in sour conditions. Sour conditions results in low pH; however, this pH can be still higher than depassivation pH of material containing Mo. Hence, Mo alloys may have good resistance to SSC. Another study (Baldy et al. 1981) conducted on N-80 and special N-80 material (N-80-Mo) containing a higher Mo content is in agreement with the findings of Hashizume et al. (2000). Tensile strength tests performed on N-80 and N-90-Mo showed the improvement of threshold stress (i.e. critical stress for initiation of SSC) with Mo content.

Effect of pH

A number of SSC corrosion studied (Vera and Castro 1997; Morana and Nice 2009; Cane and Cayard 1998; Hashizume et al. 2000) were performed at room and elevated temperature using different steel grades, including Q-125, and P-110. In these studies, test specimens were subjected high stress (90% of yield strength) and harsh corrosive conditions. Results (**Table 3.1**) showed good performance of Q-125 under corrosive environment when partial pressure of H_2S was maintained below 0.005 bars. P-110 performed slightly better than Q-125. With increasing pH, the stress intensity factor reduced. This means that, as the pH increases, lesser stress is required for crack propagation in the material. Temperature effect has been studied by Cane and Cayard (1998). **Figure**

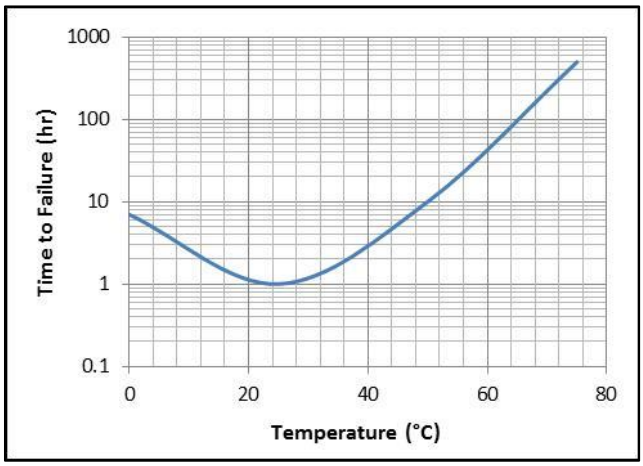

Fig. 3.2: Temperature effect on time to failure

3.2 shows temperature versus time to failure trend. High temperatures (greater than 25°C), improve the life of the material. However, this trend changes at low temperatures (less than 25°C).

Table 3.1: Comparison of P-110and Q-125 performance

	P110			Q125		
	pH			pH		
P_{H2S} in bars	3.5	4.5	5.5	3.5	4.5	5.5
0.001	-	-	-	NF	NF	
0.005	NF	-	-	-	NF	-
0.010	452	627	NF	-	575	NF
0.100	-	21-38	NF	-	-	72
0.500	-	-	25	-	-	-

NF = no failure in 720 hours

Effects of Temperature and Material Composition

Szklarz (1998) studied SSC resistance of tubulars in underbalanced drilling using Double Cantilever Beam (DCB) test. SSC resistance of L-80A, L-80B, X95, C105 and S135 materials were evaluated. Composition of each alloy is given in **Table 3.2**. Experiments were performed under simulated downhole conditions and standard conditions as recommended by NACE. Simulated conditions consist of an autoclave pressurized at 27.6 MPa with different test temperatures. The pH of test solution was set to 3. Corrosion coupons were completely submerged into test solution and solution was stirred at 500 rpm.

Table 3.2: Compositions of steel alloys (Dezhi et al. 2012; Tucroni et al. 2001; Szklarz 1988)

	L80-A	L80-B	X95	C105	S135	C110	HSLA
C	0.27	0.27	0.28	0.34	0.39	0.26	0.22-0.28
Si	0.27	0.2	0.27	0.23	0.22	0.22	0.16-0.3
Mn	1.36	1.34	0.45	0.65	0.62	0.46	0.36-0.5
P	0.011	0.011	0.01	0.016	0.013	0.011	50-100 ppm
S	0.01	0.003	0.005	0.003	0.006	0.002	10-30 ppm
Cr	0.79	0.003	1	1.02	1.09	0.45	0.9-1
Ni	0.02	0.003	-	-	1.12	0.04	
Mo	0.18	-	0.3	0.16	0.22	0.72	0.6-0.7
Al	0.028	0.027	-	0.006	0.017	0.016	
Cu	0.01	0.003	-	-	-	0.1	
Ti	-	-	-	-	-	0.01	0.01-0.025
V	-	-	-	-	-	0.08	
Nb	-	-	-	-	-	0.015	0.02-0.035

Results of experiments show that the critical stress intensity factor (K_{ISSC}) increases with temperature (**Fig. 3.3**). Increase in K_{ISSC} implies that more stress is required for crack to propagate through coupons as the temperature increases. Thus, increase in temperature leads to increase in SSC resistance. In addition, the figure compares performance of different alloys. It can be deduced that L-80A and L-80B showed best performance in sour environment. S135 exhibited poor SSC resistance. X95 performed better than S135, however, not as good as L-80 alloy.

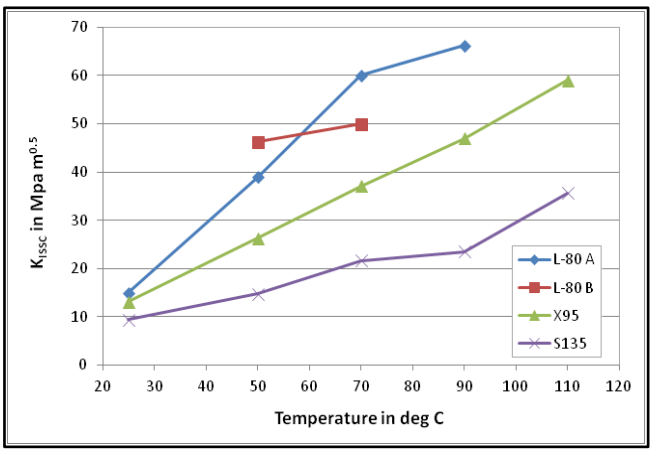

Fig. 3.3: Effect of temperature on critical stress intensity factor for different materials (Szklarz 1998)

Effect of Inhibitors

Deeper drilling makes the use of high strength steel tubulars mandatory. Various factors, which affect the SSC resistance, were listed in previous. Apart from metallurgical and environmental factors, some researchers have studied the impact of corrosion inhibitors against SSC. Inhibitors are often added into drilling fluid. The function of the inhibitors is to reduce the concentration of hydrogen at the metal surface. Zeng et al. (2012) and Szklarz (1998) have observed effects of inhibitors on SSC resistance of steels. DCB tests were performed by Zeng at al. (2012) using C110 material to study the impact of inhibitors on the SSC resistance of C110. Results showed significant increase in the value of K_{ISSC} when inhibitors were used. Thus, more stress is required for crack propagation in presence of inhibitor. Szklarz (1988) observed effect of amine inhibitor on SSC resistance L-80A, L-80B, X95, C105 and S135 materials. Composition of each alloy is given in Table 3.2. Different concentrations of amine inhibitor were used in the study. **Figure 3.4** depicts the effect of amine inhibitor concentration on K_{ISSC}. As the inhibitor concentration increased, the K_{ISSC} values increased indicating improvement of SSC resistance. Similar trends were observed for all the materials considered in the study. Thus, it can be concluded that addition of amine inhibitor helps against sulfide stress cracking.

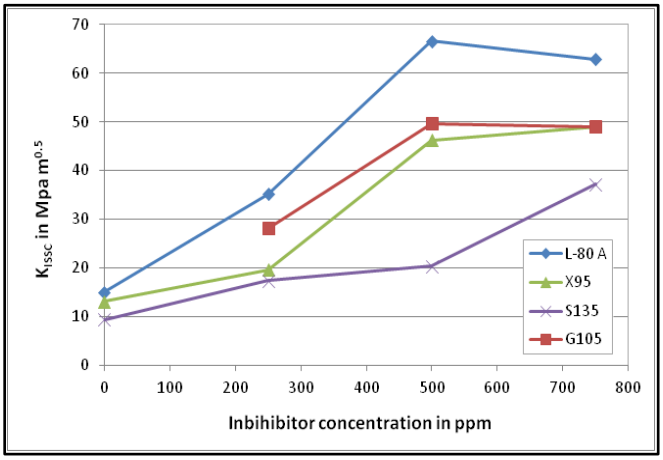

Fig. 3.4: Effect of inhibitor concentration on Kissc for different materials at 250°C (Szklarz 1998)

3.2.1.2. Theoretical Background

Sulfide stress cracking (SSC) is hydrogen embrittlement phenomenon caused by combine effect of stress and atomic hydrogen penetration into the metal lattice following corrosion by wet H_2S. Conditions that

favor sulfide stress cracking include: i) tensile stress loading imposed by either applied forces or residual stresses; ii) susceptible material; and iii) adsorption of atomic hydrogen via exposure to an environment containing a sufficient quantity of hydrogen sulfide.

Chemical Reactions Involved

Often sulfide stress cracking leads to cathodic cracking. Metals react with H_2S forming atomic hydrogen and metallic sulfides at the surface. During SSC corrosion, free H+ ions in the aqueous solution take away electron from the metal. Those H^+ ions, which take away electrons form H_2 molecule. If the concentration of H_2 at surface is sufficiently high, then hydrogen atoms diffuse through the metal leading to embrittlement. The cracking occurs, when critical concentration of H_2 diffusion is reached and the tensile stress level is above the threshold value for SSC to occur.

Sulfide stress cracking (SSC) is one the major issues in the oil and gas Industry limiting the applications of high strength steels and steel alloys. Sulfide stress cracking involves complex corrosion mechanism. The following chemical reactions show initiation of SSC at the steel surface:

Step 1: H_2S dissociation in water

$H_2S \rightarrow 2H^+ + S^{2-}$ ..... (3.1)

Step 2: Oxidation of steel in presence of water

$Fe \rightarrow Fe^{2+} + 2e^-$ ..... (3.2)

Step 3: Reduction of Hydrogen ion

$H^+ + 2e^- \rightarrow 2H$ ..... (3.3)

Step 4: Ferrous ion and sulfide ions combine to form H_2S

$Fe^{2+} + S^{2-} \rightarrow FeS$ ..... (3.4)

Overall reaction is given by:

$H_2S + Fe \rightarrow 2H + FeS$ ..... (3.5)

Furthermore, the first four reactions represent mechanism for localized corrosion attack. Hydrogen ions reduce to hydrogen atoms. Some of the atoms combine to form hydrogen molecule while others remain as free hydrogen atoms and enter into crystalline structure of steel and its alloys, resulting in the embrittlement of the metal, which leads to SSC. Thus, it can be seen that modeling of SSC must consider all these reaction steps and ionic transport processes. Therefore, in addition to the reactions, the transport processes should be considered in the model.

Mechanism of Sulfide Stress Cracking

Sulfide stress cracking (SSC) and stress corrosion cracking (SCC) are the two modes of material failure, which are very closely related to each other. It is important to understand the mechanisms involved in destruction of the material during SSC and SCC. **Figure 3.5** presents mechanism of stress corrosion cracking occurring in carbon steel. It shows a metal piece under tensile stress, which is protected by a cathodic protection layer. However, due to stretching, cathodic protection layer is removed and a small crack forms. Then, the crack is filled with corrosive solution.

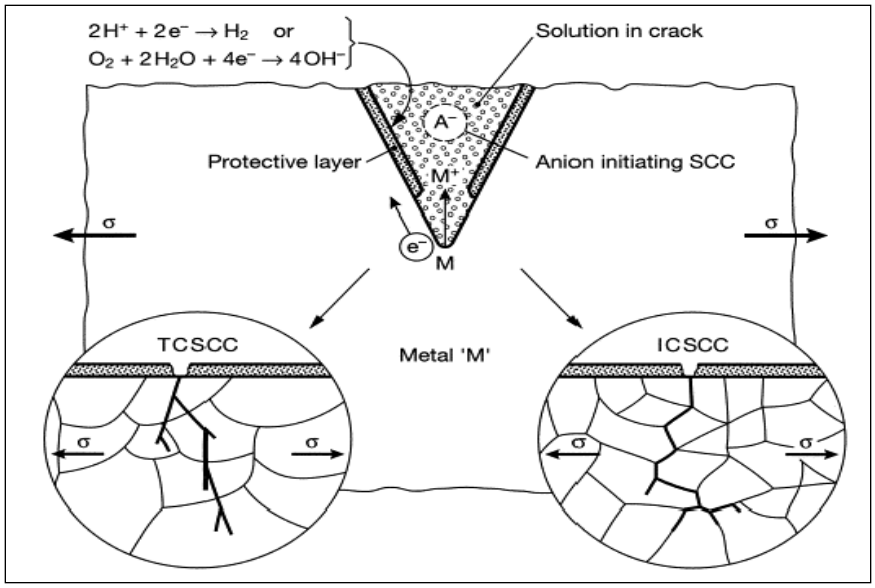

Fig. 3.5: Stress Corrosion Cracking Mechanism (Heidary et al. 2008)

Once exposed to corrosive environment, metals have a tendency to oxidize and leave free electrons on their surface. The free electros are absorbed by hydrogen ions, thereby forming hydrogen molecules as described below. Hydrogen molecules formed in the process do not interact with the metal.

$$M \longrightarrow M^{+} + e^{-} \quad \text{.....} \quad (3.6)$$

$$H^{+} + e^{-} \longrightarrow H \quad \text{.....} \quad (3.7)$$

$$H + H \longrightarrow H_2 \quad \text{.....} \quad (3.8)$$

Sulfide stress cracking has similar mechanism as SCC; however, the main difference is that, it occurs in presence of hydrogen sulfide (H_2S). The presence of H_2S hampers the reaction shown in Eq. (3.7). This leads to increase in concentration of hydrogen atoms near metal surface. As a result, small hydrogen atoms enter into lattice structure of the metal to occupy dislocations present in the structure. This leads to embrittlement of the metal leading to its failure. Furthermore, it can be seen that with increase in dislocation (caused by cold work and manufacturing defect), the susceptibility of metal towards SSC increases.

Stress Distribution in Minipipe

Cernocky et al. (2005) performed minipipe tests to find out SSC resistance. Similar experiments are performed in this project. Minipipes are subjected to tri-axial stress unlike NACE method, in which the specimen is under a uniaxial stress load.

For stress distribution purpose, minipipe can be treated as pressure vessel. In the past, a closed minipipe specimen was used by Cernocky et al. (2005). When ends of mini pipe are closed, internal pressure of fluid also contributes to overall axial tension. As a result, the following stresses develop in the minipipe: i) axial stress; ii) hoop stress; and c) radial stress. Thus, minipipe is under tri-axial stress

state similar to field loading conditions. All the above stresses can be combined to get von Mises stress. Cernocky et al. (2005) used von Mises stress criteria for minipipe failure. Stress levels are different for inside and outside part of mini pipe. Pressure inside closed mini pipe creates axial tension. Thus, total axial tension is given by:

$$Total\ Tension = Pi * \frac{\pi {D_i}^2}{4} + \text{ Frame tension} \quad \text{..... (3.9)}$$

Axial stress is same across the thickness and given by:

$$\sigma_a = \frac{Total\ Tension}{\frac{\pi({D_o}^2 - {D_i}^2)}{4}} \quad \text{..... (3.10)}$$

Hoop stress varies across the thickness of a minipipe. It is dependent on radial distance from centre. The generalized equation for hoop stress is given by:

$$\sigma_h = \frac{({P_i}^2 {r_i}^2 - {P_i}^2 {r_o}^2) * r^2 - {r_i}^2 * {r_o}^2 * (P_o - P_i)}{({r_o}^2 - {r_i}^2) * r^2} \quad \text{..... (3.11)}$$

The above equation can be simplified for inside of pipe by substituting r = r_i. Thus, hoop stress acting on inside of the minipipe is:

$$\sigma_{hi} = \frac{({r_i}^2 + {r_o}^2) * {P_i}^2 - 2 * {r_o}^2 * P_o}{({r_o}^2 - {r_i}^2)} \quad \text{..... (3.12)}$$

Similarly, the hoop stress acting on outside of the minipipe can be calculated as:

$$\sigma_{ho} = \frac{2 * {r_i}^2 * P_i - ({r_i}^2 + {r_o}^2) * {P_o}^2}{({r_o}^2 - {r_i}^2)} \quad \text{..... (3.13)}$$

Radial stress also varies in the minipipe. Generalized equation for radial stress is expressed as:

$$\sigma_r = \frac{({P_i}^2 {r_i}^2 - {P_i}^2 {r_o}^2) * r^2 - {r_i}^2 * {r_o}^2 * (P_o - P_i)}{({r_o}^2 - {r_i}^2) * r^2} \quad \text{..... (3.14)}$$

Hence, radial stresses acting inside and outside of the minipipe are: $\sigma_{ri} = -P_i$ and $\sigma_{ro} = -P_o$, respectively. All the above stress equations can be combined to determine the van Mises stress as:

$$\sigma_{von\ Mises} = \frac{1}{\sqrt{2}} * \sqrt{(\sigma_h - \sigma_r)^2 + (\sigma_h - \sigma_a)^2 + (\sigma_a - \sigma_r)^2} \quad \text{..... (3.15)}$$

Cernocky et al. (2005) theoretically studied the distribution of stresses on minipipe with ID of 0.687” and OD of 0.9”. They considered outside and inside pressures of 0 and 19,000 psig, respectively. **Figure 3.6** shows theoretically calculated stress distribution in the minipipe wall. Results show that the

von Mises stress (combined stress) is maximum in the inner part and greater than the axial stress.

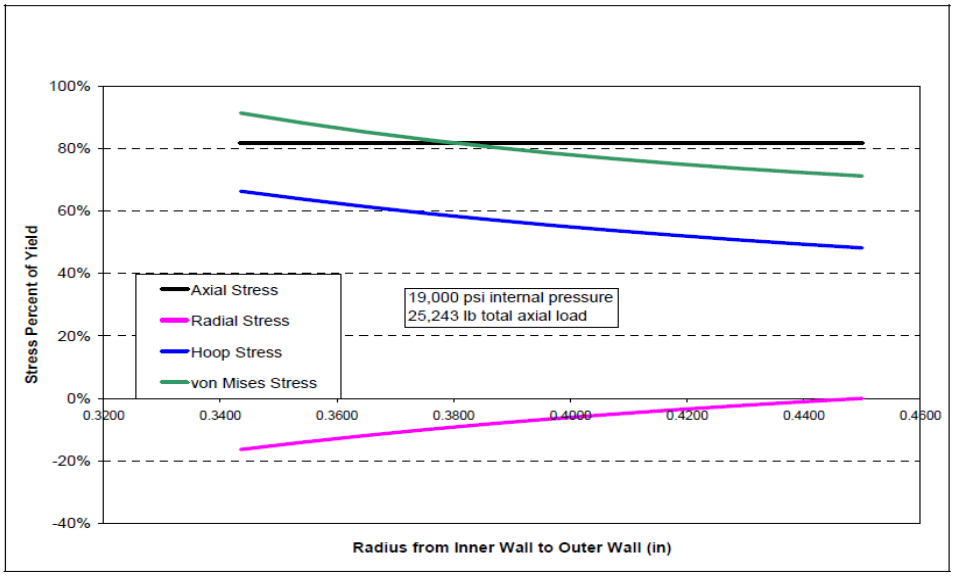

Fig. 3.6: Stress distribution in minipipe wall (Cernocky et al. 2005)

3.2.1.3. Measurement Techniques

Sulfide Stress Cracking is phenomenon, which leads to failure of materials at the stress below their yield strength. Steel alloys with high strength are more susceptible to SSC. Failure of pipeline/casing due to SSC can be harmful to the environment as well as personnel since it will lead to leak of H_2S. In order to evaluate SSC resistance of metals, different methods have been developed including: i) tensile test; ii) Double Cantilever Beam (DCB) test; iii) C-ring test; iv) Crack propagation test; and v) Four Point Bend (FPB) Test and vi) Microstructural analysis. These tests are most commonly used method for the SSC resistance evaluation.

Tensile Test

Tensile test has been used by Kim et al. (2010), Kimura et al. (1996) and Tsay et al. (2005) for evaluating SSC resistance of different steel alloys. According NACE TM0177, during tensile testing, the specimen is exposed to corrosive environment while subjected to tensile stress. The standard corrosive environment is defined as standard solution saturated with H_2S gas. **Figure 3.7** shows a setup for typical SSC test. During experiment, H_2S gas is continuously bubbled into the test solution. Standard experimental duration is 720 hours or until the sample fails. Sample failure time and stress at failure point are recorded as SSC results. The lesser the duration of failure, the lesser the resistance to sulfide stress cracking.

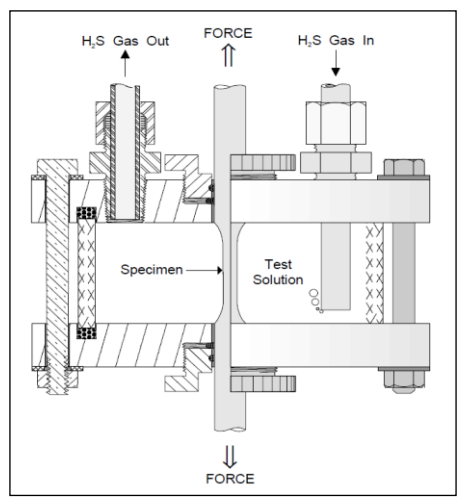

Fig. 3.7: Tensile test specimen in an environmental chamber (Kim et al. 2010)

In standard NACE tensile test involves keeping the specimen in corrosive environment under tension. Specimen

is subjected to 80-90% of its specified minimum yield strength (SMYS). NACE recommends using standard corrosive solution (5% of NaCl and 0.5% glacial acetic acid) saturated with H_2S. Temperature is maintained around 85°F and pH is maintained in the range of 2.5 to 3.5. Low pH tests provide conservative results since they increase vulnerability to SSC. During the test, if the specimen fails before 30 days, the test is stopped. Results are reported as time required for failure under a given stress condition. Samples that do not fail in 30 days are etched with Nital solution. Then, they are cross-sectioned and visually examined using a microscope for presence of cracks. Conclusions are drawn based on presence of crack or failure of specimen. Presence of cracks or failure at particular applied tensile stress shows that material is not suitable for applications in sour environment under high stress condition (i.e. more than or equal to the tensile stress applied during SSC test). If the cracks do not develop, then the applied stress is below threshold stress of material. This means the material can be used safely up to the stress level used in the test. Thus, the aim of NACE Method A is to determine threshold stress for the material. NACE has made it mandatory for the manufacturers to perform Method A test on all the materials before using them in the field.

Crack-initiation (rupture limit) and corrosion rate measurements are common techniques used to evaluate the corrosion resistance of oil field tubulars. During crack-initiation experiments, pipe specimens are subjected to tensile stresses they experience in regular well service. The tests are conducted using a real-pipe (**Fig. 3.8**) or mini-pipe (**Fig. 3.9**) specimen that has geometric similarity with the real pipe. Ten years ago, API carried out crack-initiation experiments (Maldonado and Bruno 2005) using real-pipe specimens to evaluate the accuracy of the Failure Assessment Diagram (FAD) in a sour gas environment. The FAD equation defines a load-stress intensity envelope within which a material is not expected to fail under normal HPHT well conditions. The experiments demonstrated that the FAD equation is inadequate to predict the load-stress intensity envelope in a sour gas environment. Test specimens failed at exceptionally low percentages of historical API/ISO pipe performance ratings.

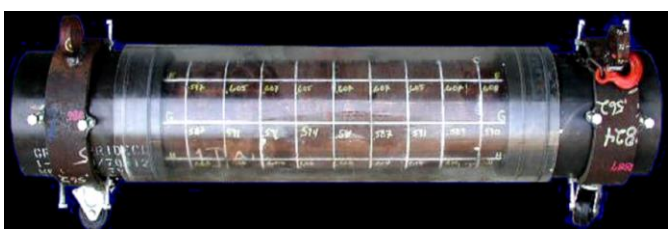

Fig. 3.8: Real-pipe specimen (Maldonado and Bruno 2005)

Fig. 3.9: Mini-pipe specimen (Cernocky et al. 2007)

In addition to the full-scale study, crack-initiation of tubulars was investigated (Edwards and Espelid 1997; Cernocky et al. 2005; Cernocky et al. 2007) using mini-pipes. One of the studies conducted on mini-pipe (Cernocky et al. 2007) showed good agreement with full-scale API pass-and-fail tests. Mini-pipes exposed to H_2S and loaded to the same percentage of the yield pressure as the full-size casing failed, while the ones loaded to a lower percentage of the yield did not. Mini-pipe tests of the same material demonstrated that the pipe performs significantly better under one-sided H_2S exposure than under two-sided (i.e. internal–external H_2S exposure). Another study (Edwards and Espelid 1997) evaluated the sulfide stress-cracking (SSC) resistance of different casing and drill pipe materials corresponding to API 5D/5CT grades C-95 to S-135. Temperature and H_2S concentration in the gas phase

were varied from ambient to 220°F and 100 to 0.1% by mol, respectively. The results showed that the SSC resistance of specially modified carbon steels that were marketed as "sulfide resistant" was poorer than anticipated. The study emphasized the need for further investigation and testing of steel materials used in the field.

Crack Propagation Test

NACE Method D provides threshold crack intensity, which is the minimum stress intensity required at the tip of preexisting crack for its propagation (NACE 2005). A pre-cracked mini-pipe specimen can provide the threshold crack intensity to evaluate accuracy of fracture mechanics models. An experimental setup developed by Cernocky et al. (2005) was used to perform mini-pipe tests to evaluate performance of material in sour environment. Combined effects of principal stresses (axial, hoop and radial stresses) on crack initiation and its propagation in presence of H_2S were determined. Results showed significant data scatter due to bending moment, which is generated from the force imbalance. As a result, bending moments were measured and monitored during experiment to examine their effect on the SSC measurements.

The setup developed by Cernocky et al. (2005) uses a frame with four springs (**Fig. 3.10**) for applying the axial load required for the test. These springs with carbon steel are needed for loading process. The carbon steel rod when loaded beyond proportional limit may show presence of creep strain. This strain is often small but if rods have high stiffness, even small strain can unload specimen significantly. This leads to erroneous results. During the test, H_2S exposure was on the outside of the mini-pipe under low-pressure condition. H_2S exposure direction can be on one side or both sides of a mini-pipe specimen. Tests showed failure pattern can vary with the exposure direction. This is useful to understand mechanism of H_2S corrosion. Cernocky et al. pressured the internal part of the mini-pipe using water and NACE test solution. Mini-pipe internal pressure was monitored continuously using pressure sensor placed inside the specimen. In addition, temperature in the room was monitored.

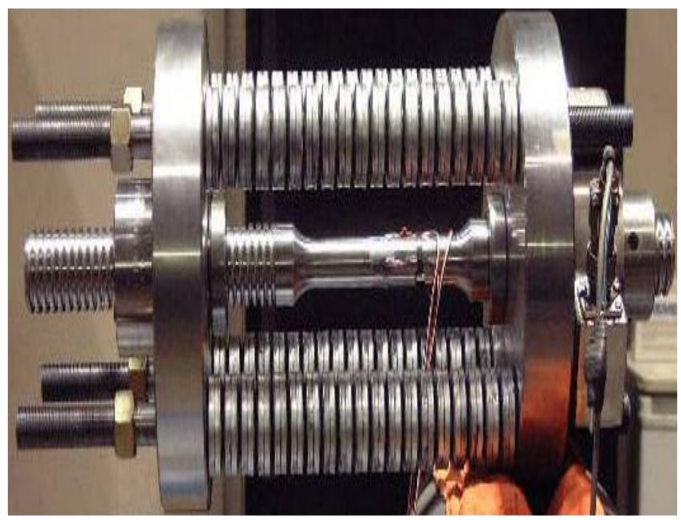

Fig. 3.10: Mini-pipe without sleeve in frame (Cernocky et al. 2005)

Recently conducted SSC study (Been and Crozier 2014) used axial force, which is applied using a motor (**Fig. 3.11**). Mini-pipe specimens were exposed to H_2S on their outside. Experiments were performed using specimens made of API casing (L-80), placed in NACE solution B saturated H_2S containing gas at 25 psi. Solution pH was ranging from 3.4 to 3.6. The specimens were subjected to stress level of 90% yield strength. H_2S concentration in the gas phase and temperature were varied during the course of the study.

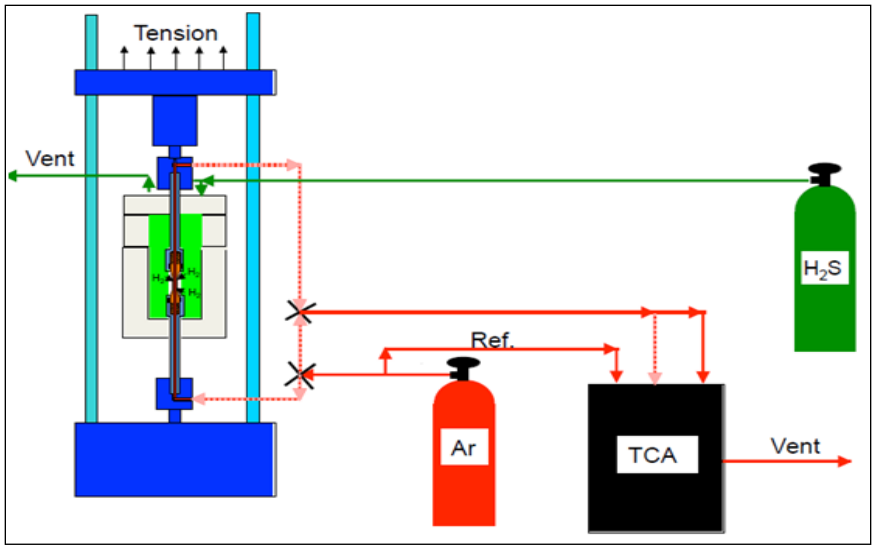

Fig. 3.11: Experimental set up for testing mini-pipe specimens (Been and Crozier 2014)

Results showed that the rate of hydrogen permeation (**Fig. 3.12**) increases with time, specimen stress loading level and H_2S pressure. Higher hydrogen permeation rate means higher susceptibility to SSC. Increase in temperature, initially resulted in rapid increase in hydrogen permeation, followed by a more gradual decrease. Similar observations were reported by other studies (Morana and Nice 2009; Hashizume et al. 2000). The studies found that increase in H_2S concentration increases susceptibility towards SSC.

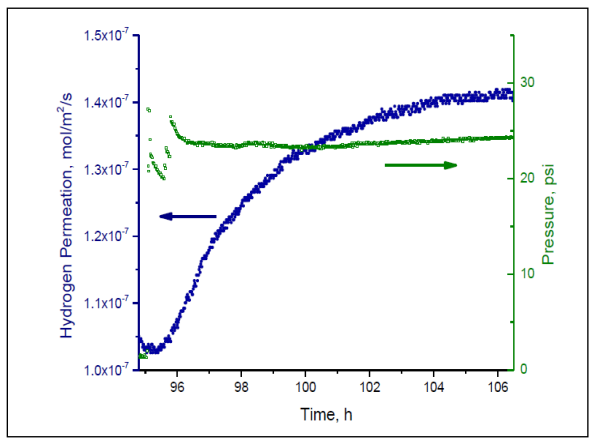

Fig. 3.12: Hydrogen permeation vs time (Been and Crozier 2014)

Cane and Cayard (1998) studied the effect of temperature on SSC. They found that SSC susceptibility is the highest near room temperature and as temperature increases susceptibility decreases. Moreover, results from mini-pipe tests were similar with those obtained from standard NACE tests that use a cylindrical rod specimen.

DCB Test

Kimura et al. (1996) used DCB test to determine the SSC resistance of steel alloys. As per NACE TM0177, DCB test gives critical stress intensity factor (i.e. K_{ISSC}). DCB test is similar to the tensile test. It is done in vessel containing standard solution saturated with H_2S. A groove is made on the specimen and then it is fatigue pricked. Initial arm displacement is measured, which is the distance between the holes of two arms. A wedge is inserted into the groove and is flushed with end of specimen until desired arm displacement is achieved. For each material, standard arm displacements are given in NACE TM0177. Wedge dimensions are based on arm displacement. Crack length and pressure required for specified displacement are measured. Based on these parameters, K_{ISSC} is calculated.

C-ring Test

C-ring test is also one of commonly used SSC measuring techniques (Muraki et al. 2006). NACE TM0177 provides a detailed procedure for standard C-ring test. As the name suggest, specimen is C-shaped. **Figure 3.13** shows typical specimen for C-ring test. Holes are drilled at 180° on the specimen. During the C-ring test, a bolt is inserted into the ring holes and tightened to increase the stress level. The ring and bolt assembly is kept in vessel containing standard solution saturated with H_2S. Experimental duration is 720 hours or until the sample exhibit failure. Sample failure time and stress at failure is noted down as result.

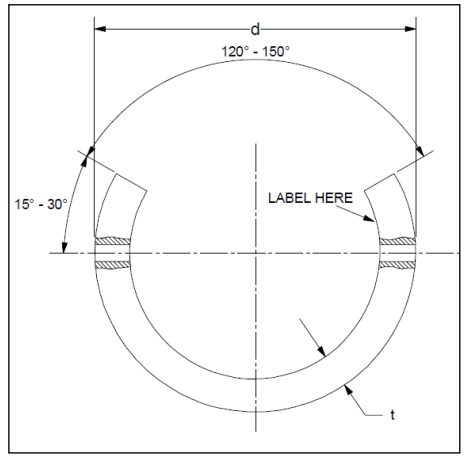

Fig. 3.13: C-ring test specimen (NACE TM0177)

Four Point Bend Test

Four Point Bend (FPB) test is another approach to determine SSC resistance of material. The FPB approach facilitates testing of small area because of its compact size (NACE TM0177 2005). **Figure 3.14** shows experimental setup for FPB test. A pusher block applies the push force from the top. The force is applied using action bolts and measured using a load cell. Four blocks are placed above and below the specimen as shown in the figure. Lower part of the figure shows bending stress distribution. The maximum stress is constant between the inner two points. Stress outside these inner points linearly reduces to zero.

During the experiment, the entire test assembly is immersed for 720 hours in NACE solution, which is saturated with H_2S at a desired pH. The test is often conducted at room temperature since the SSC rate is the highest. Test results are presented as failure or no failure case. The maximum stress developed during four point bending stress test is given by:

$$S = 3aF/(bd^2), \quad \ldots\ldots\ldots\ldots\ldots\ldots\ldots\ldots (3.16)$$

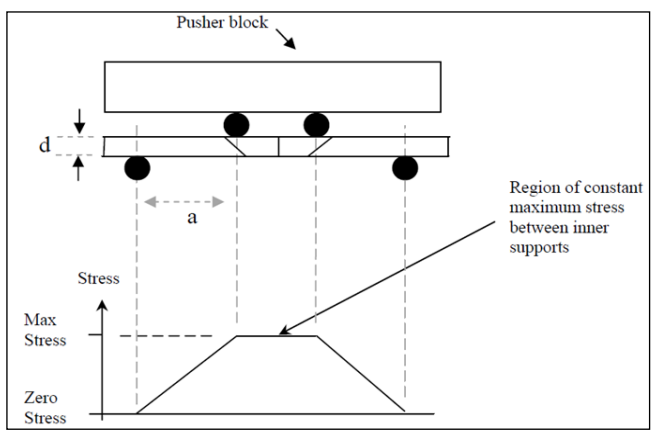

Fig. 3.14: FPB test experimental set up (Skogsberg et al. 2001)

where, S is tensile stress on bottom of tensile stress (psi); a is distance between outer support and nearest inner support (in); F is applied force (lbf); and b is testing sample width (in).

Microstructural Analysis

SSC is affected by microstructure and hardness of the material. In addition, some alloys are more resistant to SSC than steel (Kimura et al. 1996), which makes chemical composition analysis important factor for SSC resistance evaluation.

Several studies (Masouri and Zafar 2004; 2005) performed microstructural analysis using Scanning Electron Microscope (SEM). The SEM technique gives information about grain structure of the

material. In addition, inter-lath layer constituents deposited on grain boundaries can act as nucleation site for cracks. Hence, microstructure examination is essential.

Slow Strain Rate Test

Although the tensile test is the most widely used methods, it requires long test duration (approximately 1 month). This limits number of specimens that can be tested. Therefore, a method with shorter test duration is desired to investigate SSC.

Slow strain rate test is commonly referred as Constant Extension Rate Test (CERT). The test involves straining the samples slowly until failure. Usually, this test is used for stress cracking corrosion (SCC). The corrosion mechanisms of SCC and SSC are closely related to each other. Thus, with slight modification, this test method can be used for the use in measuring the SSC resistance. Existing literatures show that some researchers have used CERT for SSC testing. The common procedure is to strain the specimen until it fails in air and in corrosive environment (H_2S). Comparing stress versus strain relationships obtained under different conditions reveals if the material has undergone SSC. CERT has laid the foundation for a new testing approach, which required short time (7 – 10 days)

Horstemeier et al. (2010) performed SSC experiments on grades with SMYS of 110, 125 and 140 ksi. Both NACE Method A and CERT tests were performed on the materials in order to validate use of CERT for SSC resistance measurement. SSC resistance tests were conducted using nine different materials, which were similar in chemical composition but different in hardness and strength (**Table 3.3**).

Table 3.3: Properties of tested materials (Horstemeier et al. 2010)

Designation	Material	Grade	Origin	YS (ksi)	UTS (ksi)
A	C110	110	Pipe	113	127
B	C110	110	Pipe	113	129
C	C110	110	Pipe	121	134
D	35C-Mo	125	Plate	134	142
E	35C-Cr	125	Plate	131	148
F	45C-Mo	125	Plate	134	141
G	45C-Mo	140	Plate	147	155
H	35C-Mo-Si-Mn	140	Plate	148	155
I	45C-Mo-Si-Mn	140	Plate	151	158

Furthermore, CERT experiments were used by Koh et al. (2003) to study SSC of steels. API grade steels were used to make four different type of microstructure, which have similar chemical composition but different heat treatment. Results obtained from CERT and other methods are compared in **Fig. 3.15**. Each material has two curves. One curve presents stress-strain data of a sample exposed to corrosive solution while other curve shows specimen behavior when exposed to air. All the samples, which were exposed to corrosive solution, showed brittle failure (reduced plastic strain to failure) meaning all of them were susceptible to SSC.

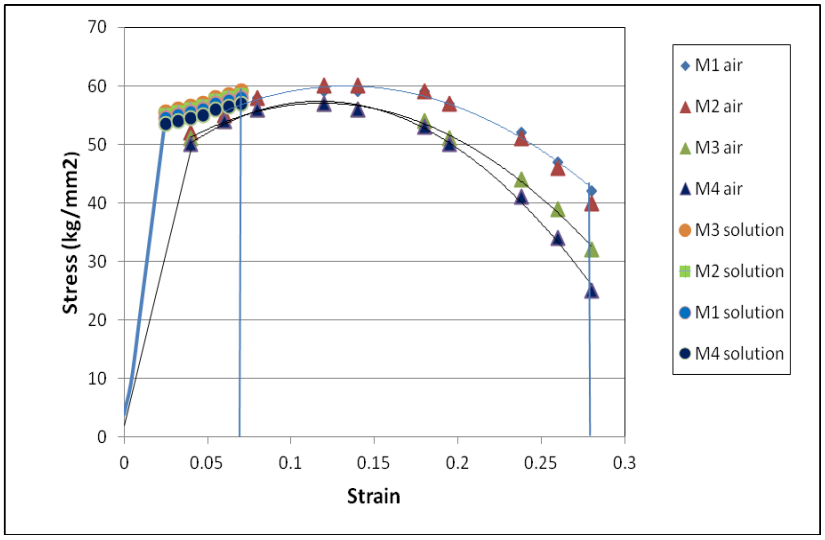

Fig. 3.15: Stress vs. strain for API grade steels (Koh et.al. 2003)

Another similar study was conducted by Kermani and MacCuish (1990). CERT tests were performed to determine SSC resistance of API grade steel (L-80). Tests were performed in corrosive NACE solution with H_2S partial pressure of 100 KPa and pH of 5.5 and 3.5, and in air. **Figure 3.16** shows stress versus strain data for the three cases. Samples showed more brittle failure in presence corrosive solution than in presence of air. Thus, change in ductility can be measured as plastic strain to failure (PST) to detect vulnerability towards SSC.

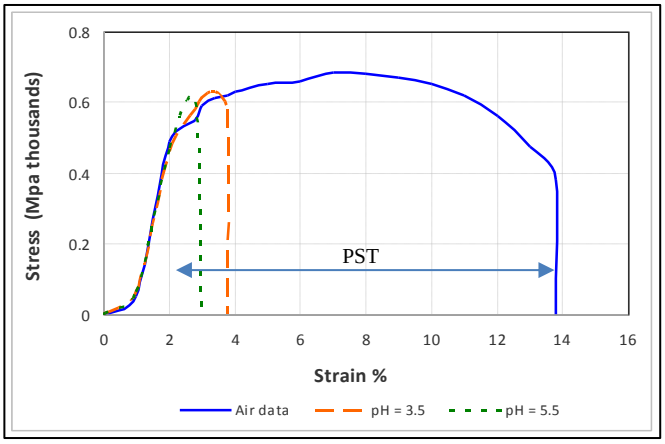

Fig. 3.16: Stress vs. strain curves for L-80 in NACE solutions and air (re-drawn from Kermani and MacCuish 1990)

Modified Slow Strain Rate Test

Based on the slow strain-rate-test technique, a new method for SSC testing has been established during this investigation. The method involves three main steps:

Step 1: sample is strained until the stress reaches 80% of SMYS in air.
Step 2: Sample kept under tensile stress (85% of SMYS) in corrosive solution for 8 days.
Step 3: After 8 days, the sample is taken from the corrosive solution and strained to failure in air.

Step 2 is closely related NACE standard tensile test. However, it lasts for 8 days. Materials which are susceptible to SSC expected to develop crack in first one to 200 hours of exposure (Kermani and MacCuish, 1990); hence, time interval of 8 days is selected. Hydrogen penetrates the steel matrix leading to occurrence of H_2S embrittlement. However, if material fails during Step 2, there is no need for Step 3. Samples that do not fail in Step 2 are strained to failure in Step 3. This step is similar to CERT

test. If material is susceptible to SSC, it shows measurable change in ductility. Moreover, in Step 1, tensile stress tests are performed on material before exposing them to corrosive solution. If a material shows shift in stress-strain curve during Step 3, then it is an indication of susceptible to SSC under given conditions.

3.2.2. Experimental Investigations

3.2.2.1. Test Conditions

Experimental study on sulfide stress cracking (SSC) behavior of three API carbon steels (T95, C110 and Q125) has been performed. **Table 3.4** summarizes all SSC tests conducted in the study. It provides detailed information on experimental conditions in which specimens were exposed.

Table 3.4: Specimen corrosion testing conditions

Test #	Label	Temp. (°F)	Pressure (psi)		Gas Composition			Time	Remarks
			Inside	Outside	H_2S (ppm)	CH_4 (%)	CO_2 (%)	(Days)	
1	01-C110-07/25-08/06	100	6000	4000	0	100	0	15	
2	02-C110-08/25-08/25	-	-	-	-	-	-	-	Baseline for C110
3	03-C110-08/27-09/03	100	6000	4000	270	90	10	7	Sample failed after 7 days
4	04-C110-09/05-09/12	100	6000	4000	300	100	0	7	
5	05-C110-09/05-09/13	100	6000	4000	285	95	5	7	
6	06-C110-09/05-09/14	100	6000	4000	270	90	10	7	Brine completely leaked out
7	07-C110-10/17-10/24	100	6000	4000	255	85	15	7	
8	08-C110-10/28-11/04	100	6000	4000	270	90	10	7	
9	09-C110-11/05-11/12	100	6000	4000	293	97.5	2.5	7	
10	10-C110-11/13-11/20	100	6000	4000	270	90	10	7	Sample failed after 7 days
11	11-C110-12/02-12/09	100	6000	4000	255	85	15	7	
12	12-Q125-11/24-	-	-	-	-	-	-	-	Baseline for Q125
13	13- Q125-11/24-	100	6000	4000	270	90	10	7	
14	14- Q125-12/10-	100	6000	4000	0	100	0	7	
15	15 - T95-12/10-12/10	-	-	-	-	-	-	-	Baseline for T95
16	16- Q125-12/17-	100	6000	4000	300	100	0	7	
17	17 - T95-01/05-01/12	100	6000	4000	0	100	0	7	
18	18 - T95-01/13-01/20	100	6000	4000	300	100	0	7	
19	19- Q125-01/20-	100	6000	4000	293	97.5	2.5	7	
20	20 - T95-01/27-02/03	100	6000	4000	293	97.5	2.5	7	
21	21-Q125-0203-0210	100	6000	4000	300	95	5	7	
22	22-Q125-0210-0217	100	6000	4000	300	85	15	7	
23	23-T95-0217-0224	100	6000	4000	300	95	5	7	
24	24-T95-0224-0303	100	6000	4000	300	90	10	7	
25	25-T95-0311-0318	100	6000	4000	300	85	15	7	
26	26-Q125-0325-0401	100	6000	4000	300	75	25	7	Sample failed after 7 days

Twenty six mini-pipe specimens were tested varying CO_2 concentration and steel grade. Internal and external pressures of specimen were maintained at 4000 and 6000 psi, respectively. Carbon dioxide concentration was varied from 0 to 15%. Q125 carbon steel was tested up to 25% CO_2. H_2S and salt concentrations were 300 ppm (roughly) and 2% NaCl. Temperature was maintained at 100°F. SSC occurs due to simultaneous exposure of corrosive environment containing H_2S and high tensile stress loading. In order to create SSC condition, all specimens were exposed to stress level of 85% of their minimum yield strength (i.e. specified by the manufacturers). The specimens were cleaned before the test. Mechanical properties of baseline samples (un-corroded) were measured using tensile strength testing (TST) apparatus. Ultimate tensile strength (UTS) and plastic strain to failure (PSF) were obtained from TST experiment. Hence, they were only measured after exposing specimens to corrosive environment. These are key measurements, which are correlated with sulfide stress cracking phenomenon, which occurs at high tensile stress loading.

3.2.2.2. Measurement Technique

A new SSC testing procedure has been developed in this investigation. The procedure involves the application of a constant tensile load (i.e. tensile stress) during exposure to corrosive environment. The method combines tensile and Constant Extension Rate Test (CERT) procedures. The tensile procedure is commonly used for SSC experiments; however, this method requires 1 month to obtain results while the new method provides results in 7 days. Literatures that are related to CERT (Horstemeier et al. 2010, Kermani and MacGuish 1990) procedure were presented in Section 3.2.1.3. The CERT tests were conducted under ambient conditions using tensile strength testing (TST). Mini-pipe specimens are used in this project instead of solid cylindrical ones that are used in standard NACE method. This is because mini-pipe can simulate the wellbore conditions better than the cylindrical ones. The new SSC testing method involves the following three steps:

Step 1: The specimen is stretched to 80% of elastic limit in air using TST apparatus
Step 2: The specimen is stretched (85% of MYS) and kept in corrosive solution for 7 days
Step 3: The specimen is taken out of the solution and stretched to failure in air using the TST.

Step 1 involves stretching the sample until the stress level reaches 80% of its yield stress limit and recording the stress-strain data. This step is repeated 3 times to get an average measurement. One un-corroded (baseline) specimen of each material was stretched to failure in order to measure the yield stress and ultimate tensile strength. The measurements confirmed the material properties provided by the manufacturer. They are used as reference values for evaluating embrittlement. The stress-strain curves of uncorroded specimens show ductile failure. Step 2 is performed in SSC cell where the specimen is exposed to corrosive environment for 7 days. Materials, which are susceptible to SSC, develop cracks in the first 200 hours of exposure (Kermani and MacGuish 1990). Hence, test duration of 7 days is selected. After exposure to H_2S environment, hydrogen atoms penetrate into the steel surface and occupy positions in steel matrix (crystal structure) leading to embrittlement.

3.2.2.3. Experimental Set Up

A new corrosion test setup has been developed in the course of this project. The new setup use the existing auxiliary facilities such as heating system, gas supply and injection system, instrumentation

system, and data acquisition (DAQ) system, which are used by cement aging system. **Figure 3.17** shows the schematics of cement degradation and tubular corrosion testing setups. The experimental setups reasonably simulate actual field conditions varying pressure, temperature, and aging/test fluid composition.

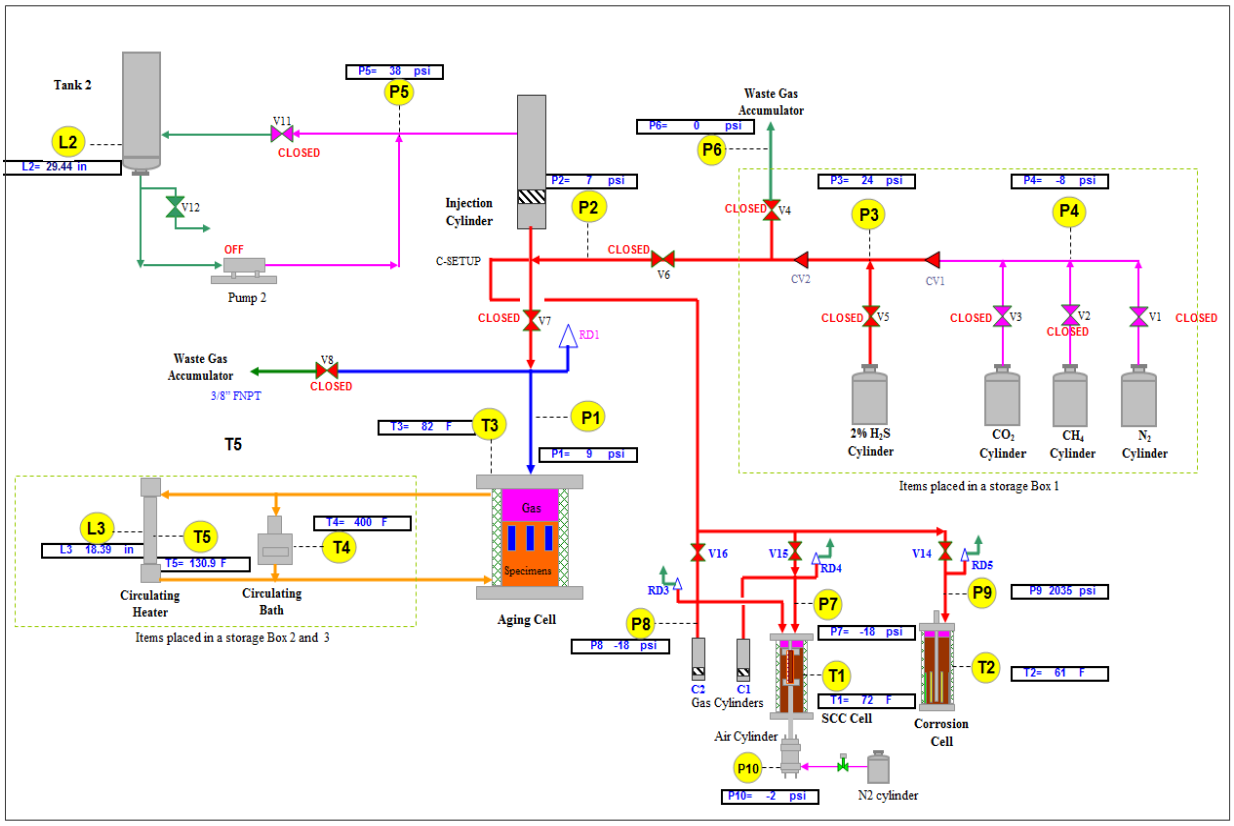

Fig. 3.17: Schematics of cement degradation and tubular corrosion facilities

The new test setup (**Fig. 3.18**) consists of two experimental setups for studying: i) stress cracking corrosion; and ii) uniform corrosion under static and dynamic conditions. The setup (**Fig. 3.19**) consist of: two corrosion test cells, two gas accumulators, a pneumatic cylinder with regulator and nitrogen supply cylinder, and magnetic drive system with air motor. Both test setups have capabilities to operate under HPHT sour gas environments. Specimens used for corrosion experiments have the same material (T95, C110 and Q125) as conventional well casings and tubulars. The setups are connected to the existing DAQ system to display and record all the experimental parameters. Critical test parameters are automatically controlled from the DAQ system.

Stress Cracking Corrosion (SCC) Setup

Mini-pipe specimens are used for stress-cracking tests. One end (the bottom end when assembled) of the mini-pipe is plugged. During the experiment, both ends of a mini-pipe are attached to a pulling rod (7/8 inch diameter) installed at the bottom of the cell (**Fig. 3.20**). The rod is connected to a power cylinder (**Fig. 3.21**) to apply the force required to generate the desired stress level in the specimen. A double acting pneumatic cylinder with 4½ inches bore diameter and 1 inch rod diameter, and maximum force of 3780 lbf (at 250 psi) is used to provide the force. The cylinder applies a pull force to put the specimen under a constant tensile stress. Nitrogen from a supply cylinder (maximum 2500 psi) is used as a pneumatic fluid to actuate the cylinder. A pressure regulator is installed to reduce the output pressure (P10) and maintain between 0 to 250 psi.

Fig. 3.18: Corrosion test setup

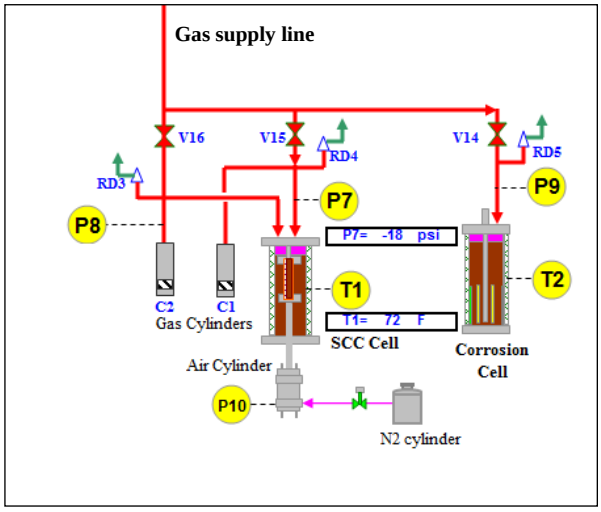

Fig. 3.19: Schematic of tubular corrosion test facility

To prevent the cylinder from over-pressurization, two pressure relief valves (set at 275 psi) are installed on the inlets of the cylinder. Over-pressurization can occur due to high nitrogen supply pressure or axial force acting on the rod resulting from hydraulic pressure inside the pressure cell. It is important to note that, in addition to the cylinder, the hydraulic pressure acting on the pipe bottom and pulling rod create a considerable tensile force on the specimen.

During the test, the internal (P7) and external (P8) sides of the specimen are pressurized and maintained at different pressure levels. This helps to simulate the underbalanced and overbalanced wellbore conditions between the wellbore and formation fluid pressures. Moreover, the pressure differential helps to reliably detect the stress cracking point as pressure begins to communicate between interior and exterior parts of the specimen. Both internal and external sides of the specimen are exposed to brine solution (2% NaCl) saturated with sour gases. Inner parts of the specimen and the pressure cell (SCC cell in which the specimen placed) are approximately 90% filled with the brine to maximize the exposure area for corrosion. Moreover, the interface between the brine solution and the gas should be in the specimen and the cell to facilitate the dissolution of gas in the liquid. Because of limited volume in the specimen and the SCC cell, two gas accumulators (C1 and C2),

with volume capacity 250 ml, are directly connected to the inside of the specimen and SCC cell (Fig. 3.19). The gas accumulators are filled with test gas using the injection cylinder. Two rapture disks (RD3 and RD4 with burst pressure of 10,500 psi) are installed on both accumulator inlet lines to prevent over pressurization. The gas inlet to the accumulators is regulated using remotely controlled valves (V15 and V16).

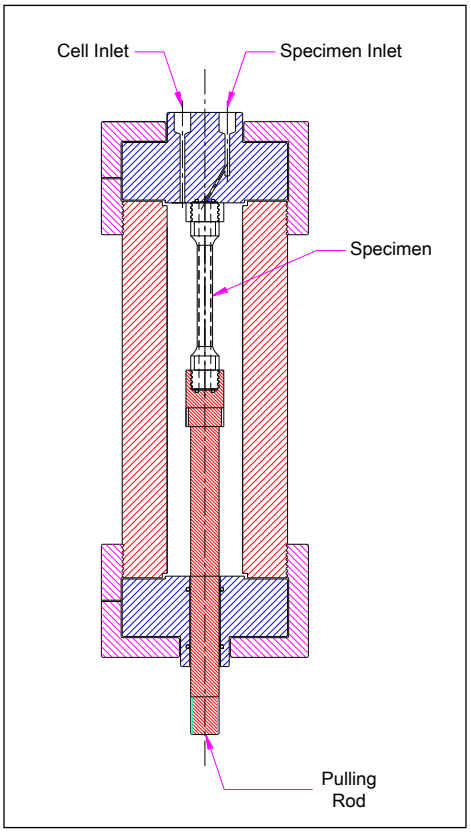

Fig. 3.20: Design of SCC cell

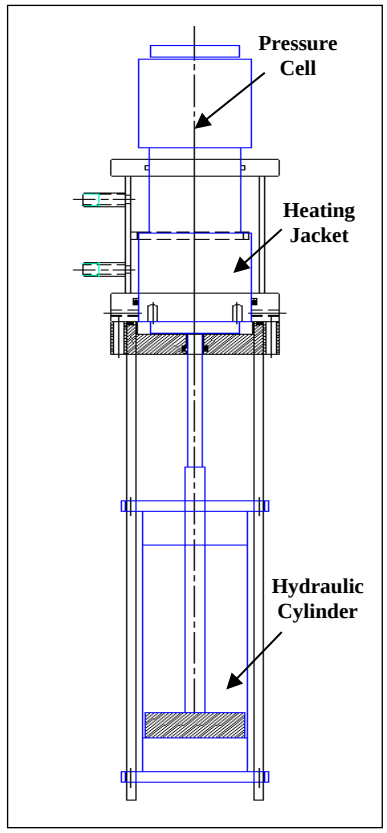

Fig. 3.21: Assembly of SCC cell with heating jacket and hydraulic cylinder

The SCC cell is placed in a heating jacket to control test temperature. The jacket completely covers the cell except the top lid part. The bottom part of the cell, including the cylinder rod inlet, is covered with the jacked. The maximum pressure rating of the jacket is 100 psi. In the case of high pressure fluid leak form the rod seal of the cell, there is a possibility of over-pressurization of the jacket and the entire heating system. In order to avoid this situation, a relief valve is installed at the inlet line of the jacket. The existing heating system provides the heating medium for controlling the temperature. Temperature in the cell is measured using a thermocouple.

Stress Analysis in the Mini-Pipe

The axial stress developed in the mini-pipe specimen is a function of cell pressure, specimen internal pressure, and the force applied by the cylinder (F_{cyd}). Considering a control volume shown in **Fig. 3.22**, the force balance in the vertical axis for equilibrium condition yields the following equation:

$$T + P_o * \frac{\Pi}{4} * (D_c^2 - D_{rod}^2) = P_o * \frac{\Pi}{4} * (D_c^2 - D_o^2) + P_i * \frac{\Pi}{4} * D_{in}^2 + P_{cyd} * \frac{\Pi}{4} * (D_{cyl}^2 - D_{p,Rod}^2) \quad \text{..... (3.17)}$$

where T is the tension in the mini-pipe. The second term on the left side of Eq. (3.17) is upward pressure force at Point 2 acting on the bottom of the adapter; the first term on the right side of the equation is the downward pressure force acting on the top of the adapter at Point 1; the second term on the right side of the equation represents the downward pressure force acting on the bottom of the mini-pipe; and the last term in the equation is the cylinder force acting downward. D_{cyl} and D_{in} denote the cylinder bore diameter and inner diameter of the mini-pipe. The buoyancy force, friction force and weight of the assembly are negligible compared to the pressure forces. Then, the axial stress is given by:

$$\sigma_{axial} = \frac{T}{\left\{\frac{\Pi}{4} * (D_o^2 - D_{in}^2)\right\}} \quad \text{..... (3.18)}$$

The force balance in lateral direction yields an expression for the circumferential stress.

$$\sigma_{\text{circumferential}} = (P_i - P_o) * \frac{D_{in}}{2t} \quad \text{..... (3.19)}$$

where t denotes the wall thickness of the mini-pipe at the mid-section.

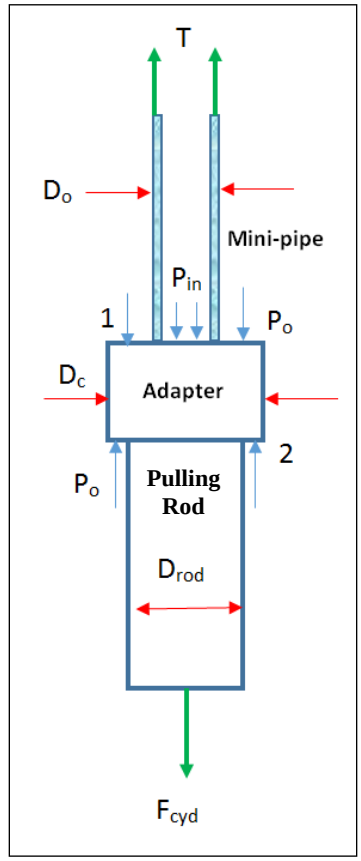

Fig. 3.22: Control volume for mini-pipe, adapter and pulling rod assembly

3.2.2.4. Specimen Preparation and Placement Procedures

The specimens were manufactured from API grade (T95, C110 and Q125) casings. To prevent atmospheric corrosion occurring before the test, specimens were placed in vacuum storage containers, which contain silica gel adsorbent. Mini-pipe specimens (**Fig. 3.23**) were stretched during the test to induce stress cracking corrosion. Two mini-pipe holders (**Fig. 3.24**), were used to apply tension force on the mini-pipe during the test. The holders were made of Hastelloy (HC-276) to withstand the corrosive environment in the test cell. They were screwed to the mini-pipe on both ends. The bottom of the mini-pipe is plugged. Holder placed on the top of the mini pipe has a sealing mechanism to prevent pressure communication between the outside and inside of the mini pipe.

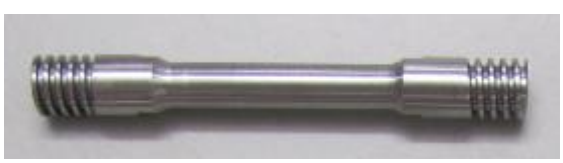

Fig. 3.23: Mini-pipe specimen

Fig. 3.24: Mini-pipe holders

Mechanical properties of mini-pipes were measured before and after the corrosion experiment. The changes occurring in ultimate strength and plastic strain to failure (PSF) after the test are used to investigate the corrosion process and determine the corrosion mechanisms.

During the experiment, one end (bottom) of the mini-pipe was attached to a pulling rod (7/8 inch diameter) installed at the bottom of the cell while the other end was connected to the lid of the corrosion testing vessel (**Fig. 3.25**). The mini-pipe was completely immersed in 2% NaCl solution during the experiment. The outer surface of the mini-pipe was cleaned using organic solvent to remove oil and grease used during its installation. The corrosion test was completed in eight days. The specimen was recovered after the test and its mechanical properties were measured.

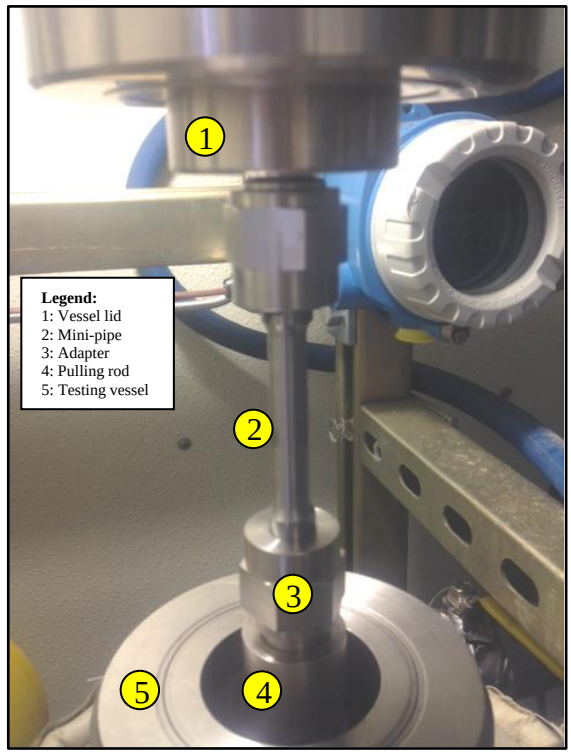

Fig. 3.25: Assembly of mini-pipe, adapters, pulling rod and vessel lid

3.2.2.5. SCC Test Procedure

When the experiment was carried out, a specimen was assembled in the SCC cell. First, the hydraulic cylinder rod was raised to attach the specimen, and then the specimen was mounted on the pulling rod by screwing. Subsequently, the SCC cell lid was assembled on the top of the specimen, after placing appropriate hydraulic seals to isolate the inner and outer parts of the specimen. The assembly was lowered and lid cover was mounted. 340 and 4.5 ml of 2% brine (sodium chloride) was injected into the cell and inside of the mini-pipe, respectively. Then, the inlets were connected to the gas accumulators and the heating system was turned on. While heating, both inside and outside of the mini-pipe were purged twice with 1800 psi of nitrogen for 15 minutes.

After purging for 30 minutes, the cell temperature was gradually increased above the critical temperature of CO_2, and then gas was injected into the accumulators to pressurize the cell and inner part of the specimen simultaneously. This was performed by opening V15 and V16 (Fig. 3.19), and injecting the gas phase through the supply line. This was conducted while heating the cell to test temperature. When the desired cell temperature and pressure were established, the pressure inside the specimen was increased separately by closing V16 and continuing the gas injection through V15 until the required pressure was reached. The supply gas pressure is limited to 2500 psi (maximum). The injection system was used to pressurize the cell and the mini-pipe to a higher pressure, which is greater than the supply pressure. The procedure of gas metering and injection involves: i) filling the cylinder with the supply gas by opening V6, V11 and one of the supply gas cylinder valves; ii) pressurization by closing V6 and V11, and pumping oil into the top side of the injection cylinder; and iii) gas injection by opening V15 and V16 simultaneously while pumping the hydraulic oil into the injection cylinder until it reaches its full stroke. Subsequently, V15 and V16 were closed and V11 and V6 were opened for charging the cylinder with the gas. These steps were repeated until the desired pressure was

established in the cell.

To increase the stress level in the specimen, nitrogen was supplied to the hydraulic cylinder. The pressure at the inlet of the cylinder (P10) was regulated so that the stress level in the specimen is 85% of the minimum yield stress.

The SCC test was completed in 8 days. After completion of the SCC test, the pressures inside the specimen and SCC cell were equalized by opening V15 and V16. Then, the heating system was shut down to cool the cell and depressurization begins by opening V15, V16, V6 and V4. The gas in the cell was sent to waste gas accumulator, in which it was slowly vented to the atmosphere after being mixed with air to maintain H_2S emission concentration of less than 10 ppm. After completion of the test, the specimen was examined using a microscope to study the crack pattern and structure. Each specimen should be photographed and all of the relevant information about that specimen was properly documented.

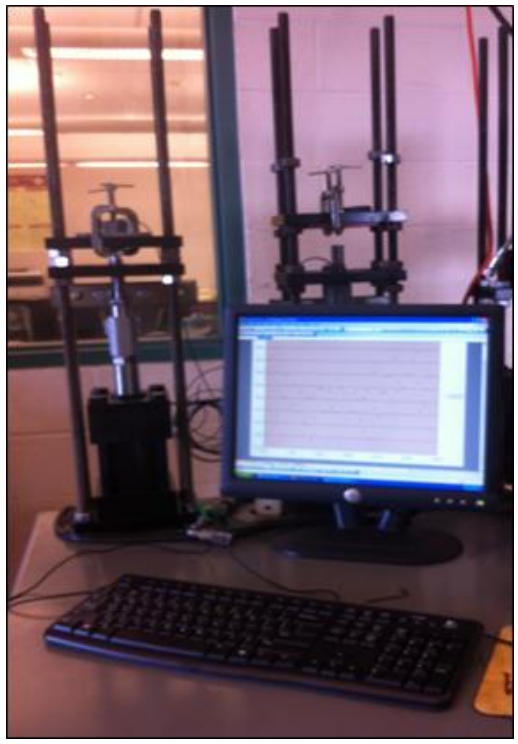

Fig. 3.26: TST apparatus

3.2.2.6. TST Setup and Procedure

Mechanical properties of the specimen were measured using TST (Tensile Strength Test) setup, which is shown in **Fig. 3.26**. The setup consists of: i) hydraulic cylinder, which applies tensile load that increases at a controlled rate; ii) syringe pump with a variable speed drive; iii) data acquisition (DAQ) system; iv) mini-pipe holders and adapters; and v) support frame.

In order to perform the test, top side of a mini-pipe specimen is first screwed into a holder, which is attached to the support frame. On the bottom side, the specimen is connected to piston rod of the hydraulic cylinder using an adapter and coupler (**Fig. 3.27**). The cylinder pressure increases with time as the specimen is being stretched. The pressure is precisely controlled by the syringe pump using the variable speed drive, which is controlled by the DAQ computer. The stress loading rate is maintained at approximately 55,000 psi/min according to the ASTM recommendations (ASTM E8/E8M). A displacement sensor is connected to the coupler to measure the elevation change during the test. Changes in elevation readings are converted into strain values using the effective specimen length (i.e. length of the narrow zone). The cylinder pressure is measured using pressure transmitter and recorded

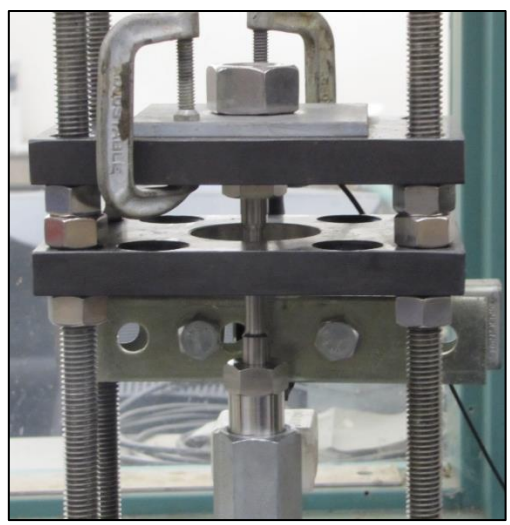

Fig. 3.27: TST apparatus

by the DAQ system. Pressure readings are converted to stress values using cross-section area of the specimen (i.e. measured in the narrow zone) and area of the cylinder.

3.2.2.7. Results

Table 3.5 shows mechanical properties of samples before and after corrosion test. After the test, most of the specimens did not fail. Therefore, the specimens were tested with the tensile strength testing (TST) apparatus. Stress-strain plot of Minipipe 1 is shown in **Fig. 3.28**. The data shows ductile behavior of the specimen indicating absence of hydrogen embrittlement. Uncorroded sample (Mini-pipe 2) was stretched to failure in the TST apparatus to measure the ultimate and yield strengths, plastic strain to failure and Young's modulus. The specimen serves as a reference; hence, it was not exposed to corrosive environment. Stress-strain data of the specimen is presented in **Fig. 3.29**. The material displayed expected yield strength. To determine its average elastic properties, Mini-pipe 3 was stretched three times to 80% of its yield stress in the TST apparatus. One set of stress-strain measurement is shown in **Fig. 3.30**. For initial stress values, very small strain was observed, later strain increased linearly with stress. Average of three measurements is obtained (Table 3.5).

Table 3.5: Mechanical properties of samples before and after corrosion test

Minipipe No.	Before Exposure				After Exposure			
	YS (psi)	UTS (psi)	PSF	E (psi)	YS (psi)	UTS (psi)	PSF	E* (psi)
1	-	-	-	-	109,855	127,619	0.030	11,785,921
2	111,529	130,156	0.040	11,842,002	-	-	-	-
3	-	-	-	11,704,810	-	100799	0.000	-
4	-	-	-	12,594,080	112768	134981	0.043	12,078,823
5	-	-	-	10,911,219	102217	114424	0.023	11,368,960
6	-	-	-	11,599,401	110686	130118	0.049	11,444,081
7	-	-	-	11,221,136	102,741	115479	0.014	11,561,000
8	-	-	-	12,044,218	106,709	120026	0.069	11,441,529
9	-	-	-	11,889,201	100,011	116742	0.036	11,255,892
10	-	-	-	12,928,070	-	100799	0.000	-
11	-	-	-	13,377,764	100,772	118484	0.035	13,527,372
12	150,072	169,282	0.051	13,580,537	-	-	-	-
13	-	-	-	13,594,795	132,903	152,493	0.028	11,757,738
14	-	-	-	13,890,878	144,533	165,460	0.080	7,321,033
15	95,399	121,115	0.058	12,125,404	-	-	-	-
16	-	-	-	10,613,970	144,528	164,641	0.084	10,642,228
17	-	-	-	8,916,085	105,167	122,075	0.135	7,031,822
18	-	-	-	7,477,965	101,540	121,952	0.137	10,000,342
19	-	-	-	10,431,875	141,344	162,711	0.066	6,395,980
20	-	-	-	7,676,120	105,217	119,540	0.126	7,580,194
21	-	-	-	6,744,550	136,403	156,584	0.049	8,431,876
22	-	-	-	9,507,949	134,333	156,737	0.050	8,740,819
23	-	-	-	8,724,446	103,495	117,293	0.126	9,335,596
24	-	-	-	8,366,828	101,594	115,885	0.106	8,796,036
25	-	-	-	8,562,738	103,133	117,799	0.116	9,205,450
26	-	-	-	9,052,546	-	109,037	0.000	-

UTS = Ultimate tensile strength, PSF = Plastic strain to failure, YS = Yield strength, E = Young's modulus before exposure, E* = Young's modulus after exposure

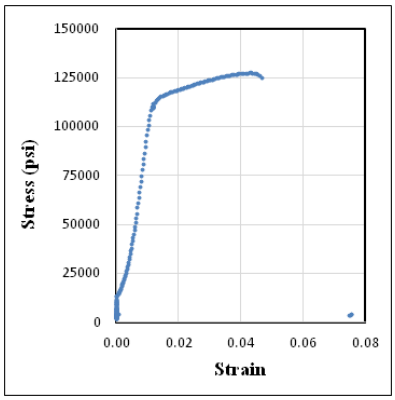

Fig. 3.28: Stress vs. strain for corroded sample (Mini-pipe 1)

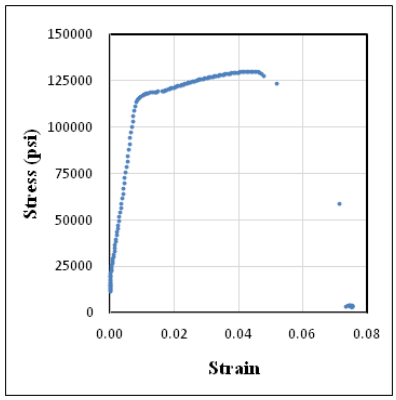

Fig. 3.29: Stress vs. strain for un-corroded sample (Mini-pipe 2)

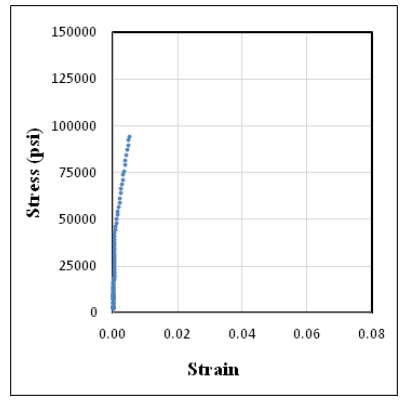

Fig. 3.30: Stress vs. strain for un-corroded sample (Mini-pipe 3)

Mini-pipe 3 was the first specimen to be exposed to sour environment in the SSC cell. The specimen was subjected to a stress equal to 85% of its yield strength. It failed in the cell on the 7th day of the test indicating the susceptible of the material to SSC. Magnified image of broken edge of the specimen was compared (**Fig. 3.31**) with images of other specimens which were not exposed to sour environment (unbrittled) but stretched to failure using the TST apparatus. The unbrittled specimens (Mini-pipes 1 and 2) show fibrous region around the crack. Furthermore, they show noticeable elongation around the failure region indicating ductility of the material. For Mini-pipe 3, crack seems to develop instantaneously without elongating the specimen. The failure line was almost perpendicular to direction of stress.

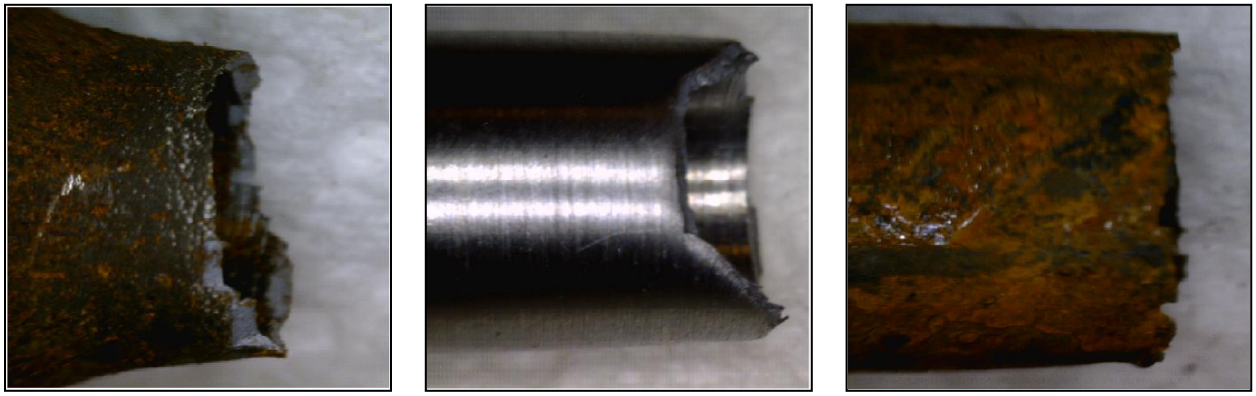

Mini-pipe 1 Mini-pipe 2 Mini-pipe 3

Fig. 3.31: Crack characteristics of broken mini-pipe specimens

SSC is hydrogen embrittlement caused by combined effects of stress and hydrogen atom, which diffuses into lattice structure of a metal in the presence of acidic solution containing H_2S. Requirements for SSC to occur include high tensile stress (i.e. greater than 75% of yield strength), susceptible material with structural defect, and formation and entry of atomic hydrogen into lattice structure. In this study, specimens were exposed to stress level of up to 85% of their minimum yield strength. Specimens 17

and 18 were strained to failure after exposure to corrosive environment with and without the presence of H_2S. The specimens showed (Table 3.5) very similar ultimate tensile strength (UTS) and plastic strain to failure (PSF). This indicates that, in addition to the presence of 300 ppm H_2S, carbon dioxide or other material, which reduces pH, is needed to create favorable condition for the occurrence of SSC. A number of studies (Morana and Nice 2009; Snape 1967; Hashizume and Inohara 2000) demonstrated reduction in SSC resistance of carbon steels with decrease in pH. In addition to pH, the concentration (i.e. partial pressure) of H_2S affects SSC corrosion of steels. **Figure 3.32** presents safe operating zone for Q-125 (Morana and Nice 2009). The area on left side of the green line represents zone where the metal is not vulnerable to SSC while the area on right side of the red line represents zone where it is highly susceptible to SSC. The area in between the two lines is intermediate zone where there is moderate level of vulnerability to SSC. Q-125 can be safely used in the area identified as No SSC zone.

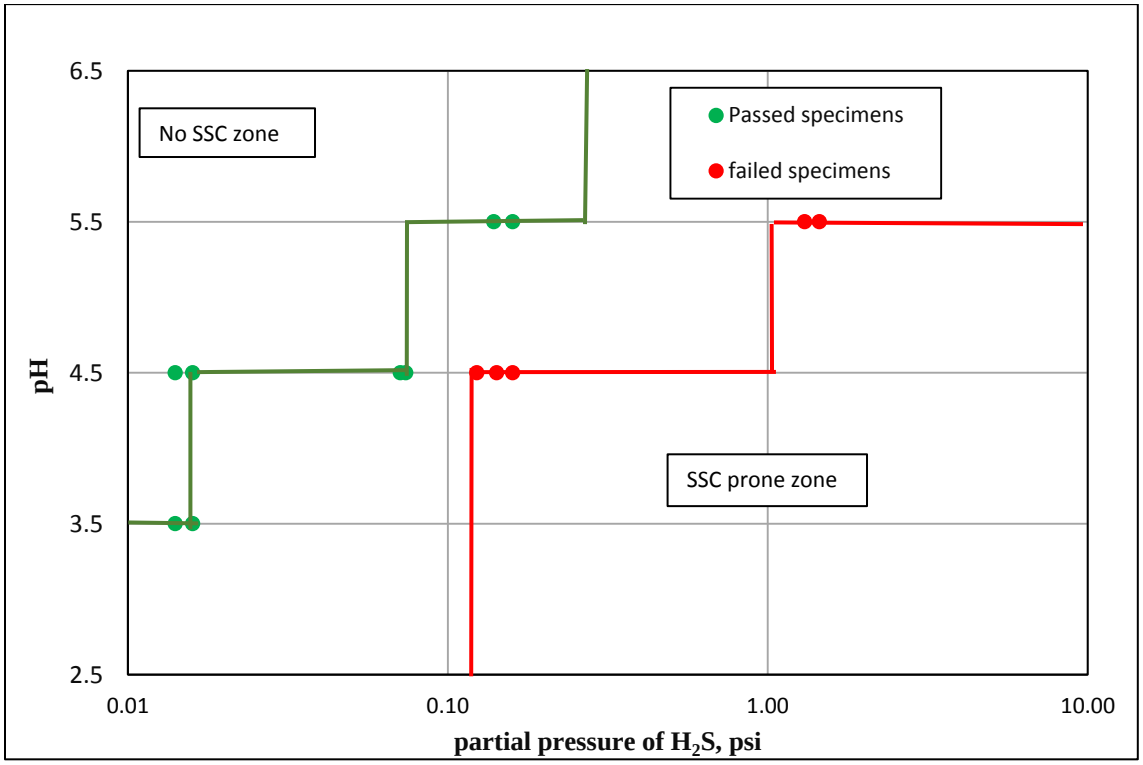

Fig. 3.32: Operating window of Q-125 (Redrawn from Morana and Nice 2009)

Concentration of CO_2 was varied in this investigation to examine its effect on SSC susceptibility. After exposure to sour environment, some specimens were broken in the corrosion cell. Unbroken specimens were strained to failure to measure their mechanical properties. The corroded specimen (**Fig. 3.33a**) showed lower ultimate tensile strength (UTS) and plastic strain to failure (PSF) than the baseline (**Fig. 3.33b**), which indicate embrittlement. As a result, UTS and PSF were used to assess the susceptibility of material towards SSC in sour conditions.

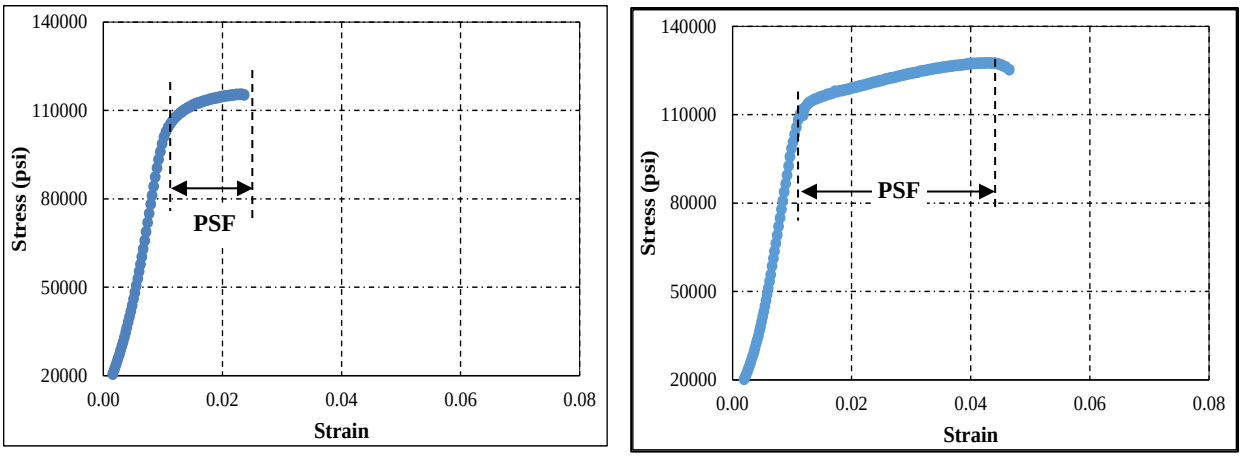

(a) (b)

Fig. 3.33: Stress vs. strain of mini-pipes: a) Mini-pipe 7 (corroded); and b) Mini-pipe 2 (baseline/uncorroded)

Figure 3.34 presents measured PSF of different carbon steel grades (T95, C110 and Q125) as a function of CO_2 concentration. PSF represents the maximum plastic deformation strain occurring during tensile strength test. Different steel grades showed similar PSF trend.

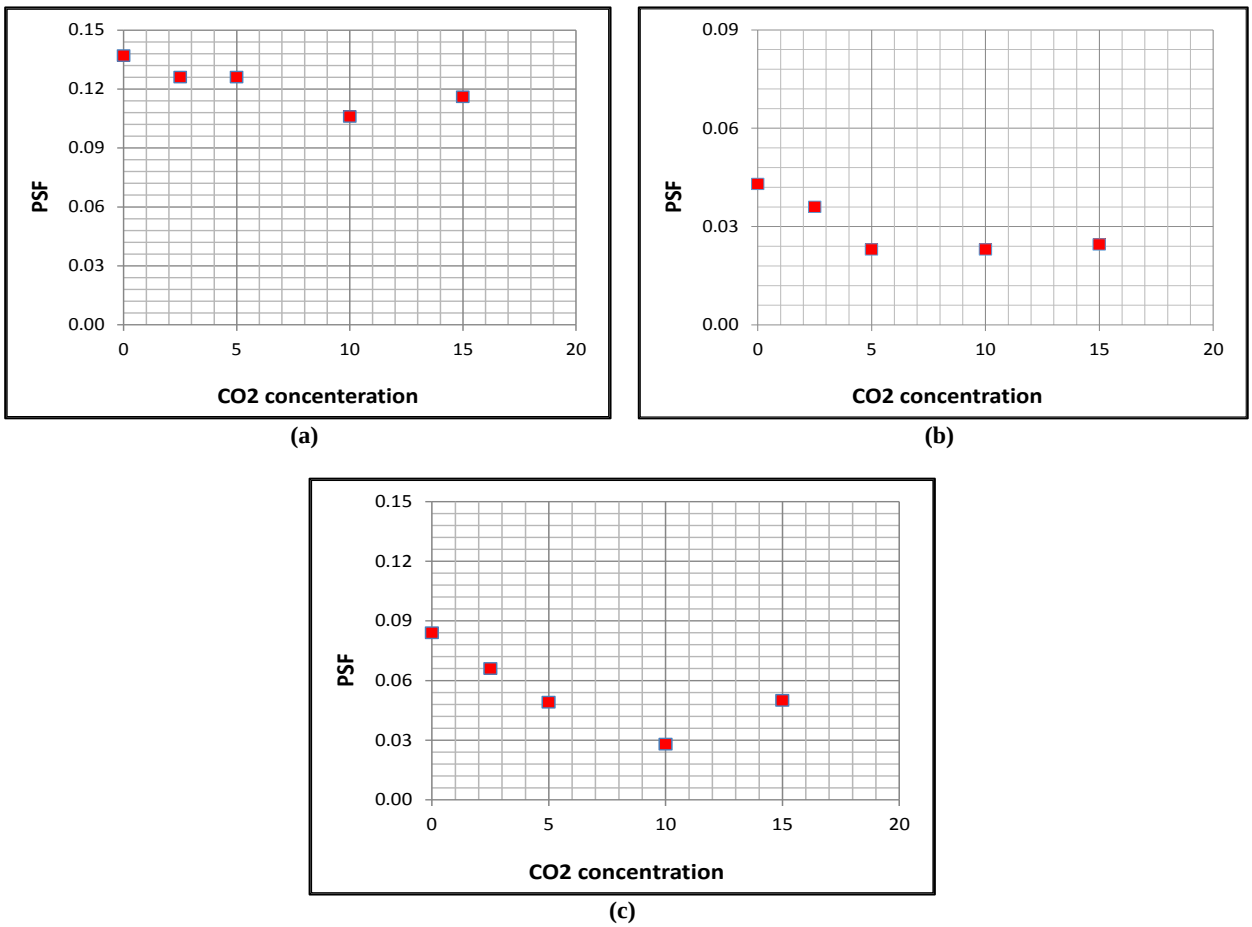

(a) (b) (c)

Fig. 3.34: Plastic strain to failure versus CO_2 concentration: a) T95; b) C110; and b) Q125

At low concentration (0 to 10% CO_2), PSF of the steels reduced with concentration. The reduction trend indicates the embrittlement occurring in the material. For C110, as CO_2 content was increased above 10%, the trend was reversed and slight improvement in PSF was observed (Fig. 3.34b). Initially, the trend reversal was thought to be due to dilution effect, which reduced H_2S content below 300 ppm (Table 3.4) in the gas as CO_2 concentration increased when supply (methane) gas containing 300 ppm H_2S was used. However, experiments conducted with T95 and Q125 at constant H_2S concentration (i.e. using 500 ppm H_2S supply gas) showed similar trend (Fig. 3.34c). Above 10% CO_2, PSF of Q125 substantially increased with concentration. Therefore, the trend reversal could be due to corrosion related phenomena, which maximize the sulfide stress cracking corrosion around 10% CO_2 for these particular sets of experiments. Two C110 specimens completely failed at this concentration when subjected to stress level of 85 percent of their minimum yield stress. This indicates the occurrence of severe sulfide stress cracking corrosion at approximately 10% CO_2.

Figure 3.35 presents ultimate tensile strength (UTS) of corroded specimens of API grade steels as a function of CO_2 concentration. The trends of UTS and PSF with CO_2 concentration are very similar. Consistent with PSF measurements, minimum UTS values were observed at approximately 10% CO_2.

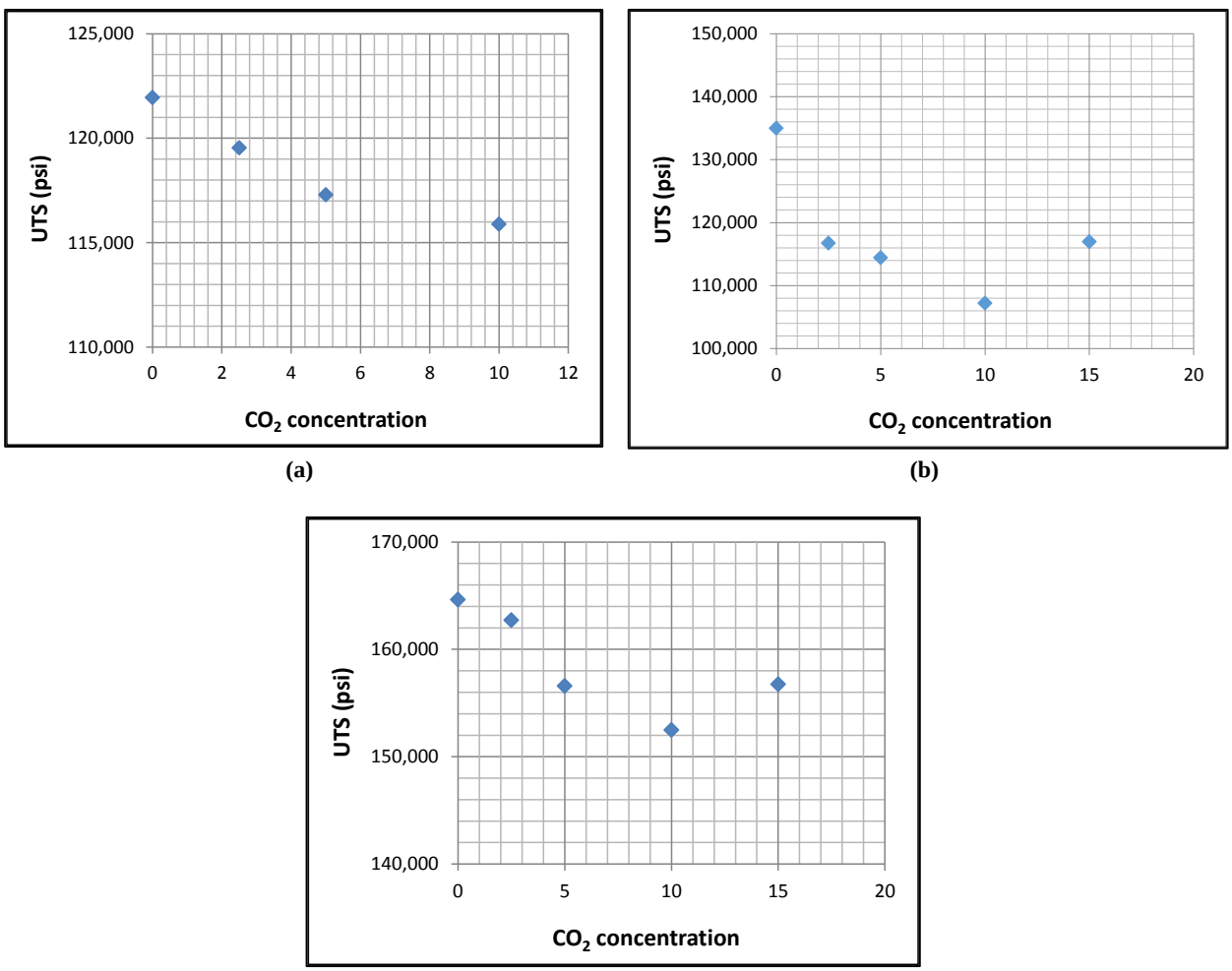

Fig. 3.35: Ultimate tensile strength versus CO_2 concentration: a) T95; b) C110; and b) Q125

In general, results suggest sulfide embrittlement tends to decrease the UTS of the steels. This observation is in agreement with published research results in the area of sulfide stress cracking corrosion. Moreover, it is important to note that the UTS measurements are consistent with the API grade number assignment (i.e. Q125 exhibited the highest UTS and T95 showed the lowest). However, PSF measurements did not follow API grade numbering. C110 displayed the lowest PSF value at all concentrations. Moreover, it was the only steel grade, which showed a complete failure when tested at 10% CO_2.

Furthermore, PSF trend shown in Fig. 3.34b demonstrates the embrittlement occurred in the specimens. With increasing the CO_2 content, the PSF substantially reduced indicating the level of embrittlement. Increasing the CO_2 content decreases pH of brine solution (surrounding fluid), which has significant effect on SSC.

3.2.3. SSC Model

Based on experimental results and theoretical analysis, a mathematical model has been developed to predict the susceptibility of materials towards SSC under different environmental conditions. Asahi et al. (1994) developed a SSC model to predict hydrogen atom concentration in steel matrix. Asahi model has been modified in order to extend its range of applicability. Differences between the modified Asahi model (SSC model developed in this study) and the original Asahi model are: i) The modified Asahi model predicts H_2S concentration using modified Raoult's law which is applicable for wide range of pressures (14.7 to 900 psi) while the original uses the Henry's law which is limited to low pressures (less than 30 psi); and ii) The modified model accounts for the presence of salt and predicts pH of the solution based on partial pressure of CO_2 while original Asahi model requires pH as an input parameter.

The modified Asahi model formulation consists of three calculation procedures involving: i) determination of H_2S and CO_2 concentrations and pH using solubility and pH models presented elsewhere (Tale 2014); and ii) calculation of the hydrogen concentration in steel using hydrogen permeation model. Critical concentration of hydrogen in steel is used as criteria for determination of SSC susceptibility of a material. The model is applicable up to 80°C (176°F). Most of commonly used steel grades (Q-125, T-95 and C-110) do not exhibit SSC above this temperature (Morana and Nice 2009). The model is valid for H_2S and CO_2 partial pressures ranging from 0 to 870 psig and 0 to 2175 psig, respectively. Partial pressure limitations of the model have been maintained as high as possible. The model has been validated by comparing its results with published experimental studies.

3.2.3.1. Hydrogen Permeation Model

Hydrogen permeation model predicts the hydrogen concentration in steel matrix for specific pH and concentration of H_2S in the solution. In addition, it compares the hydrogen concentration in steel with predetermined critical hydrogen concentration values. If the hydrogen concentration is more than the critical value, the steel is susceptible to SSC in that specific environment. Based on experimental data, Asahi et al. (1994) developed the following equation for hydrogen content of steel.

$$H_{Fe} = 13 * (H^+ * C_{H_2S})^{0.26} \quad \text{.....} \quad (3.20)$$

where H_{Fe} is hydrogen content of steel, H^+ is hydrogen ion concentration and C_{H_2S} is concentration of

H_2S in solution. The factor of 13 in Eq. (3.20) varies with steel type. Moreover, H_{Fe} is independent of temperature.

Critical hydrogen content is the hydrogen concentration in steel below which the metal does not fail at a stress level equal to its yield strength. The following equations are proposed to determine the critical hydrogen concentration at different temperatures:

$$\log H_c = -4.05 * 10^{-3} * MYS + 4.01 \; at \; 25°C \quad \text{.....} \quad (3.21)$$

$$\log H_c = -3.45 * 10^{-3} * MYS + 3.89 \; at \; 50°C \quad \text{.....} \quad (3.22)$$

$$\log H_c = -3.14 * 10^{-3} * MYS + 3.91 \; at \; 80°C \quad \text{.....} \quad (3.23)$$

where MYS is maximum yield strength. If maximum yield strength for steel is known, critical hydrogen content for that particular steel can be predicted.

3.2.3.2. Numerical Procedures

In order to obtain a numerical solution, the model executes the following steps: i) predicting CO_2 solubility in brine solution at a given CO_2 partial pressure, temperature and salt concentration; ii), calculating pH of the solution using the CO_2 concentration; iii) computing H_2S solubility in brine at a given H_2S partial pressure, temperature and salt concentration; iv) Determining concentration of hydrogen atom present inside the steel using calculated H_2S concentration and pH; and v) Comparing hydrogen content of metal with its critical hydrogen content to determine the susceptibility of the material towards SSC. For a given material (known maximum yield strength), critical hydrogen content can be computed using Eqs. (3.21) to (3.23). Conditions in which hydrogen content of a metal is less than its critical hydrogen content are designated as safe operating conditions.

3.2.3.3. Validation of SSC model

Experimental data from literature survey is used to validate the SSC model predictions. Experimental studies (Morana and Nice 2009; Skogsberg 2004) were performed on P-110 and Q-125 steel at various pH and partial pressure of H_2S conditions. The SSC model can be used to predict susceptibility of the material in these environments. It can be concluded that SSC model susceptibility predictions are in agreement with measurements presented in the literature (**Figs. 3.36**). Some of the specimens which passed the NACE test are predicted to be susceptible to SSC in the given environments. The model generates conservative results since it assumes maximum hydrogen permeation rate for SSC.

Horstemeier et al. (2010) presented SSC measurements for C-110 material in sour conditions (Fig. 3.36c). Model prediction shows good match with the measurements. The model can predict the susceptibility towards SSC under different partial pressure of CO_2 and H_2S (Fig. 3.36d). Masouri and Zafari (2005) presented measurements showing the failure of L-80 steel under sour conditions. Partial pressures of CO_2 and H_2S for the sour conditions were reported. Using this information, the model reasonably provided predicted susceptibility of the material to SSC under sour conditions.

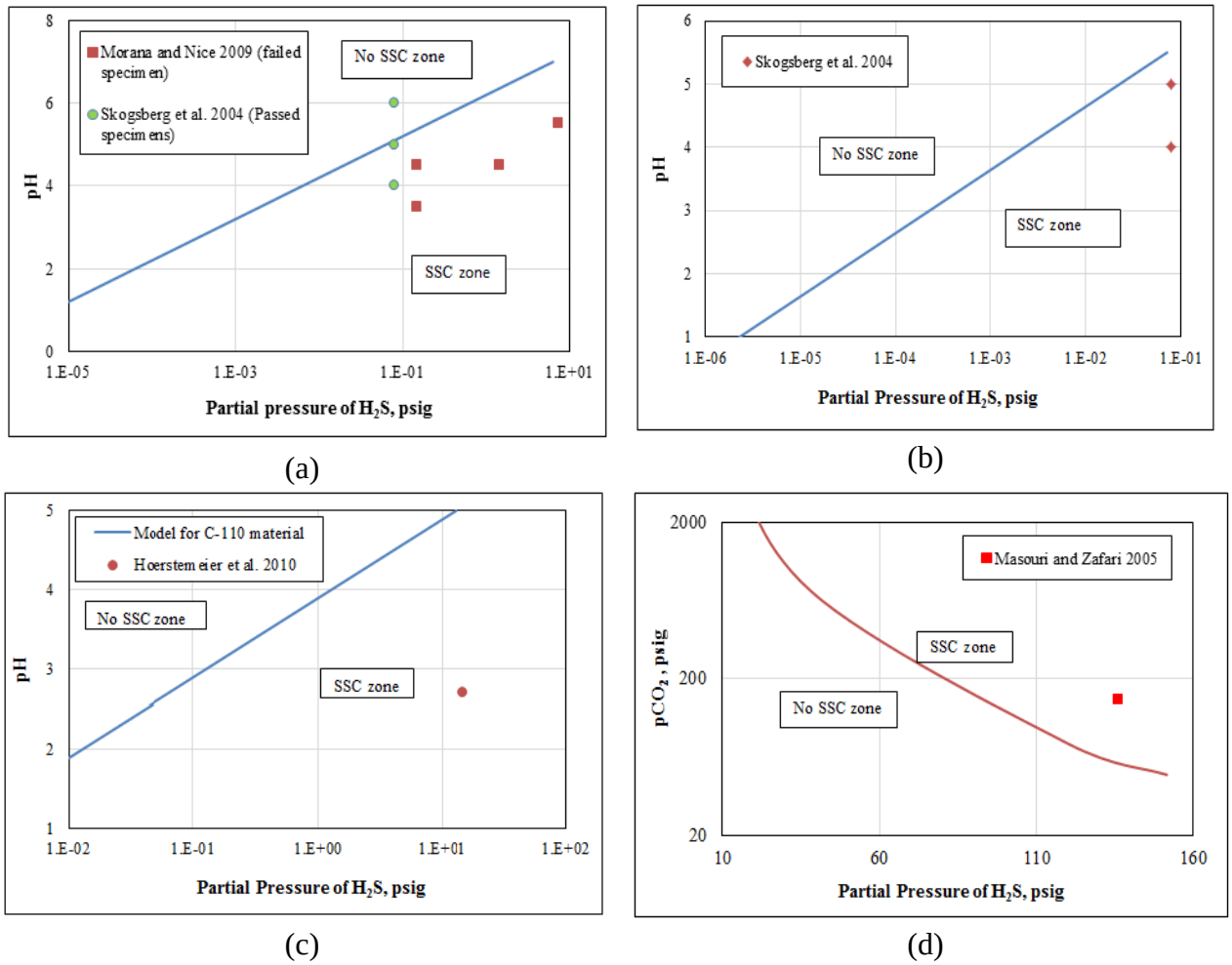

Fig. 3.36: Comparison of model susceptibility prediction with experimental data: a) P-110; b) Q-125; c) C110; and d) L-80

3.2.3.4. Sensitivity Analysis

Sensitivity analysis has been performed varying different parameters that affect the SSC resistance of a metal including: i) H_2S partial pressure; ii) CO_2 partial pressure (which controls pH); iii) temperature; and iv) salt concentration. The analysis is performed to examine the effect of each parameter on hydrogen content of steel. Sensitivity analysis is carried out at different H_2S-CO_2 pressure ratios (1/6, 1/3 and 1/1). Partial pressure ratio of 1/6 is the base case, which consists of H_2S partial pressure of 100 psig and CO_2 partial pressure of 600 psig, 2% brine solution and temperature of 104°F. **Figure 3.37** shows the percentage variation of hydrogen content of steel with percentage variation in different input parameters: H_2S and CO_2 partial pressure, temperature and salt concentration.

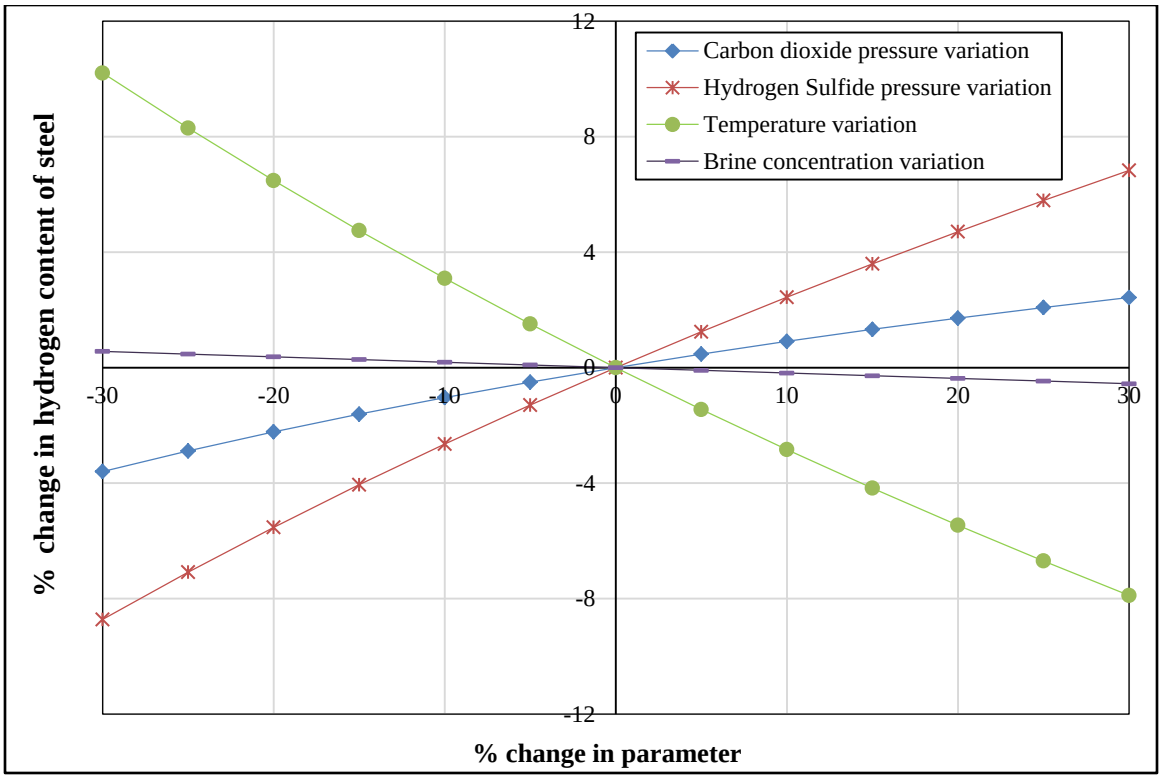

Fig. 3.37: Sensitivity analysis for SSC model at pressure ratio of 1/6

Effect of Temperature:

As shown in Fig. 3.37, hydrogen concentration in steel is most sensitive to the change in temperature. Temperature affects the solubility of all the gases in solution. Increase in temperature reduces the H_2S solubility at base case pressure (**Fig. 3.38**). Reduction in H_2S solubility implies that reduced concentration of H_2S in the solution. According to the mechanism of SSC presented in Section 3.2.1.2, H_2S is needed to retard hydrogen recombination reaction; and hence, it promotes hydrogen entry inside the steel. Increase in temperature also reduces the CO_2 solubility (Fig. 3.38), which results in increase in pH of the solution. Higher pH implies lower concentration of hydrogen ions in the solution. Thus, increase in temperature not only reduces hydrogen atom entry inside the metal but also reduces hydrogen ion concentration in the solution. Moreover, sensitivity with respect to temperature shows that hydrogen content in the steel is more sensitive to temperature at low temperatures (below 104°F). The reason behind this phenomenon is displayed in Fig. 3.38**.** Slope of the solubility curves is higher at lower temperatures and it gradually reduces. Thus, effect of temperature is more at lower temperatures.

Effects of H_2S and CO_2 Partial Pressures

Variation in H_2S partial pressure significantly affects hydrogen content in steel. Equation (3.20) shows direct relationship between the hydrogen content and H_2S concentration. Moreover, variations in CO_2 concentration also affect the hydrogen content in steel but the effect is not as strong as that of H_2S. Change in CO_2 content of the gas phase varies the carbonic acid concentration and pH of the solution.

To compare the sensitivity of hydrogen content to change in H_2S and CO_2 partial pressures, the effects of these parameters on H_2S solubility and pH has been examined (**Figs. 3.39 and 3.40**). There is approximately linear variation of H_2S solubility with respect to its partial pressure. Figure 3.40 shows the impact of variation in CO_2 partial pressure on hydrogen ion concentration of the solution. Comparing the Figs. 3.39 and 3.40**,** it can be concluded that the impact of H_2S partial pressure on its solubility is higher than the impact of CO_2 partial pressure on pH of the solution.

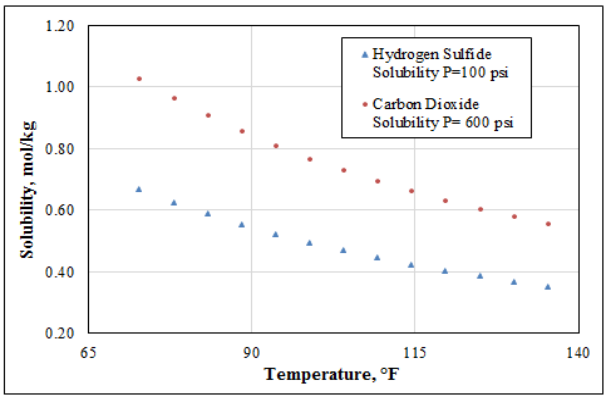

Fig. 3.38: Solubility of H_2S and CO_2 vs. temperature

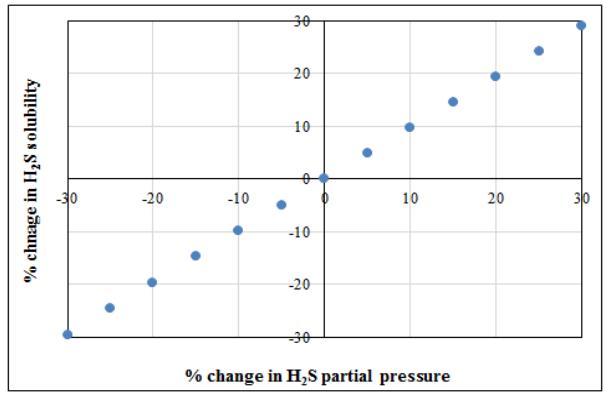

Fig. 3.39: Change in H_2S solubility vs. change in H_2S partial pressure

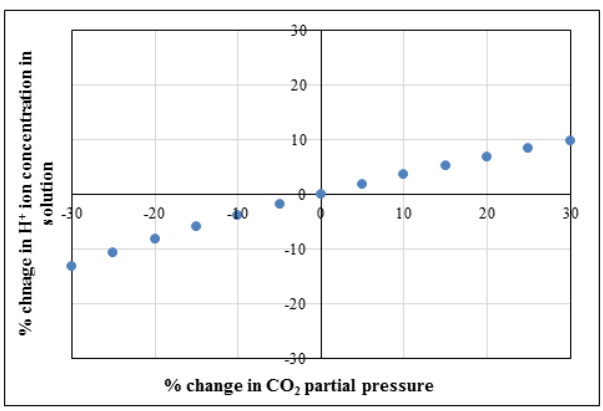

Fig. 3.40: Variation in pH vs. variation in CO_2 partial pressure

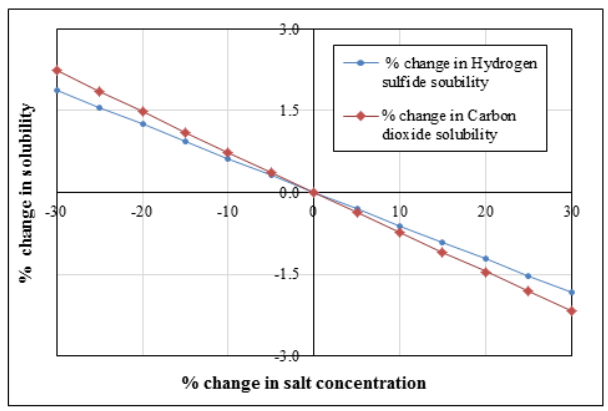

Fig. 3.41: Change in solubility of H_2S and CO_2 with variation in salt concentration

<u>Effect of Salt Concentration</u>

Salt concentration mildly affects the hydrogen content (Fig. 3.37). Increase in salt content reduces the solubilities of H_2S and CO_2 in the solution. The impact of salt is similar to the effect of temperature; however, the impact of temperature on gas solubility is more significant than that of salt concentration. **Figure 3.41** shows the impact of change in salt concentration on solubilities of H_2S and CO_2 in brine. 30% change in salt concentration results in 2.22% and 1.87% change in CO_2 and H_2S solubility, respectively. This explains why salt concentration does not affect the hydrogen content significantly.

3.2.4. Conclusions

The following conclusions are drawn based on theoretical analysis of experimental investigation:

- UTS and PSF are reliable indicators of SSC. SSC reduces PSF and UTS of steel.
- Sulfide stress cracking (SSC) corrosion requires acidic environment (low pH). In absence of CO_2, hydrogen embrittlement was not observed.
- SSC is significantly affected by CO_2 concentration. It is maximized at 10% CO_2 concentration.
- C110 grade steel is more susceptible to SSC corrosion than other grades (T95 and Q125). C110 displayed the lowest PSF values at all CO_2 concentrations.
- At low and intermediate temperatures (approximately less than 350°F), increase in temperature reduces solubility of acidic gases; and hence, it is expected to improve the SSC resistance of steel.

3.3. Uniform Corrosion

3.3.1. Literature Review

Rate of uniform corrosion in an environment containing H_2S and CO_2 is influenced by: i) electrochemistry of the corrosion process; ii) water chemistry including formation of protective scales; iii) environmental factors such as temperature, CO_2 partial pressure, and pH. Corrosion products can be insoluble or soluble materials. Insoluble solids precipitate on the corroded surface. As a result, tubular corrosion is often accompanied by the formation of scales such as iron carbonate ($FeCO_3$). The scales can be protective or non-protective depending on their physicochemical characteristics. The most common type of protective scale formed during CO_2 corrosion is iron carbonate (Nešić 2007). The scale covers the corroded surface and prevents the diffusion of species involved in the corrosion process. There are many factors that influence the formation of iron carbonate scale including water chemistry and temperature. Both water chemistry and temperature affect the solubility of iron carbonate. High temperature favors the rapid precipitation of iron carbonate and the formation of impermeable protective film. However, at low temperatures (less than 60°C), precipitation occurs slowly resulting in the formation of non-protective film on the corroded surface. The most important parameters affecting the CO_2 corrosion behavior are NaCl concentration, pH, temperature, flow velocity, flow regime, and CO_2 pressure.

3.3.1.1. Effect of NaCl on CO_2 Corrosion

Formation fluids usually contain large amounts of brine. Chloride concentration can vary significantly. On average, produced brine during oil and gas production contains 50,000 mg/L chloride (Hudak and Wachal 2001), which is highly corrosive to metals. Previous work by Uhlig et al. (1985) reported decreased oxygen corrosion with increased NaCl concentration in brine solutions. The study showed that increasing the amount of chloride in solution increases the conductivity and consequently the corrosion rate until a critical concentration of NaCl (3 wt%); and increasing the chloride content above the critical concentration decreases the corrosion rate by decreasing the solubility of the corrosive agent (oxygen in their investigation). Hassani et al. (2011) reported a slight reduction in CO_2 corrosion rate of carbon steel by increasing the NaCl concentration from 3 to 18% (by weight). On the other hands, Fang et al. (2010) reported a considerable change in corrosion rate by increasing the NaCl concentration in brine solution. Increasing the NaCl concentration from 1 to 10 wt% was reported to reduce the CO_2

corrosion rate by changing the density and viscosity, which affect the mass transfer processes, from an increase in ionic strength, which reduces the amount of dissolved CO_2, and from chloride ion adsorption onto the metal surface. At 20°C, with increasing salt concentration, the corrosion mechanism slowly changes from mixed-charge transfer (limiting current) control to pure-charge transfer control.

Increasing salt concentration reduces rates of heterogeneous charge transfer, homogenous chemical reactions, and mass transfer. Previous investigations on the effect of high ionic strength on CO_2 corrosion show that iron carbonate scale formation is a function of the ionic strength of the solution. In general, higher salt concentrations lead to higher value of solubility limit for precipitation and growth of $FeCO_3$ scale (Silva et al. 2002; Sun et al. 2009). Fosbøl et al. (2009) discussed the effect of high ionic strength on the diffusion process during CO_2 corrosion and the importance of including this effect in mechanistic models for CO_2 corrosion prediction.

3.3.1.2. Effect of pH on CO_2 Corrosion

The pH of a solution has substantial effect on CO_2 corrosion behavior. At high pH, the CO_2 corrosion substantially decreases with the formation of iron carbonate scale. However at low pH (below 4), direct reduction of H^+ ions occurs particularly at lower CO_2 concentration and the pH directly affects the corrosion rate. The pH influence is indirectly related to how pH affect the formation of iron carbonate scales. High pH results in a decreased solubility of iron carbonate resulting in increased precipitation rate and higher tendency for scaling formation. Experimental results by Chokshi et al. (2005) obtained at pH of 6.0 indicated that at lower super-saturations, the corrosion rate does not change considerably with time, even if some iron carbonate precipitation occurs, it forms relatively porous, lose and non-protective scale. Results obtained at higher pH (pH = 6.6) and higher super-saturation indicated faster precipitation and formation of more protective scales, reflected by a rapid decrease in the corrosion rate with time.

Furthermore, pH also has indirect effect on corrosion. Lower corrosion rate is usually expected at higher pH, which makes pH control technique an effective method for controlling CO_2 corrosion. However, it can lead to excessive scaling and can limited application in controlling corrosion caused by formation fluid systems (Nešić 2007).

3.3.1.3. Effect of Temperature on CO_2 Corrosion

Temperature affects corrosion behavior by facilitating most of the phenomena involved in the process of corrosion, including electrochemical, chemical, and transport processes. Increasing the temperature may increase or decrease the CO_2 corrosion rate depending upon the precipitation of iron carbonate scale. At low pH, protective scale does not form; and hence, the corrosion rate measured using conventional method (i.e. weight loss technique) increases with temperature (**Fig. 3.42**). At high pH, the trend changes noticeably when solubility of iron carbonate is exceeded; and increase in temperature improves the kinetics of precipitation and protective scale formation, resulting in decreased corrosion rate. The maximum corrosion rate is usually observed between 60°C and 80°C depending on composition of the fluid system and flow conditions.

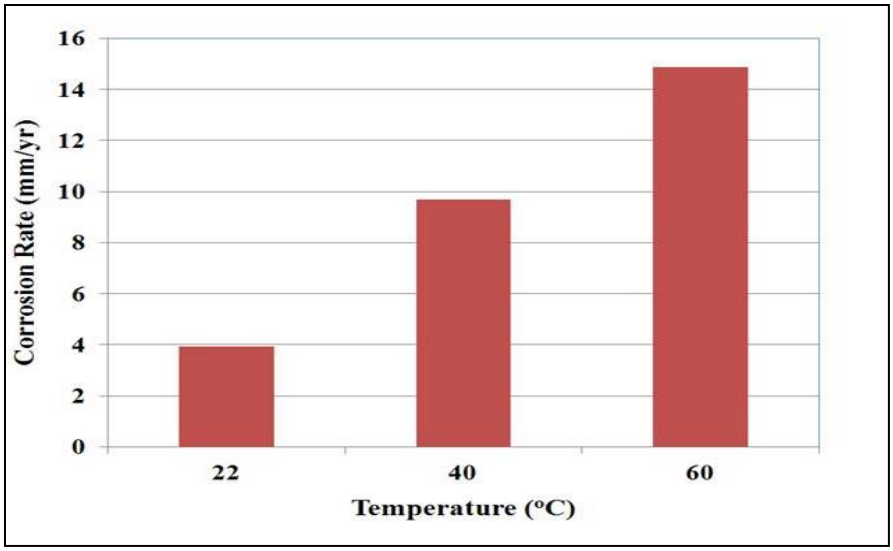

Fig. 3.42: Corrosion rates vs. temperature, pH 4, P_{CO2}=1 bar, C_{Fe2+} < 5ppm, 100 ppm acetic species (HAc + Ac^-), v = 0.5 m/s (Nešić 2007)

3.3.1.4. Effect of Flow Velocity and Flow Regime on CO_2 Corrosion

Flow velocity may affect CO_2 corrosion through two mechanisms, which can be identified based on the formation of protective scale or not. Turbulent flow condition favors the transport of species towards and away from the metal surface and without formation of protective scale (which usually happens at low pH), higher corrosion rate is expected as presented in **Fig. 3.43**. The figure compares model predictions (Nešić et al. 1996) with published experimental results (Nešić 2007).

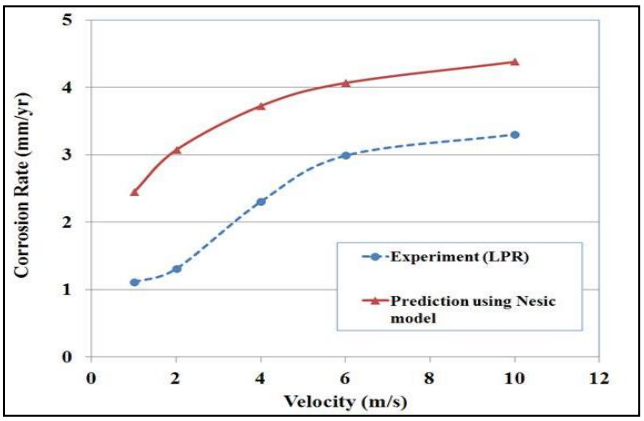

Fig. 3.43: Predicted and measured corrosion rates showing the effect of fluid velocity in the absence of iron carbonate scales at 20°C, P_{CO2}=1 bar, CFe2+ < 2 ppm

Modification of flow distribution system such as constrictions, bends, elbows, plugged tees, valves, expansions, extractions, etc. is a usual approach for reducing flow-accelerated corrosion effects. Unsteady slug flow can also lead to considerable fluctuations in wall shear stress and removes the protective surface scale layer or the protective inhibitor films from carbon steel substrate.

Zhang and Cheng (2009) studied the effects of flow velocity and impact angle on CO_2 corrosion for direct impingement geometry using computational fluid dynamics and corrosion experiments in CO_2 saturated systems. The role of fluid hydrodynamics in the CO_2-containing solution depends on its effect on the iron-carbonate scale formation. Increasing fluid velocity and shear stress prevents the formation of thick scale, thus increasing corrosion rate.

3.3.1.5. Effect of CO_2 Partial Pressure on CO_2 Corrosion

The impacts of temperature and CO_2 partial pressure on corrosion rate of carbon steel are shown **in Fig. 3.44** as presented by Ropital (2010). In the case of CO_2 corrosion without protective scale, increase in CO_2 partial pressure typically leads to increase in corrosion rate. The explanation for this observation is that increasing the partial pressure, increases the concentration of H_2CO_3 and accelerates the cathodic reaction, which aggravates the corrosion of the metal. The effect of P_{CO2} is illustrated in **Fig. 3.45**. The figure compares experimental data (Wang et al. 2004) with model prediction (Dayalan et al. 1998). However, when other conditions favor the formation of iron carbonate scales, increased P_{CO2} can have a beneficial effect in hindering the corrosion process. At a high pH, higher P_{CO2} causes increase in bicarbonate and carbonate ion concentrations, which accelerates precipitation and scale formation.

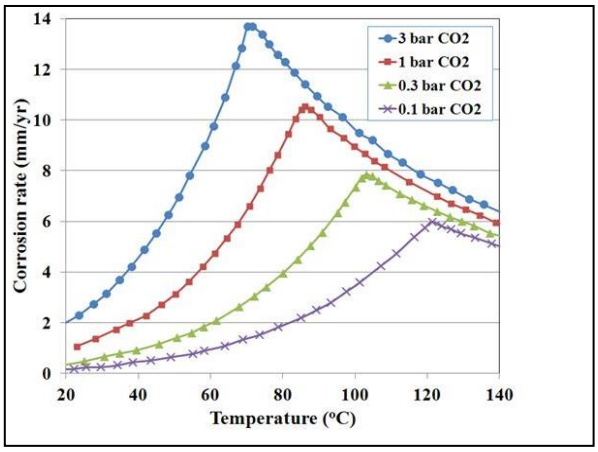

Fig. 3.44: Influence of temperature and CO_2 partial pressure on the rate of corrosion (Ropital 2010)

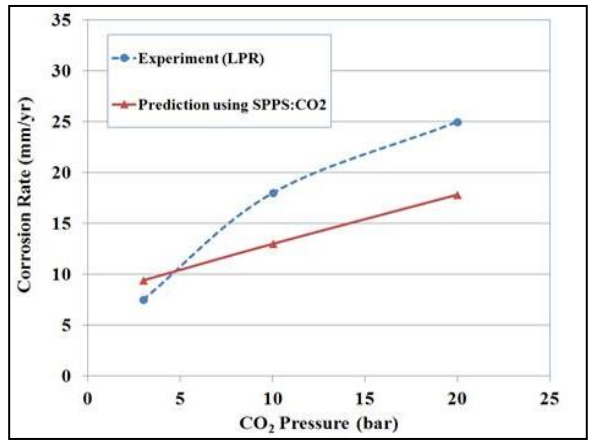

Fig. 3.45: Predicted and measured corrosion rates vs. CO_2 partial pressure at 60°C, pH 5, 1 m/s

3.3.2. Theoretical Studies

3.3.2.1. H_2S-CO_2 corrosion

The presence of carbon dioxide with or without hydrogen sulfide represents the actual condition in the oil field. The internal CO_2 corrosion of mild steel in the presence of H_2S along with formation water causes corrosion problem in the oil and gas industry. H_2S-CO_2 corrosion process is often controlled by the H_2S concentration due to formation of different types of scales on steel surface. Several studies demonstrated the existence of a critical H_2S concentration, which indicates the corrosive gas or mechanism that controls the corrosion rate.

Sun and Nešić (2007) investigated the mechanism and kinetics of mild steel corrosion in H_2S environment. They developed model to predict the corrosion rate of H_2S in the presence of iron sulfide scale. **Figure 3.46** shows a schematic of H_2S corrosion process. Earlier, Nešić et al. (1996) conducted an experimental study to investigate the protective scale that forms due H_2S corrosion process. Based on the experimental results, 'mackinawite' was found as the predominant type of the iron sulfide scale. It is formed due to the direct reaction of H_2S with the underlying steel. The model shows that the H_2S corrosion of mild steel is a function of H_2S gas concentration, temperature, velocity and the protectiveness of the scale. More recently, Sun and Nešić (2009) developed a model to predict H_2S-CO_2

corrosion rate by adding CO_2 term to the H_2S model. The model assumes that mackinawite layer still protects the steel surface from corrosion in mixed H_2S-CO_2 system. With the formation of mackinawite layer, the presence of CO_2 in the system has a little effect on corrosion rate.

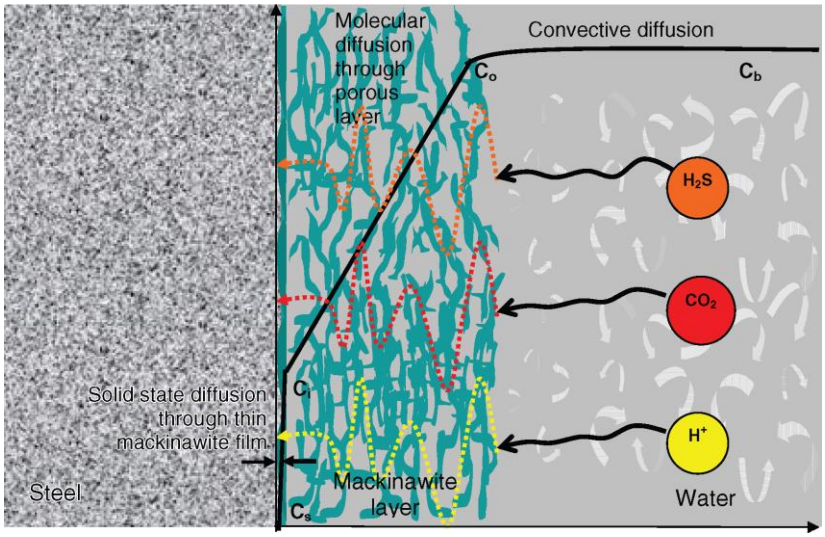

Fig. 3.46: Schematic of the H_2S-CO_2 corrosion process (Sun and Nesic 2009)

Furthermore, in H_2S-CO_2 corrosion of mild steel, there is a possibility for both iron carbonate and iron sulfide to be formed on the steel surface. A number of studies (Smith and Joosten 2006; Lee 2004) were conducted on the kinetic of layer formation and its effect on the corrosion kinetics. The studies demonstrated that protective layer formation is one of the key factors governing the corrosion rate. Smith and Joosten (2006) published a review article that described the research work performed in the area of H_2S-CO_2 corrosion in harsh oil field environment. It was concluded that the mechanism of H_2S-CO_2 corrosion remains unclear. In the case of H_2S, an extensive review on the mechanism of iron sulfide formation is conducted by Lee (2004). The study indicated the existence of many types of iron sulfide layers that may form as a product of H_2S corrosion. It was found that mackinawite is the most prevalent iron sulfide that is formed on the steel surface. Mackinawite can be converted to another form of iron sulfide depending on H_2S activity, temperature and duration of exposure.

Protective Layer

Based on the experimental work that was conducted by Nešić et al. (1996) on the H_2S corrosion, a mathematical model has been constructed. The experimental results demonstrate the formation of a Mackinawite layer on the steel surface as a product of H_2S corrosion. In their recent study, Sun and Nešić (2009) concluded that mackinawite can be the predominant iron sulfide species. However, other types of iron sulfide may form on the steel surface when attacked by H_2S, especially if the exposure is for a long duration. In general, a protective layer forms due to fast, direct and homogenous reaction of H_2S solution with steel surface. Often two types of Mackinawite layers form on the steel surface: i) very thin (much less than 1 µm) and tight inner film; and ii) thick (much greater than 1 µm) outer layer, which is loose and very porous.

The outer layer can be intermixed with any type of iron sulfide or iron carbonate that may have

precipitated. In brine saturated with H_2S and CO_2, both iron sulfide and iron carbonate may form on the steel surface depending on water chemistry, critical H_2S concentration and competitiveness of iron carbonate and iron sulfide. Sun and Nešić (2009) found that mackinawite layer formation is the dominant process in the most cases of mixed H_2S-CO_2 corrosion. In other cases, iron carbonate crystals may form intermixed with the mackinawite.

Critical H_2S Concentration

Prediction of corrosion rate in oil and gas industry is a key factor in determining the lifetime of oil field tubulars. Adding trace amount of H_2S into brine saturated with CO_2 tends to accelerate or inhibit the corrosion process. Ramirez and Ruiz (1998) determine the critical H_2S concentration that maximizes the corrosion rate. Corrosion rate experiments were conducted using A-516 steel in aqueous solution containing 5% NaCl. Test temperature and H_2S concentration were varied from 50°C to 200°C and 0 to 40 ppm, respectively. The maximum corrosion rate was observed at approximately 10 ppm (**Fig. 3.47**), regardless of the test temperature. The corrosion rate reduction at higher H_2S concentration is related to the formation of protective film (Kvarekval and Videm 1995). The maximum corrosion rate depends on the temperature, which reduces the solubility of H_2S. As a result, corrosion rate decreases with an increase in temperature. The influence of temperature on the corrosion rate is more pronounced than that of the H_2S concentration. The impact of temperature on the corrosion process is complicated as it affects gas solubility, acid dissociation and other physical and electrochemical reactions.

Formation of corrosion scale on the metal surface (porous layer) is usually a determining factor in corrosion reaction since corrosive species have to diffuse through the layer. In oil and gas production, corrosion layer formed during corrosion is usually iron carbonate, iron sulfide or iron oxide. The type of corrosion scale depends on partial pressures of H_2S and CO_2. Dunlop et al. (1983) found out that if partial pressure ratio (ratio of CO_2 partial pressure to H_2S partial pressure) is lower than 500, iron sulfide forms on metal surface; and if the partial pressure ratio is greater than 500, iron carbonate forms. Dunlop et al. (1983) developed a method to determine the iron-carbonate-iron-sulfide boundary for conditions where stable iron carbonate and iron sulfide scales form. However, the method is applicable under room temperature (25°C) and when H_2S and CO_2 gases behave like ideal gas. Smith (1993) proposed an improved version of iron-carbonate-iron-sulfide equilibrium as:

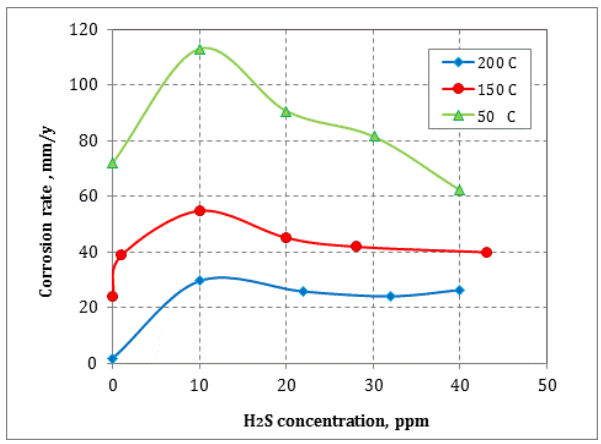

Fig. 3.47: Corrosion rate vs. H_2S concentrations in CO_2 saturated brine (5% NaCl) (Ramirez and Ruiz 1998)

$$K_{FeS/FeCO3} = \frac{a_{H2O} \times K_{CO2,aq/CO2,vap} \times a_{CO2,vap}}{K_{H2CO3,aq} \times K_{H2S,aq/H2S,vap} \times a_{H2S,vap}} \quad (3.24)$$

where $K_{FeS/FeCO3}$ is equilibrium constant between FeS and $FeCO_3$, a_{H2O} is activity of water, $K_{CO2,aq/CO2,vap}$ is equilibrium constant between CO_2 in liquid and gas phase, $a_{CO2,vap}$ is activity of CO_2 in gas phase, $K_{H2CO3,aq}$

is equilibrium constant for carbonic acid formation, $K_{H2S,aq/H2S,vap}$ is equilibrium constant between H_2S in liquid and gas phase, and $a_{H2S,vap}$ is activity of H_2S in gas phase. Assuming that activity of water is equal to one and combining all the equilibrium constants in one constant, Eq. 3.24 can be written as:

$$K_{FeS/FeCO3} = C \times \frac{a_{CO2,vap}}{a_{H2S,vap}} \quad (3.25)$$

where C a temperature dependent parameters.

Smith and Pacheco (2002) used the **Fig. 3.48** to explain corrosion-product stability regions of carbon steel in H_2S-CO_2 saturated environments. Iron carbonate scale is the most well-known corrosion product in CO_2 saturated systems. Mackinawite, pyrrhotite, pyrite, and cubic FeS are common H_2S corrosion products occurring in oil and gas applications. Mackinawite is a corrosion product of carbon steel in slightly sour system. In addition, mackinawite exists as an iron excess form ($Fe_{1+x}S$). Mackinawite is a thermodynamically semi-stable form of FeS, which is formed when the concentration of Fe^{2+} and H_2S are still below the saturation point. It is ferromagnetic and reacts with oxygen immediately when it is exposed to air forming magnetite as it is shown in the following equation.

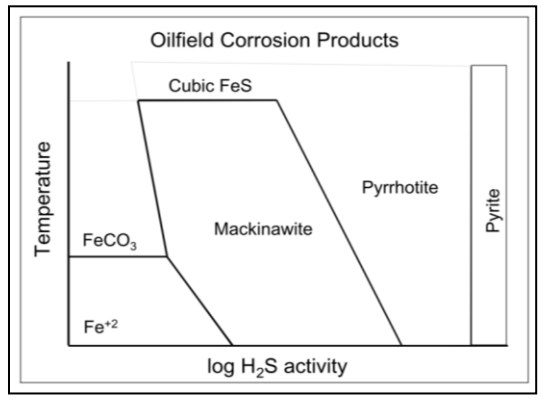

Fig. 3.48: Corrosion product diagram for H_2S-CO_2 environment (Smith 1993)

$$3FeS+2O_2 \rightarrow Fe_3O_4+3S \quad (3.26)$$

Pyrite scale formation is possible when elemental sulfur presents in the system. Pyrrhotite forms at high H_2S concentration environment and it is a stable form of H_2S corrosion product. Cubic FeS is formed at high temperature and slightly sour system. Critical temperature for the formation of cubic FeS not only depends on the thermodynamic but also the kinetics of the reaction. Different studies have reported various critical temperatures for the cubic FeS formation in the range of 110-200°C.

Smith and Pacheo (2002) developed a model for prediction of minimum H_2S required for iron sulfide corrosion product formation based on the stoichiometric FeS formation reaction:

$$Fe^{2+}+H_2S \rightarrow FeS+2H^+ \quad (3.27)$$

Reaction rate constant for Eq. (3.27) can be written as follow

$$K_{FeS/Fe^{2+}} = \frac{[H^+]^2}{[Fe^{2+}][H_2S]} \quad (3.28)$$

where $[H_2S]$ can be calculated using the following equation

$$[H_2S] = (K_{H2S,aq/H2S,vap}).(ppH_2S_{vap}).(\gamma_{H2S}) \quad (3.29)$$

where $K_{H2S,aq/H2S,vap}$ is reaction rate constant for H_2S dissolution reaction, ppH_2S_{vap} is partial pressure of H_2S, γ_{H2S} is fugacity coefficient of H_2S. Critical partial pressure of H_2S can be calculated by combining and rearranging Eqs. 3.28 and 3.29.

$$\left(ppH_2S_{vap}\right) = \frac{[H^+]^2}{K_{FeS/Fe^{2+}}[Fe^{2+}]\left(K_{H2S,aq/H2S,vap}\right).\left(\gamma_{H2S}\right)} \quad (3.30)$$

The model assumes iron ion concentration of one. It also assumes equilibrium condition between the gas and liquid phase activities of H_2S. Hydrogen concentration is simply related to log of pH, therefore, Eq. 3.30 can be written in a simpler form as:

$$\left(ppH_2S_{ap}\right) = \frac{10^{-pH}}{K_{FeS/Fe^{2+}}\left(K_{H2S,aq/H2S,vap}\right).\left(\gamma_{H2S}\right)} \quad (3.31)$$

Reaction rate constant is a function of Gibbs free energy. For the formation of iron sulfide scale, change of Gibbs free energy can be written as:

$$\Delta G_{reaction} = \Delta G_{FeS} + 2\Delta G_{H^+} - \Delta G_{Fe^{2+}} - \Delta G_{H_2S} \quad (3.32)$$

Smith and Pacheco (2002) suggested the following equation for predicting the partial pressure that corresponds to the critical H_2S concentration. This equation is derived from Eq. (3.31) by calculating the Gibbs free energy and it is a function of total pressure, temperature, pH, and fugacity coefficient of H_2S. Following equation shows the boundary between Fe^{2+} ions and Mackinawite scale.

$$\left(ppH_2S_{vap}\right) = \frac{P.10^{\frac{\Delta G}{4.757T}-2pH}}{\left(\gamma_{H2S}\right)} \quad (3.33)$$

where ΔG can be calculated using the following equation

$$\Delta G = 961.1 + 93.473T - 11.297TlnT - 0.135T^2 - \frac{4.196\times10^5}{T} + \frac{2.147\times10^7}{T^2} + 0.0196T^2lnT + 7.2\times10^4\frac{lnT}{T} \quad (3.34)$$

More recent study (Smith et al. 2011) showed the effect of pH on the mackinawite stability region (**Fig. 3.49**). Accordingly, mackinawite is more stable at lower pH. Mackinawite stability limit models are presented in Appendix E.

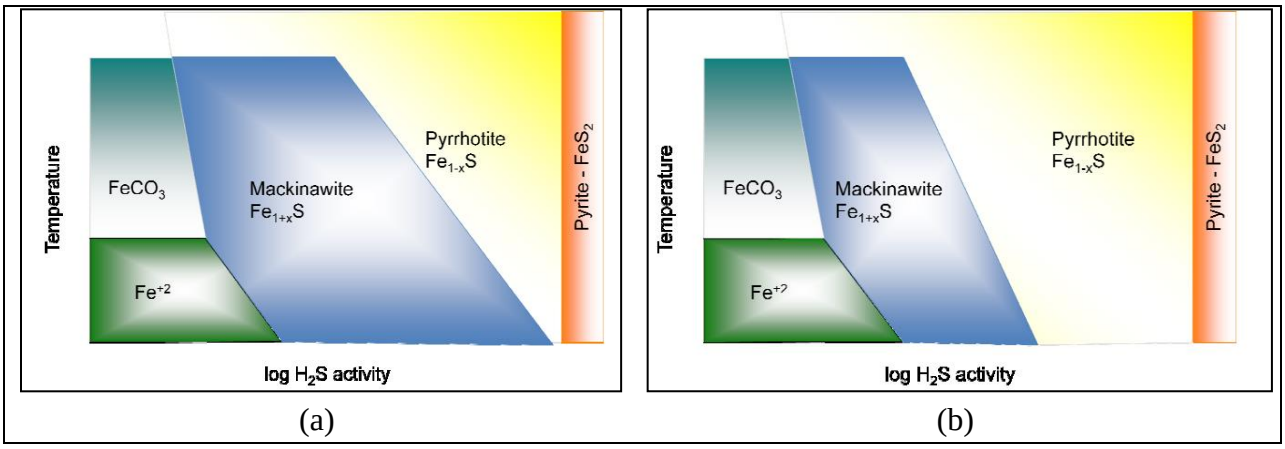

Fig. 3.49: Corrosion product diagram for H_2S-CO_2 environment (a) pH=4 and (b) pH=7 (Smith et al. 2011)

3.3.2.2 Electrochemistry of CO_2 Corrosion

The overall reaction equation describing the CO_2 corrosion of carbon steel in aqueous solution is expressed as:

$$Fe + CO_2 + H_2O \rightarrow FeCO_3 + H_2 \quad (3.35)$$

The type of corrosion process involves anodic and cathodic reaction of iron and hydrogen, respectively. A number of studies have been conducted to investigate the anodic dissolution of iron in acidic environment (shown below). Several multi-step mechanisms have been proposed to explain experimental results.

$$Fe \rightarrow Fe^{2+} + 2e^- \quad (3.36)$$

In acidic solutions, the above reaction is pH dependent with a reaction order with respect to OH^- between 1 and 2, and decreasing toward 1 and 0 at pH > 4 (Nešić 2007). The anodic dissolution of iron is influenced by the presence of carbonic acid. The carbonic species acts as a catalyst for the dissolution creating different solubility kinetics in CO_2 solutions. It is assumed that an intermediate reaction product (ligand), $Fe_L = Fe–CO_2$, forms at the electrode surface. The concentrations of H_2CO_3 and dissolved CO_2 are independent of pH. Therefore, formation of the ligand is independent of pH. Several detailed multi-step models have been presented to explain the various findings. The following corrosion mechanism has been developed by Nešić et al. (1996) to explain the experimental results for pH > 5.

$$\mathrm{Fe + CO_2 \Leftrightarrow Fe_L} \quad (3.37a)$$

$$\mathrm{Fe_L + H_2O \Leftrightarrow Fe_LOH_{ad} + H^+ + e^-} \quad (3.37b)$$

$$\mathrm{Fe_LOH_{ad} \xrightarrow{rds} Fe_LOH_{ad}^+ + e^-} \quad (3.37c)$$

$$Fe_L OH^+_{ad} + H_2O \Leftrightarrow Fe_L(OH)_{2ad} + H^+ \quad \text{(3.37d)}$$

$$Fe_L(OH)_{2ad} \Leftrightarrow Fe_L(OH)_{2sol} \quad \text{(3.37e)}$$

$$Fe_L(OH)_{2sol} + 2H^+ \Leftrightarrow Fe^{2+} + CO_2 + 2H_2O \quad \text{(3.37f)}$$

The presence of CO_2 increases the rate of corrosion of iron in aqueous solutions by increasing the rate of the hydrogen evolution reaction. In strong acids, which are completely dissociated, the rate of hydrogen evolution cannot exceed the rate of mass transfer at which H^+ ions can be transported to the surface from the bulk solution. In solutions with a pH > 4, the mass-transfer-controlled limiting current is small and the presence of H_2CO_3 enables hydrogen evolution at a much higher rate. Thus, at a given pH, the presence of CO_2 leads to a much higher corrosion rate than would be found in a solution of a strong acid. Despite more than three decades of intense research, it is still not known with absolute certainty whether H_2CO_3 is reduced directly or the final step in the reaction follows the dissociation of the H_2CO_3. Many studies (Nešić 2007, Gray et al. 1989; Bonis and Crolet 1989) assumed the two reactions are independent and the net cathodic current is the sum of the currents for the two reactions.

$$2H^+ + 2e^- \rightarrow H_2 \quad \text{(3.38)}$$

$$2\,H_2CO_3 + 2e^- \rightarrow H_2 + 2HCO_3 \quad \text{(3.39)}$$

For pH greater than 5 and very low partial pressures of CO_2, hydrogen evolution from the direct reduction of water, which occurs at lower potentials becomes important (Schmitt and Rothmann 1977; Nešić et al. 1996). Thus:

$$2H_2O + 2e^- \rightarrow H_2 + 2OH^- \quad \text{(3.40)}$$

Gray et al. (1989) have suggested that at higher pH in CO_2 solutions, the direct reduction of the bicarbonate ion becomes important:

$$2HCO_3^- + 2e^- \rightarrow H_2 + 2CO_3^{2-} \quad \text{(3.41)}$$

Because of increasing concentrations of bicarbonate at higher pH, it is difficult to distinguish the reaction path for hydrogen evolution experimentally. It has been observed that in the pH range of 4 to 7, the corrosion rates steadily decrease with increasing pH, which indicates the significance of the reaction shown in Eq. (3.41) in the overall reaction, while the concentration of bicarbonate ion steadily increases.

3.3.2.3 Electrochemistry of H_2S Corrosion

Fast and direct heterogeneous chemical corrosion reaction of H_2S with carbon steel causes the

formation of mackinawite corrosion product scale on the metal surface. The overall reaction can be written as:

$$FeS(S) + H_2S \rightarrow FeS(s) + H_2 \quad (3.42)$$

This reaction can be referred as a "solid state corrosion reaction" since both the initial and final state of Fe is solid. The mackinawite formed during corrosion reaction may dissolve depending on the level of solution saturation. Oilfield brines have the typical pH range of 4 to 7, which is usually supersaturated with respect to iron sulfide. Therefore, mackinawite scale layer does not dissolve (Brown et al. 2004). The mackinawite formed during corrosion reaction starts dissolving for pH below 4. Mackinawite dissolution increases with decreasing pH up to the pH of 2 to 3 in which all the mackinawite dissolve in brine (Shoesmith et al. 1980).

3.3.2.4 Uniform Corrosion under Dynamic Flow Conditions

High fluid velocity exacerbates CO_2 corrosion under HPHT conditions. Resistance of steel materials to CO_2 corrosion is often evaluated in terms of corrosion rate measured under dynamic flow conditions varying fluid velocity. Studies show (Kvarekval et al. 2002; Das & Khanna 2004) that the severity of corrosion in a sour gas environment strongly depends on various parameters such as pH, temperature, pressure, gas composition, and brine concentration. Increased temperature and CO_2 concentration tend to increase corrosion rate (Das & Khanna 2004). The presence of a small amount of H_2S increases the corrosion rate significantly. The API X-60 grade steel showed better corrosion resistance compared to other carbon steels.

3.3.3. Uniform Corrosion Models

A number of CO_2 and H_2S corrosion models available in the literature to predict corrosion rate, and thickness and properties of protective layer. Nyborg (2010) summarized several corrosion models (de Waard and Milliams 1975; de Waard et al. 1991; de Waard et al. 1995; Norsok 1998; Halvorsen and Søntvedt 1999; Pots 1995: Pots et al. 2002: Pots and Kapusta 2005; Bonis and Crolet 1989; Crolet and Bonis 1991; Gunaltun 1996; Hedges et al. 2005; Nordsveen et al. 2003; Nesic et al. 2003; de Waard et al. 2003; Smith and de Waard 2005; Srinivasan and Kane 1996; Sangita and Srinivasan 2000; Srinivasan and Kane 2003; Dayalan et al. 1995; Dayalan et al. 1998; Adsani et al. 2006; Perkins et al. 1996; Garber et al. 1998; Gartland and Salomonsen 1999; Gartland et al. 2003; Anderko and Young 1999; Anderko 2000; John et al. 1998) used in the industry and discussed the capabilities and limitations of these models. Most of the models are applicable for pure CO_2 corrosion.

3.3.3.1. CO_2 Corrosion Model for Non-Scale Forming Condition

Original Model

Dalayan et al. (1995) proposed a mechanistic model for CO_2 corrosion rate prediction. According to this model, the overall CO_2 corrosion process has four main steps (**Fig. 3.50**). The first step in CO_2 corrosion process is the formation of reactive species in the bulk. In this step CO_2 gas dissolves in water and then hydrate to form carbonic acid. Carbonic acid can directly reduce on metal surface or it can dissociate to bicarbonate ions first and then reduce on the metal surface as a cathodic reaction. The second step in

CO_2 corrosion process is the transportation of cathodic reaction species (reactants) from the bulk to the surface of metal. The driving force for transporting these species to the metal surface is consumption of these species on the surface by cathodic reaction of corrosion, which causes a concentration gradient between bulk and metal surface. The third step is electrochemical corrosion reaction on the metal surface. Electrochemical corrosion reaction can be divided into two main categories as anodic and cathodic reactions. The last step is transportation of corrosion products from the metal surface to the bulk solution. The driving force for this transportation is concentration difference between metal surface and bulk solution.

Based on two main hypotheses, Dayalan et al. (1995) developed the mechanistic corrosion model consists of a system of fifteen equations and fifteen unknowns. The model is valid for steady state corrosion. It incorporates chemical and electrochemical reactions, and mass transport (Eqs. 3.43 through 3.57). CO_2 corrosion rate can be predicted for non-scale forming conditions by solving the system equations. The main hypotheses in this model are: i) the sum of the mass transfer rates of the reactants must be equal to the sum of the electrochemical reaction rates (for both cathodic and anodic reactions); and ii) the sum of the mass transfer rates of carbonic acid and bicarbonate is equal to the mass transfer rate of carbonate ions. According to the first hypothesis, mass transfer rate of Fe^{2+} is equal to electrochemical reaction rate of the iron dissolution. Therefore:

$$K_{mt,Fe^{2+}}([Fe^{2+}]_s - [Fe^{2+}]_b) = 2 \times 10^{-3} F.K_{Fe^{2+}}[Fe^{2+}]_s exp\left\{\frac{(2-B)F(E_{corr}-E_{Fe^{2+}})}{RT}\right\} \quad (3.43)$$

where K_{mt} is mass transfer coefficient which can be different for different ions. $[Fe^{2+}]_s$ is iron ion concentration on the metal surface, $[Fe^{2+}]_b$ is iron ion in the bulk solution, F is Faraday constant, K_{Fe} is electrochemical reaction rate constant of iron ions, B is transfer coefficient (the value of B is 0.5 for most of the reactions), R is the universal gas constant, T is absolute temperature, E_{corr} is corrosion potential, and E^o_{Fe} is standard potential of iron at temperature T.

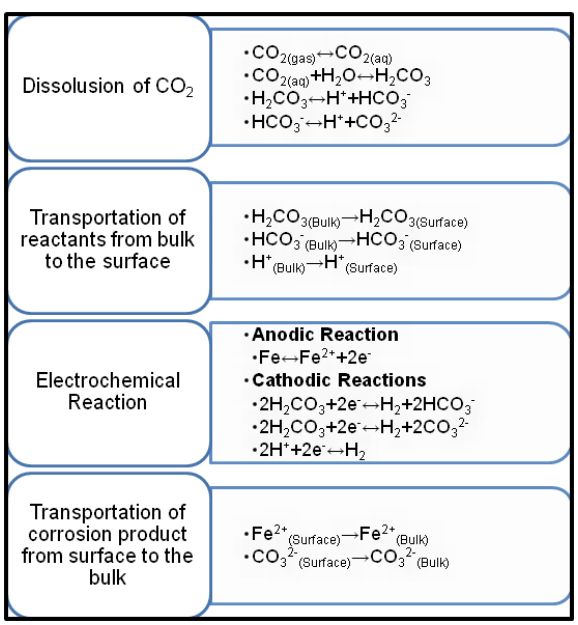

Fig.3.50: Summary of overall CO_2 corrosion process

From the second hypothesis, the sum of mass transfer rates of ([H_2CO_3], [HCO_3^-], [H^+]) are equal to the sum of electrochemical reaction rates of ([H_2CO_3],[HCO_3^-],[H^+]). Therefore:

$$K_{mt,H_2CO_3}([H_2CO_3]_b - [H_2CO_3]_s) + K_{mt,HCO_3^-}([HCO_3^-]_b - [HCO_3^-]_s) + K_{mt,H^+}([H^+]_b - [H^+]_s) = 2 \times 10^{-3}F.K_{H_2CO_3}[H_2CO_3]_s exp\left\{\frac{-BF(E_{corr}-E_{H_2CO_3})}{RT}\right\} + 2 \times 10^{-3}F.K_{HCO_3^-}[HCO_3^-]_s exp\left\{\frac{-BF(E_{corr}-E_{HCO_3^-})}{RT}\right\} + 2 \times 10^{-3}F.K_{H^+}[H^+]_s exp\left\{\frac{-BF(E_{corr}-E_{H^+})}{RT}\right\} \quad (3.44)$$

Similarly, the sum of mass transfer rates of (H_2CO_3, HCO_3^-) is equal to the mass transfer rate of CO_3^{2-}. Therefore:

$$K_{mt,H_2CO_3}([H_2CO_3]_b - [H_2CO_3]_s) + K_{mt,HCO_3^-}([HCO_3^-]_b - [HCO_3^-]_s) = K_{mt,CO_3^{2-}}([CO_3^{2-}]_b - [CO_3^{2-}]_s) \quad (3.45)$$

In addition, the sum of the cathodic reaction rates is equal to the sum of anodic reaction rates and it is equal to corrosion current density.

$$I_{H_2CO_3} + I_{HCO_3^-} + I_{H^+} = I_{Fe^{2+}} = 2 \times 10^{-3}F.K_{Fe^{2+}}[Fe^{2+}]_s exp\left\{\frac{(2-B)F(E_{corr}-E_{Fe^{2+}})}{RT}\right\} = 2 \times 10^{-3}F.K_{H_2CO_3}[H_2CO_3]_s exp\left\{\frac{-BF(E_{corr}-E_{H_2CO_3})}{RT}\right\} + 2 \times 10^{-3}F.K_{HCO_3^-}[HCO_3^-]_s exp\left\{\frac{-BF(E_{corr}-E_{HCO_3^-})}{RT}\right\} + 2 \times 10^{-3}F.K_{H^+}[H^+]_s exp\left\{\frac{-BF(E_{corr}-E_{H^+})}{RT}\right\} \quad (3.46)$$

Electrochemical cathodic and anodic reactions are expressed as:

$$I_{H_2CO_3} = 2 \times 10^{-3}F.K_{H_2CO_3}[H_2CO_3]_s exp\left\{\frac{-BF(E_{corr}-E_{H_2CO_3})}{RT}\right\} \quad (3.47)$$

$$I_{HCO_3^-} = 2 \times 10^{-3}F.K_{HCO_3^-}[HCO_3^-]_s exp\left\{\frac{-BF(E_{corr}-E_{HCO_3^-})}{RT}\right\} \quad (3.48)$$

$$I_{H^+} = 2 \times 10^{-3}F.K_{H^+}[H^+]_s exp\left\{\frac{-BF(E_{corr}-E_{H^+})}{RT}\right\} \quad (3.49)$$

$$I_{Fe^{2+}} = 2 \times 10^{-3}F.K_{Fe^{2+}}[Fe^{2+}]_s exp\left\{\frac{(2-B)F(E_{corr}-E_{Fe^{2+}})}{RT}\right\} \quad (3.50)$$

Carbonic acid dissociation reaction has two steps. Reaction rate constants for these two steps are:

$$K_1 = First\ Dissociation\ constant = \frac{[H^+]_s[HCO_3^-]_s}{[H_2CO_3]_s} \quad (3.51)$$

$$K_2 = Second\ Dissociation\ constant = \frac{[H^+]_s[CO_3^{2-}]_s}{[HCO_3^-]_s} \quad (3.52)$$

H^+ ions concentration also governed by water dissociation equilibrium described below.

$$K_w = water\ Dissociation\ constant = [H^+]_s[OH^-]_s \quad (3.53)$$

Equilibrium potential of all the cathodic and anodic species is a function of absolute temperature, and concentration of species based on the Nernst law, which can be expressed

mathematically as:

$$E_{H_2CO_3} = E^o_{H_2CO_3} + \frac{RT}{2F} Ln\left\{\frac{[H_2CO_3]_s{}^2}{[HCO_3^-]_s{}^2 .[H_2]}\right\} \text{..... (3.54)}$$

$$E_{HCO_3^-} = E^o_{HCO_3^-} + \frac{RT}{2F} Ln\left\{\frac{[HCO_3^-]_s{}^2}{[CO_3^{2-}]_s{}^2 .[H_2]}\right\} \text{..... (3.55)}$$

$$E_{H^+} = E^o_{H^+} + \frac{RT}{2F} Ln\left\{\frac{[H^+]_s{}^2}{[H_2]}\right\} \text{..... (3.56)}$$

$$E_{Fe^{2+}} = E^o_{Fe^{2+}} + \frac{RT}{2F} Ln\{[Fe^{2+}]_s\} \text{..... (3.57)}$$

where $E^o_{H_2CO_3}$, $E^o_{HCO_3^-}$, $E^o_{H^+}$, and $E^o_{Fe^{2+}}$ are the standard potentials for reduction and oxidation reactions.

Fifteen unknown variables are the six surface concentrations ($[H^+]_s$, $[HCO_3^-]_s$, $[Fe^{2+}]_s$, $[CO_3^{2-}]_s$, $[OH^-]_s$, $[H_2CO_3]_s$), four equilibrium potentials ($E^o_{H_2CO_3}$, $E^o_{HCO_3^-}$, $E^o_{H^+}$, and $E^o_{Fe^{2+}}$), the corrosion potential (E_{corr}), and current due to four reactions (I_{H2CO3}, I_{HCO3^-}, I_{H^+}, $I_{Fe^{2+}}$). **Figure 3.51** shows the comparison between the CO_2 corrosion rate prediction using the model proposed by Dayalan et al. (1995) and experimental data.

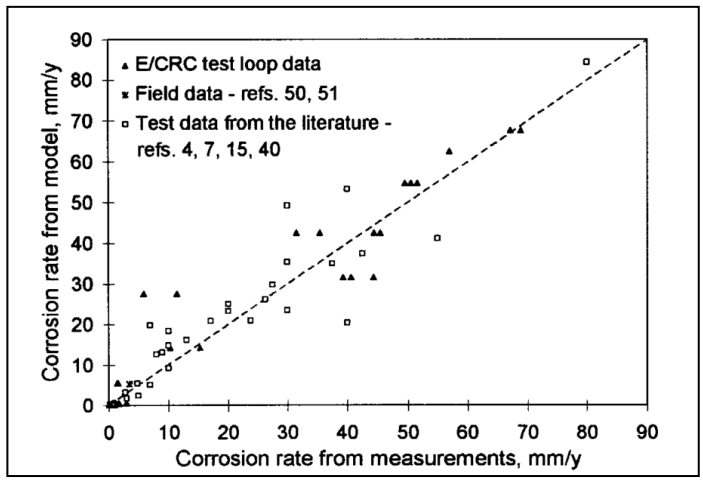

Fig.3.51: Predicted CO_2 corrosion rate vs. experimental data (Dayalan et al. 1995)

Improved Model

Based on reaction rate theory of Glasstone et al. (1941), for reactants to form products, a transitory state must be reached first, in which an intermediate product (active complex) is formed. Formation of such an activated complex requires overcoming a free energy barrier of $\Delta G^{\#}$ as shown in **Fig. 3.52**.

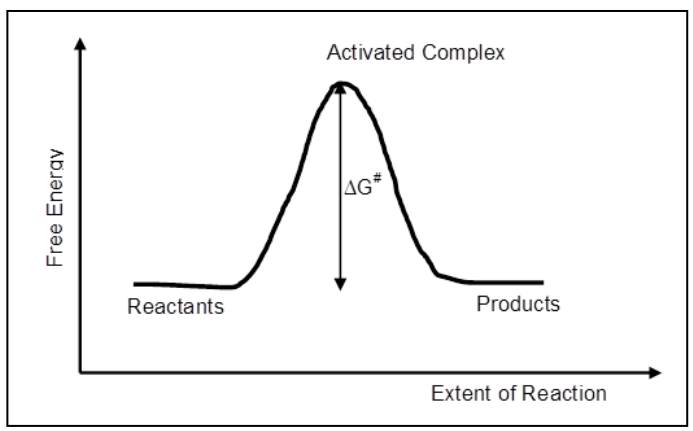

Fig. 3.52: Free energy vs. extent of reaction (Glasstone et al. 1941)

$$A + B \rightarrow [AB]^{\#} \rightarrow \text{Products} \text{ ..... (3.58)}$$

Thus, the rate of reaction (R_x) expressed as:

$$R_x = \text{(Concentration of complex)} \times \text{(Rate of passage over energy barrier)} \text{..... (3.59)}$$

When the free energy of activated complex overcomes the energy barrier, its vibration rate (h ϑ) is t

equal to the thermal energy (KT). Therefore:

$$h\vartheta = KT \quad \text{.....} \quad (3.60)$$

where h is Plank's constant, ϑ is the frequency of vibration of the complex, K is Boltzman's constant. Therefore, ϑ is the rate of passage of activated complexes over the energy barrier.

$$\vartheta = \frac{KT}{h} \quad \text{.....} \quad (3.61)$$

Using (3.58) and (3.61):

$$R_x = [AB^{\#}]\frac{KT}{h} \quad \text{.....} \quad (3.62)$$

Equilibrium constant for the formation of the activated complex is:

$$K^{\#} = \frac{[AB^{\#}]}{[A].[B]} \quad \text{.....} \quad (3.63)$$

Also from thermodynamic:

$$\Delta G^{\#} = -RTLnK^{\#} \quad \text{.....} \quad (3.64)$$

Therefore,

$$K^{\#} = exp\left\{-\frac{\Delta G^{\#}}{RT}\right\} \quad \text{.....} \quad (3.65)$$

Using Eqs. (3.62), (3.63), and (3.65)

$$R_x = [A][B] \underbrace{\frac{KT}{h} exp\left\{-\frac{\Delta G^{\#}}{RT}\right\}}_{Reaction\ Rate\ Const.} \quad \text{.....} \quad (3.66)$$

After modifying the potential from E_o to E as shown in **Fig. 3.53**, the change in free energy is determined as:

$$\Delta G^{\#} = \Delta G_o^{\#} - \alpha nF(E - E_o) \quad \text{.....} \quad (3.67)$$

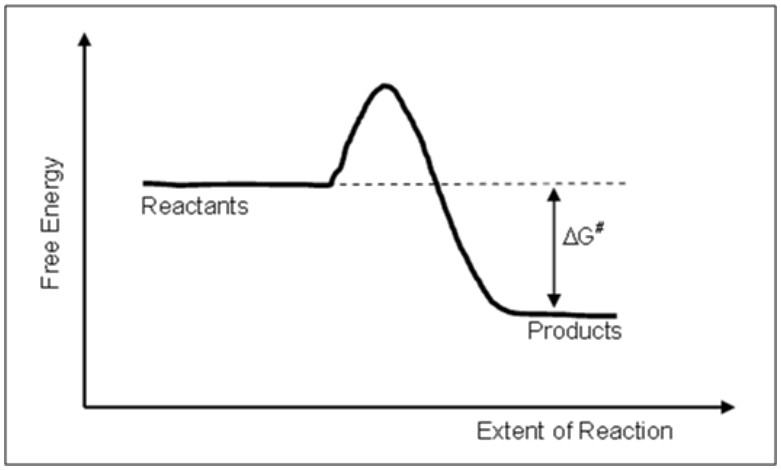

Fig. 3.53: Change in free energy as a function of extent of reaction (Glasstone et al. 1941)

Using Eqs. (3.66) and (3.67)

$$R_x = \frac{KT}{h} exp\left\{-\frac{\Delta G_o^{\#} - \alpha nF(E-E_o)}{RT}\right\} \quad (3.68)$$

where parameter α is a measure of the symmetry of the free energy barrier. When α = 0.5, the degree of decrease in the free energy barrier in the forward reaction is the same as its degree of increase in the reverse direction. The value of α is between 0 and 1; however, it is usually 0.5. Total current "I" across a surface area of A is:

$$I = (Rate\ constant).\underbrace{\left(C_{Surf}\right)}_{[A][B]} nFA \quad (3.69)$$

$$i = \frac{I}{A} = \frac{KT}{h} C_{Surf} nFexp\left\{-\frac{\Delta G_o^{\#} - \alpha nF(E-E_o)}{RT}\right\} \quad (3.70)$$

or

$$i = \underbrace{\frac{KT}{h} exp\left\{-\frac{\Delta G_o^{\#}}{RT}\right\} C_{Surf} nF}_{i_o} exp\left\{\frac{\alpha nF(E-E_o)}{RT}\right\} \quad (3.71)$$

i_o is called the exchange current density. The exchange current density represents the reaction rate in either direction at the equilibrium open circuit potential E_o. Equation (3.71) can be used in CO_2 corrosion model for modeling the current density of anodic and cathodic reaction.

Mass transfer rate of Fe^{2+} is equal to electrochemical reaction rate of the iron dissolution. Therefore:

$$K_{mt,Fe^{2+}}([Fe^{2+}]_s - [Fe^{2+}]_b) = nF\frac{KT}{h} exp\left\{-\frac{\Delta G_{Fe^{2+}}^{\#}}{RT}\right\}[Fe^{2+}]_s exp\left\{\frac{\alpha nF(E_{corr} - E_{Fe^{2+}})}{RT}\right\} \quad (3.72)$$

Dayalan et al. (1995) assumed that the sum of mass transfer rates of ($[H_2CO_3]$, $[HCO_3^-]$, $[H^+]$) is equal to the sum of electrochemical reaction rates of ($[H_2CO_3]$, $[HCO_3^-]$, $[H^+]$) whereas cathodic reduction of carbonic acid produces bicarbonate and also cathodic reaction of bicarbonate produces carbonate ions

which is not considered in this hypothesis. In this study, the proposed hypothesis by Dayalan et al. (1995) was modified by assuming that mass transfer rate of each of the cathodic species is equal to the electrochemical reaction rate of that species under steady state conditions.

$$K_{mt,\,H_2CO_3}([\,H_2CO_3]_b - [\,H_2CO_3]_s) = \frac{KT}{h} exp\left\{-\frac{\Delta G^{\#}_{H_2CO_3}}{RT}\right\}[\,H_2CO_3]_s nFexp\left\{\frac{\alpha nF(E_{corr}-E_{H_2CO_3})}{RT}\right\} \quad (3.73)$$

$$K_{mt,H^+}([H^+]_b - [H^+]_s) = \frac{KT}{h} exp\left\{-\frac{\Delta G^{\#}_{H^+}}{RT}\right\}[H^+]_s nFexp\left\{\frac{\alpha nF(E_{corr}-E_{H^+})}{RT}\right\} \quad (3.74)$$

Therefore, one more equation can be added to the system of fifteen equations (3.43) to (3.57) and there is no need for one of the hypotheses in which the sum of mass transfer rates of (H_2CO_3, HCO_3^-) is equal to the mass transfer rate of CO_3^{2-} (Eq. 3.45). Rest of the model formulation is similar to that of Dayalan et al. (1995).

3.3.3.2. CO_2 Corrosion Models for Scale-Forming Conditions

This modeling approach considers seven main steps (**Fig. 3.54**) for the overall CO_2-corrosion process under scale forming conditions (Dayalan et al. 1998). The first step in CO_2-corrosion process is formation of reactive species in the bulk, which is modeled in similar manner as the CO_2-corrosion under non-scale forming conditions (Section 3.3.3.1). In this step, CO_2 gas dissolves in water and then hydrates to form carbonic acid. Subsequently, the acid can directly reduce on metal surface or dissociate to bicarbonate ions first and then reduce on the metal surface as a cathodic reaction. Dayalan et al. (1998) assumed that carbonic acid reduction may also happen on the scale surface. The second and third steps are the transportation of cathodic reaction species (reactants) from the bulk to the scale surface and from scale surface to the metal surface, respectively. Transportation of reaction species from scale surface to metal surface has to be through the iron-carbonate scale, which is a porous medium. The driving force for transporting these species to the metal surface is consumption of these species on the metal surface by cathodic reaction of corrosion, which causes a concentration gradient between bulk and metal surface. The forth step is electrochemical corrosion reaction on the scale surface and the fifth step is electrochemical corrosion reaction on the metal surface. Electrochemical corrosion reaction can be divided into two main categories as anodic and cathodic reactions. The last step is the transportation of corrosion products from the metal surface to the scale surface and then from the scale surface to the bulk solution. The driving force for this transportation is concentration difference between metal surface, scale surface, and bulk solution because of electrochemical reactions on metal surface.

Dissolusion of CO_2	• $CO_{2(gas)} \leftrightarrow CO_{2(aq)}$ • $CO_{2(aq)} + H_2O \leftrightarrow H_2CO_3$ • $H_2CO_3 \leftrightarrow H^+ + HCO_3^-$ • $HCO_3^- \leftrightarrow H^+ + CO_3^{2-}$
Transportation of reactants from bulk to the scale surface	• $H_2CO_{3(Bulk)} \rightarrow H_2CO_{3(Scale)}$ • $HCO_3^{-}{}_{(Bulk)} \rightarrow HCO_3^{-}{}_{(Scale)}$ • $H^+{}_{(Bulk)} \rightarrow H^+{}_{(Scale)}$
Transportation of reactants from scale surface to the metal surface	• $H_2CO_{3(scale)} \rightarrow H_2CO_{3(Surface)}$ • $HCO_3^{-}{}_{(scale)} \rightarrow HCO_3^{-}{}_{(Surface)}$ • $H^+{}_{(scale)} \rightarrow H^+{}_{(Surface)}$
Electrochemical Reaction on the scale surface	• **Cathodic Reactions** • $2H_2CO_3 + 2e^- \leftrightarrow H_2 + 2HCO_3^-$ • $2H_2CO_3 + 2e^- \leftrightarrow H_2 + 2CO_3^{2-}$ • $2H^+ + 2e^- \leftrightarrow H_2$
Electrochemical Reaction on the metal surface	• **Anodic Reaction** • $Fe \leftrightarrow Fe^{2+} + 2e^-$ • **Cathodic Reactions** • $2H_2CO_3 + 2e^- \leftrightarrow H_2 + 2HCO_3^-$ • $2H_2CO_3 + 2e^- \leftrightarrow H_2 + 2CO_3^{2-}$ • $2H^+ + 2e^- \leftrightarrow H_2$
Transportation of corrosion product from the metal surface to the scale surface	• $Fe^{2+}{}_{(Surface)} \rightarrow Fe^{2+}{}_{(Scale)}$ • $CO_3^{2-}{}_{(Surface)} \rightarrow CO_3^{2-}{}_{(Scale)}$
Transportation of corrosion product from the scale surface to the bulk	• $Fe^{2+}{}_{(Scale)} \rightarrow Fe^{2+}{}_{(Surface)}$ • $CO_3^{2-}{}_{(Scale)} \rightarrow CO_3^{2-}{}_{(Surface)}$

Fig. 3.54: Steps of overall CO_2-corrosion process under scale forming conditions

Based on two main hypotheses, Dayalan et al. (1998) developed their CO_2-corrosion model consisting of a system of twenty equations and twenty unknowns (Eqs. 3.75 through 3.94). CO_2-corrosion rate can be predicted for scale-forming conditions by solving the system of twenty non-linear equations.

The main hypotheses in this modeling approach are: i) the sum of the mass transfer rates of the reactants must be equal to the sum of the electrochemical reaction rates (for both cathodic and anodic reactions); and ii) the sum of the mass transfer rates of carbonic acid and bicarbonate is equal to the mass transfer rate of carbonate ions. The twenty unknown variables are the six metal surface concentrations ($[H^+]_s$, $[HCO_3^-]_s$, $[Fe^{2+}]_s$, $[CO_3^{2-}]_s$, $[OH^-]_s$, $[H_2CO_3]_s$), five scale surface concentrations ($[H^+]_{sc}$, $[HCO_3^-]_{sc}$, $[CO_3^{2-}]_{sc}$, $[OH^-]_{sc}$, $[H_2CO_3]_{sc}$), the corrosion potential (E_{corr}),

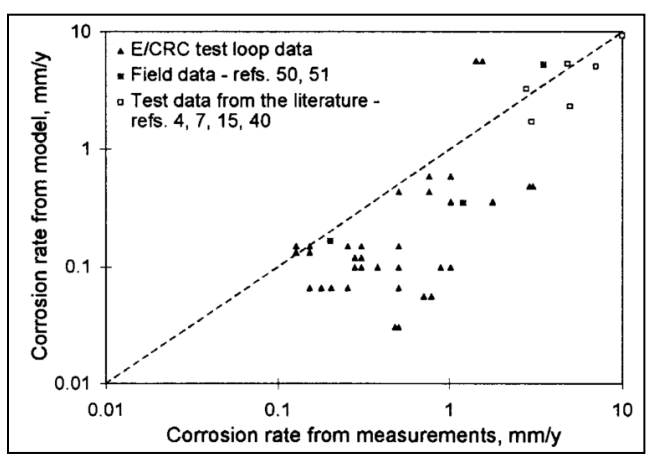

Fig. 3.55: Predicted CO_2 corrosion rate vs. experimental data (Dayalan et al. 1998)

and current due to four reactions ($I_{H2CO3,s}$, $I_{HCO3^-,s}$, $I_{H^+,s}$, $I_{Fe^{2+},s}$, $I_{H2CO3,sc}$, $I_{HCO3^-,sc}$, $I_{H^+,sc}$). **Figure 3.55** shows the comparison between predictions of this model and experimental data.

$$2F \times 10^{-3} \times K_{mt,Fe^{2+},liquid}([Fe^{2+}]_{sc} - [Fe^{2+}]_b) = I_{Fe^{2+}} \quad (3.75)$$

$$2F \times 10^{-3} \times K_{mt,Fe^{2+},scale}([Fe^{2+}]_s - [Fe^{2+}]_{sc}) = I_{Fe^{2+}} \quad (3.76)$$

$$2 \times F \times K_{mt,H_2CO_3}([H_2CO_3]_{sc} - [H_2CO_3]_s) + K_{mt,HCO_3^-}([HCO_3^-]_{sc} - [HCO_3^-]_s) + K_{mt,H^+}([H^+]_{sc} - [H^+]_s) = I_{H_2CO_3,S} + I_{HCO_3^-,S} + I_{H^+,S} \quad (3.77)$$

$$K_{mt,\ _2CO_3}([H_2CO_3]_b - [H_2CO_3]_s) + K_{mt,HCO_3^-}([HCO_3^-]_b - [HCO_3^-]_s) = K_{mt,CO_3^{2-}}([CO_3^{2-}]_s - [CO_3^{2-}]_b) \quad (3.78)$$

$$K_{mt,H_2CO_3}([H_2CO_3]_{sc} - [H_2CO_3]_s) + K_{mt,HCO_3^-}([HCO_3^-]_{sc} - [HCO_3^-]_s) = K_{mt,CO_3^{2-}}([CO_3^{2-}]_s - [CO_3^{2-}]_{sc}) \quad (3.79)$$

$$\left(I_{H_2CO_3,S} + I_{HCO_3^-,S} + I_{H^+,S}\right) + \left(I_{H_2CO_3,SC} + I_{HCO_3^-,SC} + I_{H^+,SC}\right) = I_{Fe^{2+}} \quad (3.80)$$

$$\left(I_{H_2CO_3,S} + I_{HCO_3^-,S} + I_{H^+,S}\right) + \left(I_{H_2CO_3,SC} + I_{HCO_3^-,SC} + I_{H^+,SC}\right)$$

$$= 2 \times 10^{-3} F.K_{Fe^{2+}}[Fe^{2+}]_s exp\left\{\frac{(2-B)F(E_{corr}-E_{Fe^{2+}})}{RT}\right\}$$

$$= \left(2 \times 10^{-3} F.K_{H_2CO_3}[H_2CO_3]_s exp\left\{\frac{-BF\left(E_{corr} - E_{H_2CO_3}\right)}{RT}\right\} + 2 \times 10^{-3} F.K_{HCO_3^-}[HCO_3^-]_s exp\left\{\frac{-BF\left(E_{corr} - E_{HCO_3^-}\right)}{RT}\right\} + 2 \times 10^{-3} F.K_{H^+}[H^+]_s exp\left\{\frac{-BF(E_{corr} - E_{H^+})}{RT}\right\}\right)$$
$$+ \left(2 \times 10^{-3} F.K_{H_2CO_3}[H_2CO_3]_{sc} exp\left\{\frac{-BF\left(E_{corr} - E_{H_2CO_3}\right)}{RT}\right\} + 2 \times 10^{-3} F.K_{HCO_3^-}[HCO_3^-]_{sc} exp\left\{\frac{-BF(E_{corr} - E_{HCO_3^-})}{RT}\right\} + 2 \times 10^{-3} F.K_{H^+}[H^+]_{sc} exp\left\{\frac{-BF(E_{corr} - E_{H^+})}{RT}\right\}\right) \quad (3.81)$$

$$I_{H_2CO_3,S} = 2 \times 10^{-3} F.K_{H_2CO_3}[H_2CO_3]_s exp\left\{\frac{-BF(E_{corr}-E_{H_2CO_3})}{RT}\right\} \quad (3.82)$$

$$I_{HCO_3^-,S} = 2 \times 10^{-3} F.K_{HCO_3^-}[HCO_3^-]_s exp\left\{\frac{-BF(E_{corr}-E_{HCO_3^-})}{RT}\right\} \quad (3.83)$$

$$I_{H^+,S} = 2 \times 10^{-3} F.K_{H^+}[H^+]_s exp\left\{\frac{-BF(E_{corr}-E_{H^+})}{RT}\right\} \quad (3.84)$$

$$I_{H_2CO_3,SC} = 2 \times 10^{-3} F.K_{H_2CO_3}[H_2CO_3]_{sc} exp\left\{\frac{-BF(E_{corr}-E_{H_2CO_3})}{RT}\right\} \quad (3.85)$$

$$I_{HCO_3^-,SC} = 2 \times 10^{-3} F.K_{HCO_3^-}[HCO_3^-]_{sc} exp\left\{\frac{-BF(E_{corr}-E_{HCO_3^-})}{RT}\right\} \quad (3.86)$$

$$I_{H^+,SC} = 2 \times 10^{-3} F.K_{H^+}[H^+]_{sc} exp\left\{\frac{-BF(E_{corr}-E_{H^+})}{RT}\right\} \quad (3.87)$$

$$I_{Fe^{2+}} = 2 \times 10^{-3} F.K_{Fe^{2+}}[Fe^{2+}]_{s} exp\left\{\frac{(2-B)F(E_{corr}-E_{Fe^{2+}})}{RT}\right\} \quad (3.88)$$

$$K_1 = First\ Dissociation\ constant = \frac{[H^+]_s[HCO_3^-]_s}{[H_2CO_3]_s} \quad (3.89)$$

$$K_2 = Second\ Dissociation\ constant = \frac{[H^+]_s[CO_3^{2-}]_s}{[HCO_3^-]_s} \quad (3.90)$$

$$K_w = water\ Dissociation\ constant = [H^+]_s[OH^-]_s \quad (3.91)$$

$$K_1 = First\ Dissociation\ constant = \frac{[H^+]_{sc}[HCO_3^-]_{sc}}{[H_2CO_3]_{sc}} \quad (3.92)$$

$$K_2 = Second\ Dissociation\ constant = \frac{[H^+]_{sc}[CO_3^{2-}]_{sc}}{[HCO_3^-]_{sc}} \quad (3.93)$$

$$K_w = water\ Dissociation\ constant = [H^+]_{sc}[OH^-]_{sc} \quad (3.94)$$

Formation of iron carbonate ($FeCO_3$) scale changes corrosion mechanism because it reduces the area of metal surface exposed to the corrosive environment and limits diffusion of corrosion products. If the concentration of Fe^{2+} and CO_3^{2-} at the metal surface exceeds the solubility limit (K_{sp}), insoluble $FeCO_3$ scale forms on the metal surface. The thermodynamic of iron carbonate scale formation is important in corrosion study because the effect of the scale on corrosion rate and mechanisms can be substantial.

$$K_{sp} = [Fe^{2+}]_s[CO_3^{2-}]_s \quad (3.95)$$

where $[Fe^{2+}]_s$ is surface concentration of Fe^{2+}, $[CO_3^{2-}]_s$ is surface concentration of CO_3^{2-} , and K_{sp} is solubility product of $FeCO_3$ at the given temperature. The K_{sp} is a function of temperature, and ionic strength of the solution:

$$\log K_{sp} = -59.3498 - 0.041377T_k - \frac{2.1963}{T_k} + 24.5724\log T_k + 2.51I^{0.5} - 0.6571 \quad (3.96)$$

where T_k is temperature in Kelvin and I is ionic strength expressed in molarity and can be calculated as:

$$I = \tfrac{1}{2}\sum_i C_i Z_i^2 = \tfrac{1}{2}(C_1Z_1^2 + C_2Z_2^2 + ...) \quad (3.97)$$

where C_i are the concentrations of different species in the aqueous solution expressed in mol/L, and Z_i are the species' charges.

The entire surface of the metal is available for the anodic reaction (iron dissolution reaction to form Fe^{2+}) and for the cathodic reactions (reduction of H^+, H_2CO_3, and HCO_3^-). The surface covered by scale is not available for the anodic reaction. In addition, this area is not available for cathodic reactions on the metal surface. Nevertheless, cathodic reactions can take place on the scale surface (the rates are considerably lower than on metal surfaces) (Dayalan et al. 1998). Corrosion continuously creates voids under scale and undermines the scale as the steel surface corrodes. On the other hands, precipitation of corrosion products also continuously fills up the voids. If the rate of precipitation of corrosion products is higher than the rate of destruction of the scale due to environmental conditions, then a dense and protective corrosion product forms on the surface. However, if the rate of destruction is higher than the rate of precipitation, a thin and non-protective scale forms on the surface (Nešić 2007).

There are some limitations in the CO_2-corrosion models presented by Dayalan et al. (1995) and (1998) including temperature range (up to 250°F), and some of the assumptions made in formulating the models. Dayalan et al. (1998) assumed that some of the cathodic reaction happens on the iron carbonate scale surface. This assumption is unrealistic because iron carbonate scale is a non-conductive ceramic.

In order to adapt the model presented by Dayalan et al. (1998) for high temperature conditions, the first step is improving models used for predicting pH and concentration of corrosion species in bulk solution. The system of five equations and five unknowns for carbonic acid's first and second dissociation, water dissociation, carbon balance, and electroneutrality (Eqs. 3.98 through 3.102) can be solved to predict the pH of the solution. The models used for CO_2 dissolution and dissociation are applicable for HPHT conditions. Therefore, pH prediction is expected to be valid for HPHT conditions. Model predictions are compared with experimental data in **Figs. 3.56 and 3.57**. Model predictions show a good agreement with experimental data.

$$K_1 = First\ Dissociation\ constant = \frac{[H^+]_{bulk}[HCO_3^-]_{bulk}}{[H_2CO_3]_{bulk}} \quad (3.98)$$

$$K_2 = Second\ Dissociation\ constant = \frac{[H^+]_{bulk}[CO_3^{2-}]_{bulk}}{[HCO_3^-]_{bulk}} \quad (3.99)$$

$$K_w = water\ Dissociation\ constant = [H^+]_{bulk}[OH^-]_{bulk} \quad (3.100)$$

$$[CO_3^{2-}]_{bulk} + [HCO_3^-]_{bulk} + [H_2CO_3]_{bulk} = [CO_2]_{bulk} \quad (3.101)$$

$$[H^+]_{bulk} = 2[CO_3^{2-}]_{bulk} + [HCO_3^-]_{bulk} + [OH^-]_{bulk} \quad (3.102)$$

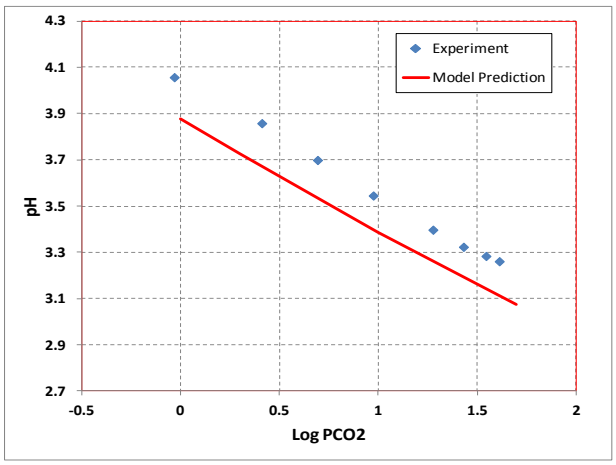

Fig. 3.56: Model predictions and experimental data at 347K and 0.5 molar NaCl concentration

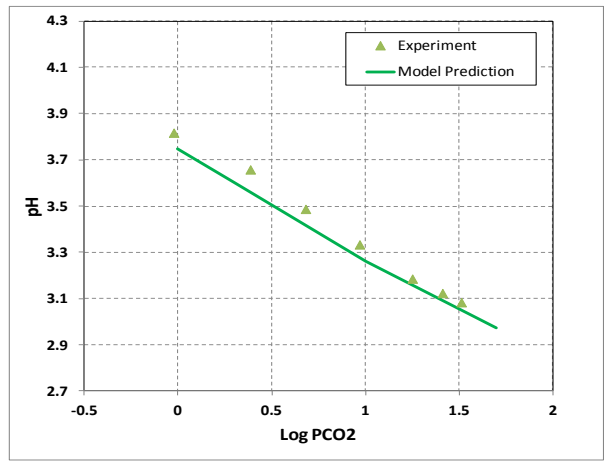

Fig. 3.57: Model predictions and experimental data at 299K and 0.5 molar NaCl concentration

3.3.3.3. H_2S Corrosion Model

Hydrogen sulfide corrosion of mild steel is considered to be solid state reaction which means the initial and final form of iron is solid.

$$Fe + H_2S \leftrightarrow FeS_{(s)} + H_2 \quad \text{.....} \quad (3.103)$$

Sun and Nešić (2007) proposed a model for H_2S corrosion. Based on this model, adsorption of H_2S onto the carbon steel metal surface immediately forms a protective non-stoichiometric layer of iron with thickness significantly less 1 µm. The protective layer is known as Mackinawite. The formation of Mackinawite reduces the corrosion rate by producing a compact diffusion barrier. Environmental conditions erode the scale and forms a new mackinawite later. New layer of Mackinawite builds up internal stress, which causes cracking and consequently delamination of scale layer. The process of scale build-up and cracking creates a thick and porous scale. Sun and Nešić (2007) assumed the formation of two different layers of Mackinawite during H_2S corrosion process including porous outer layer and compact inner layer. They also assumed that H_2S corrosion is controlled only by mass transfer of ions through the scale layer and liquid boundary layer. Figure 3.46 shows the mechanism of H_2S corrosion process. Equations (3.104) through (3.106) show the flux of H_2S through the boundary layer, porous outer mackinawite, and inner mackinawite layer, respectively.

$$Flux_{H_2S} = K_{m(H_2S)}\left[C_{b,H_2S} - C_{O,H_2S}\right] \quad \text{.....} \quad (3.104)$$

$$Flux_{\ \ _2S} = \frac{D_{H_2S}\varepsilon\psi}{\delta_{OS}}\left[C_{O,H_2S} - C_{i,H_2S}\right] \quad \text{.....} \quad (3.105)$$

$$Flux_{H_2S} = A_{H_2S} Ln\left(\frac{C_{i,H_2S}}{C_{s,H_2S}}\right) e^{\frac{-B_{H_2S}}{RT_K}} \quad \text{.....} \quad (3.106)$$

where $Flux_{H_2S}$ is expressed in mole/(m^{2}s), $K_{m(H_2S)}$ is the mass transfer coefficient for H_2S in the

hydrodynamic boundary layer. Under nearly stagnant condition, $K_{m(H_2S)} = 10^{-4} m/s$. C_{b,H_2S} is bulk concentration of H_2S in the liquid phase in mole/m^3. C_{O,H_2S} is interfacial concentration of H_2S at the outer scale/solution interface in mole/m^3. D_{H_2S} is the diffusion coefficient of dissolved H_2S in water, which is $2 \times 10^{-9} m^2/s$. ε is porosity of the outer Mackinawite scale, ψ is tortuosity factor of the outer mackinawite, C_{i,H_2S} is interfacial concentration of H_2S at the inner-scale film-interface in mole/m^3. δ_{OS} is the thickness of Mackinawite scale in m.

$$\delta_{OS} = \frac{m_{OS}}{(\rho_{FeS} A)} \quad \text{.....} \quad (3.107)$$

M_{OS} is mass of the Mackinawite scale in kg, A is surface area (m^2), A_{H_2S} and B_{H_2S} are Arrhenius constants ($A_{H_2S} = 1.3 \times 10^{-4} \frac{mole}{m^2.s}$, $B_{H_2S} = 15500 \frac{Jouls}{mole}$). T_K is temperature (in Kelvin), C_{s,H_2S} is the concentration of H_2S on the steel surface, which is typically 10^{-7} mole/m^3. Under steady state situation, three fluxes are equal to each other and are equal to the rate of H_2S consumption due to corrosion. Based on this analysis, the H_2S corrosion rate can be expressed as:

$$CR_{H_2S} = (A_{H_2S}) e^{\frac{-B_{H_2S}}{RT_K}} Ln\left(\frac{C_{b,H_2S} - CR_{H_2S}\left[\frac{\delta_{0.5}}{D_{H_2S}\varepsilon\psi} + \frac{1}{K_{m(H_2S)}}\right]}{C_{s,H_2S}}\right) \quad \text{.....} \quad (3.108)$$

The unknown properties of the outer Mackinawite, which changes with time, are calculated separately. Mackinawite retention rate (SSR) is equal to the difference of scale formation (SFR) and scale damage rate (SDR). Experimental results by Sun and Nešić (2007) showed that even in stagnant conditions, about half of the sulfide scale layer removed by spalling. For corrosion occurring under flowing condition, the scale removal rate can be written as:

$$SDR_m = 0.5(1 + C.V^a) CR_{H_2S} \quad \text{.....} \quad (3.109)$$

where SDR_m is mechanical scale damage rate. The constants c and a are determined experimentally. For flow between rotating cylinders, the values of "c" and "a" are approximately 0.55 and 0.2, respectively. The change in mass of the outer scale is:

$$\Delta m_{os} = (SRR) M_{FeS} A \Delta t \quad \text{.....} \quad (3.110)$$

where M_{FeS} is molar mass of iron sulfide (kg/mole) and Δt is the time interval (s).

Sun and Nešić (2007) found that the porosity of the outer Mackinawite scale is very high (0.9). However, due to its layered structure, the tortuosity factor was found to be very low ψ = 0.003. They suggested the following steps to predict H_2S corrosion rate under scale forming conditions:

Step 1: The corrosion rate without scale (assuming $\delta_{OS} = 0$) is calculated using Eqn. A.49.
Step 2: Δm_{os} is computed using Eqn. A.51 in Δt time interval.
Step 3: δ_{OS} is determined from Δm_{os} and new corrosion rate can be predicted using Eqn. A.49.

Step 4: Steps 2 and 3 are repeated for a new time interval.

Modeling becomes complicated when iron sulfide forms and controls the corrosion rate at very low H_2S gas concentrations (in ppm_w range). In addition, the corrosion process is substantially affected by the reduction of protons. Following the procedure suggested by Sun and Nešić (2007), corrosion rate equation presented below can be developed for corrosion driven by protons and controlled by the presence of the iron sulfide scale.

$$CR_{H^+} = (A_{H^+})e^{\frac{-B_{H^+}}{RT_K}} Ln\left(\frac{C_{b,H^+} - CR_{H^+}\left[\frac{\delta_{0.5}}{D_{H^+}\varepsilon\psi} + \frac{1}{K_{m(H^+)}}\right]}{C_{s,H^+}}\right) \quad \text{..... (3.111)}$$

where $K_{m(H^+)} = 3 \times 10^{-4}$ for nearly stagnant condition, $D_{H^+} = 2.8 \times 10^{-8}\, m^2/s$, $A_{H^+} = 3.9 \times 10^{-4}\, mole/(m^2.s)$, $B_{H^+} = 15500\, Joules/Mole$, C_{s,H^+} is set to $10^{-7}\, mole/(m^3)$. Therefore, total corrosion rate is equal to sum of corrosion rates resulting from scale removal and reduction of protons.

$$CR = CR_{H^+} + CR_{H_2S} \quad \text{..... (3.112)}$$

Sun and Nešić (2007) compared experimental data and model predicted corrosion and scale-retention rates at different H_2S concentrations (**Figs. 3.58** through **3.60**).

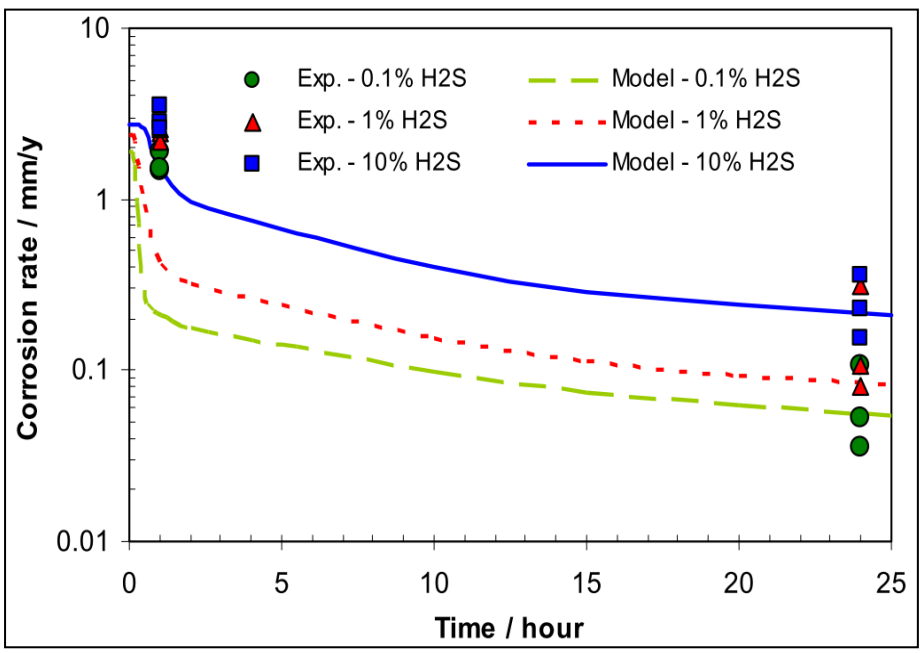

Fig. 3.58: Measured and prediction corrosion rate vs. time for different H_2S gas concentrations under stagnant conditions (P = 1 bar, T = 80ºC, and pH 5.0-5.5) reaction times of 1 and 24 hours (Sun and Nešić 2007)

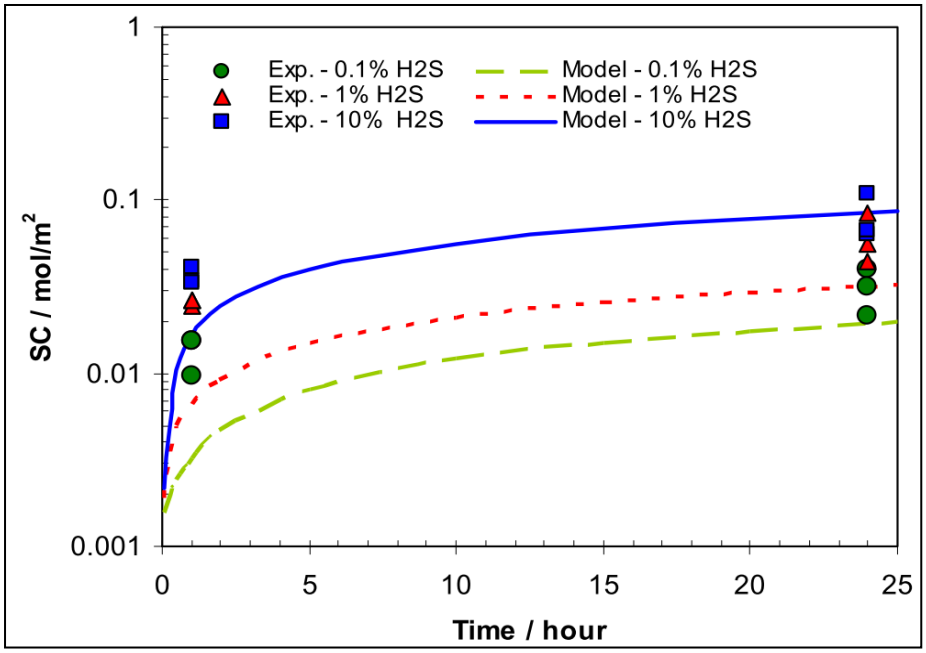

Fig. 3.59: Measured and predicted scale retention vs. time for different H_2S gas concentrations under stagnant conditions (P = 1 bar, T = 80ºC, and pH 5.0-5.5) reaction time of 1 and 24 hours (Sun and Nešić 2007)

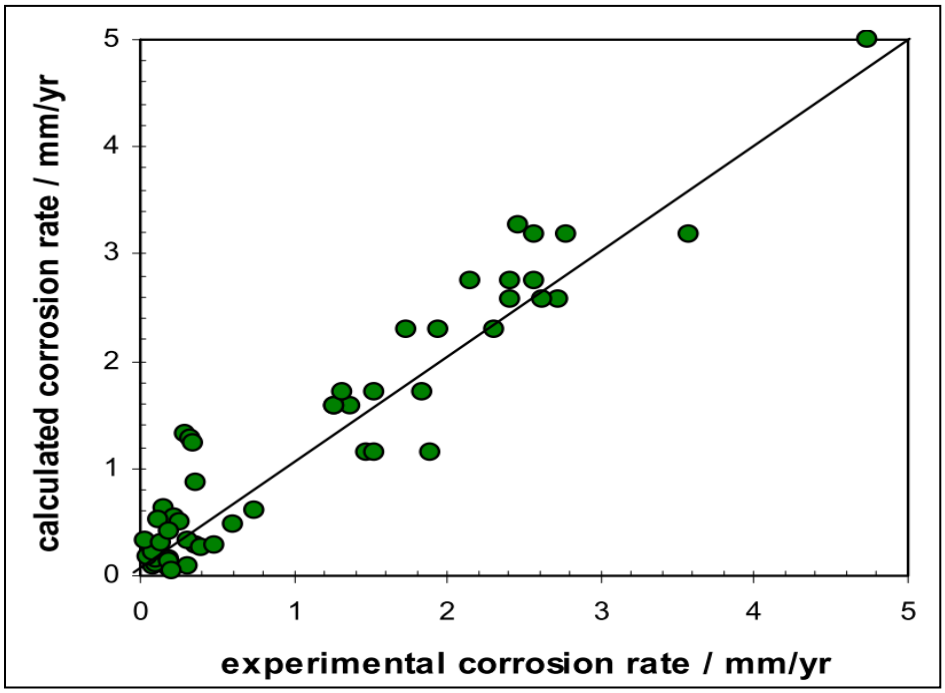

Fig. 3.60: Predicted vs. measured corrosion rate (P = 1 bar, H_2S concentration ranging from 0.0075% to 10%, temperature 25°C, 60°C, and 80°C, reaction time of 1 hour and 24 hours, pH from 5.0 to 5.5, and velocity from 0 to 8000 rpm) (Sun et al. 2007)

3.3.3.4. H_2S-CO_2 Corrosion Models

I. Mass Transfer Based Model

Due to the presence of the inner mackinawite film and porous outer layer, it is assumed that the corrosion rate of steel in H_2S solution is always more affected by mass-transfer than electrochemical process. The corrosion is also influenced by the direct reaction of H_2S and CO_2 with steel surface as well as the reduction of protons (H^+). Therefore, a model can be established based on the mass transfer flux of the three elements (H^+, H_2S and CO_2), resulting from: i) convective mass transfer through the boundary layer, ii) molecular diffusion through the liquid in pores in the outer layer, and iii) solid-state diffusion through the inner mackinawite layer. Under the steady state condition, the three fluxes of each element are equal and proportional to the corrosion rate. The flux of H_2S can be expressed as:

$$Flux_{H2S} = A_{H2S}.e^{-\frac{B_{H2S}}{RT_K}}.\ln\frac{C_{b,H2S} - Flux_{H_2S}\left(\frac{\delta_{0.5}}{D_{H_2S}.\varepsilon\psi} + \frac{1}{K_{m,H_2S}}\right)}{C_{s,H_2S}} \quad (3.113)$$

Rate of corrosion resulting from H_2S is given as: $CR_{H2S} = Flux_{H2S}.M_{Fe}/\rho_{Fe}$. The amount of Mackinawite retained on the steel surface changes with time and it depends on deposition and removal rates. The amount of Mackinawite retained is expressed as:

$$SRR = SFR - SDR \quad (3.114)$$

where SRR is sulfide layer retention rate, SFR is the sulfide layer formation rate, which is equivalent to the corrosion rate and SDR is the sulfide layer removal rate, which is half of the corrosion rate. By knowing the layer retention rate, the change in mass of the outer sulfide layer can be calculated as:

$$\Delta m_{os} = SRR.M_{FeS}.A.\Delta t \quad (3.115)$$

where M_{Fes} is the molar mass of iron sulfide in kg/mol and Δt is the time interval in seconds. Then thickness of the formation is calculated as:

$$\delta_{0.5} = \Delta m_{os}/(\rho_{FeS}.A) \quad (3.116)$$

Similarly, the flux of H^+ can be expressed as:

$$Flux_{H^+} = A_{H^+}.e^{-\frac{B_{H+}}{RT_K}}.\ln\frac{C_{b,H^+} - Flux_{H^+}\left(\frac{\delta_{0.5}}{D_{H^+}.\varepsilon\psi} + \frac{1}{K_{m,H^+}}\right)}{C_{s,H^+}} \quad (3.117)$$

The flux of H+ is equivalent to the rate corrosion resulting from hydrogen ion:

$$CR_{H^+} = \frac{Flux_{H^+}}{2}.\frac{M_{Fe}}{\rho_{Fe}} \quad (3.118)$$

Correspondingly, the flux of CO_2 can be expressed as:

$$Flux_{CO2} = A_{CO2}.e^{-\frac{B_{CO2}}{RT_K}}.\ln\frac{C_{b,CO2} - Flux_{CO2}\left(\frac{\delta_{0.5}}{D_{CO2}.\varepsilon\psi} + \frac{1}{K_{m,CO2}}\right)}{C_{s,CO2}} \quad (3.119)$$

In case of H_2S, the pure mass transfer is assumed and $C_{s,H2S}$ and $C_{s,H}^{+}$ are set to be in very small quantity, which is 1×10^{-7} mol/m^3. In CO_2 corrosion, CO_2 hydrates and forms H_2CO_3 at the steel surface. This process is considered very slow; and hence expected to control the process. Therefore, the flux of CO_2 can be expressed as:

$$Flux_{CO2} = C_{s,CO2}\left(D_{H2CO3}.\varepsilon.\psi.K_{hyd}^{f}.K_{hyd}\right)^{0.5} \quad (3.120)$$

By combining Eqs. (3.119) and (3.120), the flux of CO_2 can be given as:

$$Flux_{CO2} = A_{CO2}.e^{-\frac{B_{CO2}}{RT_K}}.\ln\frac{C_{b,CO2} - Flux_{CO2}\left(\frac{\delta_{0.5}}{D_{CO2}.\varepsilon\psi} + \frac{1}{K_{m,CO2}}\right)}{\frac{Flux_{CO2}}{\left(D_{H2CO3}.\varepsilon.\psi.K_{hyd}^{f}.K_{hyd}\right)^{0.5}}} \quad (3.121)$$

The bulk concentration of CO_2 in the solution, $C_{b,CO2}$ (mol/bar) can be estimated applying Henry's law as:

$$C_{b,CO2} = P_{CO2} \times K_{sol} \quad (3.122)$$

where P_{CO2} is the partial pressure of carbon dioxide in bar, K_{sol} is a Henry's constant which is a function of temperature (°F) and ionic strength (mol/L).

$$K_{sol} = \frac{14.5}{1.00258} \times 10^{-(2.27+5.65\times10^{-3}T_f - 8.06\times10^{-6}T_f^2 + 0.075\times I)} \quad (3.123)$$

Other parameters, which are required to estimate flux of CO_2 such as diffusion coefficient of H_2CO_3, equilibrium constant for the CO_2 hydration reaction and forward reaction rate for the CO_2 hydration reaction are presented in **Table 3.6**.

Table 3.6: Parameters of Flux equations

Parameter identification	Constant	Source
Equilibrium constant of CO_2 hydration	$K_{hyd} = 2.58\times10^{-3}$	Palmer and Van Eldik(1983)
Forward reaction rate for CO_2 hydration reaction	$K_{f\ hyd} = 10^{329.85-110.54\times\log T_K - \frac{17265.4}{T_K}}$	Palmer and Van Eldik(1983)
Diffusion constant of H_2CO_3 at 20°C, (m^2/s)	$D_{ref} = 2.00\times10^{-9}$	KvareKval (1997)
Diffusion constant of H^+ at 20°C, (m^2/s)	$D_{ref} = 9.312\times10^{-9}$	Newman (1991)
Diffusion constant of CO_2 at 20°C, (m^2/s)	$D_{ref} = 1.96\times10^{-9}$	Perry (1984)
Diffusion constant of HS^- at 20°C, (m^2/s)	$D_{ref} = 2.00\times10^{-9}$	Nordsveen et al. (2001)

The influence of temperature on diffusion coefficient can be obtained from the Stokes-Einstein equation:

$$D = D_{ref} \times \frac{T}{T_{ref}} \times \frac{\mu_{ref}}{\mu} \quad \text{(3.124)}$$

where T_{ref} is a reference temperature = 20°C, the dynamic viscosity of water is μ_{ref} = 1.002 Kg/(m.s) and the diffusion coefficient can be obtained from Table 3.6. Dynamic water viscosity as a function of temperature is given as:

$$\mu = \mu_{ref} \times 10^{\frac{1.3272.(20-T)-0.001053.(20-T)^2}{T+105}} \quad \text{(3.125)}$$

Then, total corrosion rate in mixed H_2S-CO_2 saturated brine environment is the sum of individual corrosion rate resulting from each element. Thus:

$$CR_T = CR_{H_2S} + CR_{H^+} + CR_{CO2} \quad \text{(3.126)}$$

<u>Numerical Procedure</u>

The flow chart presented in **Fig. 3.61** demonstrates H_2S-CO_2 corrosion model computational procedure that can be summarized as:

- Determination of the bulk concentration of CO_2, H_2S and H^+ in the solution at desirable conditions.
- Computation of H_2S corrosion rate in the absence of formation layer using Eq. (3.113).
- Estimation of the level of protective scale formed over time using Eq. (3.116).
- Calculation of H_2S corrosion rate in the presence of scale using Eq. (3.113).
- Determination of H^+ and CO_2 corrosion rate using Eqs. (3.117) & (3.118), and then the total

corrosion rate by adding the corrosion rates of H_2S, CO_2 and H^+.

- Steps from 3 to 5 are repeated to estimate the total corrosion rate over new time interval.

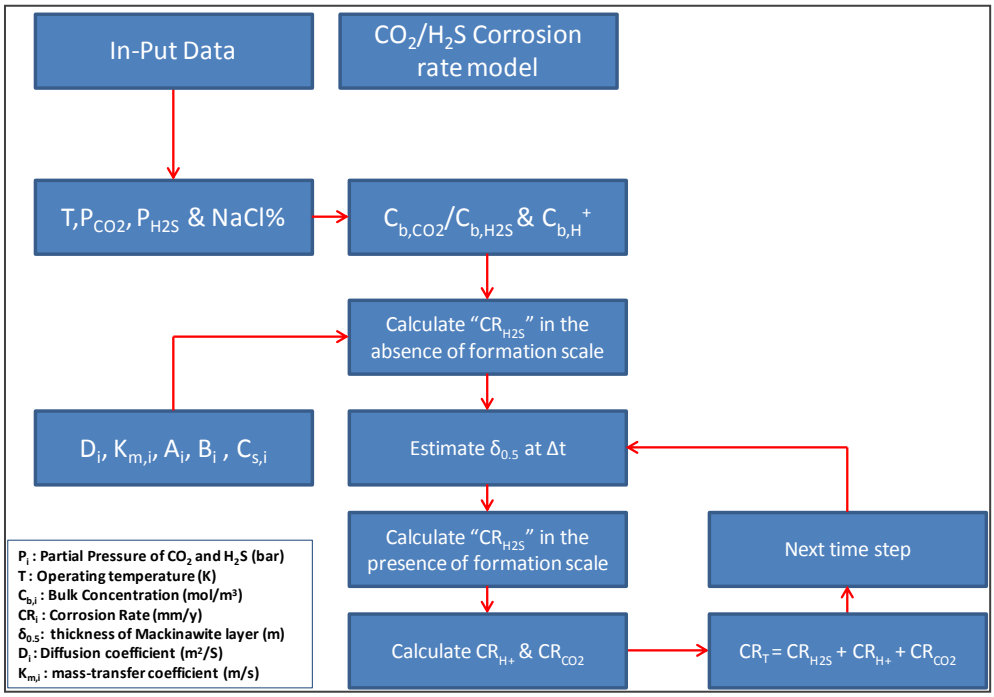

Fig. 3.61: Schematic of H_2S-CO_2 model computational procedure

Model Assumptions and Limitations

- The model assumes uniform H_2S and H_2S-CO_2 corrosion. It cannot be used to predict localized corrosion.
- The model is applicable in the range of partial pressure of 0.01-10 bar for both hydrogen sulfide and carbon dioxide.
- The model does not account for any precipitation of iron sulfide, iron carbonate, or any other scale.
- The model also does not account for various transformation of sulfide from one type to another that depends on H_2S concentration, temperature and period of exposure.
- The model is valid for pH range of 3-7, because it does not account for dissolution of iron sulfide layer that may occur at very low pH.

Model Modification

In order to improve this model to be valid for high pressure and high temperature applications, the model formulations has been modified: i) The bulk concentrations of CO_2, H_2S and H^+ are estimated at high temperature conditions; and the influence of H_2S concentration and temperature on formation of iron sulfide layer is estimated.

Model Verification

Model proposed by Sun and Nešić (2009) calculates the H_2S solubility in the brine to predict the corrosion rate. The model is improved in this study. Model predictions for H_2S-CO_2 system are

compared with experimental data obtained at P_{CO2} = 29 bar, P_{H2S} = 0.0441 – 1 psi, T = 158°C, pH = 4.2 – 4.9, and liquid velocity = 0.3 m/s (**Fig. 3.62**). Comparison of the improved model predictions with measurements showed significant enhancement in corrosion rate prediction after 300 hours. The model is more accurate in predicting corrosion rate for longer time periods.

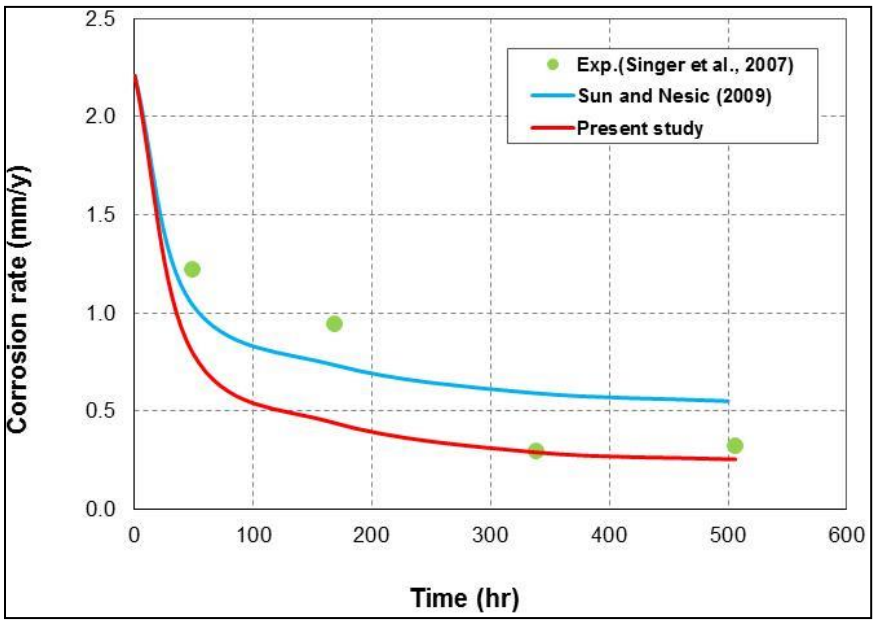

Fig. 3.62: Comparison between experimental data (Singer et al. 2007), Sun and Nešić model (2009), and prediction using modified model

Modified H_2S-CO_2 corrosion model is also compared with experimental data by Kvarekval et al. (2003) at P_{CO2}=101 psi, P_{H2S} = 20 - 62 psi, T = 248°F, pH = 3.95 – 4.6, and liquid velocity = 10 m/s (**Fig. 3.63**). Modified H_2S-CO_2 corrosion model showed better agreement with experimental data in comparison with the existing model (Sun and Nešić 2009).

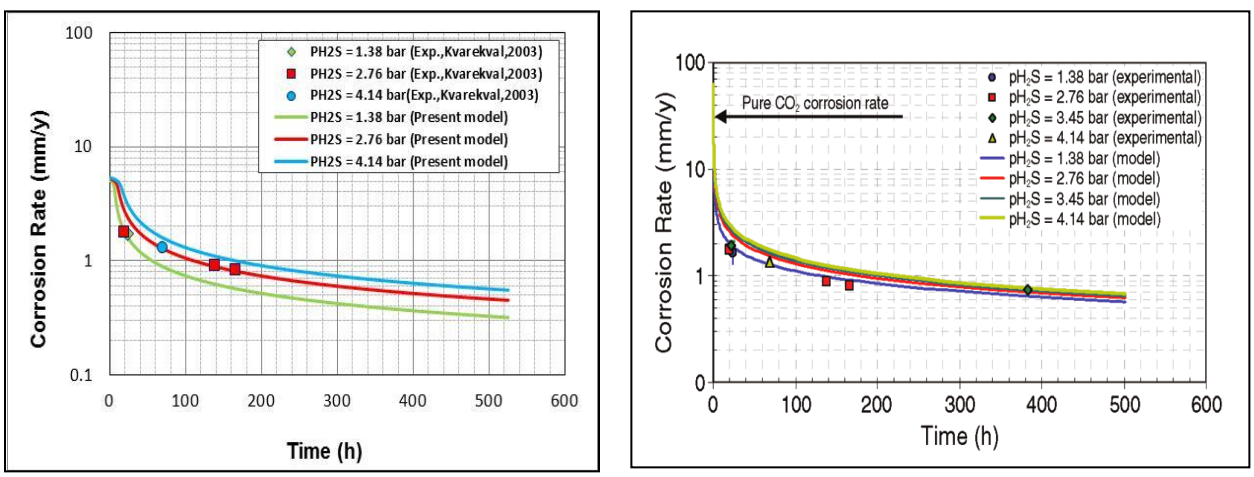

(a) **(b)**

Fig. 3.63: Comparison between predictions and measurements: a) data (Kvarekval et al. 2003); and b) data (Kvarekval et al. 2003; Sun and Nešić model 2009)

II. Thermodynamic and Electrochemical Based Model

Anderko and Young (1998) model combines thermodynamic and electrochemical modeling approaches to describe the partial cathodic and anodic processes on the steel surface. It predicts uniform corrosion rates of carbon steels in the presence of carbon dioxide and hydrogen sulfide. It also provides the expected corrosion scale (iron carbonate and iron sulfide) using the corrosion rate. The model is presented in Appendix F.

III. Mechanistic CO_2-H_2S Corrosion Model

Recently, a new CO_2-H_2S Corrosion model has been developed (Sina et al. 2012) to predict uniform corrosion rate in CO_2-H_2S containing corrosive environment. The model considers transient chemical reactions that occur in the bulk solution, transport of ions and active species towards and away from the metal surface, and electrochemical reactions at the surface. In addition, it accounts for the formation of corrosion scale and its effect on the corrosion rate. The model is presented in Appendices G and H. An improved version of this model is presented in Appendix I.

3.3.4. Measurement Techniques

Uniform corrosion measurement techniques can be divided into two main categories known as non-electrochemical and electrochemical. Non-electrochemical techniques are including weight loss measurement, 3D profilometer of surface, visual observations, electrical resistance probes and ultrasonic measurement techniques. The electrochemical measurement techniques are: Linear Polarization Resistance (LPR), Electrochemical Impedance Spectroscopy (EIS), Potentiodynamic polarization, Electrochemical Frequency Modulation (EFM), Harmonics and electrochemical noise. Summary of two important electrochemical measurement techniques used in this study are discussed in the following sections. More details about electrochemical measurement techniques can be found in ASTM G3, Standard Practice for Conventions Applicable to Electrochemical Measurements in Corrosion Testing.

3.3.4.1. Linear Polarization Resistance

A commonly used polarization technique is linear polarization resistance (LPR). The polarization resistance of a metal is defined as the gradient of the potential–current density (E-i) curve (which is often called Tafel slop) at the free corrosion potential (**Fig. 3.64**), resulting in the polarization resistance R_p, which is related to the corrosion current as:

$$R_p = \frac{B}{i_{corr}} = \frac{\Delta E}{(\Delta i)_{\Delta E \to 0}} \quad \text{..... (3.127)}$$

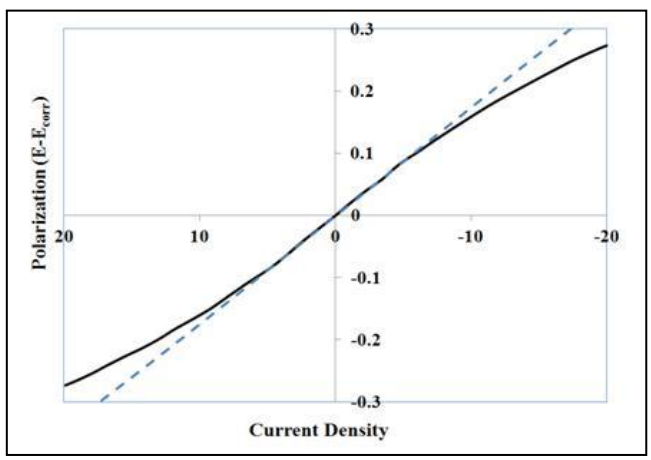

Fig. 3.64: Linear polarization plot (Roberge 1999)

where R_p is polarization resistance, I_{corr} is corrosion current, and B is an empirical polarization resistance constant that can be related to the anodic (b_a) and cathodic (b_c) Tafel slopes with:

$$B = \frac{b_a b_c}{2.3(b_a + b_c)} \quad \text{.....} \quad (3.128)$$

The Tafel slopes themselves can be evaluated experimentally using real polarization plots similar to those presented in **Fig. 3.65** and **3.66** or obtained from literature (Roberge 1999).

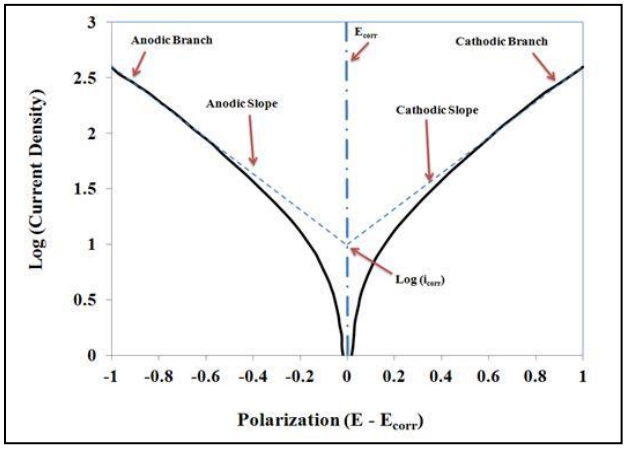

Fig. 3.65: Polarization diagram for an active system with anodic and cathodic branches (Roberge 1999)

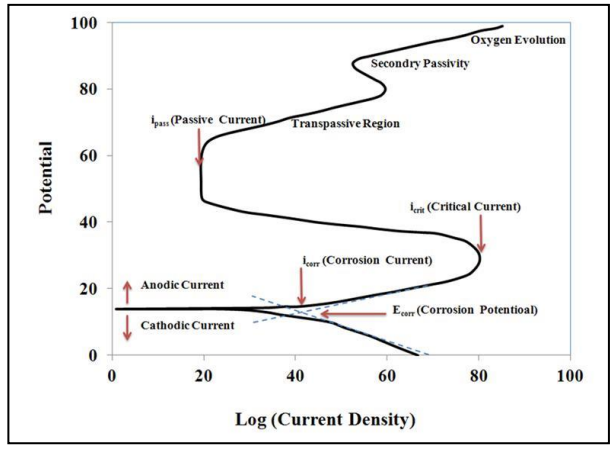

Fig. 3.66: Hypothetical polarization diagram for a passivating system with anodic and cathodic branches (Roberge 1999)

3.3.4.2. Electrochemical Impedance Spectroscopy

Electrochemical impedance spectroscopy (EIS) is one of the methods used to study of corrosion since early seventies. The method has been proven to be reliable and accurate in measuring corrosion rate. However, to compute the charge transfer resistance or polarization resistance R_p, which is linearly related to the corrosion rate, EIS results have to be interpreted using an interface model. EIS method is becoming popular in corrosion laboratories around the world (Epelboin et al. 1972). The main benefit of EIS over other methods is the use of very small-amplitude signals without significantly affecting the measurement. To make an EIS measurement, a small-amplitude signal, usually a voltage between 5 and 50 mV, is applied to a specimen over a range of frequencies from 0.001 to 100,000 Hz.

The EIS technique monitors the real (resistance) and imaginary (capacitance) parts of the impedance response of the system. An electrical circuit model or circuit description code and initial circuit parameters are assumed depending upon the shape of the EIS spectrum. A computer program can be used to fit the best frequency response to the given EIS spectrum to calculate the EIS spectrum parameters. Depending upon how well the fitting curve overlaps the original spectrum, the quality of the fitting can be judged. It is possible to obtain a set of parameters by fitting the EIS data, which can be correlated with the corrosion of the substrate, electrochemical reactions, and the coating condition (if a coating is present). Only a few numerous equivalent circuits really apply in the context of a freely corroding interface at or close to kinetic equilibrium to describe electrochemical interfaces. The first circuit (**Fig. 3.67a**) corresponds to the simplest equivalent circuit that can describe a metal/electrolyte interface. The component *Q* describes the "leaky capacitor" behavior representing the presence of a constant phase element. The admittance representation *Y** of the CPE behavior with frequency can be

described by Eq. (3.129). For n = (1-β), Eq. (3.129) displays the behavior of a resistor with $R = Y_o^{-1}$ and for $n = \beta$, that of a capacitor with $C = Y_o$. For n = 0.5, Eq. (3.129) becomes the expression of a Warburg (W) component, and when $n=-\beta$, it emulates an inductance with $L = Y_o^{1.25}$ (Epelboin et al. 1972).

$$Y^*(\omega) = Y_o\, \omega^{n} \cos(n\pi/2) + jY_o\, \omega^{n} \sin(n\pi/2) \quad (3.129)$$

Figure 3.68 shows the complex-plane display of EIS simulated data generated for the model circuit shown in Fig. 3.67a when R_s =10 Ω, R_p =100 kΩ, and Q decomposes into C_{dl} = 40 μF and n = 0.8, and **Fig. 3.69** suggests how the same data can be presented in a Bode plot format (Epelboin et al. 1972).

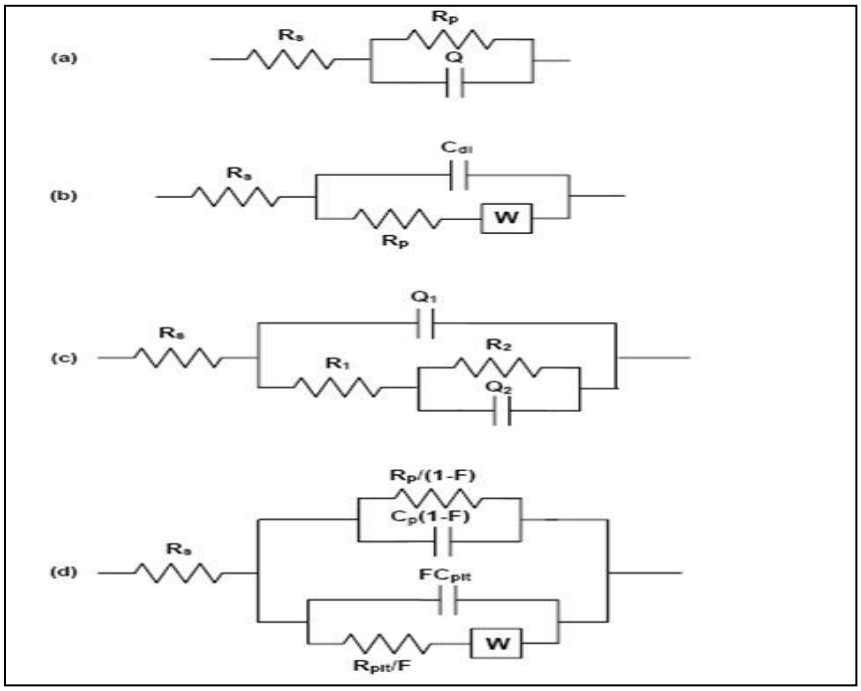

Fig. 3.67: Equivalent circuit models proposed for the interpretation of EIS results measured in corroding systems: (a) simplest representation of an electrochemical interface; (b) one relaxation time constant with extended diffusion; (c) two relaxation time constants; and (d) the impedance of pitting processes of Al-based materials (Epelboin et al. 1972)

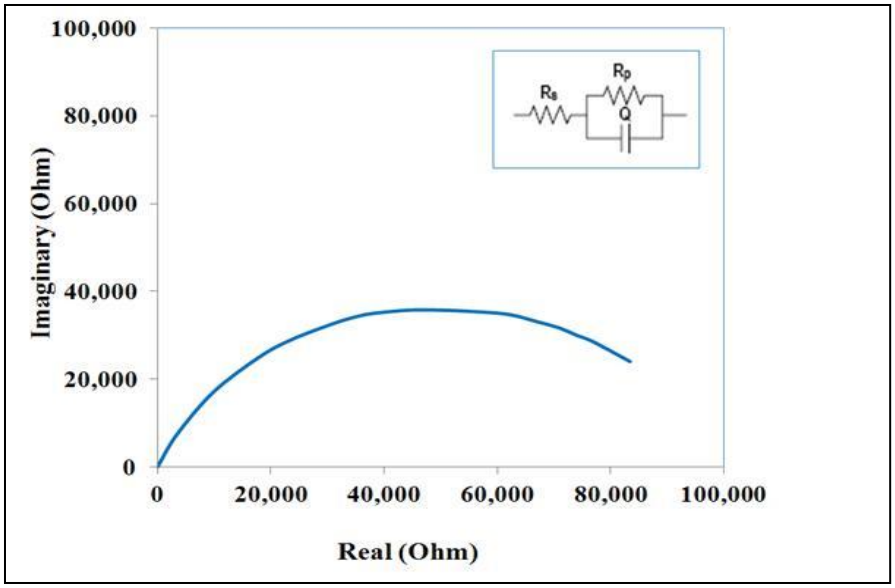

Fig. 3.68: Complex-plane presentation of simulated data corresponding to the model circuit in Fig. 3.67a when Rs=10 Ω, Rp= 100 KΩ, and Q decomposes into Cdl=40µF and n=0.8 (Epelboin et al. 1972)

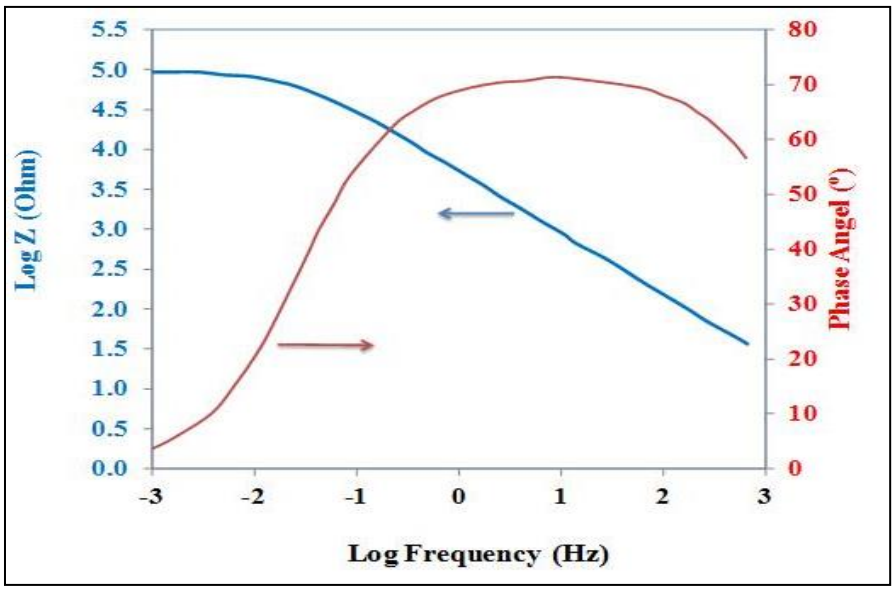

Fig. 3.69: Bode representation of the same data illustrated in Fig. 3.68 in complex plane format (Epelboin et al. 1972)

3.3.5. Experimental Study at Low Pressure

Low-pressure corrosion experiments were conducted using both weight loss (WL) and electrical measurement techniques. Tests were performed with nitrogen purged nickel-plated aluminum autoclave. The description of the experimental setup is presented in Section 3.3.5.4. The effects of the carbon dioxide concentration (0 to 100%), temperature (78 to 176°F), and brine concentration (1% and 2%) on corrosion of the carbon steel have been investigated.

3.3.5.1. Test Conditions

Corrosion rate of common carbon steel was measured under different experimental conditions. The average corrosion rate was determined using linear polarization resistance (LPR) and weight loss techniques. To examine the effects of temperature, CO_2 and salt concentrations on corrosion rate, 54 tests were performed at a constant pressure of 120 psi. Test parameters of the experiments are presented in **Table 3.7**.

Table 3.7: Test parameters of low-pressure corrosion experiments

Exp. #	Temp. (ºF)	Pressure (psi)	Partial Pressure %		Brine Conc. (%)	Test Period (days)
			N_2	CO_2		
12	78	120	100	0	2	187
13	78	120	50	50	2	187
14	78	120	25	75	2	187
15	78	120	25	75	2	187
16	78	120	0	100	2	187
17	78	240	0	100	2	187
18	78	120	75	25	2	187
19	110	120	75	25	2	187
20	110	120	25	75	2	187
21	110	120	100	0	2	187
22	110	120	75	25	2	187
23	110	120	50	50	2	187
24	110	120	25	75	2	187
25	110	120	0	100	2	187
26	176	120	100	0	2	187
27	176	120	75	25	2	187
28	176	120	50	50	2	187
29	176	120	25	75	2	187
30	176	120	0	100	2	187
31	140	120	100	0	2	187
32	140	120	75	25	2	187
33	140	120	50	50	2	187
34	140	120	25	75	2	187
35	140	120	0	100	2	187
36	140	120	100	0	1	187
37	140	120	75	25	1	187
38	140	120	75	25	1	187
39	140	120	50	50	1	187
40	140	120	25	75	1	187
41	140	120	0	100	1	187
42	176	120	0	100	1	187
43	176	120	25	75	1	187
44	176	120	50	50	1	187
45	176	120	75	25	1	187
46	176	120	100	0	1	187
47	176	120	75	25	1	187
48	110	120	25	75	1	187
49	110	120	0	100	1	187
50	110	120	50	50	1	187
51	110	120	100	0	1	187
52	110	120	75	25	1	187
53	110	120	50	50	1	187
54	110	120	25	75	1	187
55	110	120	0	100	1	187

3.3.5.2. Measurement Techniques

Linear polarization resistance (LPR) and weight loss (WL) methods were used to measure corrosion rate under low-pressure condition (120 psi). The LPR technique is non-destructive, widely applicable and indirect corrosion measurement method. In contrary to the WL technique, this method provides the corrosion rate measurements as a function of time (i.e. instantaneous corrosion rate), which makes it suitable for applications demanding on-line and real-time measurement, monitoring and recording of the corrosion rate. It facilitates determination of instant interfacial reaction rates (corrosion) and the exchange of current densities from a single experiment. It is based on polarization technique, which involves systematic variation of the potential of an electrode from its value at open circuit. A polarized electrode causes the current at the electrode surface to flow through the electrochemical reactions. The kinetics of the reaction controls the current along with the diffusion of the reactants. Cathodic and anodic currents are generated by one of the electrochemical reactions at equilibrium that controls the open circuit potential in a corrosion system undergoing uniform corrosion at open circuit. The open potential terminates at mixed potential, which is a potential where the values of anodic and cathodic currents are equivalent. Thus, corrosion current is electrical current developed due to this reaction. For two kinetically controlled reactions, the potential of the corrosion system is determined by Eq. (3.130). Corrosion rate can be determined using the calculated value of I_{corr}.

$$I = I_{corr}\left(e^{\frac{-2.303(E-E_{OC})}{\beta a}} - e^{\frac{-2.303(E-E_{OC})}{\beta c}}\right) \quad (3.130)$$

where,

I - measured current in amps,

I_{corr} - corrosion current in amps,

E_{oc} - open circuit potential in volts,

β_a - anodic Beta coefficient in volts/decade

β_c - cathodic Beta coefficient in volts/decade.

Applying Faraday's law, the rate of uniform corrosion is determined as:

$$CR = K\frac{I_{corr} \cdot EW}{d \cdot A} \quad (3.131)$$

where

CR - corrosion rate. Units relate to K

I_{corr} - corrosion current in amperes

K - constant =3272 mm/yr

EW - equivalent weight in grams/equivalent

D - density in grams /cm^3

A - exposed sample area in cm^2

To carry out LPR measurement, test specimens (carbon steel Grade 1045) were utilized as the working electrode. A graphite rod and high-temperature Ag/AgCl were used as counter and reference electrodes, respectively. To reduce the impact of atmospheric oxygen on the measurement, the

autoclave was first purged with nitrogen gas. Inside the autoclave, the specimen (working-electrode) was inserted into brine (NaCl) solution. A potentiostat (Gamry Series G300) was used to measure corrosion rate using LPR technique. The test duration was 187 hours as required by the LPR method. Average initial weight of the specimens was approximately 13.5 grams. After completion of each experiment, the specimen was taken out and standard mechanical cleaning procedure was applied. It was mechanically cleaned using soft brush and detergent. After cleaning, the sample was weighed to determine the corrosion rate using WL method. Based on weight loss, the average corrosion rate was determined. The Potentiostat provided instantaneous corrosion rate (CR). The average corrosion rates measured from both LPR and WL methods showed good agreement with selection of appropriate Potentiostat calibration constant, which varies with salt concentration.

Plots of corrosion potential and corrosion rate generated by the LPR instrument are shown in **Fig. 3.70**. The CR trend in the figure shows the initial corrosion rate of approximately 7 mpy. The rate decreased gradually because of formation of protective scales until the rate reach approximately 1 mpy (i.e. approximately 12 hours of exposure) and remained roughly at a constant corrosion rate until the end of the experiment. A very important observation from this experiment is that the measurement was very stable. This shows the absence of chemically induced corrosion such as pitting.

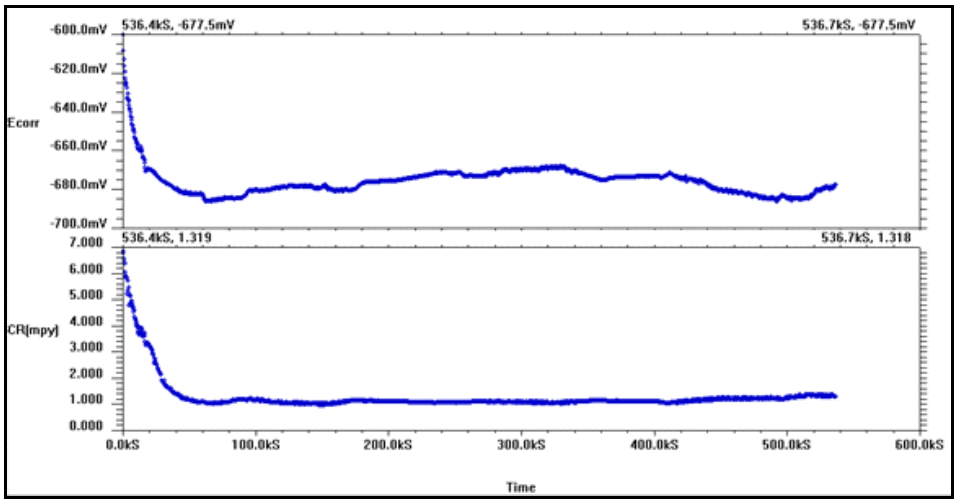

Fig. 3.70: Instantaneous corrosion rate vs. time (LPR data)

3.3.5.3. Specimen Preparation and Placement Procedures

A high-carbon steel, Grade 1045 cylindrical specimen (D = 0.25” x L = 3”) was used to determine the corrosion rate. It was used as working electrode for the LPR instrument. The specimen was cut from a ¼-inch carbon steel rod and polished to have uniform surface roughness. The same procedure was used for preparing all the specimens used for the experimental investigation. Chemical composition of Grade 1045 carbon steel is provided in **Table 3.8**.

During the test, a specimen was cleaned using organic solvent before mounting on a holder (**Fig. 3.71**). A cylindrical Teflon rod (a cylindrical PTFE block of 3.3” diameter and 1.5” height with drilled holes) is used as a specimen/electrode holder.

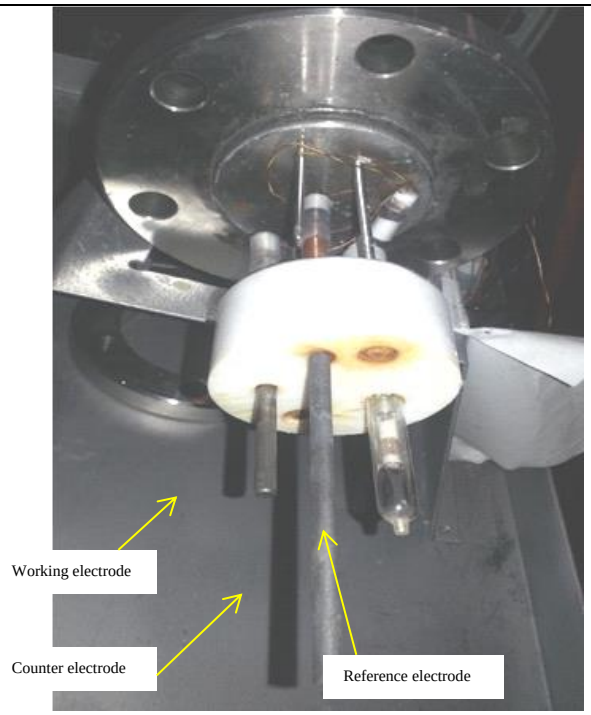

Fig. 3.71: Cylindrical PTFE block with electrodes

Table 3.8: Chemical composition of Grade 1045 carbon steel

Element	Content
Carbon, C	0.420 - 0.50 %
Iron, Fe	98.51 - 98.98 %
Manganese, Mn	0.60 - 0.90 %
Phosphorous, P	≤ 0.040 %
Sulfur, S	≤ 0.050 %

3.3.5.4. Experimental Set Up

The test setup (**Fig. 3.72**) consists of: i) a corrosion cell (autoclave) with a 3.5-in. diameter and 13-in. height; ii) circulating bath equipped with temperature controller; iii) gas supply cylinders; and iv) computer with LPR system. A cylindrical autoclave (Height = 13 in., Diameter = 3.5 in.) made of aluminum (body) and 304 stainless steel (lid) is used as the corrosion cell, the pressure rating of the autoclave is 3000 psi. The autoclave together with the PVC jacket is mounted on a uni-strut frame in which the heating fluid is circulated using the circulating bathe (**Fig. 3.73**) in order to maintain desired temperature. The autoclave was nickel plated inside to prevent it from corrosion resulting from the test fluid (brine saturated with CO_2) under elevated pressures and temperatures. Before starting the experimental program, the autoclave was pressure tested at 1100 psi for 60 minutes to ensure its integrity and safety.

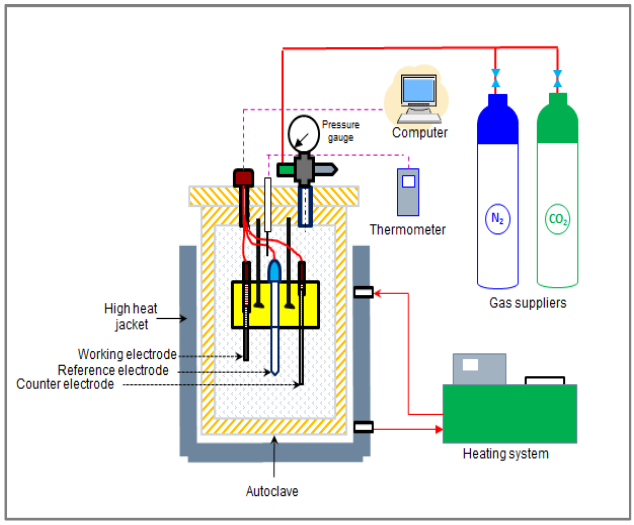

Fig. 3.72: Schematic of moderate pressure experimental setup

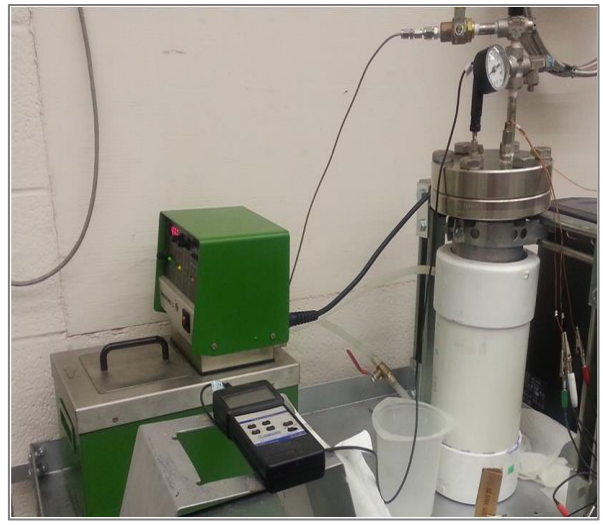

Fig. 3.73: Modified test setup for low pressure corrosion study

Glycol is used as the heating fluid. A temperature sensor is installed on the autoclave to record and monitor test temperature. Precise temperature control is needed to eliminate anomalies (spikes in corrosion rate shown in **Fig. 3.74**), which were observed during corrosion rate measurements obtained under ambient conditions without precise temperature control. Pressure gauges are also mounted on the top of the autoclave to monitor the pressure.

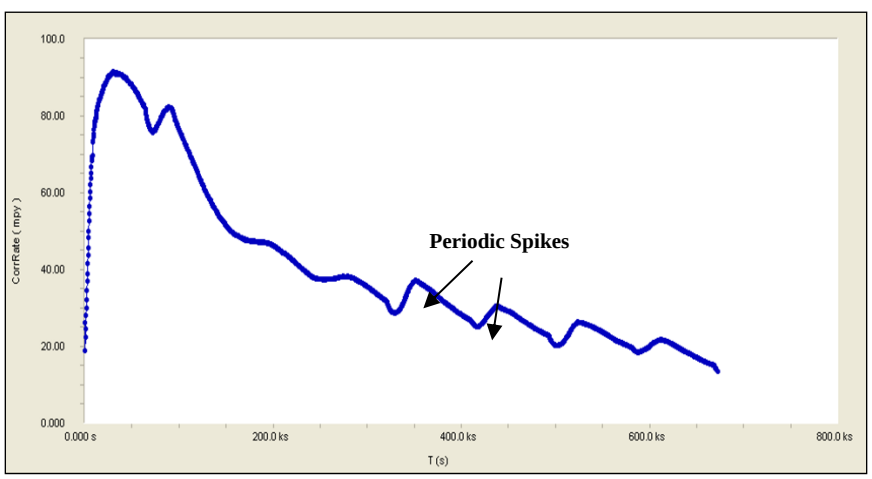

Fig. 3.74: Corrosion rate vs. time obtained before installing a heating jacket

Electrodes: The experiments were conducted using LPR system with three electrodes: i) working electrode, ii) counter electrode, and iii) reference electrode. The working electrode is the test specimen (sample) that undergoes corrosion during the experiment. Cylindrical specimens (Length = 3 in. and Diameter = 0.25 in.) in were made from Grade-1045 medium carbon steel. A graphite rod (Length = 5.5 in. and Diameter = 0.25 in.) is used as a counter electrode. The experiments were performed at ambient and elevated temperature (176°F). Therefore, a high temperature Ag/AgCl cell (Fischer scientific ™ accumet ™ glass body Ag/AgCl reference electrode, USA) is used as a reference electrode, instead of a

standard hydrogen electrode (SHE). The electrode provides better accuracy and stability at higher temperatures (Lundstrom et al. 2008). The operating temperature range for this reference electrode is 23°F to 230°F.

In order to suspend all the electrodes inside the autoclave, a cylindrical Teflon (PTFE) block with length of 3.0 in. and diameter of 0.25 in. was drilled with holes slightly larger than the diameter of each electrode (**Fig. 3.75**). As the internal diameter of the autoclave is 3.5 in., the size of the PTFE block offers a stable mount for the electrodes while maintaining reasonable distance between them. The block is suspended from the lid of the autoclave with two stainless steel threaded rods in such a way that they are not immersed into the brine solution as part of the corrosion system; two copper tube sleeves were cut, soldered to LPR lead wires for measurements. These sleeves served as holders for the working and counter electrodes as shown in Fig. 3.75. High-pressure sealing gland (rated at 6000 psi) is used to connect safely the signal leads from all the electrodes running from the inside of the autoclave through the lid to the outside of it, allowing direct connection from the electrodes to the potentiostat (GAMRY G300) for LPR measurements.

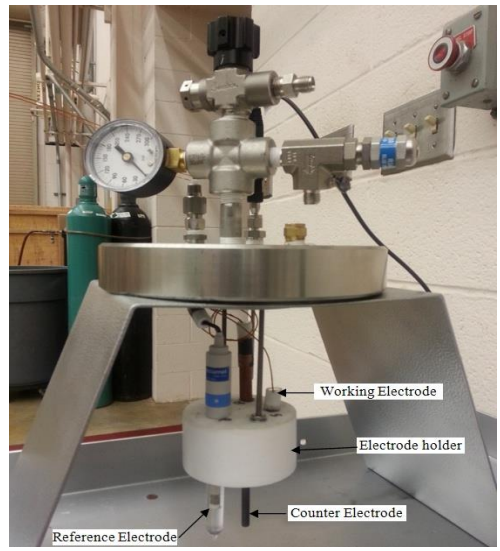

Fig. 3.75: Autoclave cover with PTFE block

All the experiments were conducted using the potentiostat (**Fig. 3.76**), which is installed on the CPU unit of a personal computer. It was calibrated using master calibration kit provided by GAMRY to measure the corrosion current. It was fine-tuned to the suitable current range. All potentiostat functions are composed by software package (DC-105), which facilitates easy comparison of multiple experiments for parametric study of the corrosion trend for varying temperature or CO_2 concentration. The potential range for the LPR measurements are from -0.02 to 0.02 V and a scan rate of 0.125 mV/s. To validate the LPR measurements, comparison between WL and LPR measurements were made.

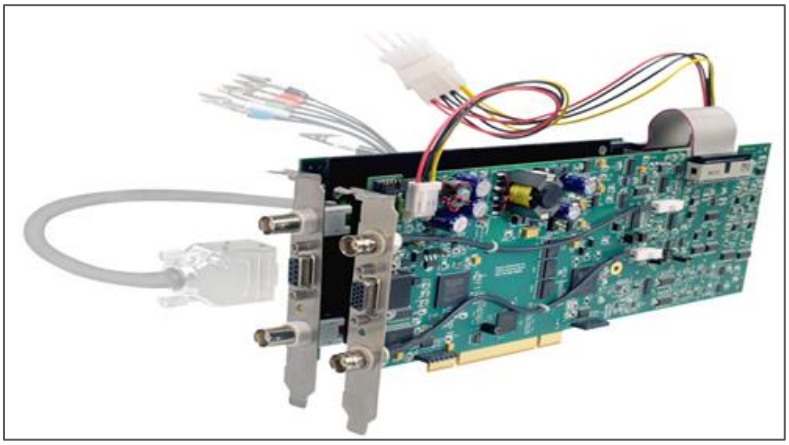
Fig. 3.76: GAMRY G300 Potentiostat for LPR measurement (Courtesy GAMRY Instrument)

3.3.5.5. Test Procedure

The following ten-step test procedure was developed to carry out the corrosion experiments conducted in this study:

Step 1: Sample Preparation: A test specimen (0.25-inch diameter and 3" length carbon steel) was cut from ¼" rod. The specimen surface was then polished using a grinding machine to remove oxidation products and make the sample surface clean and smooth. The sample was then washed with tap water and dried.

Step 2: Sample Weighing: After the sample was prepared and ready to be installed inside the autoclave, it was weighed up to four decimal points (0.0001 g) and the weight of the sample was recorded to be used for WL measurements. The sample was then inserted into the copper sleeve connected to the LPR lead and supported by the Teflon block.

Step 3: Preparation of Electrodes: The reference electrode (Ag/AgCl) was installed on the Teflon block permanently. Before each experiment, the level of KCl solution inside the reference electrode was checked and topped up when it was necessary. The counter electrode was cleaned with water for every new experiment and inserted in to the copper sleeve connected to the LPR lead (sealing gland) that is installed on the lid of the autoclave.

Step 4: Continuity Testing: Both working and counter electrodes were checked for continuity using a multi meter to ensure the signals transfer from the electrodes to the LPR leads and to avoid any short circuit between either of the electrodes and the autoclave lid.

Step 5: Electrolyte Preparation: 1000 ml brine solution (2% NaCl by weight) was prepared as a standard electrolyte for the experiments. The autoclave was partially filled with the solution, the lid was then bolted, and the setup was ready for gas injection.

Step 6: Nitrogen Purging: The presence of oxygen inside the autoclave may accelerate pitting corrosion, purging of the autoclave was required to avoid this. The purging was done by injecting nitrogen gas into the autoclave and venting it through a relief valve.

Step 7: N_2 and CO_2 Injection: N_2 and CO_2 gas were injected respectively into the autoclave. The percentage of each gas injected varied for each experiment as per its demand. The experiments were conducted at 120 psi operating pressure varying CO_2 concentration and temperature.

Step 8: LPR Measurement Initiation: Following the injection of gas in the autoclave, variables were preset in the DC-105 software for initiation of the measurement. These variables (**Fig. 3.77**) included sample surface area, LPR scan rate, duration, and equivalent weight of the sample material.

Step 9: Sample Recovery and Weight Measurement: After 187 hours of experiment, the autoclave was de-pressurized gradually and opened. The sample was carefully taken out of the copper holder. The iron carbonate deposits were removed by washing the sample with tap water and scrubbing it gently. Identical sample cleaning procedure was maintained for all the experiments conducted. The sample was dried and weighed and WL calculations were performed to determine the rate of corrosion.

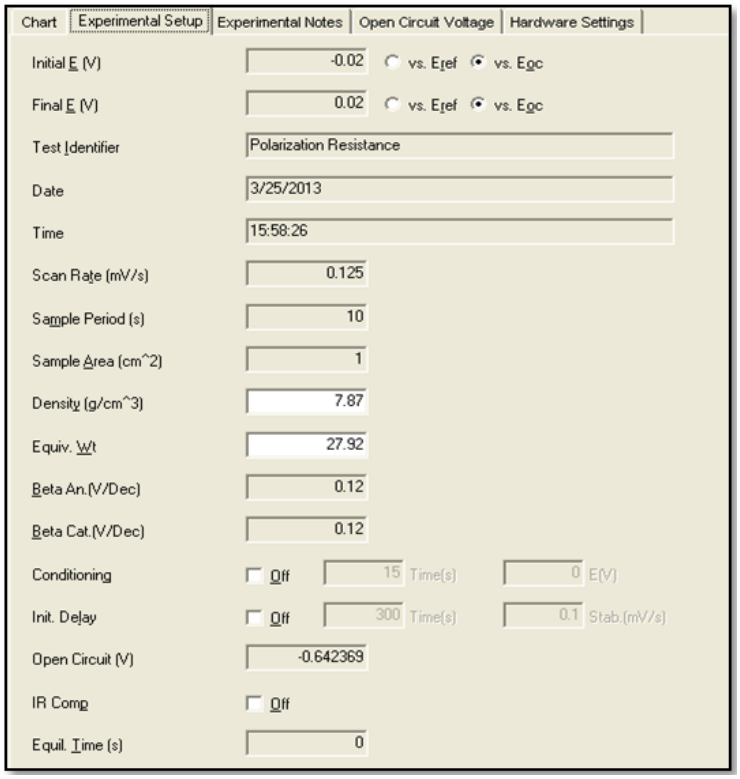

Fig. 3.77: GAMRY DC-105 startup interface

3.3.5.6. Results

Corrosion rate of common carbon steel (Grade 1045) was measured under different experimental conditions. The average corrosion rate was measured using linear polarization resistance (LPR) and weight loss techniques. Forty-three successful experiments were conducted to examine the effects of CO_2 and salt concentrations and temperature on corrosion rate. The tests were performed at a constant pressure of 120 psi. Test parameters and results of the experiments are presented in **Table 3.9**.

Table 3.9: Test parameters and results of low-pressure corrosion experiments conducted to date

Exp. #	Temp. (ºF)	Pressure (psi)	Partial Pressure %		Brine Conc. (%)	Test Period (days)	Results (mpy)	
			N_2	CO_2			LPR	WL
12	78	120	100	0	2	187	2.6	4.1
13	78	120	50	50	2	187	32.0	27.6
14	78	120	25	75	2	187	40.3	48.1
15	78	120	25	75	2	187	40.30	31.91
16	78	120	0	100	2	187	39.18	32.18
17	78	240	0	100	2	187	N/A	N/A
18	78	120	75	25	2	187	22.92	21.83
19	110	120	75	25	2	187	31.78	23.78
20	110	120	25	75	2	187	53.16	43.22
21	110	120	100	0	2	187	12.37	15.40
22	110	120	75	25	2	187	31.07	23.78
23	110	120	50	50	2	187	70.35	43.39
24	110	120	25	75	2	187	53.16	43.22
25	110	120	0	100	2	187	44.92	32.49
26	176	120	100	0	2	187	4.04	3.10
27	176	120	75	25	2	187	16.53	11.77
28	176	120	50	50	2	187	24.23	12.71
29	176	120	25	75	2	187	17.39	10.87
30	176	120	0	100	2	187	22.56	12.04
31	140	120	100	0	2	187	2.58	2.72
32	140	120	75	25	2	187	11.00	6.33
33	140	120	50	50	2	187	13.33	14.30
34	140	120	25	75	2	187	38.48	26.76
35	140	120	0	100	2	187	24.40	24.23
36	140	120	100	0	1	187	3.69	1.23
37	140	120	75	25	1	187	5.16	20.97
38	140	120	75	25	1	187	9.86	25.13
39	140	120	50	50	1	187	6.40	21.24
40	140	120	25	75	1	187	6.50	23.78
41	140	120	0	100	1	187	4.31	14.77
42	176	120	0	100	1	187	1.76	4.63
43	176	120	25	75	1	187	2.79	9.00
44	176	120	50	50	1	187	4.95	12.59
45	176	120	75	25	1	187	17.79	36.98
46	176	120	100	0	1	187	0.69	2.60
47	176	120	75	25	1	187	5.79	14.90
48	110	120	25	75	1	187	8.55	33.23
49	110	120	0	100	1	187	6.21	30.81
50	110	120	50	50	1	187	22.23	46.88
51	110	120	100	0	1	187	6.57	6.51
52	110	120	75	25	1	187	78.62	101.78
53	110	120	50	50	1	187	31.86	34.62
54	110	120	25	75	1	187	20.88	33.18
55	110	120	0	100	1	187	38.82	41.99

Effect of CO_2 Concentration

Figures 3.78 and **3.79** compares corrosion rate measurements obtained from electrochemical (LPR) and weight loss (WL) methods at various CO_2 concentrations and temperature. With increasing CO_2 concentration, the corrosion rate slightly reduced at high concentrations. Both measuring techniques provided similar trends. Even though the corrosion rate reduction with CO_2 concentration is not common, similar corrosion rate trend has been reported previously (Seiersten 2001). No explanation was provided for this type of corrosion rate trend. One of the possible explanations is that the concentration of Fe^{2+} increases with the increase in CO_2 concentration, resulting in reduction of

corrosion rate. At 100% CO_2 concentration, the super-saturation exceeds the solubility limit of Fe^{2+} and; therefore, porous corrosion scale can be formed under these conditions, significantly diminishing the corrosion rate. Furthermore, increase in CO_2 concentration enhances the dissolution of CO_2 and the formation of carbonic acid, which reduces the pH. The reduction in pH results in increase in iron carbonate solubility, which facilitates the corrosion process by preventing the formation of protective scale. However, as CO_2 concentration approaches 100%, pH reduction with the CO_2 concentration diminishes, causing the corrosion rate to stabilize or reduce.

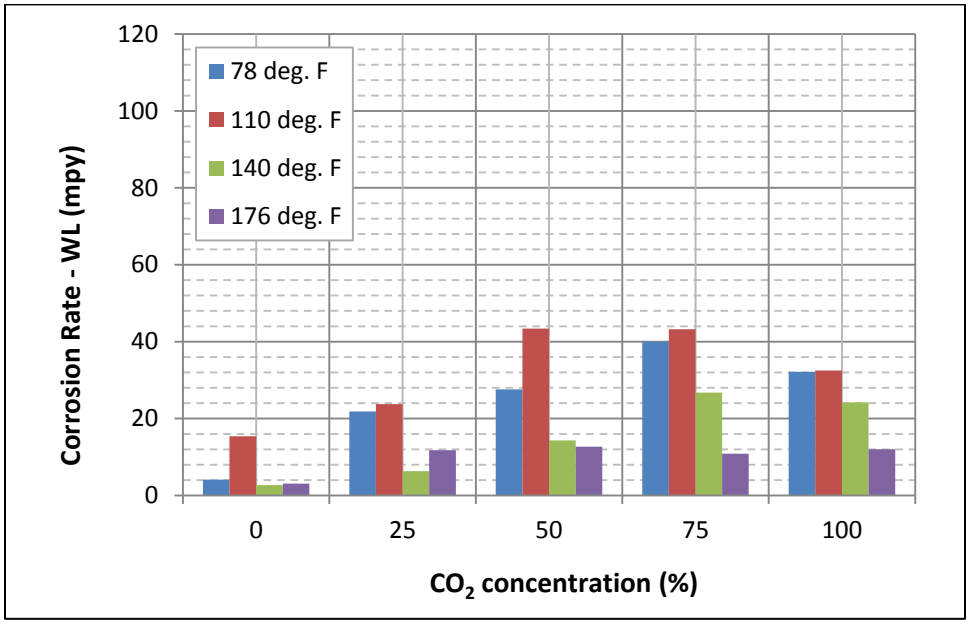

Fig. 3.78: Corrosion rate versus CO_2 concentration and temperature for 2% NaCl solution (WL method)

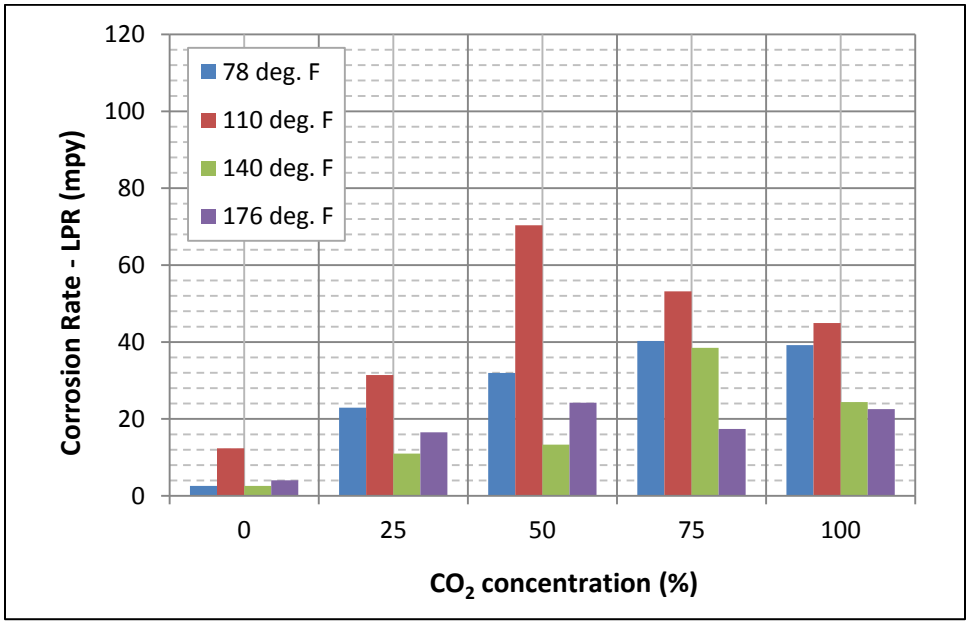

Fig. 3.79: Corrosion rate versus CO_2 concentration and temperature for 2% NaCl solution (LPR Method)

Effect of Salt Concentration

In general, corrosion rate is strongly affected by the salt concentration with or without the presence of carbon dioxide. **Figure 3.80** shows the corrosion rate measured using the weight loss method as a function of CO_2 concentration for 1% salt concentration. For 0% carbon dioxide (pure nitrogen), the average corrosion rates decreased with the reduction in salt concentration. According to Fang (2006), the activity coefficient of H^+ ion decreases with reduction in the salt concentration, which leads to pH increase and subsequently decrease in corrosion rate. However, in the presence of carbon dioxide, a reverse trend was predominantly observed when the salt concentration was reduced from 2 to 1 wt%. These observations are consistent with previously published results (Fang 2006; Fang et al. 2010). The presence of salt retards both the anodic and cathodic reactions, which primarily determine the rate of CO_2 corrosion (Fang et al. 2010). Hence, CO_2 corrosion rates decreased with increase in the salt concentration. The relationship between CO_2 concentration and corrosion rate is strongly influenced by temperature and salt concentration.

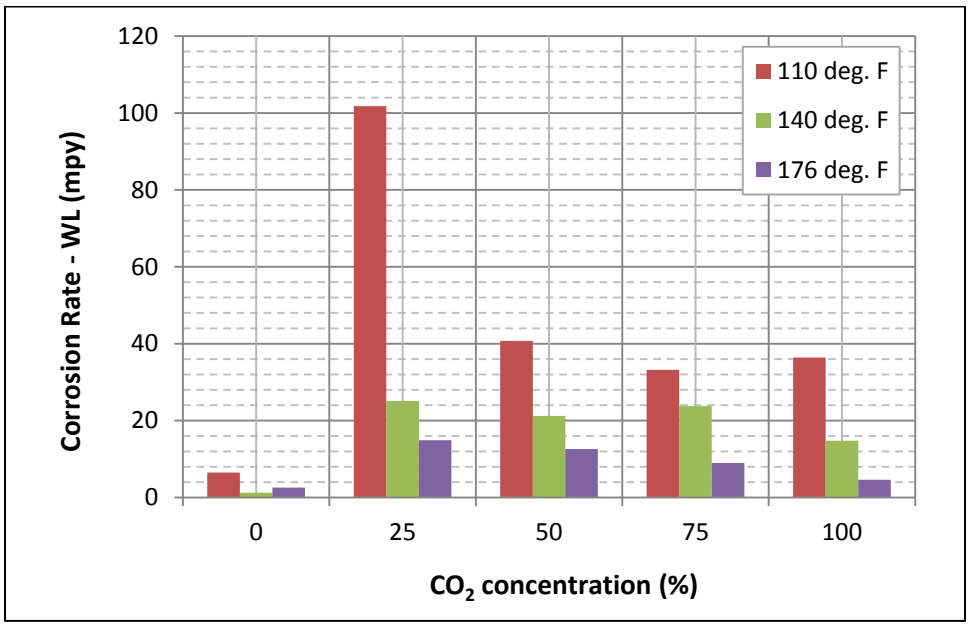

Fig. 3.80: Corrosion rate versus CO_2 concentration and temperature for 1% NaCl solution (WL method)

Effect of Temperature

Temperature has major effect on corrosion. Increase in temperature facilitates the corrosion reactions and transport of species (molecular diffusion); hence, it facilitates corrosion process. On the other hand, increase in temperature accelerates precipitation of corrosion product and formation of protective scale, resulting in reduction of corrosion rate. In pure CO_2 system, the corrosion products such as iron carbonate ($FeCO_3$) precipitate and deposit on the metal surface after their solubility limit is reached. Johnson and Tomson (1991) reported extreme sensitivity of rate of iron carbonate precipitation to temperature. Moreover, with increasing temperature, CO_2 solubility decreases causing reduction in carbonic acid concentration and increase in pH, which have negative impact on corrosion process. According to Valdes et al. (1998), the severity of corrosion in carbonic acid environment is higher in low-temperature than high-temperature. In the presence of CO_2, results obtained from 1% salt

concentration corroborate with the findings of Valdes et al. (1998). However, measurements at 2% salt concentration show mixed but consistent trend. At low CO_2 concentrations (0 to 50%), with increasing temperature from 78 to 176°F, the corrosion rate trend displayed increase from 78 to 110°F, decrease from 110 to 140°F and increase from 140 to 176°F. Regardless of the salt and CO_2 concentrations, the maximum corrosion rate was observed at 110°F. The reduction in corrosion rate above 110°F is attributed to the decrease in iron carbonate solubility, which promotes the formation of protective scale that can limit further corrosion of the material. In addition, the increase in temperature has a negative impact on the solubility of CO_2. The reduction in the solubility of CO_2 tends to increase the pH of the solution thereby slowing the corrosion process.

Comparison of Measurements

The difference between LPR and WL measurements shown in **Fig. 3.81a** and **3.81b** could be attributed to the use of calibration factor B (30 mV) in determining the corrosion rate from the LPR instrument. Comparison of the corrosion rate measurements obtained from electrochemical (LPR) and weight loss (WL) methods (Fig. 3.81) at different CO_2 concentration and temperatures showed significant variation. For 1% NaCl solution, WL method provided higher corrosion rate than the LPR technique. However for 2% NaCl solution, lower corrosion rate was obtained with the WL method.

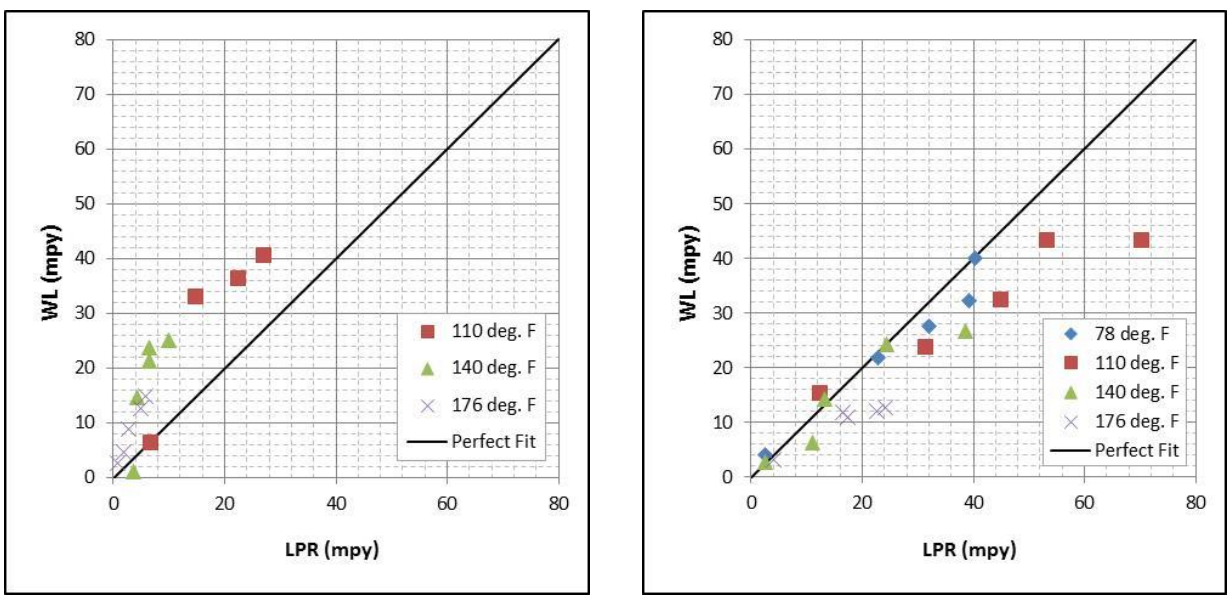

(a) (b)

Fig. 3.81: WL vs. LPR corrosion rate measurements: a) 1% NaCl; and b) 2% NaCl

The LPR measurements show better agreements with WL data for 2% than 1% NaCl solution. Reduced accuracy with LPR measurements is attributed to calibration challenge with the instrument, as salt concentration was reduced from 2% to 1%. When salt concentration was 2%, LPR instrument reference voltage of 30 mV (B = 30 mV) was used for determining the corrosion rate from the electrochemical measurements. This reference value was obtained after performing calibration tests using the two-point method. Similar calibration was not conducted at salt concentration of 1% and resultant in reduced accuracy. Moreover, two-point calibration method seems inadequate. For 2% NaCl

solution, LPR measurements were mostly higher than WL data points. Better result can be obtained by performing multi-point calibration covering wide range of corrosion rate data points.

3.3.6. Experimental Study at High Pressure

The major objective of high-pressure test is to determine the effects of pressure, CO_2 and H_2S concentrations on the corrosion rate of common oil field tubulars. Test temperature and salt concentration were maintained at 100°F and 2% NaCl, respectively. Results from low-pressure study (Section 3.3.5.6) showed that corrosion of carbon steel is maximum at approximately 100°F.

3.3.6.1. Test Conditions

High-pressure uniform corrosion experiments were conducted to assess corrosion behavior of API carbon steels in CO_2 and H_2S environment. Experiments were performed by varying pressure (3000 to 9000 psi), CO_2 concentration (0 to 100%) and H_2S concentration (0 and 50 ppm). In addition, one batch of dynamic corrosion test was carried out. Corrosion behavior of three grades of carbon steel (T95, C110 and Q125) were investigated. **Table 3.10** summarizes test conditions of the experiments.

Table 3.10: Test conditions for HPHT uniform corrosion tests

Batch No.	Material	Pressure (psi)	Temp. (°F)	Duration (Days)	CO_2 Conc. (%)	CH_4 Conc. (%)	H_2S Conc. (ppm)
001	C110	6000	100	7	100	0	0
002	C110	6000	100	7	50	50	0
003	C110	6000	100	7	0	100	0
004	C110	6000	100	7	25	75	0
005	C110	6000	100	7	75	25	0
006	C110	9000	100	7	100	0	0
007	C110	3000	100	7	0	100	0
008	C110	9000	100	7	75	25	0
009	C110	9000	100	7	50	50	0
010	C110	9000	100	7	25	75	0
011	C110	9000	100	7	0	100	0
012	C110	3000	100	7	75	25	0
013	C110	3000	100	7	100	0	0
014	Q125	6000	100	7	50	50	0
015	Q125	9000	100	7	50	50	0
016	T95	6000	100	7	50	50	0
017	T95	9000	100	7	50	50	0
018	C110	6000	100	7	50	0	10
019	C110	6000	100	7	50	0	50
020	Q125	6000	100	7	75	25	0
021	Q125	6000	100	7	100	0	0
022	Q125	6000	100	7	0	100	0
023	Q125	6000	100	7	25	75	0
024	T95	6000	100	7	75	25	0

025	T95	6000	100	7	100	0	0
026	T95	6000	100	7	25	75	0
027	T95	6000	100	7	0	100	0
028	Q125	6000	100	7	50	0	10
029	Q125	6000	100	7	50	0	50
030	T95	6000	100	7	50	-	10
031*	Q125	6000	100	7	50	50	0
032	T95	6000	100	7	50	-	50

* Batch 031 was conducted under dynamic condition (rotor speed of 1000 rpm)

3.3.6.2. Measurement Techniques

Corrosion rate was measured using weight loss methods. Initial and final weights of the coupons were measured using an electronic balance with accuracy of ±0.0001 mg to determine the corrosion rate based on weight loss technique. The final weights of the coupons were measured, after removing protective coating and corrosion scale. Based on the initial and final weights, the average corrosion rate is calculated as:

$$CR = \frac{438.78 \times (w_1 - w_2)}{t \times A} \quad \text{.....} \quad (3.132)$$

where CR is average corrosion rate in mpy; w_1 and w_2 are initial and final coupon weight in milligrams, respectively; t is the test duration in hours; and A is the exposed surface area in cm^2. In addition to weight loss measurement, tensile strength tests were conducted on the specimens before and after corrosion experiments to measure mechanical properties of the coupon materials.

3.3.6.3. Specimen Preparation and Placement Procedures

Samples (corrosion coupons) were mechanically cleaned using organic solvent, and weighted and tested before and after exposure to corrosive environment to determine their corrosion rate and assess the effect of corrosion on their mechanical properties. Before the corrosion experiment, coupons were covered with protective coating except the exposure area (i.e. one-side of the narrow test section shown in **Fig. 3.82**). The samples were weighed before applying the coating. The exposure area has 192 mm^2 surface. Before the experiment, the test section of each specimen was cleaned with solvent and dried. Three or two specimens were mounted on the inside of a sleeve (**Fig. 3.83**) using high-temperature silicone seal.

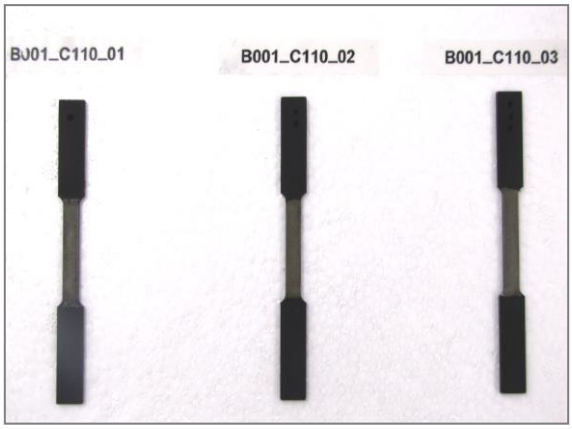

Fig. 3.82: Corrosion coupon covered with protective coating

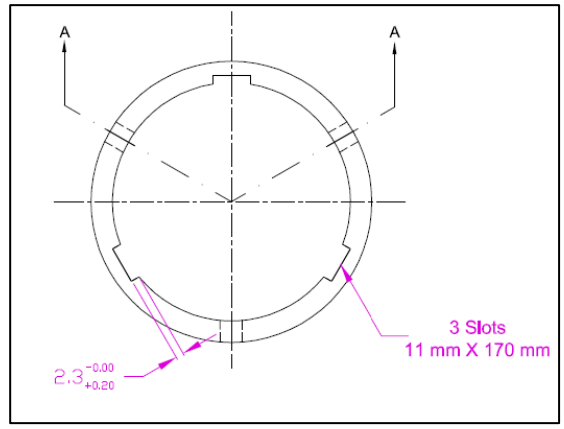

Fig. 3.83: Specimen holder

3.3.3.4. Experimental Setup

The static and dynamic (SD) corrosion test setup is a facility developed to carry out uniform corrosion studies under HPHT conditions in the presence of acidic gases. During the development of the setup, two different methods (fluid circulating in a pipe section or fluid shearing between two rotating co-axial cylinders) were considered for creating the dynamic flow under HPHT conditions.

To develop a facility with fluid recirculation, different companies were contacted to provide price quotes for high-pressure recirculation pump. There were two main limitations for a high-pressure recirculation pump including low system pressure, and low flow rate and material compatibility for brine saturated with sour gases. With market available circulation pumps such as Micropump, the maximum pressure is 5000 psi, the maximum average fluid velocity that can be achieved using a Micropump in an 1/8 inch pipe test section is 0.3 m/s, which is very low for simulating the shear stress occurring in the oil and gas drilling and production systems. On the other hand, available high-pressure circulation pump with 10,000 psi system pressure such as WITTE gear pump is not designed for low viscosity liquids. Hence, it is not suitable for pumping brine solution. We also considered using injection cylinder as a pump, acquiring a custom-made pump or syringe type pump that meets the desired specifications. However, the low flow capacity and pressure pulsation are the limiting factors for piston or syringe type pumping systems.

After considering all these alternatives, the best option left was using rotating coaxial cylinder system. The system uses a magnetic drive to rotate a cylinder placed in the HPHT autoclave. The drive rotates the cylinder at high-speed creating Couette flow that can generate wall shear stress level, which is often experienced in real life. Different vendors were contacted to supply the magnetic drive. Due to their air gap limitation, maximum pressure rating for magnetic drives made of Hastelloy is 5000 psi. Magnetic drives with a higher pressure rating (10,000 psi) are available in stainless steel 316 or A286 version. Corrosion studies conducted to evaluate the performance of these materials in sour gas environment show good corrosion resistance of A286 at ambient and high temperature (up to 300°F) conditions. Stainless steel 316 exhibited pitting when exposed to brine saturated with sour gas.

After choosing the Couette flow type corrosion cell, the design of the HPHT corrosion test setup (**Fig. 3.84**) was finalized. The dynamic corrosion cell that has a rotating cylinder inside installed in the corrosion setup presented in Fig. 3.19. Three specimens can be attached to a Teflon coated specimen holder (Fig. 3.83) and placed in the cell. The clearance between the cylinder and the holder is 3.4 mm. The rotation of the cylinder generates turbulence and wall shear stress needed to facilitate the removal of corrosion products and accelerate the corrosion process. As shown in Fig. 3.84, magnetic coupling with an air motor is installed on the top of the cell to simulate dynamic condition. The speed of the motor is controlled by the air supply pressure and flow rate, which are controlled by a pressure regulator and air inlet valve, respectively.

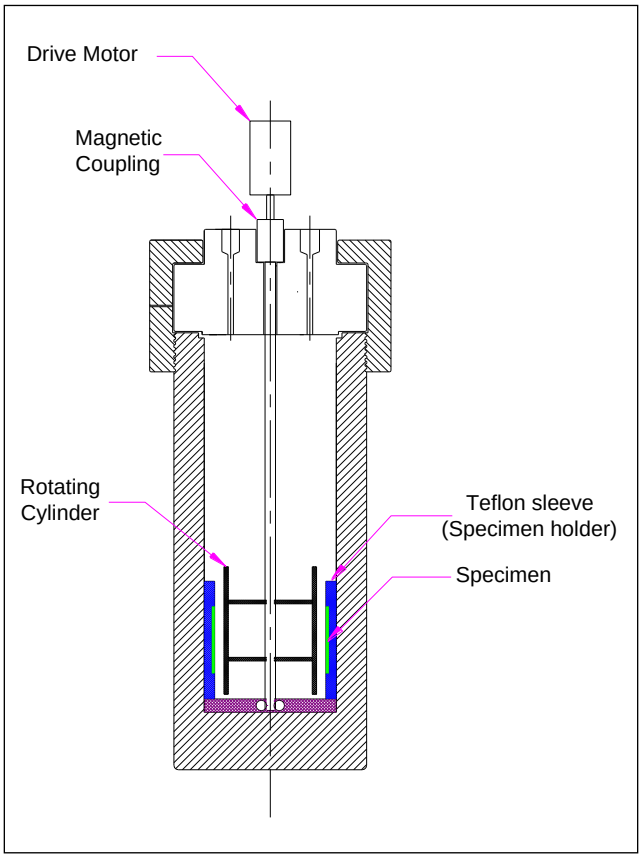

Fig. 3.84: Dynamic corrosion cell

The SD corrosion cell is placed in a heating jacket to control the temperature. The jacket completely covers the side and bottom parts of the cell. The jacket is rated for 100 psi. Hydraulic pressure acting on the bottom creates a force that can lift the vessel. In order to prevent the lifting, the jacket is clapped to the vessel and the hydraulic pressure is limited to 15 psi using a rupture disk. The rupture disk is installed at the inlet of the jacket. The heating medium is circulated through the jacket to control the temperature. Temperature is measured using a thermocouple sensor placed in the cell.

3.3.3.5. Test Procedure

To perform the static and dynamic corrosion experiment, corrosion coupons (**Fig. 3.85**) were cleaned with appropriate solvent. The coupons have two end sections (heads) and one middle test section.

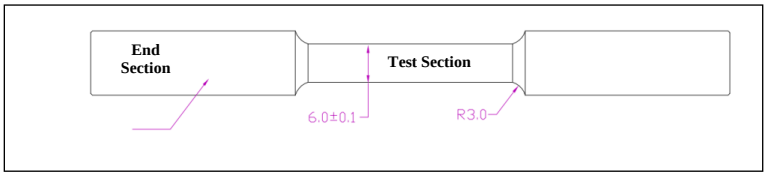

Fig. 3.85: Coupon used for static and dynamic corrosion test

The heads are used to hold the coupons during tensile strength test, which was carried out after the corrosion experiment was completed. After cleaning the coupons, the weight of each coupon was measured. The rear-side and end sections of the coupons were coated with high-temperature anti-corrosion paint. Only the front part of the test section was exposed to the test fluid during the test. Then, the coupons were inserted into specimen slots of the holder. High temperature sealant is used to attach the coupon with the specimen holder.

After setting, the sleeve together with the coupons was inserted into the autoclave and a cylindrical rotor was inserted in the middle of the sleeve. The autoclave was filled with 950 mL of brine solution, which was prepared with deionized water and 2 wt% of NaCl. The solution was deoxygenated by purging the cell with pure nitrogen for 30 minutes. Then, the test cell was heated to 100°F (±5°F) and pressurized by injecting CH_4 and CO_2 up to the desired pressure. The corrosion test lasted for 168 hours (7 days). The testing conditions are shown in Table 3.10.

Once the coupons were attached to the holder, the base (**Fig. 3.86**) of the specimen holder was installed. The base acts as a bearing for the cylinder (**Fig. 3.87**). It is equipped with trust bearing to reduce the mechanical friction between the holder base and cylinder base. Subsequently, the base and the rotating cylinder was assembled and attached to the drive shaft. The vessel was filled (approximately 70%) with brine solution and the specimen assembled was slowly lowered to the bottom of the vessel. Then, the bolts on the lid of the vessel were tightened.

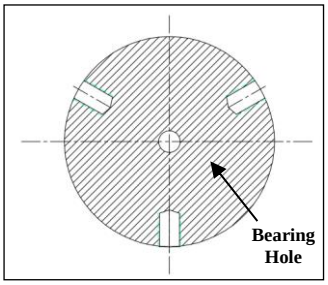

Fig. 3.86: Base of the specimen holder

When the vessel is ready for gas injection, the heater was turned on to bring the cell temperature to the desired level. After that, gas from one of the supply tanks was allowed to fill the vessel by opening V14 (Fig. 3.19). Injection cylinder is needed to increase the vessel pressure above the supply pressure. The operation of the injection cylinder is similar to the one described in Section 2.3.6. When the desired pressure and temperature condition is established, the air is supplied to the drive motor to rotate the inner cylinder. The speed of the motor is controlled using inlet air valve and supply pressure.

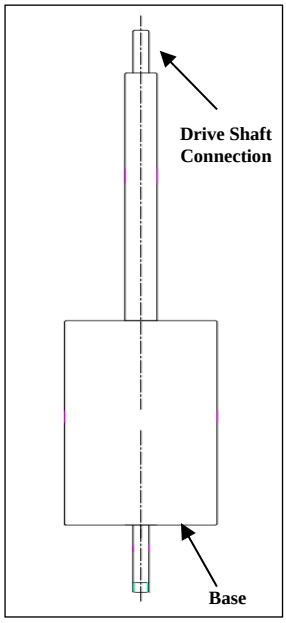

Fig. 3.87: Rotating cylinder

One SD corrosion test was completed in one week. After completion of the test, the air supply to the motor was cut-off and the heater was shut down to cool the cell. The corrosion cell is depressurized opening V14, V6 and V4. The gas from the vessel was sent to the waste gas accumulator for gradual venting. After completion of the test, the coupons were examined using a microscope to study the corrosion scale characteristics. Each specimen was photographed. The corrosion scale was carefully removed and preserved for further studies. After cleaning the corrosion scale, the final weight of the coupon was measured. Subsequently, the tensile strength of the couple was measured using TST apparatus.

3.3.3.6. TST Setup and Procedure

The tensile strength testing (TST) setup presented in Section 3.2.2.6 has been developed to evaluate the change occurring in mechanical properties of flat coupons after acid attack. To carry out the experiments, the coupon was assembled with special grips (**Fig. 3.88**) that are designed and manufactured to work with the TST setup. Then, the assembly was attached to the TST for testing mechanical properties of the coupon.

Fig. 3.88: Grips for flat coupons

Tensile strength tests were performed on specimens, according to the ASTM E8M specification. The tensile strength tests were conducted by applying tensile load on the specimen and the corresponding elongation or change in length was recorded (**Fig. 3.89**). Loading rate of approximately 100,000 psi/min was used during the test. The main objective of performing the test is to assess change occurring in mechanical properties (Young's modulus, yield strength, tensile strength, and elongation to failure) of the specimens after exposure to corrosive environment. Result clearly shows the elastic and plastic deformation regimes.

Tensile strengths of the specimens were measured before and after the corrosion experiments to assess the impact of the corrosion on mechanical properties of C110 alloy. Prior to the test, each coupon was stretched three times by applying force equivalent to 75% of its yield strength in order to measure the initial modulus of elasticity.

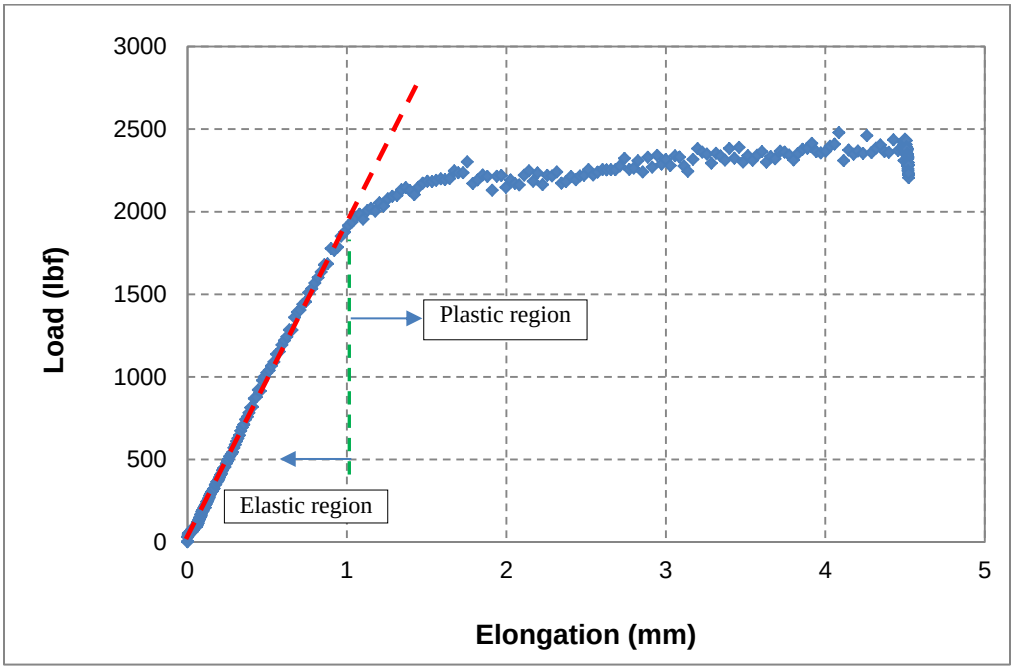

Fig. 3.89: Applied instantaneous load versus elongation for C110 coupon

3.3.3.7. Results and Analysis

A total of 32 successful high-pressure corrosion experiments were conducted. **Table 3.11** presents corrosion rate measurements and mechanical properties of specimens measured before and after exposure to the corrosive environment. Results demonstrate the occurrence of significant corrosion after the exposure as exhibited by considerable reduction in weight and change in mechanical measurements after exposure. Due to the pressure effect, corrosion rates measured at high pressure is significantly higher than those measured at low-pressure (120 psi). The maximum corrosion rate obtained during low-pressure test was 102 mpy, whereas at high-pressure, rate of corrosion of more than 600 mpy was observed.

Table 3.11: Corrosion rate and mechanical properties of specimens before and after corrosion test

Batch No.	Specimen No.	CO_2 Con.%	Initial weight gm	Final weight gm	CR (mpy)	E (psi)	E* (psi)	Yield strength (psi)	Tensile Strength (psi)
001	C110-1	100	13.3848	13.2129	234	5.79E+06	9.91E+06	107,560	123,600
	C110-2		13.4397	13.2212	297	6.02E+06	8.62E+06	105,950	119,933
	C110-3		13.4478	13.2323	293	7.71E+06	9.44E+06	108,140	120,673
002	C110-1	50	13.4875	13.1076	517	1.07E+07	8.57E+06	104,960	117,283
	C110-2		13.3884	13.0029	524	5.10E+06	9.01E+06	97,180	116,388
	C110-3		13.3376	12.9835	482	5.54E+06	8.25E+06	95,140	116,198
003	C110-1	0	13.4459	13.3916	74	1.00E+07	7.76E+06	93,250	130,891
	C110-2		13.4196	13.3924	37	1.15E+07	8.43E+06	96,780	131,917
	C110-3		13.3234	13.2680	75	1.07E+07	8.25E+06	96,940	129,187
004	C110-1	25	13.3739	12.949	578	8.75E+06	8.13E+06	91,000	113,833
	C110-2		13.3092	12.9818	445	8.48E+06	6.99E+06	95,510	116,450
	C110-3		13.4018	13.0782	440	8.15E+06	8.44E+06	94,880	117,009
005	C110-1	75	13.4127	13.1079	415	8.71E+06	8.09E+06	103,240	111,286
	C110-2		13.4881	13.2212	363	1.10E+07	6.52E+06	101,290	112,891
	C110-3		13.4635	12.9808	657	8.43E+06	6.01E+06	101,000	111,062
006	C110-1	100	13.4039	13.1518	343	1.14E+07	8.43E+06	100,000	116,283
	C110-2		13.3703	12.9598	558	1.08E+07	8.57E+06	96,410	113,007
	C110-3		13.4606	13.2294	315	1.10E+07	6.36E+06	95,570	117,066
007	C110-1	0	13.4169	13.3859	42	9.98E+06	6.96E+06	100,920	130,212
	C110-2		13.4447	13.4144	41	9.29E+06	6.94E+06	100,530	130,658
	C110-3		13.4041	13.3635	55	9.47E+06	7.05E+06	101,170	128,982
008	C110-1	75	13.3681	12.9327	592	7.74E+06	8.37E+06	97,530	110,554
	C110-2		13.4538	13.0456	555	7.97E+06	8.67E+06	99,660	110,922
	C110-3		13.3742	12.9952	516	8.44E+06	9.24E+06	100,480	112,723
009	C110-1	50	13.4238	12.9867	595	1.14E+07	8.15E+06	97,480	111,270
	C110-2		13.2956	13.0504	334	8.45E+06	8.55E+06	98,740	118,488
	C110-3		13.4920	13.1036	528	8.47E+06	8.35E+06	102,700	113,291
010	C110-1	25	13.3937	13.092	410	9.30E+06	8.33E+06	99,250	119,451
	C110-2		13.3812	12.9699	559	1.23E+07	7.15E+06	101,270	114,472
	C110-3		13.3518	12.9320	571	1.25E+07	7.36E+06	100,120	112,456
011	C110-1	0	13.4399	13.4033	50	8.81E+06	5.89E+06	107,870	129,910
	C110-2		13.3882	13.3497	52	9.25E+06	7.43E+06	110,000	128,725
	C110-3		13.4730	13.4332	54	1.10E+07	8.06E+06	106,890	127,023

Batch No.	Specimen No.	CO_2 Con.%	Initial weight gm	Final weight gm	CR (mpy)	E (psi)	E* (psi)	Yield strength (psi)	Tensile Strength (psi)
012	C110-1	100	13.3637	12.9442	571	1.20E+07	7.52E+06	99,760	110,045
	C110-2		13.3376	12.9346	548	1.19E+07	5.62E+06	100,570	111,029
013	C110-1	75	13.3668	13.2191	201	1.10E+07	6.20E+06	101,540	121,867
	C110-2		13.3789	13.1548	305	1.01E+07	6.31E+06	101,200	120,463
014	Q125 -1	50	13.2108	13.1086	139	1.07E+07	8.20E+06	117,600	155,273
	Q125-2		12.9513	12.8756	103	9.03E+06	7.88E+06	116,830	151,903
015	Q125-1	50	13.0443	12.9842	82	1.18E+07	8.28E+06	117,070	151,036
	Q125-2		13.2890	13.2249	87	9.03E+06	9.19E+06	120,140	157,005
016	T95-1	50	13.5557	13.1052	613	8.58E+06	7.37E+06	93,240	103,405
	T95-2		13.1735	12.7736	544	7.35E+06	8.24E+06	90,980	103,170
017	T95-1	50	13.3376	13.0653	370	6.21E+06	7.44E+06	90,190	109,001
	T95-2		13.2942	12.9121	520	5.40E+06	7.33E+06	90,170	105,425
018	C110-1	50	13.3801	12.9783	547	8.60E+06	8.48E+06	100,050	114,088
	C110-2		13.4545	13.0451	557	8.06E+06	8.05E+06	102,670	114,466
019	C110-1	50	13.246	12.9677	379	8.21E+06	9.65E+06	100,300	112,331
	C110-2		13.2357	12.9752	354	8.04E+06	9.26E+06	107,350	114,472
020	Q125 -1	75	13.3003	13.0650	320	8.78E+06	9.25E+06	126,180	148,642
	Q125-2		13.2306	12.9783	343	8.07E+06	8.83E+06	125,720	145,371
021	Q125 -1	100	13.1388	12.8640	374	8.12E+06	8.85E+06	122,660	142,615
	Q125-2		12.9428	12.6524	395	8.64E+06	7.64E+06	122,990	140,851
022	Q125 -1	0	12.9684	12.8976	96	8.23E+06	7.67E+06	130,800	151,123
	Q125-2		13.2393	13.1888	69	8.30E+06	7.96E+06	133,100	157,469
023	Q125 -1	25	13.2973	12.9259	505	9.45E+06	8.80E+06	127,700	141,463
	Q125-2		13.2585	12.8393	570	8.51E+06	8.11E+06	120,500	140,209
024	T95-1	75	13.2812	12.6815	816	8.59E+06	7.83E+06	87,500	96,891
	T95-2		13.1886	12.6272	764	8.59E+06	7.18E+06	87,830	98,713
025	T95-1	100	13.1777	12.4770	953	7.53E+06	7.00E+06	83,840	92,673
	T95-2		13.5060	12.8808	850	8.60E+06	7.58E+06	86,600	96,532
026	T95-1	25	13.1866	12.6496	730	9.03E+06	8.35E+06	89,610	98,581
	T95-2		13.2638	12.7952	637	8.64E+06	7.77E+06	91,660	102,082
027	T95-1	0	13.1711	12.8920	380	8.59E+06	8.63E+06	96,050	107,909
	T95-2		13.6589	13.3721	390	8.47E+06	7.49E+06	101,110	111,145
028	Q125 -1	50	13.0742	12.8092	360	7.67E+06	8.72E+06	125,490	141,986
	Q125-2		13.0549	12.7815	372	9.30E+06	8.15E+06	124,980	144,785
029	Q125 -1	50	13.0385	12.7462	398	8.79E+06	8.06E+06	122,070	142,666
	Q125-2		13.0300	12.7461	386	8.38E+06	8.42E+06	123,750	136,764
030	T95-1	50	13.2402	12.6493	804	8.64E+06	8.49E+06	88,330	95,708
	T95-2		13.2607	12.6008	898	9.46E+06	8.04E+06	83,600	92,865
031*	Q125 -1	50	13.2407	12.5630	922	8.17E+06	7.12E+06	121,600	134,114
	Q125-2		13.2171	12.7181	679	9.36E+06	8.30E+06	122,620	133,815
032	T95-1	50	13.2512	12.8109	599	8.51E+06	8.12E+06	87,290	97,884
	T95-2		13.2402	12.6493	804	8.40E+06	8.64E+06	91,270	100,457

E and E* are Young's modulus measured before and after exposure, respectively. * Batch 031 was conducted under dynamic condition (rotor speed of 1000 rpm)

Effect of Pressure and CO_2 Concentration

Figure 3.90 presents the corrosion rates of different API grade steels (T95, C110 and Q125) as a function of CO_2 concentration in 2% NaCl solution saturated with methane containing CO_2 at 6000 psi and 100°F. T95 and Q125 grades demonstrated similar corrosion rate trend with concentration. At low concentration (less than 25% CO_2), corrosion rate increased with increasing CO_2 concentration. However, above 25% CO_2, increasing CO_2 content reduced corrosion rate. As the concentration increased above 50%, this trend changed and the rate increased. These results are consistent with low-pressure corrosion rate measurements obtained when high-strength carbon steel (grade 1045), which meets properties of ASTM A108, was tested in 1% NaCl solution saturated with nitrogen gas containing carbon dioxide (**Fig. 3.91**). Maximum corrosion rate was recorded at 25% CO_2. Grade 1045 carbon steel has minimum yield strength of 77,000 psi. Furthermore, Q125 showed consistently higher corrosion resistance than T95.

Figure 3.90c shows the influence of CO_2 concentration on corrosion rate of Q125 grade steel. The corrosion rate increased with CO_2 concentration resulting from increased solubility of CO_2 in the brine, which reduces the pH and facilitates the corrosion process. As the CO_2 concentration increases, carbonic acid concentration in the solution increases, accelerating the cathodic reactions and therefore increasing the corrosion rate. The corrosion rate increasing-trend with CO_2 concentration has been found consistent with previous studies.

Grade C 110 showed slightly different corrosion rate trend (Fig. 3.90b). At low CO_2 concentration (less than 25%), the average corrosion rate greatly increased with CO_2 concentration. In the intermediate concentration

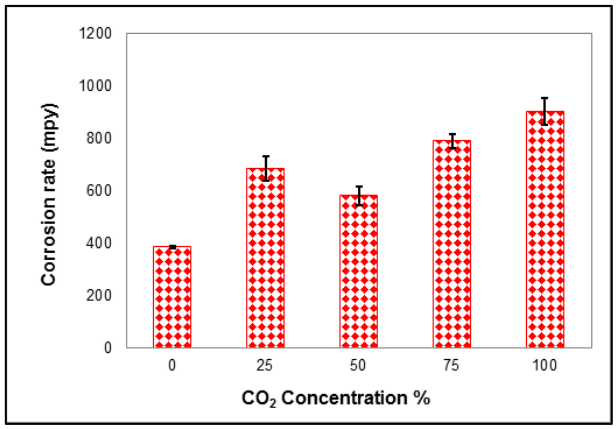

(a)

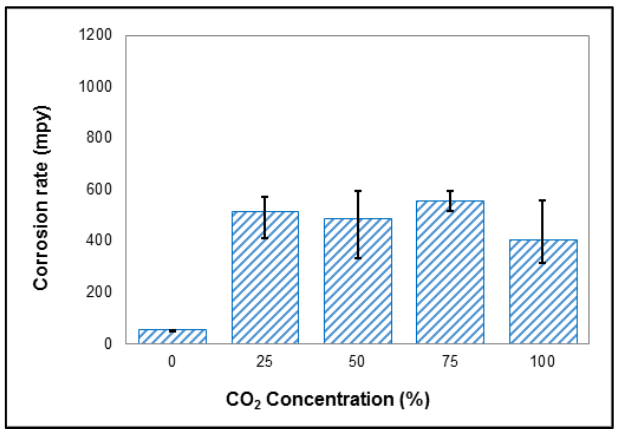

(b)

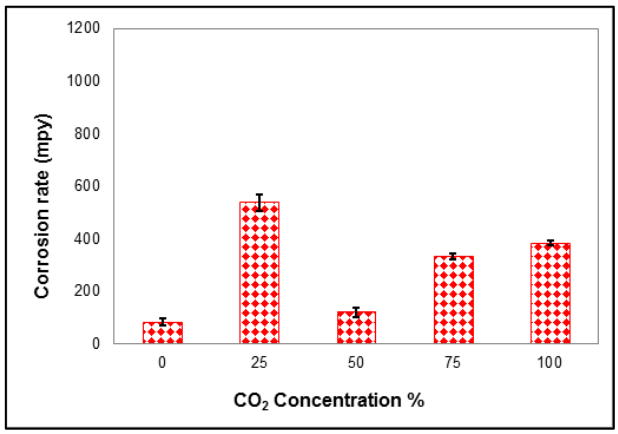

(c)

Fig. 3.90: Corrosion rates of API grade steels as function CO_2 concentration measured at 6000 psi and 100°F: a) T95; b) C110; and c) Q125

range (25 to 75%), the corrosion rate was approximately constant. Slight reduction in the corrosion rate was observed when the concentration was increased above 75%. **Figure 3.92** compares the corrosion rate measurements obtained at different pressures (6000 and 9000 psi). In general, the effect of pressure on corrosion rate is minimal. However, at CO_2 concentration above 50%, a slight increase in corrosion rate was observed when the pressure was raised from 6000 to 9000 psi. The increase in corrosion rate can be attributed to the increase in carbonic acid concentration. As the pressure increases, the concentration of the acid also increases to due to increased solubility. This condition accelerates the cathodic reactions and therefore increasing the corrosion rate.

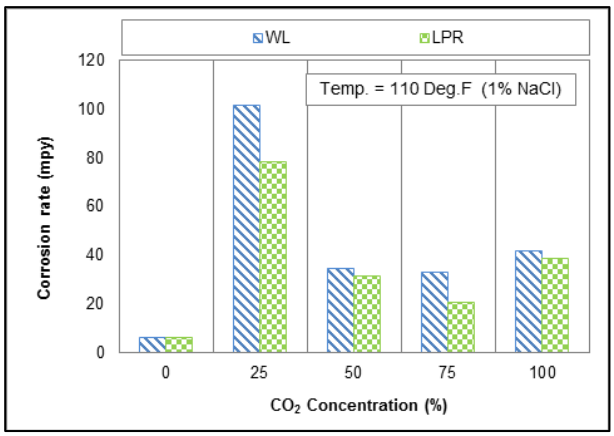

Fig. 3.91: Comparison of corrosion rate measurements at different CO_2 concentrations (Carbon steel 1045)

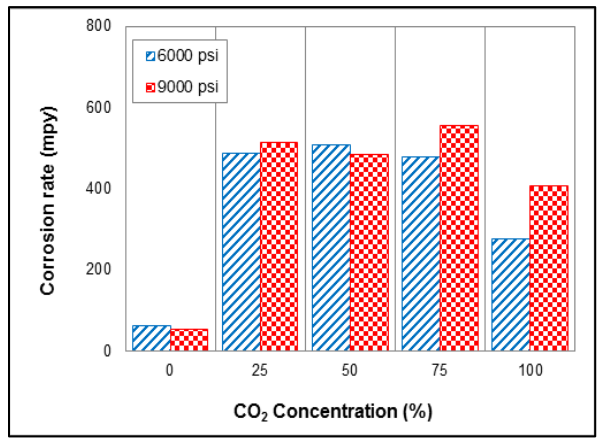

Fig. 3.92: Corrosion rate of C110 versus CO_2 concentration at 100°F and different pressures

Figure 3.93 presents corrosion rate of C110 as a function of CO_2 concentration at 3000 psi. The corrosion rate increased with the CO_2 concentration due to increase in carbonic acid concentration (H_2CO_3). As the partial pressure of CO_2 increases, the acid concentration also increases, accelerating the cathodic reactions and therefore increasing the corrosion rate. This corrosion rate trend is consistent with previous measurements available in the literature (Choi et al. 2014; Huang et al. 2014; Schmitt and Horstemeier 2006). However, the corrosion rate trend at 3000 psi was found to be different from our previous observations at 6000 and 9000 psi, in which the corrosion rate increased at low and intermediate CO_2 concentrations and decreased as the concentration approached 100%.

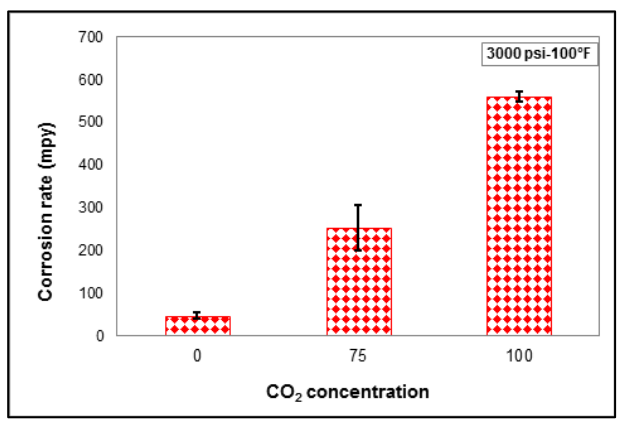

Fig. 3.93: Corrosion rate of C110 as a function CO_2 concentration (3000 psi and 100°F)

Figure 3.94 compares the corrosion rates of different API grade steels (T95, C110 and Q125) in 2% NaCl solution saturated with methane containing 50% CO_2 at 6000 and 9000 psi, and 100°F. Under these conditions, Q125 showed the highest corrosion resistance. Increasing pressure slightly reduced the corrosion rate in all steel grades. This is unexpected because increased pressure improves suitability of CO_2 leading to lower pH and higher acidity, which are favorable for corrosion. Results obtained at 100% CO_2 concentration show a different trend (**Fig. 3.95**). The highest corrosion rate was recorded at 3000 psi. In addition to electrochemical reaction and ionic diffusion, the formation of protective scale on the surface of a metal determines the corrosion rate. When tested at low-pressure (3000 psi), only loose protective corrosion scale was formed on the specimen surface whereas at 6000 psi, more compact and dense scale was formed resulting in the lowest corrosion rate.

In the absence of CO_2, pressure slightly affects the corrosion process. Tests conducted under different pressures (**Fig. 3.96**) demonstrated the influence of pressure on corrosion rate of C110 in the absence of carbon dioxide (brine saturated with pure methane). Slight variation in corrosion rate was observed as the pressure was increased from 3000 to 9000 psi. One possible explanation for this phenomenon could be the improvement in molecular diffusion in the brine as more methane is dissolved due to increased pressure.

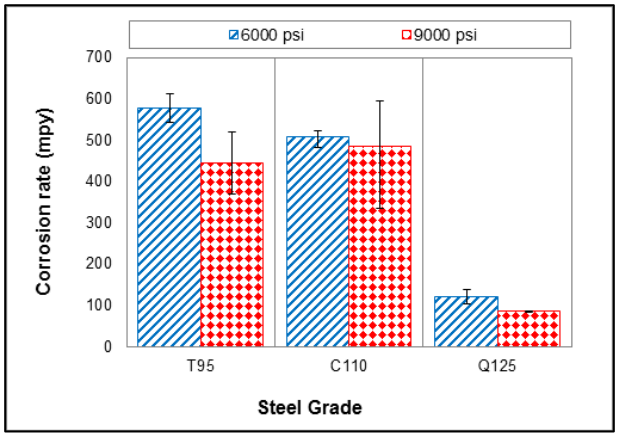

Fig. 3.94: Corrosion rates of API grade steels at different pressures (50% CO_2 and 100°F)

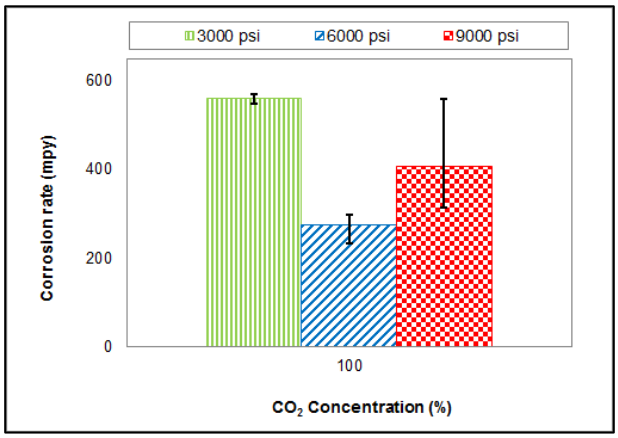

Fig. 3.95: Corrosion rate of C110 at different pressures (100% CO_2 and 100°F)

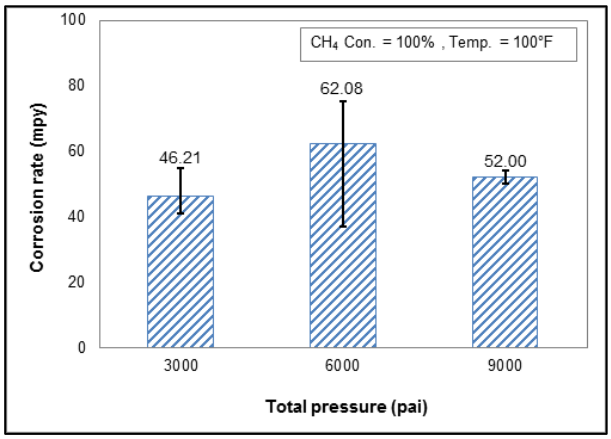

Fig. 3.96: Corrosion rate versus pressure at 100°F and 0% CO_2

Effect of H_2S Concentration

Figure 3.97 presents the impact of H_2S concentration on uniform corrosion rate of T95 in 2% NaCl solution saturated with mixed gas containing 50% CO_2 and 50% methane. These measurements were obtained from tests conducted at 6000 psi and 100°F. The results demonstrate a corrosion rate trend, which is very similar to that of C110 (**Fig. 3.98**). At low H_2S concentration (less than 10 ppm), the rate increased with increasing concentration of hydrogen sulfide. Above 10 ppm of H_2S, the corrosion rate declined as the H_2S concentration was increased. The reduction in the corrosion rate occurs due to the formation of a protective corrosion scale. The corrosion rate trend observed in these experiments is consistent with published results obtained from tests performed at low pressure (Valdes et al. 1998).

Figure 3.99 presents the impact of H_2S concentration on the CO_2 corrosion rate of Q125 grade steel. At low H_2S concentration (less than 10 ppm), the corrosion rate sharply increased with increase in H_2S concentration. However, above 10 ppm, the rate displayed only slight increase with the concentration. Measurements obtained from T95 and C110 showed reduction in corrosion rate at high CO_2 concentration. The presence of maximum corrosion rate for carbon steel at approximately 10 ppm H_2S concentration has been previously reported (Valdes et al. 1998).

Effect of Fluid Velocity

Furthermore, the influence of fluid movement (i.e. wall shear stress and turbulence) on the corrosion rate of Q125 at 6000 psi and 50% CO_2 concentration was investigated (**Fig. 3.100**). As presented in Section 3.3.3.4, the uniform corrosion cell is equipped with a rotating inner bob. Under dynamic condition, remarkably high corrosion rate (nearly ten-fold) was observed as rotor speed was increased from 0 to 1000 rpm.

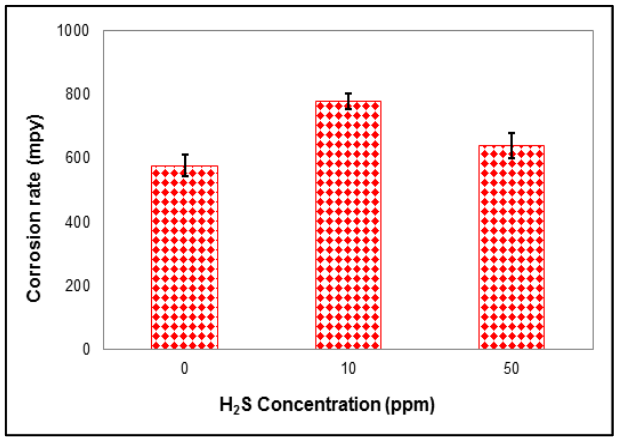

Fig. 3.97: Corrosion rate of T95 as a function of H_2S concentration (100°F, 50% CO_2 and 6000 psi)

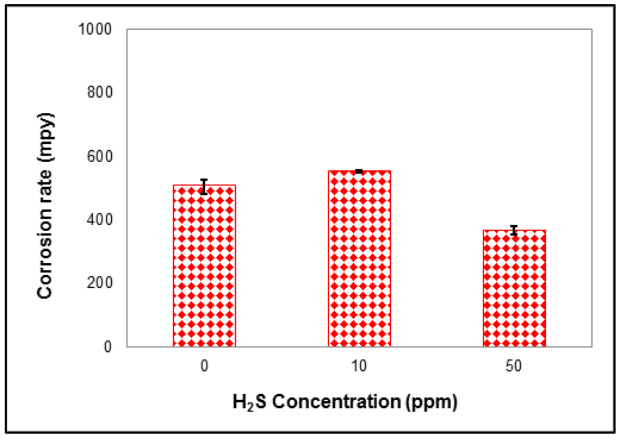

Fig. 3.98: Corrosion rate of C110 as a function of H_2S concentration (100°F, 50% CO_2 and 6000 psi)

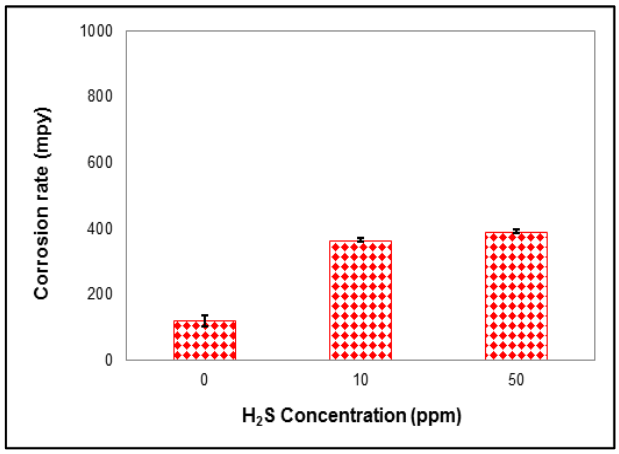

Fig. 3.99: Corrosion rate of Q125 as a function of H_2S concentration (100°F, 50% CO_2 and 6000 psi)

Possible explanation for the sharp increase in corrosion rate can be the occurrence of two natural phenomena, namely diffusion enhancement and prevention of protective scale formation. Often, corrosion process is controlled by corrosive species (ions) transport rate (diffusion rate). Corrosion occurs when corrosive species reach the steel surface from the bulk (i.e. mass transfer rate). Increasing the rotational speed under turbulent flow condition increases momentum and species diffusion. Improved diffusion rate tends to increase the corrosion rate through the enhancement of the rate-controlling phenomenon. In addition, the development of higher wall shear stress at the metal surface can affect the integrity and formation of the corrosion scale. The results obtained from these experiments are consistent with published experimental studies (Nor et al. 2011; Nor et al. 2012 and Farelas et al. 2013) conducted at low pressure.

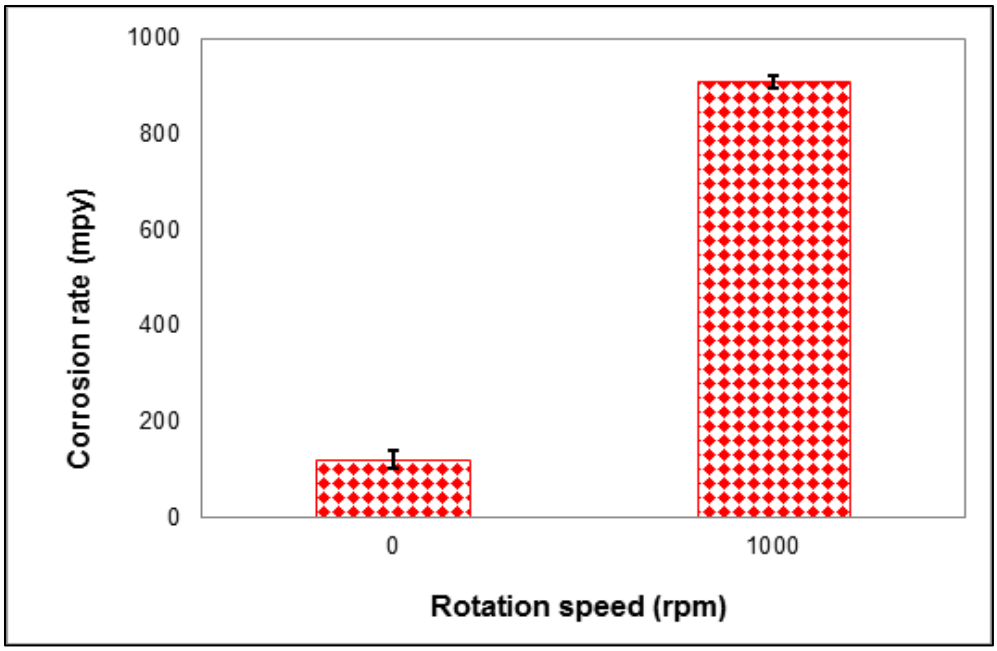

Fig. 3.100: Effect of rotational speed on corrosion rate of Q125 at 6000 psi, 100°F and 50% CO_2

Determination of Wall Shear Stress at the Coupon Surface

Dynamic flow condition strongly affects some types of corrosion by preventing scale development on corroded surface of a metal. The disruption of the scale formation process is related to a number of factors including fluid properties (viscosity and density) and flow parameters such as rotation speed of the cylinder and annular clearance between the rotating cylinder and coupon holder. Studies show that CO_2 corrosion rate under dynamic conditions is strongly related to the wall shear stress. Due to low fluid viscosity and high rotational speed of the rotating cylinder, flow during the corrosion test is predominately under turbulent flow condition. For turbulent flow, the wall shear stress is related to the fluid viscosity and density, annular clearance and rotational speed of the cylinder. For the sake of simplicity, a narrow annular flow is often approximated using a parallel plate flow (**Fig. 3.101**).

The velocity distribution developed between two parallel plates (moving and stationary plates) under turbulent flow condition follow a logarithmic profile. Near wall velocity profiles of simple turbulent flows are modeled using the wall equations. Spalding (94) developed a generalized formulation of the law of the wall that is valid for the whole turbulent boundary layer including the viscous sublayer. Spalding equation is expressed in simplified form as:

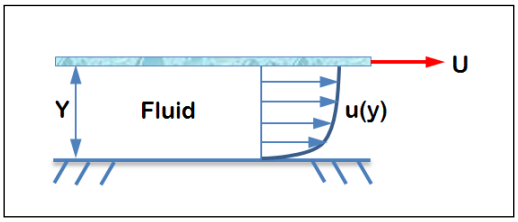

Fig. 3.101: Flow between parallel plates

$$y^{+} = \frac{w}{\kappa} + A(e^{w} - 1 - w - 0.5w^{2} - 0.33w^{3} - 0.0417w^{4}) \quad \text{..... (3.133)}$$

where the parameter $w = u^{+}\kappa$, constant $A = 0.1108$, and $\kappa = 0.4$. u^{+} and y^{+} are dimensionless local velocity and dimensionless distance from the wall, respectively. Dimensionless flow parameters (u^{+} and y^{+}) are defined as: $u^{+} = u/u^{*}$; and $y^{+} = yu^{+}\rho/\mu$. The friction velocity is determined from the wall shear stress as: $u^{*} = (\tau_w/\rho)^{0.5}$. The moving plate velocity is approximately, $U = \omega R_{cyl}$, where R_{cyl} and ω are the radius and rotation speed of the rotating cylinder. Hence, the wall shear is numerically determined from the above equation knowing the values of U, Y, ρ and μ.

3.3.7. Modeling

3.3.7.1. Model Description

The possible CO_2 corrosion mechanism and different reactions that take place near and away from the steel surface are extensively studied in the past few years. Based on the literature review, the most prominent CO_2 mechanism involves cathodic reaction (reduction of H^{+}, H_2CO_3 and HCO_3^{-}) and anodic reaction (iron dissolution, Fe^{2+}). The overall corrosion process includes four steps: i) chemical reactions in the bulk solution; ii) mass transport of corrosive species from the bulk to steel surface; iii) electrochemical reaction at the steel surface; and iv) transport of corrosion products to the bulk solution.

3.3.7.2. Assumptions and Limitations

The model presented in this study predicts the corrosion rate assuming no corrosion scale formation and static fluid. It considers only hydrogen ion reduction and iron dissolution for the electrochemical reactions. Furthermore, the following assumptions are utilized in model formulation: i) The sum of the current due to the cathodic reactions must be equal to the current due the anodic reaction, which in turn is equal to the corrosion current; and ii) The sum of the mass transfer rate of reactant must be equal to the sum of the electrochemical reaction rates.

3.3.7.3. Model Formulation

Physicochemical Reactions

The following equations summarize the model formulation to determine the corrosion rate (Wang et al. 2004):

Step I: - Formation of Reactive species in the bulk

$CO_2 + H_2O = H_2CO_3$ ..... (3.134)

$H_2CO_3 = H^+ + H_{CO3}^-$ ..... (3.135)

$HCO^3- = H^+ + CO_3^-$ ..... (3.136)

Step II: - Transportation of Reactants (Bulk to Surface)

$H^+_{(bulk)} \rightarrow H^+_{(Surface)}$ ..... (3.137)

Step III: - Electro-Chemical Reaction at the Surface

Cathodic reaction

$2H^+ + 2e = H_2$ ..... (3.138)

Anodic reaction

$Fe = Fe^{2+} + 2e$ ..... (3.139)

Step IV: - Transportation of Products (Surface to Bulk)

$Fe^{2+}_{(Surface)} \rightarrow Fe^{2+}_{(Bulk)}$ ..... (3.140)

Electrochemical Reactions

The concentrations of corrosive species produced due to the chemical reactions presented in the first step are proportional to CO_2 partial pressure and temperature, according to the solubility model presented in this study (Appendix B). The electrochemical reactions are characterized by anodic and cathodic current. The current density due to electrochemical reactions (Step III) can be estimated using Butler-Volmer equation as:

$$i_a = 2FK_{e,Fe2+}\left[Fe^{2+}\right]_s \exp\left[\frac{2\times(1-\alpha)\times F\times(E_{corr}-E_{Fe^{2+}})}{R\times T}\right] \quad (3.141)$$

$$i_c = 2FK_{e,H^+}\left[H^+\right]_s \exp\left[\frac{-2\alpha\times F\times(E_{corr}-E_{H^+})}{R\times T}\right] \quad (3.142)$$

where

i_a is anodic current density (A/m^2)

i_c is cathodic current density (A/m^2)

$\left[Fe^{2+}\right]_s$ is surface concentration of Fe^{2+} (mol/m^3)

$\left[H^+\right]_s$ is surface concentration of H^+ (mol/m^3)

E_{corr} is corrosion potential (V)

α is transfer coefficient (=0.5 most cases)

F is Faraday's constant (=96500 C/mol)

R is universal gas constant (=8.314 J/mol-K)

T is temperature (K)

$E_{Fe^{2+}}$ is potential for the anodic reaction (V)

E_{H^+} is potential for the cathodic reaction (V)

$K_{e,Fe^{2+}}$ is rate constant for the anodic reaction (m/s)

K_{e,H^+} is rate constant for the cathodic reaction (m/s)

The values of the rate constants are not available in the literature for all temperature and material types. The values of $K_{e,Fe^{2+}}$ and K_{e,H^+} that have been used in this study are listed in **Table 3.12**.

Table 3.12: Values of rate constant of the electrochemical reactions

Temperature (°C)	$K_{e,Fe^{2+}}$ (cm/s)	K_{e,H^+} (cm/s)	Reference
40	0.0259	2×10^{-5}	Dayalan et al.(1995)
60	0.259	2×10^{-4}	Dayalan et al.(1995)
80	2.59	2×10^{-3}	Dayalan et al.(1995)

The equilibrium potentials E_{H^+} and $E_{Fe^{2+}}$ are given by the Nernst equations:

$$E_{H^+} = E^0_{H^+} + \frac{RT}{nF}\ln\frac{[H^+]_s^2}{[H_2]} \quad (3.143)$$

$$E_{Fe^{2+}} = E^0_{Fe^{2+}} + \frac{RT}{nF}\ln[Fe^{2+}]_s \quad (3.144)$$

Ionic Diffusion

Surface reactions consume and produce chemical species. As a result, variation in the species concentration, which is normal to the steel surface is created. This generates flux to/away from the surface (steps II and IV). Mass transfer is one of the key processes that affect the rate of corrosion. The mass transfer rate of the reactant and product species are given by the following equations:

The mass transfer rate of Fe^{2+} = $2FK_{mt,Fe^{2+}}\left([Fe^{2+}]_s - [Fe^{2+}]_b\right)$ ..... (3.145)

The mass transfer rate of H^+ = $FK_{mt,H^+}\left([H^+]_b - [H^+]_s\right)$ ..... (3.146)

where $K_{mt,Fe^{2+}}$ and K_{mt,H^+} are the mass transfer coefficient of the iron and hydrogen ions, respectively. It should be noted that both constants are set to be 1×10^{-4} m/s. The subscripts s and b represents the surface and bulk. The model assumes steady state condition. Under this condition, the following assumptions can be made:

I. The sum of the current due to the cathodic reactions must be equal to the current due the anodic reaction, which in turn is equal to the corrosion current.

$$i_c = i_a = i_{corr} \quad (3.147)$$

II. The sum of the mass transfer rate of reactant must be equal to the sum of the electrochemical reaction rates.

The current density for anodic reaction is expressed as:

$$i_a = 2FK_{mt,Fe^{2+}}\left(\left[Fe^{2+}\right]_s - \left[Fe^{2+}\right]_b\right) \quad (3.148)$$

Similarly, the current density for cathodic reaction is given by:

$$i_c = FK_{mt,H^+}\left(\left[H^+\right]_b - \left[H^+\right]_s\right) \quad (3.149)$$

There are three unknowns in a set of three nonlinear equations above (Eqs. 3.147-3.149). The unknowns are surface concentrations of iron and hydrogen ions, and the corrosion potential (E_{corr}). The unknowns are obtained by solving these equations numerically using the Newton-Raphson method to determine the corrosion rate as:

$$CR = \frac{i_a}{2F}\frac{M_{Fe}}{\rho_{Fe}} \times 3600 \times 24 \times 365 = 1.16 \times i_a \quad (3.150)$$

where

CR is corrosion rate (mm/y)

i_a is anodic current density (A/m^2)

M_{Fe} is iron molecular weight (=55.85 kg/kmol)

ρ_{Fe} is iron mass density (=7800 kg/m^3)

The electrochemical model was implemented in Matlab software in order to solve the set of equations numerically and predict the corrosion rate and surface concentrations. The main code (corrosion model) is linked to other sub-codes (solubility model, pH model and gas compressibility model) to find the bulk concentration of the corrosive species as well as compressibility factor and fugacity coefficient. The model requires as input: gas composition, temperature, salt concentration and initial concentration of iron ion.

3.3.7.4. Model Validation and Testing

To ensure the model performance and its accuracy, the present model predictions where compared with measurements of corrosion experiments, which were performed in this study under high-pressure condition, varying CO_2 concentration. **Figure 3.102** compares the model prediction with experimental data at 3000 psi and 75% and 100% of CO_2 concentration. As displayed on the figure, model predictions show some discrepancies with the experimental data, even though the trend prediction is in agreement with the measurements. **Figures 3.103** to **3.104** compare model predictions with experimental data for different test materials (T95, C110 and Q125) at 6000 psi and various CO_2 concentrations (25 – 100%). The model provides reasonable corrosion rate predictions for C110 at various CO_2 concentrations, though its corrosion-rate-trend prediction is not consistent with the measurements. As a result, the model slightly overestimates the corrosion rate at 100% CO_2 because the impact of the model neglects the effect of corrosion scale. In the case of T95, the model underestimates the corrosion rate.

However, the corrosion rate trend is still consistent with the measurement (i.e. the corrosion rate tends to increase with the increase in the CO_2 concentration). Limited agreement is observed when model predictions compared with experimental data of Q125 (**Fig. 3.105**). Measurements show mixed corrosion rate (CR) trend while predictions show unique CR trend. The model does not account for material property variations such as tensile strength, hardness or elasticity. Model prediction is compared with experimental data (**Fig. 3.106**) obtained from different steel grades at high-pressure condition (i.e. 9000 psi, 100°F and 50% CO_2 concentration). The results show that the model closely predicts corrosion rate of T95 and C110 and substantially overestimates the corrosion of Q125.

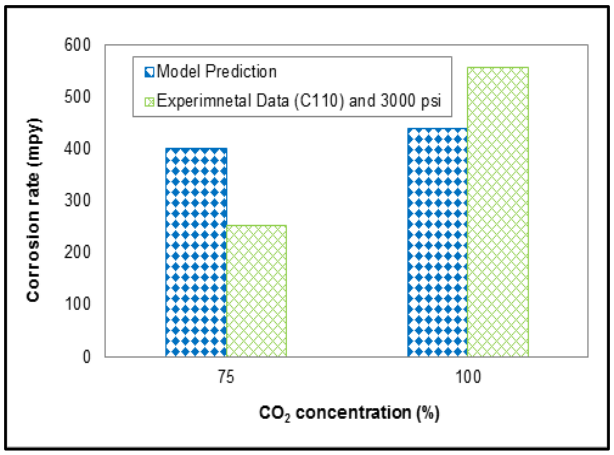

Fig. 3.102: Model prediction and measurements for C110 at 3000 psi, 100°F and different CO_2 concentrations

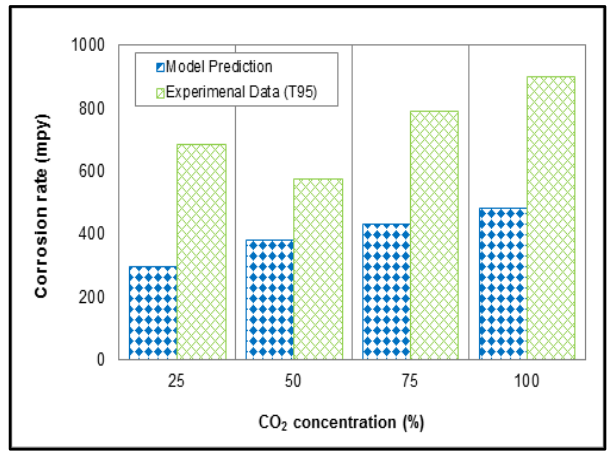

Fig. 3.103: Model prediction and measurements for T95 at 6000 psi, 100°F and different CO_2 concentrations

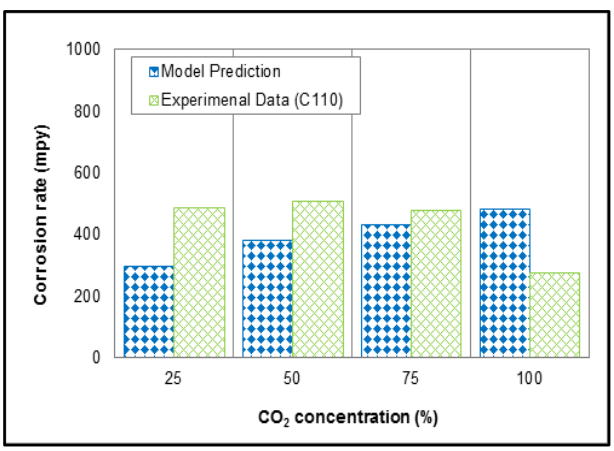

Fig. 3.104: Model prediction and measurements for C110 at 6000 psi, 100°F and different CO_2 concentrations

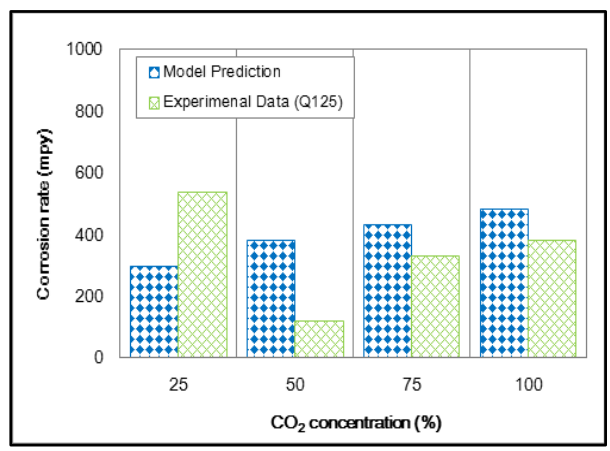

Fig. 3.105: Model prediction and measurements for Q125 at 6000 psi, 100°F and different CO_2 concentrations

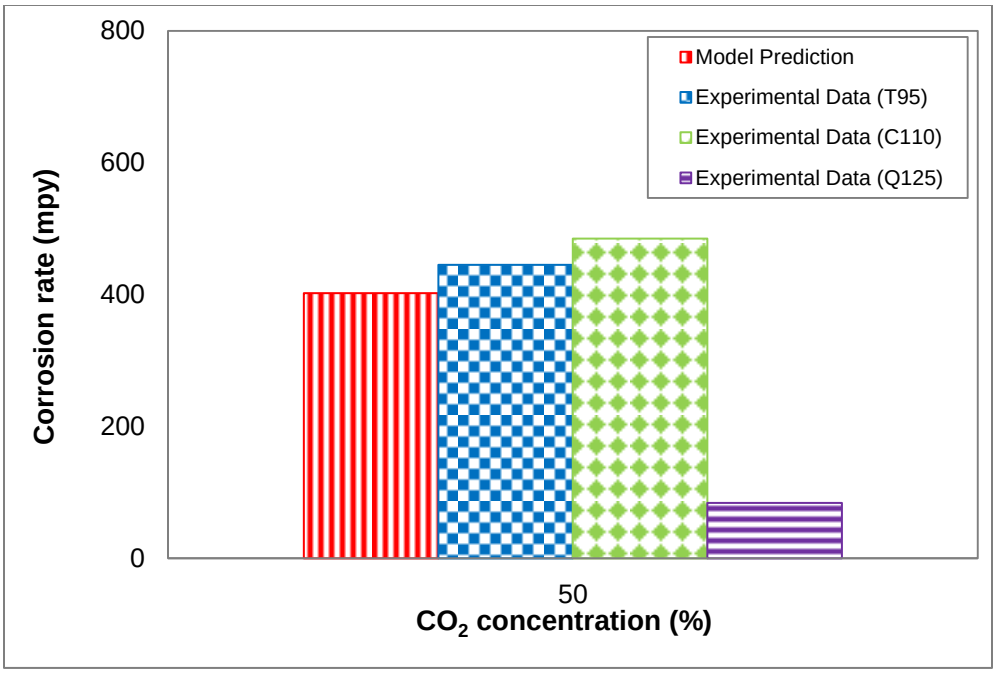

Fig. 3.106: Model prediction and measurements at 9000 psi, 100°F, 50% CO_2 and different materials

3.3.7.5. Summary

A mechanistic model has been developed to predict the rate of corrosion of carbon steel for non-scale forming conditions in CO_2 environments under the influence of NaCl brine in elevated temperature and pressure condition. The model is based on mass transfer in the bulk solution and electrochemical reaction occurring on the metal surface. The model predictions have been compared with measurements. The model predictions predominantly exhibit reasonable agreement with the experimental measurement. However, in some cases considerable discrepancies have been noticed.

3.3.8. Conclusions

The following conclusions are drawn from the results of this investigation:

- Corrosion rate is strongly affected by the salt concentration with or without the presence of carbon dioxide. CO_2 corrosion rates decreases with the increase in the salt concentration.
- The Impact of CO_2 concentration and corrosion rate is strongly influenced by temperature and salt concentration.
- Increase in temperature facilitates the corrosion reactions and transport of species (molecular diffusion); hence, it facilitates corrosion process.
- Regardless of the salt and CO_2 concentrations, the maximum corrosion rate was observed at 110°F.
- T95 and Q125 grade steels demonstrated similar corrosion rate trend with CO_2 concentration. Q125 showed consistently higher corrosion resistance than T95.
- The presence of small amount of H_2S (less than 10 ppm) is sufficient to influence corrosion rate due to the formation of protective corrosion scale.
- Dynamic condition remarkably increased corrosion rate because of enhancement in diffusion process and prevention of protective scale formation.

NOMENCLATURES

Acronyms

BWOC	By weight of cement
CH	Calcium hydroxide
CSH	Calcium silicate hydrate
FTIR	Fourier Transform Infra-Red
GHO	Class G cement with hydroxyapatite
GS	Class G cement with silica flour
GSMG	Class G cement with silica flour and magnesium oxide
GSLM	Class G cement with silica flour, latex and micro-silica
GSLT	Class G cement with latex
HHO	Class H cement with hydroxyapatite
HPHT	High-pressure high-temperature
HS	Class H cement with silica flour
HSHO	Class H cement with silica flour and hydroxyapatite
HSMG	Class H cement with silica flour and magnesium oxide
HSLM	Class H cement with silica flour, latex and micro-silica
HSLT	Class H cement with latex
LPR	Linear polarization resistance
LTMS	Cement with latex and micro-silica additives
mpy	mils per year
MGO	Magnesium oxide containing cement
MGO-5	Cement containing 5% BWOC MgO as additive
MGO-10	Cement containing 10% BWOC MgO as additive
MS	Micro-silica containing cement
MS-10	Cement containing 10% BWOC micro-silica as additive
NACE	National Association of Corrosion Engineers
SBS	Shear bonding strength
SD	Static and dynamic
SEM	Scanning Electron Microscope
SCC	stress corrosion cracking
XRD	X-Ray diffraction

Symbols

K_H	Henry's constant
K_h	Dissociation constant of CO_2
K_{a1}	First dissociation constant of H_2CO_3
K_{a2}	Second dissociation constant of H_2CO_3
t	Time from commencement of degradation process
D	Effective diffusion coefficient component in each direction
U	Bulk fluid velocity component in each direction
Cs	Specie concentration in solid phase

x, y, z	Distance from the edge of the sample in each direction
k	Thermal conductivity
Blaine	Cement fineness
E_a	Activation energy
R	Universal gas constant
W/C	Water–to-cement ratio
K_{sp}	Solubility constant of calcium hydroxide
C_{NaCl}	Concentration of sodium chloride in wt%
K_{spc}	Solubility constant of calcium carbonate
K_w	Solubility constant of water
$[Ca^{2+}]$	Concentration of Ca^{2+}
$[H^+_{(aq)}]$	Concentration of H^+
$[HCO^-_{3(aq)}]$	Concentration of HCO^-_3
$[CO^{2-}_{3(aq)}]$	Concentration of CO^{2-}_3
$[OH^-_{(aq)}]$	Concentration of OH^-
$[H_2CO_{3(aq)}]$	Concentration of H_2CO_3
$[CO_{2(aq)}]$	Concentration of CO_2
C_{total}	Solid phase total calcium concentration
x_d	Degradation depth
D	Effective diffusion coefficient
$C_{s,0}$	Initial solid – phase calcium concentration (mol/L)
$C_s(x,t)$	Calcium concentration at any time and location (mol/L)
C_{satu}	Saturated liquid phase calcium ion concentration (mmol/L)
$\bar{C}_l$	Dimensionless liquid phase calcium concentration
C_l	Liquid phase calcium concentration
C_{CH}	Amount of calcium in the solid phase of the calcium hydroxide (mmol/L)
C_{CSH}	Amount of calcium in the solid phase of the C-S-H gel (mmol/L)
x_1	Liquid phase Ca^{+2} concentration when C-S-H begins to convert into silica (mmol/L)
x_2	Liquid phase Ca^{+2} concentration when he dissolution of CSH gel begins (mmol/L)
X_c	Weight fraction of Portland cement
X_{SF}	Weight fraction of silica flour
X_{C2S}	Volume fraction of C_2S
X_{C3S}	volume fraction of C_3S
K	Empirical parameter
v_{chsh}	Chemical shrinkage
T	Absolute Temperature, K
P	Total pressure, bar
y	Mole fraction of CO_2 in vapor phase
m	Molality of brine solution
C_{NaCl}	Weight percentage of NaCl
σ	Compressive strength of control sample
r	Radius of cement sample

r_1, r_2, r_3	Distance of each leached zone from edge of the sample
D_c	Diameter of mini-pipe adapter
D_{in}	Inner diameter of a mini-pipe
D_o	outer diameter a mini-pipe
D_{rod}	Diameter of the pulling rod
$D_{p,rod}$	Diameter of the piston rod
P_{cyl}	Pressure is pneumatic cylinder
P_{in}	Pressure inside the mini-pipe
P_o	Pressure in the SCC vessel
t	Annular clearance between rotating cylinder and corrosion coupon holder
T	Tension at the middle of a mini-pipe
u	Local fluid velocity in narrow slot
u+	Dimensionless velocity at the moving plate
u*	Friction velocity
U	Mean fluid velocity in narrow slot
y	Distance of any arbitrary point from the stationary plate
Y+	Dimensionless distance between the moving and stationary plates
Y	Distance between the moving and stationary plates

<u>Greek Symbols</u>

α	Degree of hydration
ξ_d	Dimensionless degraded depth
ε	Dimensionless variable
$\xi_{CO_2-Na-Cl}$	Interaction parameter
ϕ	Fugacity coefficient
$\emptyset_0$	Initial porosity of cement
$\emptyset$	Porosity of cement at current time step
κ	Von Karman constant
λ_{CO_2-Na}	Interaction parameter
μ	Fluid viscosity
μ	Chemical potential
$\frac{\mu_{CO_2}^{1(0)}}{RT}$	Interaction parameter
ρ	Fluid density
σ_o	Initial uniform stress in sample
σ_{T-P}	First Intermediate stress achieved in leaching zone
σ_{T-CP}	Minimum stress achieved in leaching zone
$\sigma_{T-P'}$	Second Intermediate stress achieved in leaching zone
σ_T	Stress in sound zone
σ_∞	Ultimate strength
σ_{axial}	Axial stress in a mini-pipe
$\sigma_{circumferential}$	Circumferential stress in a mini-pipe
τ_w	Wall shear stress acting on a corrosion coupon

REFERENCES

Abdul Rahman, R. and Chong, A. 1997. Cementing Multilateral Well With Latex Cement. Paper SPE 37623 presented at SPE/IADC Drilling Conference, Amsterdam, Netherlands, March, 4 to 6. http://dx.doi.org/10.2118/37623-MS.

Adsani, E., Shirazi, S.A. Shadley, J.R., Rybicki, E.F. 2006. Validation of Mass Transfer Coefficient Models used in Predicting CO_2 Corrosion in Vertical Two-Phase Flow in the Oil and Gas Production, Paper 06573, presented at the NACE Corrosion conference, Houston, TX.

Agzamov, F., Karimov, N.and Akchurin, K. 2013. Preparation of expanding oil well cements. Oil and Gas Business Journal (published online December 11, 2001).

Ahmed, R. M., Takach, N. E., Khan, U. M, Taoutaou, S., James, S., Saasen, A. and Godøy, R. 2009. Rheology of Foamed cement, Cement and Concrete Research, Volume 39, Issue 4, Pages 353-361.

Akkaya, Y., Voigt, T., Subramaniam, K. V. and Shah, S. P. 2003. Nondestructive Measurement of Concrete Strength Gain by an Ultrasonic Wave Reflection Method.

Ali, M.M. and Mullick, A.K. 1998. Volume Stabilization of High MgO Cement: Effect of Curing Conditions and Fly Ash Addition, Cement and Concrete Research 28 (11): 1585-1594.

Allan, M.L. 1997. Rheology of Latex Modified Grouts, Cement and Concrete Research 27 (12): 1875 – 1884.

Amri, J., Kvarekval, J. and Malki, B. 2011. Simulation of Solid-State Growth of Iron Sulfides in Sour Corrosion Conditions, paper No. 78, March 13 - 17, Houston, Texas.

Anderko, A. and Young, R. D. 1999. Simulation of CO_2/H_2S Corrosion Using Thermodynamic and Electrochemical Models, Paper No. 31, presented at the NACE CORROSION conference, Houston, TX.

Anderko, A. 2000. Simulation of $FeCO_3$/FeS Scale Formation Using Thermodynamic and Electrochemical Models, Paper No. 102, presented at the NACE CORROSION conference, Houston, TX.

API RP 10B, Recommended Practice for Testing Well Cements, Standard by American Petroleum Institute (1997).

Arliguie, G. and Grandet, J. 1985. Etude par calorimetrie de l'hydratation du ciment Portland en presence de zinc, Cement and Concrete Research, Volume 15, Issue 5, September, Pages 825–832.

Asahi, H., Ueno, M.and Yonezawa, T. 1994. Prediction of Sulfide Stress Cracking in High-strength tubulars. Corrosion 50 (7): 537-545.

ASTM Standard C39/C39M-12. 2012. Standard Test Method for Compressive Strength of Cylindrical Concrete Specimens.

ASTM E8/E8M. 2013. Standard Test Methods for Tension Testing of Metallic Materials, ASTM International.

Baldy, M.F., Tuttle, R.N. and Kane, R.D. 1981. H_2S corrosion in Oil and Gas production- A compilation of classic papers, National Association of Corrosion Engineers, pp 614-618, Houston, Texas.

Barlèt-Gouédard, V., Rimmelé, G., Goffé, B. and Porcherie, O. 2006. Mitigation Strategies for the Risk of CO_2 Migration through Wellbores, paper *IADC/SPE 98924* presented at the IADC/SPE Drilling Conference, Miami, Florida, U.S.A., 21–23 February.

Basheeduzzafar Dakhil F.D., Bader M.A. and Khan M.M. 1992. Performance of Corrosion Resisting Steels in chloride Bearing Concrete. ACI Materials Journal. 89(5): 439-448.

Been, J. and Crozier, B. 2014. Thermal Well Casing Corrosion Evaluation Using Hydrogen Permeation in Mini-Pipe Specimens, Alberta Innovates Technology Futures, AITF, Calgary, Alberta http://www.atimetals.com/news/corrosion-conference/Documents/CSC11-pdfs/presentation_5b_been.pdf, last accessed on 01-18-2014.

Benning, L. G., Wilkin, R. T. and Barnes, H. L. 2000. Reaction pathways in the Fe-S below 100 °C, Chem. Geol., 167, 25-51.

Bensted, J. and Barnes, P. 2002. *Structure and Performance of Cements*. Second Edition, London: SPON Press.

Berger, F.P. K. and Hau, F. F.L., 1977.Mass Transfer in Turbulent Pipe Flow Measured by the Electrochemical Method, Int. J. Heat Mass Transfer, Vol. 20; pp. 1,185-1194.

Bich, N.N. and Goerz, K. 1996. Caroline Pipeline Failure: Finding on Corrosion Mechanism in Wet Sour Gas Systems Containing Significant CO_2, paper No. 26, March 24 - 29, Denver, Co.

Black, L., Breen, C., Yarwood, J., Grave, K., and Stemmermann, P. 2007. Structural Features of CSH(I) and its Carbonation in air - A Raman Spectroscopic Study - Part II: Carbonated Phases, J. of American Ceramic Society, Soc. 90: 908 - 917.

Bockris, J.O'M., Drazic, D. and Despic, A.R., 1961. The Electrode Kinetics of the Deposition and Dissolution of Iron, ElectrochimicaActa, Vol. 4, pp. 325 to 361.

Bonis, M. R. and Crolet, J. L. 1989. Basics of the Prediction of the Risks of CO_2 Corrosion in Oil and Gas Wells. Paper No. 466, presented at the NACE CORROSION conference, Houston, TX.

Bourgoyne, T.A. Jr., Chenevert M.E., Millheim K.K. and Young F.S.Jr. 1986. *Applied Drilling Engineering*, Second Printing, Richardson, Texas: Textbook Series, SPE.

Brandl, A., Cutler, J., Seholm, A., Sansil, M. and Braun, G. 2010. Cementing Solutions for Corrosive Well Environments. Paper SPE 132228-MS presented at International Oil & Gas Conference and Exhibition, China, June, 8 to 10. http://dx.doi.org/10.2118/132228-MS.

Brown, B., Reddy, S. and Nešić, S. 2004. CO_2 Corrosion In The Presence of Trace Amounts of H_2S, paper No. 04736, presented at the NACE International conference, CORROSION 2004, Phoenix, AZ.

Bruce, E. and Urband, P.E. 1999. High Strength Sour Service C110 casing, paper SPE/IADC 52843 presented at the SPE/IADCE Drilling Conference, 9-11 March, Amsterdam, Holland.

Bruckdorfer, R. A. 1986. Carbon Dioxide Corrosion In Oil Well Cements, SPE 15176 Billings, MT, May 19 – 21.

Buntoro, A. and Rubiandini, R.S. 2001. The Effect of Neat Magnesium Oxide (MgO) as Expanding Additive With Burning Temperature 1200°C and 1300°C on Cement Shear Bond Strength at High Pressure and Temperature. Proceedings of the 5th INAGA Annual Scientific Conference and Exhibitions, Yogyakarta, Indonesia, March 7-10.

Cane R.D. and Cayard M.S. 1998. Roles of H_2S in Behavior of engineering alloys: A review of literature and experience, Paper no. 274, NACE International Annual Conference, March 22 - 27, 1998, San Diego, CA.

Carde, C., Francois, R. and Torrenti, J M. 1996. Leaching of both calcium hydroxide and C-S-H from cement paste: Modeling the mechanical behavior, Cement and Concrete Research, Volume: 26, Issue: 8, Pages: 1257-1268.

Cernocky, E., Aaron, V., Paslay, P.and Wink, R. 2005. Combined Axial Tension/Compression and Internal Pressure Testing of Mini-Pipe Specimens in H_2S Environment to Determine Three Dimensional (Triaxial) Stress States which Produce Crack Initiation Failure: Explanation of the New Test Fixture Mini-Pipe Specimen and Preliminary Test Results. Paper presented at the SPE High Pressure/High Temperature Sour Well Design Applied Technology Workshop, Woodlands, Texas, 17-19 May.

Cernocky, E. P., Moore, P.W. and Cernocky, L.J. 2007. Correlation of Half-Inch Diameter, Mini-Pipe Tests with API Full-Size Tests of Casing with Internal Pressure in H2s Environment, Paper No. 07111, NACE International, CORROSION 2007, March 11 - 15, Nashville, Tennessee.

Chauveau, E., Koschel, D., Bouvier, N. and Mesquita, T.J. 2012. Influence of Metallurgy and Chemical Composition on the Sulphide Stress Cracking Resistance of Two Supermartensitics Stainless Steels, paper No. C2012-0001284, presented at NACE International Conference and Exposition.

Cheremisinoff, P. N. 1995. *Handbook of Water and Wastewater Treatment Technology*. New York: Marcel Decker Inc.

Cheung, Ping- Sun. 1999. Expanding Additive for Cement Composition. US Patent No. 5942031.

Choi, Y.S., Farelas, F., Nešić S., Magalhães, A. A. O., and Andrade C. D. 2014. Corrosion Behavior of Deep Water Oil Production Tubing Material under Supercritical CO_2 Environment: Part I. Effect of Pressure and Temperature, paper No. 2380, NACE International, 17-21 March, Orlando, Florida.

Chokshi, K., W. Sun, S. Nešić, 2005. Iron carbonate film growth and the effect of inhibition in CO_2 corrosion of mild steel, NACE International corrosion conference: Houston, TX.

Ciaraldi, S.W. 1986. Some factors that affect sour service performance of Carbon Steel Oil Country tubulars, SPE Drilling Engineering, Vol. 1, Num. 3, Pages 233-241.

Clark A.H. 1966. Stability Field of Monoclinic Pyrrhotite, Transactions of the Institute of Mining and Metallurgy, Vol. 75, pp. B232-235.

Collepardi, M. 2003. A state-of-the-art review on delayed ettringite attack on concrete. Cement and Concrete Composites, 25: 401-407.

Craig, B. 2005. Metallurgical Limits to Increasing Tubular Strength While Maintaining SSC Resistance. Paper SPE-97580-MS presented at the SPE High Pressure/High Temperature Sour Well Design Applied Technology Workshop, The Woodlands, Texas, 17-19 May.

Crolet, J. L., Bonis, M. R., 1991. Prediction of the Risks of CO_2 Corrosion in Oil and Gas Well.SPE Production Engineering, Vol. 6, No. 4, p. 449.

Danjusevsky, V.S. 1983. Gefuege und Eigenshaften hydraulicer Bindemitel nach dem Erhaerten Bei Boheren Temperaturen und Laengeren Zeiten, ITEFachberiche, Vol-107, No: 10, Moskow.

Daou, F., and Plot, B., 2009, “Cement Slurry Performance and Set-Cement Properties vs. Mircosilica Densification”, SPE Drilling & Completion.

Das, G.S. & Khanna, A.S. 2004. Parametric Study of CO_2/H_2S Corrosion of Carbon Steel Used for Pipeline Application, International Symposium of Research Students on Materials Science and Engineering, December 20-22, 2004, Chennai, India.

Dayalan, E., Vani, G., Shadley, J.R., Shirazi, S.A. and Rybicki, E.F. 1995. Modeling CO_2 corrosion of carbon steel in pipe flow, Paper No. 118, presented at the NACE corrosion conference.

Dayalan, E., de Moraes, F.D., Shadley, J.R., Shirazi, S.A., Rybicki, E.F., 1998. CO_2 Corrosion Prediction in Pipe Flow Under $FeCO_3$ Scale-Forming Conditions, Paper no. 51, presented at the NACE

CORROSION conference, Houston, TX.
de Waard, C. and Milliams, D. E. 1975. Carbonic Acid Corrosion of Steel, CORROSION, vol. 31, pp. 131.
de Waard, C, Lotz, U., Milliams, D.E., Corrosion 47 (1991): p. 976.
de Waard, C, Lotz, U. and Dugstad, A. 1995. Influence of Liquid Flow Velocity on CO_2 Corrosion: A Semi-Empirical Model, Paper No. 128, presented at the NACE CORROSION conference, Houston, TX.
de Waard, C., Smith, L. and Craig, B.D. 2003. The Influence of Crude Oil on Well Tubing Corrosion Rates, Paper No. 03629, presented at the NACE CORROSION conference, Houston, TX.
DeWaard, C. and Milliams, D. E. 1975. Carbonic Acid Corrosion of Steel, Corrosion, Vol. 31, p.131.
Dezhi, Z., Chen, Z., Zhang, Z., Shao, L., Li, G., Tian,G. and She, T., 2012. Research on Stress Corrosion Sensitivity of C110 Casing in Wellbore Protection Fluid,
Dillenbeck III, R.L., Mueller, D.T. and Orr, B.R. 1990. The Effect of Micro-Silica on the Thermal Stability of Lightweight Cement Systems, paper SPE 21597 presented at International Technical Meeting, Petroleum Society of CIM and SPE, Calgary, 10-13 June.
Duan, Z., and Sun, R. 2003. An improved model calculating CO_2 solubility in pure water and aqueous NaCl solutions from 257 to 533 K and from 0 to 2000 bar. Chem. Geol. 193, 257–271.
Duan Z. and Mao, S., 2006. A thermodynamic model for calculating methane solubility, density and gas phase composition of methane-bearing aqueous fluids from 273 to 523K and from 1 to 2000bar. Geochimica et Cosmochimica Acta 70 3369–3386.
Duan, Z., Sun, R., Liu, R.and Zhu, C. 2007. Accurate Thermodynamic Model for the Calculation of H_2S solubility in pure Water and Brines. Energy & Fuels 21 (4): 2056-2065.
Dubois, N., Bouygues, Noik, Ch. and Rivereau, A. 1999. Improvement of low-permeable cement for zonal isolation at high-temperature Conditions, Paper SPE 50782, presnted at the SPE International Symposium on Oilfield Chemistry held in Houston, Texas, February 16–19.
Duguid, A., Radonjic, M., Scherer G. 2005. Degradation of Well Cements Exposed to Carbonated Brine. Fourth Annual Conference on Carbon Capture and Sequestration DOE/NETL May 2-5.
Duguid, A. 2008. The Effect of Carbonic Acid on Well Cements as Identified Through Lab and Field Studies, paper SPE 119504 presented at the 2008 SPE Eastern Regional/AAPG Eastern Section Joint Meeting, Pittsburgh, Pennsylvania, USA, 11–15 October.
Duguid, A. 2009. An estimate of the time to degrade the cement sheath in a well exposed to carbonated brine. Energy Procedia 1, 3181–3188.
Dunlop, A.K., Hassell, H.L. and Rhodes, P.R., 1983. Fundamental Considerations in Sweet Gas Well Corrosion, paper No. 46, NACE International Annual Conference.
Edwards, J.D. and Espelid, B. 1997. Operational Limits for Casing and Drill Pipe Steels in H2s Containing Environments, Paper No.42, CORROSION 97.
Eilers, L.H. and Root, R.L. 1976. Long-Term Effects of High Temperature on Strength Retrogression of Cements. Paper SPE 5871 presented at SPE California Regional Meeting, Long Beach, California, 7-9 April.
Eilers, L.H., Nelson, E.B. and Moran, L.K. 1983. High Temperature Cement Compositions – Pectolite, Scawtite, Truscotite or Xonoloite: Which Do You Want? Journal of Petroleum Technology 35 (7): 1373-1377.
Epelboin, I., M. Keddam, and H. Takenouti, 1972. Use of impedance measurements for the determination of the instant rate of metal corrosion Journal of Applied Electrochemistry, 2: p.

71-79.

Fakhreldin, Y., Al-Sharji, H., Ruwehy, A.M., et al. 2010. Advanced Cement system for Acid Gas Injection Wells. Paper SPE 132345 presented at SPE Asia Pacific Oil & Gas Conference and Exhibition, Queensland, Australia, 18-20 October.

Fang, H. 2006. Low Temperature and High Salt Concentration Effects on General CO_2 Corrosion for Carbon Steel, thesis, November, Ohio University.

Fang, H., Brown B., and Nešić, S. 2010. High Salt Concentration Effects on CO_2 Corrosion and H_2S Corrosion, paper No. 276, 14-18 March, San Antonio, Texas.

Fardisi, S., Tajallipour, N. and Teevens, P. 2012. Predicting General Corrosion Rates in Sour Environments with the Growth of a Protective Iron Sulphide Film, paper No.1471, March 11 - 15, Salt Lake City, Utah.

Farelas, F., Choi Y.-S. Nešić, S., Magalhães A. A.O., and de Azevedo Andrade C. 2013. Corrosion Behavior of Deep Water Oil Production Tubing Material under Supercritical CO_2 Environment: Part II. Effect of Crude Oil and Flow, NACE paper No. 2381, 17-21 March, Orlando, Florida.

Fosbøl, P.L., Thomsen, K., Stenby, E. H., 2009. Improving mechanistic CO_2 corrosion Models.

Fuquan, S., Guangming, L. and Jianzhou, J. 2006. Application and Research of Latex Tenacity Cement Slurry System, paper SPE 104434, presented at the SPE International Oil & Gas Conference and Exhibition, Beijing, China.

Garber, J.D., Polaki, V., Adams, C. and Varanasi, N.R. 1998. Modeling Corrosion Rates in Non-Annular Gas Condensate Wells Containing CO_2, Paper No. 53, presented at the NACE CORROSION conference, Houston, TX.

Garev, K., Stemmermann, P., Black, L. and Yarwood, J. 2007. Structural Features of CSH(I) and its Carbonation in air - A Raman Spectroscopic Study - Part I: Fresh Phases, J. of American Ceramic Society, Soc. 90: 900 - 908.

Gartland, P.O. and Salomonsen, J. E. 1999. A Pipeline Integrity Management Strategy Based on Multiphase Fluid Flow and Corrosion Modelling, Paper No. 622, prestned at CORROSION conference, Houston, TX.

Gartland, P.O., Johnsen, R. and Øvstetun, I., 2003. Application of Internal Corrosion Modeling in the Risk Assessment of Pipelines, Paper No. 03179, presented at the NACE CORROSION conference, Houston, TX.

Ghofrani, R. and Plack, H. 1993. CaO- and/ or MgO- Swelling Cements: A Key for Providing a Better Annular Sealing? Paper SPE 25697 presented at SPE/IADC Drilling Conference, Amsterdam, February, 22 to 25.

Glasser, F. P., Marchand, J. and Samson, E. 2008. Durability of Concrete - Degradation phenomena involving detrimental chemical reactions. Cement and Concrete Research, 38: 226-246.

Glasstone, S., Laidler, K.J. and Eyring, H. 1941. The Theory of Rate Processes McGraw-Hill, New York.

Grabowski, E. and Gillott, J. E. 1989. Effect of Replacement of Silica Flour with Silica Fume on Engineering Properties of Oil Well Cements at Normal and Elevated Temperatures and Pressures, Cement and Concrete Research, Vol. 19, pp 333-344.

Gray, L.G.S., B.G. Anderson, M.J. Danysh, P.G. Tremaine, 1989. Mechanism of carbon steel corrosion in brines containing dissolved carbon dioxide at pH 4, NACE International corrosion conference: Houston, TX.

Gunaltun, Y. M., 1996. Combining research and field data for corrosion rate prediction. Paper No. 27, presented at the NACE CORROSION conference, Houston, TX.

Halvorsen, A.M.K., Søntvedt, T., 1999. CO_2 Corrosion Model for Carbon Steel Including a Wall Shear Stress Model for Multiphase Flow and Limits for Production Rate to Avoid Mesa Attack, Paper No. 42, presented at the NACE CORROSION conference, Houston, TX.

Hamilton, I.E. and Sammes, N.M. 1999. Encapsulation of steel foundary bag house dusts in cement mortar, Cement Concrete Research 29, 55-61.

Harker, R.l. 1965. Scawtite and its Synthesis, *Mineral Magazine,* 34, 232.

Hashimoto, H., Komaki, E., Hayashi, F. and Uematsu, T. 1980, "Partial Decomposition of Dolomite in CO_2", Journal of Solid State Chemistry 33, 181-188.

Hashizume, S., Inohara, Y. and Masamura, K. 2000. Effects of pH and PH_2S on SSC Resistance of Martensitic Stainless Steels, paper No.130, NACE International Annual Conference, March 26 - 31, Orlando, Fl.

Hassani, S., Roberts K.P., Shirazi S.A., Shadley J.R., Rybicki E.F., Joia C., 2011. Flow Loop Study of Chloride Concentration Effect on Erosion, Corrosion and Erosion-Corrosion of carbon Steel in CO_2 Saturated Systems, NACE International corrosion conference, Houston, TX.

Hedges, B. Chapman, R., Harrop, D., Mohammed, I., Sun, Y., 2005. A Prophetic CO_2 Corrosion Tool - But When is it to be Believed?, Paper No. 05552, presented at the NACE CORROSION conference, Houston, TX, April 3 - 7.

Heidary, H., Oskouei, A. and Ahmadi, M. 2008. Mechanism detection of Stress Corrosion Cracking by acoustic emission and effect of manufacturing process on AE signals, Acoustics conference, June 29- July 4, Paris, France.

Heidersbach, R., 2011. Metallurgy and Corrosion Control in Oil and Gas Production. Hoboken, NJ: Wiley.

Horstemeier, M., Bosch, C., Orlans, B. and Delattre, L. 2010. Validation of the Constant Extension Rate Test (CERT) for high strength OCTG steels as a ranking tool for SSC resistance, NACE paper no. 10309, presented at NACE corrosion conference and expo, Houston.

Hou, W., Fuquan, S., Gao, Y., Zeng, J., Huo, M. and Wang, J. 2010. Research of High Temperature Tolerance Latex Slurry System. In Twentieth International Offshore and Polar Engineering Conference, Beijing, China, June 20 to 25.

Huang, J., Guraieb, P., Yan, C., Contreras, E., Tomson, M. B., and Tomson, R. 2014. Corrosion Testing of Deepwater Tubing Materials under Extreme Pressure and Temperature Conditions, SPE paper OTC-25193-MS, 05-08 May, Houston, Texas.

Hudak, P.F. and D.J. Wachal, 2001. Effects of brine injection wells, dry holes, and plugged oil/gas wells on chloride, bromide, and barium concentrations in the Gulf Coast Aquifer, southeast Texas, USA. Environment International, 26(7-8): p. 497-503.

Jacquemet, N., Pironon, J. and Caroli, E. 2005. A New Experiment Procedure for Simulation of H_2S +CO_2 Geological Survey. Oil & Gas Science Technology- Rev. IFP, 60 (1): 193-206.

Jacquemet, N., Pironon, J., Lagneau, V., et al. 2011. Armouring of well cement in H_2S–CO_2 saturated brine by calcite coating. Applied Geochemistry, 27: 782-795.

Jennings, S. S., Al-Ansari, A. A. and Al-Yami, A. S. 2003. Gas Migration after Cementing Greatly Reduced, Paper SPE 81414 presented at the SPE 13th Middle East Oil Show and Conference, Baharain, April 5 to 8.

Jennings S.S., 2005. Long-Term High-Temperature Laboratory Cement Data Aid in the Selection of Optimized Cements, paper SPE 95816 presented at the 2005 SPE Annual Technical Conference and Exhibition held in Dallas, Texas, U.S.A., 9 – 12 October 2005.

John, R.C., Jordan, K. G., Young, A. L., Kapusta, S. D. and Thompson, W. T. 1998. SweetCor: An Information System for the Analysis of Corrosion of Steels by Water and Carbon Dioxide, Paper No. 20, presented at the NACE CORROSION conference, Houston, TX.

John Lee, K.L. 2004. A Mechanistic Modeling of CO_2 Corrosion of Mild Steel in the Presence of H_2S, PhD dissertation, Ohio University.

Johnson M. L. and Tomson, M. B. 1991. Ferrous Carbonate Precipitation Kinetics and its Impact CO_2 Corrosion, paper No. 268, NACE international, Houston, Texas.

Johnson, R, M., and Garvin, T, R. 1972. Cementing Practices, SPE AIME-MMIJ Meeting, May 25-27, Tokyo, Japan.

Jones, R.R. and Carpenter, A.B. 1991, "New Latex, Expanding Thixotropic Cement Systems Improve Job Performance and Reduce Costs", SPE 21010.

Kermani, M.B. and MacCuish, R.G., 1990. Materials Assessment for Sour Service Applications, SPE paper no. 20457, 65th Annual Technical Conference and Exhibition, New Orleans.

Kim, W. K., Park, G., Koh, S. U., Jung, H. G.and Kim, K. Y. 2010. Determination of Critical Factors Affecting on Hydrogen Induced Cracking and Type I Sulfide Stress Cracking of High Strength Linepipe Steel. Paper presented at the The Twentieth International Offshore and Polar Engineering Conference, Beijing, 20-25 June.

Kimura, M., Kataoka, Y.and Nakano, Y. 1996. Sulfide Stress Corrosion Cracking Resistance of Low Cr Steel. Paper NACE-96060 presented at the Corrosion, Denver, Colorado, 24-29 March.

Koh, S.U., Kim, J.S., Yang, K.Y. and Kim, K.Y, 2003. Effect of Line Pipe Steel Microstructure on susceptibility to Sulfide Stress Cracking, Corrosion, Vol. 3, 244-253.

Krilov, Z., Loncaric, B., INA-Naftaplin and Miksa, Z. 2000. Investigation of a Long-Term Cement Deterioration under a High-Temperature, Sour Gas Downhole Environment, paper SPE 58771 prepared for presentation at the 2000 SPE International Symposium on Formation Damage Control, Lafayette, Louisiana 23–24 February.

Kutchko, B.G., Strazisar, B.R., Dzombak, D.A., Lowry, G.V. and Thaulow, N. 2007. Degradation of Well Cement by CO_2 under Geologic Sequestration Conditions. Environ. Sci. Technol. 41: 4787-4792.

Kutchko, B.G., Strazisar, B.R., Hawthorne, S.B., Lopano, C.L., Miller, D.J., Hakala, A. and Guthrie, G.D. 2011. H_2S–CO_2 reaction with hydrated Class H well cement: Acid-gas injection and CO_2 Co-sequestration, International Journal of Greenhouse Gas Control, Vol. 5, Issue 4, Pages 880–888.

Kvarekval. J. and Videm, K., 1995. Corrosion of Carbon Steel in Carbon Dioxide-Saturated Solutions Containing Small Amounts of Hydrogen Sulfide. NACE international, April.

Kvarekval, J., Nyborg, R. and Seiersten, M. 2002. Corrosion Product Films on Carbon Steel In Semi-Sour CO_2/H_2S Environments, Paper No. 02296, Corrosion 2002, NACE International, 24 - 29, Denver, Colorado.

Kvarekval, J. and Nyborg, R. and Choi, H. 2003. Formation of Multilayer Iron Sulfide Films during High Temperature CO_2/H_2S Corrosion of Carbon Steel, paper No. 339, March, San Diego Ca.

Lea, F.M. 1971. The Chemistry of Cement and Concrete, third edition, Chemical Publishing Co., New York City, 177-202.

Lécolier E., Rivereau A., Ferrer N., Audibert A. and Longaygue X., 2006. Durability of Oilwell Cement Formulations Aged in H_2S-Containing Fluids, paper SPE 99105 presented at the IADC/SPE Drilling Conference, Miami, Florida, February 21–23.

Lécolier E., Rivereau A., Ferrer N., Audibert A., Longaygue X., (2008) Study of New Solutions for Acid-Resistant Cements. SPE 116066, Annual Technical Conference and Exhibition, Denver, Colorado, USA, 21-24 September 2008.

Lécolier, E., Rivereau, A., Ferrer, N., Audibert, A., & Longaygue, X. 2010. Durability of Oilwell Cement Formulations Aged in H2S-Containing Fluids. SPE drilling and completion, Volume 25, Issue01. doi:10.2118/99105-PA.

Lerch, W. Ford, C.L., 1948. Long-term study of cement performance in concrete: chapter 3. Chemical and physical tests of the cements, ACI Journal 19 (8) 745–795.

Lin, F., Meyer, C., 2009. Hydration kinetics modeling of Portland cement considering the effects of curing temperature and applied pressure, Cement and Concrete Research 39, 255–265.

Lundstrom, M., Aromaa, J. and Forsen, O. 2008. Redox Potential Characteristics of Cupric Chloride Solutions. Hydrometallurgy, Vol. 95, pp. 285-289.

Mack, R., Filippov, A. and Kendziora, L. 2000. In-Situ Expansion of Casing and Tubing-Effect on Mechanical Properties and Resistance to Sulfide Stress Cracking, paper No. 164, NACE International Annual Conference, March 26 - 31, Orlando, Fl.

Maekawa, K., Ishida, T. and Kishi, T. 2009. *Multi-scale Modeling of Structural Concrete*. London and New York: Taylor and Francis Group.

Mainguy, M. and Coussy, O. 2000. Propagation fronts during Calcium Leaching and Chloride Penetration. Journal of Engineering Mechanics, 126 (3): 250-257.

Maldonado, J.G. and Bruno, T.V. 2005. Evaluation of the Accuracy of the ISO DIS 10400 Failure Assessment Diagram Through Full Scale Testing of Pipe Containing Surface Imperfections, API PRAC Project 2002-100300, Final Report to the American Petroleum Institute Production Research Advisory Committee.

Martin, R. I. and Brown, P. W. 1995. Mechanical properties of Hydroxyapatite formed at physiological temperature. Journal of Material Science: Materials in Medicine, 6: 138-143.

Masouri, D.and Zafari, M. 2004. Sulfide Stress Cracking Of Stainless Steel 410 In Sour Crude Oil. Paper NACE-04121 presented at the Corrosion, New Orleans, Louisiana, 28 March- 1 April.

Masouri, D.and Zafari, M. 2005. Sulfide Stress Cracking of Tubular Product-Case Histories. Paper NACE-05460 presented at the Corrosion, Houston, Texas, 3-7 April.

Matteo, E. N., Scherer, G. W., Huet, B., and Pel, L. 2011. Understanding Boundary Condition Effects on the Corrosion Kinetics of Class H Well Cement. *Energy Procedia 4. 5370–5376.*

Matteo, E. N. and Scherer, G. W. 2012. Experimental study of the diffusion controlled acid degradation of Class H Portland cement. International Journal of Greenhouse Gas Control 7: 181-191.

Mehta, P. K. 1983. Mechanism of Sulphate Attack on Cement and Concrete - Another look. Cement and Concrete Research 13: 401-406.

Mehta, P.K. and Monteiro, P.J.M. 2006. *Concrete: Microstructure, Properties and Materials*. Third Edition, Tata McGraw Hill.

Meller, N., Hall, C., Kyritsis, K., Giriat, G., Jakobsen, H. J. and Skibsted, J. 2007. Incorporation of Aluminium Guest-ions in Nominally Alumina-free Calcium Silicate Hydrates: Effects on Crystal

Structure and Thermal Stability, In 12th International Congress on the Chemistry of Cement.

Millero, F., Huang, F., Graham, T., Pierrot, D., 2007, The dissociation of carbonic acid in NaCl solutions as a function of concentration and temperature, *Geochimica et Cosmochimica Acta* 71 pp. 46-55.

Morales, M., Morris, W., Criado, M. A., Robles, J., Bianchi, G. 2003. Improving the Sulfate Resistance Performance of API Cement Class A upon Appropriate Slurry Design, paper SPE 81000, presented at the SPE Latin American and Caribbean Petroleum Engineering Conference held in Port-of-Spain, Trinidad, West Indies, April 27-30.

Morana R. and Nice P.I. 2009. Corrosion assessment of High Strength Carbon Steel Grades P-110, Q-125,140 and 150 for H_2S containing producing well environments, paper No. 9093, presented at the NACE International Conference and Expo, 22-26 March, Atlanta, Georgia.

Mueller, D.T. and Dillenbeck III, R.L. 1991. The Versatility of Silica Fume as an Oilwell Cement Admixture. Paper SPE 21688 presented at SPE Production Operations Symposium, Oklahoma City, Oklahoma, April, 7 to 9. http://dx.doi.org/10.2118/21688-MS.

Muraki, T., Tsuru, E.and Asahi, H. 2006. Sulfide Stress Cracking Resistance of Post-Expanded Low Alloy Steel Tubulars. Paper NACE-06153 presented at the Corrosion, San Diego, California, 12-16 March.

Myneni, S. C. B., Traina, S. J., Waychunas, G. A., et al. 1998. Vibrational spectroscopy of functional group chemistry and arsenate coordination in ettringite. Geochimica et Cosmochimica. Acta 62 (21/22): 3499-3514.

NACE Standard TM0177, 2005. Laboratory Testing of Metals for Resistance to Sulfide Stress Cracking and Stress Corrosion Cracking in H_2S Environments.

Naik, N. 2003. Sulfate Attack on Portland Cement-Based Materials: Mechanisms of Damage and Long-Term Performance. PhD dissertation, Georgia Institute of Technology, Georgia (August 2003).

Nakarai, K., Ishida, T., Maekawa, K. 2006. Modeling of Calcium Leaching from Cement Hydrates Coupled with Micro-Pore Formation. Journal of Advanced Concrete Technology, 4 (3): 395-407.

Nelson, E. B., Eilers, L. H. and Kalousek, G. L. 1981. Formation and Behavior of Calcium Silicate Hydrates in a Geothermal Environment, Cem. Concr. Res. 11, 371 – 381.

Nešić, S., Postlethwaite J. and Olsen, S. 1995. An Electrochemical Model for Prediction of CO_2 Corrosion, Paper No. 131 presented at the NACE CORROSION/95 conference, Houston, TX.

Nešić, S., Postlethwaite, J. and Olsen, S. 1996. An Electrochemical Model for Prediction of Corrosion of Mild Steel in Aqueous Carbon Dioxide Solutions, CORROSION, Vol. 52, pp. 280-294, April.

Nešić, S. and Lee, K.L.J. 2003. A Mechanistic Model for Carbon Dioxide Corrosion of Mild Steel in the Presence of Protective Iron Carbonate Films – Part 3: Film Growth Model, CORROSION, Vol. 59, No. 7, pp. 616-628, June.

Nešić, S. 2007. Key issues related to modelling of internal corrosion of oil and gas pipelines, Corrosion Science, Vol. 49, Issue 12, December 2007, Pages 4308–4338.

Neville, A. M. 2004. *Properties of Concrete, 4th* edition. New York: John Wiley and Sons.

Noik, Ch., and Rivereau, A. 1999. Oil well Cement Durability, paper SPE 56538, presented at the SPE Annual Technical Conference and Exhibition held in Houston, Texas, October 3–6.

Nokken, M.R. 2010. Expansion of MgO in Cement Pastes Measured by Different Methods. ACI Materials Journal, 107 (1): 80-84.

Nor , A. M., Suhor, M.F., Mohamed, M.F., Singer, M. and Nešić, S. 2011. Corrosion of Carbon Steel in

High CO_2 Environment: Flow Effect, NACE paper No. 11242, 13-17 March, Houston, Texas.

Nor, A. M., Suhor, M.F., Mohamed, M.F., Singer, M. and Nešić, S. 2012. Corrosion Of Carbon Steel In High CO_2 Containing Environments - The Effect Of High Flow Rate, NACE paper No. 1683, 11-15 March, Salt Lake City, Utah.

Nordsveen, M., Nešić, S., Nyborg, R., Stangeland, A., 2003. A Mechanistic Model for CO_2 Corrosion with Protective Iron Carbonate Films - Part 1: Theory and Verification. Corrosion, Vol. 59, No. 5, pp. 443-456.

NORSOK Standard no. M-506. 1998. CO_2 Corrosion Rate Calculation Model. Norwegian Technology Standards Institution, http://www.nts.no/norsok.

Nyborg, R. 2010. CO_2 Corrosion Models for Oil and Gas Production Systems, Paper No 10371, presented at the NACE corrosion conference, March 14 - 18, San Antonio, TX.

Oddo, J.E. and Tomson, M.B. 1982. Simplified Calculation of CaCO3 Saturation at High Temperatures and Pressures in Brine Solutions, SPE of AIME, Society of Petroleum Engineers, p. 1,583, Richardson, Texas.

Olmo, F., Chacon, E. and Irabien, A. 2001. Influence of lead, zinc, iron (III) and chromium (III) oxides on the setting time and strength development of Portland cement, Cement and Concrete Research, Volume 31, Number 8, August, pp. 1213-1219.

Palmer D. A., van Eldik R. 1983. The chemistry of metal carbonate and carbon dioxide complexes, Chem. Rev. 83, p. 651.

Pavlock, C., Tennison, B., Thompson, J. and Darbe, R. 2012. Latex Base Cement Design – Meeting the Challenges of the Haynesville Shale. Paper SPE 152730 presented at SPE America's Unconventional Resources Conference, Pittsburgh, Pennsylvania, June, 5 to 7.

Perkins, R.S., Fang, C.S., Garber, J. D., Singh, R. K., 1996. Predicting Tubing Life in Annular-Flow Gas Condensate Wells Containing Carbon Dioxide, Corrosion, Vol. 52, No. 10, p. 801.

Ping, X. and Beaudoin, J. J. 1992. Mechanism of sulfate expansion. Cement and Concrete Research, 22: 631-640.

Planel, D., Sercombe, J., Le Bescop, P., et al. 2006. Long-term performance of cement paste during combined calcium leaching - sulfate attack: Kinetics and size effect. Cement and Concrete Research 36: 137-143.

Pots, B.F.M., 1995. Mechanistic Models for the Prediction of CO_2 Corrosion Rates under Multi-Phase Flow Conditions, Paper No. 137, NACE CORROSION conference, Houston, TX.

Pots, B.F.M., John, R.C., Rippon, I.J., Thomas, J.S., Kapusta, S. D., Girgis, M. M. and Whitham, T. 2002. Improvements on de Waard - Milliams Corrosion Prediction and Applications to Corrosion Management, Paper No. 02235, presented at the NACE CORROSION conference, Houston, TX.

Pots, B.F.M. and Kapusta, S. D., 2005. Prediction of Corrosion Rates of the Main Corrosion Mechanisms in Upstream applications, Paper No. 05550, presented at the NACE CORROSION conference, Houston, TX.

Powers T. C. 1958. *The Physical Structure and Engineering Properties of Concrete.* PCA Research & Development Laboratories, Bulletin 90, Chicago.

Prausnitz, J.M., Lichtenthaler, R.N. & de Azevedo, E.G. 1986. Molecular thermodynamics of fluid-phase equilibria. 2nd ed. Englewood Cliffs (N.J.): Prentice-Hall.

Ramirez, M. and Ruiz, A., 1998. The Effect of Small Amounts of H_2S on CO_2 Corrosion of a Carbon Steel.

NACE international.

Ray, I. and Gupta, A.P. 1994. Effect of Latex and Super-plasticiser on Portland Cement Mortar in the Fresh State. Cement and Concrete Composites 16: 309-316.

Reddy, B. R., Lewis, S. J., Santra, A., Palmer, A. V., 2010. (Halliburton Energy Services Inc.); "Wellbore Sealant Compositions Containing Cationic Latexes", US Patent 7687440.

Renpu, W. 2011. Advanced Well Completion Engineering, Gulf Professional Publishing; 3rd Edition, Gulf Professional Publishing.

Richardson, I. G. 2008. The Calcium Silicate Hydrates, Cem. Concr. Res. 38, 137 – 158.

Rickard, D. and Luther, G. W. 1997. Kinetics of Pyrite formation by the H_2S oxidation of iron (ll) monosulfide in aqueous solutions between 25 and 125 C: the mechanism. Geochimica et Cosmochimica Acta, 61: 135-147.

Rimmelé, G., Barlet-Gouedard, V., Porcherie, O., Goffe, B. and Brunet, F. 2008, Heterogeneous Porosity Distribution in Portland Cement Exposed to CO_2-Rich Fluids, Cement and Concrete Research, 38, 1038-1048.

Roberge, P.R., 1999. Handbook of Corrosion Engineering. New York: McGrow-Hill.

Roger, J. 1996. Cements treated with high-pressure CO_2. US Patent 5,518,540, 21 May.

Ropital, F., 2010. Corrosion and degradation of metallic materials: Understanding of the phenomena and applications in petroleum and process industries.

Rossignolo, J.A. and Agnesini, M.V.C. 2002. Mechanical properties of polymer-modified lightweight aggregate concrete. Cement and Concrete Research 32: 329-334.

Rossignolo, J.A., Agnesini, M.V.C. and Morais, J.A. 2003. Properties of high-performance LWAC for precast structures with Brazilian lightweight aggregates. Cement and Concrete Research 25: 77-82.

Rossignolo, J.A. and Agnesini, M.V.C. 2004. Durability of polymer-modified lightweight aggregate concrete. Cement and Concrete Research 26: 375-380.

Rossignolo, J.A. 2009. Interfacial interactions in concretes with silica fume and SBR Latex. Construction and Building Material 23: 817-821.

Rubiandini, R., Siregar, S., Suhascaryo, N. and Efrial, D. 2005. The Effect of CaO and MgO as Expanding Additives to Improve Cement Isolation Strength under HPHT Exposure. PROC. ITB Eng. Science 37B (1): 29-48.

Sanders, L. D. and Smothers, W. J. 1957. Effect of Tobermorite on the Mechanical Strength of Autoclaves Portland Cement-Silica Mixtures, J. Am. Conc. Inst. 28, 127-134.

Sangita, K. A. and Srinivasan, S., 2000. An Analytical Model to Experimentally Emulate Flow Effects in Multiphase CO_2/H_2S Systems. Paper No. 58, presented at the NACE CORROSION conference, Houston, TX.

Santra, A., Reddy, B.R., Liang, F. and Fitzgerald, R. 2009. Reaction of CO_2 with Portland cement at Down-hole Conditions and the role of Pozzolanic Supplements. Paper SPE 121103 presented at SPE International Symposium on Oilfield Chemistry, Woodlands, Texas, USA, April, 20 to 22.

Santra, A. and Sweatman, R. 2011. Understanding the Long-Term Chemical and Mechanical Integrity of Cement in a CCS Environment. Energy Procedia 4: 5243-5250.

Sasaki, S., Kobayashi, W. and Okabayashi, S. 1985. Effects of various Factors on Thickening time and Strength of Silica Cement under High Temperature. SPE Publication 015335.

Sasaoka, E., 1994, "Characterization of Reaction between Zinc Oxide and Hydrogen Sulfide", Energy & Fuels, 8, 1100-1105.

Sauki, A., Irawan, S. 2010. Effects of pressure and temperature on well cement degradation by supercritical CO_2, *International Journal of Engineering & Technology*, Vol. 10 pp.53-61.

Schmitt, G. and B. Rothmann, 1977. Corrosion Mechanism of Unalloyed Steel in Oxygen-Free Carbon Dioxide Solutions - 1. Untersuchungen Zum Korrosionsmechanismus Von Unlegiertem Stahl In Sauerstoffreinen Kohlensaeureloesungen - 1. Kinetik Der Wasserstoffabscheidung., 28(12): p. 816-822.

Schmitt, G. and Horstemeier, M. 2006. Fundamental Aspects of CO_2 Metal Loss Corrosion - Part II: Influence of Different Parameters on CO_2 Corrosion Mechanisms, paper No.06112, NACE International, 12-16 March, San Diego, California.

Seiersten, M. 2001. Materials Selection for Separation, Transportation and Disposal of CO_2, paper No. 042, 11-16 March, Houston, Texas.

Shadizadeh, S. R., Kholghi, M., and Salehi Kassaei, M. H. 2010, "Experimental Investigation of Silica Fume as a Cement Extender for Liner Cementing in Iranian Oil/Gas Wells", Iranian Journal of Chemical Engineering, Vol. 7, No. 1 (Winter), IAChE.

Shahriar, A. 2011. Investigation on Rheology of Oil Well Cement Slurries, PhD Dissertation, The University of Western Ontario, School of Graduate and Postdoctoral Studies, London, Ontario.

Shoesmith, D.W., Taylor, P., Bailey, M.G., Owen, D.G., 1980. The formation of ferrous monosulfide polymorphs during the corrosion of iron by aqueous hydrogen sulfide at 21 C, J. Electrochem. Soc. 127, 1007–1015.

Siddique, R. and Khan, M. I. 2011. Supplementary Cementing Materials. Springer- Verlag, Berlin-Heidelberg.

Silva, C.A.R., X. Liu, and F.J. Millero, 2002. Solubility of Siderite in NaCl Solutions. Journal of Solution Chemistry, 31(2): p. 97-108.

Skogsberg, L. 2004. Fitness for Purpose Sulfide Stress Corrosion Testing for Alloys in Existing Wells in Deep Water Gulf of Mexico. Paper NACE-04148 presented at the CORROSION 2004, New Orleans, Louisiana, 28 March-1 April.

Smith, D. K. 1991. Worldwide Cementing Practices, First Ed., American Petroleum Institute, January, p. 11.

Smith, S. N. 1993. A Proposed Mechanism for Corrosion in Slightly Sour Oil and Gas Production, paper NACE No. 385,Twelfth International Corrosion Congress, Houston, Texas, Sep. 19 – 24.

Smith, S., and Wright, E.J., 1994. Prediction of minimum H_2S levels required for slightly sour corrosion systems, NACE International corrosion conference, Paper 11, Baltimore, MD.

Smith, S., and Pacheco, 2002. Prediction of Corrosion in Slightly Sour systems, NACE International Corrosion conference, Paper No. 02241.

Smith, L. and de Waard, C. 2005. Corrosion Prediction and Materials Selection for Oil and Gas Producing Environments, Paper No. 05648, presented at the NACE CORROSION conference, Houston, TX.

Smith, S. N. and Joosten, M. 2006. Corrosion of carbon steel by H_2S in CO_2 containing oilfield environments, Corrosion/2006, Paper no. 06115, NACE International, Houston, Texas, 2006.

Smith, S., Brown, B., Sun, W., 2011. Corrosion at higher H_2S concentrations and moderate temperatures, NACE International Corrosion conference, Paper No. 11081.

Snape, E. 1967. Sulfide Stress Corrosion of Some Medium and Low Alloy Steels. Corrosion 23 (6): 154-172.

Song, F.M. 2010. A Comprehensive Model for Predicting CO_2 Corrosion Rate in Oil and Gas Production and Transportation Systems, ElectroChimica Acta 55, p. 689.

Spaldings, D. 1961. A single formula for the law of the wall, ASME C: J. Appl. Mech. Vol. 28, Issue 3, 455-458.

Spycher, N., K. Pruess and J. Ennis-King. 2003. CO_2-H_2O Mixtures in the Geological Sequestration of $_{CO2}$. I. Assessment and Calculation of Mutual Solubilities from 12 to 100°C and up to 600 bar, Geochim. Cosmochim. Acta, Vol. 67, No. 16, pp. 3015 - 3031, doi:10.1016/S0016-7037(03)00273-4.

Srinivasan, S. and Kane, R. D., 1996. Prediction of Corrosivity of CO_2 / H_2S Production environments. Paper No. 11, presented at the NACE CORROSION conference, Houston, TX.

Srinivasan S. and Kane, R. D. 2003. Critical Issues in the Application and Evaluation of a Corrosion Prediction Model for Oil and Gas Systems. Paper No. 03640, presented at the NACE CORROSION conference, Houston, TX.

Strazisar, B., Kutchko, B., and Huerta, N., 2009. Chemical Reactions of Wellbore Cement Under CO_2 Storage Conditions: Effects of Cement Additives. Energy Procedia 1, 3603-3607.

Sugama, T. and Carciello, N.R. 1992. Carbonation of Hydrothermally Treated Phosphate-Bonded Calcium Aluminate Cements. Cement and Concrete Research 22: 783-792.

Sugama, T. and Carciello, N.R. 1993. Carbonation of Calcium Phosphate Cements after Long Term Exposure to Na_2CO_3-Laden Water at 250°C. Cement and Concrete Research 23: 1409-1417.

Sugama, T. 2006. Advanced Cements for Geothermal Wells. BNL-77901-2007-IR.

Suleimenov, O. M. and R. E. Krupp. 1994. Solubility of hydrogen sulfide in pure water and in NaCl solutions, from 20 to 320°C and at saturation pressures. Geochim. Cosmochim. Acta, 58, 2433–2444.

Suleimenov, O. M. and Seward, T. M. 1997. A spectrophotometric study of hydrogen sulfide ionization in aqueous solutions to 350 °C. Geochim. Cosmochim. Acta, 61, 5187-5198.

Sun, W., Nesic, S., Papavinasam, S. 2006. Kinetics of Iron Sulfide and Mixed Iron Sulfide/Carbonate Scale Precipitation in CO_2/H_2S Corrosion, paper NACE No. 06644, Houston, Texas.

Sun, W., Nešić, S. 2007. A Mechanistic Model of H_2S Corrosion of Mild Steel, Paper No. 7655, presented at the NACE corrosion conference, March 11 - 15, Nashville, TN.

Sun, W., Nešić, S. 2008. A Mechanistic Model of Uniform Hydrogen Sulfide/ Carbon Dioxide Corrosion of Mild Steel, Corrosion Journal, Vol. 65. No, 5.

Sun, W. and Nešić, S. 2009. A Mechanistic Model of Uniform Hydrogen Sulfide/Carbon Dioxide Corrosion of Mild Steel. NACE international.

Sun, W., S. Nešić, and R.C. Woollam, 2009. The effect of temperature and ionic strength on iron carbonate ($FeCO_3$) solubility limit. Corrosion Science, 51(6): p. 1273-1276.

Svenningsen, G., Palencsar, A. and Kvarekval, J. 2009. Investigation of Iron Sulfide Surface Layer Growth in Aqueous H_2S/CO_2 Environments, paper No. 359, March 22 - 26, Atlanta, GA Vestergaard, B. and Robinson, T. 2003. CO_2 in Refrigeration Applications, Air Conditioning, Heating and Refrigeration News, October 2, available at: http://www.achrnews.com, Last accessed 06/11/2013.

Szklarz K.E. 1988. SSC resistance of drilling material in a simulated underbalanced drilling, paper no.

104, NACE International Annual Conference.

Takeno S., Zoka, H. and Niihara T. 1970. Metastable Cubic Iron Sulfide with Special Reference to Mackinawite, American Mineralogist, Vol. 55, pp. 1639-1649.

Tale, S. 2014. Sulfide Stress Cracking Behavior of Grade C-110 Steel Tubulars under High-Pressure Conditions, MS Thesis, University of Oklahoma, Norman, Oklahoma.

Taylor, H. F. W. 1964. The Chemistry of Cements. London: Academic Press, Ltd., 106-122.

Taylor, H. F. W. 1997. *Cement Chemistry*, 2nd Edition. London: Thomas Telford Publishing.

Taylor P. 1980. The stereochemistry of iron sulfides - a structural rationale for the crystallization of some metastable phases from aqueous solution, American Mineralogist, 65, pp 1026-1030.

Teraoka, K., Ito, A., Maekawa, K., Onuma, K., Tateishi, T. and Tsutsumi, S. 1998. Mechanical Properties of Hydroxyapatite and OH-Carbonated Hydroxyapatite Single Crystals. Journal of Dental Research 77 (7): 1560-1568.

Tixier, R. 2000. Microstructural Development and Sulfate Attack Modeling in Blended Cement-Based Materials. MS Thesis, Arizona State University, Arizona (December 2000).

Tsay, L.W., Chi, M.Y., Chen H.R. and Chen, C. 2005. Investigation of Hydrogen sulfide stress corrosion cracking of PH 13-8 Mo stainless steel, Materials and Science Engineering A, Vol. 416, 155-160.

Tucroni, G.L., Cumino, G., Echaniz, G. , Anneli, E., Scoppio, L. and Perez,T., 2001. Improvement of Resistance to SSC Initiation and Propagation of High Strength OCTG through Microstructure and Precipitation Control, paper no. 1077, NACE International Annual Conference.

Uhlig, H.H.a.R.W.R., 1985. Corrosion and corrosion control: An introduction to corrosion science and engineering. 4th ed. Hoboken, NJ: John Wiley & Sons.

Valdes, A., Case, R., Ramirez, M., and Ruiz, A. 1998. The Effect of Small Amounts of H_2S on CO_2 Corrosion of a Carbon Steel, paper No.22, March 22 - 27, San Diego CA.

Vera, J.R and Castro, J. 1997. The Relationship between Hydrogen permeation and Sulfide Stress cracking Susceptibility of OCTG materials at different temperatures and pH Values, Paper No. 47, NACE International Conference, Houston, TX.

Videm, K. 1993. Fundamental Studies Aimed at Improving Models for Prediction of CO_2 Corrosion, in Progress in the Understanding and Prevention of Corrosion, Proc. 10th Europ. Corros. Cong., vol. 1, pp. 513, London, England.

Voigt, T., Shah, S. P. 2003. Nondestructive Monitoring of Setting and Hardening of Portland Cement Mortar with Sonic Methods.

Waid, G.M and Stiglitz, R.J. 1979. The Development of High Strength Casing Steels with Improved H_2S cracking resistance for Sour Service, paper OTC 3509, presented at the 11th Annual OTC, April 30 – May 3, Houston, Texas.

Wan, R. 2011. Production Casing and Cementing. In *Advanced Well Completion Engineering*, Chapter 5, 221-294, Third Edition, Waltham, Massachusetts: Gulf Professional Publishing.

Wang, H. L., Fan, H. B. and Zheng, J. S. 2002. Corrosion inhibition of mild steel in hydrochloric acid solution by a mercapto-triazole compound. *Materials Chemistry and Physics*, Vol. 77, 655–661.

Wang, J. G. 1994. Sulfate Attack on Hardened Cement Paste. Cement and Concrete Research 24 (4): 735-742.

Wang, S., K. George, S. Nešić, 2004. High pressure CO_2 corrosion electrochemistry and the effect of acetic acid, NACE International corrosion conference: Houston, TX.

Woollam, R.; Tummala, K.; Vera, J. and Hernandez, S. 2011. Thermodynamic Prediction of FeCO3/FeS Corrosion Product Films, paper NACE No.076, Houston, Texas.

Zeng, D., Chen, R., Zhang, Z., Shao, L., Li, G., Tian, G.and Shi, T. 2012. Research on Stress Corrosion Sensitivity of C-110 Casing in Wellbore Protection Fluid. Energy Procedia 16: 816-821.

Zeng, J., Sun, F., Li, P., Liu, A. and Gao, Y. 2012. Study of Salt-tolerable Latex Cement Slurries. In 22nd International Offshore and Polar Engineering Conference, Greece, June 17 to 22.

Zhang, G.A. and Y.F. Cheng, 2009. Electrochemical corrosion of X65 pipe steel in oil/water emulsion. Corrosion Science, 51(4): p. 901-907.

Zhang, L., Dzombak, D. A., Nakle, D.V., et al. 2013. Characterization of Pozzolan - amended Wellbore Cement exposed to CO_2 and H_2S gas Mixtures under Geologic Carbon Storage Conditions. International Journal of Greenhouse Gas Control, 19: 358-368.

Zhang, Z., Xu, L. and Tang, M. 2011. Effect of Particle Size on Expansive Behavior of MgO-Based Expansive Agent in Cement Paste. Advanced Materials Research 194-196: 1143-1146.

Zhang, Z., Xu, L., Liu, F. and Tang, M. 2012. Effect of Amount on Expansion Property of MgO- type Expansive Agent Used in Cement- based Materials. Advanced Materials Research 391-392: 803-806.

Zhou, Q. and Glasser, F. P. 2001. Thermal stability and decomposition mechanisms of ettringite at <120 °C. Cement and Concrete Research 31: 1333-1339.

Zirrahi, M., Azin, R., Hassanzadeh, H. and Moshfeghian, M., 2012 Mutual solubility of CH_4, CO_2, H_2S, and their mixtures in brine under subsurface disposal conditions. Fluid Phase Equilibria 324 80– 93.

APPENDIX A: EXPERIMENTAL DATABASE

APPENDIX B: GAS SOLUBILITY MODELS

APPENDIX C: NUMERICAL SCHEME FOR DEGRADATION DEPTH MODEL

APPENDIX D: MECHANICAL STRENGTH DEGRADATION MODEL

APPENDIX E: MACKINAWITE STABILITY LIMIT MODELS

APPENDIX F: CORROSION BEHAVIOR OF TUBULARS UNDER SOUR GAS ENVIRONMENT

APPENDIX G: MECHANISTIC CO2-H2S CORROSION MODEL

APPENDIX H: PARAMETERS USED TO PREDICT CORROSION RATE

APPENDIX I: IMPROVED MECHANISTIC CO2-H2S CORROSION MODEL